ERDC/CHL TR-03-12

Coastal and Hydraulics Laboratory

US Army Corps
of Engineers®
Engineer Research and
Development Center

20031112 095

North Jetty Performance and Entrance Navigation Channel Maintenance, Grays Harbor, Washington

Volume I: Main Text

Nicholas C. Kraus and Hiram T. Arden, editors
With contributions by (in alphabetical order)
Hiram T. Arden, Jessica L. Baker, Mark R. Byrnes,
Mary A. Cialone, Julie A. Cohen, Michael H. Davies,
David Hericks, Nicholas C. Kraus, Neil J. McDonald,
Philip D. Osborne, Ty V. Wamsley, and Donald L. Ward

September 2003

Approved for public release; distribution is unlimited.

ERDC/CHL TR-03-12
September 2003

North Jetty Performance and Entrance Navigation Channel Maintenance, Grays Harbor, Washington

Volume I: Main Text

Nicholas C. Kraus and Hiram T. Arden, editors
With contributions by (in alphabetical order)
Hiram T. Arden, Jessica L. Baker, Mark R. Byrnes, Mary A. Cialone, Julie A. Cohen, Michael H. Davies, David Hericks, Nicholas C. Kraus, Neil J. McDonald, Philip D. Osborne, Ty V. Wamsley, and Donald L. Ward

Coastal and Hydraulics Laboratory
U.S. Army Engineer Research and Development Center
3909 Halls Ferry Road
Vicksburg, MS 39180-6199

Final report

Approved for public release; distribution is unlimited

REPRODUCED FROM
BEST AVAILABLE COPY

Prepared for U.S. Army Engineer District, Seattle
P.O. Box 8755, Seattle, WA 98124-3755

ABSTRACT: This report documents a study performed for the U.S. Army Engineer District, Seattle to identify and evaluate feasible methods for reducing annual maintenance dredging in the outer Federal navigation channel at Grays Harbor, WA, by modification of the north jetty. Main interest was in potential reduction of southward sand bypassing the north jetty and preservation of the jetty should the neighboring beach erode. Considerable information and predictive capability were generated concerning the behavior of the Federal navigation channel and adjacent coastal and inlet shorelines. The study was conducted as a coordinated multi-disciplinary approach involving field measurement, physical modeling of the hydrodynamics and potential sediment pathways, geomorphic analysis and sediment budget formulation, and numerical modeling of waves, circulation and sediment transport, including modeling of shoreline change and bypassing.

Numerous alternatives were considered and subjected to a screening process to identify feasible engineering and physically constructible alternatives within broad criteria. Six alternatives passed the screening and were evaluated. The alternatives concerned an innovative submerged spur that would be placed parallel to the shoreline along the north jetty, partial and full rehabilitation of the north jetty, and a combination of these alternatives with structures of different lengths.

The sediment-control alternatives were evaluated relative to the existing condition. The study revealed many wide-area processes controlling sedimentation in and around Grays Harbor. The scale of change in southward-directed bypassing of sediment expected to occur after construction of any of the evaluated alternatives was found to be small compared to the scale of transport at the Grays Harbor entrance from sources originating outside the entrance or by being reworked and redistributed within the entrance. Modification of the north jetty is one of relatively few options for controlling sedimentation in the outer navigation channel; others include channel realignment and modifications to the south jetty.

DISCLAIMER: The contents of this report are not to be used for advertising, publication, or promotional purposes. Citation of trade names does not constitute an official endorsement or approval of the use of such commercial products. All product names and trademarks cited are the property of their respective owners. The findings of this report are not to be construed as an official Department of the Army position unless so designated by other authorized documents.

Contents

Conversion Factors, Non-SI to SI Units of Measurement xxviii

Preface xxix

1—Introduction 1-1

Background 1-1
Purpose of Study 1-4
Study Procedure 1-5
Development of Alternatives 1-6
Units of Measurement 1-7
Contents of Volume II 1-8
References 1-8

2—Grays Harbor and Chehalis River Navigation Project 2-1

Grays Harbor Navigation Project 2-1
Dredging and Disposal 2-4
North Jetty History and Existing Conditions 2-13
Development of Design Optimization for Control of Southward Bypassing 2-21
Jetty Rehabilitation Alternatives (Alts 3A and 3B) 2-22
Spur Alternatives and Combined Alternative (Alts 2A, 2B, and 4) 2-22
References 2-25

3—Inlet and Nearshore Morphodynamics 3-1

Introduction 3-1
Setting 3-2
Sediments 3-3
History and engineering activities 3-10
Sediment-volume changes 3-14
Scope 3-17
Data Sources 3-18
Shoreline position 3-18
Bathymetry 3-19
Shoreline Evolution 3-20
Regional trends 3-21

Seasonal variability 3-28
Shoreline change at Damon Point 3-28
Inlet and Nearshore Morphology 3-32
Shoal and Channel Evolution 3-40
Sediment Transport Pathways 3-51
Sediment Budget 3-58
Summary 3-63
References 3-67

4—Oceanographic Setting, Field Data Collection, and Analysis 4-1

Regional Setting 4-1
Grays Harbor Wave Climate 4-2
Seasonal variability 4-3
Extremal analysis 4-4
Interannual variability and long-term trends 4-8
Wave height and water level anomalies 4-10
Current and Tide 4-10
Ocean circulation 4-12
Tides and inlet circulation 4-17
Seasonal and long-term variability 4-18
Sediment Transport 4-22
Field Measurements of Coastal Processes 4-23
Analysis Methods 4-24
Waves 4-24
Currents 4-25
Suspended sediments 4-26
Sediment grain size 4-26
Bed elevation 4-28
Sediment transport 4-28
Results 4-29
Waves and wave-dominated currents 4-29
Tides and tidal currents 4-37
Mixed wave and tide regimes 4-45
Sediment transport 4-45
Summary 4-50
References 4-52

5—Physical Modeling of North Beach and Jetty 5-1

Introduction 5-1
Facilities and Equipment 5-2
Description of model 5-2
Wave and current generation and data acquisition equipment 5-3
Selection of Storms for Model Runs 5-5
Calibration of Physical Model 5-10
Coal Tracer and Dye Studies 5-10
Coal tracer studies 5-10
Dye studies 5-12
Web cameras 5-12
Description of Alternative Structures in Physical Model 5-13

Alternative 1: Existing conditions 5-13
Alternative 2A: Long rubble mound submerged spur dike 5-13
Alternative 2A': Long rubble mound submerged spur dike at sta 162+50 5-13
Alternative 3B: Full jetty rehabilitation 5-17
Alternative 2A with projected shoreline 5-17
Results and Discussion 5-17
Storms from west-northwest 5-17
Storms from southwest 5-40
Alternative 2A with GENESIS 5-year projected shoreline 5-54
Summary 5-60
References 5-62

6—Longshore Sand Transport and Shoreline Change Modeling 6-1

Model Overview 6-1
Boundary conditions 6-4
Breakwaters in GENESIS-T 6-5
Time-dependent wave transmission coefficient 6-5
Waves 6-8
Representative offshore wave time series 6-8
STWAVE modeling 6-10
Tidal Currents 6-11
Cross-shore Transport Processes 6-12
Littoral feeding 6-12
Rip current transport 6-13
Model Configuration 6-14
Spatial domain 6-14
Additional input parameters 6-15
Model Calibration 6-16
Calibration (1976 to 1985) 6-17
Verification (1985 to 1995) 6-17
Existing condition (Alt 1) 6-18
Longshore Sand Transport 6-20
Results and Sensitivity Analysis 6-22
Spur configuration (Alts 2A and 2B) 6-23
Jetty rehabilitation (Alts 3A and 3B) 6-27
Combination structure (Alt 4) 6-30
Sensitivity analysis 6-31
Discussion 6-35
References 6-37

7—Wave, Circulation, and Sediment Transport Modeling 7-1

Oceanographic Setting of Grays Harbor 7-2
Tides 7-2
Local wind and freshwater inflow 7-2
Tidal Circulation Model 7-5
ADCIRC Mesh Development 7-5
ADCIRC Model Calibration 7-9
Comparison of Measured and Calculated Water Level and Current 7-9

Wave Transformation Model 7-21
Bathymetry grid 7-21
Input wave spectra 7-22
Tide 7-23
Wave Model Validation 7-23
Linkage of Wave and Circulation Models in SMS 7-27
2001 Calibration of Linked Models 7-28
Simulation of Alternatives 7-28
Plan view maps 7-31
Statistical analysis at selected locations 7-46
Time series of velocity components 7-65
Global difference plan view maps 7-65
Westerly waves 7-76
Simulations with 5-Year and 30-Year Shoreline 7-80
Simulation of 5-year shoreline 7-80
Simulation of 30-year shoreline 7-82
Comparison to Physical Model 7-82
Analysis of Predicted Sediment Transport Pathways at Grays Harbor 7-84
Model Description – PSed 7-84
Circulation Patterns and Sediment Pathways 7-86
Grain-size map 7-86
Sediment sources 7-86
Catchment analysis 7-86
Tidal forcing 7-90
Existing Condition 7-90
Sediment mobility maps 7-90
North jetty 7-92
Inner estuary 7-98
Sediment trap analysis 7-98
Evaluation of Alternatives 7-99
Summary 7-103
References 7-110

8—Annualized Circulation and Sediment Bypassing at North Jetty 8-1

Annualized Circulation at North Jetty 8-1
CoastL grid development for north jetty 8-2
Offshore model 8-4
Inshore model 8-4
Inshore simulations 8-5
Development of a representative annual climate 8-10
Simulation of nearshore currents at north jetty 8-10
Simulation of nearshore circulation – existing condition 8-12
Evaluation of alternatives 8-17
Submerged spur (Alts 2A and 2B) 8-17
Jetty rehabilitation (Alts 3A and 3B) 8-28
Combination structure (Alt 4) 8-35
Simulations with 2001 bathymetry 8-35
Simulations with 2004 and 2029 bathymetry 8-35
Annual change in bypassing flow 8-47
Sediment transport potential 8-55

Methodology 8-55
Evaluation of alternatives 8-55
Annual potential transport climate 8-61
Lagrangian transport analysis 8-67
Lagrangian bypassing rate analysis 8-74
Post-project bathymetries 8-77
Review of assumptions 8-78
Summary 8-79
References 8-80

9—Synthesis of Study Results and Conclusions 9-1

Findings of This Study 9-1
Key processes 9-2
Evaluation of alternatives 9-3
Conclusions 9-4
Discussion 9-5

List of Figures

Figure 1-1. Regional location map for Grays Harbor, Washington 1-2

Figure 2-1. Grays Harbor Navigation Channel 2-2

Figure 2-2. Annual maintenance dredging volumes between 1977 and 2002 for Bar Channel, Entrance and Point Chehalis Reaches, South Reach, Crossover Reach, and total for outer reaches 2-7

Figure 2-3. Average annual volume of dredged sediment distributed along each channel reach 2-9

Figure 2-4 Annual sedimentation rates between 1991 and 2001 for Bar Channel, Entrance and Point Chehalis Reaches, South Reach, and Crossover Channel 2-10

Figure 2-5. Location of dredged material disposal areas in and near Grays Harbor entrance 2-11

Figure 2-6. North jetty profile and cross sections based on a 1940 condition survey 2-15

Figure 2-7. North jetty profile showing original bottom profile and crest elevation from a 1953 survey 2-16

Figure 2-8. North jetty profile showing crest elevation between sta 100+00 and 160+00 based on a 1973 survey 2-17

Figure 2-9. Elevation contours developed from aerial topographic and bathymetric multi-beam surveys conducted by USAED, Seattle (1996-2000) 2-19

Figure 2-10. North jetty longitudinal cross section west of sta 150+00 in 2000 2-19

Figure 2-11. North jetty cross sections at sta 140+00, 150+00, and 160+00 based on 1996 condition survey compared with 1975 design cross section 2-20

Figure 2-12. Forecast of reduction in average annual maintenance dredging volume with increase in jetty length from sta 160+00 for 1975 rehabilitation 2-23

Figure 2-13. Annual change in southward bypassing rate and change in annual dredging volume for Alt 3A and Alt 3B 2-24

Figure 3-1. Location diagram illustrating barrier beach trends for outer coast of Washington 3-2

Figure 3-2. Distribution of median grain size for Washington-Oregon continental shelf 3-4

Figure 3-3. Sediment accumulation rates for southwest Washington continental shelf using Pb-210 geochronology 3-5

Figure 3-4. Diagram illustrating surficial geology of shelf deposits within CRLC in relation to surface grab samples 3-6

Figure 3-5. Surface sediment composition on lower beach face 3-7

Figure 3-6. Inner-shelf sand samples offshore Grays Harbor 3-7

Figure 3-7. Sediment samples offshore northwest of Grays Harbor illustrating characteristics of gravel patch 3-8

Figure 3-8. Sediment composition characteristic of inner ebb-shoal deposits; 95 to 100 percent sand and median diameter of about 0.21 mm 3-9

Figure 3-9. Provinces of sand deposition in Grays Harbor 3-10

Figure 3-10. Map prepared by Captain George Vancouver in 1798 3-11

Figure 3-11. Changes in crest elevation along south jetty since 1902 3-14

Figure 3-12. Areas for temporal comparison of sediment volumes 3-16

Figure 3-13. Changes in sediment volume for regions shown in Figure 3-12 combining data from CTH (1967) with that derived by Burch and Sherwood (1992) 3-16

Figure 3-14. Comparison of 1950s shorelines along north beach from USC&GS (July 1950), Seattle District (August 1954), and April 1950 aerial photograph 3-20

Figure 3-15. Shoreline position change prior to jetty construction north and south of Grays Harbor entrance, 1862 to 1898 (Epoch I) 3-21

Figure 3-16. Shoreline position change associated with jetty construction north and south of Grays Harbor entrance, 1898 to 1916 (Epoch II) 3-23

Figure 3-17. Shoreline position change associated with jetty deterioration north and south of Grays Harbor entrance, 1916 to 1942 (Epoch III) 3-23

Figure 3-18. Shoreline position change associated with jetty rehabilitation north and south of Grays Harbor entrance, 1942 to 1965 (Epoch IV) 3-25

Figure 3-19. Shoreline position change associated with second jetty rehabilitation north and south of Grays Harbor entrance, 1965 to 1987 (Epoch V) 3-25

Figure 3-20. Shoreline position change associated with detailed sediment budget developed for Grays Harbor entrance, 1987 to 2001 (Epoch VI) 3-26

Figure 3-21. Cumulative shoreline change north and south of Grays Harbor entrance, 1862 to 2001 3-27

Figure 3-22. Seasonal variability in high-water shoreline position along north beach at Transect D 3-29

Figure 3-23. Evolution of Damon Point sand spit between completion of north jetty in 1916 and reconstruction in 1942, and post-reconstruction shoreline response by 1950 3-31

Figure 3-24. Evolution of Damon Point sand spit between 1950 and 1981 ... 3-31

Figure 3-25. Evolution of Damon Point sand spit, 1981 to 2001 3-32

Figure 3-26. Bathymetric surface morphology for Grays Harbor entrance prior to jetty construction, 1862 and 1894 3-34

Figure 3-27. Bathymetric surface morphology for Grays Harbor entrance half way through construction of south jetty, 1900 3-35

Figure 3-28. Bathymetric surface morphology for Grays Harbor entrance after construction of north and south jetties, 1921 3-36

Figure 3-29. Bathymetric surface morphology for Grays Harbor entrance prior to reconstruction of north and south jetties, 1940 3-37

Figure 3-30. Bathymetric surface morphology for Grays Harbor entrance after reconstruction of north and south jetties, 1954/56 3-38

Figure 3-31. Bathymetric surface morphology for Grays Harbor entrance (1987) after partial rehabilitation of north and south jetties in 1965 and 1976 3-39

Figure 3-32. Most recent bathymetric surface morphology for Grays Harbor entrance (2002) 3-40

Figure 3-33. Cross-section locations for documenting channel and shoal development and movement between 1900 and 2002 3-41

Figure 3-34. Change in bathymetry along Inlet Cross-section 1 from 1900 to 2002 3-42
Figure 3-35. Change in bathymetry along Inlet Cross-section 2 from 1900 to 2002 3-44
Figure 3-36. Change in bathymetry along Inlet Cross-section 3 from 1900 to 2002 3-45
Figure 3-37. Change in bathymetry along Inlet Cross-section 4 from 1900 to 2002 3-47
Figure 3-38. Change in bathymetry along ebb shoal Cross-section 5 from 1900 to 2002 3-48
Figure 3-39. Change in bathymetry along Inlet Cross-section 6 from 1900 to 2002 3-49
Figure 3-40. Change in bathymetry along Inlet Cross-section 7 from 1900 to 2002 3-50
Figure 3-41. Bathymetric change at Grays Harbor entrance, 1862 to 1900 ... 3-52
Figure 3-42. Bathymetric change at Grays Harbor entrance, 1900 to 1921 ... 3-54
Figure 3-43. Bathymetric change at Grays Harbor entrance, 1921 to 1940 ... 3-54
Figure 3-44. Bathymetric change at Grays Harbor entrance, 1940 to 1954/56 3-56
Figure 3-45. Bathymetric change at Grays Harbor entrance, 1900 to 1954/56 3-56
Figure 3-46. Bathymetric change at Grays Harbor entrance, 1954/56 to 1987 3-57
Figure 3-47. Bathymetric change at Grays Harbor entrance, 1987 to 2002 ... 3-57
Figure 3-48. Grays Harbor sediment budget, 1987 to 2002 3-59
Figure 3-49. Cumulative shoreline change within 3,000 ft of north jetty, and associated sand accumulation volume between 1940 and 2002 3-60
Figure 3-50. Sediment deposition at eastern margin of sediment budget region on Sand Island Shoal, 1987 to 2002 3-61
Figure 3-51. Bathymetric change at Grays Harbor entrance, 1954/56 to 2002 3-63
Figure 3-52. Bathymetric change at Grays Harbor entrance, 1954/56 to 1987 3-64
Figure 4-1. Monthly statistics of H_s, T_p, and Dir from 1994-2001 at CDIP buoy 3601 4-5
Figure 4-2. Joint distribution of H_s and T_p for measurements at Grays Harbor CDIP buoy 3601 between January 1994 and December 2001 4-6
Figure 4-3. Wave rose showing percent frequency of occurrence for all waves in 11.25-deg bands 4-6

Figure 4-4. Wave rose showing percent frequency of occurrence for waves greater than 5 m only in 11.25-deg bands 4-7

Figure 4-5. Annual wave statistics of CDIP buoy 3601 wave measurements from 1 January 1985 to 30 November 2001 4-9

Figure 4-6. Annual wave statistics of CDIP buoy 3601 wave measurements from 1 January 1985 to 30 November 2001 4-9

Figure 4-7. Time series of significant wave height at CDIP buoy 3601 and water level anomaly at Toke Point in Willapa Bay; measured and predicted water levels and water level anomaly at Toke Point between 16 October 2001 and 4 January 2002 4-11

Figure 4-8. Water level anomaly at Toke Point as a function of H_s at CDIP buoy 3601 for 20 October to 16 December 2001 4-12

Figure 4-9. Aerial photographs illustrating circulation patterns and suspended sediment transport regime typical of summer upwelling conditions and west-northwest waves 4-13

Figure 4-10. Average speed and direction of monthly winds along Washington/Oregon continental shelf 4-15

Figure 4-11. Currents determined by Corps of Engineers Drogue Studies between 1974-1981 and 1984-1085. 4-19

Figure 4-12. Location of instrument deployment in and near Grays Harbor 4-25

Figure 4-13. Joint occurrence of H_s and DIR measured at Grays Harbor CDIP buoy 3601 for all observations between 1994 and 2001 4-30

Figure 4-14. Time series of h, H_s, and DIR 4-32

Figure 4-15. Time series of U_o, τ_{cw}, and τ_w at north jetty during spring deployment in May 2001 4-33

Figure 4-16. Time series of current vectors during storm of 10-27 to 11-03 1999, in inlet entrance ebb shoal and h and H_s at sta 1 and 2 inlet entrance stations 4-35

Figure 4-17. Nearshore measurements during spring 2001 deployment on north beach 4-36

Figure 4-18. Time series of direction of wave approach (α_w) measured at Grays Harbor CDIP buoy 3601 and current direction (α_c) measured at sta OS 4 in May 2001 4-37

Figure 4-19. Near-bed (ADVO) and depth-averaged (ADP) tidal current ellipses (12-14 September 1999) 4-38

Figure 4-20. Compass plots of average peak flood and average peak ebb velocity vectors 4-40

Figure 4-21. View looking south of current speed and direction during 12 May 2001 flood 4-40

Figure 4-22. Depth-averaged current vectors along ADP transects on 12 May 2001 between 2126 and 2208 UTC 4-41
Figure 4-23. Depth-averaged current vectors along ADP transects on 18-20 September 2001 representing peak flood currents during a spring tide 4-42
Figure 4-24. Depth-averaged current vectors along ADP transects on 18-20 September 2001 representing peak ebb currents during a spring tide 4-43
Figure 4-25. View looking west of current speed and direction profiles along ADP transect C1 between Westport and Damon Point on 18 September 2001during ebb tide 4-44
Figure 4-26. Time series of current vectors h and H_s from 29 March 2002 to 2 May 2002 on Damon Point and H_s measured at CDIP buoy 3601 4-46
Figure 4-27. Measured near-bed concentration, C, and wave Shields parameter, θ_w 4-47
Figure 4-28. Comparison between at-a-point measurements of suspended sediment flux due to current with predicted sediment flux at same elevation using van Rijn formula at sta OS 5 4-48
Figure 4-29. Flux vectors computed using van Rijn formula and integrated over a 45-day period from mid-October to end of November 1999 4-49
Figure 4-30. Cumulative fluxes computed using at-a-point measurements, van Rijn and Bailard algorithms at sta OS 5 and OS 6 near north jetty – Ocean Shores, during May 2001 4-50
Figure 5-1. Area of prototype reproduced in physical model 5-2
Figure 5-2. Basin layout for physical model 5-4
Figure 5-3. Wave gauge and ADV arrangement for waves from west-northwest 5-6
Figure 5-4. Wave gauge and ADV arrangement for waves from southwest 5-7
Figure 5-5. Frequency of occurrence of incident waves by height and direction 5-8
Figure 5-6. Incident direction for storms with significant wave heights greater than or equal to 3 m 5-9
Figure 5-7. Layout of coal tracer lines at start of a run 5-12
Figure 5-8. Physical model layout of Alt 1 5-14
Figure 5-9. Physical model layout of Alt 2A 5-15
Figure 5-10. Physical model layout of Alt 2A' 5-16
Figure 5-11. Physical model layout of Alt 3B 5-18

Figure 5-12 Physical model layout of Alt 2A with GENESIS 5-year projected shoreline 5-19

Figure 5-13. Longshore current with Alt 2A and 5-m, 13-sec waves from west-northwest at mhw 5-20

Figure 5-14. Dye placed shore-parallel north of jetty 5-20

Figure 5-15. Rip current carrying dye seaward 5-21

Figure 5-16. At seaward edge of rip current, dye is carried back towards jetty 5-21

Figure 5-17. Near jetty, dye is carried shoreward completing gyre 5-22

Figure 5-18. Complete counter-clockwise gyre and longshore current north of gyre 5-22

Figure 5-19. Rip current with 2-m, 9-sec waves from west-northwest at mtl with full flood current 5-24

Figure 5-20. Rip current with 3-m, 13-sec waves from west-northwest at mtl with full flood current 5-24

Figure 5-21. Rip current with 5-m, 13-sec waves from west-northwest at mtl with full flood current 5-25

Figure 5-22. Coal patterns of shoreward transport north of gyre, counter-clockwise circulation in gyre, and some coal carried across jetty remnants 5-25

Figure 5-23. Coal tracer patterns from mild storm waves at mllw 5-26

Figure 5-24. Difference in wave heights between Alt 2A and Alt 1 as a percentage of Alt 1 for waves from west-northwest at mllw for wave heights of 2-m, 9-sec; 3-m, 13-sec; and 5-m, 13-sec combined 5-36

Figure 5-25. Difference in wave heights between Alt 2A and Alt 1 as a percentage of Alt 1 for waves from west-northwest at mtl for wave heights of 2 m, 9 sec; 3 m, 13 sec; and 5 m, 13 sec combined 5-37

Figure 5-26. Difference in wave heights between Alt 2A and Alt 1 as a percentage of Alt 1 for waves from west-northwest at mhw for wave heights of 2 m, 9 sec; 3 m, 13 sec; and 5 m, 13 sec combined 5-38

Figure 5-27. Change in average velocity magnitude with Alt 2A relative to Alt 1 5-40

Figure 5-28. Initial placement of dye lines for a run with 3-m, 12-sec waves from southwest at mllw 5-41

Figure 5-29. Dye pattern with 3-m, 12-sec waves from southwest at mllw taken 2 min, 10 sec (prototype) after Figure 5-28 5-41

Figure 5-30. Dye pattern with 3-m, 12-sec waves from southwest at mllw taken 8 min, 40 sec (prototype) after Figure 5-28 5-42

Figure 5-31. Dye pattern with 3-m, 12-sec waves from southwest at mllw taken 13 min (prototype) after Figure 5-28 5-42

Figure 5-32. Initial placement of dye for a run with 3-m, 12-sec waves from southwest at mtl with full flood current 5-44

Figure 5-33. Dye pattern with 3-m, 12-sec waves from southwest at mtl with full flood current taken 8 min 40 sec (prototype) after Figure 5-32 5-44

Figure 5-34. Difference in wave heights between Alt 2A and Alt 1 as a percentage of Alt 1 for waves from southwest at mllw for wave heights of 2 m, 9 sec; 3 m, 12 sec; and 6 m, 16 sec combined 5-48

Figure 5-35. Difference in wave heights between Alt 2A and Alt 1 as a percentage of Alt 1 for waves from southwest at mtl for wave heights of 2 m, 9 sec; 3 m, 12 sec; and 6 m, 16 sec combined .. 5-49

Figure 5-36. Difference in wave heights between Alt 2A and Alt 1 as a percentage of Alt 1 for waves from southwest at mhw for wave heights of 2 m, 9 sec; 3 m, 12 sec; and 6 m, 16 sec combined 5-50

Figure 5-37. Difference in wave heights between Alt 3B and Alt 1 as a percentage of Alt 1 for waves from southwest at mllw for wave heights of 2 m, 9 sec; 3 m, 12 sec; 6 m, 16 sec combined 5-51

Figure 5-38. Difference in wave heights between Alt 3B and Alt 1 as a percentage of Alt 1 for waves from southwest at mtl for wave heights of 2 m, 9 sec; 3 m, 12 sec; 6 m, 16 sec combined 5-52

Figure 5-39. Difference in wave heights between Alt 3B and Alt 1 as a percentage of Alt 1 for waves from southwest at mhw for wave heights of 2 m, 9 sec; 3 m, 12 sec; 6 m, 16 sec combined 5-53

Figure 5-40. Velocity differences with Alt 2A relative to Alt 1 for 2-m, 9-sec waves; 3-m, 12-sec waves; and 6-m, 16-sec waves combined 5-55

Figure 5-41. Velocity differences with Alt 3B relative to Alt 1 for 2-m, 9-sec waves; 3-m, 12-sec waves; and 6-m, 16-sec waves combined 5-55

Figure 5-42. Average wave heights shoreward of spur with existing shoreline and 5-year projected shoreline for waves from west-northwest 5-57

Figure 5-43. Average wave heights shoreward of spur with existing shoreline and 5-year projected shoreline for waves from southwest 5-60

Figure 6-1. Notation for wave transmission predictive formulas 6-6

Figure 6-2. Transmission coefficient calculations 6-7

Figure 6-3. Frequency distribution of depth of active sand movement 6-16

Figure 6-4. Measured and predicted 1985 shorelines 6-18

Figure 6-5. Measured and predicted 1995 shorelines 6-19

Figure 6-6. Existing condition 5-year predicted shorelines for various onshore feeding rates 6-19
Figure 6-7. Net longshore sand transport 6-20
Figure 6-8. Southbound longshore sand transport 6-22
Figure 6-9. Short-term change in shoreline position relative to Alt 1 6-24
Figure 6-10. Net longshore sand transport 6-24
Figure 6-11. Short-term percent change in south-directed transport relative to Alt 1 6-25
Figure 6-12. Short-term percent change in south-directed transport relative to Alt 1 for K_1 value equal to 0.11 6-26
Figure 6-13. Long-term change in shoreline position relative to Alt 1 6-27
Figure 6-14. Short-term change in shoreline position relative to Alt 1 6-28
Figure 6-15. Long-term change in shoreline position relative to Alt 1 6-29
Figure 6-16. Short-term percent change in south-directed transport relative to Alt 1 6-29
Figure 6-17. Short- and long-term changes in shoreline position for Alt 4 relative to Alt 1 6-30
Figure 6-18. Short-term percent change in south-directed longshore transport for Alt 4 relative to Alt 1 for different values of K_1 6-31
Figure 6-19. Change in shoreline position for Alt 2A relative to Alt 1 for various wave cases 6-32
Figure 6-20. Change in shoreline position for Alt 2B relative to Alt 1 for various wave cases 6-33
Figure 6-21. Change in shoreline position for Alt 3B relative to Alt 1 for various wave cases 6-34
Figure 6-22. Change in shoreline position for Alt 4 relative to Alt 1 for various wave cases 6-35
Figure 6-23. Schematic of sediment pathways and transport volumes 6-36
Figure 7-1. Mean daily stream flow for Chehalis River, WA 7-4
Figure 7-2. ADCIRC grid for Grays Harbor application 7-6
Figure 7-3. Regional view of ADCIRC grid showing variation in resolution 7-7
Figure 7-4. Detail of ADCIRC grid for Grays Harbor 7-7
Figure 7-5. Grays Harbor Bay bathymetric contours from 1999 data 7-8
Figure 7-6. Grays Harbor entrance bathymetric contours from 1999 data 7-8
Figure 7-7. Water level measurement locations 7-10
Figure 7-8. Current measurement locations 7-10
Figure 7-9. Measured and calculated water level time series at tide sta 1 7-13

Figure 7-10. Measured and calculated water level time series at tide sta 2....7-13
Figure 7-11. Measured and calculated water level time series at tide sta 3....7-14
Figure 7-12. Measured and calculated water level time series at tide sta 4....7-14
Figure 7-13. Measured and calculated current speed at velocity sta 1 for a 15-day period....7-15
Figure 7-14. Measured and calculated current speed at velocity sta 1 for a 5-day period....7-15
Figure 7-15. Measured and calculated current speed at velocity sta 2 for a 15-day period....7-16
Figure 7-16. Measured and calculated current speed at velocity sta 2 for a 5-day period....7-16
Figure 7-17. Measured and calculated current speed at velocity sta 3 for a 15-day period....7-17
Figure 7-18. Measured and calculated current speed at velocity sta 3 for a 5-day period....7-17
Figure 7-19. Measured and calculated current speed at velocity sta 4 for a 15-day period....7-18
Figure 7-20. Measured and calculated current speed at velocity sta 4 for a 5-day period....7-18
Figure 7-21. Measured and calculated current speed at velocity sta 5 for a 15-day period....7-19
Figure 7-22. Measured and calculated current speed at velocity sta 5 for a 5-day period....7-19
Figure 7-23. Measured and calculated current speed at velocity sta 6 for a 15-day period....7-20
Figure 7-24. Measured and calculated current speed at velocity sta 6 for a 5-day period....7-20
Figure 7-25. STWAVE existing condition bathymetry grid....7-22
Figure 7-26. Measured and calculated wave height at sta 0....7-24
Figure 7-27. Measured and calculated wave height at sta 1....7-24
Figure 7-28. Measured and calculated wave height at sta 2....7-25
Figure 7-29. Measured and calculated wave height at sta 3....7-25
Figure 7-30. Measured and calculated wave height at sta 4....7-26
Figure 7-31. Measured and calculated wave height at sta 5....7-26
Figure 7-32. Measured and calculated wave height at sta 6....7-27
Figure 7-33. Measured and calculated north-south velocity component at sta OS 5....7-29
Figure 7-34. Measured and calculated east-west velocity component at sta OS 5....7-29

Figure 7-35. Measured and calculated north-south velocity component at sta OS 6 7-30
Figure 7-36. Measured and calculated east-west velocity component at sta OS 6 7-30
Figure 7-37. Existing condition bathymetry 7-34
Figure 7-38. Alternative 2A bathymetry 7-34
Figure 7-39. Alternative 2B bathymetry 7-35
Figure 7-40. Alternative 3A bathymetry 7-35
Figure 7-41. Alternative 3B bathymetry 7-36
Figure 7-42. Alternative 4A bathymetry 7-36
Figure 7-43. ADCIRC grid node locations for statistical analysis 7-37
Figure 7-44. Run 104 (west-northwest, spring tide), inlet view of flood tide 7-38
Figure 7-45. Run 104 (west-northwest, spring tide), north jetty view of flood tide 7-38
Figure 7-46. Run 104 (west-northwest, spring tide), inlet view of ebb tide ... 7-39
Figure 7-47. Run 104 (west-northwest, spring tide), north jetty view of ebb tide 7-39
Figure 7-48. Run 105 (west-southwest, spring tide), inlet view of flood tide 7-40
Figure 7-49. Run 105 (west-southwest, spring tide), north jetty view of flood tide 7-40
Figure 7-50. Run 105 (west-southwest, spring tide), inlet view of ebb tide ... 7-41
Figure 7-51. Run 105 (west-southwest, spring tide), north jetty view of ebb tide 7-41
Figure 7-52. Run 106 (west-northwest, neap tide), inlet view of flood tide ... 7-42
Figure 7-53. Run 106 (west-northwest, neap tide), north jetty view of flood tide 7-42
Figure 7-54. Run 106 (west-northwest, neap tide), inlet view of ebb tide 7-43
Figure 7-55. Run 106 (west-northwest, neap tide), north jetty view of ebb tide 7-43
Figure 7-56. Run 107 (west-southwest, neap tide), inlet view of flood tide ... 7-44
Figure 7-57. Run 107 (west-southwest, neap tide), north jetty view of flood tide 7-44
Figure 7-58. Run 107 (west-southwest, neap tide), inlet view of ebb tide 7-45
Figure 7-59. Run 107 (west-southwest, neap tide), north jetty view of ebb tide 7-45
Figure 7-60. Mean currents for Run 104 7-48

Figure 7-61. Mean currents for Run 105 7-48
Figure 7-62. Mean currents for Run 106 7-49
Figure 7-63. Mean currents for Run 107 7-49
Figure 7-64. Mean currents for existing (Run 104) versus Alt 2A (Run 108) 7-50
Figure 7-65. Mean currents for existing (Run 105) versus Alt 2A (Run 109) 7-50
Figure 7-66. Mean currents for existing (Run 106) versus Alt 2A (Run 110) 7-51
Figure 7-67. Mean currents for existing (Run 107) versus Alt 2A (Run 111) 7-51
Figure 7-68. Mean currents for existing (Run 104) versus Alt 2B (Run 112) 7-52
Figure 7-69. Mean currents for existing (Run 105) versus Alt 2B (Run 113) 7-52
Figure 7-70. Mean currents for existing (Run 106) versus Alt 2B (Run 114) 7-53
Figure 7-71. Mean currents for existing (Run 107) versus Alt 2B (Run 115) 7-53
Figure 7-72. Mean currents for existing (Run 104) versus Alt 3A (Run 116) 7-54
Figure 7-73. Mean currents for existing (Run 105) versus Alt 3A (Run 117) 7-54
Figure 7-74. Mean currents for existing (Run 106) versus Alt 3A (Run 118) 7-55
Figure 7-75. Mean currents for existing (Run 107) versus Alt 3A (Run 119) 7-55
Figure 7-76. Mean currents for existing (Run 104) versus Alt 3B (Run 120) 7-56
Figure 7-77. Mean currents for existing (Run 105) versus Alt 3B (Run 121) 7-56
Figure 7-78. Mean currents for existing (Run 106) versus Alt 3B (Run 122) 7-57
Figure 7-79. Mean currents for existing (Run 107) versus Alt 3B (Run 123) 7-57
Figure 7-80. Mean currents for existing (Run 104) versus Alt 4A (Run 124) 7-58
Figure 7-81. Mean currents for existing (Run 105) versus Alt 4A (Run 125) 7-58
Figure 7-82. Mean currents for existing (Run 106) versus Alt 4A (Run 126) 7-59

Figure 7-83. Mean currents for existing (Run 107) versus Alt 4A (Run 127) 7-59
Figure 7-84 Time series of north-south velocity component at node 11421 for spring tide and west-northwest waves 7-66
Figure 7-85. Time series of east-west velocity component at node 11421 for spring tide and west-northwest waves 7-66
Figure 7-86. Time series of north-south velocity component at node 11421 for spring tide and west-southwest waves 7-67
Figure 7-87. Time series of east-west velocity component at node 11421 for spring tide and west-southwest waves 7-67
Figure 7-88. Time series of north-south velocity component at node 11421 for neap tide and west-northwest waves 7-68
Figure 7-89. Time series of east-west velocity component at node 11421 for neap tide and west-northwest waves 7-68
Figure 7-90. Time series of north-south velocity component at node 11421 for neap tide and west-southwest waves 7-69
Figure 7-91. Time series of east-west velocity component at node 11421 for neap tide and west-southwest waves 7-69
Figure 7-92. Difference map Alt 2A – existing (Run 108 – Run 104) for peak flood 7-71
Figure 7-93. Difference map Alt 2A – existing (Run 108 – Run 104) for peak ebb 7-71
Figure 7-94. Difference map Alt 2B – existing (Run 112 – Run 104) for peak flood 7-72
Figure 7-95. Difference map Alt 2B – existing (Run 112 – Run 104) for peak ebb 7-72
Figure 7-96. Difference map Alt 3A – existing (Run 116 – Run 104) for peak flood 7-73
Figure 7-97. Difference map Alt 3A – existing (Run 116 – Run 104) for peak ebb 7-73
Figure 7-98. Difference map Alt 3B – existing (Run 120 – Run 104) for peak flood 7-74
Figure 7-99. Difference map Alt 3B – existing (Run 120 – Run 104) for peak ebb 7-74
Figure 7-100. Difference map Alt 4A – existing (Run 124 – Run 104) for peak flood 7-75
Figure 7-101. Difference map Alt 4A – existing (Run 124 – Run 104) for peak ebb 7-75
Figure 7-102. Run 128 (existing, west, spring tide) north jetty view of flood tide 7-77

Figure 7-103. Run 128 (existing, west, spring tide) north jetty view of ebb tide 7-77
Figure 7-104. Flowchart for PSed calculation 7-85
Figure 7-105. Grain size map for PSed simulations 7-87
Figure 7-106. Point sources releasing sediment within estuary 7-89
Figure 7-107. Catchment areas for sediment trap analysis 7-89
Figure 7-108. Offshore water surface time series, spring tide (Run 104) 7-91
Figure 7-109. Offshore water surface time series, neap tide (Run 106) 7-91
Figure 7-110. Temporally averaged (residual) sediment mobility for 0.3-mm sand (Run 104) 7-93
Figure 7-111. Sediment parcel locations during flood tide for Run 104 superimposed on a contour map of residual mobility 7-93
Figure 7-112. Mean currents for Run 104 7-94
Figure 7-113. Mean current vectors for Run 104 7-95
Figure 7-114. Final sediment parcel locations for Run 104, sand source at north jetty 7-95
Figure 7-115. Final sediment parcel locations for Run 104, sand source at Damon Point 7-96
Figure 7-116. Final sediment parcel locations for Run 104, sand source at south jetty 7-96
Figure 7-117. Final sediment parcel locations for Run 104, sand source at lower reach 7-97
Figure 7-118. Final sediment parcel locations for Run 104 with sand source at Point Chehalis 7-97
Figure 7-119. Sand pathways at end of 5-day simulation for sources within estuary, Run 104 (spring tide, waves H_s = 5m, T_p = 13 sec from west-northwest) 7-98
Figure 7-120. Comparison of sediment pathways at north jetty for existing condition and Alt 2A for west-northwest waves on a neap tide (Runs 106 and 110, respectively) 7-100
Figure 7-121. Comparison of sediment pathways at north jetty for existing condition and Alt 2B for west-northwest waves on a neap tide (Runs 110 and 114, respectively) 7-101
Figure 7-122. Comparison of sediment pathways at north jetty for existing condition and Alt 3A for west-northwest waves on a neap tide (Runs 106 and 118, respectively) 7-102
Figure 7-123. Comparison of sediment pathways at north jetty for existing condition and Alt 3B for west-northwest waves on a neap tide (Runs 106 and 122, respectively) 7-104

Figure 7-124. Comparison of sediment pathways at north jetty for existing condition and Alt 4 for west-northwest waves on a neap tide (Runs 106 and 126, respectively) 7-105

Figure 7-125. Comparison of sediment pathways at Day 1, 5.5 hr for all project alternatives against existing condition for neap tide with waves from west-northwest 7-106

Figure 8-1. Location of offshore 100-m grid and inshore 20-m grid 8-3

Figure 8-2. Bathymetry of offshore 100-m grid 8-3

Figure 8-3. Computed significant wave height from 100-m offshore model for incident wave condition H_S = 5.0 m, T_p = 13.0 sec, and direction = 280 deg 8-5

Figure 8-4. Existing condition 1999 bathymetry 8-6

Figure 8-5. Alternative 2A 1999 bathymetry 8-6

Figure 8-6. Alternative 2B 1999 bathymetry 8-7

Figure 8-7. Alternative 3A 1999 bathymetry 8-7

Figure 8-8. Alternative 3B 1999 bathymetry 8-7

Figure 8-9. Alternative 4 1999 bathymetry 8-7

Figure 8-10. Alternative 1 2001 bathymetry 8-7

Figure 8-11. Alternative 2A 2001 bathymetry 8-7

Figure 8-12. Alternative 2A 2004 bathymetry 8-8

Figure 8-13. Alternative 2A 2029 bathymetry 8-8

Figure 8-14. Alternative 2B 2004 bathymetry 8-8

Figure 8-15. Alternative 2B 2029 bathymetry 8-8

Figure 8-16. Alternative 3A 2004 bathymetry 8-8

Figure 8-17. Alternative 3A 2029 bathymetry 8-8

Figure 8-18. Alternative 3B 2004 bathymetry 8-9

Figure 8-19. Alternative 3B 2029 bathymetry 8-9

Figure 8-20. Alternative 4 2004 bathymetry 8-9

Figure 8-21. Alternative 4 2029 bathymetry 8-9

Figure 8-22. Wave-induced current pattern on 1999 bathymetry for offshore waves with direction of azimuth 300 deg, H_S of 5 m, and T_p of 13 sec at high water slack 8-13

Figure 8-23. Wave-induced current pattern on 1999 bathymetry for offshore waves with direction of azimuth 210 deg, H_S of 5 m, and T_p of 13 sec at high water slack 8-14

Figure 8-24. Wave-induced current pattern on 1999 bathymetry for offshore waves with direction of azimuth 280 deg, H_S of 2 m, and T_p of 18 sec at low water slack 8-15

Figure 8-25. Wave-induced current pattern on 2001 bathymetry for offshore waves with direction of azimuth 300 deg, H_S of 5 m, and T_p of 13 sec at high water slack 8-16

Figure 8-26. Shore-normal cross-sections from bathymetric grids taken 135 m north of north jetty 8-16

Figure 8-27. Results for waves of H_s = 5 m, T_p = 13 sec from azimuth 300 deg for low water slack: (a) H_s for existing condition, (b) H_s for Alt 2A, and (c) difference in H_s between Alt 2A and existing condition 8-18

Figure 8-28. Results for waves of H_s = 5 m, T_p = 13 sec from azimuth 300 deg for peak ebb 8-19

Figure 8-29. Results for waves of H_s = 5 m, T_p = 13 sec from azimuth 300 deg for peak flood 8-20

Figure 8-30. Results for waves of H_s = 5 m, T_p = 13 sec from azimuth 300 deg for high water slack 8-21

Figure 8-31. Change in current speed between Alt 2A and existing condition for H_s = 5 m, T_p = 13 sec, from azimuth 300 deg for peak flood 8-23

Figure 8-32. Current patterns for H_s = 5 m, T_p = 13 sec from azimuth 300 deg for peak flood 8-24

Figure 8-33. Results for waves of H_s = 5 m, T_p = 13 sec from azimuth 300 deg for peak flood 8-25

Figure 8-34. Current patterns for H_s = 5 m, T_p = 13 sec from azimuth 300 deg for peak flood 8-26

Figure 8-35. Change in current speed between Alt 2B and existing condition for H_s = 5 m, T_p = 13 sec from azimuth 300 deg for peak flood 8-27

Figure 8-36. Change in current speed between Alt 2A and Alt 2B for H_s = 5 m, T_p = 13 sec from azimuth 300 deg for peak flood 8-27

Figure 8-37. Results for waves of H_s = 5 m, T_p = 13 sec from azimuth 300 deg for peak flood: (a) H_s for existing condition, (b) H_s for Alt 2B, and (c) difference in H_s between Alt 2B and existing condition 8-29

Figure 8-38. Current patterns for H_s = 5 m, T_p = 13 sec from azimuth 300 deg for peak flood: (a) existing condition, (b) Alt 3A, and (c) Alt 3A and existing condition 8-30

Figure 8-39. Change in current speed between Alt 3A and existing condition for H_s = 5 m, T_p = 13 sec from azimuth 300 deg for peak flood 8-31

Figure 8-40. Results for waves of H_s = 5 m, T_p = 13 sec from azimuth 300 deg for peak flood: (a) H_s for existing condition, (b) H_s for Alt 3A, and (c) difference in H_s between Alt 3A and existing condition 8-32

Figure 8-41. Current patterns for H_s = 5 m, T_p = 13 sec from azimuth 300 deg for peak flood: (a) existing condition, (b) Alt 3B, and (c) Alt 3B and existing condition 8-33

Figure 8-42. Change in current speed between Alt 3B and existing condition for H_s = 5 m, T_p = 13 sec from azimuth 300 deg for peak flood 8-34

Figure 8-43. Results for waves of H_s = 5 m, T_p = 13 sec from azimuth 300 deg for peak flood: (a) H_s for existing condition, (b) H_s for Alt 3B, and (c) difference in H_s between Alt 3B and existing condition 8-36

Figure 8-44. Current patterns for H_s = 5 m, T_p = 13 sec from azimuth 300 deg for peak flood: (a) existing condition, (b) Alt 4, and (c) Alt 4 and existing condition 8-37

Figure 8-45. Change in current speed between Alt 4 and existing condition for H_s = 5 m, T_p = 13 sec from azimuth 300 deg for peak flood 8-38

Figure 8-46. Results for waves of H_s = 5 m, T_p = 13 sec from azimuth 300 deg for peak flood: (a) H_s for existing condition, (b) H_s for Alt 4, and (c) difference in H_s between Alt 4 and existing condition 8-39

Figure 8-47. Change in current speed between Alt 4 and 2001 conditions for H_s = 5 m, T_p = 13 sec from azimuth 300 deg for peak flood 8-40

Figure 8-48. Current patterns for H_s = 5 m, T_p = 13 sec from azimuth 300 deg for peak flood: (a) 2001 conditions, (b) Alt 2A, and (c) Alt 2A and 2001 conditions 8-41

Figure 8-49. Results for waves of H_s = 5 m, T_p = 13 sec from azimuth 300 deg for peak flood: (a) H_s for 2001 conditions, (b) H_s for Alt 2A, and (c) difference in H_s between Alt 2A and 2001 conditions 8-42

Figure 8-50. Current patterns for H_s = 5 m, T_p = 13 sec from azimuth 300 deg for peak flood: (a) 1999 existing condition, (b) 2004 with Alt 2A, and (c) both 8-43

Figure 8-51. Current patterns for H_s = 5 m, T_p = 13 sec from azimuth 300 deg for peak flood: (a) 1999 existing condition, (b) 2029 with Alt 2A, and (c) both 8-44

Figure 8-52. Current patterns for H_s = 5 m, T_p = 13 sec from azimuth 300 deg for peak flood: (a) 1999 existing condition, (b) 2004 with Alt 3B, and (c) both 8-45

Figure 8-53. Current patterns for H_s = 5 m, T_p = 13 sec from azimuth 300 deg for peak flood: (a) 1999 existing condition, (b) 2029 with Alt 3B, and (c) both 8-46

Figure 8-54. (a) Average current speed for 1999 existing condition, (b) average current speed for 1999 with Alt 2A, and (c) difference in average current speed between Alt 2A and 1999 existing condition 8-48

Figure 8-55. (a) Average current speed for 1999 existing condition, (b) average current speed for 1999 with Alt 2B, and (c) difference in average current speed between Alt 2B and 1999 existing condition 8-50

Figure 8-56. (a) Average current speed for 1999 existing condition, (b) average current speed for 1999 with Alt 3A, and (c) difference in average current speed between Alt 3A and 1999 existing condition 8-51

Figure 8-57. (a) Average current speed for 1999 existing condition, (b) average current speed for 1999 with Alt 3B, and (c) difference in average current speed between Alt 3B and 1999 existing condition 8-52

Figure 8-58. (a) Average current speed for 1999 existing conditions, (b) average current speed for 1999 with Alt 4, and (c) difference in average current speed between Alt 4 and 1999 existing condition 8-53

Figure 8-59. (a) Average current speed for 2001 existing condition, (b) average current speed for 2001 with Alt 2A, and (c) difference in average current speed between Alt 2A and 2001 existing condition 8-54

Figure 8-60. Transport potential results for waves of H_s = 5 m, T_p = 13 sec from azimuth 300 deg for peak flood: (a) q_s for 1999 existing condition, (b) q_s for Alt 2A, and (c) difference in q_s between Alt 2A and 1999 existing condition 8-56

Figure 8-61. Transport potential results for waves of H_s = 5 m, T_p = 13 sec from azimuth 300 deg for peak flood: (a) q_s for 1999 existing condition, (b) q_s for Alt 2B, and (c) difference in q_s between Alt 2B and 1999 existing condition 8-57

Figure 8-62. Transport potential results for waves of H_s = 5 m, T_p = 13 sec from azimuth 300 deg for peak flood: (a) q_s for 1999 existing conditions, (b) q_s for Alt 3A, and (c) difference in q_s between Alt 3A and 1999 existing condition 8-58

Figure 8-63. Transport potential results for waves of H_s = 5 m, T_p = 13 sec from azimuth 300 deg for peak flood: (a) q_s for 1999 existing condition, (b) q_s for Alt 3B, and (c) difference in q_s between Alt 3B and 1999 existing condition 8-59

Figure 8-64. Transport potential results for waves of H_s = 5 m, T_p = 13 sec from azimuth 300 deg for peak flood: (a) q_s for 1999 existing condition, (b) q_s for Alt 4, and (c) difference in q_s between Alt 4 and 1999 existing condition 8-60

Figure 8-65. Expected annual change in q_s: (a) q_s for 1999 existing condition, (b) q_s for Alt 2A, and (c) difference in q_s between Alt 2A and 1999 existing condition 8-62

Figure 8-66. Expected annual change in q_s: (a) q_s for 1999 existing condition, (b) q_s for Alt 2B, and (c) difference in q_s between Alt 2B and 1999 existing condition 8-63

Figure 8-67. Expected annual change in q_s: (a) q_s for 1999 existing condition, (b) q_s for Alt 3A, and (c) difference in q_s between Alt 3A and 1999 existing condition 8-64

Figure 8-68. Expected annual change in q_s: (a) q_s for 1999 existing condition, (b) q_s for Alt 3B, and (c) difference in q_s between Alt 3B and 1999 existing condition 8-65

Figure 8-69. Expected annual change in q_s: (a) q_s for 1999 existing condition, (b) q_s for Alt 4, and (c) difference in q_s between Alt 4 and 1999 existing condition 8-66

Figure 8-70. Expected annual change in q_s: (a) q_s for 2001 existing condition, (b) q_s for Alt 2A, and (c) difference in q_s between Alt 2A and 2001 existing condition 8-68

Figure 8-71. Sediment source locations for Lagrangian modeling 8-70

Figure 8-72. Lagrangian sediment parcel paths for H_s = 5 m, T_p = 13 sec from Az 300 deg for peak flood, existing condition, 1999 bathymetry 8-71

Figure 8-73. Lagrangian sediment parcel paths for H_s = 5 m, T_p = 13 sec from Az 300 deg for peak flood, Alt 2A, 1999 bathymetry 8-71

Figure 8-74. Lagrangian sediment parcel paths for H_s = 5 m, T_p = 13 sec from Az 300 deg for peak flood, Alt 2B, 1999 bathymetry 8-72

Figure 8-75. Lagrangian sediment parcel paths for H_s = 5 m, T_p = 13 sec from Az 300 deg for peak flood, Alt 3A, 1999 bathymetry 8-72

Figure 8-76. Lagrangian sediment parcel paths for H_s = 5 m, T_p = 13 sec from Az 300 deg for peak flood, Alt 3B, 1999 bathymetry 8-73

Figure 8-77. Lagrangian sediment parcels for H_s = 5 m, T_p = 13 sec from Az 300 deg for peak flood, Alt 4, 1999 bathymetry 8-73

Figure 8-78. Example of time-averaged trap collection rate 8-74

List of Tables

Table 1-1. Alternatives Evaluated 1-7

Table 2-1. Summary of Tidal Datum Planes for Grays Harbor, Washington 2-3

Table 2-2. Grays Harbor Navigation Channel Dimensions 2-4

Table 2-3. 1991-2001 Annual Maintenance Dredging Volumes and Decadal Statistics by Reach 2-8

Table 2-4. Disposal Site Annual Volumes and Sources 1991-2002 2-12

Table 2-5. History of North Jetty 2-13
Table 2-6. Estimated Average Annual Dredging Volumes for Various Jetty Rehabilitation Alternatives for 1975 Rehabilitation 2-23
Table 2-7. Extrapolated Changes in Dredging Volumes for Each Alternative 2-24
Table 3-1. Construction and Rehabilitation History, Grays Harbor, Washington 3-12
Table 3-2. Epoch Delineation for Shoreline and Bathymetric Change Analysis at Grays Harbor, Washington 3-18
Table 3-3. Volume Change at Grays Harbor Entrance, 1987 to 2002 3-62
Table 3-4. Volume Change at Grays Harbor Entrance, 1954/56 to 2002 3-64
Table 3-5. Summary of Morphologic Changes by Epoch 3-66
Table 4-1. Wave Buoy Site Characteristics 4-3
Table 4-2. Extreme Significant Wave Height Analysis 4-7
Table 4-3. Grain Size Statistics 4-27
Table 4-4. Summary Statistics of Descriptive Wave Parameters 4-30
Table 4-5. Percentage of Time τ_c Exceeded During Deployment 4-34
Table 5-1. Froude Scaling Relationships 5-5
Table 5-2. Storm Wave Data from CDIP Buoy 5-8
Table 5-3. Wave Heights and Periods in Physical Model Experiments 5-9
Table 6-1. Selection of Representative Wave Time Series 6-9
Table 6-2. Wave Band Limits 6-11
Table 6-3. Summary of Model Input 6-17
Table 6-4. Incident Wave Cases for Sensitivity Analysis 6-31
Table 7-1. Tidal Constituent Amplitudes, at Aberdeen, Toke Point, and Neah Bay 7-3
Table 7-2. Tidal Datums for Willapa Tide Gauges 7-4
Table 7-3. Wave Model Validation for Tide Stations 1 Through 4 7-12
Table 7-4. Current Model Validation for Velocity Stations 1 Through 6 7-12
Table 7-5. Values of *nn* Defining Representative Spectra 7-23
Table 7-6. Steering Module Simulations 7-32
Table 7-7. Mean Currents at Select Node Locations 7-60
Table 7-8. Difference in Current Magnitude Between Alternatives and Existing Condition 7-62
Table 7-9. Mean Currents for Westerly Waves and Difference in Mean Currents Between Alternatives and Existing Condition 7-79

Table 7-10. Endpoints of Line Sources of Sediment for PSed Analysis of Pathways 7-87
Table 7-11. Point Sources of Sediment for PSed Analysis of Pathways 7-88
Table 7-12. ADCIRC/STWAVE Runs Input to PSed Analysis 7-92
Table 7-13. Sediment Trap Results for Simulations with Run 104 Hydrodynamics 7-99
Table 7-14. Sediment Trap Results for a Point Source at North Jetty 7-107
Table 7-15. Sediment Trap Results for a Line Source North of North Jetty 7-107
Table 8-1. Hydrodynamic Conditions for Offshore CoastL Model Simulations 8-4
Table 8-2. Bathymetric Configurations Studied with Inshore CoastL Model 8-6
Table 8-3. Frequency of Occurrence of Selected Wave Conditions from CDIP Measurements (1994-2002) 8-11
Table 8-4. Hydrodynamic Conditions for Inshore CoastL Model Simulations 8-11
Table 8-5. Number of Simulations with Inshore CoastL Model 8-12
Table 8-6. Total Annual Change in Sediment Transport Potential to North of Jetty 8-67
Table 8-7. Change in Bypassing Rate for Southward Transport Conditions 8-75
Table 8-8. Change in Bypassing Expressed as Percentage of Total Bypassing, 1999 Bathymetry 8-76
Table 8-9. Change in Bypassing Expressed as Percentage of Total Bypassing, 2001 Bathymetry 8-77
Table 8-10. Change in Bypassing Expressed as Percentage of Total Bypassing, 2004 Bathymetry 8-77
Table 8-11. Change in Bypassing Expressed as Percentage of Total Bypassing, 2029 Bathymetry 8-78
Table 9-1. Predicted Changes in Key Performance Criteria Relative to Existing Conditions 9-6

Conversion Factors, Non-SI to SI Units of Measurement

Non-SI units of measurement used in this report can be converted to SI units as follows:

Multiply	By	To Obtain
acres	4,046.873	square meters
cubic yards	0.7645549	cubic meters
feet	0.3048	meters
inches	2.54	centimeters
miles (U.S. statute)	1.609347	kilometers
pounds (2,000 pound, mass)	4.5359×10^2	grams
tons	907.1847	kilograms
square miles	2,589,998	square meters

Preface

This report describes a multidisciplinary study of the sediment retention and bypassing functioning of the north jetty at Grays Harbor, WA, and its relation to sediment shoaling in the federally authorized deep-draft navigation channel at Grays Harbor. The report consists of two volumes. Volume I contains the main text, references, and conclusions of the study. Volume II contains eight appendices providing further information in text, figures, photographs, and tables.

The study was conducted for the U.S. Army Engineer District, Seattle (NWS) by the U.S. Army Engineer Research and Development Center (ERDC), Coastal and Hydraulics Laboratory (CHL), Vicksburg, MS. Mr. Hiram T. Arden was the NWS project manager for this study, and Ms. Aimee T. Kinney, and Messrs. George A. Hart, Eric E. Nelson, and Robert M. Parry, provided NWS technical assistance and review of this report.

The ERDC study team was under the technical direction of Dr. Nicholas C. Kraus, Senior Scientists Group, CHL. Contributors to this report are identified on the first page of each chapter. Contributors were Mr. Arden, NWS, and Dr. Kraus, CHL, for engineering and dredging; Ms. Jessica L. Baker and Dr. Mark R. Byrnes, Applied Coastal Research and Engineering, Inc., Mashpee, MA, for morphologic analysis; Ms. Mary A. Cialone, Coastal Processes Branch (CPB), CHL, for wave and circulation numerical modeling; Ms. Julie A. Cohen and Dr. Donald L. Ward, Coastal Harbors and Structures Branch (CHSB), CHL, for physical modeling; Dr. Michael H. Davies, Mr. David Hericks, Dr. Neil J. McDonald, Dr. Philip D. Osborne, and Dr. Vladimir Shepsis, formerly Pacific International (PI) Engineering, PLLC, Edmonds, WA, presently Coast and Harbor Engineering, Inc., for field measurement, literature review, dredged volume analysis, and particle tracking modeling; and Mr. Ty V. Wamsley (CPB) for numerical modeling of shoreline change. Dr. Osborne was the project coordinator at PI Engineering. Mr. Terry Larson, captain of the vessel *Tricia Rae*, and Mr. Dave Mullins, Mullins Guide Service, provided support of field data collection. U.S. Coast Guard Station Astoria provided helicopter pilots and crews to assist with instrument deployment and recovery.

Dr. Kraus and Mr. Arden were the report technical editors. Mr. Dennis G. Markle, Chief, CHSB, assisted Dr. Kraus in administrative aspects of the study. Ms. J. Holley Messing, Coastal Engineering Branch, CHL, completed final report word processing and formatting for both volumes. The Information Technology Laboratory (ITL) technical editor was Ms. Linda L. Wheatley.

The study was conducted from October 2000 through December 2002 under the administrative supervision of Mr. Thomas W. Richardson, Director of CHL, and Dr. William D. Martin, Deputy Director, CHL.

At the time of publication of this report, COL James R. Rowan, EN, was Commander and Executive Director of ERDC and Dr. James R. Houston was Director.

1 Introduction[1]

This chapter presents the background of a study performed for the U.S. Army Engineer District, Seattle to identify and evaluate feasible methods for reducing annual maintenance dredging in the outer Federal navigation channel at Grays Harbor, Washington, by modification of the north jetty. Main interest was in potential reduction of southward sand bypassing the north jetty and preservation of the jetty should the neighboring beach erode. Considerable information and predictive capability were generated concerning the behavior of the Federal navigation channel and adjacent coastal and inlet shorelines.

Included in this chapter are an overview of the study site, background to the engineering need, and orientation to the technical chapters, Chapters 2-8, of this report. Conclusions are given in Chapter 9. This report is divided into two volumes. Volume I contains the main narrative text of the study in nine chapters, and Volume II consists of eight appendices for further and more detailed information and documentation of procedures and results described in Volume I.

Background

The entrance to Grays Harbor is approximately 72 km north of the Columbia River entrance and 177 km south of the Strait of Juan de Fuca (Figure 1-1). Grays Harbor is a large estuary and possesses one of the greatest tidal prisms in the United States at approximately 5.7×10^8 cu m (Jarrett 1976) owing to the large bay area (236 sq km at mean higher high water to 98 sq km at mean lower low water (mllw)) and relatively large diurnal tidal range of approximately 2.8 m. Pacific Ocean waves incident along the northwest Washington coast produce an annual gross longshore transport rate on the order of 1 million cu m. Comprehensive information about the navigation project and oceanography of the area is contained in Chapter 2 of this report. Chapter 3 presents analysis of morphology change and the regional sediment process; and Chapters 3, 4, 6, 7, and 8 describe various aspects of sediment transport ranging from field measurement and calculation of sediment pathways to calculation and prediction of shoreline change.

[1] Written by Nicholas C. Kraus, Coastal and Hydraulics Laboratory, U.S. Army Engineer Research and Development Center, Vicksburg, MS, and by Hiram T. Arden, U.S. Army Engineer District, Seattle, WA.

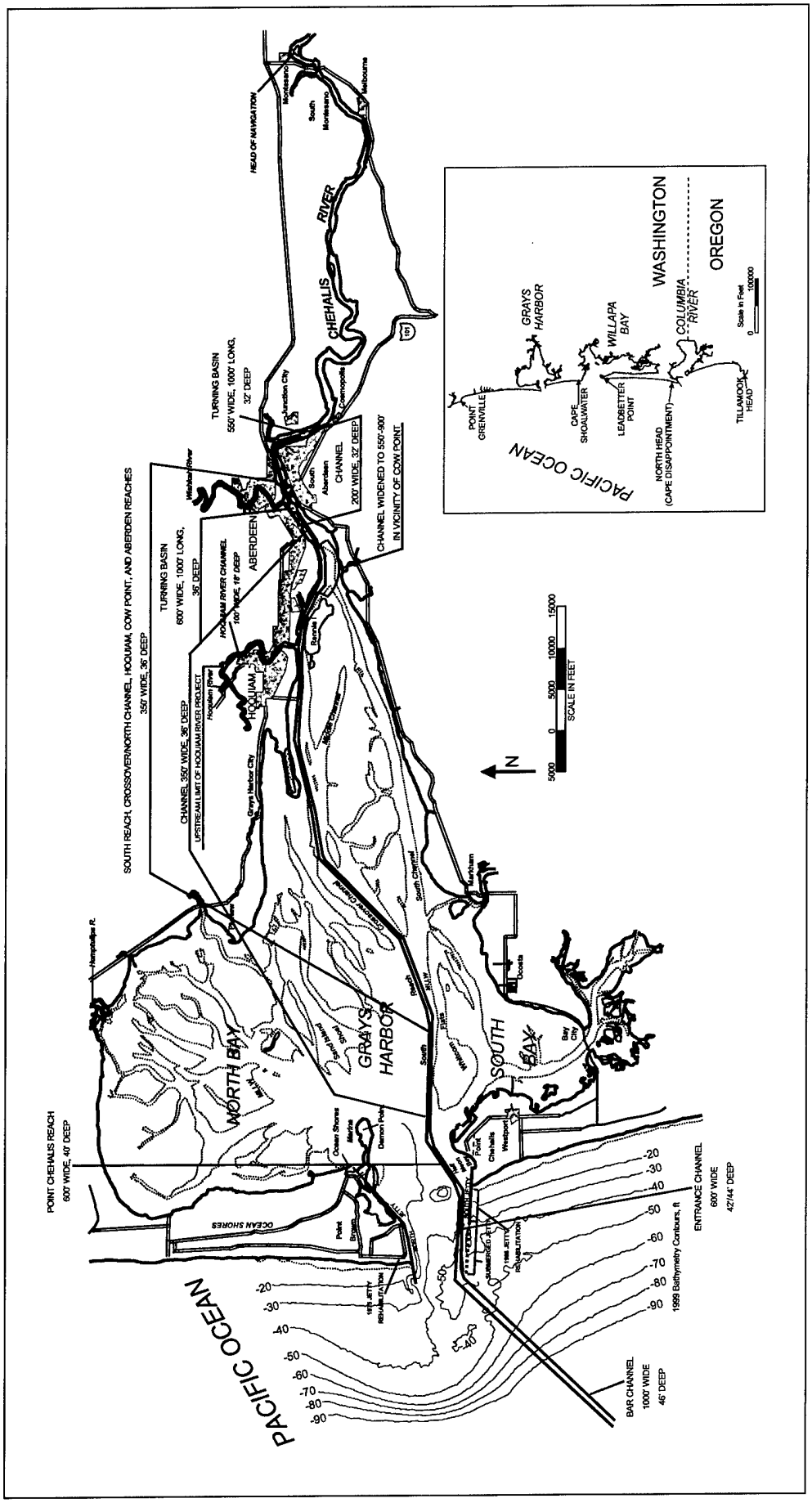

Figure 1-1. Regional location map for Grays Harbor, Washington

The Grays Harbor and Chehalis River Navigation Project is a federally constructed and maintained navigation channel that supports deep-draft shipping through the outer bar, Grays Harbor estuary, and the Chehalis River to Cosmopolis. Authorized depth of the outer harbor navigation channel tapers from 46 ft[1] mllw at the Bar Reach to 36 ft mllw at the South and Crossover Reaches, the channel length is of primary interest in this study. Chapter 2 further describes the navigation channel reaches and stationing. Structure-related sediment and morphologic processes for the south jetty at Grays Harbor were recently reviewed and analyzed by Osborne, Wamsley, and Arden (2003).

Stabilization of the entrance was authorized in 1896. Net longshore transport was believed to be from south to north (subsequently verified – see Chapters 2 and 3), and construction of the south jetty was completed in 1904. The solitary south jetty was found to be inadequate to stabilize the large entrance bar (ebb-tidal shoal), so a north jetty was constructed between 1907 and 1913. The north jetty was designed to block southward movement of littoral drift and aid in maintaining the entrance channel between the jetties (U.S. Army Engineer District, Seattle (USAED, Seattle, 1973). The north and south jetties were constructed to provide a reliable, safe, and low-maintenance navigable channel over the Bar, Entrance, Point Chehalis, South, and Crossover Reaches. Reconstruction of the western submerged sections of the jetties has not been recommended, but the eastern sections have been rehabilitated several times (Chapters 2 and 3).

The Seattle District has formulated a maintenance dredging and disposal program for the Grays Harbor and Chehalis River Navigation Project to reduce dredging volumes and cost. After navigation project deepening in 1990, projections indicated that, 10 years after construction, outer harbor channel dredging requirements would diminish to zero, which has not happened. The expectation was that the tidal prism and reduction of sediment around the pre-jetty ebb shoal would result in a self-scouring channel with little input. Continued dredging at present volumes is expected if no other engineering interventions are taken.

An estimated 1.1 million cu yd of sediment is dredged annually from the outer harbor and will continue to be necessary for the foreseeable future, resulting in continued adverse environmental conditions for Dungeness crab (*Cancer magister*), the most commercially significant crab in Washington State territorial waters. Although the Seattle District has entered into an interagency agreement[2] to mitigate the impact of channel dredging on Dungeness crab, the preferred management approach is to minimize dredging to the most practicable extent. On the other hand, opportunities and demands exist for beneficial uses of sand dredged from the outer entrance channel. For example, some of this dredged material is disposed at Half Moon Bay to preserve the integrity of the barrier spit and south jetty (Osborne, Wamsley, and Arden 2003). Thus, sand management at Grays Harbor must be performed with a wide perspective in

---

[1] Engineering quantities in this report are given in American Customary (non-SI) units of measure. A table for converting non-SI units to SI units of measure is given on page lxx.
[2] U.S. Army Corps of Engineers, Seattle District, and others, September 1998, "Revised crab mitigation strategy agreement," Seattle, WA.

recognition of dredged material as a valuable environmental resource (Arden 2003).

The seaward ends of both the north and south jetties have deteriorated and settled in the century since they were constructed. Although portions of the jetties have been rehabilitated a number of times, the seaward portions have been allowed to sink and now provide minimal obstruction to waves, longshore current, and longshore sand transport. The submerged portions are charted as submerged obstructions. Osborne, Wamsley, and Arden (2003) give the chronology of construction and rehabilitation of the south jetty, and Chapters 2 and 3 of this report document the north jetty construction and rehabilitation.

Previous Seattle District studies (USAED, Seattle, 1973, 1974) concluded that significantly lengthening the north jetty (by 6,000 to 7,800 ft) would reduce annual maintenance dredging in the South and Crossover Reaches by as much as 360,000 to 660,000 cu yd, respectively. The conclusions were based mainly on limited data and a simple empirical relationship between channel dredging volume and jetty length before and after jetty rehabilitation. Modeling was recommended to further quantify and confirm the results. The present study was performed with an array of modern analysis and modeling tools to consider feasible alternatives for reducing shoaling in the outer harbor channel, as recommended in the Seattle District studies.

Purpose of Study

The purpose of this study was to identify and evaluate engineering alternatives for reducing annual maintenance of the Federal navigation channel by reducing the amount of sand bypassing the north jetty. A potential secondary benefit of such a project would be protection of the north jetty from scour during times of beach erosion and shoreline recession.

For an alternative or combination of alternatives to be recommended, the selection must meet several criteria. The alternative must:

a. Reduce southward sediment bypassing of the north jetty to reduce channel dredging. The alternative would provide a significant reduction in costs associated with maintenance of the navigation project features, including the channel and jetties. The reduction in cost would be further evaluated in a cost-benefit analysis not part of the present coastal and inlet physical processes study.

b. Maintain the depth in the inlet channel.

c. Reduce adverse environmental impacts associated with the Grays Harbor Navigation Project.

d. Avoid or minimize additional environmental impacts, such as breaching of Damon Point.

e. Avoid creating or increasing beach erosion adjacent to the north jetty.

f. Ensure that the Seattle District will continue to meet its dredged material maintenance obligations for beach nourishment and infrastructure protection.

g. Comply with all applicable Federal, state, and local government regulations.

Some of these criteria were represented by quantities directly related to the physical processes of waves, current (longshore and cross shore), and sediment transport.

Supplemental project benefits include the possible reduction of erosion and damage from El Niño-induced storms to the beaches and infrastructure located adjacent to the north jetty. An optimal alternative would preferably lend itself to regional sediment management initiatives for beneficial uses of dredged material.

Study Procedure

Similar to the navigation channel reliability study recently performed by the ERDC for the Seattle District (Kraus 2000), the Grays Harbor north jetty study required the expertise of several specialists who participated as a team in developing approaches and procedures, and in conducting the required work. Meetings and briefings were held at the study site and at the Seattle District, as well as at the Coastal and Hydraulics Laboratory (CHL).

The study was developed as a simultaneous multidisciplinary effort conducted in tasks such as engineering analysis; physical modeling; numerical modeling of waves, currents, and sediment transport; and analysis of historical and recent geomorphology changes. The tasks can be summarized with reference to chapters comprised by the report as:

a. Critical and comprehensive review of the literature and engineering activities, including the dredging records, and the relations between maintenance of the outer harbor channel and condition of the beach adjacent to the north jetty (Chapter 2).

b. Analysis of long-term evolution and behavior of inlet morphology, including the ebb-tidal shoal, channels, nearshore, and shoreline, leading to development of historic and existing-condition inlet sediment budgets and quantification of inlet sediment pathways (Chapter 3).

c. Characterization of the oceanographic and nearshore setting (waves, wind, tide, currents, sediment, and sediment transport) (Chapter 4).

d. Short-term field measurement and associated analysis of the waves, current, and sediment transport at and around the north jetty and in the outer harbor for understanding of the acting processes and for verifying predictive numerical models (Chapter 4).

e. Physical modeling of the waves and circulation along the beach north of the north jetty, together with inferences of wide-area currents and sediment transport through dye and tracer studies of the various engineering alternatives considered (Chapter 5).

f. Numerical modeling of longshore sand transport, sand bypassing at the north jetty, and shoreline change in response to the various engineering alternatives considered (Chapter 6).

g. Numerical modeling of nearshore wave transformation around the entrance and propagation through the harbor entrance; numerical modeling of water circulation under combined forcing of tide, waves, and wind, including local changes in waves and circulation in response to the various engineering alternatives considered; and sediment transport pathways as driven by the calculated circulation (Chapter 7).

h. Numerical modeling of sediment pathways through a Lagrangian particle tracking approach in response to the various engineering alternatives considered (Chapter 8).

i. Integrated summary with respect to the project study purpose and criteria as stated in the previous section (Chapter 9).

The numerical modeling and geomorphic analysis components of this study benefited greatly from bathymetric data collected in 1999, 2000, and 2001 by the Seattle District's Hydrosurvey Unit, Navigation Section, Operations Division in operation of their survey vessels, including the *Shoalhunter*. Additional technical information on procedures and results is compiled in Volume II of this report.

Several major modeling, measurement, and analysis capabilities were improved in support of this complex study. A helicopter-based instrument deployment was successful in placing instruments near to the jetty under the typically rough wave conditions and strong currents (Osborne, Hericks, and Kraus 2002). A coupled wave-current circulation model was developed and implemented to compute the total circulation at the entrance (Cialone and Kraus 2001; Cialone et al. 2003). Calculation procedures for wave transmission (Wamsley and Ahrens 2003) over submerged breakwaters were developed, as well as implementation of time-dependent wave transmission in the GENESIS[1] model of shoreline change (Wamsley and Hanson 2002).

Development of Alternatives

Over the course of the first year of the study, numerous alternatives were proposed and subjected to a screening process to identify feasible engineering and physically constructible alternatives within broad criteria. Six alternatives passed the screening and are listed in Table 1-1.

An innovative geotextile construction technique or stone rubble-mound spur alternative was developed based upon the concept of a submerged detached breakwater that would run parallel to the trend of the shore adjacent to the north jetty. A submerged spur is expected to have the favorable properties of (a) reducing the height of waves behind it, thus promoting accumulation of coarser sediment (sand), (b) posing a minimal navigation hazard and maintaining an unobstructed view of the ocean (no aesthetic consequence), (c) having considerably lower construction cost as compared to an emergent structure, and (d) having a maintenance cost lower than an emergent structure.

---

[1] GENESIS simulates shoreline change as produced by differences in the longshore sediment transport rate alongshore that it calculates from obliquely incident waves and boundary conditions (Hanson and Kraus 1989).

Table 1-1
Alternatives Evaluated

Alternative (Alt)	Description	Comments
1	Existing condition (do nothing)	None
2A	Long rubble mound submerged jetty spur	Nominal length of 1,500 ft
2B	Short rubble mound submerged jetty spur	Nominal length of 800 ft
3A	Partial rehabilitation of north jetty	Nominal length of 500 ft
3B	Full rehabilitation of north jetty	Nominal length of 1,200 ft
4	Combination: Short spur (Alt 2B) and partial jetty rehabilitation (Alt 3A)	None

The spur would be placed at a location offshore corresponding to north jetty sta 165+00 and in water depths ranging from approximately 18 to 31 ft mllw. The crest width of the evaluated design is 30 ft, and the depth over the crest is 10 ft mllw. Environmental conditions for such a deeply submerged nearshore structure, with the relatively long period and high waves that prevail along the Pacific southwest coast of Washington, exceeded the empirical foundation of available stability criteria for coastal structures. Therefore, physical model stability tests were conducted, supported by the local communities, with observation by a CHL staff member. A long rubble-mound submerged jetty spur (Alt 2A) and a short jetty spur (Alt 2B) were considered.

Another alternative identified for blocking the southward movement of sediment was to rehabilitate the north jetty. Two lengths of rehabilitation were examined, denoted as Alt 3A (partial rehabilitation) and Alt 3B (full rehabilitation). Jetty rehabilitation has the advantage of fewer regulatory constraints as compared to spur construction. A combination (Alt 4) of a short submerged spur and partial jetty rehabilitation was also evaluated.

This study concerns functional design, which is the evaluation of a concept (alternative) within the acting physical processes to determine if the design will perform as intended. Through comparison of alternatives with the same analysis procedures, both relative and absolute performance can be estimated. Construction costs and procedures were evaluated only to the extent of a rough estimation.

Units of Measurement

In this report, dimensions and quantities originally published in American Customary (non-SI) units in engineering documents and in the general literature are retained. These quantities concern length of structures or channel, depth, dredging volume, and rate of sediment transport. A table of conversion factors from non-SI to SI units is given on page lxx. Oceanographic and meteorologic measurements and calculations (e.g., of waves, water current, and wind speed) are expressed in SI units.

Contents of Volume II

Volume II consolidates information in eight appendices that supplement material contained in the main text of this report (Volume I). Appendix A documents a stability analysis for the submerged spur alternative. Appendix B contains discussion and plots documenting the physical model study of all alternatives examined. Appendix C is a review of the literature of sediment transport in rip currents. Appendix D provides additional data plots and metadata for the field data collection. Appendix F contains additional plots and metadata on vertical datums, as well as an uncertainity analysis for bathymetry volume change calculations. Appendix G describes calculations of longshore sediment transport and shoreline change performed to examine sensitivity of such calculations to variations in cross-shore distribution of the longshore sediment transport rate. Appendix H collects and describes the governing equations of the circulation, wave transformation, and associated sediment transport numerical models applied in this study.

References

Arden, H. T. (2003). "South jetty breach fill at Grays Harbor, Washington: Doing the right thing with dredged material," *Shore & Beach* 71(1), 3-5.

Cialone, M. A., and Kraus, N. C. (2001). "Engineering study of inlet entrance hydrodynamics: Grays Harbor, Washington, USA," *Proceedings Coastal Dynamics '01*, ASCE, 413-422.

Cialone, M. A., Militello, A., Brown, M. E., and Kraus, N. C. (2003). "Coupling of wave and circulation numerical models at Grays Harbor Entrance, Washington, USA," *Proceedings 28th International Coastal Engineering Conference,* World Scientific, 1,279-1,291.

Jarrett, J. T. (1976). "Tidal prism-inlet area relationships." GITI Report 3, U.S. Army Engineer Waterways Experiment Station, Vicksburg, MS.

Kraus, N. C. (Editor). (2000). "Study of navigation channel feasibility, Willapa Bay, Washington," Technical Report ERDC/CHL TR-00-6, Coastal and Hydraulics Laboratory, U.S. Army Engineer Research and Development Center, Vicksburg, MS, 440 p.

Osborne, P. D., Hericks, D. B., and Kraus, N. C. (2002). "Deployment of oceanographic instruments in high energy environments," Technical Note ERDC/CHL CHETN-IV-46, Coastal and Hydraulics Laboratory, U.S. Army Engineer Research and Development Center, Vicksburg, MS. http://chl.wes.army.mil/library/publications/chetn.

Osborne, P. D., Wamsley, T. V., and Arden, H. T. (2003). "South jetty sediment processes study, Grays Harbor, Washington: Evaluation of engineering structures and maintenance measures," Technical Report ERDC/CHL TR-03-4, Coastal and Hydraulics Laboratory, U.S. Army Engineer Research and Development Center, Vicksburg, MS.

U.S. Army Engineer District, Seattle. (1973). "Grays Harbor (Chehalis and Hoquiam Rivers) north jetty rehabilitation report," Seattle, WA, September.

_____. (1974). "Grays Harbor (Chehalis and Hoquiam Rivers) north jetty rehabilitation," Technical Design Memorandum, Seattle, WA, September.

Wamsley, T. V., and Hanson, H. (2002). "Evaluation of proposed submerged jetty spur on shoreline evolution, Grays Harbor, Washington," *Proceedings 28th International Coastal Engineering Conference,* World Scientific, 2,625-2,637.

Wamsley, T. V., and Ahrens, J. (2003). "Computation of wave transmission coefficients at detached breakwaters for shoreline response modeling," *Proceedings Coastal Structures '03*, ASCE, in press.

2 Grays Harbor and Chehalis River Navigation Project[1]

This chapter describes the history and current status of the Grays Harbor and Chehalis River Navigation Project and reviews dredging and disposal activities associated with maintenance dredging and new work. Focus is primarily on the history and status of the north jetty and its relationship to sedimentation occurring in the navigation channel. Relationships between the north jetty length and channel dredging derived from a previous study (USAED, Seattle, 1973) are applied to alternatives developed for this study as a means of preliminary comparing alternatives for optimal design of southward bypassing.

Grays Harbor Navigation Project

The Grays Harbor Navigation Project is a federally constructed and maintained navigation channel that allows deep-draft shipping through the outer bar, Grays Harbor estuary, and the Chehalis River to Cosmopolis. Two jetties that stabilize the harbor entrance are part of the existing project. The entrance to Grays Harbor is approximately 45 miles north of the Columbia River entrance and 110 miles south of the Strait of Juan de Fuca (Figure 1-1). Grays Harbor is one of the largest estuaries in the continental United States. The length of the estuary is approximately 15 miles (Figure 2-1), with a width of approximately 11 miles (at the widest section), and water surface area ranges from 91 square miles at mean higher high water (mhhw) to 38 square miles at mean lower low water (mllw). Tidal datum planes for Grays Harbor are summarized in Table 2-1.

The original project, authorized by Congress through the River and Harbor Act on 3 June 1896, provided for the construction of the south jetty with a top elevation of +8 ft mllw and a length of 13,734 ft. The south jetty was completed in 1904. At the time of project development, the predominant littoral drift was thought to be from south to north (USAED, Seattle, 1989), and the jetty was

[1] Written by Dr. Philip Osborne, Pacific International (PI) Engineering, PLLC, Edmonds, WA, and Hiram Arden, U.S. Army Engineer District, Seattle, WA. Dr. Vladimir Shepsis, formerly of PI Engineering, PLLC, contributed to an earlier draft of the chapter.

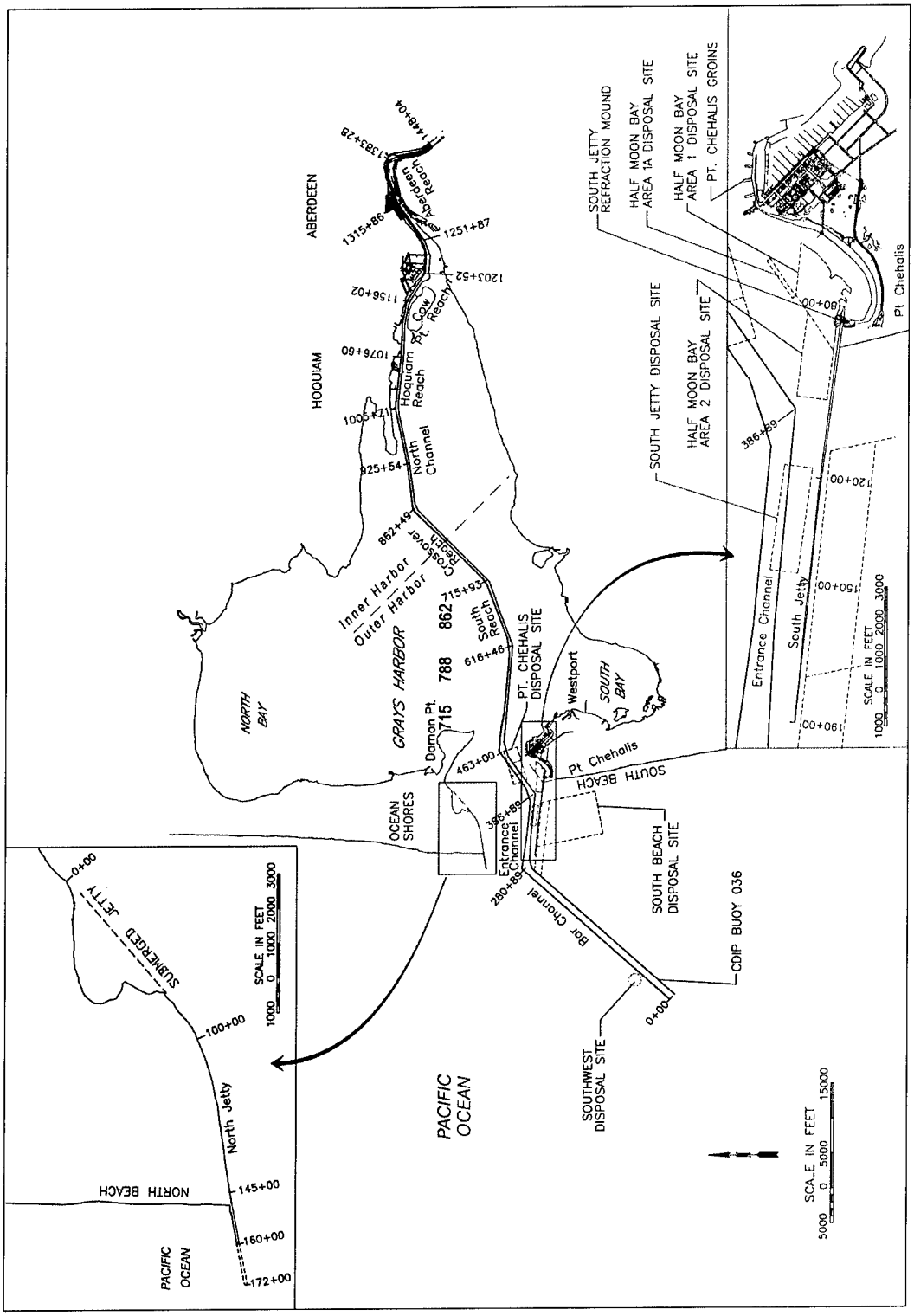

Figure 2-1. Grays Harbor Navigation Channel (modified from USAED, Seattle, 1989)

Table 2-1
Summary of Tidal Datum Planes for Grays Harbor, Washington

Tidal Datum Plane	Elevations in m (ft) Referred to mllw		
	Westport (NGS PID # SD0042)	Point Chehalis[2]	Aberdeen[2]
Highest Tide (Observed 06/20/1982)	3.35 (11.0)	4.27[3]	4.54[3]
Mean Higher High Water (mhhw)	2.79 (9.16)	2.74	3.08
Mean High Water (mhw)	2.57 (8.43)	2.50	2.87
Mean (Half) Tide Level (mtl)	1.50 (4.91)	1.46	1.66
National Geodetic Vertical Datum 1929 (NGVD 29)[1]	1.46 (4.78)		
North American Vertical Datum 1988 (NAVD 88)[1]	0.46 (1.51)		
Mean Low Water (mlw)	0.42 (1.39)	0.43	0.46
Mean Lower Low Water (mllw)	0.00 (0.00)	0.00	0.00
Lowest Tide (Observed 06/23/1982)	-0.66 (-2.18)	-1.07[3]	-0.88[3]

Notes:
[1] The NAVD 88 and the NGVD 29 elevations related to mllw were computed from Bench Mark 944 1102 TIDAL 2 1952, at the station; the elevation of mllw to NAVD 88 is -1.51 ft.
[2] USAED, Seattle (1989).
[3] Estimated.

constructed with the expectation that it would maintain the bar channel in a stable position. Soon after the south jetty was constructed, however, it became clear that the south jetty alone would not stabilize a deep channel. Therefore, construction of the north jetty was authorized through the River and Harbor Act of 2 March 1907, and the jetty was constructed between 1907 and 1913 to mid-tide elevation along a project length of 16,000 ft. The north jetty was designed to block movement of littoral drift southward into the inlet, prevent northward migration of the inlet throat, and aid in maintaining the entrance channel between the jetties (Black 1916; USAED, Seattle, 1973).

The jetties were expected to control northward and southward sediment transport toward the channel, constrain the ebb flow, and scour greater depths across the ebb shoal (USAED, Seattle, 1974). Prior to jetty construction, the shoal at the harbor entrance obstructed navigation and was a hazard for many vessels. The controlling depth on the Outer Bar varied from 12 to 26 ft mllw (Black 1916).

Although the original navigation project did not specify a depth for the channel over the outer bar, it was anticipated that a depth of at least 24 ft mllw would develop (Black 1916). In 1916, the project for the inner harbor and Chehalis River provided for a channel 18 ft deep and 200 ft wide from the bay to Cosmopolis (Board of Engineers for Rivers and Harbors 1934). Since construction of the jetties, the channel has been redesigned several times, increasing channel depth, width, and length. Presently, the navigation channel

is approximately 27 miles long, extending from the seaward end of the Outer Bar to the lower part of the Chehalis River. Figure 2-1 shows a general plan view of the channel. The navigation channel consists of several reaches as described in Table 2-2. Channel alignments, depths, and widths in the table correspond to the latest channel improvement project, completed in 1991 under authorization of Section 202 of the Water Resources Development Act, Public Law 99-662, November 1986.

Table 2-2
Grays Harbor Navigation Channel Dimensions

	Channel Reach	Stations	Length (ft)	Channel Depth (ft)	Channel Width (ft)
Outer	Bar Channel	From 0+00 to 280+89	28,089	46	1,000
	Entrance Channel	280+89 to 292+89	1,200	46	Varies
	Entrance Channel	292+89 to 342+89	5,000	44	600
	Entrance Channel	342+89 to 377+89	3,500	42	600
	Entrance Channel	377+89 to 386+89	900	40	600
	Point Chehalis Reach	386+89 to 463+00	7,611	40	600
	South Reach	463+00 to 715+93	25,293	36	400
Transition	Crossover Channel	715+93 to 862+49	14,656	36	350
Inner	North Channel	862+49 to 1005+71	14,322	36	350
	Hoquiam Reach	1005+71 to 1156+02	15,031	36	350
	Cow Point Reach	1156+02 to 1231+50	7,548	36	350
	Cow Point Reach	1231+50 to 1251+87	2,837	32	Varies
	Aberdeen Reach	1251+87 to 1315+86	6,399	32	200
	Upper S. Aberdeen Reach	1315+86 to 1439+65	12,379	32	300

Note: Dredging of the outer harbor reaches is performed by hopper dredge, while inner harbor reaches are dredged by clamshell.

The design vessel for the 1991 Navigation Channel Improvement Project was a timber carrier with 625 ft length, 100 ft beam, and 37 ft draft. The largest vessel recorded to have called at the Port of Grays Harbor had a dry weight tonnage of 50,250 tons, a 686 ft length, 100 ft beam, and 39.8 ft draft.

Further details of the history of the navigation channel, dredging and disposal practices, and the history, evolution, and existing conditions at the north jetty are provided below. Detailed description of the south jetty history, evolution, and existing conditions may be found in USAED, Seattle (1965, 1973, 1995, and 1997).

Dredging and Disposal

Sediment that shoals the Grays Harbor navigation channel is derived from marine and fluvial sources. Marine sediment, predominantly medium and fine sand, is delivered to Grays Harbor and the navigation channel mainly through longshore sediment drift, transported to the bay by waves, nearshore currents,

and tidal currents through the entrance (Scheidegger and Phipps 1976). Fluvial or river-borne sediment, predominantly silt and clay fractions, in the channel is primarily from the Chehalis River, which discharges at the head of the estuary. A number of small rivers and creeks discharge sediments in the upper and middle estuary. Previous studies (e.g., Beverage and Swecker 1969; Scheidegger and Phipps 1976) indicate that river-borne sediment is deposited mostly in the upper estuary and does not exit Grays Harbor in any significant amount. Sediments dredged from the inner harbor by clamshell and hopper dredges have been placed in the south jetty disposal site, and some of that material exits Grays Harbor by tidal current transport. The same studies determined that marine sediment enters the estuary and disperses as far as 10 to 14 miles upstream, resulting in deposition in all lower channel reaches up to the North Channel.

A previous study (USAED, Seattle, 1973) determined that the north jetty was effective in reducing the southward littoral drift (marine sediment) into the entrance and minimized deposition and maintenance dredging in the navigation channel. It is assumed hereafter that the north jetty can control only the delivery of marine sediment to the navigation channel, whereas it does not control any delivery of river-borne sediment. The outer navigation channel comprises the Bar Channel, Entrance, Point Chehalis, and South Reaches, while the inner channel comprises the North Channel, Hoquiam, Cow Point, and Aberdeen Reaches. According to the sand depositional provinces identified by Scheidegger and Phipps (1976; Chapter 3), Crossover Reach is at the transition between the inner and outer channel.

The earliest records of dredging within Grays Harbor date to 1905, when a 200-ft-wide channel extending 12 miles downstream from Cosmopolis was maintained by dredging to a depth of 18 ft mllw (Scheidegger and Phipps 1976; Washington Department of Ecology [WDOE] 1977). Records indicate that regular maintenance dredging of the Bar and Entrance Channels also occurred between 1916 and 1942. During this period, the average volume of maintenance dredging at the Outer Bar and Entrance Channel was approximately 850,000 cu yd/year, all of which was disposed in deep water (below 60 ft mllw) outside the harbor. Between 1916 and 1927, the bar channel was dredged to a depth of 24 ft mllw and from 1928 the dredging continued to a depth of 36 ft mllw. Following rehabilitation of the north jetty in 1942, maintenance dredging in the Entrance and Bar Channels ceased until 1990.

No data prior to 1961 on maintenance dredging at Crossover and Sand Island Reaches have been found. Between 1961 and 1974, an average of 1,040,000 cu yd/year was dredged from Crossover Reach and Sand Island Reach. Before 1978, the Sand Island Reach extended northeast from the Point Chehalis Reach to the north side of the inlet throat and then east approximately parallel with Sand Island Shoal to connect with Crossover Reach. Realignment of the channel from Sand Island Reach to South Reach was completed in 1978 because the Sand Island Reach area was shoaling while the South Reach area was eroding. Figure 2-2 shows annual maintenance dredging volumes for the outer reaches of the navigation channel and Crossover Reach. Following north jetty rehabilitation in the late 1970s, the annual volumes dredged from Crossover and South Reaches between 1980 and 1989 were 460,000 and 650,000 cu yd/year, respectively.

The most recent channel deepening improvement project was completed between 1990 and 1991. Channel dimensions were achieved as specified in

Table 2-2. As a result of the channel improvement project, maintenance dredging resumed in the Outer Bar and Entrance Channels, and the channels were dredged below existing ambient bottom elevations, creating dredge cuts that capture sediment in transport. Advance maintenance dredging has been required in parts of each reach since 1991 to maintain navigable depths of the channels for the duration of the annual maintenance. Figure 2-2 indicates that approximately 5 million cu yd of sediment were removed from the outer reaches of the navigation channel as part of the project.

Data from maintenance dredging reports and dredging contract documentation for 1991 to 2001 were analyzed to identify trends in sediment distribution along channel reaches. Average annual maintenance dredging volumes and associated 95 percent confidence limits were estimated from dredging records maintained by the Seattle District. The 95 percent confidence limits on the mean annual dredging volume ($\bar{x}$) is calculated as:

$$\bar{x} \pm z_{\alpha/2} \frac{\sigma}{\sqrt{n}} \qquad (2\text{-}1)$$

where σ is the sample standard deviation, n is the number of samples, and $z_{\alpha/2}$ has a value of 1.96. Assuming the dredging volumes are normally distributed, the 95 percent confidence limits of the annual maintenance dredging volume is interpreted as follows: 95 percent of all estimates of channel dredging volume will fall within the confidence limits and 5 percent will not.

The calculated average annual volumes of dredged sediment distributed along the channel length for each of the channel reaches are presented in Figure 2-2. The solid line in the lower part of the figure shows average volumes of maintenance dredging along channel reaches. Volumes were averaged over the reported dredging distances (station limits) for each dredging event reported over the period of record (11 years). Average annual maintenance dredging volumes and associated 95 percent confidence intervals for each channel reach are summarized in Table 2-3 and in Figure 2-3. Dredging volumes for 2002 are also shown in the table for comparison with the decadal statistics.

Dredged volumes may not accurately portray the channel shoaling rates. Annual dredging volumes depend on the availability of government dredges and funding, as well as the volume of sediment in the channel. Therefore, it is difficult to determine trends from the annual dredged volumes over a period of 12 years. Dredged volumes for 1991 to 2002 were converted to average annual sedimentation rates (expressed as a depth of sediment deposited per year) for each channel reach. The results are summarized in Figure 2-4.

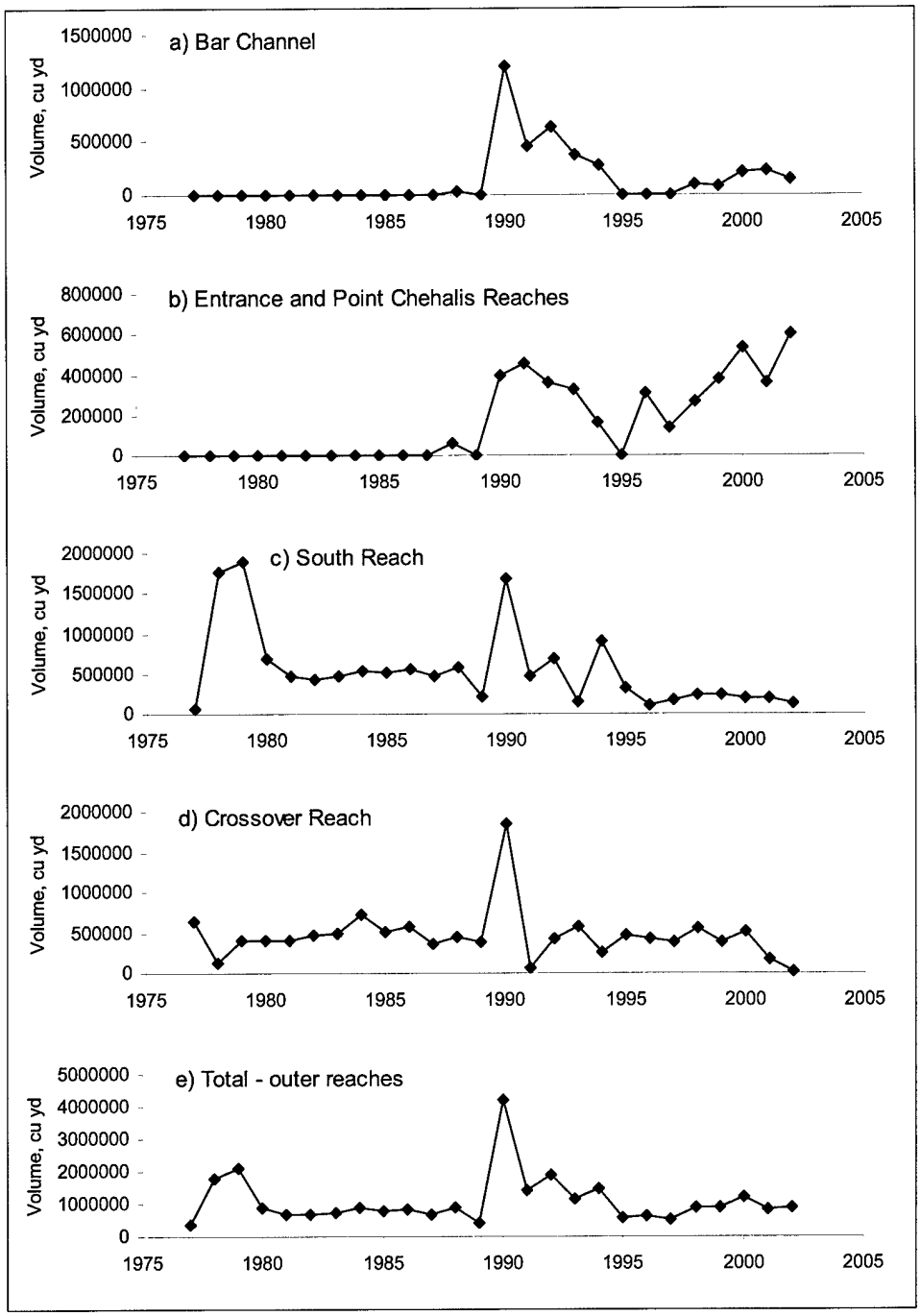

Figure 2-2. Annual maintenance dredging volumes between 1977 and 2002 for (a) Bar Channel, (b) Entrance and Point Chehalis Reaches, (c) South Reach, (d) Crossover Reach, and (e) total for outer reaches

Table 2-3
1991-2001 Annual Maintenance Dredging Volumes* and Decadal Statistics by Reach

Fiscal Year	Bar Channel, cu yd	Entrance and Point Chehalis Reach, cu yd	South Reach, cu yd	Crossover Reach, cu yd	Total, cu yd
1991	452,000	453,000	477,000	88,000	1,470,000
1992	636,000	361,000	683,000	521,000	2,201,000
1993	373,000	324,000	158,000	639,000	1,494,000
1994	277,000	163,000	903,600	364,000	1,707,600
1995	0	0	332,000	469,000	801,000
1996	0	308,000	103,600	425,000	836,600
1997	0	136,000	226,400	456,000	818,400
1998	103,000	266,000	293,000	840,000	1,502,000
1999	76,000	382,000	229,000	390,000	1,077,000
2000	209,000	537,000	231,000	463,000	1,440,000
2001	227,000	359,000	169,000	190,000	945,000
Average annual volume, cu yd/year	214,000	299,000	346,000	440,000	
Upper 95 percent confidence limit, cu yd/year	91,000	209,000	200,000	322,000	
Lower 95 percent confidence limit, cu yd/year	337,000	389,000	492,000	559,000	
FY 2002 actual volumes for comparison, cu yd	144,000	605,000	136,000	22,000	907,000

*Volumes rounded to the nearest thousand.

Maintenance dredging resumed at the Outer Bar, Entrance, and Point Chehalis Reaches as a result of the Navigation Improvement Project in the early 1990s. Shoaling rates in the Bar Channel, Entrance, and Point Chehalis Reaches show similar patterns to the dredging volumes. Following the completion of the Navigation Improvement Project, dredging volumes have remained approximately constant at Crossover Reach and decreased at South Reach. Approximately 350,000 cu yd/year on average, have been dredged from South Reach over the last decade. In 1994, approximately 900,000 cu yd was removed from South Reach, a significantly larger volume than average. Approximately 600,000 cu yd of the sediment dredged from South Reach in 1994 were used to fill the breach between the south beach and south jetty. Excluding the 1994 volume, the average annual volume dredged from South Reach is 275,000 cu yd/year. In contrast with the pattern in dredging volumes, the shoaling rates in Crossover Reach have increased since 1995 but have remained relatively constant for South Reach. Approximately 900,000 cu yd per year have been dredged from the combined Bar, Entrance, Point Chehalis, and South Reaches.

The volume of sediment dredged from the Bar Channel in 2002 was within the 95 percent confidence intervals of the decadal average. Volumes dredged from Entrance and Point Chehalis Reaches were above average while volumes dredged from South and Crossover Reaches were below average in 2002.

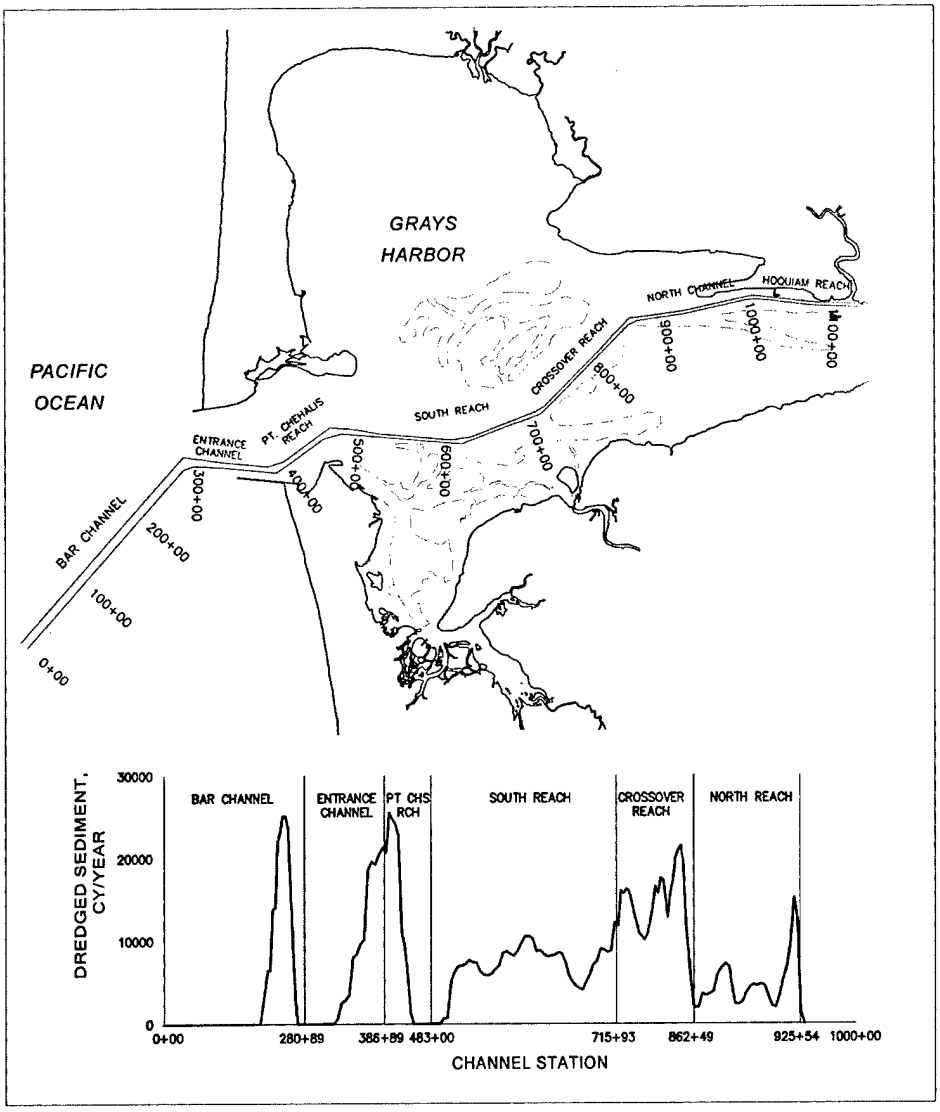

Figure 2-3. Average annual volume of dredged sediment distributed along each channel reach. Volumes were calculated with 1991 through 2001 data

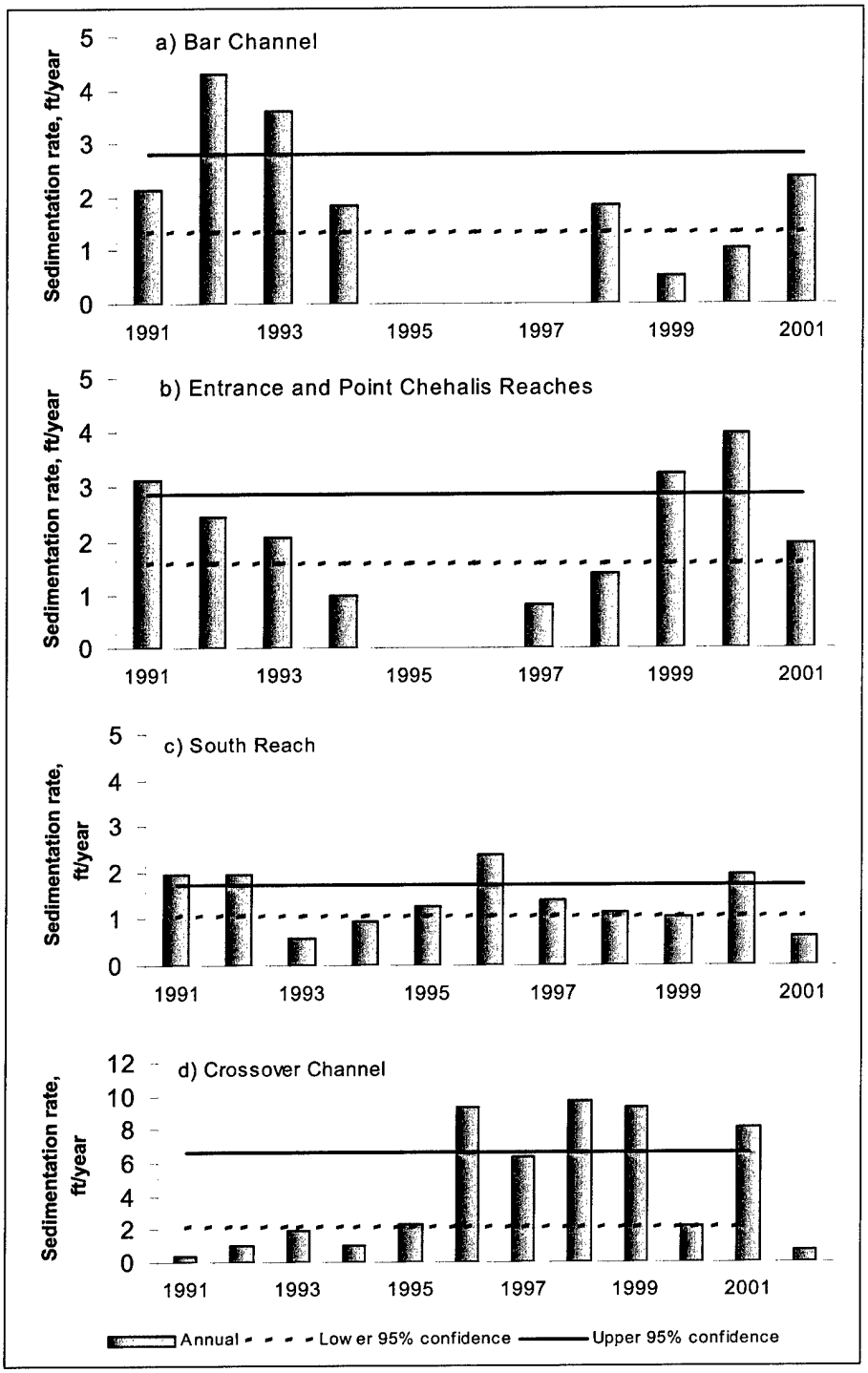

Figure 2-4. Annual sedimentation rates between 1991 and 2001 for (a) Bar Channel, (b) Entrance and Point Chehalis Reaches, (c) South Reach, and (d) Crossover Channel. Upper and lower 95 percent confidence limits for average annual maintenance dredging volume also are shown

The estimated total volume of sand material dredged from the outer reaches of the channel between 1991 and 2001 is approximately 1.1 million cu yd/year (Table 2-3). This estimate assumes that 50 percent of the dredged material from the Crossover Channel is sand and that only silt material (no sand) is dredged in the North Channel. These assumptions are based on practical experience from the Seattle District, and analysis of limited sediment grain size data for dredged sediment.

Dredged material from the channels was disposed at six different disposal sites in the Bay and in the open ocean. The locations of the disposal sites are depicted in Figure 2-5. The volume of dredged material placed at each site is summarized in Table 2-4, which also shows the source of dredged material. Currently, the Seattle District uses disposal sites at Point Chehalis, Half Moon Bay, south beach, south jetty, and the southwest site. Other disposal sites are permitted. Selection of specific disposal sites for dredged material disposal is controlled by economic and environmental considerations and an attempt to maximize a beneficial use of dredged material for habitat enhancement and beach restoration projects. For example, sites in Half Moon Bay and Point Chehalis are designated for disposal of dredged material that benefits beach nourishment and shore protection at Half Moon Bay and Point Chehalis. The amount of dredged material placed at the site is controlled by water depth that allows a hopper dredge safe maneuvering during disposal operations. Sites in Half Moon Bay receive dredged material predominately from South Reach, Point Chehalis, and Entrance Reaches, characterized by sand material typical of Half Moon Bay beach sediment.

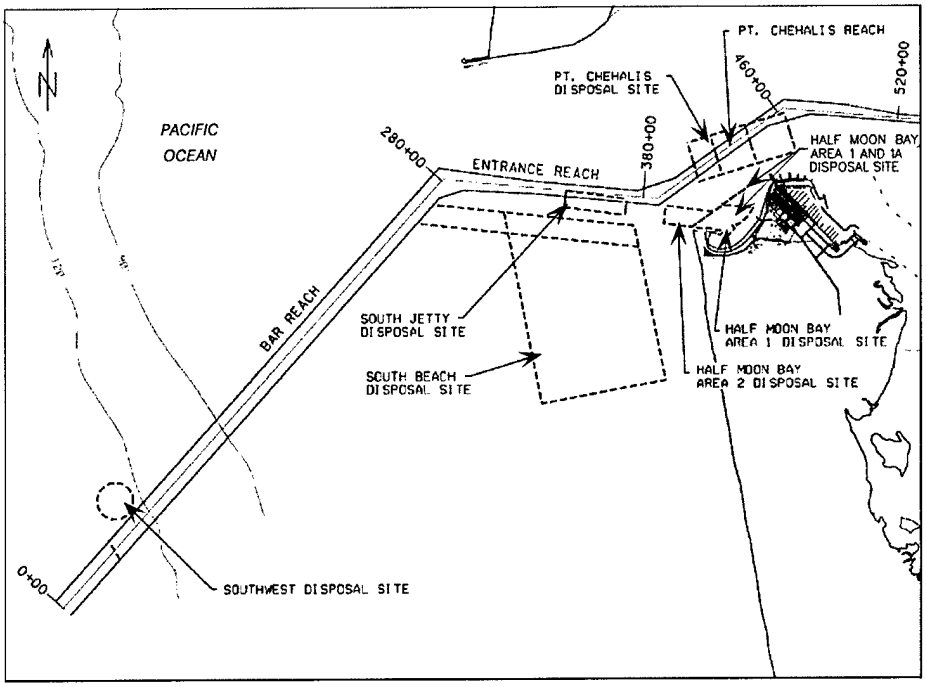

Figure 2-5. Location of dredged material disposal areas in and near Grays Harbor entrance (modified from USAED, Seattle, 1989)

Table 2-4
Disposal Site Annual Volumes* and Sources 1991-2002

Fiscal Year	Point Chehalis	South Jetty	Half Moon Bay Nearshore	Half Moon Bay Direct	Westport Fill	Breach Fill	South Beach	SW (Ocean)	Total
1991	710,000	1,109,000	0	0	0	0	0	452,000	2,271,000
1992	990,000	1,621,000	200,000	0	0	0	0	637,000	3,448,000
1993	683,000	1,120,000	0	0	0	0	373,000	0	2,176,000
1994	704,000	889,000	0	0	0	600,000	265,000	12,000	2,470,000
1995	1,181,000	392,000	0	0	300,000	0	0	0	1,874,000
1996	296,000	1,674,000	275,000	0	0	0	0	0	2,245,000
1997	599,000	959,000	309,000	0	0	0	0	0	1,866,000
1998	714,000	1,198,000	441,000	0	0	0	0	0	2,353,000
1999	1,156,000	593,000	228,000	229,000	0	0	76,000	0	2,283,000
2000	956,700	1,200,000	0	0	0	0	0	0	2,157,000
2001	668,000	359,000	0	0	0	0	0	227,000	1,254,000
2002	942,000	475,000	378,000	1,000	0	135,000	75,000	69,000	2,076,000
Total volume, cu yd	9,600,000	115,90,000	1,832,000	230,000	300,000	735,000	789,000	1,397,000	26,473,000
Reaches Dredged	Aberdeen, Cow Point, Cow Point Notch, Inner Crossover, Lower Crossover, Elliot Slough, Hoquiam, Inner Crossover, North Channel, South Reach, Turning Basin, Westport Marina	Aberdeen, Bar, Cow Point, Crossover, Elliot Slough, Entrance, Point Chehalis, Hoquiam, Inner Crossover, North Channel, South Reach	Entrance, South	Entrance, South	South	Entrance, South	Bar	Bar	

* Volumes rounded to the nearest thousand cubic yards.

North Jetty History and Existing Conditions

The chronology of engineering activities and condition of the north jetty is presented in Table 2-5. The north jetty was initially constructed to a length of 10,000 ft to mid-tide level extending to the southwest from the high water line at Point Brown. In 1910, it was evident that the extension of the jetty seaward (to the west) by 7,000 ft to a point nearly opposite the end of the south jetty would be necessary to maintain a reliable channel. The north jetty was extended to a total length of 17,000 ft from the high-water line between 1911 and 1915 to the mid-tide level. Since then, the north jetty has been repaired and rehabilitated several times. In 1916, the jetty was raised to approximately mhw (+8 ft, mllw) along its entire length. By 1934, the north jetty varied from a height of +17 ft mllw at the shoreline to -3 ft mllw at the outer end.

Table 2-5
History of North Jetty

Year	Event	Jetty Length	Jetty Crest Elevation
1907	Beginning of Construction		
1910	End of First Phase Construction	9,000 ft	+5 ft mllw
1913	End of Second Phase Construction	17,204 ft	+5 ft mllw
1916	End of Third Phase Construction	17,204 ft	+8 ft mllw
1933	Deterioration	Seaward part approximately 8,000 ft	-1.5 ft mllw
1942	Jetty Rehabilitation	Seaward part 8,228 ft	+20 ft mllw
1949	Deterioration	725 ft from seaward end including 325 ft 400 ft	Below 0.0 ft mllw +16 ft mllw
1953	Deterioration	2,050 ft from seaward end including 1,050 ft 1,000 ft	Below 0.0 mllw +10 ft mllw
1961	Deterioration	6,280 ft	Below 0.0 mllw
1971	Deterioration	8,000 ft	Below 0.0 mllw
1975	Rehabilitation	1,500 ft	+ 20 ft mllw
1996	Deterioration	140 ft from seaward end	Below 0.0 mllw
2001	Major Maintenance	5,000 ft from shoreline inland	23 ft mllw

Cross-sections of the north jetty were surveyed in July 1940 at six locations from near the jetty tip to more than 4,000 ft landward (Figure 2-6). The 1940 and 2001 shorelines and photo mosaic from aerial photographs acquired in 2000 are shown in the background for reference. The cross sections were approximately 400 ft long,, and measurements show toe elevations from the south to north sides of the jetty. Measured depths were generally 25 ft at the outer end of the jetty on the channel side. Moving eastward, near the current location of the sewage treatment plant, the depth on the channel side decreased to 10 ft. Depth at the toe on the north side of the north jetty was about 15 ft, but shallowed to 5 ft at the eastern-most cross section. These sections indicate that the bottom lowered as much as 25 ft adjacent to the jetty from the time of construction to 1940. Rehabilitation was needed by 1940 because of changes in foundation elevation, probably because the original jetty rock settled several feet into the sand. Depth of the lowermost rock in the section is not known.

In 1942, approximately 8,200 ft of the jetty were reconstructed to a crest elevation of +20 ft mllw. Following reconstruction in 1942, a deep channel developed in the entrance and across the bar, and no maintenance dredging of the Entrance and Bar channels was performed until 1990.

After reconstruction in 1942, the north jetty continued to deteriorate. In 1961, approximately 4,000 ft of rehabilitated jetty degraded to below +10 ft mllw. Figure 2-7 shows a profile of the jetty based on a 1953 survey indicating that sections of the jetty had degraded to below +10 ft mllw. A profile of the original ground elevation in the north jetty alignment is also shown in Figure 2-7. Location of the stationing noted on the profile is shown in the plan view on Figure 2-7. The ground profile shows the jetty was built on bottom as shallow as 1 ft below mllw. The original jetty was constructed by building a trestle-supported railway and random-dumping jetty stone from side-dumping rail cars. In the early part of the 20th century, an engineered toe was usually not built.

By the early 1970s, little evidence remained of the outer portion of the jetty between sta 160+00 and 172+00. The condition of the remaining portions of the jetty ranged from fair to poor (USAED, Seattle, 1974). The jetty from sta 145+00 to 160+00 was in poor condition with crest elevations low enough that most waves easily passed over the crest at high water. Several failures and lowering of the crest elevation below the constructed grade had occurred in at least three areas east of the beach line between sta 147+00 and 100+00. Figure 2-8 shows a longitudinal profile of the jetty crest between sta 100+00 and 160+00 based on a survey in 1973. In 1975, approximately 6,000 ft of the jetty, from sta 100+00 to 160+00, were reconstructed to +20 ft mllw. The design memorandum for the rehabilitation (USAED, Seattle, 1974) specified Class A stone with average weight of 14 tons for use in reconstruction of the seaward portion of the jetty. The direct impact of jetty rehabilitation in 1975 on channel maintenance dredging is unclear, owing to the realignment of South Reach and the elimination of Sand Island Reach in 1978-1979. The reduction in annual maintenance dredging volumes in the outer channel reaches following these events is estimated at approximately 0.5 million cu yd/year, from a volume of

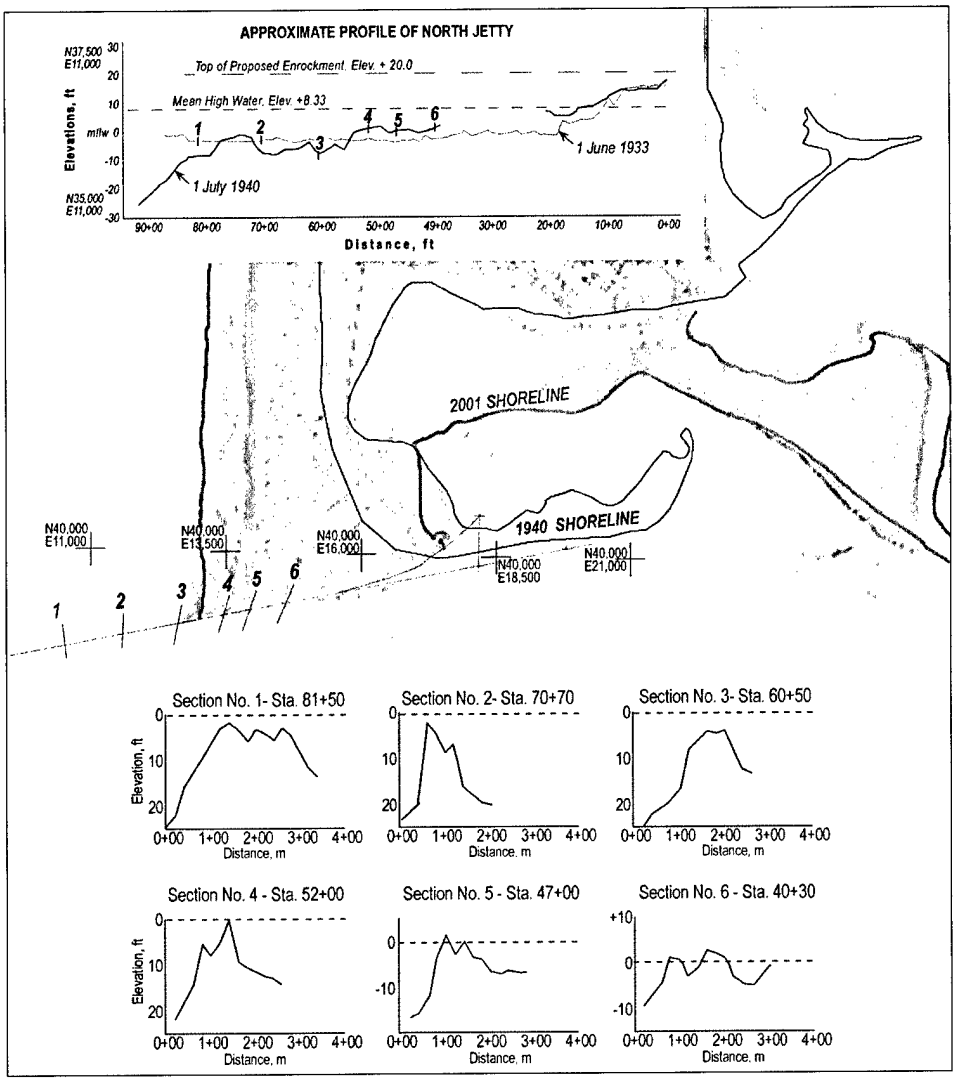

Figure 2-6. North jetty profile and cross sections based on a 1940 condition survey (modified from USAED, Seattle, 1940)

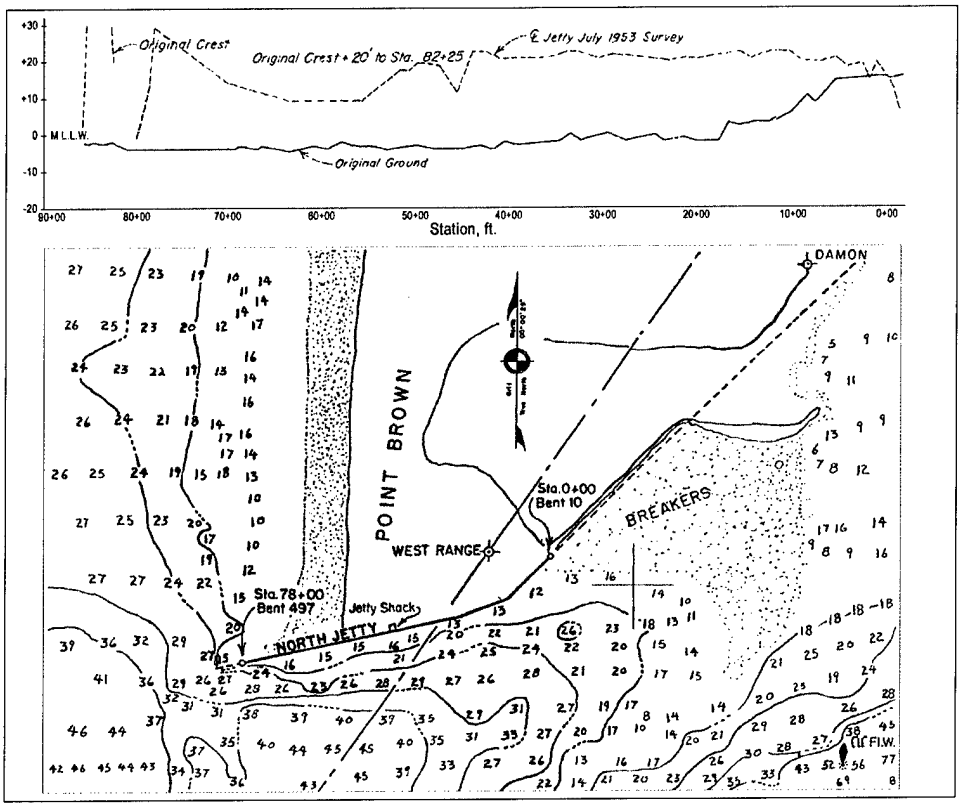

Figure 2-7. North jetty profile showing original bottom profile and crest elevation from a 1953 survey. Plan view shows location of stationing on profile and ambient seabed elevations near north jetty from 1953 annual condition survey. (Note that station locations in this figure do not follow conventions used elsewhere in this report) (modified from USAED, Seattle, 1953)

approximately 1.0 million cu yd/year prior to rehabilitation in 1975 to approximately 0.5 million cu yd/year after channel realignment in 1978. It is likely that both jetty rehabilitation and channel realignment contributed to the reduced dredging volumes in the combined outer reaches.

The most recent rehabilitation of the jetty occurred between 2000 and 2002 to the east of the present north beach shoreline. The crest elevation of the jetty from sta 95+00 to 145+00 had subsided below +20 ft mllw allowing wave overtopping and flooding of the adjacent residential area several times per year. The jetty was rehabilitated to design conditions by placing 59,000 tons of Class A rock.

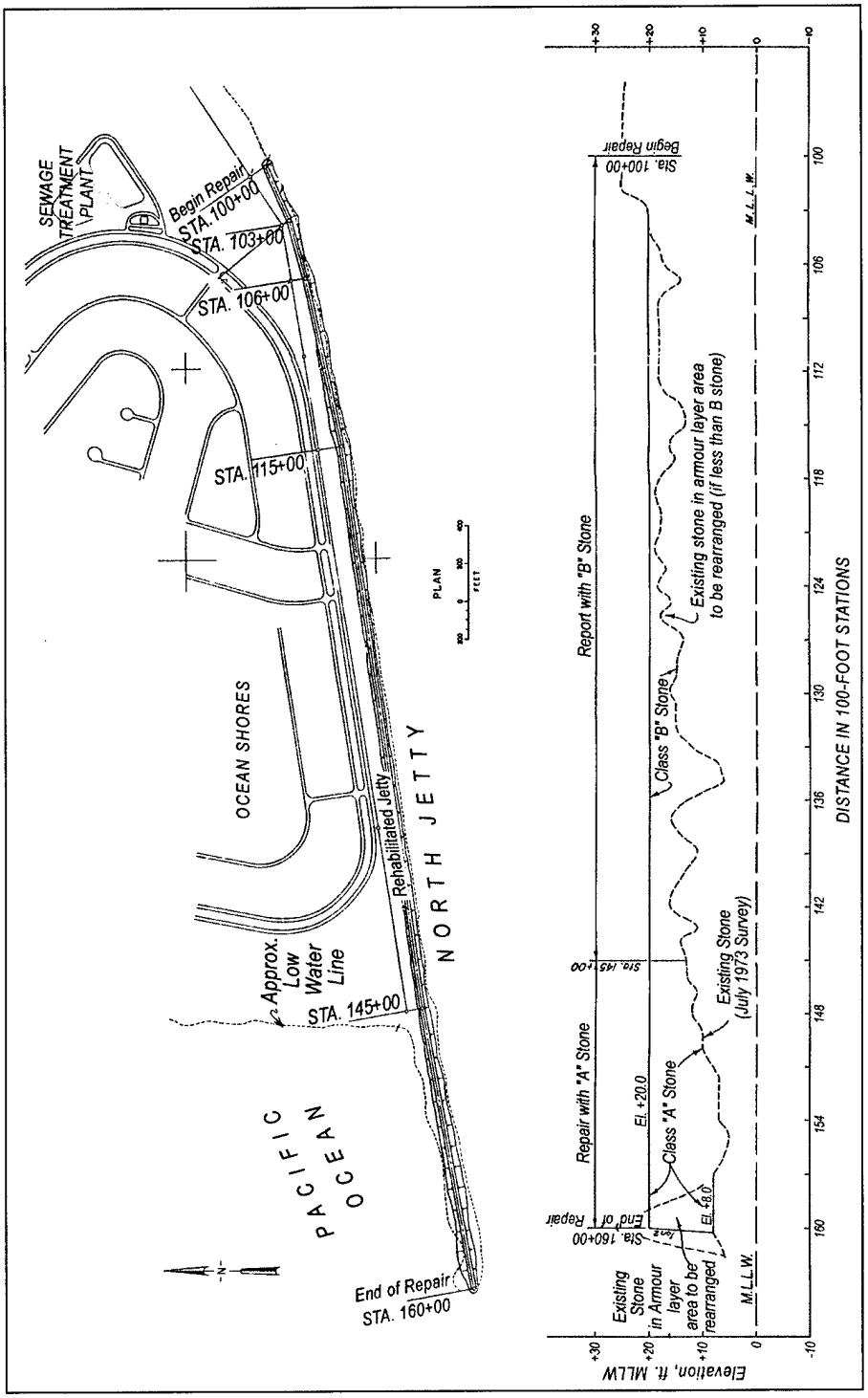

Figure 2-8. North jetty profile showing crest elevation between sta 100+00 and 160+00 based on a 1973 survey. The plan view shows station locations on profile (modified from USAED, Seattle, 1974, Plate 2)

Since the 1975 rehabilitation of the seaward part of the jetty, its profile and cross-section change has been minor. Figure 2-9 shows a combined aerial topographic and bathymetric multi-beam survey of the north jetty area conducted by USAED, Seattle in 1996. A longitudinal section along the center line of the north jetty extracted from this survey is presented in Figure 2-10. Small displacements (up to 5 ft) of crest elevation on the jetty below the design grade of +20 ft mllw are evident on the figures. These displacements may result from settlement of the jetty and/or accuracy limits of construction and surveying technique. Figure 2-11 shows cross sections of the jetty at sta 160+00, 150+00, and 140+00 from the same condition survey. This figure also depicts a design cross section from the rehabilitation project in 1975. No significant differences between the surveyed cross sections and design are evident except for some displacement of stone from the south face of the jetty at the seaward end (sta 160+00). It is unlikely that the displacements have caused any change in the ability of the jetty to retain sediment.

Deterioration of the outer end of the jetty by subsidence and wave attack has occurred over time since the original construction of the north jetty. Analysis of bathymetry changes in the inlet and shoreline changes north of the jetty over time since jetty construction and rehabilitation (Chapter 3) indicates a relationship between shoreline position north of the jetty, shoal volume in the inlet throat, and jetty condition. In general, the shoreline progrades seaward and shoal volumes are reduced for some time following major rehabilitation. Volumes of sediment dredged from the navigation channel are also reduced.

Evidence from hydraulic studies, field measurements, and analysis of historical bathymetry changes indicates that most marine sand is transported into Grays Harbor on the north side of the inlet (Chapters 3, 4, 7, and 8). Since the early 1900s, most of the marine sediment entering Grays Harbor from the north has followed a path around the north jetty to eventually reach the navigation channel. The pathways for marine sand between source and sink (navigation channel) are extremely complicated, multi-phased, and influenced by multiple processes that are subject to cycles at local and regional scale (Chapters 3 and 7). Also, the time frame for sediment transported from north beach to the channel may span several years or even decades. As a result, it is difficult to establish a strong quantitative relationship between the amount of sand bypassing the north jetty and the volume of deposition occurring in the navigation channel over a short period (less than a decade). At present, the average amount of marine sediment dredged from the lower reaches of the navigation channel is estimated at approximately 1.1 million cu yd/year. As Table 2-3 summarizes, the average amount of sediment dredged from Crossover and South Reaches is approximately 700,000 cu yd/year. Crossover Reach is within the mixed sediment region of the estuary. Assuming approximately half of the sediment dredged from Crossover Reach is of marine origin and half is of fluvial origin would indicate that approximately 500,000 cu yd/year of marine sand is dredged from South and Crossover Reaches. The approximate volume of 500,000 cu yd/year is an estimate of the deposition of marine sediment based on decadal-scale measurements of bathymetry change and includes contributions from marine sediment that entered the harbor prior to jetty construction as well as new marine

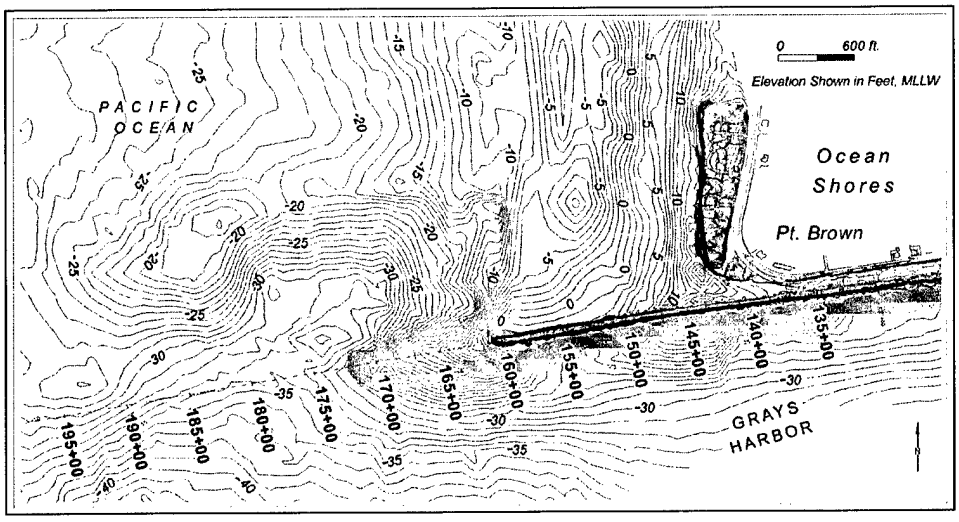

Figure 2-9. Elevation contours developed from aerial topographic and bathymetric multi-beam surveys conducted by USAED, Seattle (1996-2000)

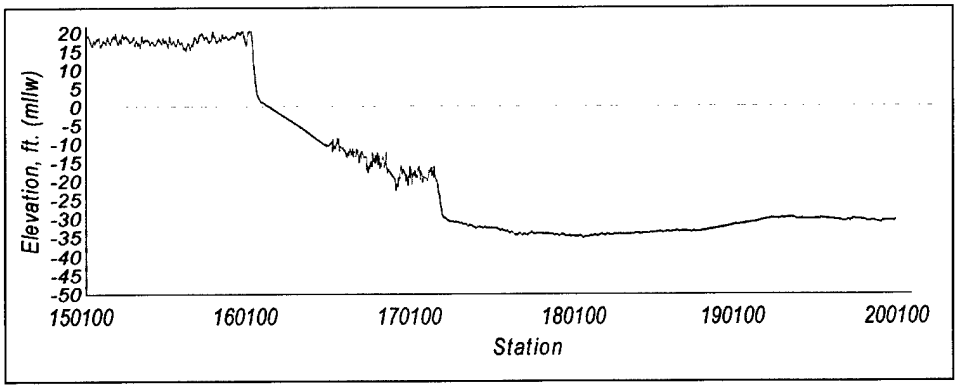

Figure 2-10. North jetty longitudinal cross section west of sta 150+00 in 2000

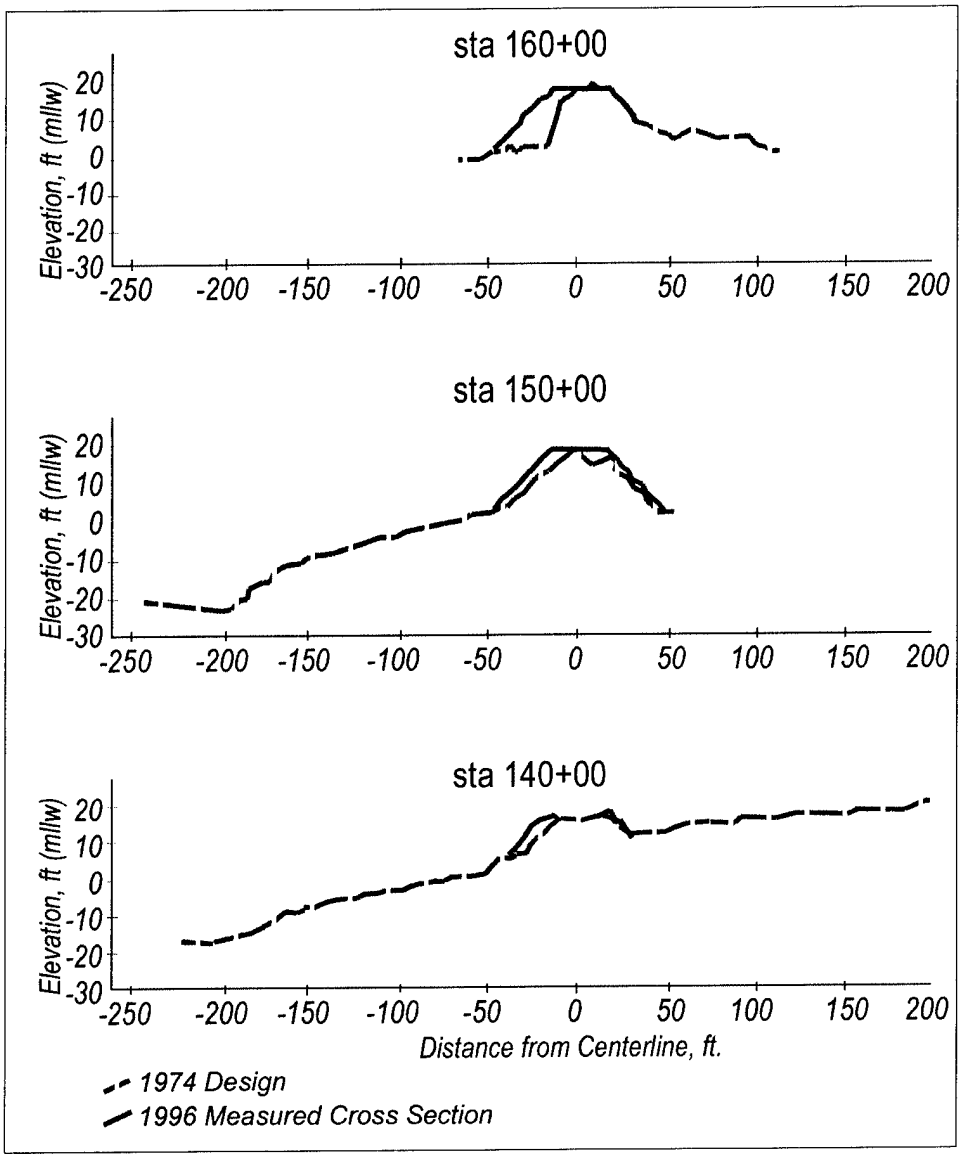

Figure 2-11. North jetty cross sections at sta 140+00, 150+00, and 160+00 based on 1996 condition survey compared with 1975 design cross section (modified from USAED, Seattle, 1996)

sediment bypassing the north jetty. It is apparent from photographic and anecdotal evidence, field measurements, and bathymetry analysis (Chapters 3 and 4) that the north jetty allows a significant quantity of southward littoral sediment movement to Grays Harbor. This evidence will be reviewed in detail in subsequent chapters of this report. It is expected that the north jetty will gradually deteriorate over time because of wave impacts, toe scour, strong currents, and other mechanisms. Assuming present levels of sediment supply, the amount of sediment bypassing would be expected to increase, thereby increasing maintenance dredging requirements in the future.

Development of Design Optimization for Control of Southward Bypassing

The reasons for considering optimization and control of sediment bypassing southward at the north jetty relate to maintenance dredging in the navigation channel and stability of the north beach shoreline, the latter associated with possible instability of the jetty. Previous empirically based knowledge, practical experience, and studies related to rehabilitation of the jetties and navigation channel improvement projects have established that marine sediment depositing in Grays Harbor results mainly from southern littoral drift from Point Brown bypassing the north jetty. A specific function of the north jetty is to control the southward movement of littoral drift and aid in maintaining the entrance channel between the jetties (USAED, Seattle, 1973).

The relationship between channel sedimentation (or dredging volumes) and jetty length developed for the 1975 rehabilitation must be considered preliminary and further analysis is required to determine if it has any applicability to present conditions of sedimentation in the inlet. However, the relationship provides a benchmark for a preliminary comparison of the potential effectiveness of the alternatives developed for this study in reducing channel sedimentation in assuming 1970s conditions. A study preceding the rehabilitation of the north jetty (USAED, Seattle, 1973) determined that changes in the jetty length affected maintenance dredging principally in the Sand Island (prior to South Reach realignment, completed in 1978) and Crossover Channel reaches of the authorized channel. This study predicted that rehabilitation of 6,000 ft of the jetty, from sta 100+00 to 160+00 would reduce maintenance dredging in these two reaches by up to 360,000 cu yd/year. The study also predicted that rehabilitation of the next 1,800 ft of the jetty from sta 160+00 to 178+00 would further reduce sedimentation in the channel reaches by approximately 300,000 cu yd/year. The study also predicted that some shoaling of the Entrance Reach might be expected with extension of the jetty.

The review of dredging data presented in this chapter shows that, following the 1975 rehabilitation of the north jetty and realignment of the channel to South Reach (1978-79), maintenance dredging in Crossover and South Reaches was reduced by approximately 500,000 cu yd/year relative to the annual volumes previously dredged from Crossover Reach and the former Sand Island Reach. (It should be noted that the 1975 rehabilitation did not alter the length of the north jetty and repairs were mainly above +8 mllw. Consequently, the rehabilitation may not have significantly altered trends in shoreline response and southward bypassing of sediment to the inlet. Also note that typically, dredging is expected to increase following dredging of a new channel because of slumping of sediment on the side slopes of the new channel cut.) Comparing the dredging data with the anticipated reduction in dredging of 360,000 cu yd/year, it is possible that the 1975 north jetty rehabilitation achieved some of the anticipated reduction of maintenance dredging requirement. It remains to be determined, however, whether the relationship between the north jetty length and estimated volume of maintenance dredging in the Navigation Channel obtained in the 1973 study is applicable. The relationship developed for the 1973 study is applied below for the purpose of a preliminary comparison of alternatives assuming

1970s conditions. The estimated average annual maintenance dredging volumes for jetty lengths beyond sta 160+00 and the respective change in dredging volume, based on the 1973 relationship, are summarized in Table 2-6 and Figure 2-12.

Jetty Rehabilitation Alternatives (Alts 3A and 3B)

The north jetty is approximately 1,600 ft shorter than the authorized length. Rehabilitating the jetty to its authorized length is an alternative for reducing channel sedimentation and coastal erosion. The forecast in Table 2-7 and Figure 2-12, based on the 1973 analysis, provides a simple and direct means of evaluating the potential reduction in maintenance dredging volumes associated with jetty rehabilitation alternatives assuming the 1970s conditions.

Two jetty rehabilitation alternatives are compared by applying the 1975 forecasts. Alternative 3A, a partial rehabilitation from sta 160+00 to 165+00, would reduce average annual maintenance dredging by approximately 130,000 cu yd. Alternative 3B, a full rehabilitation to sta 170+00, would reduce average annual maintenance dredging by approximately 200,000 cu yd.

Spur Alternatives and Combined Alternative (Alts 2A, 2B, and 4)

In this chapter, the relationship between change in dredging volumes and bypassing rates as controlled by jetty length is extended for the purpose of comparing the other alternatives. This is accomplished by assuming that the forecast change in annual dredging volume for each of the jetty rehabilitation alternatives (summarized in Table 2-7) is linearly related to the relative changes in annual southward sediment bypassing estimated by numerical modeling (Chapter 8).

The relationship determined for the jetty rehabilitation alternatives (Alt 3A and Alt 3B) is shown in Figure 2-13. Figure 2-13 also shows the estimated values of the change in bypassing determined for other alternatives (Alt 2A, 2B, and 4) based on relative changes in southward bypassing determined by the numerical modeling of sediment transport (Chapter 8).

Application of the above method assumes that the present sediment bypassing potential of the north jetty is similar to the 1975 condition. The method also assumes that the relationship between jetty length and channel sedimentation volumes developed in the early 1970s is correct and applicable to present conditions.

The forecasts for the 1975 rehabilitation design are based on the premise that an increase in the volume of the north beach results in an increase in bypassing of the north jetty and therefore an increase in channel dredging of the navigation channel in the Sand Island and Crossover Channel Reaches. The relationship was based on dredging records, historical north jetty condition, and the north beach

Table 2-6
Estimated Average Annual Dredging Volumes for Various Jetty Rehabilitation Alternatives for 1975 Rehabilitation (USAED, Seattle, 1973)

Rehabilitation or Extension from sta 100+00 to sta:	Increase in Jetty Length Relative to sta 160+00 (ft)	Average Annual Maintenance Dredging Volume (cu yd/year)	Change in Dredging Volume with Increase in Jetty Length (cu yd)
160+00	0	680,000	
166+00	600	540,000	-140,000
172+00	1,200	460,000	-220,000
178+00	1,800	410,000	-270,000
190+00	3,000	360,000	-320,000

Adapted from Table 1, p 18, USAED, Seattle, 1973.

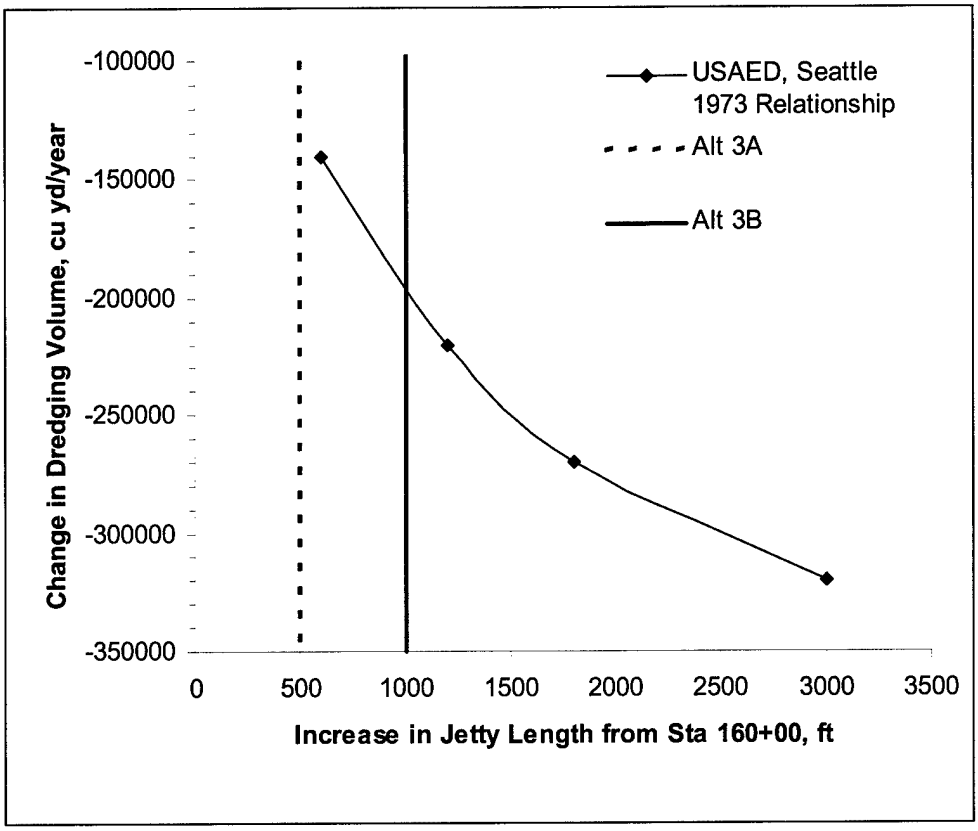

Figure 2-12. Forecast of reduction in average annual maintenance dredging volume with increase in jetty length from sta 160+00 for 1975 rehabilitation (USAED, Seattle, 1973)

Table 2-7
Extrapolated Changes in Dredging Volumes for Each Alternative

Alternative	Change in Dredging Volume with increase in Jetty Length USAED, Seattle (1973) (cu yd)	Relative Change in Southward Bypassing (percent)	Extrapolated Change in Annual Dredging for Alternatives (cu yd)
3A	-140,000	15	
3B	-200,000	38	
2A		6	-113,000
2B		3	-105,000
4 (2A + 3A)		17	-143,000

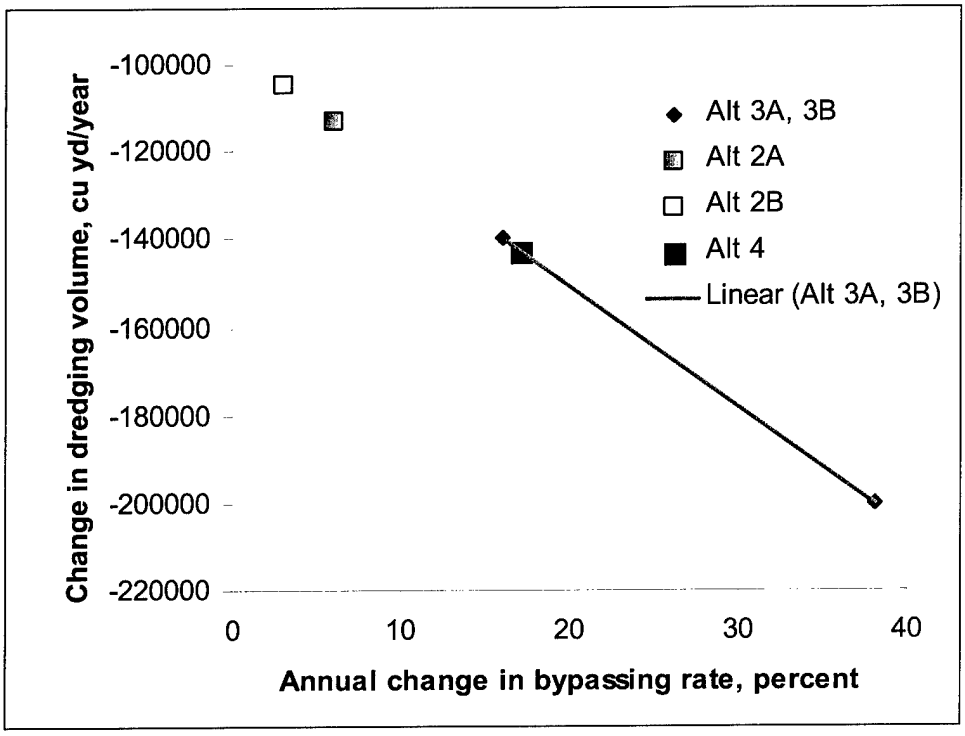

Figure 2-13. Annual change in southward bypassing rate and change in annual dredging volume for Alt 3A and Alt 3B

volume changes between 1942 and 1972 (USAED, Seattle, 1973). North beach volumes were determined from the annual condition surveys. (Note that only hand-drawn contours were used to determine volumes from bathymetry data in 1973, not digitized depths.) This relationship will be examined in greater detail in later chapters of this report.

The extension of the forecasts for the 1975 rehabilitation to the analyzed alternatives should be treated with caution because the assumptions concerning the 1975 forecasts have not been verified in detail. Similarly the extrapolation of the results in combination with the bypassing results determined by numerical modeling is intended only as a relative guide for comparing potential changes in dredging.

A second aspect of southward bypass optimization and control relates to inlet shoal and shoreline stability issues. This aspect should be addressed through estimates of the amount of sediment required to maintain the existing balance of sediment in the Grays Harbor littoral system in a way to preclude any detrimental changes in existing morphological condition in the harbor. In other words, the amount of sediment bypassing the jetty to the harbor consists of two components: sediment that maintains the littoral system and sediment deposited in the channel. Sediment maintained in the littoral system contributes to the development and evolution of natural morphological features in the bay, for example, Damon Point. The goal of optimization would be to reduce the bypassing constituent that contributes to the deposited and dredged sediment without causing significant adverse impact to Damon Point.

References

Beverage, J., and Swecker, M. (1969). "Estuarine studies in Upper Grays Harbor Washington," U.S. Geological Survey Water Supply Paper 1873-B, 90 p.

Black, W. M. (1916). Letter to the Secretary of War, in Letter from Secretary of War transmitted to Congress, 12 December 1916.

Board of Engineers for Rivers and Harbors. (1934). "Report of the Board of Engineers for Rivers and Harbors to the Chief of Engineers, United States Army, Subject: Grays Harbor, Washington, June 26, 1934," in letter transmitted to Committee on Rivers and Harbors, 74th Congress, 17 July 1934.

Scheidegger, K. F., and Phipps, J. B. (1976). "Dispersal patterns of sand in Grays Harbor estuary, Washington," *Journal of Sedimentary Petrology* 46(1), 163-166.

U.S. Army Engineer District, Seattle. (1940). "North jetty condition, July 1940," U.S. Engineer Office, Seattle, Field Book File No. 20-225.

_____. (1953). "Bar and entrance condition, August 1953," File No. E-5-7-124.

_____. (1965). "South jetty rehabilitation," Grays Harbor and Chehalis River Washington General Design Memorandum, Seattle, WA.

_____. (1973). "North jetty rehabilitation, Grays Harbor and Chehalis River and Hoquiam River, Washington," Seattle, WA, September, 34 p.

_____. (1974). "Design Memorandum: North jetty rehabilitation," Seattle, WA, August, 16 p.

_____. (1989). "General design memorandum and environmental impact statement supplement: Grays Harbor, Washington Navigation Improvement Project," Volume 1, Appendix B: Design Analysis, Seattle, WA, TC 202.S42 G72.

_____. (1995). "Alternatives for the long term maintenance of the Federal Navigation Project at Grays Harbor, Washington," Seattle, WA, April.

_____. (1997). "Long-term maintenance of the south jetty at Grays Harbor, Washington," Evaluation Report, Seattle, WA.

Washington Department of Ecology. (1977). "Maintenance dredging and the environment of Grays Harbor Washington summary report," prepared for the U.S. Army Engineer District, Seattle, Contract No. DACW67-74-C-0086, 102 p.

3 Inlet and Nearshore Morphodynamics[1]

Introduction

The most direct method for evaluating regional sediment transport pathways and quantifying long-term net transport rates at and adjacent to an inlet entrance is by quantifying historical changes in inlet and nearshore morphology with a time series of shoreline and bathymetric surveys. Data are typically lacking for drawing detailed and confident conclusions regarding the evolution of inlet systems relative to channel shoaling and adjacent beach changes. Grays Harbor, Washington is an exception, however, where shoreline and bathymetry surveys have been collected on an approximately annual basis since 1894. Availability of such comprehensive data at high frequency for such a long time span is rare and demonstrates the concern for navigation by the U.S. Army Engineer District, Seattle.

This chapter presents results from a geomorphic investigation of inlet and beach sedimentation patterns at Grays Harbor within the context of dredging and construction engineering activities. Geomorphic analyses presented in this chapter are based on a more comprehensive data set than previous studies because (a) a greater number of shoreline and bathymetry data sets from the Seattle District were generated in digital format, (b) historical maps were registered consistently within a common horizontal coordinate system and vertical reference plane (Appendix F), (c) recent shoreline, intertidal topography, and annual bathymetric survey data were incorporated, and (d) all data from bathymetric maps were analyzed in digital format (not just depth contours). Change analysis specifically identifies trends in seafloor erosion and accretion, quantifies shoreline response to structure placement and reconstruction, and establishes a detailed sediment budget with sediment pathways for the periods 1954/56 to 1987 and 1987 to 2002.

[1] This chapter was written by Mark R. Byrnes and Jessica L. Baker, Applied Coastal Research and Engineering, Mashpee, MA.

Setting

The outer coast of Washington extends from the Straits of Juan de Fuca in the north to the mouth of the Columbia River at the border with Oregon. The southern half of this area, from Point Grenville south to the Columbia River, encompasses barrier beaches formed by the reworking of fluvial sediment by marine wave and current processes (Kachel and Smith 1989). The regional north-south shoreline is divided into three slightly concave westward segments separated by the channels and shoals present at Grays Harbor, Willapa Bay, and the Columbia River (Figure 3-1).

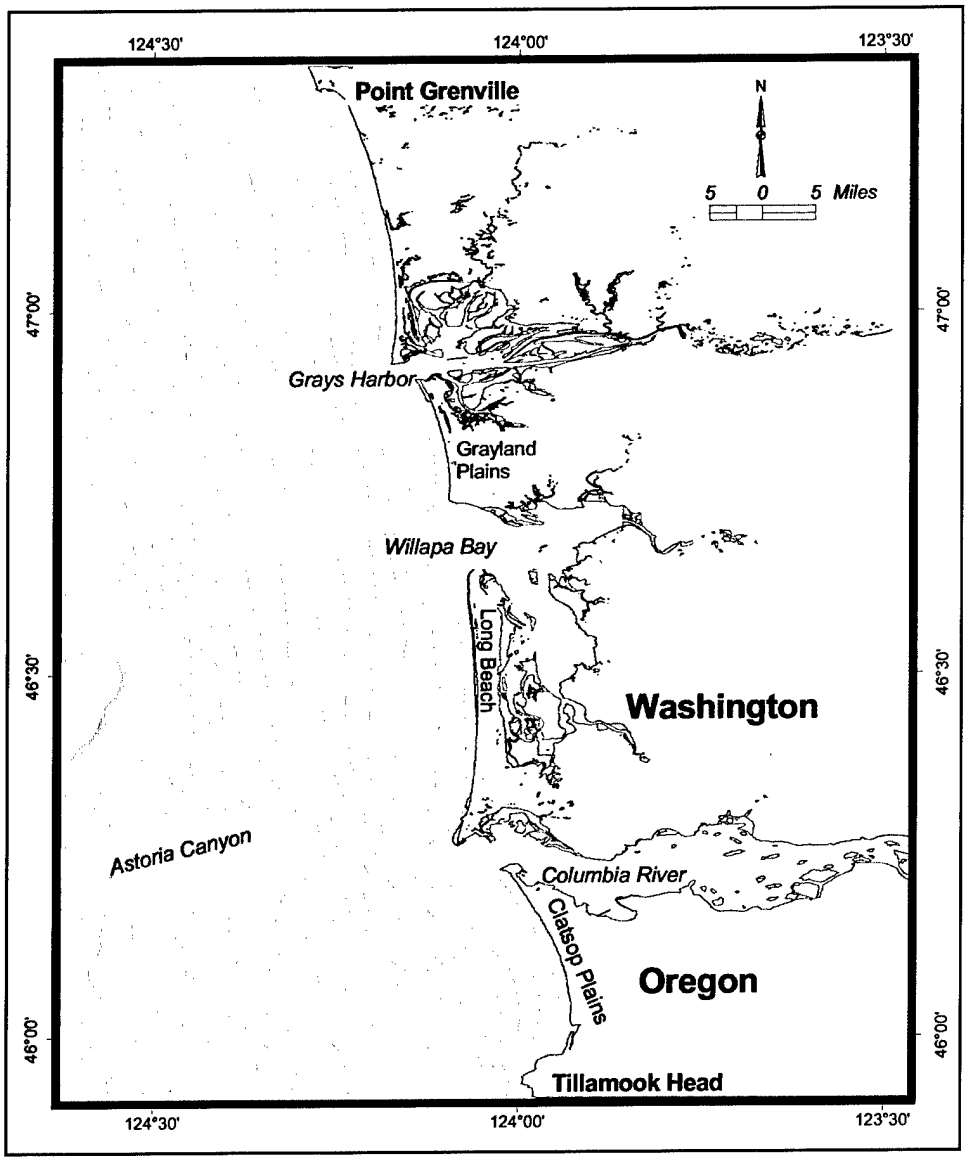

Figure 3-1. Location diagram illustrating barrier beach trends for outer coast of Washington

The continental shelf seaward of the coast varies in width from about 20 to 45 miles, with a shelf break depth of 500 to 650 ft (Byrne 1963; McManus 1972). The nearshore slope is about 0.004 except where depth contours protrude seaward around ebb-shoal deposits off Grays Harbor, Willapa Bay, and the Columbia River. The heads of submarine canyons along the outer edge of the continental shelf are at depths of about 600 ft (Hands 2000). Generally, the bathymetry of the Washington continental shelf within the Columbia River Littoral Cell (CRLC) is smooth, with contour lines trending approximately 15 deg west of north (McManus 1972). Modern deposits in the CRLC are as much as 165 ft thick, and surface sediment varies from silty sand on the middle and outer shield to fine sand on the beaches and inner shelf (Nittrouer 1978; Sternberg 1986).

The southwest Washington coast is wave dominated with significant wave heights ranging from about 10 to 22 ft (Ruggiero et al. 1997). Seasonally variable wave approach produces longshore currents that transport sand to the north during winter months and to the south in the summer. Because the northerly component of littoral transport is driven by high-energy winter waves, the predominant drift direction is to the north. Ballard (1964) documented that the dominant source of sand for beach and offshore environments in southwest Washington is from the Columbia River, and that sand is moved northward in a net sense by seasonally reversing longshore currents.

Sediments

Fluvial sediment originating from the Columbia River has been the primary source of material for the southwest Washington shelf during the Holocene at an estimated average annual sediment discharge rate of 0.55 to 2.3 x 10^7 tons/year (Van Winkle 1914; Judson and Ritter 1964; Karlin 1980). General surface sediment distribution on the shelf contains a nearshore sand unit extending north along the coast seaward to a depth of about 160 ft. Typical wave energy levels in this region prevent significant deposition of silt landward of the 160-ft-depth contour (Figure 3-2; Kachel and Smith 1989). This area was defined by Creager and Sternberg (1972) as the landward region with median grain size ranging from 0.12 to 0.25 mm (<10 percent silt). Between 160 and 425 ft water depth, Nittrouer (1978) identified measurable sediment accumulation rates and the presence of clay and silt characteristic of a Columbia River source (Figure 3-3). Creager and Sternberg (1972) found that the silt component in this central zone increased to 40 to 70 percent from that of the landward region. Sandy sediment generally occupies the outer shelf environment as relict deposits in depths greater than 425 ft (Kachel and Smith 1989).

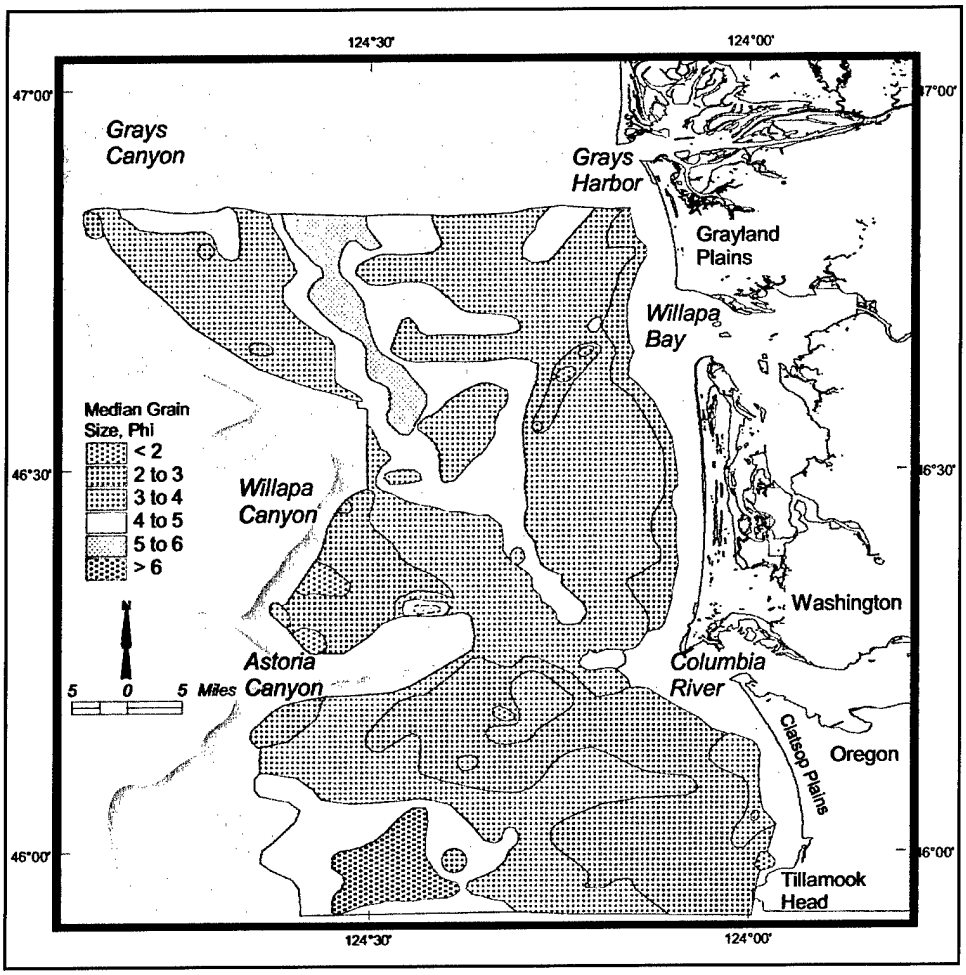

Figure 3-2. Distribution of median grain size for Washington-Oregon continental shelf (from McManus 1972)

Twitchell, Cross, and Parolski (2000) collected sidescan sonar imagery, surface sediment samples, and bottom photographs within the CRLC to describe the surficial geology of the inner shelf. Historical sediment samples of Roberts (1974) and Nittrouer (1978) supplemented acquired data to define eight distinctive sedimentary units on the shelf (Figure 3-4). Three of these units are particularly relevant to the sediment budget. Lower beach face deposits represent the shoreward zone of analysis that extends seaward to about the 60-ft-depth contour. Mean grain size ranges from about 0.25 mm in the nearshore (<30 ft) to 0.12 mm near the offshore boundary (Twitchell, Cross, and Parolski 2000), north and south of Grays Harbor. Concentrations of sand dollars are common throughout the lower beach face unit (Figure 3-5).

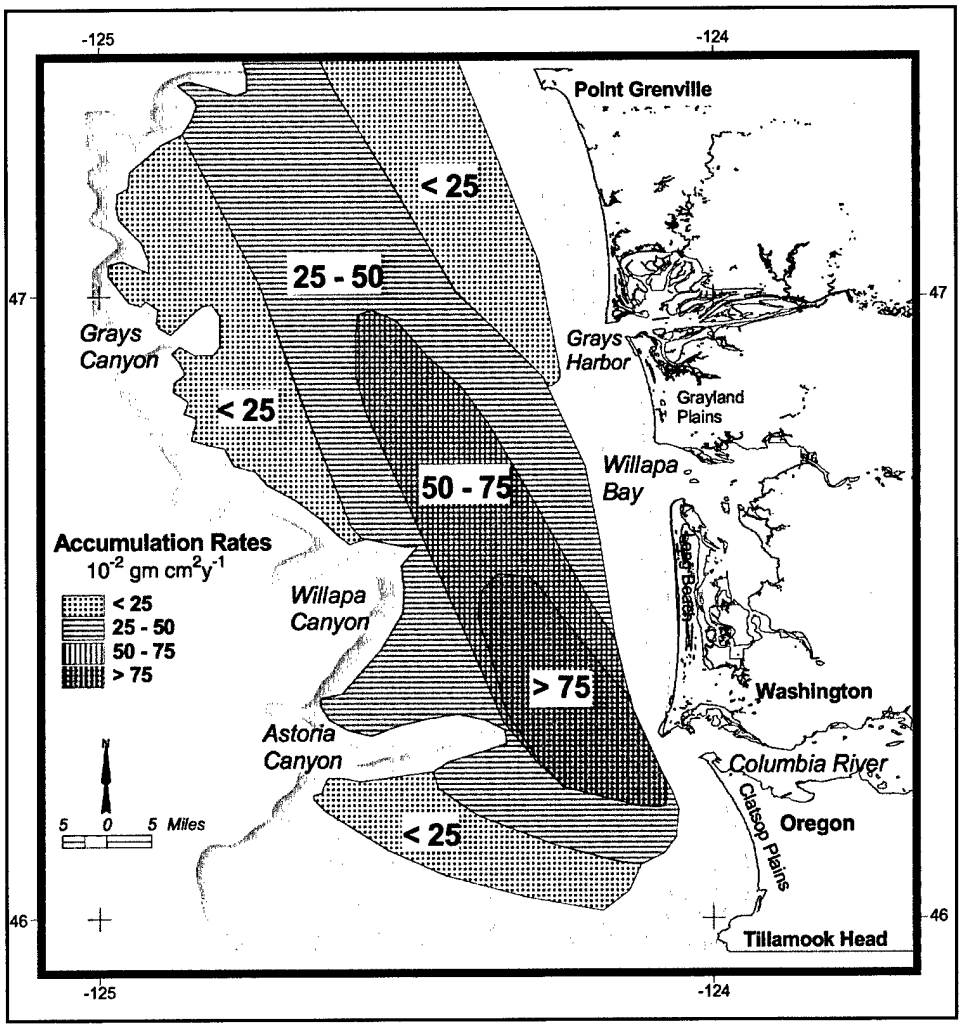

Figure 3-3. Sediment accumulation rates for southwest Washington continental shelf using Pb-210 geochronology (after Nittrouer 1978)

Very fine sand dominates surface sediment samples seaward of the 60-ft-depth contour to a distance offshore where silt and clay become more than 25 percent of the sample distribution (Figure 3-6). Twitchell, Cross, and Parolski (2000) observed that the fine sand fraction decreased gradually from 40 to 65 percent in 60 to 80 ft water depth to 5 to 10 percent in 180 to 230-ft water depth. Conversely, the very fine sand fraction increases from 30 to 52 percent to 55 to 70 percent for the same depth intervals. The silt and clay content gradually increases with depth from about 7 percent near the boundary with the lower beach face to as much as 39 percent at the seaward boundary with the mid-shelf silty sand unit. Twitchell, Cross, and Parolski (2000) also noted that biological reworking of the seafloor increased with increasing water depth throughout the inner-shelf sand unit.

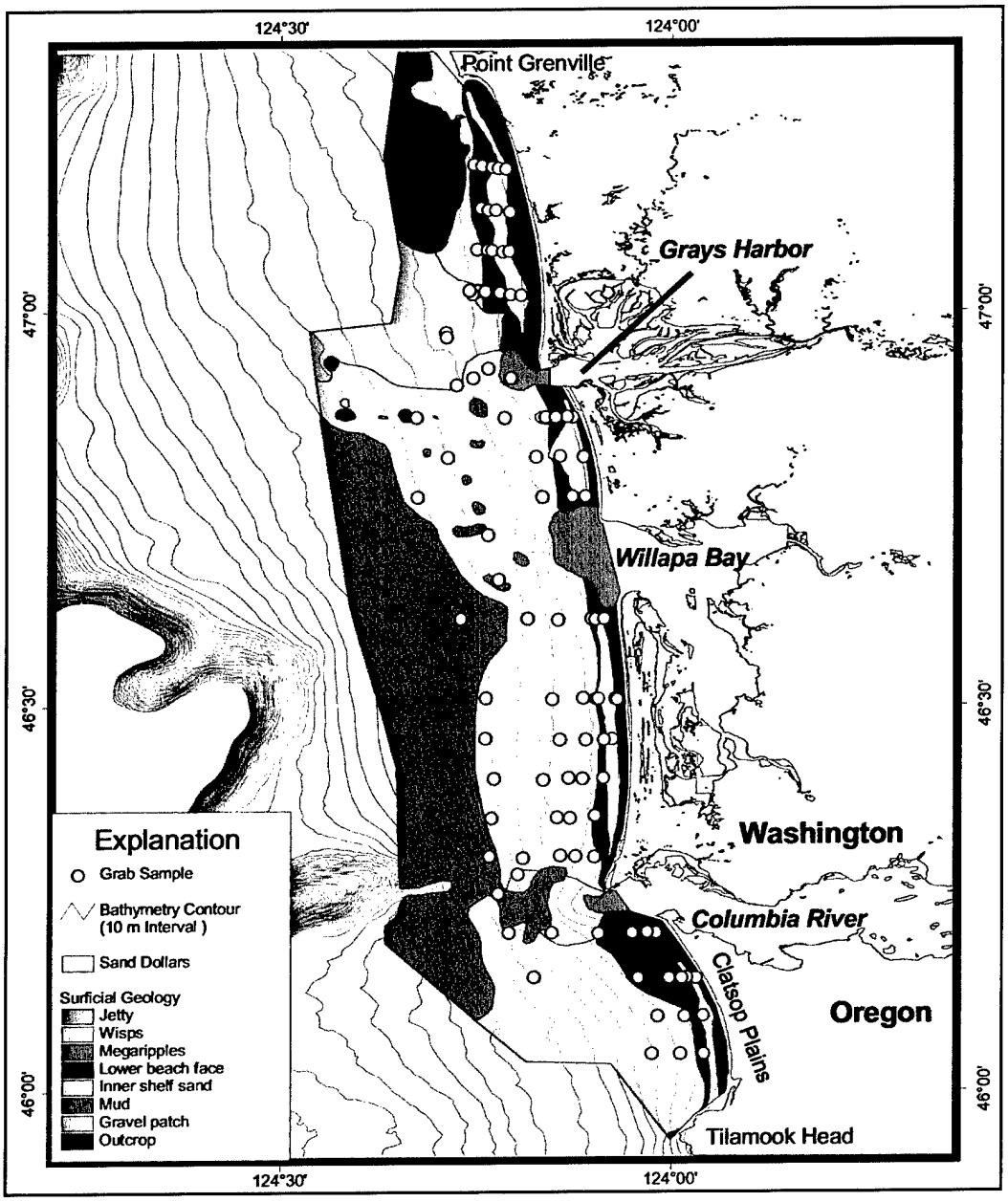

Figure 3-4. Diagram illustrating surficial geology of shelf deposits within CRLC in relation to surface grab samples (modified after Twitchell, Cross, and Parolski 2000)

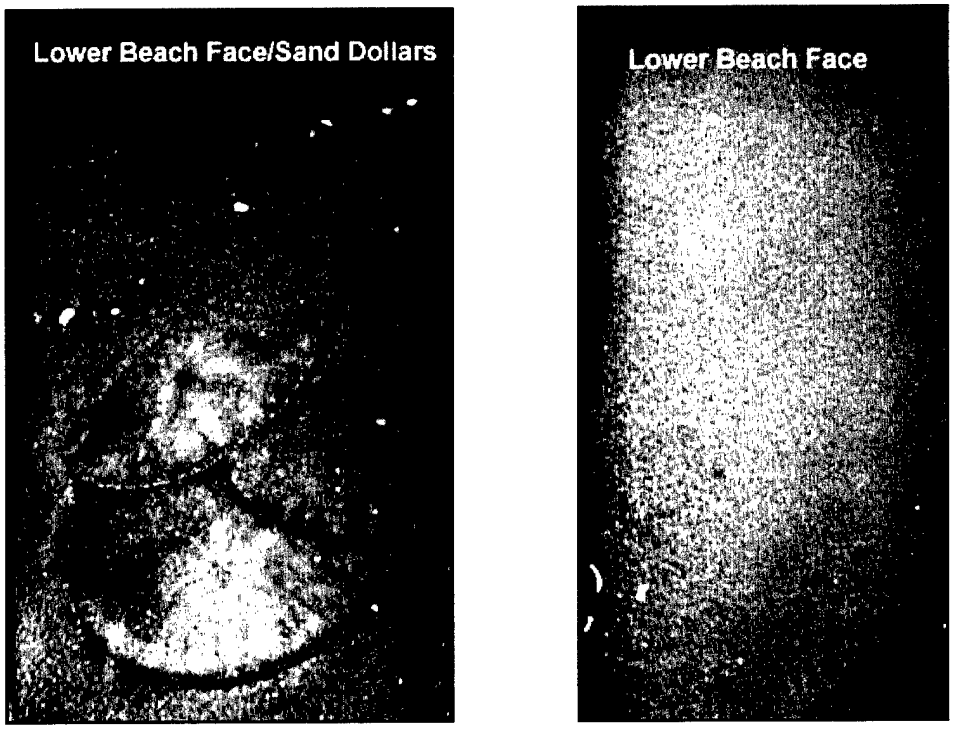

Figure 3-5. Surface sediment composition on lower beach face (modified from Twitchell, Cross, and Parolski 2000). Mean grain size ranges between 0.12 and 0.25 mm with <10 percent silt and clay

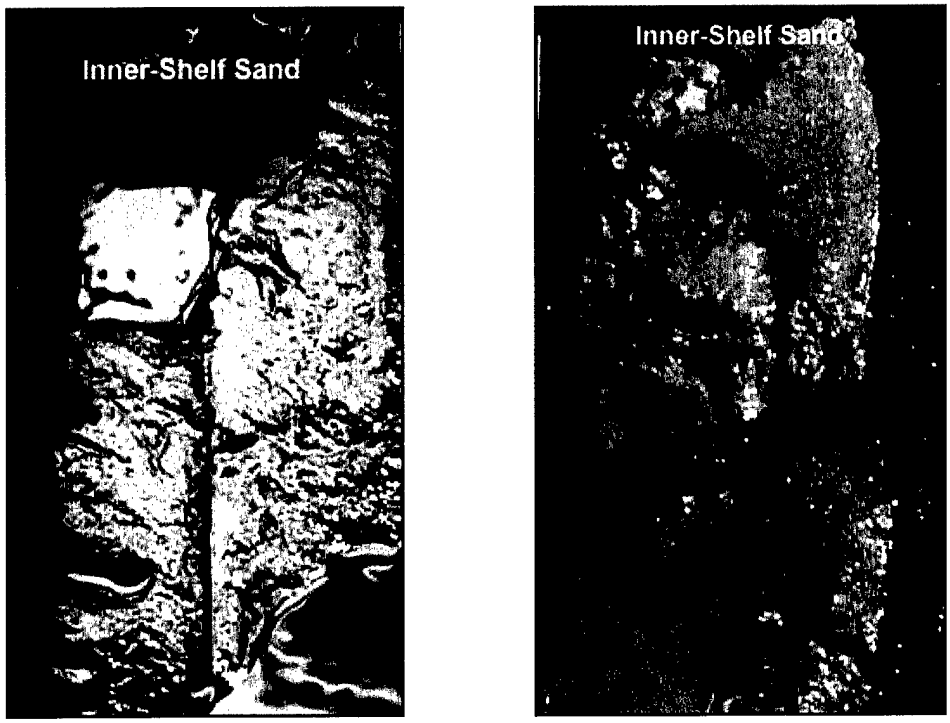

Figure 3-6. Inner-shelf sand samples offshore Grays Harbor, as defined by Twitchell, Cross, and Parolski (2000). Samples illustrate very fine deposits with <25 percent silt and clay

Two other areas of interest regarding the sediment budget include a gravel area west-northwest of Grays Harbor entrance and the ebb shoal seaward of the entrance jetties. As outlined by Twitchell, Cross, and Parolski (2000), the gravel patch offshore Grays Harbor appears quite extensive. However, only three samples define the sedimentologic characteristics of the area (Figure 3-7), and limited sidescan data define the acoustic character of the surface. In fact, one of the three sediment samples within the gravel area is more characteristic of the lower beach face zone (0.15 mm median grain size), emphasizing the patchiness of relict gravel deposits. One sediment sample collected from the inner portion of the ebb shoal reflects the sediment type available for bypassing the entrance. Median grain size for that sample is 0.21 mm, and it contains 100 percent sand (Figure 3-8). These textural characteristics are most similar to the lower beach face, the source of sand to the net north-directed littoral drift system.

The Grays Harbor estuary is a drowned river valley that formed as a consequence of sea level rise and filled during the Holocene with coarse-grained sediment of fluvial and marine origin (Scheidegger and Phipps 1976; Peterson, Scheidegger, and Komar 1984; Peterson and Phipps 1992). Sediment dispersal patterns during the Holocene resulted in distinct zones of marine, mixed, and fluvial sediment throughout the estuary. Scheidegger and Phipps (1976) identified sediment sources and dispersal patterns from the composition of heavy minerals in 77 surface samples. The two primary sources identified included one from rivers flowing into the northern and eastern parts of the estuary (Chehalis and Humptulips Rivers) and the other from the Columbia River.

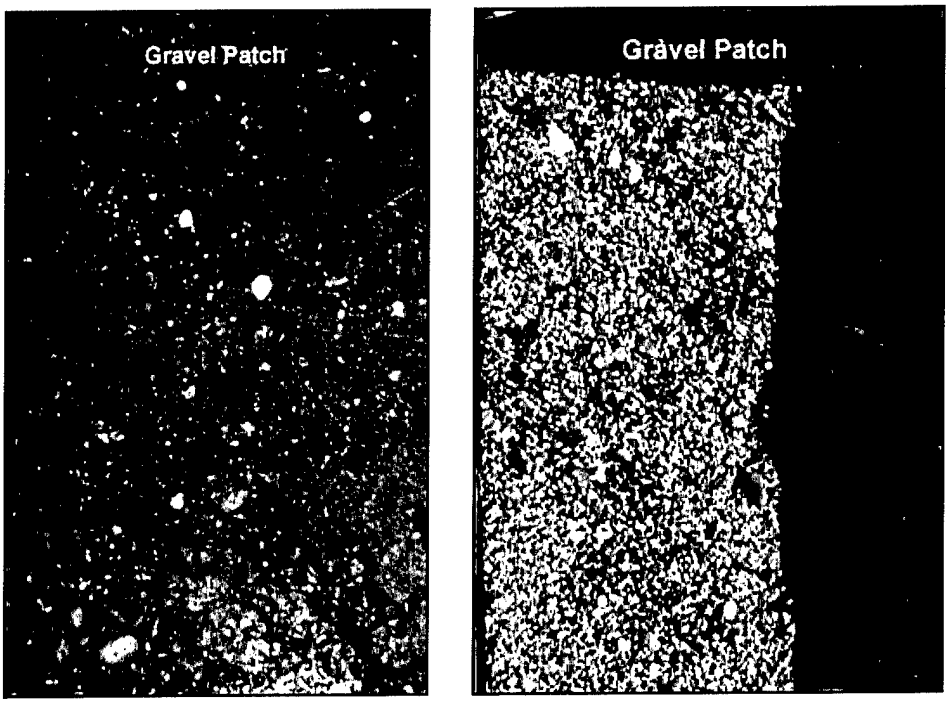

Figure 3-7. Sediment samples offshore northwest of Grays Harbor illustrating characteristics of gravel patch defined by Twitchell, Cross, and Parolski (2000). Deposits are most abundant in areas of relict sediment outcrops

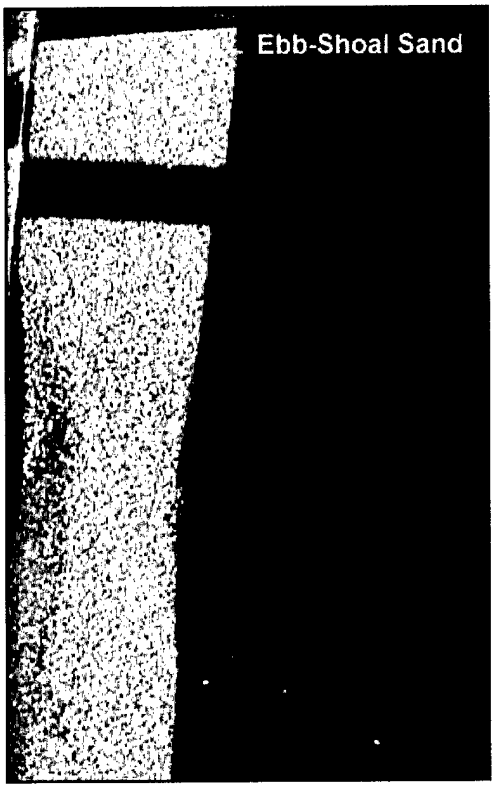

Figure 3-8. Sediment composition characteristic of inner ebb-shoal deposits; 95 to 100 percent sand and median diameter of about 0.21 mm. Sand is very similar to that present on lower beach face (modified from Twitchell, Cross, and Parolski 2000)

Sediment from the Columbia River entered Grays Harbor as a marine source from the beaches and nearshore zone adjacent to the bay entrance. Two distinct heavy mineral assemblages resulted in the identification of three sand depositional provinces within the estuary (Figure 3-9). A marine province is associated with the entrance area, and a local fluvial province extends bayward from the northern and eastern margin of the estuary. Scheidegger and Phipps (1976) identified the transition zone between these two mineralogical end members as mixed. Peterson, Scheidegger, and Komar (1984) state that depositional patterns in Grays Harbor result from seasonal variations in estuarine hydrography. During winter months, when fluvial discharge is high, sand and gravel from local rivers are transported down the estuary. During summer months, beach and nearshore sand is transported into the estuary by flood-tidal currents.

Peterson and Phipps (1992) completed basic textural analysis on 290 samples from 17 drill-core sites to document dominant sediment characteristics of Holocene fill in Grays Harbor basin. Overall, mud-rich deposits (greater than 50 percent silt and clay) were limited to the top 110 ft of basin fill in the upper half of the bay and the bottom 110 ft in the lower bay. Conversely, sand and gravel deposits dominate the lower 110 ft of the basin fill in the upper estuary and the upper 110 ft of fill in the lower reaches of the estuary. This three-dimensional pattern of basin fill indicates that two different sources of sediment have contributed to basin infilling.

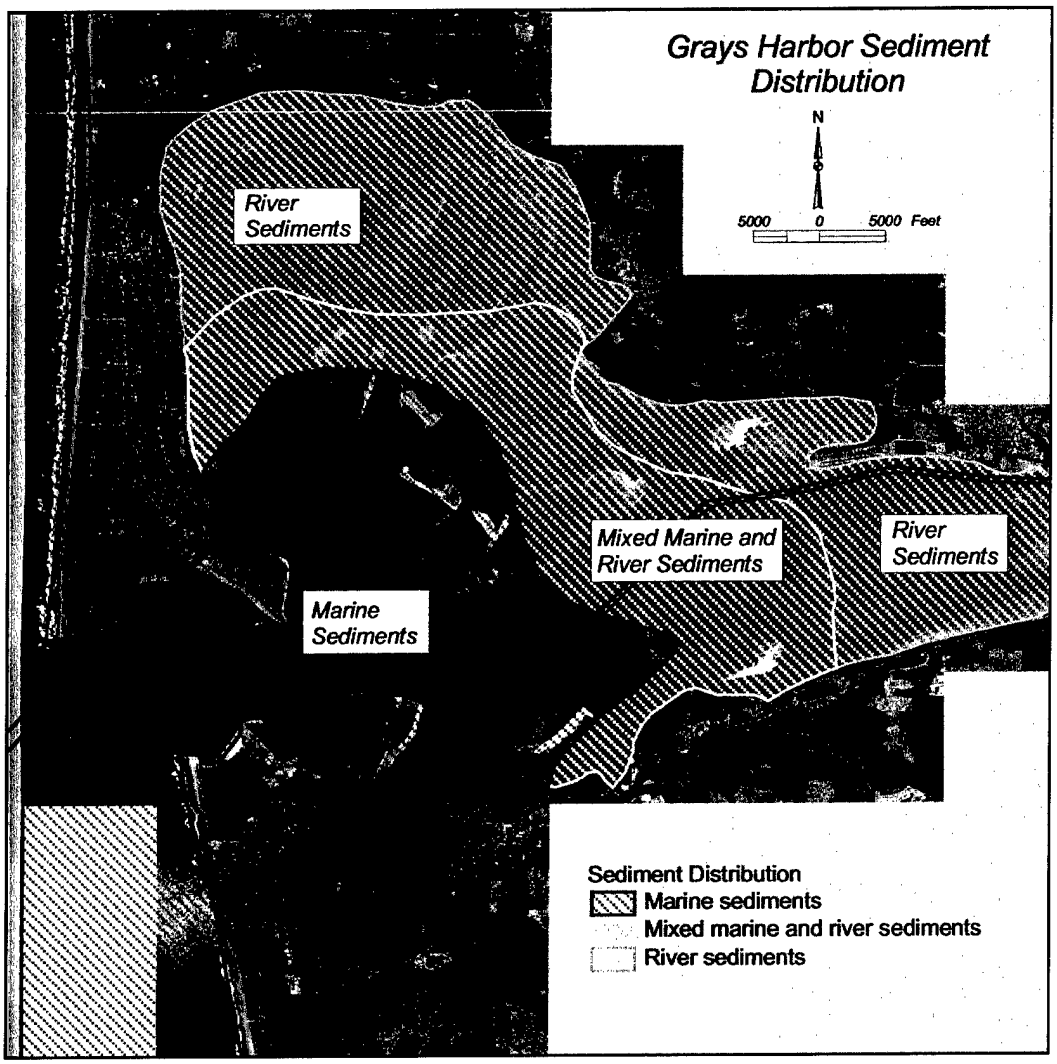

Figure 3-9. Provinces of sand deposition in Grays Harbor as described by Scheidegger and Phipps (1976)

History and engineering activities

In the late 1780s, the Boston Fur Company was formed to engage the Pacific Northwest natives in the trading of sea otter furs. On 7 May 1792, Captain Robert Gray, a New England native, sailed his ship, the Columbia, into Bullfinch Harbor (later renamed Grays Harbor). Searching for still more trading partners, Gray sailed into the mouth of the Columbia River, advancing some 15 miles by 10 May 1792, just 3 days after he had sailed into Grays Harbor. To commemorate the event, the river was named Columbia in honor of the ship (Bohlander 1984).

A chart prepared by Captain George Vancouver, dated 1798, illustrates many of the same major features and shapes in the estuary that exist today (Figure 3-10). The first extensive mapping of the harbor was completed about a century later in 1883 by the U.S Coast and Geodetic Survey (USC&GS), again illustrating relatively few geomorphic changes relative to present conditions. The most significant changes are those associated with the construction of jetties at the entrance (USAED, Seattle, 1974, 1989; Buijsman, Kaminsky, and Gelfenbaum 2003).

Since 1894, the Seattle District has been surveying the harbor and entrance area to monitor shoreline position and changes in shoal and channel morphology. Jetty construction in the early 1900s was undertaken to improve channel navigability. The structures imposed substantial influence on estuarine hydrography and channel characteristics, creating a self-scouring inlet that has moved the crest of the offshore bar seaward into deeper water and significant sand deposition along the beaches north and south of the harbor. Most geomorphic changes recorded at the entrance were anticipated (Burch and Sherwood 1992). Table 3-1 summarizes the construction and rehabilitation history for the entrance jetties since authorization. The history is for reference with long-term changes in sediment transport trends documented throughout this chapter and the report. Interpretation of geomorphic change is described in terms of key engineering events as documented in the table.

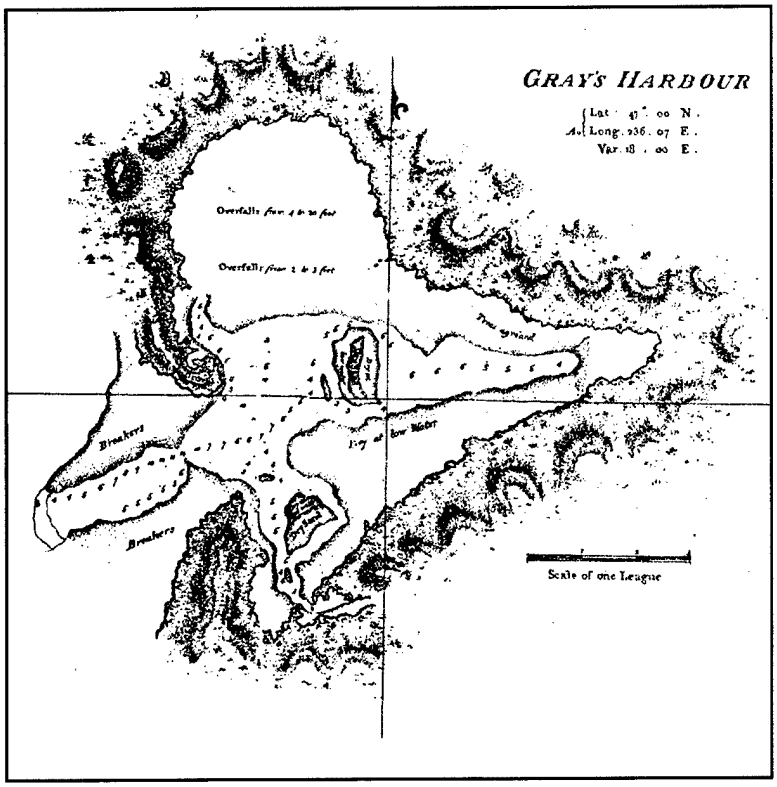

Figure 3-10. Map prepared by Captain George Vancouver in 1798 (modified from Washington State Archives)

Table 3-1
Construction and Rehabilitation History, Grays Harbor, Washington

3 June 1896	The River and Harbor Act authorized the original Grays Harbor navigation project, including a channel across the bar (self-scouring to a depth of about 18 ft mean lower low water [mllw]) and construction of a single jetty extending 18,154 ft seaward from Point Hansen (now called Point Chehalis) peninsula along the southern margin of the entrance to Grays Harbor. At this time, predominant longshore transport was determined to be from south-to-north, and the south jetty was considered responsible for preventing shoaling in the navigation bar channel (USAED, Seattle, 1965).
1898 – 1902	The south jetty was constructed between May 1898 and September 1902. It was completed to a height of +8 ft mllw and a total length of 13,734 ft, of which 11,950 ft extended seaward of the high-water line in 1902. During construction, the channel adjacent to the jetty undermined the structure causing material overruns that depleted project funds before the design length of 18,154 ft could be reached. A groin (spur) pointing into the channel was constructed 11,952 ft from the high-water line in 1902.
1902 – 1906	Between 1898 and 1904, depth over the ebb-shoal increased from 12 to 22 ft mllw as a result of jetty construction, meeting the stated purpose of the project. In addition, the beach south of the jetty accreted, creating a 3,000-ft seaward progradation of the high-water shoreline. However, deterioration of the jetty began around 1904. By 1906, the south jetty had settled due to scour, and the bar channel began to widen and shoal. This unfavorable shoaling led to construction of the north jetty (USACE 1934).
2 March 1907	The River and Harbor Act authorized construction of the north jetty 9,000 ft long from the ordinary high-water line to an elevation of +5 ft mllw and an 18-ft deep navigation channel.
1907 – 1910	Construction of 10,000 ft of the north jetty completed to +5 ft mllw.
25 June 1910	The River and Harbor Act authorized an extension of 7,000 ft to the north jetty.
1910 – 1913	The north jetty was completed to a project length of 16,000 ft and an elevation of +5 ft mllw.
1913 – 1916	The north jetty was reconstructed to +8 ft mllw and extended to a length of 17,204 ft. Construction period for the entire jetty extends from May 1907 to January 1916. After reconstruction of the north jetty, the channel adjacent to the south jetty shoaled, and a new wider and deeper channel developed north of the old channel to about -24 ft mllw. Depth over the bar was again about -22 ft mllw, and it remained that way until about 1924.
8 August 1917	River and Harbor Act authorized dredging of the bar channel.
1916	As jetties continued to deteriorate and were inadequate to maintain project dimensions in the bar channel, dredging commenced (57,000 cu yd) and continued at regular intervals until 1926 (except for 1918 and 1919).
1926 - 1942	The bar channel required almost continuous dredging between 1926 and 1942. The total quantity dredged from the entrance between 1916 and 1942 was approximately 22 x 10^6 cu yd; maximum dredging occurred between 1934 and 1936. The minimum quantity dredged in a year was 22,000 cu yd, and the maximum was 1,964,000 cu yd (Committee on Tidal Hydraulics 1967).
1933	By 1933, the south jetty had subsided to an average depth of 5 to 10 ft below mllw (+6 ft mllw at the high-water shoreline and -10 ft mllw at the outer end; Figure 3-11).
1934	The outer 8,000 ft of the north jetty, between the high water shoreline and the tip of the jetty, subsided to approximately -1.5 ft mllw.
30 August 1935	River and Harbor Act authorized reconstruction of the north and south jetties and maintenance of a 26-ft deep channel below Aberdeen.

(Continued)

[1] Reconstructed refers to major changes in jetty dimensions along the length of the structure.
[2] Rehabilitated refers to changes implemented to maintain a portion of the jetty and its general dimensions.

Table 3-1 (Concluded)	
1936 – 1939	A 12,656-ft section of the south jetty (about sta 80+00 to 220+00) was reconstructed to an elevation of +20 ft mllw. Jetty reconstruction blocked the supply of sand to Point Chehalis, causing serious erosion of Point Chehalis. A 32-ft section of the jetty was removed to try to restore the supply of sand, but it was quickly blocked by accretion south of the jetty.
1939 – 1946	The outer 900 ft of the south jetty was destroyed, and crest rock was displaced to +2 ft mllw over the next 2,656 ft.
1940	The inner 7,300 ft of the north jetty, shoreward of the high-water shoreline, was impounded with sand.
1941 - 1942	The north jetty was reconstructed between February 1941 and May 1942 to +20 ft mllw for 7,700 ft seaward of the high-water shoreline, then +30 ft mllw for an additional 528 ft. A 412 ft segment seaward of the reconstructed section was at mllw and was not restored. The structure landward of the high-water shoreline was not rebuilt.
1942	Maintenance dredging of the bar and entrance channels was no longer required due to scouring effects of the jetties.
1942 – 1949	The outer 325 ft of the north jetty was leveled, and about 400 ft of the reconstructed section was lowered 4 ft below grade.
1946 – 1951	An additional 900 ft of the south jetty was destroyed, and the next 4,100 ft subsided to 0 to +10 ft mllw.
1951 – 1953	An additional 900 ft of the outer south jetty was destroyed, and the next 4,500 ft subsided to 0 to 2 ft mllw. The next 2,400 ft subsided to +4 ft mllw.
1949 - 1953	An additional 325 ft of outer end of the north jetty was leveled, and more than 1,000 ft of the remaining section subsided to +10 ft mllw.
1952 - 1954	More than 300 ft of the south jetty (between sta 70+00 and 80+00) was dismantled, and the rock used for construction of the Point Chehalis revetment.
1959	An additional 30 x 106 cu yd of sand had accumulated north of the north jetty as a result of jetty reconstruction completed in 1942.
1961	Only 2,100 ft of the reconstructed portion of the north jetty remained at or near grade (+20 ft mllw).
1962	By April 1962, average elevation of the south jetty between 135+00 and 198+00 (6,300 ft) was about mllw; seaward of this point from 198+00 to 220+00 (2,200 ft), crest elevation ranged from -6 ft mllw to -48 ft mllw. The landward section from about 88+00 (high-water shoreline) to 135+00 (4,700 ft) was near grade (Figure 3-11).
1966	A 4,000-ft section of the south jetty (from sta 110+00 to 150+00) was rehabilitated to +20 ft mllw, leaving the outer 7,000 ft in a degraded condition (-10 ft mllw or deeper).
1974	A section of the north jetty, about 1,300 ft seaward of the high-water shoreline, ranged from +3 to +14 ft mllw. The jetty seaward of this point was below mllw.
1975 - 1976	A 6,000-ft section of the north jetty, from the high-water shoreline seaward, was rehabilitated to an elevation of +20 mllw.
1991	Maintenance dredging of the bar and entrance channel reactivated.
December 1993	A breach occurred between the ocean and Half Moon Bay adjacent to the south jetty. The breach was filled with 600,000 cu yd of sand dredged from the channel in 1994.
March 1999	Storm lowered a 200 ft section of the south jetty to about +9 ft mllw and damaged the jetty where it intersected the shoreline.
2000	A 3,500-ft section of the south jetty seaward of the high-water shoreline was raised to an elevation of +23 ft mllw. Approximately 5,000 ft of the north jetty landward of the high-water line was raised to an elevation of +23 ft mllw.

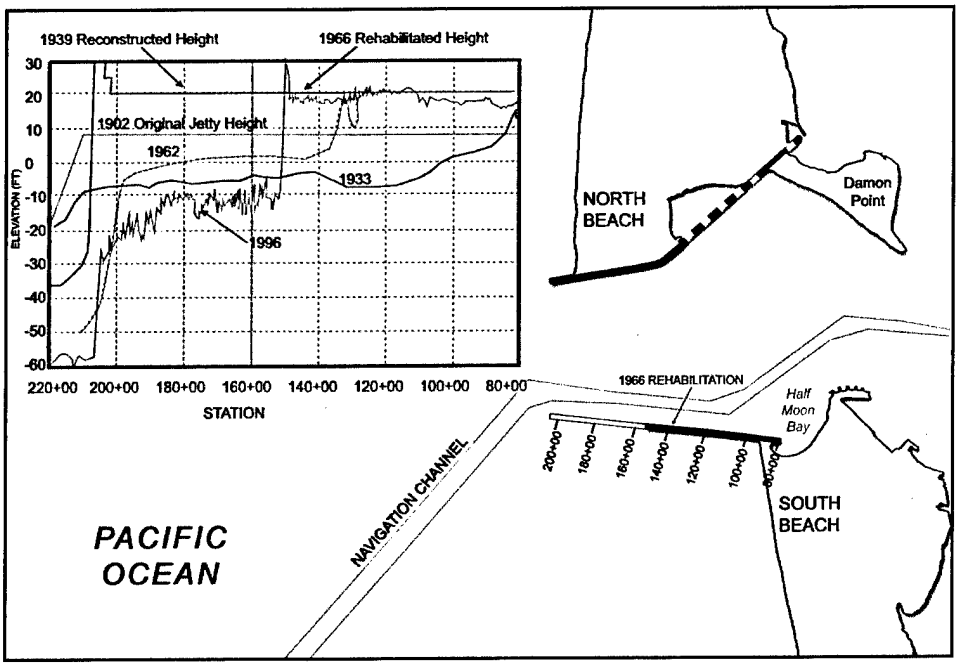

Figure 3-11. Changes in crest elevation along south jetty since 1902 (USAED, Seattle, 1997)

Construction of the jetties stabilized the entrance by confining flows in and out of the estuary and by blocking littoral drift from shoaling the navigation channel. Maintenance dredging has been required at times since jetty construction to maintain authorized project dimensions (Chapter 2). After construction of the north jetty in 1916, channel depth increased to 24 ft. However, shoaling increased between 1917 and 1924, and in 1924/25, approximately 1 million cu yd was dredged from the bar channel to create a channel depth of 36 ft. According to the Chief of Engineers Report to Congress in 1934, dredging was practically continuous from 1927 to 1933 to maintain a 30-ft-deep channel. Overall between 1916 and 1942, dredging in the bar channel amounted to about 22 million cu yd (USAED, Seattle, 1974). Following reconstruction of the jetties to +20 ft mean lower low water (mllw), the bar and entrance reaches did not require dredging between 1942 and 1989. However, the channel was deepened to 46 ft mllw and widened in 1990, resulting in average annual dredging since 1991 of about 0.6 million cu yd for the bar and entrance channel. Since jetty construction, depths over all parts of the ebb shoal have increased and it has moved seaward by about 1.5 miles.

Sediment-volume changes

Two previous studies summarized morphologic changes for the Grays Harbor entrance area based on analysis of Seattle District and USC&GS bathymetric surveys. The Committee on Tidal Hydraulics (CTH) produced a report in 1967 that summarized net scour and fill trends for subregions at the entrance from 1862 to 1960. Burch and Sherwood (1992) augmented this data

set by including surveys between 1960 and 1990. Methods applied by the CTH (1967) to register and digitize shoreline and bathymetric map data are not described, but Burch and Sherwood (1992) compiled surveys that overlapped with the CTH and found volume estimates to be in relatively good agreement.

Burch and Sherwood (1992) compiled data by digitizing bathymetric contours at 6-ft intervals from each map (as opposed to depth measurements from each map). Areas between contour intervals within each of the sediment volume analysis regions were measured with planimetry software, and areas were multiplied by the average water depth to determine the overlying water volumes. All water volumes were summed for an analysis region to obtain total water volume. Changes in water volume between survey years were then interpreted as changes in sediment volume (Burch and Sherwood 1992). It is assumed that similar procedures were applied in the CTH analysis (CTH 1967).

Changes that occurred from 1900 to 1990 for four regions defining the entrance area at Grays Harbor were summarized by Burch and Sherwood (1992) (Figures 3-12 and 3-13). The regions identified include nearshore areas, not the beach and shoreline. As illustrated in Figure 3-13, only the north beach nearshore region shows net accretion for the period of record (about 24 million cu yd), and about half of that accumulated between 1944 and 1948. The entrance region exhibited relatively steady erosion at a rate of about 380,000 cu yd/year. The south beach nearshore region also eroded from 1900 to 1990 at a rate of about 680,000 cu yd/year, and the bar translated offshore, outside the bar region, resulting in an overall sediment loss of about 75 million cu yd. According to Burch and Sherwood (1992), erosion in these regions amounts to about 153 million cu yd, of which 97 million cu yd occurred between 1900 and 1928.

Buijsman et al. (2003) completed a regional analysis of geomorphic change in the CRLC between the late 1800s and 1999. For the Grays Harbor area, they reported massive sand accumulation north of the entrance associated with south-to-north directed littoral transport and bypassing of the entrance. Following construction of the jetties, the entrance channel eroded and the ebb shoal translated offshore in response to the changed estuarine hydrodynamic regime (CTH 1967). South of the entrance, the beach and nearshore region to about 100-ft water depth were net erosional, although the upper shoreface (less than 30-ft water depth) showed net accretion. For the entire time period, the Grays Harbor study area was a net sink for sediment from the Columbia River, Grayland Plains, and the Grays Harbor estuary (Buijsman et al. 2003).

A critical component of the sediment transport regime at the entrance that has been addressed repeatedly since the earliest surveys of the harbor has been the magnitude and direction of net littoral drift. Before the jetties were constructed, Seattle District personnel recognized the dominant direction of transport as south-to-north (USAED, Seattle, 1965). However, the CTH (1967) stated that the predominant direction of littoral drift was from north to south. Presumably, this observation was based on sand accumulation trends north of the Grays Harbor entrance after the north jetty was constructed. Sand accumulation north of the jetty was extensive between 1908 and 1960; however, most of the sand that

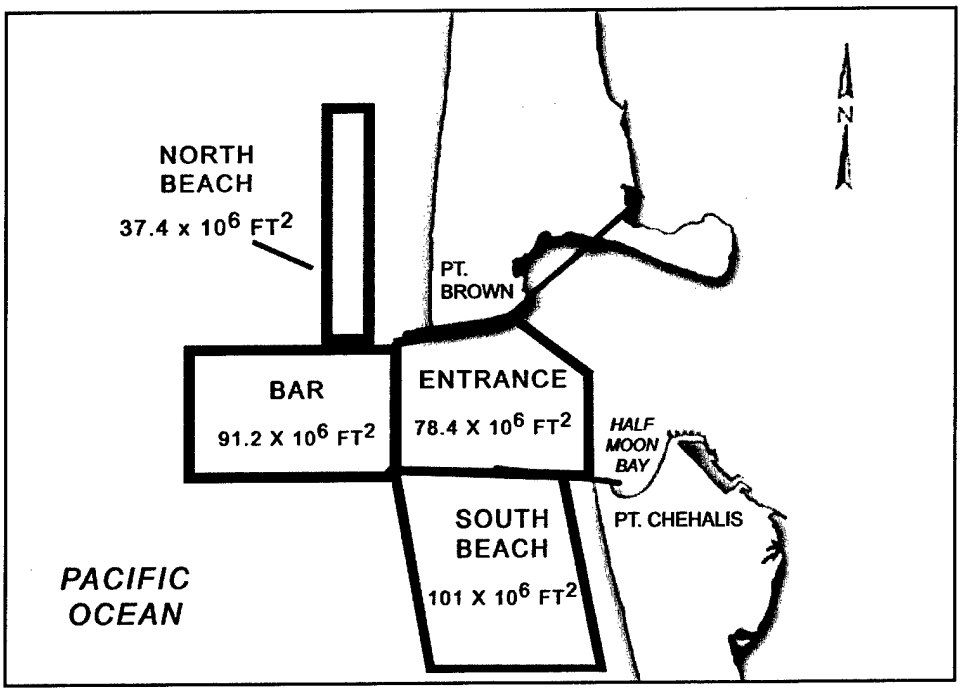

Figure 3-12. Areas for temporal comparison of sediment volumes (modified from Burch and Sherwood 1992)

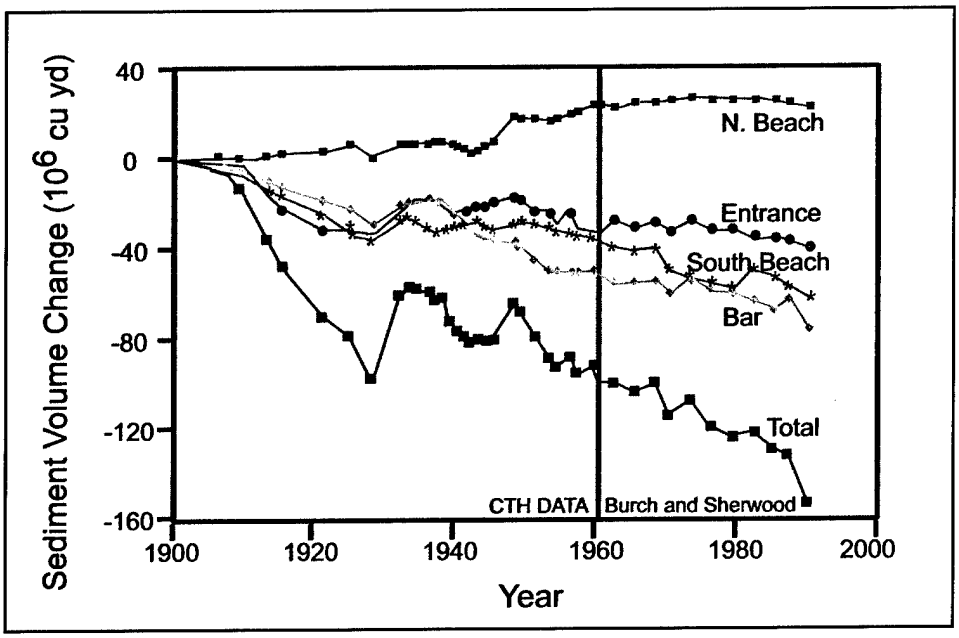

Figure 3-13. Changes in sediment volume for regions shown in Figure 3-12 combining data from CTH (1967) with that derived by Burch and Sherwood (1992) (modified from Burch and Sherwood 1992)

deposited along the north beach was the result of onshore transport from ebb shoals as the outer bar adjusted to changing hydrodynamic conditions in the estuary, not regional littoral drift (presented in the sections on Sediment Transport Pathways and Sediment Budget). As such, the estimate of 2 million cu yd/year net southward transport by the CTH (1967) grossly overestimates the actual littoral transport rate north of the entrance. South-directed longshore transport within about a mile north of the north jetty does transport sand toward the jetty and into the entrance (Schwartz and Bronson 1984), but the net direction of regional littoral drift is to the north everywhere within the CRLC (Burch and Sherwood 1992; Pacific International Engineering (PIE) 2000; Buijsman et al. 2003).

Gross and net longshore transport have been estimated with wave gauge and hindcast data by predicting potential transport (unlimited sediment supply and regular bathymetry) analytically and modeling long-term shoreline change relative to historical surveys (Chapter 6). In all cases, potential transport rate calculations (not calibrated against shoreline change trends) have overestimated rates (1 to 10 million cu yd/year; e.g., PIE 2000) relative to calibrated numerical model runs (Kaminsky, Buijsman, and Ruggiero 2000; also see Chapter 6 of this report). If wave information, transformed over variable bathymetry, is input to shoreline change prediction models, net longshore transport rates north and south of the entrance are found to be around 400,000 cu yd/year directed to the north.

Scope

This chapter documents geomorphic change at and adjacent to the entrance to Grays Harbor from 1862 to 2002. Historical shoreline and bathymetry surveys are analyzed to quantify beach and nearshore sediment-volume changes. Sediment erosion and accretion were documented within the context of major engineering events since 1898 (Table 3-2). Changes recorded prior to engineering activities were evaluated to quantify natural variability in shoreline and shoal movement at the entrance (Epoch I). Epoch II includes changes associated with construction of the north and south jetties. Epoch III summarizes changes that occurred during the first reconstruction of the jetties, and Epoch IV includes changes between the first and second jetty rehabilitations. Epoch V encompasses erosion and accretion trends that occurred after jetty rehabilitation in 1965 and before channel deepening in 1990. Epoch VI includes changes between 1987 and 2002 resulting from channel deepening and relatively minor rehabilitations to the north and south jetties. Detailed sediment budgets are presented for the periods 1954/56 to 1987 and 1987 to 2002 that describe sediment transport rates and pathways throughout the entrance area. This information documents existing conditions in the study area for evaluating potential structural alternatives to the north jetty for reducing channel shoaling and annual dredging requirements, and for assessing the response of the shoreline along the north beach.

Table 3-2
Epoch Delineation for Shoreline and Bathymetric Change Analysis at Grays Harbor, Washington

Epoch	Time Range (Shoreline)	Time Range (Bathymetry)	Description
I	1862 to 1898	1862 to 1900	Entrance condition prior to jetty construction. Reflects natural variability in shoreline and shoal movement.
II	1898 to 1916	1900 to 1921	Entrance condition during north and south jetty construction. Reflects initial response of shoreline and shoals to construction of jetties.
III	1916 to 1942	1921 to 1940	Entrance condition following north and south jetties construction, including subsequent deterioration and reconstruction (south jetty in 1939; north jetty in 1942). Illustrates shoreline and entrance area response during settling and deterioration of the jetties.
IV	1942 to 1965	1940 to 1954/56	Entrance condition after reconstruction of the jetties but prior to subsequent jetty rehabilitation. Shows response of inlet system to reconstructed jetties followed by a period of deterioration and settling.
V	1965 to 1987	1954/56 to 1987	Entrance condition during and immediately after jetty rehabilitation (south jetty in 1966; north jetty in 1976). Illustrates inlet system response to jetty rehabilitation.
VI	1987 to 2001	1987 to 2002	Entrance condition during the most recent time period. Illustrates recent changes in entrance conditions, including renewed dredging in 1991. A sediment budget for the entrance area was developed for this time period.

Data Sources

During the course of this study, it was found that shoreline and bathymetric surveys collected by the Seattle District and the USC&GS for Grays Harbor entrance and offshore bar provided the most complete coverage of inlet and nearshore morphodynamics for any known inlet in the United States. Surveys of the offshore bar and entrance area have been completed annually since construction began on the south jetty in 1898 (Appendix F). The time series of change associated with construction and rehabilitation of the jetties isolates sediment transport trends that reflect the performance of navigation structures. Shoreline and bathymetry surveys have been analyzed to document sediment transport patterns relative to engineering activities for developing comprehensive channel navigation and environmental management plans.

Shoreline position

Forty-two high-water shorelines for the 1862 to 2001 period document changes north and south of Grays Harbor resulting from natural processes and engineering activities. A description of each survey is summarized in Appendix F (Table F-1), and shorelines are plotted relative to the 1999 orthophotography. Shoreline data include 30 Seattle District field survey

shorelines, nine shorelines interpreted from aerial photography, one Light Detection And Ranging (LiDAR) survey shoreline, two shorelines developed from USC&GS topographic sheets, and one shoreline derived from a USC&GS hydrographic sheet. Positional accuracy estimates were based on procedures presented in Byrnes and Hiland (1994). The positional uncertainty estimate for 1:24,000 Seattle District field surveys is ±54 ft. For the 1:10,000 USC&GS shoreline surveys, positional uncertainty is ±32 ft. The nine shorelines derived from aerial photography were controlled with points derived from the 1:10,000 maps, resulting in a positional uncertainty of ±27 ft.

In years when more than one set of shoreline data were available, each was compared with rectified aerial photography (when available) and known ground control point locations to determine the best source for analysis. In most cases, if USC&GS data overlapped Seattle District data, the USC&GS data were chosen because shorelines on topographic sheets typically contained more detail and could be compared with geo-referenced scans of original maps. Shorelines developed from aerial photographs take precedent over USC&GS and Seattle District maps because spatial overlays between the registered aerial photograph and the interpreted shoreline can be evaluated.

An example of this procedure involved the July 1950 T-sheet (topographic maps developed by the USC&GS and the 1954 Seattle District field survey. The position of the 1950 T-sheet shoreline and the 1954 USACE field survey shoreline showed an offset of approximately 350 to 400 ft. To reconcile this discrepancy, the two data sources were overlaid on a registered aerial photograph from April 1950, and positions were compared with a shoreline interpreted from the photograph. The position of the 1954 Seattle District data to the shoreline interpreted from aerial photography was close; however, the Seattle District data were relatively small scale and some of the shoreline detail was lost. As such, the shoreline interpreted from aerial photography was used as the position for 1950 (Figure 3-14).

An independent shoreline change analysis was completed to document the evolution of Damon Point from 1921 to 2001. Damon Point is a sand spit that has formed along the northeast margin of the interior segment of the north jetty (Figure 3-14). Nineteen surveys were analyzed to represent the development of the spit in response to engineering activities. Available data sets are summarized in Table F-2 of Appendix F. Uncertainties in horizontal position are the same as presented above.

Bathymetry

Forty data sets were available for bathymetric surface comparison from 1862 to 2002. Of these, nine surfaces were selected to represent eight time periods of bathymetric change. Time periods were chosen to give the best representation of change throughout the study area during significant inlet engineering events (Table 3-2). The history of north and south jetty construction and rehabilitation, along with channel dredging records and data coverage, were all considered in determining representative epochs. A timeline detailing significant engineering events in the evolution of Grays Harbor is presented in Table 3-1. All available digital data and source information are summarized in Appendix F under the

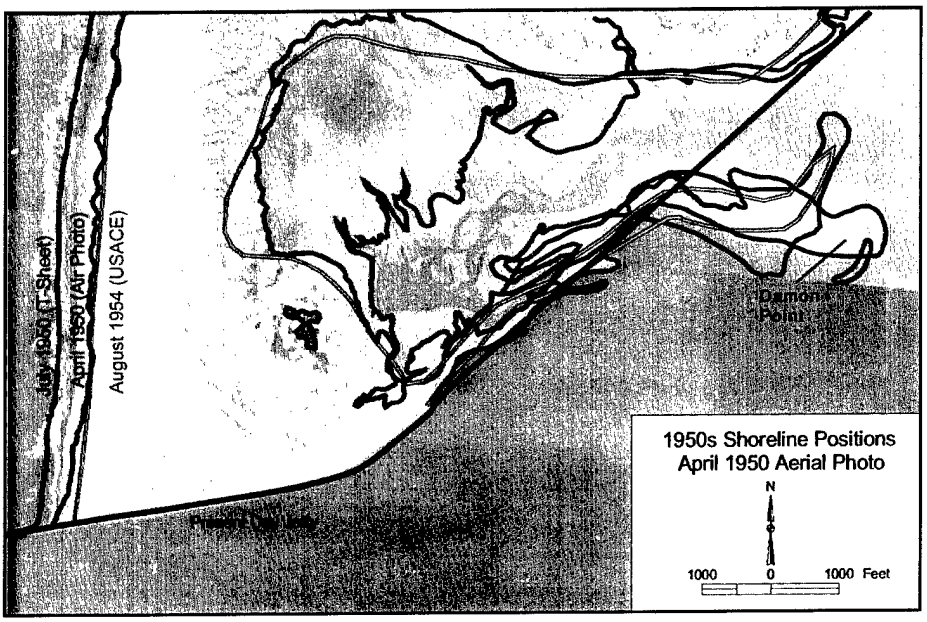

Figure 3-14. Comparison of 1950s shorelines along north beach from USC&GS (July 1950), Seattle District (August 1954), and April 1950 aerial photograph

section "Bathymetry Data Sources." The reference vertical datum for all bathymetric surfaces described below in the section "Inlet and Nearshore Morphology" is the North American Vertical Datum (NAVD). Analysis of bathymetric uncertainty associated with surface comparisons is described in Appendix F under the section "Bathymetric Surface Error and Uncertainty Estimates." Potential uncertainty was estimated for the 1954/1956 (±1.5 ft), 1987 (±1.3 ft), and 2002 (±1.3 ft) bathymetric surfaces, and a root mean square (rms) error was calculated for the 1954/1956 to 1987 (±2.0 ft), 1987 to 2002 (±2.0 ft), and 1954/1956 to 2002 (±1.8 ft) change surfaces.

Shoreline Evolution

Phipps and Smith (1978) first documented regional changes in shoreline erosion and accretion along the southwest Washington coast, examining the interval 1862 and 1977. Phipps (1990) updated the earlier study to 1987 using aerial photography, and Buijsman et al. (2003) included 1995 aerial photography to update regional change trends. In the present study, the high-water shoreline position change adjacent to Grays Harbor entrance was evaluated within the context of six major time periods defined by engineering activities.

The period 1862 to 1898 represents natural variability in shoreline response to littoral currents that move sediment on beaches adjacent to the harbor and by tidal exchange between the estuary and offshore area prior to jetty construction. Between 1898 and 1916, the south and north jetties were constructed to increase flow and promote scouring in the entrance channel. Concurrently, sediment feeding to the littoral-transport system adjacent to the entrance started accumulating along the downdrift sides of the jetties. The period 1916 to 1942

is the time after jetty construction when both structures were settling and deteriorating, followed by rehabilitation of the south jetty in 1939 and the north jetty in 1942. During most of this time, the jetties were so porous that significant quantities of sediment were transported through and over the structures, resulting in large accumulations of sand within the entrance (Appendix F, Grays Harbor regional analysis). The period 1942 to 1965 is a time of minimal engineering activity after major modifications to both jetties. Between 1965 and 1987, portions of both jetties were again rehabilitated (Table 3-1). The most recent period (1987 to 2002) encompasses a time of renewed dredging after the navigation channel was authorized to -46 ft mllw in 1990. It also is the time period adopted in this study for formulation of a sediment budget.

Regional trends

Shoreline changes between 1862 and 2001 were evaluated at shore-perpendicular transects along beaches north and south of the harbor. Transects A through D on the north beach were spaced evenly from 2.5 miles north of the north jetty (Transect A) to directly north of the jetty (Transect D). An extra transect (E) was established for the period 1862 to 1898 to evaluate shoreline position change south of Point Brown (Figure 3-15). On the south beach, Transects A through D were spaced evenly from 2.0 miles south of the south jetty (Transect D) to directly south of the jetty (Transect A). Transect locations were kept consistent through time periods to facilitate change comparisons.

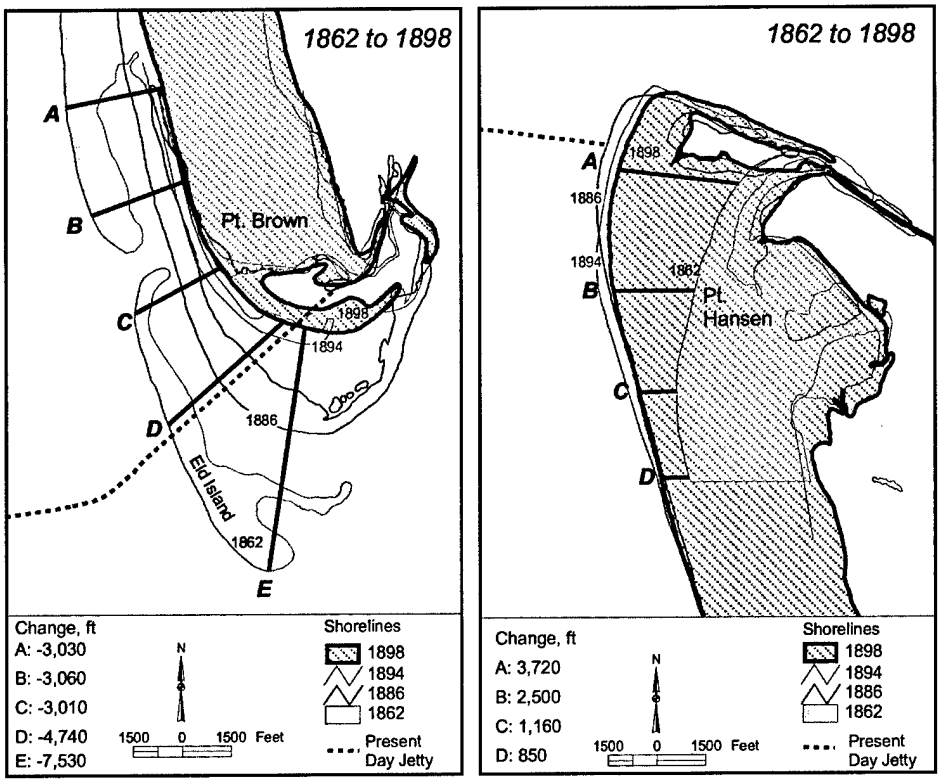

Figure 3-15. Shoreline position change prior to jetty construction north and south of Grays Harbor entrance, 1862 to 1898 (Epoch I)

Between 1862 and 1898 (Epoch I), prior to implementing navigation channel improvements, beaches adjacent to the entrance illustrated rapid change in response to channel and shoal migration forced by tidal currents and incident wave processes. The shoreline along the northern margin of the entrance, south of Point Brown, receded consistently prior to jetty construction at a rate of about 210 ft/year (Transect E; Figure 3-15). Although the magnitude of change decreased with distance from the inlet, change at Transect A (located 2.5 miles north of the present jetty position) experienced net recession at a rate of 84 ft/year. Along the south side of the inlet, the beaches fronting Point Hansen accreted rapidly from south-to-north-directed littoral transport. Two miles south of the present position of the south jetty (Transect D), the beach was accreting at a rate of about 24 ft/year between 1862 and 1898. Shoreline advance increased to about 3,700 ft (103 ft/year) near the present jetty location (Transect A), and this change was a minimum relative to two earlier surveys (Figure 3-15). Deposition along beaches fronting Point Hansen and shoreline recession seaward of Point Brown illustrate the predominance of south-to-north longshore transport and the tremendous variability in shoreline movement that existed prior to engineering activities.

Epoch II (1898 to 1916) encompasses the period required to complete the south and north jetties. The south jetty was constructed first to a height of +8 ft mllw between May 1898 and September 1902. North jetty construction began in March 1907 and was completed in January 1916 to the same crest height (Table 3-1). As inlet shoals were adjusting to new hydrodynamic conditions imposed by the entrance jetties, sand transport from south-to-north began supplying beaches north of the Harbor with sand from ebb shoals. The beaches west of Point Brown began accreting at rates of between 170 and 200 ft/year (Transects A and B; Figure 3-16). The very southern extension of Point Brown continued to recede as in Epoch I, but the recession rate was reduced to about 59 ft/year. By 1916, a small subaerial island was mapped near the bend in the north jetty, indicating that substantial quantities of sand likely were deposited below the mapped high-water line in this area.

Beaches on the south side of the entrance also accreted in response to south jetty construction. Seaward of Point Hansen, the 1903 shoreline on Figure 3-16 exhibits the initial response of beaches south of the south jetty to structure placement. Overall, the shoreline continues to advance into the harbor as sand is transported over and through the south jetty. Shoreline advance was continual at Transects B through D (54 to 70 ft/year) for the entire time period, but at Transect A, net accretion of about 120 ft/year between 1898 and 1916 was associated with incremental shoreline recession from 1909 to 1914 (Figure 3-16).

Epoch III (1916 to 1942) is a period of continual jetty deterioration (Table 3-1 and Appendix F) until jetty reconstruction was completed in 1939 and 1942 for the south and north structures, respectively. Beaches north of the north jetty experienced greatest change south of Transect B where shoreline advance ranged from about 4,500 to 7,600 ft over the 26-year period (Figure 3-17). Most change occurred between 1916 and 1921, immediately after construction of the north jetty. About 2.5 miles north of the north jetty, shoreline advance was recorded at

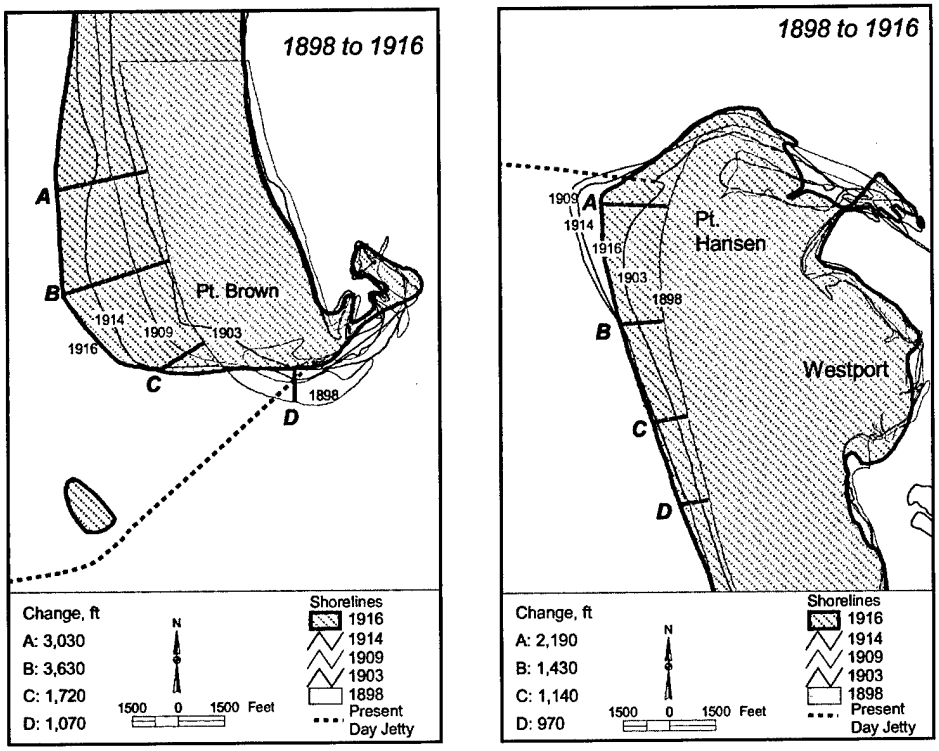

Figure 3-16. Shoreline position change associated with jetty construction north and south of Grays Harbor entrance, 1898 to 1916 (Epoch II)

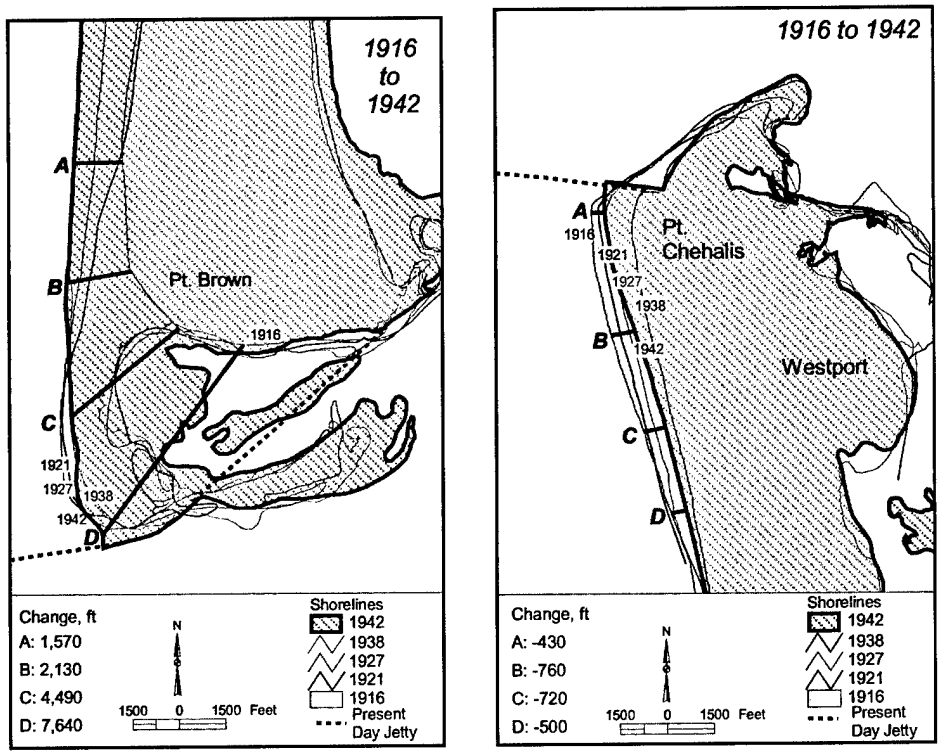

Figure 3-17. Shoreline position change associated with jetty deterioration north and south of Grays Harbor entrance, 1916 to 1942 (Epoch III)

about 60 ft/year. In addition, an extensive sand spit (the beginning of what is presently referred to as Damon Point) had developed east of the jetty as sand was transported over and through the deteriorated structure. A small section of the spit was visible in the 1921 shoreline and continued to grow significantly throughout the time period. Progradation of the spit tip between 1921 and 1942 was approximately 1 mile.

Along the south side of the harbor entrance, shoreline recession was continuous between 1916 and 1938 (Figure 3-17). Greatest changes were recorded along Transect A where the beach receded at a rate of about 62 ft/year. Along Transect D (2 miles south of the south jetty), the recession rate decreased to about 37 ft/year between 1916 and 1938. The recession trend changed to accretion between 1938 and 1942 in response to completion of south jetty reconstruction in 1939. At Transect A, the shoreline advanced 950 ft between 1938 and 1942; this accretionary trend decreased to 210 ft at Transect D. Although the shoreline north of the south jetty, along the western margin of Point Chehalis, experienced significant erosion between 1916 and 1942, Half Moon Bay did not begin to form until after 1942.

Between 1942 and 1965 (Epoch IV; Figure 3-18), shoreline response on either side of the Grays Harbor entrance was controlled by jetty reconstruction and its influence on localized littoral sand transport processes. Both jetties were reconstructed to an elevation of +20 ft mllw along their entire length seaward of the high-water shoreline. The shoreline along the north beach continued to advance, but at a rate 3 times slower than that for Epoch III (Figure 3-18). The beach at Transect A advanced at about 14 ft/year, and shoreline advance steadily increased to the south to a rate of 96 ft/year at Transect D. Littoral sand feeding Damon Point was blocked by the rehabilitated jetty, so the sand spit eroded rapidly and migrated northeast along the north jetty. Along the south beach, the magnitude of shoreline advance was smaller than to the north and varied between 10 and 20 ft/year (Transects D and A, respectively). As the beach south of the harbor accreted, Point Chehalis experienced significant erosion and had to be armored in the 1950s. Half Moon Bay started forming between 1942 and 1946, and by 1965, substantial erosion had occurred as the result of wave diffraction around the eastern end of the south jetty (Figure 3-18).

Epoch V (1965 to 1987) includes the second rehabilitation event for the north and south jetties (Table 3-1). The 1975 rehabilitation of the north jetty reconstructed a 6,000 ft section seaward of the high-water line to +20 ft mllw. In contrast to earlier rehabilitation events, shoreline change showed only moderate accretion at Transect D from 1975 to 1987 (about 18 ft/year). However, Damon Point nearly doubled in aerial extent (Figure 3-19). Although south jetty rehabilitation was completed along a 4,000-ft section seaward of the high-water line in 1966 (Table 3-1), the shoreline along the south beach was much less dynamic than that to the north. In contrast to changes recorded after the 1936/39 reconstruction event at the south jetty, the shoreline was primarily erosional between 1965 and 1987. Within about 2,000 ft of the south jetty, net shoreline recession of about 20 ft/year was recorded. South of this point to Transect D, shoreline response ranged from no change to minimal advance (Figure 3-19).

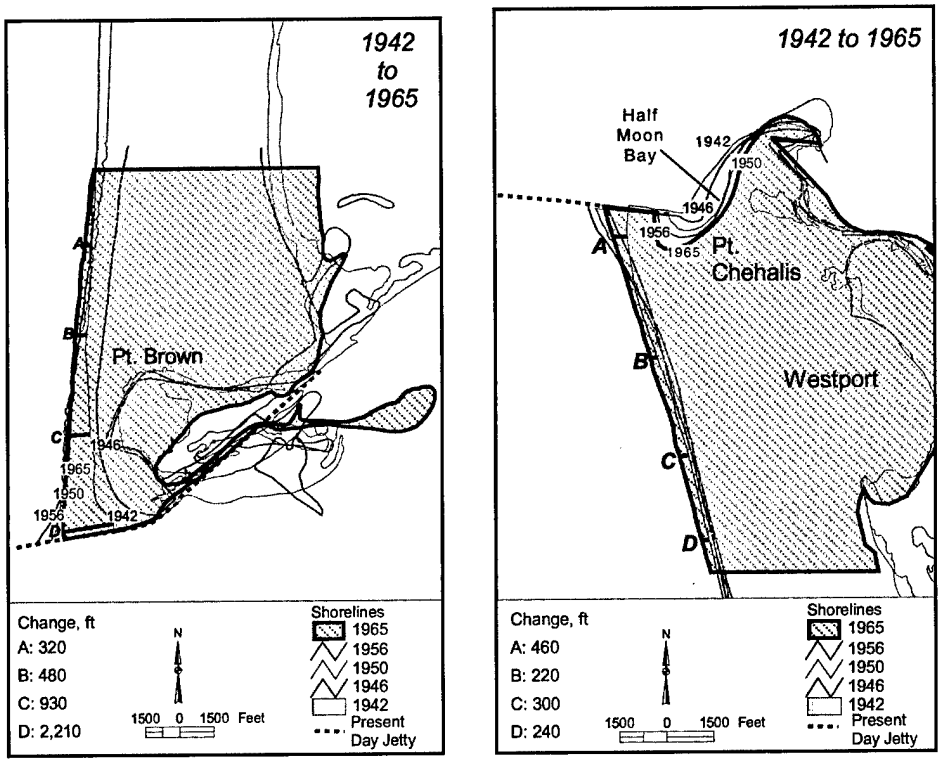

Figure 3-18. Shoreline position change associated with jetty rehabilitation north and south of Grays Harbor entrance, 1942 to 1965 (Epoch IV)

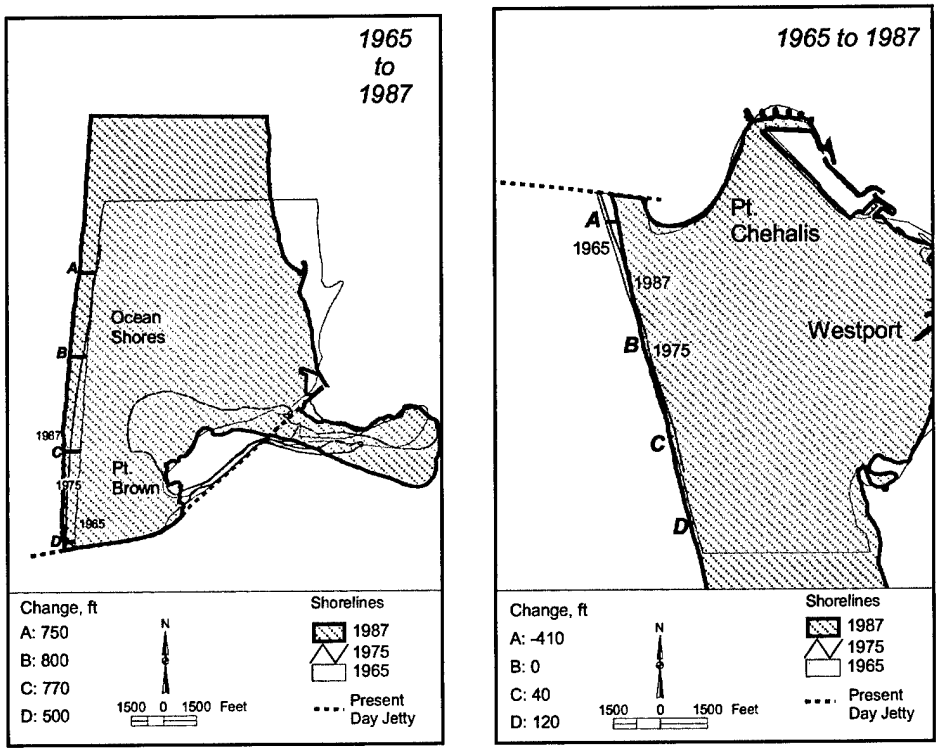

Figure 3-19. Shoreline position change associated with second jetty rehabilitation north and south of Grays Harbor entrance, 1965 to 1987 (Epoch V)

Between 1987 and 2001 (Epoch VI), the rate of shoreline advance along the north beach had decreased to about 10 to 15 ft/year (Figure 3-20). Damon Point continued to erode along its southwestern margin and accrete to the southeast. The extent of shoreline recession along the south beach increased south past Transect B in response to the breach that occurred south of the south jetty in December 1993 (visible on the July 1994 aerial photograph in Appendix F). Minor changes in shoreline position were recorded between 1995 and 2001 (USAED, Seattle, 1997). The shoreline recession rate increased from about 20 ft/year at Transect B to 27 ft/year at Transect A. No significant changes in shoreline position occurred at Transects C and D.

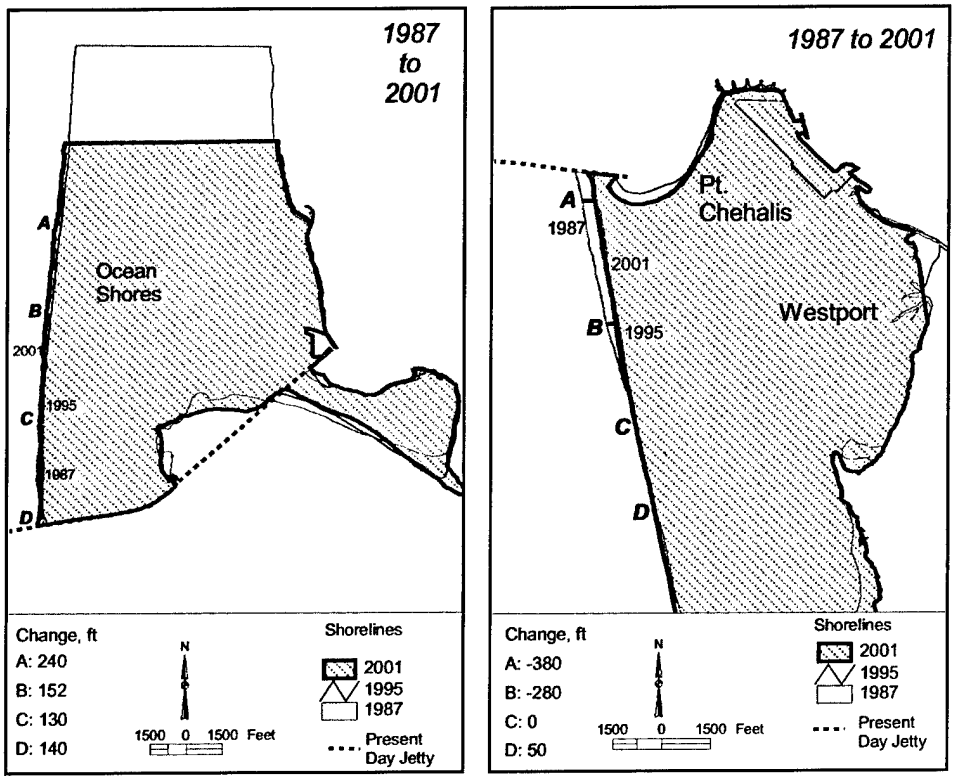

Figure 3-20. Shoreline position change associated with detailed sediment budget developed for Grays Harbor entrance, 1987 to 2001 (Epoch VI)

Cumulative changes in shoreline position between 1862 and 2001 are summarized in Figure 3-21. Greatest variations in shoreline change are associated with preconstruction changes in shoreline position (1862 to 1898) and shoreline adjustments associated with jetty construction between 1898 and 1916. Prior to jetty construction, the north beach was receding between 85 and 130 ft/year, with the greatest changes occurring closest to the entrance at Transect D. By the time the jetties were completed in 1916, shoreline advance since 1898 nearly balanced natural recession trends prior to jetty construction, resulting in minor net accretion between 1862 and 1916 at Transects A and B. Between 1917 and 1920, rapid sediment accumulation occurred north of the north jetty resulting in no net change along Transects C and D between 1862 and 1920. By 1925, the

north beach had advanced seaward at all transects, with greatest beach accretion between 4,000 and 9,000 ft north of the jetty at Transects B and C. It was not until after reconstruction of the north jetty in 1942 that the beach at Transect D advanced seaward of all locations north of this point relative to the 1862 shoreline (Figure 3-21). Since 1948, shoreline advance along the north beach has been greatest near the jetty, decreasing in magnitude to the north.

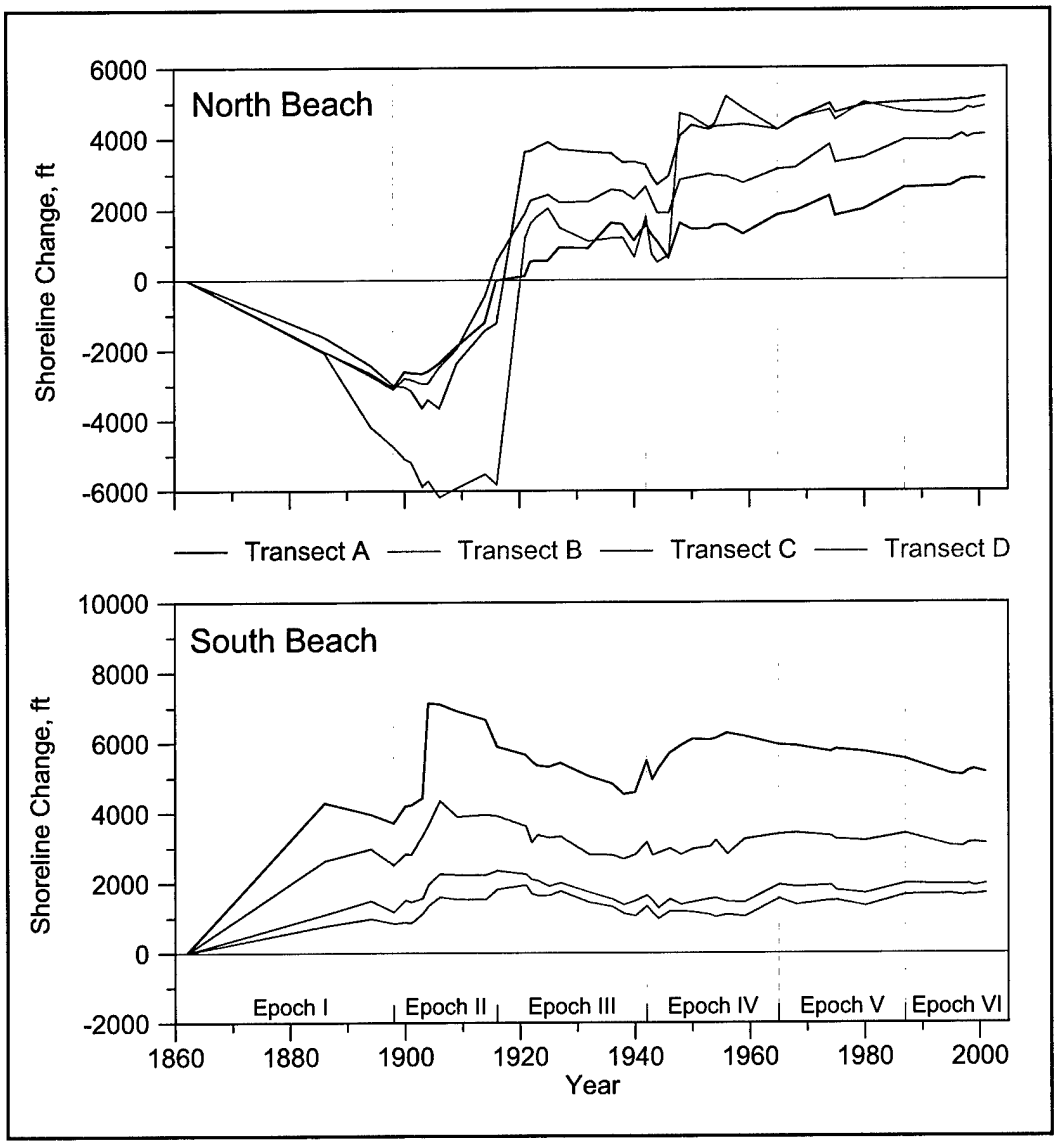

Figure 3-21. Cumulative shoreline change north and south of Grays Harbor entrance, 1862 to 2001

Along the south beach, the opposite trend was recorded. Prior to and during construction of the south jetty, shoreline advance was dominant along the south beach. By 1904, the beach at Transect A began receding and, by 1909, the beach at all transects south of the south jetty was receding. This trend of gradual erosion continued until after the jetty was rehabilitated in 1939. Since 1942, the shoreline along Transects B, C, and D has been stable to accreting. However, after continuous shoreline advance at Transect A between 1944 and 1956, recession has dominated through 2001.

Seasonal variability

Topographic survey data collected by the WDOE between 1997 and 2001 along the north beach (Ruggiero and Voigt 2000) were analyzed to evaluate seasonal variability in shoreline position for beaches adjacent to Grays Harbor. Annual trends in shoreline movement can be compared with seasonal changes to estimate the variability and existence of trends. Variations between winter and summer shoreline position at Transects A through D illustrate differences ranging from 30 to 310 ft. Transect D is located closest to the north jetty and represents the region of greatest seasonal variability (Figure 3-22). It also is the beach area of greatest interest relative to study alternatives, modeled sediment transport rates, and sediment budget analyses.

Figure 3-22 documents differences in shoreline position at Transect D for winter and summer beaches between 1997 and 2001. Shoreline change ranges from 40 to 310 ft between winter (March) and summer (September). Annual changes in shoreline position are least variable for the winter season, resulting in a maximum horizontal distance of 80 ft over 4 years (bottom graph in Figure 3-22). This number is about 25 percent of the change recorded between summer 1997 and winter 1998. Because historical shoreline surveys were performed between April and December throughout the period of record, seasonal change calculations offer a means of estimating the significance of long-term trends relative to annual variations in beach response. It also provides a way to judge the meaning of modeled shoreline change estimates for evaluating project alternatives.

Shoreline change at Damon Point

After construction was completed on the north jetty in 1916, large quantities of sand accumulated north of the jetty creating a wide low-relief beach (Figure 3-17). By 1921, sand transported to and deposited north of the jetty began to migrate through and over the northeastern extension of the jetty (+8 ft mllw elevation at this time), creating a small peninsula representing the initial formation of the feature currently known as Damon Point. Kaminsky et al. (1999) documented the evolution of Damon Point between 1967 and 1998 noting the low relief of the feature that has resulted in overtopping and washouts across the western end of the sand spit in 1997 and 1998. The evolution of Damon Point is of interest to this study because the spit has been a deposition area for eastward

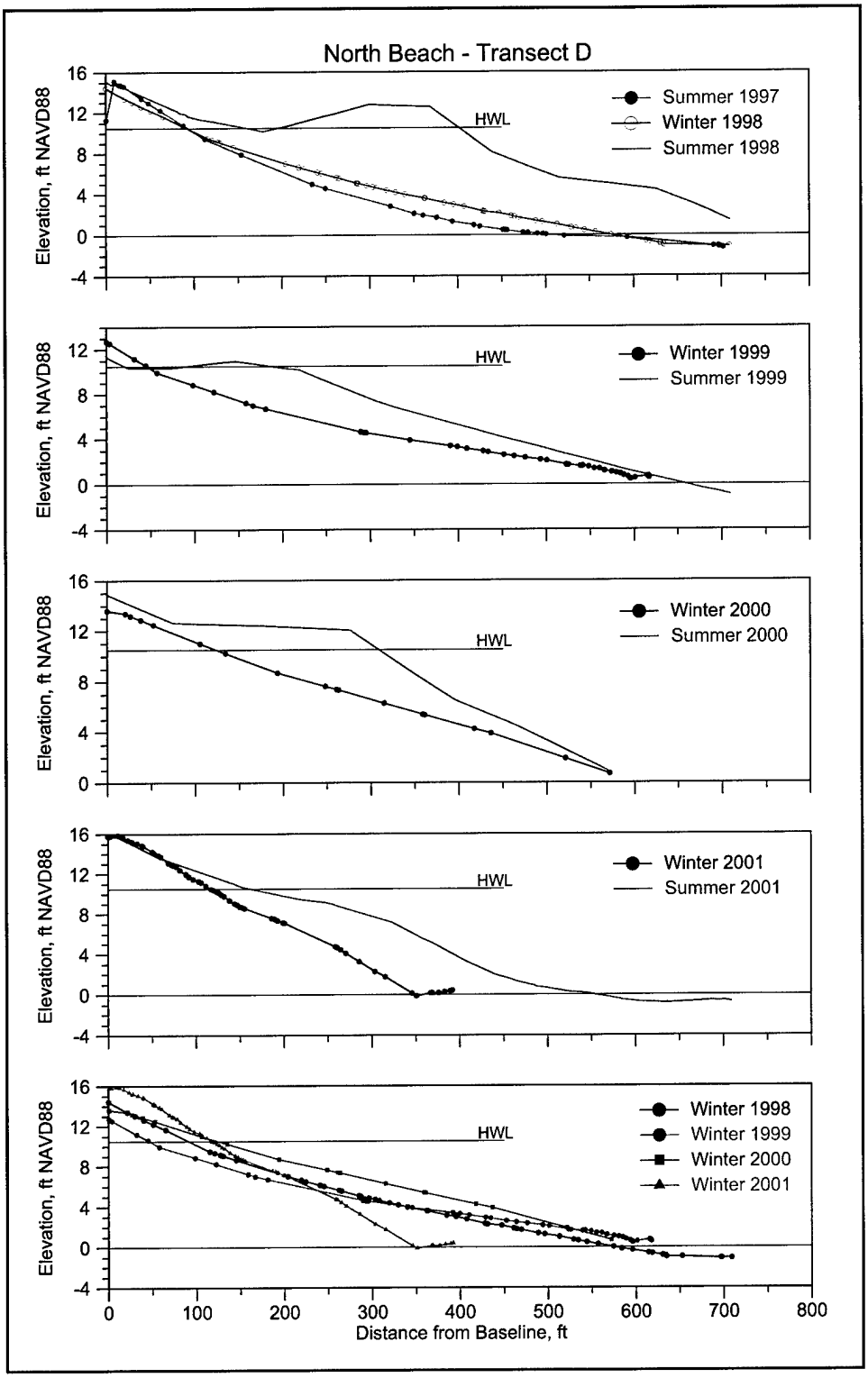

Figure 3-22. Seasonal variability in high-water shoreline position along north beach at Transect D (data from Ruggiero and Voigt 2000)

transport of sand into the estuary from the north beach over the past 80 years. As documented on bathymetric change maps and in the sediment budget for the entrance area, sand deposition in the Point Chehalis and the entrance channel reaches of the navigation channel is partially supplied by transport from Damon Point.

In 1921, transport of beach sand over and through the northeast extension of the north jetty created a small sand spit that evolved into a much larger feature by 1942. Rapid growth occurred between 1921 and 1927 as sand streamed through the jetty in an eastward direction (Figure 3-23). The sand spit continued to expand to the east and north at a slightly slower rate from 1927 to 1942, resulting in an extensive feature that accumulated at a rate of about 670,000 cu yd/year (3 August 1938 and 4 September 1943 photographs in Appendix F).

After reconstruction of the north jetty to +20 ft mllw in 1942, sand transport to Damon Point from the north beach was blocked. The 4 September 1943 aerial photograph (Appendix F) documents that a beach that had formed at the western end of the sand spit adjacent to the jetty had narrowed in response to blocked sand transport from the north beach. By 1944, the narrow beach area was breached by waves and currents, and the peninsula became an island that continued to decrease in size until 1950, when it reformed as a relatively small sand spit attached to the jetty about 4,700 ft to the northeast of its location in 1921 (Figure 3-23). Reconstruction of the north jetty in 1942 eliminated the flow of sand to Damon Point until the north beach advanced seaward enough to begin bypassing south-directed sand through and around the jetty and toward Damon Point. By 1950, this sand bypassing process was renewed and the sand spit began to widen and lengthen to the east (Figure 3-24). By 1965, the core of the modern Damon Point had formed.

Between 1965 and 1981, the sand spit continued to expand along its eastern margin to the south (Figure 3-24). Although the north jetty was rehabilitated in 1975, the width of the beach along the spit increased to the south and east as the entire deposit became more extensive. Evidently, sand transported around the jetty and into the entrance toward Damon Point was not interrupted by rehabilitation activities in 1975. This observation is corroborated by shoreline change data for the area just north of the jetty (Transect D), where no net change in high-water shoreline position was recorded between 1975 and 1987 (Figure 3-19). No net change in shoreline position suggests that sand transport to this area is flowing around the jetty and into the entrance, where dominant flood currents (Chapter 7) can transport sediment toward Damon Point.

Sand spit growth to the southeast along the eastern end of Damon Point and shoreline recession along the western half of the peninsula continued between 1981 and 1997 (Figure 3-25). The eastern shoreline of Damon Point experienced little change during this period as the terminus of littoral transport encountered strong ebb currents in a dominant north-south channel along the eastern margin of the spit. This process is known as dynamic diversion (Todd 1968), and it is the primary mechanism by which subaerial and subaqueous deposits associated with Damon Point have formed since 1967 (Figures 3-24 and 3-25). Deposition of littoral sediment began to extend the southeastern shoreline of Damon Point to the east between 1997 and 2001, and the subaqueous portion of the spit

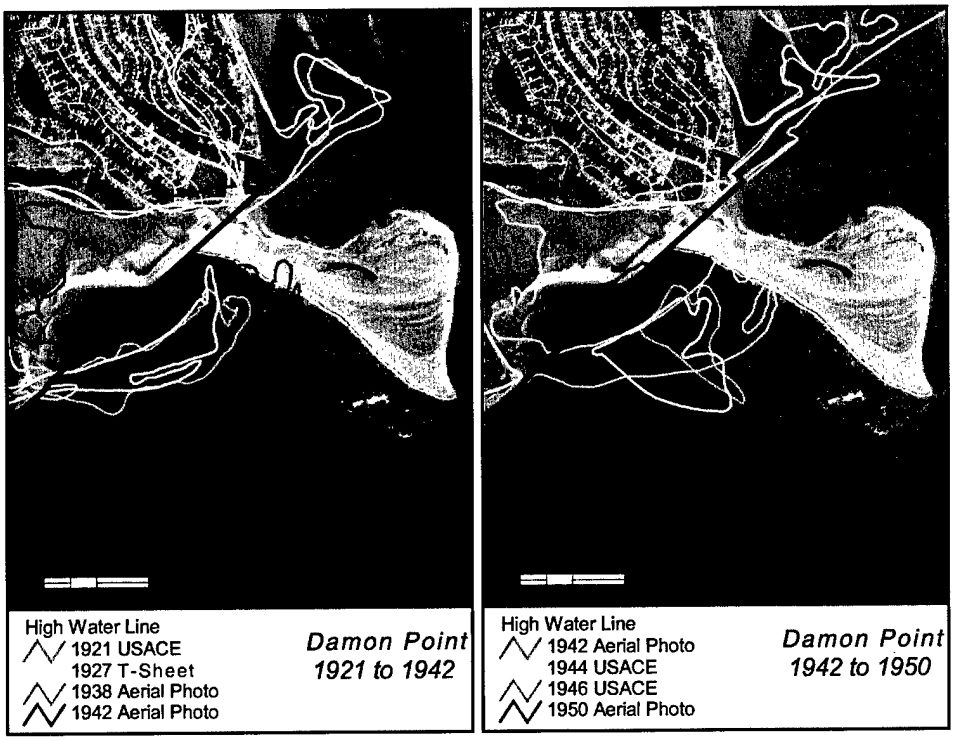

Figure 3-23. Evolution of Damon Point sand spit between completion of north jetty in 1916 and reconstruction in 1942, and post-reconstruction shoreline response by 1950

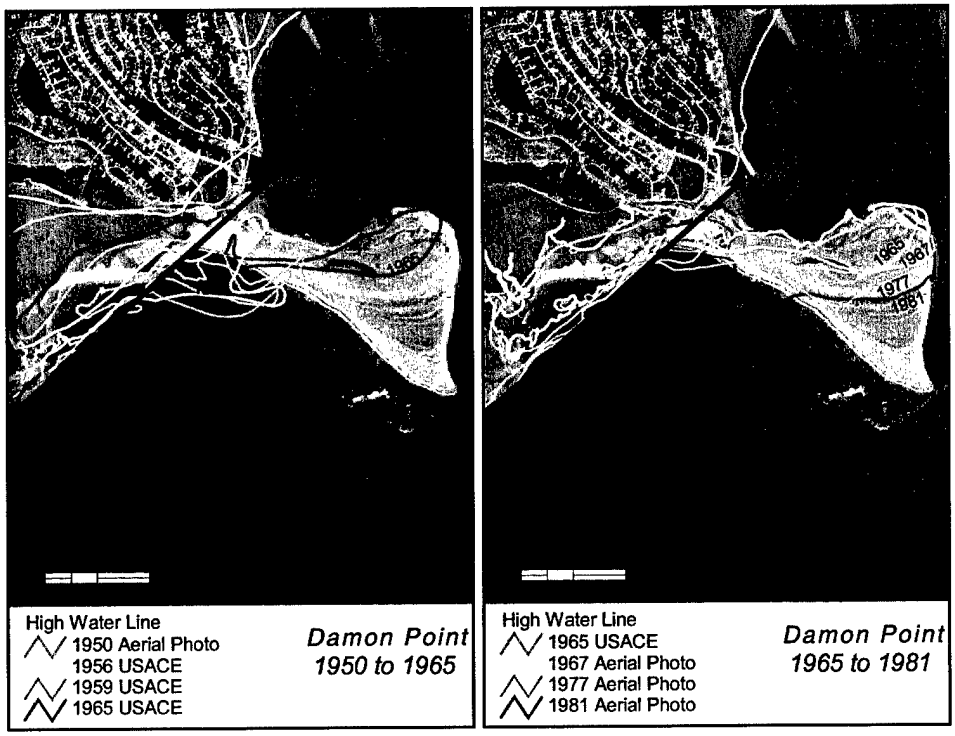

Figure 3-24. Evolution of Damon Point sand spit between 1950 and 1981

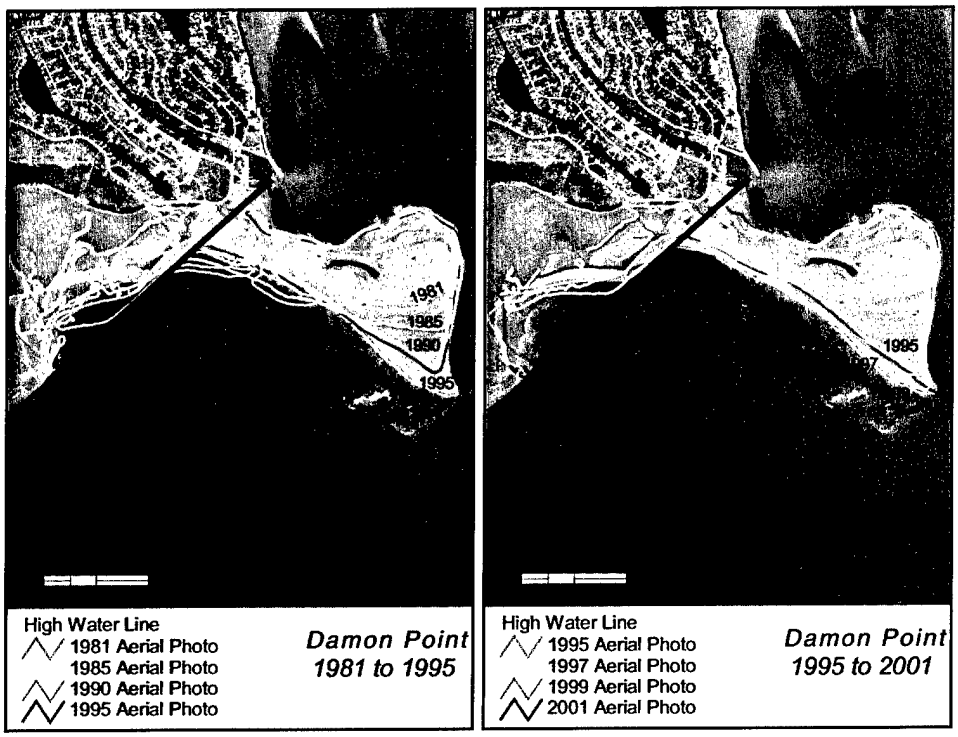

Figure 3-25. Evolution of Damon Point sand spit, 1981 to 2001

expanded substantially (see section on Sediment Transport Pathways). The beach along the western half of the spit continued to slowly erode because the net supply of sand to this region was insufficient to balance the erosive energy of waves and currents. As the western end of Damon Point continues to erode, the area will become more vulnerable to overtopping by waves and potential breaching. Kaminsky et al. (1999) discuss the character of two washover events in 1997 and 1998 along the western half of the spit that may be a precursor to a future breach in this area.

Inlet and Nearshore Morphology

Although shoreline response adjacent to entrances contains a record of the influence of coastal processes on beach response, regional patterns of inlet and nearshore morphology better reveal the dominant processes controlling the magnitude and direction of sediment transport throughout the inlet system. Analysis of long-term change in seafloor morphology provides a method of identifying net sediment transport pathways, quantifying volume changes, and evaluating sediment budgets for assessing large-scale evolution of coastal depositional systems.

Prior to jetty construction at Grays Harbor, the morphology of ebb-shoal sand deposits appeared much like those associated with other natural inlet systems separating offset barrier beaches (Hayes and Kana 1976; Hayes 1991).

Figure 3-26 illustrates the regional characteristics of nearshore morphology in the study area for 1862 and 1894. In 1862, shoals adjacent to the beaches north and south of the entrance were shallow and extensive. The shoreline and shoals north of the channel (Eld Island and North Spit) extended into the entrance about 2 miles south of Point Brown, whereas a shallow subaqueous sand spit north and west of Point Hansen (south of the channel) controlled the position of the channel as it exited the estuary. The primary channel between these shoals directed water and sediment from three secondary estuarine channels (Humptulips River Channel, Main Channel, and Ocosta Channel) through the entrance and to the northwest after it encountered a large, shallow spit seaward of the entrance called South Spit. At this time, the ebb shoal was skewed to the northwest because of the orientation of the channel. The deepest part of the channel was located at the confluence of the three estuarine channels between Eld Island and South Spit, features resulting from littoral transport north and south of the harbor. Maximum depths were about 90 ft NAVD that shoaled rapidly on the ocean side of the entrance to 10 to 20 ft NAVD. The presence of South Spit south of the channel, extending to the northwest, indicated the dominant direction of net transport in 1862 was from south-to-north.

By 1894, the shoreline at Point Hansen had advanced north and west by about 4,000 ft (Figure 3-26). The shallow subaqueous shoal labeled South Spit in 1862 still existed in 1894, but was reduced in extent. The main channel was oriented east-west at this time and had scoured to about 100 ft at its deepest point. The shoreline north of the channel retreated to the north between 1862 and 1894 about 4,100 ft, but the sand platform upon which the shoreline was perched in 1862 remained as an extensive subaqueous shoal called North Spit. The shape of the ebb shoal was well defined by the 30-ft-depth contour, with broad and shallow sand deposits dominating the ebb shoal north of the channel. Orientation of the shoal and channel indicates north-directed littoral transport and bypassing from the beach fronting Point Hansen to the beach and broad expanse of shallow sand shoals seaward of Point Brown.

By 1900, the south jetty seaward of the high-water line was completed to about half its authorized length. Hydrodynamic response to the jetty was rapid. The beach south of the jetty began to accrete in 1900, and the subaqueous sand flat seaward of Point Hansen (South Spit), as defined by the 10-ft-depth contour, had decreased in size (Figure 3-27). The greatest amount of shoreline advance south of the south jetty occurred between 1903 and 1906, just after the jetty was completed in 1902 (Figure 3-21). The main purpose for jetty construction was to constrain flow within the entrance area to create a self-scouring channel for safe navigation. In fact, after the south jetty was completed, the main channel became well defined, scouring to a maximum depth of about 110 ft and extending the ebb shoal (as defined by the 20-ft-depth contour) seaward of its position prior to jetty construction. An exit channel deeper than 20 ft formed to the northwest of the main channel by 1900 (Figure 3-27). Low-relief sand flats and shoals remained seaward and to the south of Point Brown, posing a potential hazard by shoaling in the navigation channel.

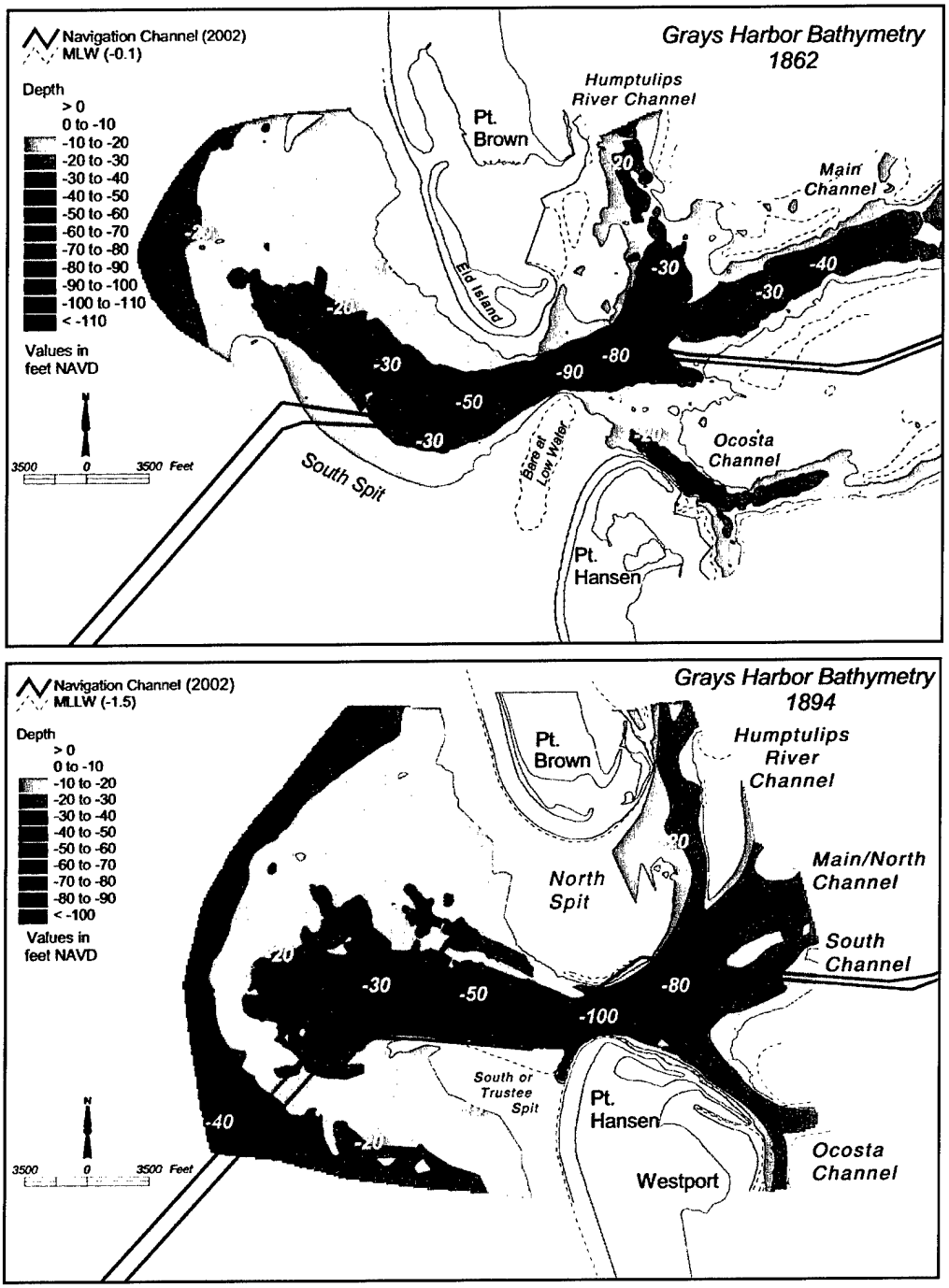

Figure 3-26. Bathymetric surface morphology for Grays Harbor entrance prior to jetty construction, 1862 and 1894

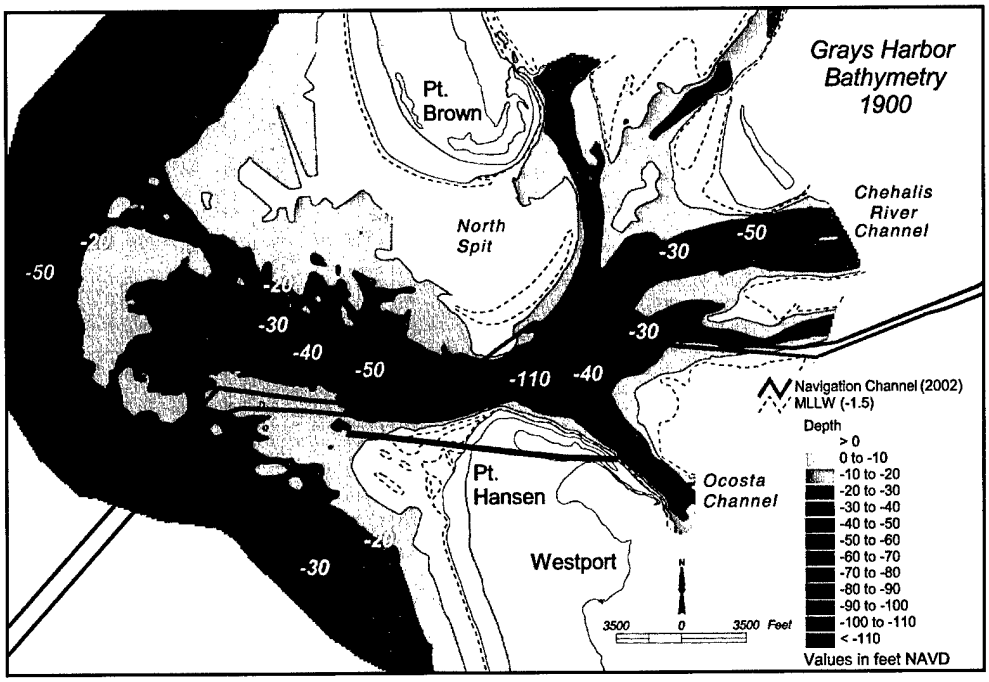

Figure 3-27. Bathymetric surface morphology for Grays Harbor entrance half way through construction of south jetty, 1900

To alleviate channel navigation hazards and reduce localized sediment transport from beaches seaward of Point Brown into the northern portion of the entrance area, construction of the north jetty was authorized in 1907 and completed in 1916. By 1921, hydrodynamics and sediment transport within the entrance area had created a self-scouring area between the jetties that was about 40 to 50 ft deep (Figure 3-28). The shoreface seaward of Point Hansen eroded after construction of the south jetty through alteration of waves and currents that had formerly deposited and redistributed sediment in this part of the inlet system.

The 40-ft-depth contour was now within about 8,500 ft of the high-water shoreline seaward of Westport in 1921, whereas the contour at this location in 1900 was at a depth of 30 ft or shallower. Beaches north of the north jetty advanced thousands of feet seaward by 1921 as a result of jetty construction (Figures 3-16 and 3-17). However, the shoreface fronting these beaches became deeper because stronger current speeds at the entrance mobilized sand from shoals 20-ft deep and shallower (ebb-shoal system of 1900) and transported sediment to the west and north of the entrance (Figure 3-28). On the 1921 bathymetric surface, the 20-ft-depth contour was not present on the ebb shoal, whereas it was a prominent feature of the ebb shoal on the 1900 bathymetric surface (Figure 3-27). A large portion of the entrance shoal system north of the channel in 1900 appears to have rapidly migrated onshore after construction of the north jetty, creating what is now known as Ocean Shores. Some of the eroded sediment was transported westward by strong ebb-tidal currents and deposited in water depths deeper than 50 ft NAVD seaward of the ebb shoal.

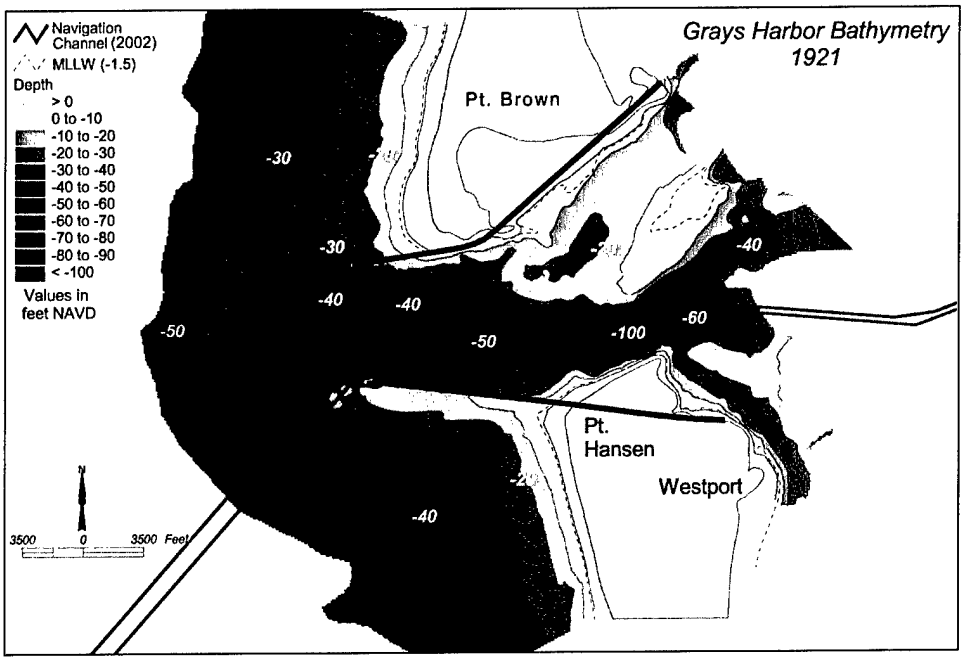

Figure 3-28. Bathymetric surface morphology for Grays Harbor entrance after construction of north and south jetties, 1921

The north and south jetties began to subside rapidly because erosion by tidal currents destabilized the foundation, and wave forces displaced individual stones (USAED, Seattle, 1965, 1974). The south jetty was reconstructed to an elevation of +20 ft mllw between 1936 and 1939, and the north jetty was reconstructed to the same elevation between 1941 and 1942. The 1940 bathymetric surface primarily documents the response of beach, nearshore, and entrance areas prior to reconstruction of the jetties (Figure 3-29). Within the entrance, a large shoal north of the channel and east of the north jetty in 1921 had nearly disappeared by 1940. However, deterioration of the north jetty provided a pathway for sediment transport through and over the jetty, and by 1940 an extensive sand spit had formed inside the entrance to the east of the north jetty (see discussion above on Damon Point).

Overall, the entrance area continued to deepen as average water depths between and just seaward of the jetties were about 40 to 50 ft (Figure 3-29). The ebb shoal, as defined by the 30-ft-depth contour, had eroded since 1921, particularly along the southern half of the feature. The northern portion of the ebb shoal seaward of Point Brown was similar to what it was in 1921, except a relatively small 30- to 40-ft deep channel separated north and south portions of the shoal in 1940. In addition, the southern portion of this feature had shoaled to -20 ft in two small areas, indicating that net sediment bypassing from south-to-north had been maintained after jetty construction. The most significant changes that occurred south of the channel were erosion of sand from the nearshore seaward of Point Chelalis and an erosion offset between the beaches north and south of the south jetty. According to Figure 3-17, this offset began forming after reconstruction of the south jetty was initiated.

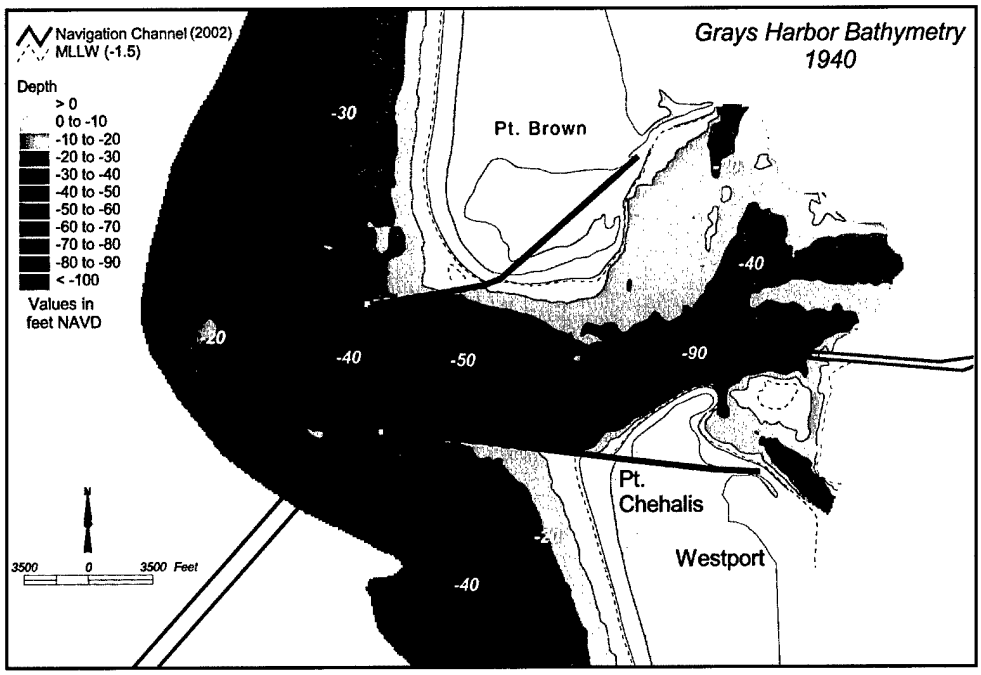

Figure 3-29. Bathymetric surface morphology for Grays Harbor entrance prior to reconstruction of north and south jetties, 1940

The 1954/56 surface documents bathymetric change after reconstruction of the north and south jetties in 1939 and 1942, respectively. At the coast, the beaches north and south of the entrance advanced seaward because sand transported toward the inlet was blocked by the jetties. The 20-ft-depth contour was at the seaward end of the north jetty at this time. The extensive sand spit eastward of the north jetty deteriorated after reconstruction of the north jetty in 1942, and it appears that much of the sand associated with this feature was transported to the southwest along the northern margin of the channel by ebb currents (Figure 3-30). Between 1940 and 1954/56, the ebb shoal within the 30-ft-depth contour eroded substantially because sand was transported north and onshore to beaches fronting Point Brown and offshore to deeper water. While the beach just south of the south jetty accreted between 1942 and 1956, impoundment of littoral transport from the south caused erosion of the Point Chehalis shoreline north of the jetty, first creating an offset between beaches on either side of the jetty which led to an erosional cove landward and south of the jetty that started between 1944 an 1946 (Appendix F).

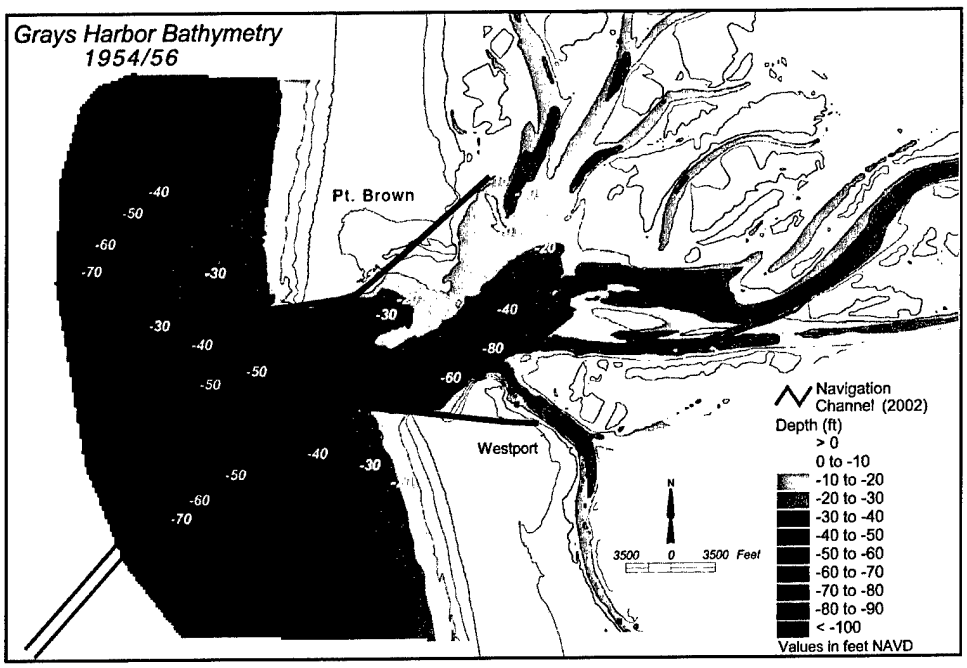

Figure 3-30. Bathymetric surface morphology for Grays Harbor entrance after reconstruction of north and south jetties, 1954/56

By 1987, the bathymetric surface describing the Grays Harbor entrance and vicinity had changed substantially (Figure 3-31). Engineering activities between 1954/56 and 1987 included rehabilitation of the north and south jetties in 1976 and 1966, respectively. Rehabilitation was not completed for the entire length of either jetty, however. As such, sand transported by the north-to-south-directed longshore current freely moved around the north jetty and into the estuary via the flood current, creating a large subaerial and subaqueous spit referred to now as Damon Point. Localized transport of sand to Damon Point has been supplied by onshore movement of sand from the ebb shoal, as indicated by erosion of the shoal and recession of the 30-ft-depth contour seaward of the beaches fronting Point Brown. In 1954/56, the 30-ft-depth contour was located about 2 miles seaward of the north jetty tip, and by 1987, the contour was just seaward of the jetty tip (Figure 3-31).

Within the entrance, the deepest portion of the channel shoaled to about 70 ft as the system continued to adjust to changing hydrodynamic conditions imposed by partial jetty rehabilitation. In addition, the channel thalweg extended to the northeast as Damon Point expanded to the east, constricting flow in Humptulips Channel between Sand Island and Damon Point. The beach and nearshore area defined by the 10-ft-depth contour south of the south jetty was generally accretional between 1956 and 1987, but erosion along the landward end of the jetty continued to a maximum in 1965, creating an erosional cove known as Half Moon Bay.

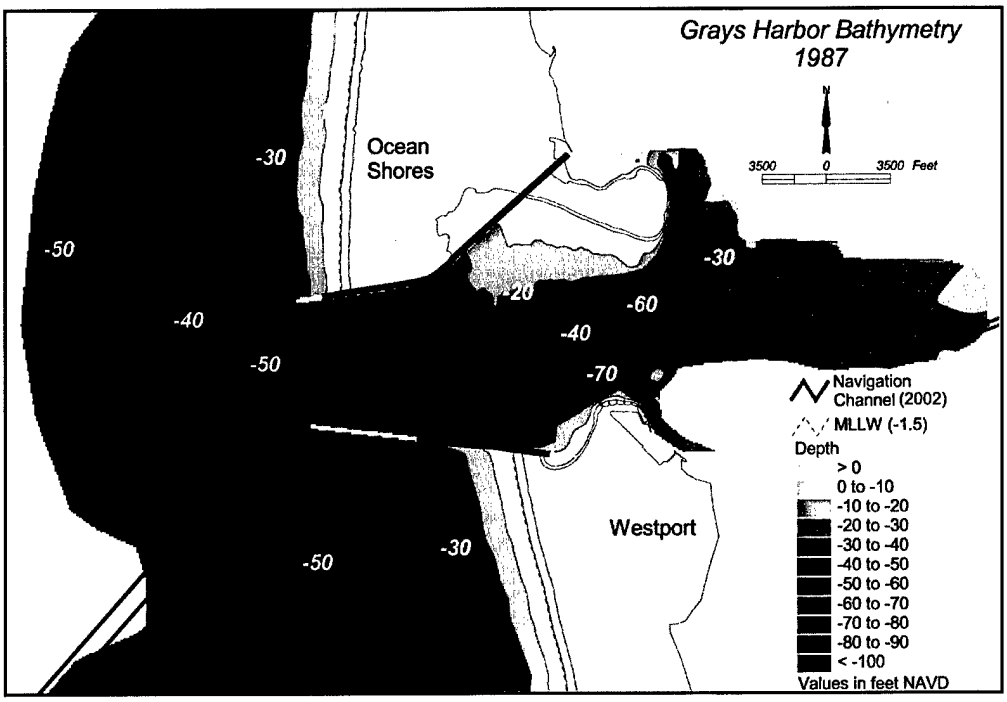

Figure 3-31. Bathymetric surface morphology for Grays Harbor entrance (1987) after partial rehabilitation of north and south jetties in 1965 and 1976, respectively. White areas seaward of jetties represent sections of original jetties that were not rehabilitated

Between 1987 and 2002, the ebb shoal continued to deflate because sediment from the shallowest portions of the shoal was eroded and transported offshore to the north and west and onshore to the nearshore and beach fronting Ocean Shores (Figure 3-32). Similar to the pattern of change displayed for the 30-ft-depth contour on the ebb shoal between 1954/56 and 1987, the 40-ft-depth contour moved north and east between 1987 and 2002 as the ebb shoal continued to erode in response to storm waves and tidal currents. East of the north jetty, an extensive subaqueous sand spit continued to expand to the southwest along the margin of the channel as Damon Point accreted to the southeast. Encroachment of the sand spit on the channel scoured the channel to depths greater than 80 ft. Sedimentation within the entrance area is strongly influenced by the evolution of Damon Point because sand is eroded from the seafloor fronting Damon Point and transported toward the channel and entrance area.

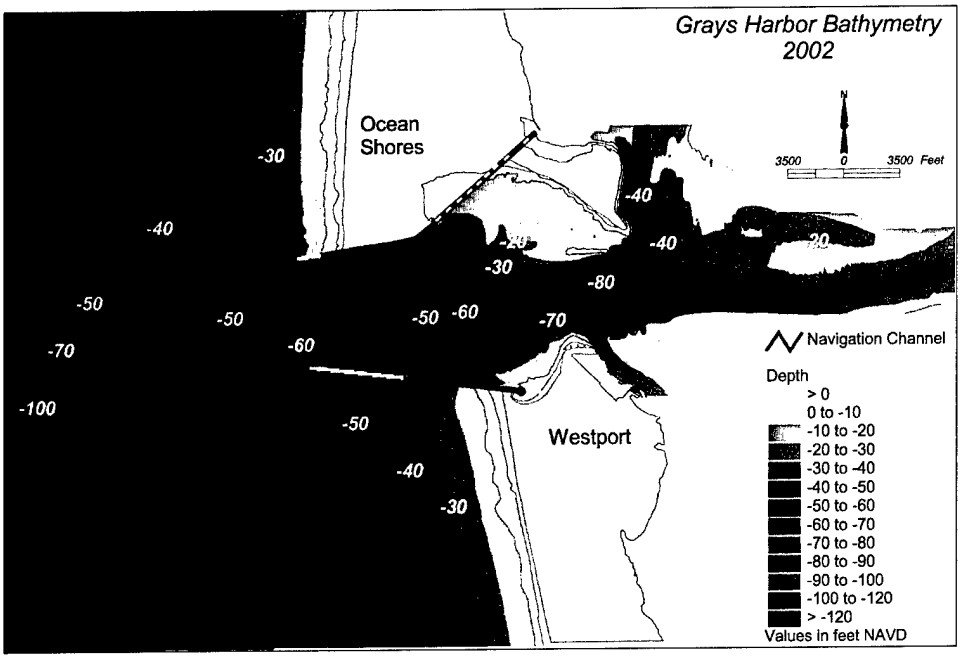

Figure 3-32. Most recent bathymetric surface morphology for Grays Harbor entrance (2002). White areas seaward of jetties represent sections of original jetties that were not rehabilitated

Shoal and Channel Evolution

Cross sections of the inlet area and nearshore were developed to document the temporal evolution of the channel and shoals associated with the Grays Harbor entrance between 1900 and 2002 (Figure 3-33). Cross-section 1 represents the evolution of the southern portion of the ebb shoal, changes within the entrance area, and development of Damon Point from a southwest to northeast approach. Cross-sections 2-4 document the evolution of the entrance area, across the ebb shoal from the 50- to 60-ft-depth contours through the inlet entrance from west to east, in the dominant direction of flow (parallel to the entrance). Cross-section 5 is oriented north-south to record the evolution of the ebb shoal. Cross-sections 6 and 7 illustrate the development of the channel and entrance area as hydrodynamic conditions changed during construction and rehabilitation of the jetties. For all cross sections, the greatest amount of change occurred between 1900 and 1954/56. Large quantities of sediment were moved throughout the entrance and on the ebb shoal as changing hydrodynamic conditions associated with jetty construction and rehabilitation scoured the entrance area. The placement of the cross sections was designed to capture significant changes in bathymetry resulting from jetty construction.

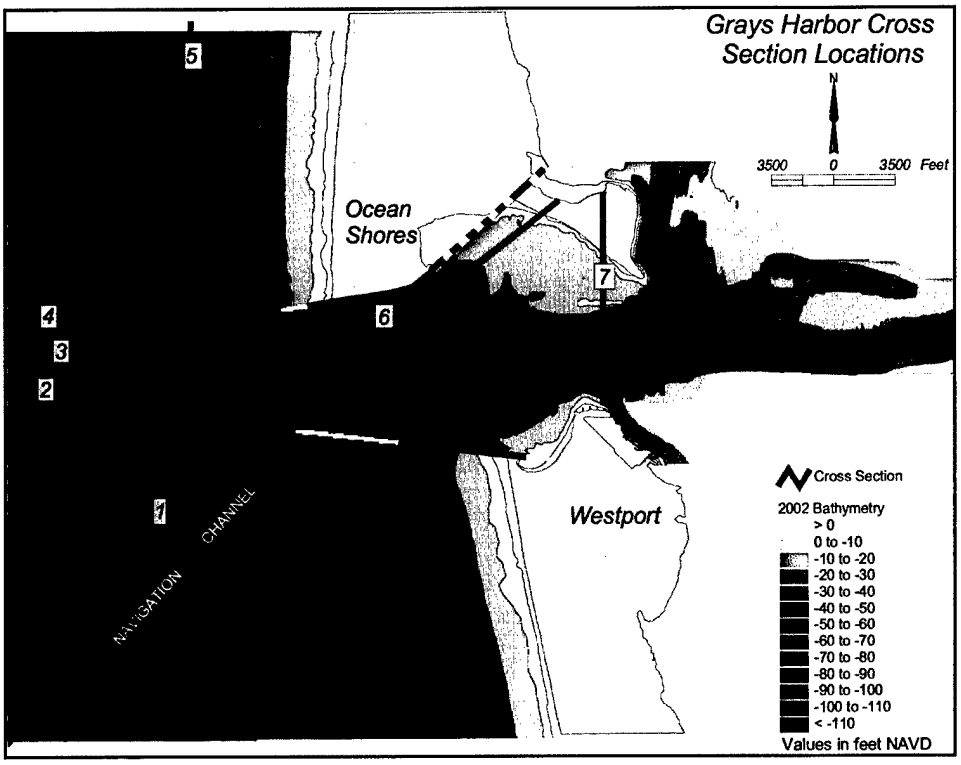

Figure 3-33. Cross-section locations for documenting channel and shoal development and movement between 1900 and 2002

Cross-section 1 documents the continuous degradation of the southern lobe of the ebb shoal after completion of the south jetty in 1902. In 1900, the minimum water depth over this portion of the ebb shoal was less than 20 ft. By 1921, minimum water depth over the southern part of the ebb shoal increased to about 25 ft to a distance 5,000 to 6,000 ft southwest of the shoal in 1900. Stronger ebb-tidal currents that were confined by the jetty eroded sediment from the ebb shoal and transported it to the north and offshore. By 1954/56, after reconstruction of the south jetty, minimum water depth over the southern portion of the ebb shoal was about 40 ft, approximately 4,500 ft seaward of the minimum depth in 1940. Minor changes in water depth have occurred since this time, resulting in a minimum depth of about 45 ft in 2002 at a distance 2,500 ft southwest of the end of the original jetty (Figure 3-34).

The northeastern end of Cross-section 1 records the development of Damon Point. By 1940, Damon Point had become an extensive subaerial and subaqueous feature. However, after sand transport to this area was stopped due to reconstruction of the north jetty in 1942, Damon Point began to degrade and migrate to the northeast under the influence of west-southwest waves and flood currents. Between 1954/56 and 1975, sand shoals fronting Damon Point appear to have migrated to the southwest toward the channel (Figure 3-34). However, shoal migration trends have not been as clear to understand along this transect since this time. Although the south and north jetties were rehabilitated in 1966 and 1976, only minor depth changes occurred in the entrance area between 1954/56 and 2002.

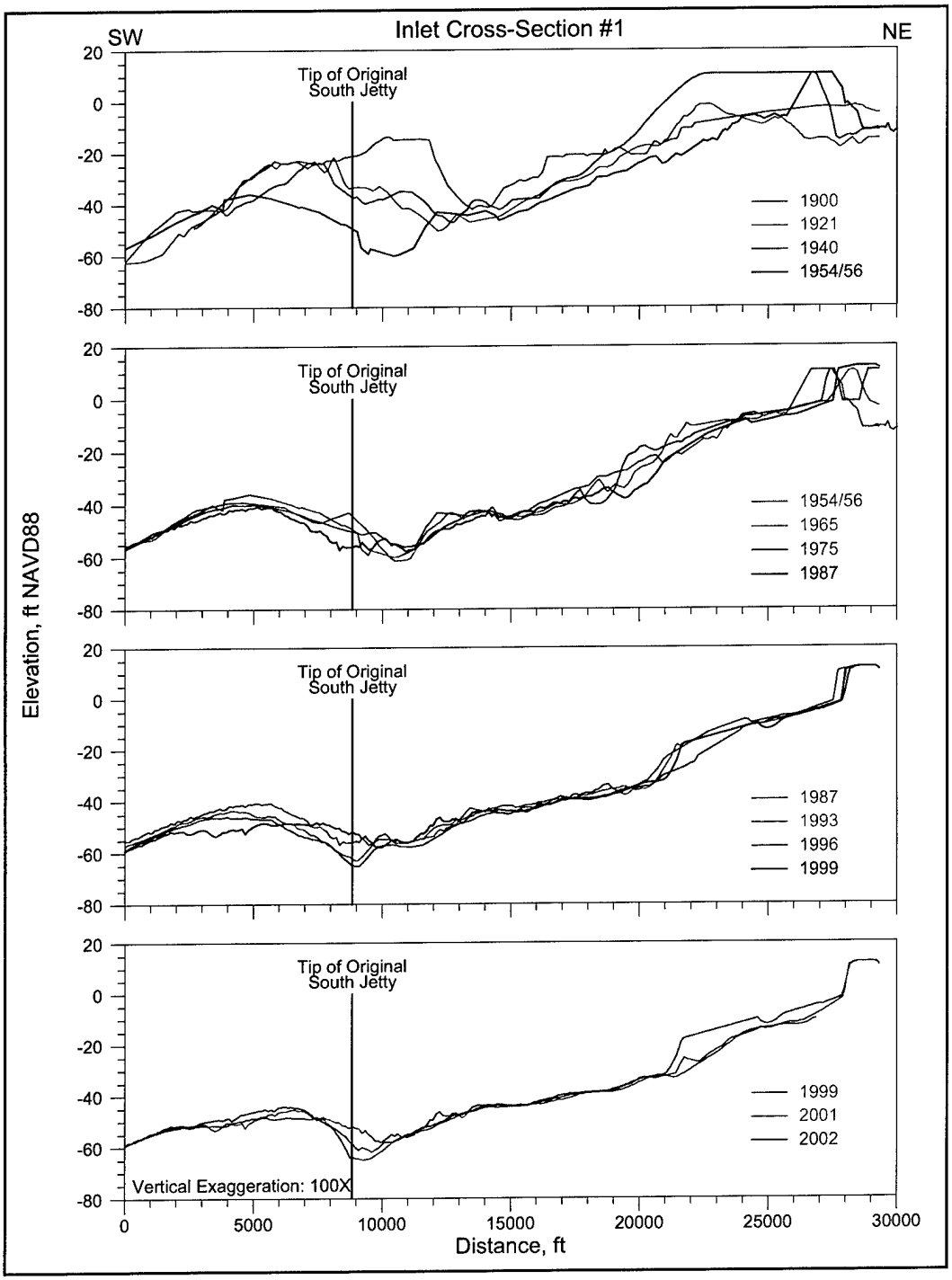

Figure 3-34. Change in bathymetry along Inlet Cross-section 1 from 1900 to 2002

Inlet Cross-sections 2, 3, and 4 document variations in bathymetry along the axis of the entrance from south-to-north, respectively. Along the southern cross section (Cross-section 2), substantial changes in shoal and channel migration occurred between 1900 and 1954/56 (Figure 3-35). In 1900, the natural channel was deepest along this cross section and located eastward of subsequent channel positions. From 1921 to 1954/56, the channel shifted westward and shoaled, and the entrance area shoaled (Figure 3-35), as sediment from the northeast side of the channel (east of Damon Point) began to fill the entrance area as a northeast-southwest elongated shoal (Figures 3-29 and 3-30).

Seaward of this point, across the southern portion of the ebb shoal, depths began to increase due to the scouring action of ebb currents constricted by the jetties. Sediment eroded from this area was transported offshore, extending the ebb shoal into deeper water and to the northwest (Figure 3-35). Between 1954/56 and 1975, channel shoaling was minimized, but it was not until 1975 that scouring in the entrance area eroded shoal deposits that had formed between the channel and the end of the south jetty between 1900 and 1965.

By 1987, sediment had filled the western half of the channel via sand transport from Damon Point, constricting flow within the channel. The supply of sand from Damon Point to the subaqueous spit north of the channel continued through 2002 (Figures 3-32), resulting in sand waves migrating west through the entrance in response to dominant ebb currents along the south side of the entrance (Figure 3-35). Between 1987 and 2002, depth changes on the ebb shoal were minor compared with sand wave formation and migration within the entrance area.

Inlet Cross-section 3 (located approximately 2,000 ft north of Cross-section 2) experienced channel deepening and migration, seafloor erosion seaward of the eastern margin of the channel, and seaward migration of the ebb shoal between 1900 and 1940 (Figure 3-36). By 1954/56, after reconstruction of the south and north jetties, the channel shoaled and deposition occurred west of the channel within the entrance area as a result of sand transport from the northeast (a pattern also recorded at Cross-section 2). The crest of the ebb shoal continued to erode, supplying sediment offshore to deeper water. Between 1954/56 and 1987, the channel experienced small fluctuations in depth and position, but the shoal along the western margin of the channel had eroded continually. The ebb shoal continued to erode and lose crest elevation under the influence of dominant ebb currents. Between 1987 and 2002, the greatest seafloor changes were occurring along the western margin of the channel because sand eroded from this area was migrating west as sand waves, similar to changes observed along Cross-section 2 (Figure 3-36). The ebb shoal intersected by this cross section was relatively unchanged during this time.

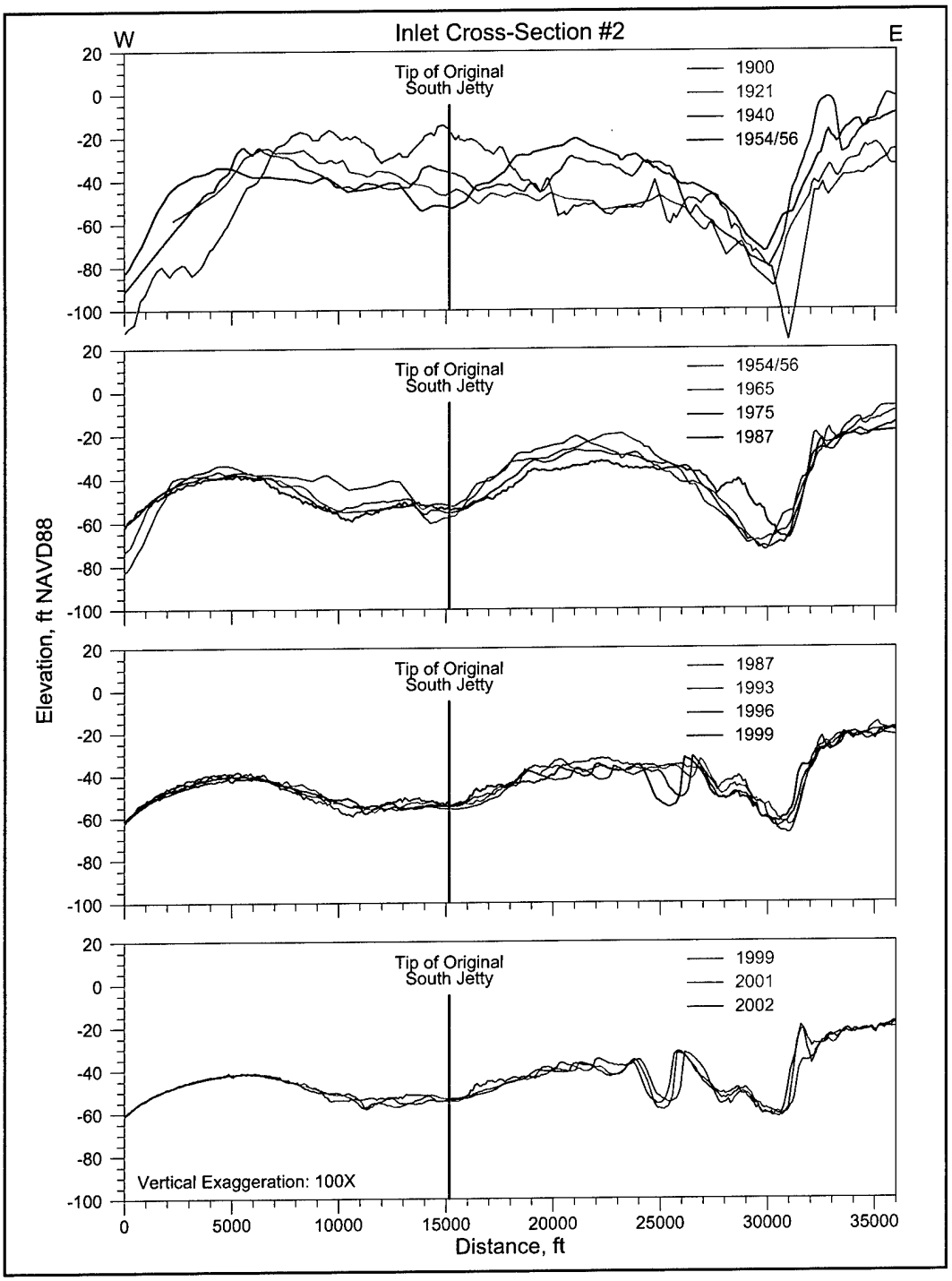

Figure 3-35. Change in bathymetry along Inlet Cross-section 2 from 1900 to 2002

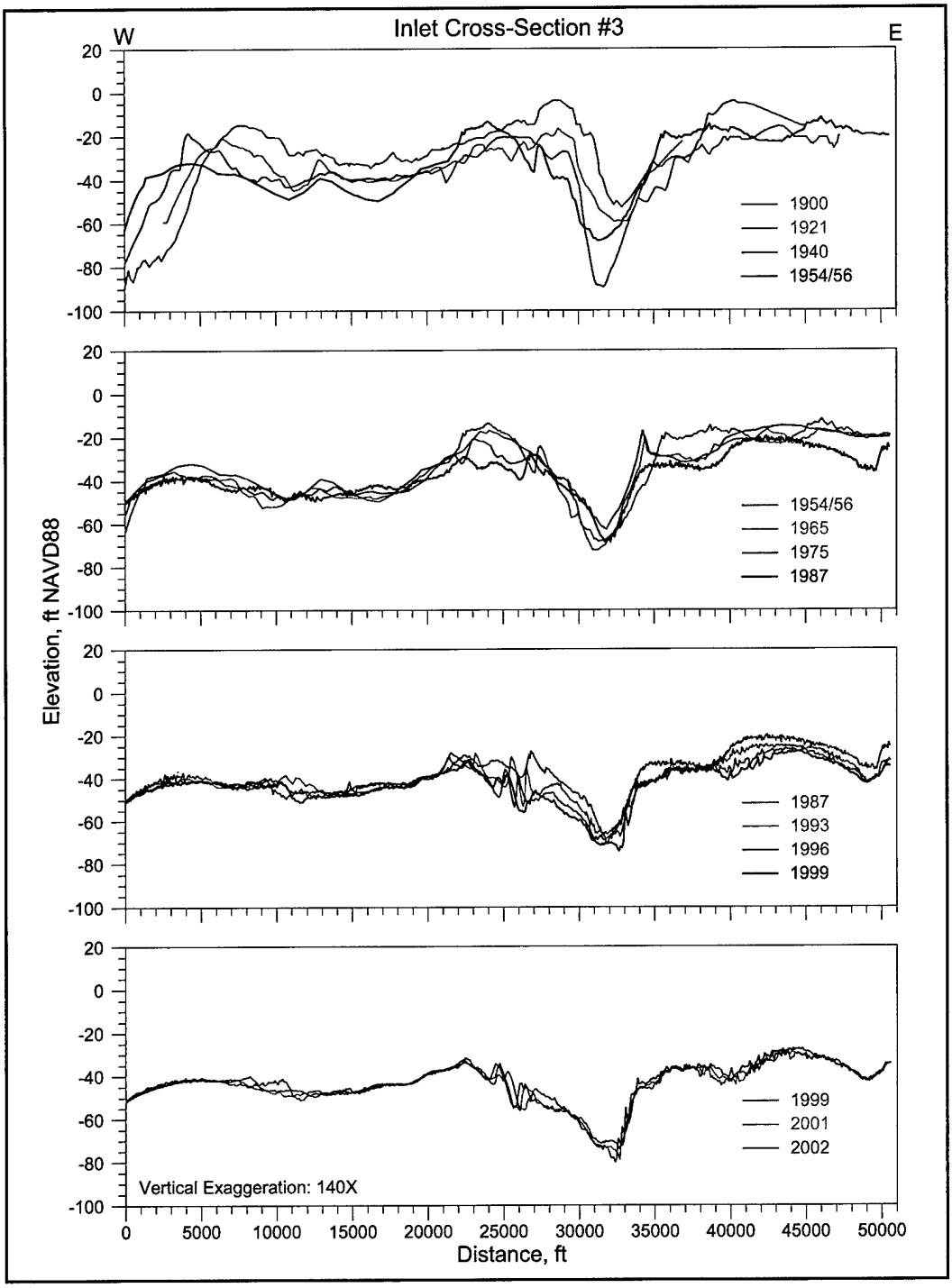

Figure 3-36. Change in bathymetry along Inlet Cross-section 3 from 1900 to 2002

The northernmost inlet cross section (Cross-section 4), located approximately 1,900 ft north of Cross-section 3, experienced continuous erosion within the entrance area and seaward translation of the ebb shoal between 1900 and 1954/56 (Figure 3-37). Sand eroded from this area by southwest waves and transported to the east by dominant flood currents (Chapters 4 and 7 of this report) along this cross section was transported by longshore currents along Damon Point to the southwest, causing shoaling in the entrance area at Cross-sections 2 and 3.

Between 1954/56 and 1987, a broad channel developed that deepened from about -45 ft in 1954/56 to about -85 ft in 2002 near the eastern side of the cross section. The channel continued to widen between 1987 and 1993, but by 1996 sand deposition along the western margin of the channel was initiated via transport from Damon Point. Between 1993 and 2002, the channel narrowed from about 5,000 ft to less than 2,000 ft as a result of subaqueous sand spit deposition from Damon Point (Figure 3-37). Eastward migrating sand waves west of the channel and near the end of the north jetty reflect the dominance of flood currents and sand transport processes along this cross section.

Longshore changes on the ebb shoal were recorded along Cross-section 5. Changes in elevation over the shoal were greatest between 1900 and 1954/56, and significant adjustments continued through 1987 (Figure 3-38). Less rapid changes occurred between 1987 and 2002, but the shoal continued to erode north of the navigation channel as sediment was transported onshore and to the northwest. As the shoal reaches dynamic equilibrium relative to the acting wave and current processes, the magnitude of seafloor changes away from the entrance become negligible, and those closest to the entrance are relatively minor.

Inlet Cross-section 6 illustrates changes between the north and south jetties in the entrance area. After construction of the jetties, seafloor erosion was present throughout the entrance area. Erosion was particularly evident along the south side of the entrance where approximately 30 to 35 ft of sand was removed between 1900 and 1921 (Figure 3-39). Scour adjacent to the south jetty continued between 1921 and 1954/56; however, deposition north of the channel was persistent during this time. Net erosion along the north side of the entrance in 1954/56 was likely the result of littoral drift blocking after reconstruction of the north jetty in 1942. Between 1954/56 and 1987, the channel and entrance area scoured to about 70 ft and 40 ft deep, respectively (Figure 3-39). Since 1987, the navigation channel has shoaled to a depth of about 60 ft, and the entrance area has scoured slightly. Accretion on the south side of the north jetty is supplied by littoral transport around the end of the jetty and into the entrance area by dominant flood tidal currents.

Inlet Cross-section 7 documents channel and shoal erosion and accretion across the inner entrance area between Damon Point and Point Chehalis (Figure 3-33). This part of the Grays Harbor entrance has been the most active throughout the period of record. Prior to jetty construction, a deep natural channel (-65 ft mllw) existed near the location of the present navigation channel, north of which was dominated by shallow sand flats. After construction of the jetties, the channel scoured to a depth of about 95 ft in 1921 (Figure 3-40). Between 1921

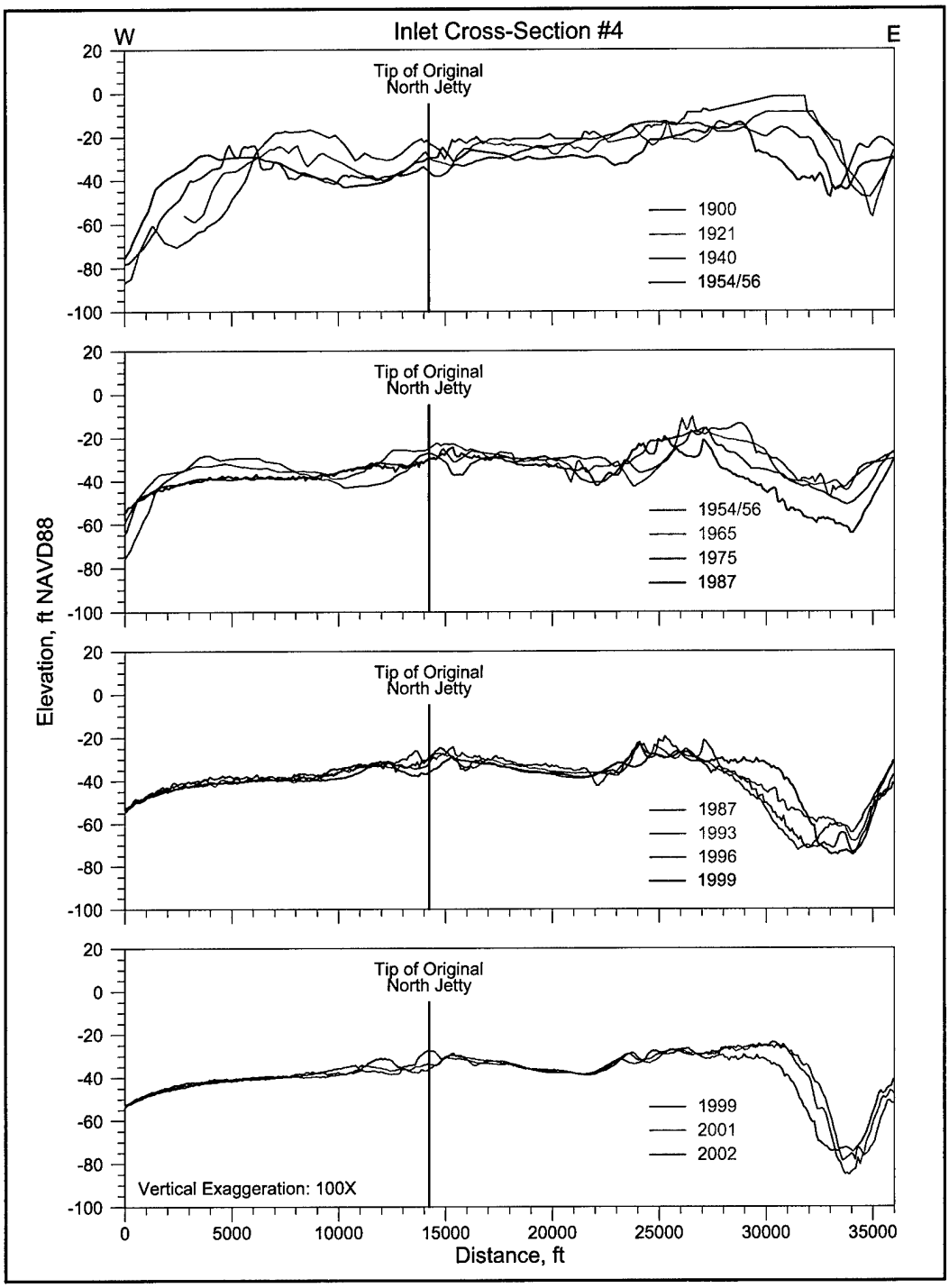

Figure 3-37. Change in bathymetry along Inlet Cross-section 4 from 1900 to 2002

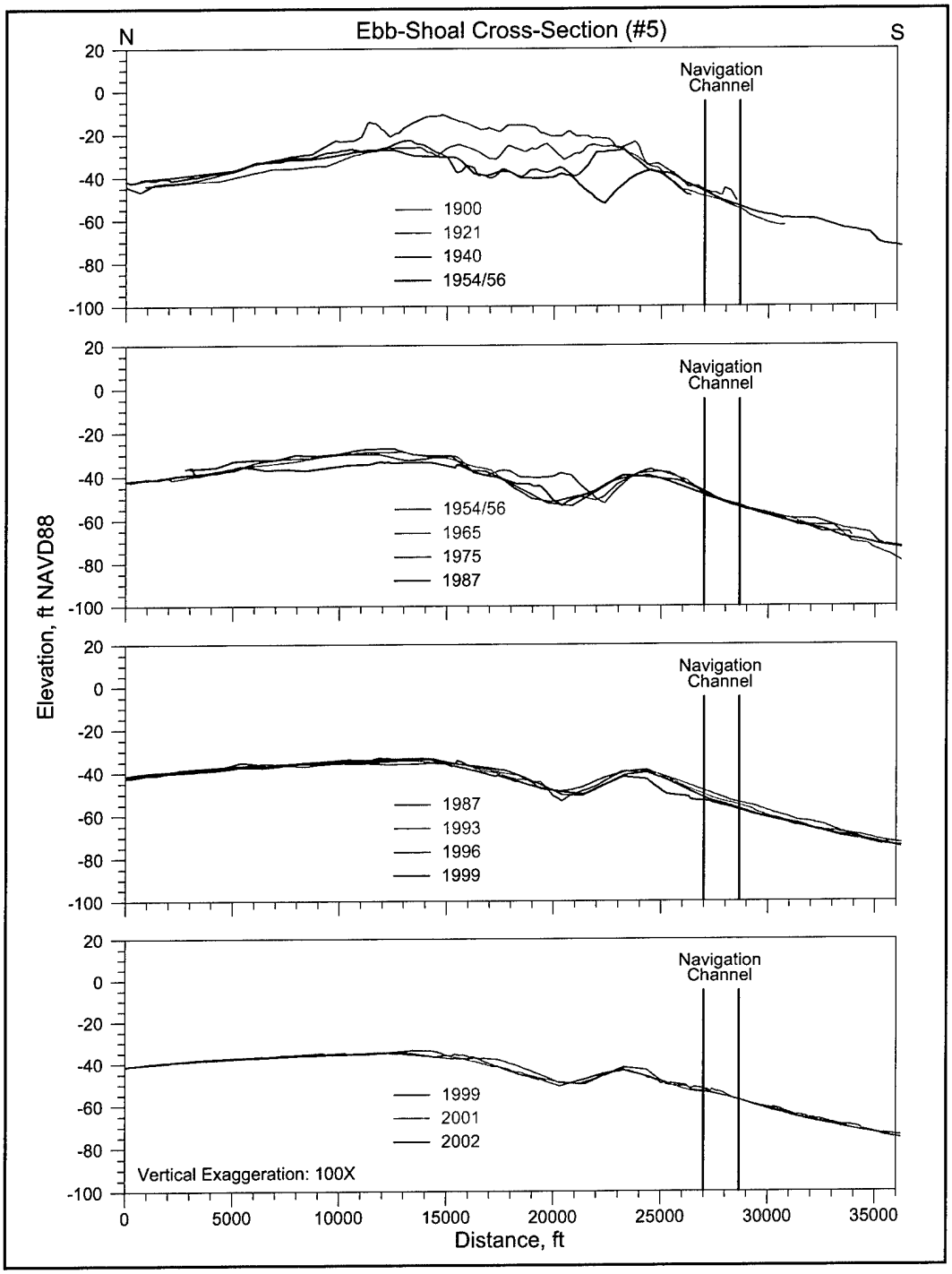

Figure 3-38. Change in bathymetry along ebb shoal Cross-section 5 from 1900 to 2002

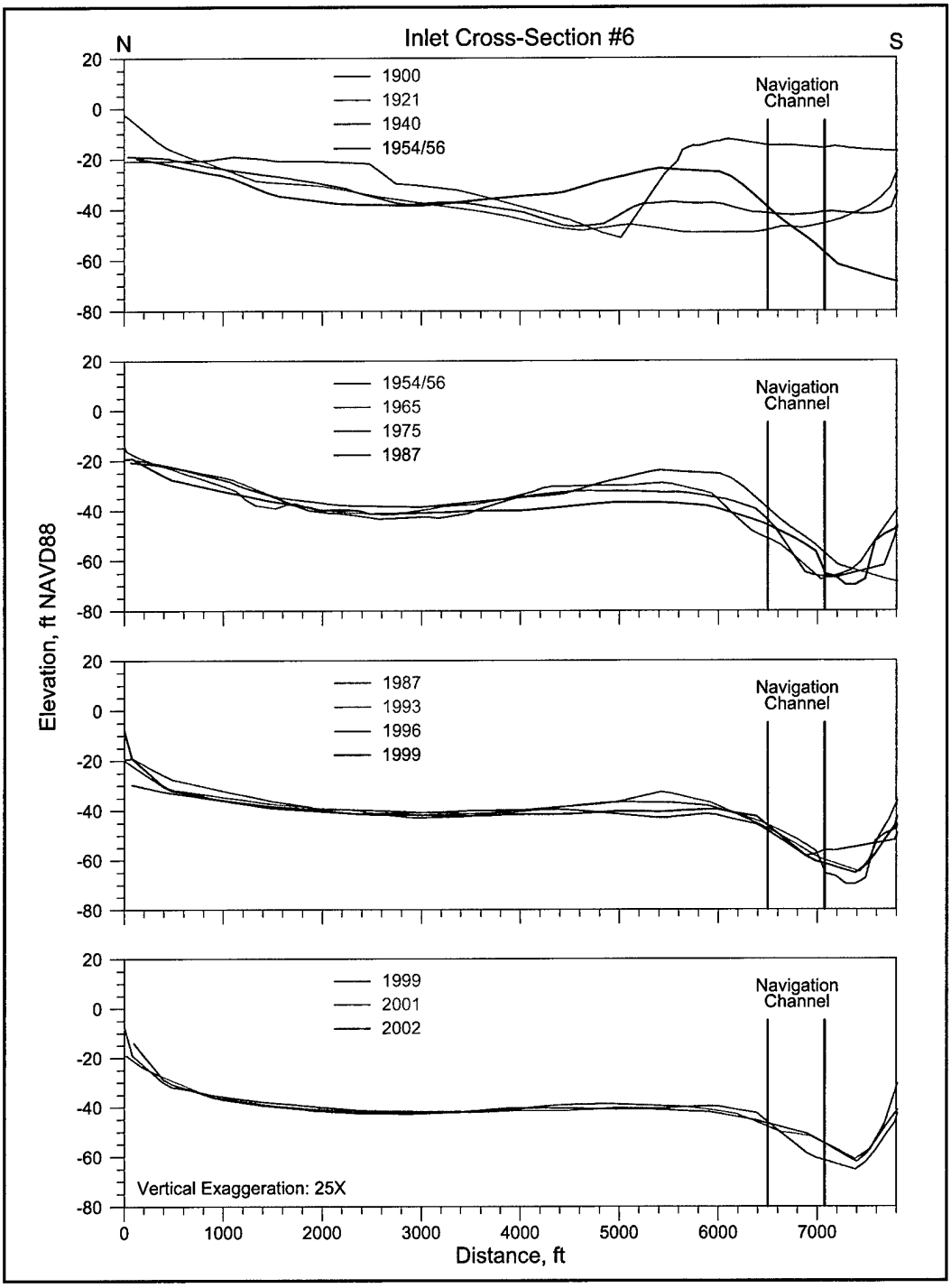

Figure 3-39. Change in bathymetry along Inlet Cross-section 6 from 1900 to 2002

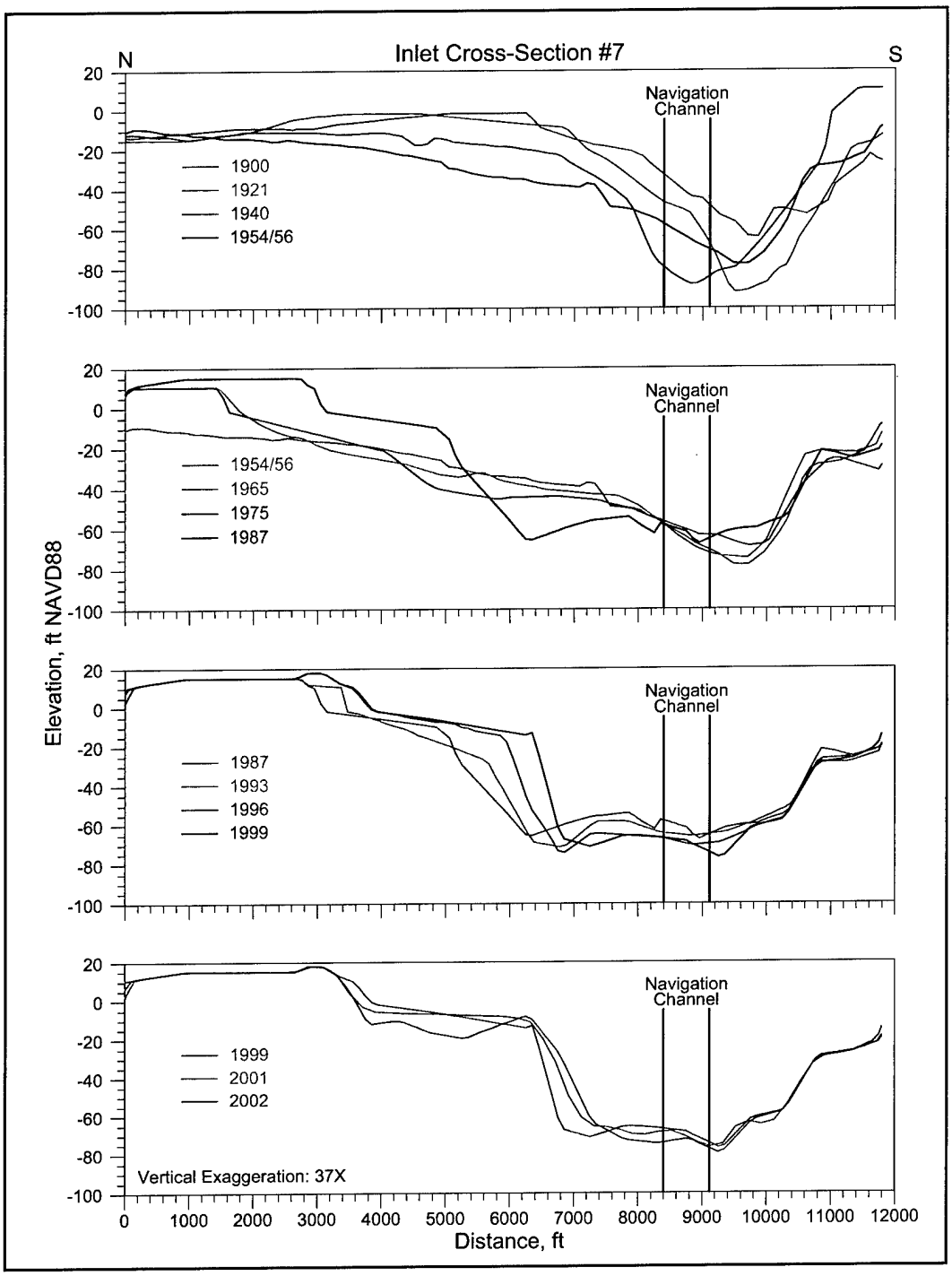

Figure 3-40. Change in bathymetry along Inlet Cross-section 7 from 1900 to 2002

and 1940, the thalweg of the channel migrated north and shoaled to a depth of about 85 ft. In addition, the shallow sand shoals north of the channel scoured 10 to 15 ft. This trend continued through 1954/56, when the channel was approximately 75 to 80 ft deep and the entrance area north of the navigation channel had eroded upwards of about 40 ft.

From 1954/56 to 1987, Damon Point accreted substantially from south-directed littoral transport just north of the north jetty. Waves and flood-tidal currents transported sand toward a small sand spit east of the north jetty. During this period, the subaerial extent of Damon Point expanded significantly, creating a large peninsula and shoal feature that began encroaching on the channel in 1987 (Figure 3-40). Since that time, the subaqueous growth of the sand spit has narrowed the channel opening by about 1,500 ft, resulting in about 10 ft of scour within the navigation channel area. Sand from this extensive deposit is transported along the northern channel margin to the west and southwest, toward the Point Chehalis and entrance reaches of the maintained navigation channel. Although significant quantities of sand transported from the subaqueous spit south of Damon Point are not causing channel shoaling problems at this time, when the deposit extends downdrift and away from maximum current speeds in the future, maintenance dredging requirements for these channel reaches can be expected to increase.

Sediment Transport Pathways

Comparisons of bathymetric surfaces from the same geographic area for different time periods document erosion and accretion patterns that reflect net sediment transport pathways. Erosion and accretion volumes define the magnitude of sediment exchange associated with these transport pathways. Together, these data describe the sediment budget for an area, constrained by import and export estimates (e.g., longshore transport) at the boundaries. Data presented in this section are derived from comparisons of bathymetric surfaces described above for time periods representative of major engineering activities since jetty construction.

The natural movement of channels and shoals at the Grays Harbor entrance was documented by comparing the 1862 and 1900 bathymetric surfaces. Although south jetty construction started in 1898, only half of the structure was completed by 1900, and no direct relationships were identified between jetty placement and inlet morphology that would mask natural sediment transport dynamics for the 38-year change record. Four primary responses were identified.

a. As channel orientation switched from northwest in 1862 to west by 1900 (and 1894; Figure 3-26), erosion was prominent along the 1900 channel axis (Figure 3-41). Two areas of deposition associated with channel migration were located northwest of the 1900 channel and offshore of the entrance as part of the ebb shoal.

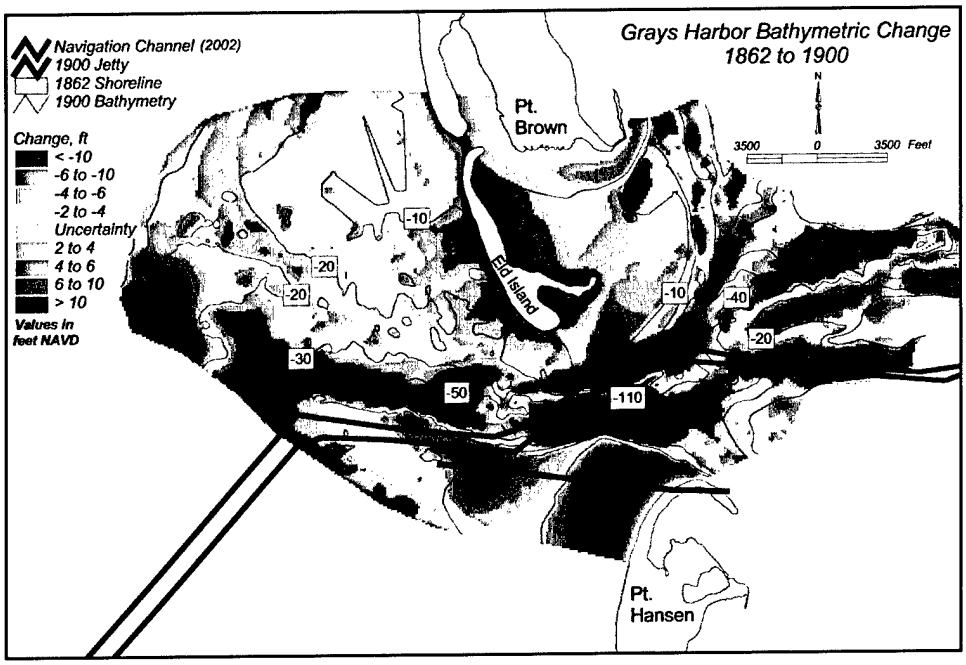

Figure 3-41. Bathymetric change at Grays Harbor entrance, 1862 to 1900

b. Deposition south of the channel and seaward of Point Hansen was significant. This pattern of bathymetric change is consistent with shoreline position change for the same period and demonstrates that the dominant direction of longshore transport is from south-to-north (Figure 3-41). Furthermore, westward extension of the zone of deposition south of the channel emphasizes the transport pathway by which sand-sized sediment is bypassed from the beach to the ebb shoal, and eventually to beaches north of the entrance.

c. The shallow area north of the channel and south of Point Brown was highly erosional prior to jetty construction. By 1900, Eld Island had eroded and receded toward Point Brown in response to channel migration from northwest to west. Ebb-shoal sediment that was deposited just offshore of Point Brown in 1862 likely supplied beaches north of the entrance with substantial quantities of sand as shoal features migrated onshore as part of the long-term south-to-north sand bypassing process. After the channel orientation switched to the west, the quantity of sand directly supplied to northern beaches was reduced, and the shoreline began to erode.

d. An area of deposition north of the channel and inside the entrance indicates transfer of sand from Eld Island and other Point Brown beaches into the entrance area during shoreline recession (Figure 3-41). Wave-induced transport along sand-spit beaches north of the channel directs sand into the entrance, and tidal currents redistribute this material relative to dominant sediment transport pathways. This subaqueous deposition feature is similar to that extending to the southwest off Damon Point in 2002 (Figure 3-32).

The 1900 to 1921 period encompasses construction of the north and south jetties. Bathymetric changes illustrated in Figure 3-42 document the primary purpose for constructing the jetties. As stated in Seattle District documents regarding Grays Harbor, the purpose of the jetties was to confine tidal currents to create scouring velocities over the bar and along the entrance channel. Scouring of the entrance was effective after the jetties were completed (CTH 1967; USAED, Seattle, 1989, 1997, page 6; also see Chapter 2 of this report). Three major changes in the morphology are observed in Figure 3-42.

a. The entrance area between Point Brown and Point Hansen was primarily erosional as increased tidal currents excavated 6 to 10 ft of sand from much of the entrance and natural ebb shoal. Sediment was transported offshore to water depths greater than 30 ft and onshore to the beaches fronting Point Brown, as seen by the volume increases in these areas.

b. Beaches north and south of the harbor accreted during this time interval. The north beaches accumulated approximately 61 million cu yd of sand from erosion of the entrance area and the old ebb shoal, creating a large offset between the north and south beaches (Figure 3-42). Most sand was impounded on the north side of the north jetty, but some leaked through the structure back into the entrance area. Deposition along beaches south of the harbor from north-directed longshore transport was about 10 percent of that to the north, supporting the idea that most accretion along the beaches north of the entrance is associated with onshore transport of sand from the entrance area and ebb shoal. Longshore transport of sand from Grayland Plains to the north accumulated along the beaches south of the jetty and inside the entrance at Point Hansen. However, the greatest sand accumulation along beaches south of the jetty was recorded adjacent to the jetty due to impoundment (Figure 3-16).

c. The offshore area south of the south jetty was highly erosional. Once sediment exchange between the inlet and offshore areas was severed by construction of the south jetty, accumulation and migration of inlet shoals (i.e., South Spit; Figure 3-26) was eliminated. However, wave and current action that redistributed sediment in this area remained, resulting in chronic seafloor erosion that continues today to a lesser degree.

Between 1921 and 1940, the jetties settled and deteriorated rapidly. The structures were not functioning as designed and channel navigation problems became an issue. Substantial quantities of sand were being deposited in the entrance from south and north through the jetties. Figure 3-43 illustrates large areas of deposition east of the north jetty and north of the south jetty. For the first time since jetty construction, beaches north of the north jetty were net erosional because littoral sand was being transported over and through the deteriorated structure. As a result, a large sand spit and shoal area formed inside the entrance. Severe erosion on both sides of the north and south jetties indicated that scour was a major factor influencing structure instability, rendering the jetties ineffective (Figure 3-43). Apparently, hydrodynamic conditions had changed throughout the entrance because net deposition was dominant at this time. However, the pre-jetty

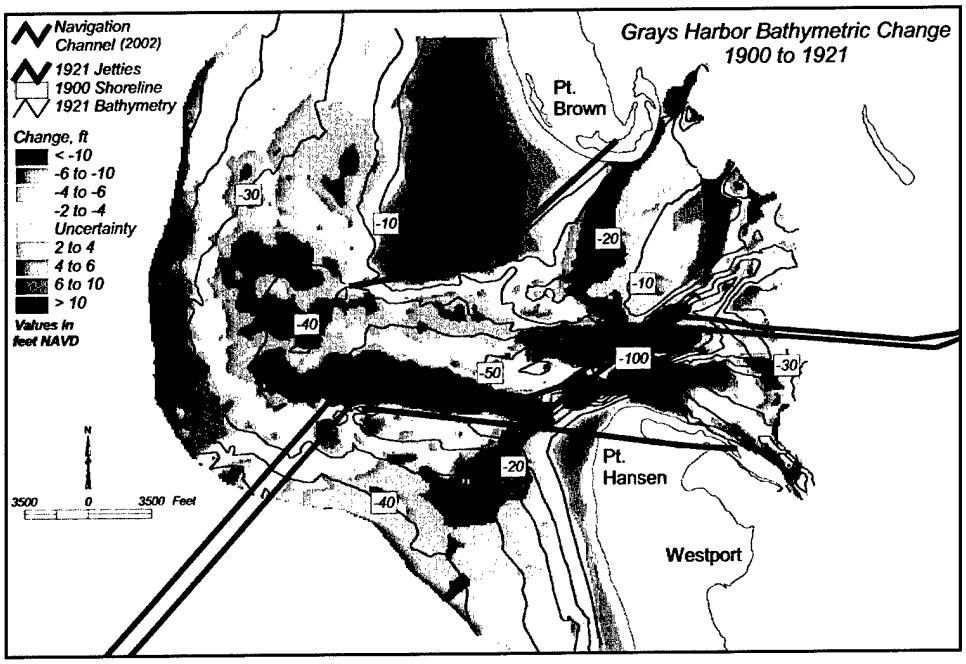

Figure 3-42. Bathymetric change at Grays Harbor entrance, 1900 to 1921

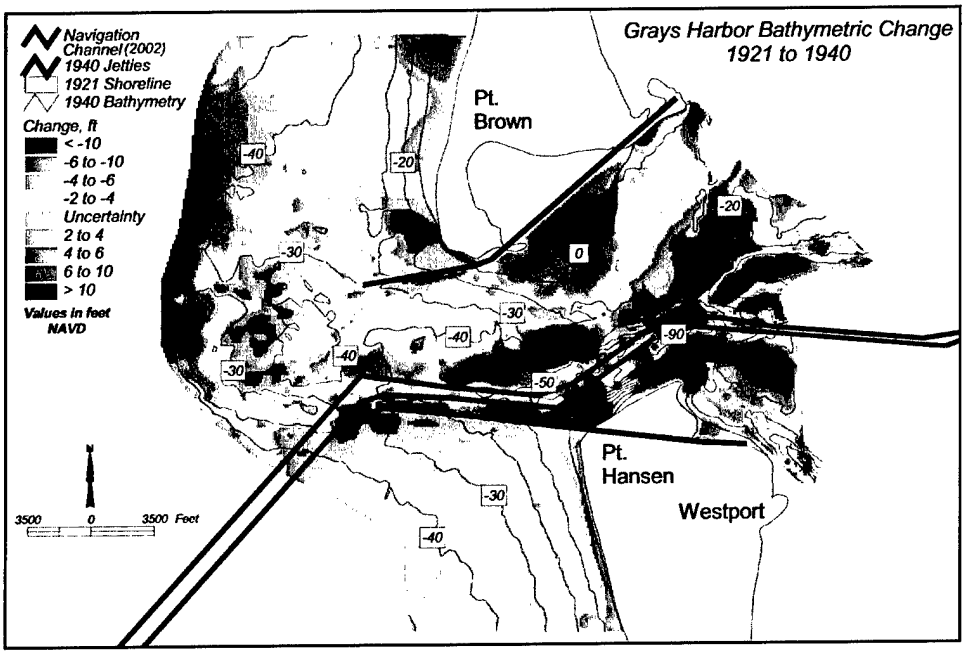

Figure 3-43. Bathymetric change at Grays Harbor entrance, 1921 to 1940

ebb shoal seaward of the structures continued, due to waves and ebb-tidal flow, to erode and deposit sediment offshore in deeper water and onshore to the beaches fronting Point Brown.

Both jetties were reconstructed to +20 ft mllw in 1939 (south) and 1942 (north) to regain channel scouring capacity and block longshore transport of sand into the entrance. The period 1940 to 1954/56 illustrated a significant reversal in trend resulting from reconstruction of the jetties (Figure 3-44). First, beaches north and south of the entrance were net accretional. As after initial jetty construction, northern beaches accreted much more than southern beaches, but the jetties were blocking littoral transport. An immediate change in sedimentation occurred east of the north jetty, where historical Damon Point eroded rapidly between 1940 and 1954/56 and migrated to the northeast as a much smaller spit feature. Much of the sand that had deposited in the entrance area between 1921 and 1940 to form the spit and subaqueous shoals eroded once the supply of littoral material was removed, creating a large sand shoal north of the channel in the entrance area (Figure 3-44). The seafloor in the vicinity of the seaward half of the south jetty remained highly erosional, and the southern half of the ebb shoal was net erosional once again. Almost the entire area seaward and north of the north jetty was net depositional, indicating that south-to-north transport of littoral sand and sediment eroded from the ebb shoal was dominant.

Comparison of bathymetric surfaces between 1900 and 1954/56 provides a summary of net changes that occurred after initial construction of the jetties and after reconstruction of the structures to +20 ft mllw. Figure 3-45 illustrates that, by 1954/56, the original position and form of the ebb shoal had changed remarkably.

Between 1954/56 and 1987, portions of the reconstructed north and south jetties were rehabilitated (Table 3-1). However, the outer portions of the structures were beyond repair (USAED, Seattle, 1965, 1974; also see Chapter 2 of this report). Flows were maintained between the shortened jetties to scour the central portion of the entrance area and the ebb shoal (Figure 3-46). Beaches north of the north jetty were slightly depositional. By 1954, the north jetty was near capacity for blocking localized longshore transport of sand to the south. Since this time, sand has been moving around the north jetty, into the northern portion of the entrance area, and on to Damon Point, creating an extensive sand spit. The channel adjacent to Damon Point maintains strong currents that have promoted scour of the central portion of the entrance. The ebb shoal and offshore area south of the south jetty continue to erode and provide sediment to the outer part of the ebb shoal (water depths greater than 50 ft) and to beaches fronting Ocean Shores (Figure 3-46). All but the northern 3,500 ft of beach south of the south jetty accreted during this period. Although deposition occurred within the Point Chehalis Reach of the navigation channel, natural depths generally remain deeper than authorized depths.

Between 1987 and 2002, most bathymetric changes occurred within the entrance area. Deposition along the southeastern margin of Damon Point has resulted in an elongated shoal that is constrained on its southern boundary by an 80-ft deep channel that has been scouring (Figure 3-47). Deposition south of the navigation channel along Point Chehalis and the entrance channel reaches is from planned dredged-material disposal by the Seattle District.

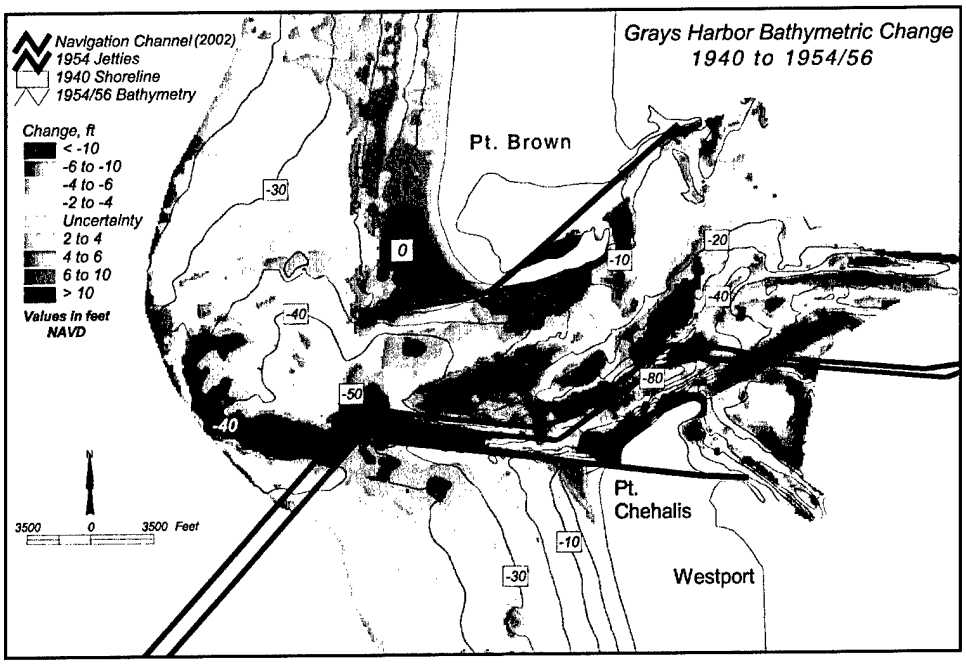

Figure 3-44. Bathymetric change at Grays Harbor entrance, 1940 to 1954/56

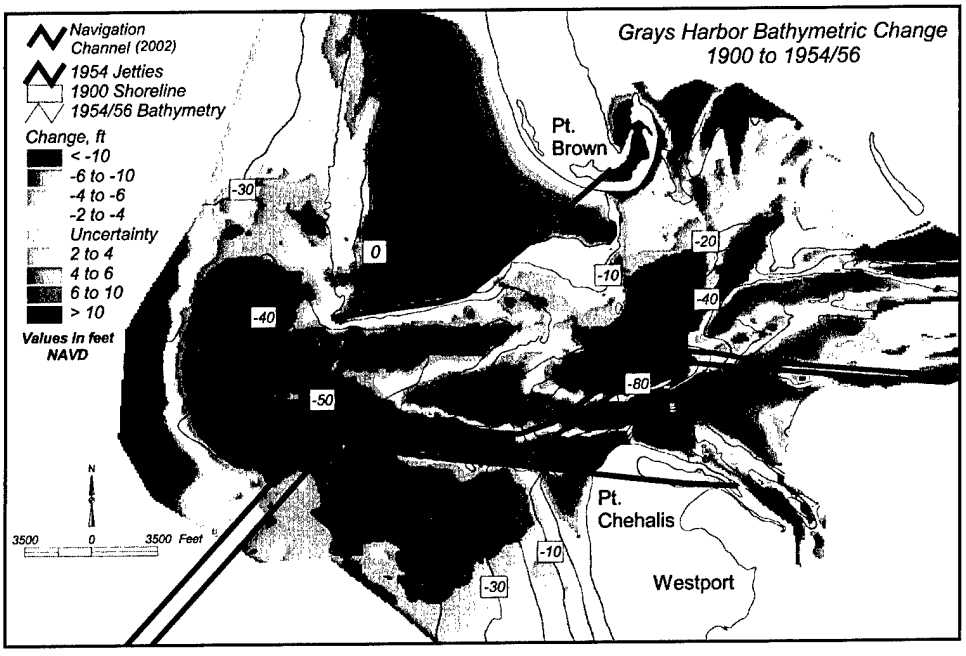

Figure 3-45. Bathymetric change at Grays Harbor entrance, 1900 to 1954/56

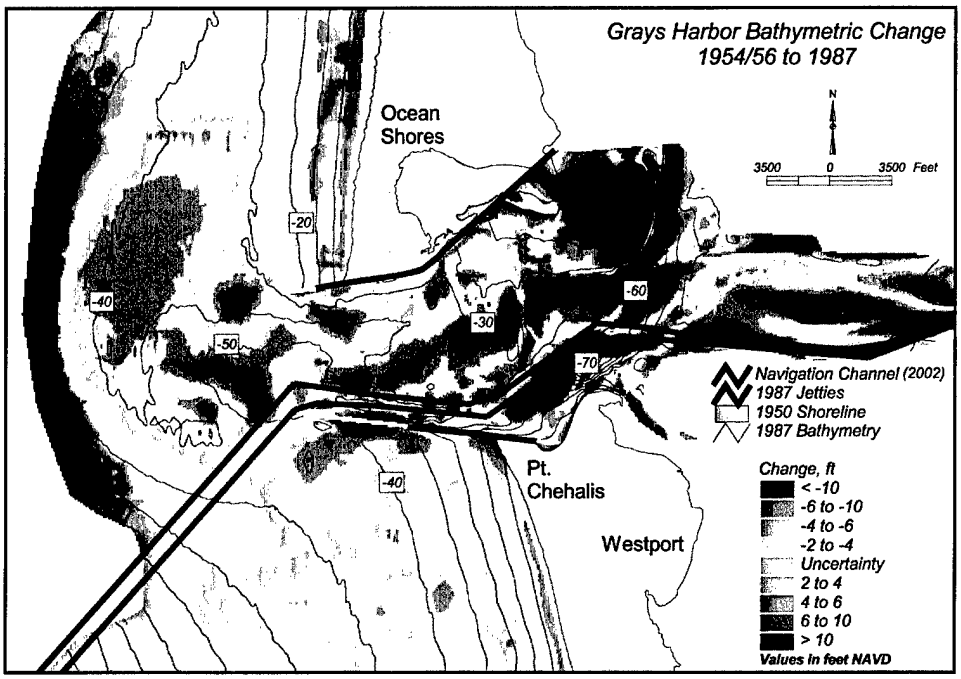

Figure 3-46. Bathymetric change at Grays Harbor entrance, 1954/56 to 1987

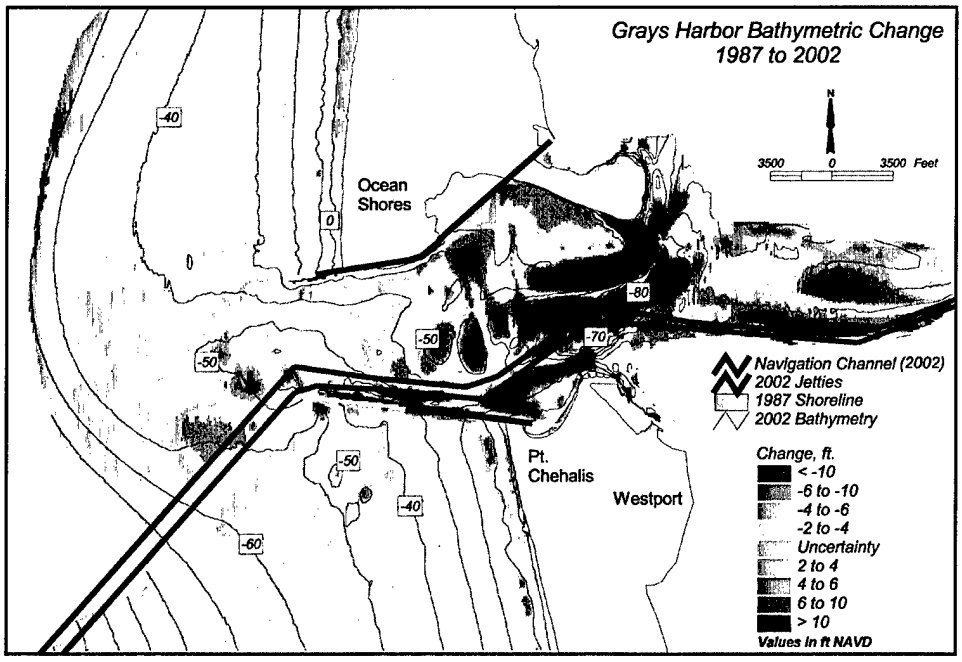

Figure 3-47. Bathymetric change at Grays Harbor entrance, 1987 to 2002

Offshore erosion continues on the southern portion of the ebb shoal, and net deposition is dominant (but relatively minor) north and offshore of the north jetty. Deposition on the inner portion of the ebb shoal just west of the navigation channel appears to be originating from the entrance area south of the channel and from erosion of the beach and shoreface along the south beach (Figure 3-47). Sediment from the inner shoal is being bypassed to the north and east on to Ocean Shores beaches. Longshore sand transport within about 0.5 miles north of the north jetty is directed to the south and into the entrance area, where sediment is transported by the flood tidal current toward Damon Point and by wave-induced currents along Damon Point to the subaqueous shoal off the southeastern end of the spit. Although there is no evidence that significant quantities of sediment are being transported from this shoal to the navigation channel at this time, historical data suggest that it may happen in the future (Figure 3-44).

Sediment Budget

Sediment budget determination for the coastal zone involves the principle of conservation of mass applied to littoral and offshore sediment (Bowen and Inman 1966; Rosati and Kraus 1999). Development of a budget at the Grays Harbor entrance and vicinity requires quantitative evaluation of various sediment sources to and losses from the study area, and a comparison of net gains or losses with observed rates of erosion or accretion. The USACE Sediment Budget Analysis System (SBAS) was operated to display transport pathways and analyze sediment volume fluxes (Rosati and Kraus 2001).

Sediment erosion and accretion volumes were quantified for the period 1987 to 2002 by comparing (differencing) bathymetric survey data (Figure 3-47). Ten zones of erosion and accretion were identified throughout the sediment budget control area based on bathymetric change analysis (Figure 3-48). Overall, the inlet throat and zones south of the entrance were net erosional. Zones north of the inlet throat and offshore were net accretional. One exception to this trend was the depositional zone adjacent to the south jetty, inside the entrance. In addition to being an area of historical deposition, this region has been the location of greatest placement of dredged material within the sediment budget control area.

Regional trends support the net movement of sand from south-to-north; however, significant volumes of sediment are transported into the inlet by local transport reversals within about 0.5 mile of the north jetty (see Chapter 6 on Longshore Sand Transport). Southward-directed sediment transport along the north beach and into the northern side of the entrance supplies sand to Damon Point, creating a rapidly migrating and expanding subaqueous spit that is a conduit for sediment transport back to the entrance area toward the maintained navigation channel (Figure 3-47). Sand-sized sediment dredged from the channel and placed in the Point Chehalis and south jetty disposal sites eventually is transported seaward to the inner and outer ebb shoal zones, and back to the north beach, where the transport cycle is repeated.

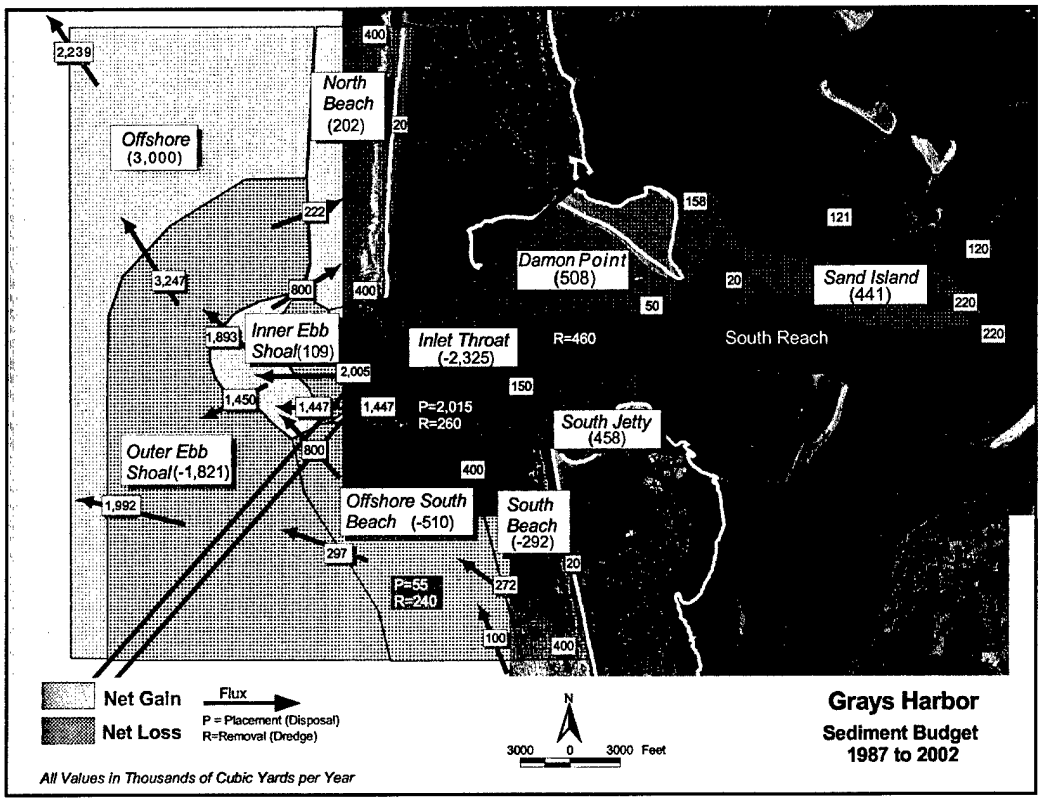

Figure 3-48. Grays Harbor sediment budget, 1987 to 2002

Sediment sources and sinks were determined for open boundaries within the sediment budget control area. Based on regional sediment transport results and numerical modeling estimates presented in Chapter 6, net littoral transport quantities were determined to be about 400,000 cu yd/year to the north. Figure 3-49 documents cumulative changes in shoreline position at Transects C and D (Figure 3 18) within about 3,000 ft of the north jetty. Estimates of sand volume change within this region between the seaward end of the north jetty and the high-water shoreline illustrate that most sand accumulated between 1940 (near the time of jetty reconstruction) and 1954 at a rate of about 400,000 to 500,000 cu yd/year. Since 1954, this portion of the north beach appears to be in a state of dynamic equilibrium, where relatively small changes in net sand volume are evident (up to 35,000 cu yd/year). As such, most south-directed sand transport at the north jetty is bypassing the jetty in transit to Damon Point via dominant flood currents along the north side of the entrance (Chapters 4 and 7).

Dredging removal and placement volumes were derived from Seattle District dredging records. Sediment input rates from the east and northeast boundaries of the control area were based on channel shoaling quantities (dredging records) and short-term bathymetric change trends near the boundaries. Figure 3-50 documents the east-to-west migration of a portion of Sand Island Shoal as it aggraded at a rate of about 200,000 cu yd/year between 1987 and 2002.

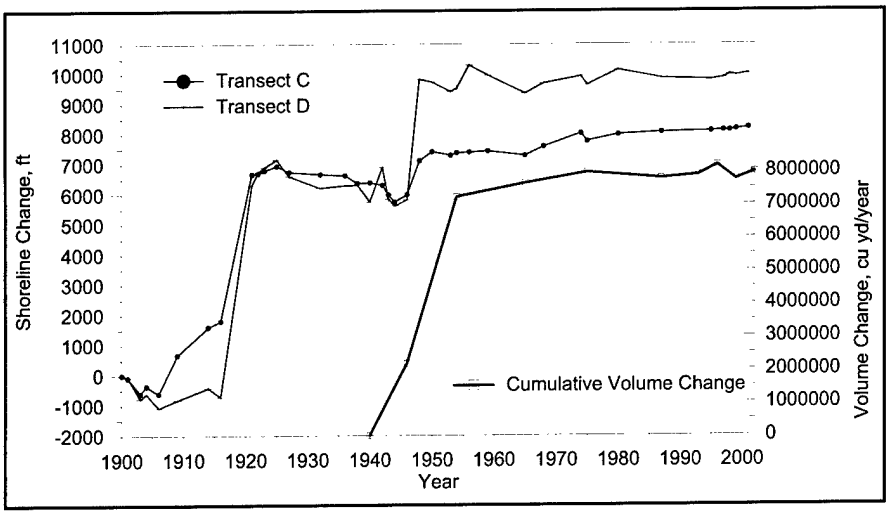

Figure 3-49. Cumulative shoreline change within 3,000 ft of north jetty, and associated sand accumulation volume between 1940 and 2002

Approximately 800,000 cu yd/year of sand is transported from the south side of the entrance (offshore south beach) north across the inner ebb shoal to the north beach (inlet bypassing). In addition, about 222,000 cu yd/year of sand is transported from the outer ebb shoal to the north beach, where an average of 202,000 cu yd/year was deposited along the shoreline between 1987 and 2002. Approximately 400,000 cu yd/year is transported to the south and into the northern side of the entrance from the north beach in response to a localized longshore transport reversal, supplying sediment to Damon Point. Along outer coast beaches, onshore transport quantities of sand by wind were estimated based on the presence of extensive aeolian deposits in the study area.

Net deposition along the southeastern end of Damon Point and on the subaqueous spit extending south and west of the shoreline has been about 508,000 cu yd/year. The greatest amount of change in the entrance and largest transport rates are associated with the inlet throat zone, where about 2.3 million cu yd/year is transported seaward across the ebb shoal to the offshore zone. The offshore zone accumulates approximately 3 million cu yd/year of sediment, and it is estimated that another 2.2 million cu yd/year of fine-grained sediment is transported seaward to deeper water on the continental shelf. As the outer ebb shoal continued to erode in response to inlet hydrodynamics, about 1.8 million cu yd/year of sand was lost to the north beach and offshore zones.

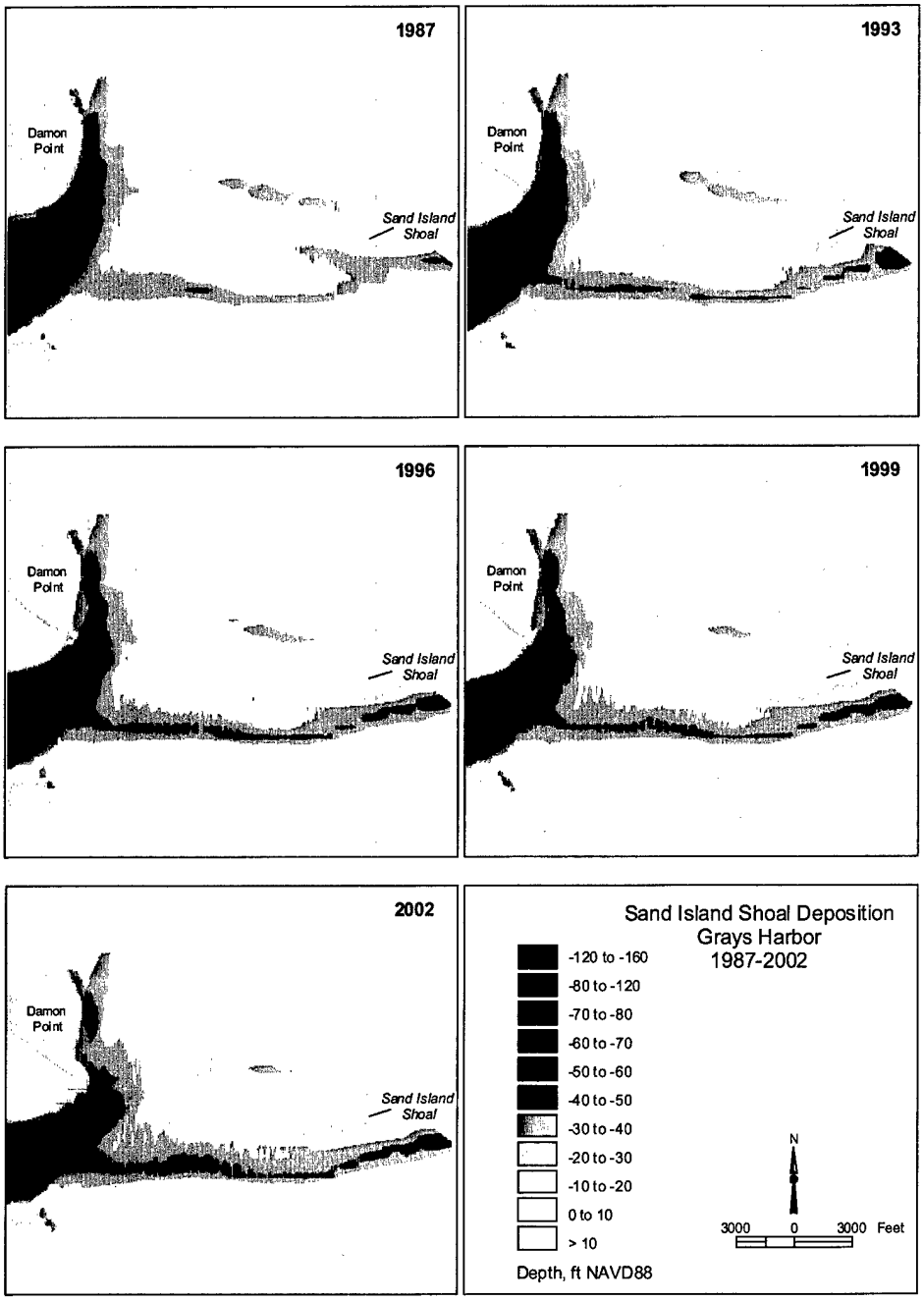

Figure 3-50. Sediment deposition at eastern margin of sediment budget region on Sand Island Shoal, 1987 to 2002

Table 3-3 summarizes volume-change results for each of the sediment budget polygons for the period 1987 to 2002. Deposition and erosion volumes were recorded as derived from surface model analysis software, with net change rounded to the nearest 1,000 units (cu yd and cu yd/year). Net deposition in the offshore zone as described above is not listed on Table 3-3 because survey data in 1987 did not extend far enough seaward to capture all offshore deposition. As such, the 1954/56 and 2002 bathymetric surfaces were compared to quantify the magnitude of offshore deposition associated with losses in the entrance area. Figure 3-51 illustrates the extent of survey coverage for the two bathymetric surfaces and the pattern of erosion and accretion for the 47-year time period. Although the entire offshore deposition zone is not encompassed by these data, the surface difference does capture the area of greatest change to the outer margin of the ebb shoal.

To estimate the quantity of offshore deposition for the 1987 to 2002 sediment budget, the ratio between deposition in the offshore zone (2,221,000 cu yd/year) and erosion associated with the inlet throat, the south beach, offshore south beach, inner ebb shoal, and outer ebb shoal polygons (3,549,000 cu yd/year) for the period 1954/56 to 2002 was multiplied by volume losses for the same polygons between 1987 and 2002. This relationship is based on the assumption that changes in erosion and offshore deposition associated with these sediment budget polygons over the last 15 years are not significantly different than those over the past 47 years. Based on this comparison, it was estimated that the amount of sediment depositing offshore between 1987 and 2002 was about 3 million cu yd/year.

Table 3-3
Volume Change at Grays Harbor Entrance, 1987 to 2002

Polygon	Area X 10^6 sq yd	Deposition		Erosion		Net	
		X10^6 cu yd	cu yd/year	X10^6 cu yd	cu yd/year	X10^6 cu yd	cu yd/year
North beach	9.787	3.966	265,000	0.939	63,000	3.027	202,000
Outer ebb shoal	33.888	0.062	4,000	27.376	1,825,000	-27.314	-1,821,000
Inner ebb shoal	3.306	2.114	141,000	0.482	32,000	1.632	109,000
Offshore south beach	13.910	0.564	38,000	8.219	548,000	-7.655	-510,000
South beach	6.638	0.492	33,000	4.869	325,000	-4.377	-292,000
Inlet throat	17.163	1.060	71,000	35.933	2,396,000	-34.873	-2,325,000
South jetty	4.162	7.253	483,000	0.378	25,000	6.875	458,000
Damon Point	11.986	19.306	1,287,000	11.686	779,000	7.620	508,000
Sand Island	4.867	7.288	486,000	0.670	45,000	6.617	441,000

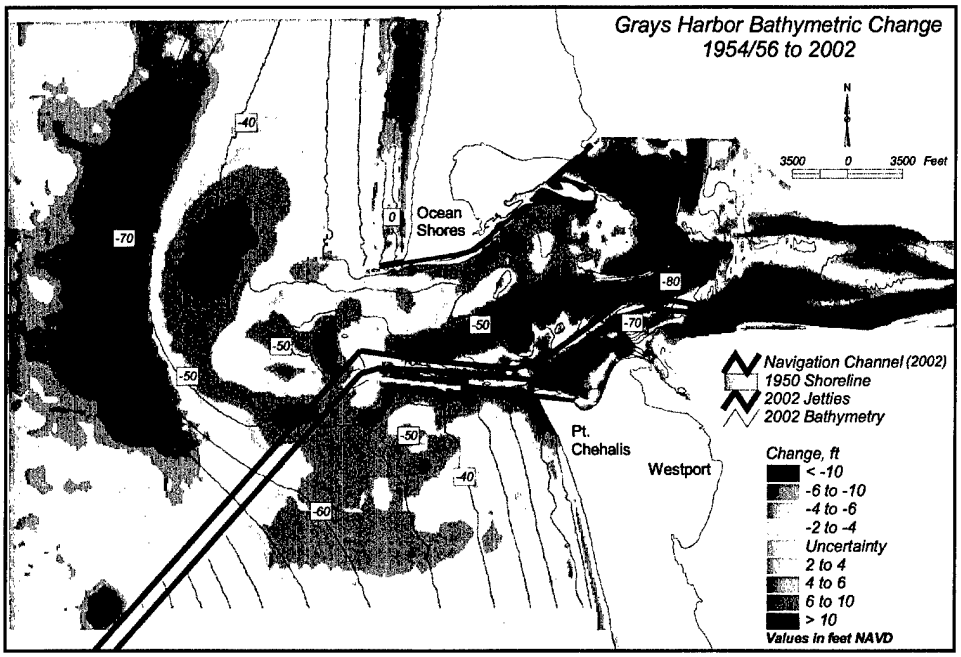

Figure 3-51. Bathymetric change at Grays Harbor entrance, 1954/56 to 2002

To test the assumption of near-constancy in processes, a sediment budget was formulated for the period 1954/56 to 1987 (Figure 3-52). Accumulation/erosion rates in each of the polygons were very similar to those documented between 1987 and 2002. Table 3-4 summarizes sediment-volume changes associated with the 1954/56 to 1987 bathymetric change map (Figure 3-47). Polygon boundaries are similar to those determined for the 1987 to 2002 sediment budget. The largest difference between the two sediment budgets is associated with the development of Sand Island Shoal, where the rate of deposition in this zone has approximately doubled for the 1987 to 2002 period, possibly as a result of navigation channel realignment in 1990.

Summary

Overall, sediment transport pathways and magnitudes of erosion and accretion at the Grays Harbor entrance and along adjacent beaches demonstrate that morphologic response was dynamic prior to and after jetty construction. Net transport along the beaches and on the continental shelf is to the north, but a local longshore transport reversal exists north of the entrance. Jetty construction on both sides of the entrance and subsequent rehabilitation works have resulted in major changes in sediment transport processes throughout the entrance area, over the ebb shoal, and along adjacent beaches.

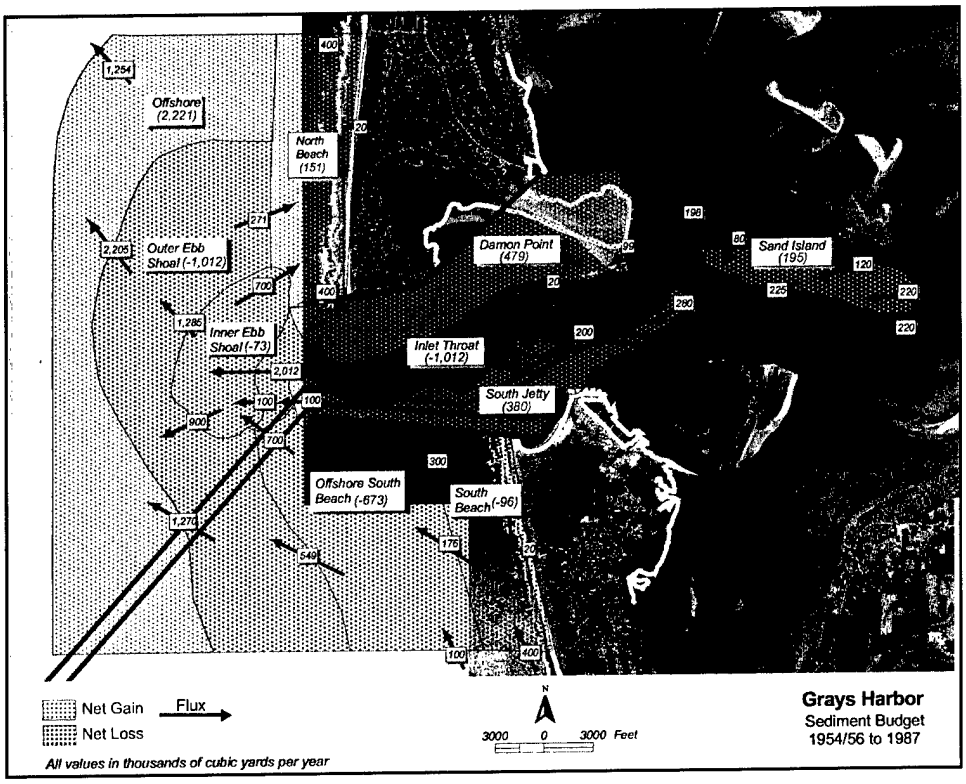

Figure 3-52. Bathymetric change at Grays Harbor entrance, 1954/56 to 1987

Table 3-4
Volume Change at Grays Harbor Entrance, 1954/56 to 1987

Polygon	Area X 10^6 sq yd	Deposition		Erosion		Net	
		X10^6 cu yd	cu yd/year	X10^6 cu yd	cu yd/year	X10^6 cu yd	cu yd/year
North beach	8.942	6.232	195,000	1.395	44,000	4.8367	151,000
Outer ebb shoal	24.648	0.531	17,000	32.910	1,029,000	-32.379	-1,012,000
Inner ebb shoal	5.314	2.883	90,000	5.210	163,000	-2.327	-73,000
Offshore south beach	14.436	0.049	2,000	21.579	675,000	-21.530	-673,000
South beach	7.017	1.330	42,000	4.410	138,000	-3.081	-96,000
Inlet throat	18.659	0.620	19,000	62.327	1,949,000	-61.707	-1,928,000
South jetty	6.572	13.557	424,000	1.394	44,000	12.163	380,000
Damon Spit	10.411	22.751	711,000	7.431	232,000	15.321	479,000
Sand Island	3.167	6.695	209,000	0.446	14,000	6.249	195,000

Table 3-5 summarizes inlet and nearshore morphology changes at the Grays Harbor entrance associated with historical time periods defined in Table 3-2. The entrance area deepened rapidly after jetty construction, starting from a deep natural channel that had existed prior to engineering activities. In response to changing hydrodynamic conditions associated with jetty construction, the ebb shoal translated seaward to water depths greater than 50 ft. Much of the sediment associated with shallow ebb shoals was transported onshore to beaches north of the north jetty between 1900 and 1921. Offshore erosion south of the entrance resulted when shoal migration and sand exchange between the entrance area and shelf seaward of the south beach was severed by construction of the south jetty. Regional transport processes continue to mobilize and bypass sand from this area to beaches north of the entrance, resulting in net erosion south of the south jetty. Post-jetty littoral transport rates to the south beach are not sufficient to compensate for natural sediment exchange processes existing at the inlet prior to jetty construction, resulting in net erosion along the beach and in the nearshore.

Although deposition along beaches north of the entrance continues, the magnitude of change is small compared with earlier time periods (Figure 3-49). Shoreline change data indicate that the north jetty has been close to impoundment since about 1954. About 40 percent of the sediment reaching the north beach from offshore is transported south around the end of the jetty and into the northern part of the entrance area. This trend is compatible with transport rates derived at the north jetty from shoreline change modeling shown in Chapter 6. Dominant flood currents and wave-induced currents (Chapters 4 and 7) along the north side of the entrance transport this sediment toward Damon Point, where it eventually deposits on an extensive subaqueous spit south and west of the point. Only minimal quantities of sediment are transported from this shoal to the navigation channel at present. However, as the shoal increases in size to the south and west (Figure 3-47) away from the location of greatest current speeds now confining deposition north of the channel, navigation channel infilling from this source may be expected to increase.

Table 3-5
Summary of Morphologic Changes by Epoch

Epoch	Conditions	Morphologic Response
I	Natural tidal currents and incident wave processes associated with natural inlet conditions and south-to-north-directed littoral transport.	Channel orientation fluctuates from northwest to west, generating subaqueous erosion and shoreline recession to the north of the entrance (about 210 ft/year). Along the south side of the entrance, subaqueous deposition and shoreline advance (about 100 ft/year near present-day jetty position) are prominent, associated with south-to-north-directed net littoral transport.
II	Jetty construction confines tidal currents to create scouring velocities in the entrance channel and over the bar.	Sediment erosion within the entrance area and on the ebb shoal is greatest of any time period. Shoreline advance prominent along both sides of the entrance. The north beach deposition is about ten times greater than that on the south beach, as sediment from the entrance and ebb shoal is directed north and onshore to the beach, and offshore toward deeper water.
III	Jetty deterioration and settling due to erosion by waves and tidal currents reduces scouring velocities within the entrance channel.	Sediment erosion within the entrance area and on the ebb shoal is greatly reduced. Erosion becomes dominant along both beaches near the jetties as they deteriorate (1927 to 1942 at the north beach; 1916 to 1938 at the south beach). Sediment transported through and over the jetties generates substantial subaqueous and subaerial deposition inside the entrance east of the north jetty (Damon Point) and north of the south jetty.
IV	Jetty reconstruction enhances channel scouring capacity and blocks longshore transport of sand into the entrance.	Beaches north and south of the entrance were net accretional; northern beaches accreted more than southern beaches. Damon Point eroded and migrated northeast between 1940 and 1954/56, then enlarged to the east-southeast between 1954/56 and 1965 as the north jetty became impounded. Scouring between the jetties and onto the ebb shoal increased, and the offshore south of the entrance remained erosional. The seafloor north of the north jetty was net depositional.
V	Inner portions of north and south jetties rehabilitated, maintaining flows between shortened structures.	Flows were maintained between the shortened jetties to scour the central portion of the entrance and the ebb shoal. Beaches adjacent to the south jetty were net erosional; northern beaches were slightly depositional. Because sand accumulation at the north jetty was near capacity by 1954/56, south-directed transport of sand around the jetty and east toward Damon Point continued to promote subaqueous deposition of the sand spit.
VI	Small portions of north and south jetties rehabilitated. Entrance and bar channel dredging commences in 1991.	Greatest bathymetric change occurred within the entrance. Deposition continued along the southeastern margin of Damon Point as a subaqueous shoal north of the navigation channel. Offshore erosion continued on the southern portion of the ebb shoal, and net deposition was dominant north and offshore of the north jetty. The south beach remained net erosional. Increased deposition occurred south of the navigation channel from dredged-material disposal by the Seattle District.

References

Ballard, R. L. (1964). "Distribution of beach sediment near the Columbia River," Technical Report No. 98, University of Washington, Department of Oceanography, Seattle, WA, 82 pp.

Bohlander, R. E., editor. (1984). *World explorers and discoverers*. Macmillan Publishing Company, New York, NY.

Bowen, A. J., and Inman, D. L. (1966). "Budget of littoral sands in the vicinity of Port Arguello, California," Technical Memorandum No. 19, U.S. Army Engineer Waterways Experiment Station, Coastal Engineering Research Center, Vicksburg, MS.

Buijsman, M. C., Sherwood, C. R., Gibbs, A. E., Gelfenbaum, G., Kaminsky, G., Ruggiero, P., and Franklin, J. (2003). "Regional sediment budget of the Columbia River littoral cell, USA, analysis of bathymetric- and topographic-volume change," Open-File Report 02-281, U.S. Geological Survey, Menlo Park, CA.

Buijsman, M. C., Kaminsky, G. M., and Gelfenbaum, G. (2003). "Shoreline change associated with jetty construction, deterioration, and rehabilitation at Grays Harbor, Washington," *Shore and Beach* 71(1), 15-22.

Burch, T. L., and Sherwood, C. R. (1992). "Historical bathymetric changes near the entrance to Grays Harbor, Washington," Batelle/Marine Sciences Laboratory Sequim, WA.

Byrne, J. V. (1963). "Coastal erosion, northern Oregon," in *Essays in Marine Geology*, T. Clements (ed.), University of Southern California Press, Los Angeles, CA, 11-33.

Byrnes, M. R., and Hiland, M. W. (1994). "Compilation and analysis of shoreline and bathymetry data (Appendix B)," in *Kings Bay Coastal and Estuarine Monitoring and Evaluation Program: Coastal Studies,* N. C. Kraus, L. T. Gorman, and J. Pope (ed.), Technical Report CERC-94-09, U.S. Army Engineer Waterways Experiment Station, Coastal Engineering Research Center, Vicksburg, MS, B1-B89.

Committee on Tidal Hydraulics. (1967). "Grays Harbor, Washington," U.S. Army Engineer Waterways Experiment Station, Vicksburg, MS.

Creager, J. S., and Sternberg, R. W. (1972). "Some specific problems in understanding bottom sediment distribution and dispersal on the continental shelf," in *Shelf Sediment Transport,* D. J. P. Swift, D. B. Duane, and O. H. Pilkey (ed.), Dowden, Hutchinson & Ross. Inc., Stroudsburg, PA, 347-362.

Hands, E. B. (2000). "Geomorphology," Chapter 3, in *Study of Navigation Channel Feasibility, Willapa Bay, Washington,* N. C. Kraus (ed.), prepared for U.S. Army Engineer District, Seattle, WA.

Hayes, M. O. (1991). "Geomorphology and sedimentation patterns of tidal inlets: A review," in *Coastal Sediments '91*, N. C. Kraus, K. J. Gingerich, and D. L. Kriebel (ed.), American Society of Civil Engineers (ASCE), New York, 1,343-1,355.

Hayes, M. O., and Kana, T. W. (1976). "Terrigenous clastic depositional environments," Technical Report CRD-11, Department of Geology, University of South Carolina, Columbia, SC, 364 pp.

Judson, S., and Ritter, R. F. (1964). "Rates of regional denudation in the United States," *Journal of Geophysical Research* 69, 3,395-3,401.

Kachel, N. B., and Smith, J. D. (1989). "Sediment transport and deposition on the Washington continental shelf," in *Coastal Oceanography of Washington and Oregon*, M. R. Landry and B. M. Hickey (ed.), Elsevier Publishing, 287-348.

Kaminsky, G. M., Ruggiero, P., McCandless, D., Lindstrum, E., McInnis, J., and Daniels, R. (1999). "Road wash-outs and shoreline change at Damon Point, Washington," report to the Washington State Parks and Recreation Commission, Olympia, WA.

Kaminsky, G. M., Buijsman, M. C., and Ruggiero, P. (2000). "Predicting shoreline change at decadal scale in the Pacific Northwest, USA," *Proceedings 27th Coastal Engineering Conference*, ASCE, 2,400-2,413.

Karlin, R. (1980). "Sediment sources and clay mineral distributions off the Oregon coast," *Journal of Sedimentary Petrology* 50(2), 543-560.

McManus, D. A. (1972). "Bottom topography and sediment texture near the Columbia River mouth," in *The Columbia River Estuary and Adjacent Ocean Regions*, D. L. Alverson and A. T. Pruter (ed.), University of Washington Press, Seattle, WA, 241-253.

Nittrouer, C. A. (1978). "The process of detrital sediment accumulation in a continental shelf environment: An examination of the Washington shelf," Ph.D. diss., University of Washington, Seattle, WA.

Pacific International Engineering. (2000). "Documentation of existing conditions: Grays Harbor north jetty spur dike feasibility study project," prepared for U.S. Army Engineer Research and Development Center, 125 pp. plus appendix.

Peterson, C. D., and Phipps J. B. (1992). "Holocene sedimentary framework of Grays Harbor basin, Washington, USA," *SEPM Special Publication No. 48*, Society for Sedimentary Geology, 273-285.

Peterson, C., Scheidegger, K., and Komar, P. (1984). "Sediment composition and hydrography in six high-gradient estuaries of the northwestern United States," *Journal of Sedimentary Petrology* 54(1), 86-97.

Phipps, J. B. (1990). "Coastal accretion and erosion in Southwest Washington: 1977-1987," Shorelands and Coastal Zone Management Program Publication Number 90-21, Washington Department of Ecology, Olympia, WA, 33 pp. plus aerial photographs.

Phipps, J. B., and Smith, J. M. (1978). "Coastal accretion and erosion in southwest Washington," Washington Department of Ecology Report No. WA/DOE/CZ-78-12, 79 pp. plus appendices.

Roberts, R. W. (1974). "Marine sedimentological data of the Washington continental shelf," Special Report 57, Department of Oceanography, University of Washington, Seattle, WA, 129 pp.

Rosati, J. D., and Kraus, N. C. (1999). "Formulation of sediment budgets at inlets," Coastal Engineering Technical Note CETN-IV-15 (Revised August 1999), U.S. Army Engineer Research and Development Center, Vicksburg, MS.

_____. (2001). "Sediment budget analysis system (SBAS): Upgrade for regional applications," Coastal and Hydraulic Engineering Technical Note CHETN-XIV-3, U.S. Army Engineer Research and Development Center, Vicksburg, MS.

Ruggiero P., Kaminsky, G. M., Komar, P. D., and McDougal, W. G. (1997). "Extreme waves and coastal erosion in the Pacific Northwest," Ocean Wave Measurement and Analysis, *Proceedings of the 3rd International Symposium Waves '97*, 947-961.

Ruggiero, P., and Voigt, B. (2000). "Beach monitoring in the Columbia River littoral cell, 1997-2000," Publication No. 00-06-26, Coastal Monitoring and Analysis Program, Washington Department of Ecology, Olympia, WA, 112p.

Scheidegger, K. F., and Phipps, J. B. (1976). "Dispersal patterns of sands in Grays Harbor estuary, Washington," *Journal of Sedimentary Petrology* 46(1), 163-166.

Schwartz, M. L., and Bronson, H. (1984). "Grays Harbor County, Washington, net shore-drift," final report by Coastal Consultants, Inc. to the Washington State Department of Ecology, Olympia, WA.

Sternberg, R. W. (1986). "Transport and accumulation of river-derived sediments on the Washington continental shelf, U.S.A.," *Journal of Geological Society of London* 143, 945-956.

Todd, T. W. (1968). "Dynamic diversion: Influence of longshore current-tidal flow interaction on chenier and barrier island plains," *Journal of Sedimentary Petrology* 38, 734-746.

Twitchell, D. C., Cross, V. A., and Parolski, K. F. (2000). "Sidescan-sonar imagery, surface sediment samples, and surficial geologic interpretation of the southwestern Washington inner continental shelf based on data collected during Corliss cruises 97007 and 98014," Open-File Report 00-167, U.S. Geological Survey, Menlo Park, CA.

U.S. Army Corps of Engineers. (1934). "The Chief of Engineers, United States Army, report of the Board of Engineers for rivers and harbors on review of reports heretofore submitted on Grays Harbor, Washington," 74th Congress, 1st Session, Committee on Rivers and Harbors, House of Representatives, Document 2.

U.S. Army Engineer District, Seattle. (1965). "South jetty rehabilitation, Grays Harbor and Chehalis River, Washington," General Design Memorandum, Seattle, WA.

_____. (1974). "North jetty rehabilitation," Grays Harbor and Chehalis River, Washington, General Design Memorandum, Seattle, WA.

_____. (1989). "Grays Harbor, Washington, navigation improvement project," General Design Memorandum and Environmental Impact Statement Supplement, Appendix B-Design Analysis, Seattle, WA.

_____. (1997). "Long-term maintenance of the south jetty at Grays Harbor, Washington," Seattle, WA.

Van Winkle, W. (1914). "Quality of the surface waters of Washington," U.S. Geological Survey, Water Supply Paper 339, Tacoma, WA.

4 Oceanographic Setting, Field Data Collection, and Analysis[1]

This chapter describes the oceanographic setting at Grays Harbor including the nearshore, inlet throat, and outer portions of the harbor. It also provides an analysis of coastal and inlet processes based on recent field measurements. An extensive review and analysis of wave climate, ocean and inlet circulation, and sediment transport rates and patterns is included. The purpose of the field measurements and their analysis is to investigate coastal processes associated with waves currents and sediment transport near the submerged end of the north jetty, in the surf zone of the adjacent beach, and in the inlet. The analysis provides information needed to test hypotheses concerning mechanisms for southward sediment bypassing of the north jetty, the relative importance of cross-shore and longshore transport on north beach, and the transport patterns and pathways on the ebb shoal and in Grays Harbor inlet during storm and nonstorm conditions. A second objective of the measurements is to provide information to verify wave, current, and transport numerical models, thereby advancing their value as design tools to aid in the evaluation of alternatives. Background information on the field data collection in and around the entrance to Grays Harbor between 2001 and 2002 is provided in Appendix A.

Regional Setting

Inundation of the seaward portion of the Chehalis River formed the Grays Harbor estuary. The harbor is pear-shaped, approximately 15 miles long and 11 miles wide, with a surface area varying from approximately 97 square miles at mean higher high water (mhhw) to 38 square miles at mean lower low water (mllw). The harbor is separated from the Pacific Ocean by two long sandy peninsulas, the termini of which are named Point Brown on the north and Point Chehalis on the south. The entrance width between the two jetties is 6,500 ft.

The Chehalis River enters at the head of the estuary and contributes approximately 80 percent of the freshwater discharge to the harbor. Other minor rivers entering the harbor include the Humptulips, Hoquiam, Wishkah, Johns, and Elk. Winter flows of the Chehalis River generally range from 10,000 to

[1] Written by Philip D. Osborne, Pacific International Engineering, PLLC, Edmonds, WA.

40,000 cu ft/sec with the 100-year peak discharge estimated at 86,000 cu ft/sec. Weaker discharges occur in summer and generally range from 2,000 to 3,000 cu ft/sec, with extreme low discharge of 1,000 cu ft/sec (USAED, Seattle, 1989).

Grays Harbor is a partially mixed to well mixed estuary, but stratification may be pronounced in the upper estuary. The saline wedge fluctuates between Hoquiam Reach to above Cosmopolis (see Figure 1-1), depending on tidal stage and Chehalis River discharge (USAED, Seattle, 1989).

Facing the northeast Pacific Ocean, the entrance to Grays Harbor experiences an extreme wave climate with winter-significant wave heights (H_s) commonly exceeding 6 m during storms. In summer, H_s is less than 2 m on average. Seasonal winds over the northeast Pacific Ocean are largely determined by circulation about the North Pacific high and the Aleutian low. In summer, the center of high pressure is situated near 30°N latitude, 150°W longitude and the Aleutian low is significantly weakened. This pressure distribution is associated with winds from the northwest and north over the coastal and offshore areas of Washington. The Aleutian low strengthens with the approach of the winter season and midlatitude storms track eastward causing considerable day-to-day variations in wind speed and direction at Grays Harbor. Strongest winds in the offshore region of Grays Harbor originate out of the southwest. The annual variation in wind and wave energy results in seasonally reversing coastal circulation and sediment transport regime (both onshore-offshore and alongshore). Longer-term (decadal) variations are forced by large-scale climate controls including El Niño and La Niña events and the changing intensity of extratropical storms (e.g., Graham and Diaz 2001; Allan and Komar 2000b).

Grays Harbor Wave Climate

Waves are a primary mechanism controlling gross and net sediment transport in the nearshore and ebb-shoal regions of tidal inlets such as Grays Harbor. Waves are responsible for the generation of nearshore currents, long-period (infragravity) waves, and water level shifts at the shoreline, the combination of which may result in episodes of erosion and accretion. Wave energy is a primary consideration for commercial navigation at Grays Harbor, as well as the construction feasibility and functional design of a stable structure. Therefore, understanding the wave climatology in deep and shallow water at Grays Harbor is fundamental for this study.

Several studies have documented the wave climate of the northeastern Pacific Ocean. Prior to the availability of long records of waves measured by offshore buoys, the wave climate was based on hindcast techniques utilizing daily weather charts and merchant marine vessel observations (e.g., USAED, Seattle, 1982; Hemsley and Brooks 1989). More recently, ocean buoy data available since the mid-1970s and early 1980s have been the subject of analyses relevant to the Pacific Northwest, including studies by Ruggiero et al. (1996), Tillotson and Komar (1997), and Allan and Komar (2000a, 2000b, 2001, 2002a, 2002b). Buoy data are available from the National Data Buoy Center (NDBC) of the National Oceanic and Atmospheric Administration (NOAA) and the Coastal Data Information Program (CDIP) of the Scripps Institution of Oceanography (e.g., Seymour et al. 1996).

Data from two buoys are most relevant to this study. The deep-water Naval Oceanographic and Meteorological Device (NOMAD) buoy, operated by NDBC off the Washington coast (46005), has been in operation since 1976. Closer to Grays Harbor, CDIP buoy 3601 has been in operation since 1981, with directional measurements available since 1994. Site characteristics of the two buoys are summarized in Table 4-1. Measurements from the NDBC buoy, together with measurements from five other deep-water buoys on the West Coast, have been reviewed and analyzed in detail by Allan and Komar (2000a, 2001, 2002b) providing an overview of large-scale and long-term seasonal and interannual variability in wave climate. CDIP measurements at buoy 3601 also were summarized and analyzed as part of the present study to describe waves local to Grays Harbor and provide local forcing for nearshore wave transformation modeling and wave-current interaction modeling (Chapter 7).

Table 4-1
Wave Buoy Site Characteristics

Station Name	Location (Latitude, Longitude)	Water Depth (m)	Period of Operation	System
NDBC 46005	46 deg 3 min 0 sec N; 131 deg 1 min 12 sec W	2,853	1976-present	6-m NOMAD buoy
CDIP 3601	46 deg 51 min 24 sec N; 124 deg 14 min 40 sec W	41.5	1981 to present (directional since 1994)	Datawell Directional Buoy

Seasonal variability

There is a strong seasonal variability in the wave climate of the eastern north Pacific (Ruggiero et al. 1996; Allan and Komar 2002b). Deep-water significant wave heights, H_s, on the Washington Coast are smallest (< 2.0 m) on average between May and August (late spring to summer), reaching a minimum in July or August. Monthly average wave heights increase between August and November and reach a maximum in December. Average monthly H_s in winter range between 3.6 and 3.8 m in the northern portion of the eastern north Pacific that includes Washington State. Winter waves also exhibit a high degree of latitudinal variation on the West Coast with smaller waves occurring to the south (southern Oregon to California) and larger waves occurring to the north (Allan and Komar 2002b).

Spectral peak wave periods, T_p, exhibit a similar seasonal variation to H_s, averaging less than 10 sec in summer months and increasing to more than 12 sec in winter months. There is also a marked seasonal variation in peak wave direction, Dir, on the Washington coast with summer waves predominately from the northwest and west-northwest while winter storm waves mostly originate from the west-southwest and southwest. Winter swell is predominately from the west-northwest and west.

Time series of monthly average H_s, T_p, and Dir based on measurements at the CDIP buoy 3601 are shown in Figure 4-1 for 1994 to 2001 when directional measurements are available. Monthly average H_s varies between 1.2 and 1.7 m in summer months (May-September) and from 2.0 to 2.9 m in winter months (October-April), approximately 24 and 44 percent lower than the respective deep water measurements published by Allan and Komar (2001). Monthly average T_p decreases in summer months ranging from 8.1 to 10.4 sec and increases to between 10.6 and 12.9 sec in winter months similar to the deep-water NOMAD measurements. Direction of wave approach at CDIP buoy 3601 (called the "Grays Harbor buoy") is mostly greater than 270 deg from April through October and often at angles less than 270 deg from November through March.

The combined H_s and T_p distribution for the CDIP measurements (Figure 4-2) indicate the largest H_s correspond with intermediate wave periods centered between 15 to 18 sec for the Washington coast (Allan and Komar 2002b). Longer T_p of 20 to 21 sec are associated with H_s between 6 and 7 m. Although T_p as long as 25 sec have been recorded, they are associated with H_s of only 2 m. The inter-relationship between H_s and T_p enters the selection of design waves for coastal structures such as a submerged spur dike, jetty, or similar sediment control structure because the potential for damage to such a structure is a function of wave height and period.

Figure 4-3 shows the percent frequency of occurrence for all H_s measured at CDIP buoy 3601 between January 1994 and December 2001 in 11.25 deg bands. The wave rose shows that most waves arriving at Grays Harbor originate from the west and west-northwest. Figure 4-4 shows percent frequency of occurrence for all H_s greater than 5 m in the same 11.25-deg bands. The extreme wave rose indicates that most of the large waves at Grays Harbor originate from the west and west-southwest.

Extremal analysis

Allan and Komar (2002b) applied the Automated Coastal Engineering System program (Leenknecht, Szuwalski, and Sherlock 1992) to estimate the 10- through 100-year extreme values for deep-water H_s based on the largest H_s measured each year for the duration of record of the deep water NDBC buoy. As part of the present study, a similar analysis was applied to the annual maximum wave heights measured at CDIP buoy 3601 near Grays Harbor. The annual maximum series of H_s was formed from January 1985 to December 2001 (a period of 17 years). An extreme wave analysis was performed by applying Fisher Tippett Type 1 (FT-1) and Weibull (for shape factor (k) = 0.75, 1.0, 1.4, 2.0) distributions to the annual maximum series (AMS). The Weibull distribution with $k = 2.0$ produces the highest correlation between theoretical and actual distribution of 0.986. A similar analysis was applied to the Peak Over Threshold (POT) for 52 storms with H_s greater than 6.0 m. In this case a Weibull distribution with $k = 1.4$ provides a correlation of 0.99. The results of the analyses for the two buoys are compared in Table 4-2. Statistics of the AMS and POT produce similar H_s for return periods of 10 years or more. There is a difference of 3 to 4 m in the extreme H_s between

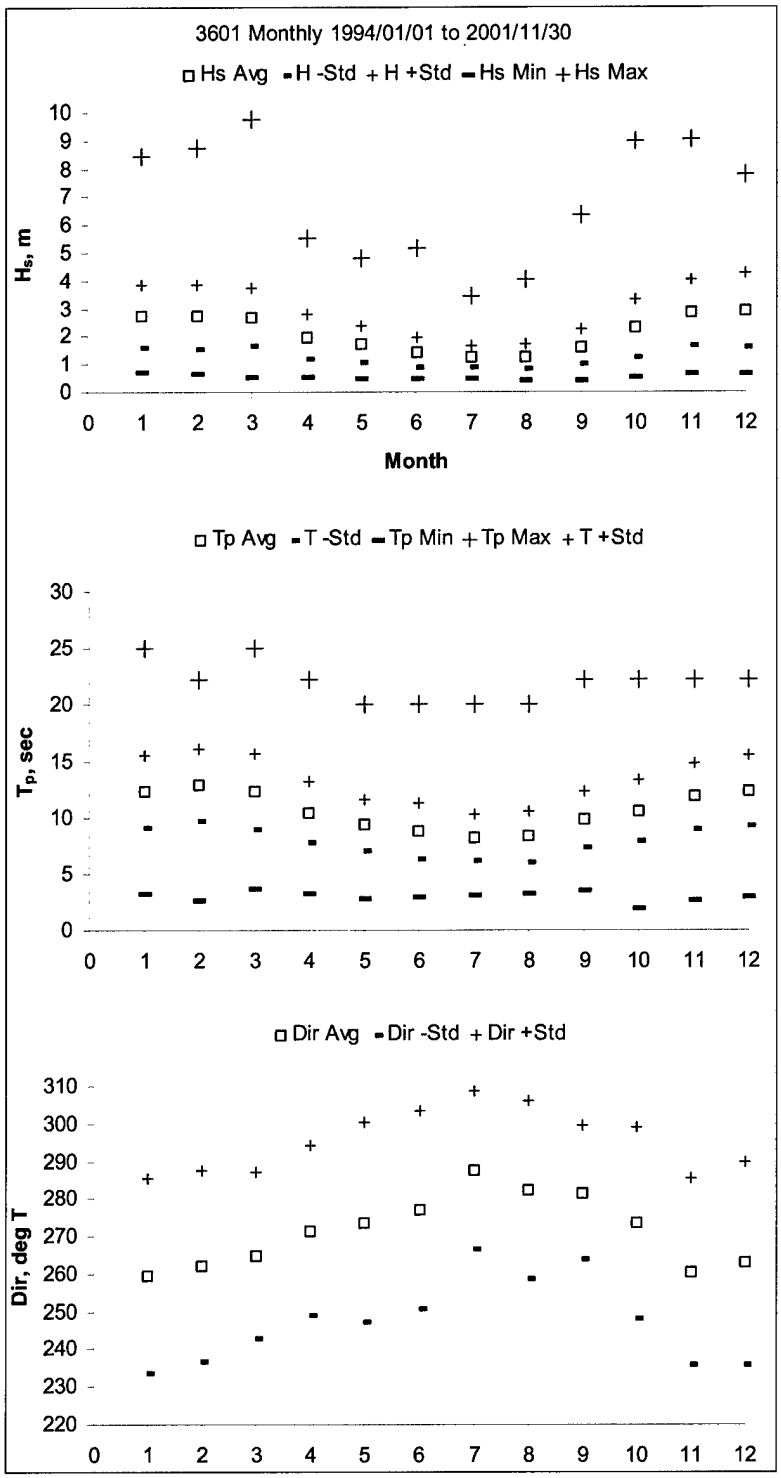

Figure 4-1. Monthly statistics of H_s, T_p, and Dir from 1994-2001 at CDIP buoy 3601

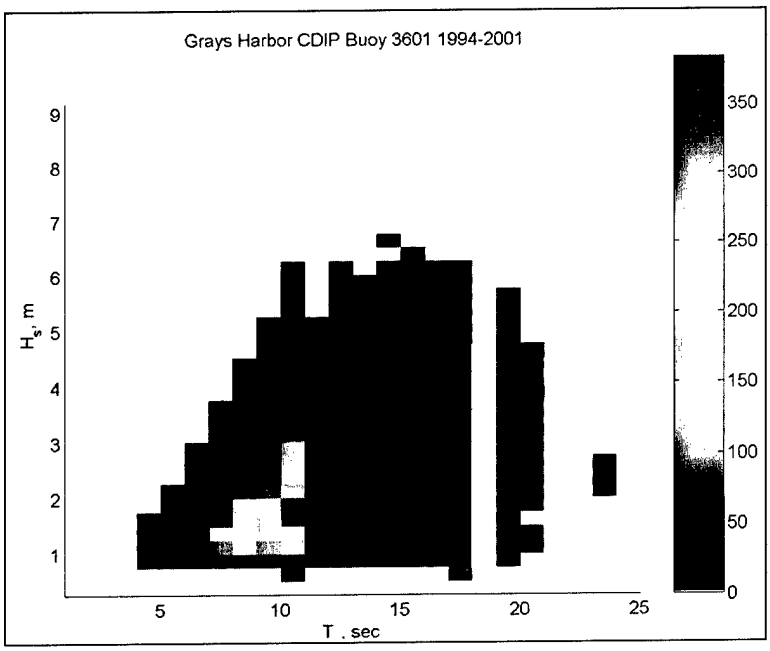

Figure 4-2. Joint distribution of H_s and T_p for measurements at Grays Harbor CDIP buoy 3601 between January 1994 and December 2001. Color scale represents number of hours per year

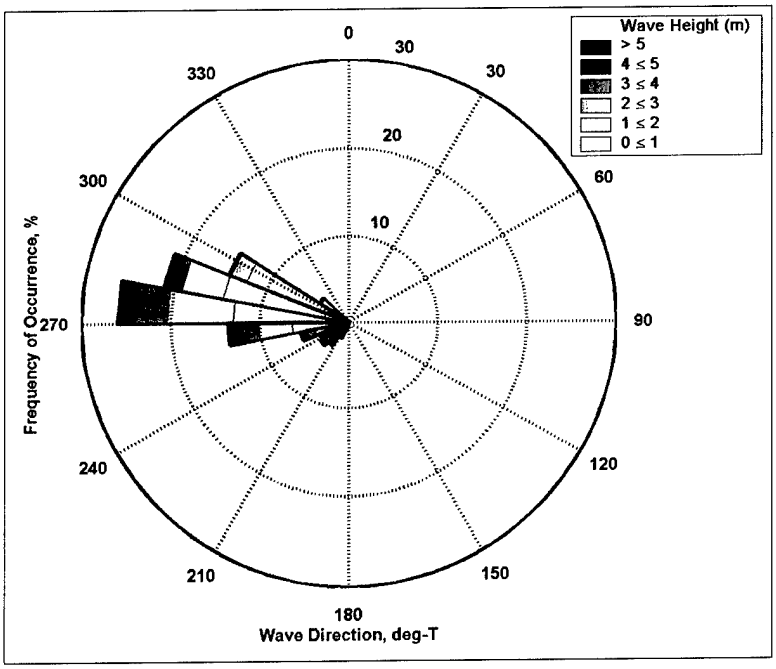

Figure 4-3. Wave rose showing percent frequency of occurrence for all waves in 11.25-deg bands

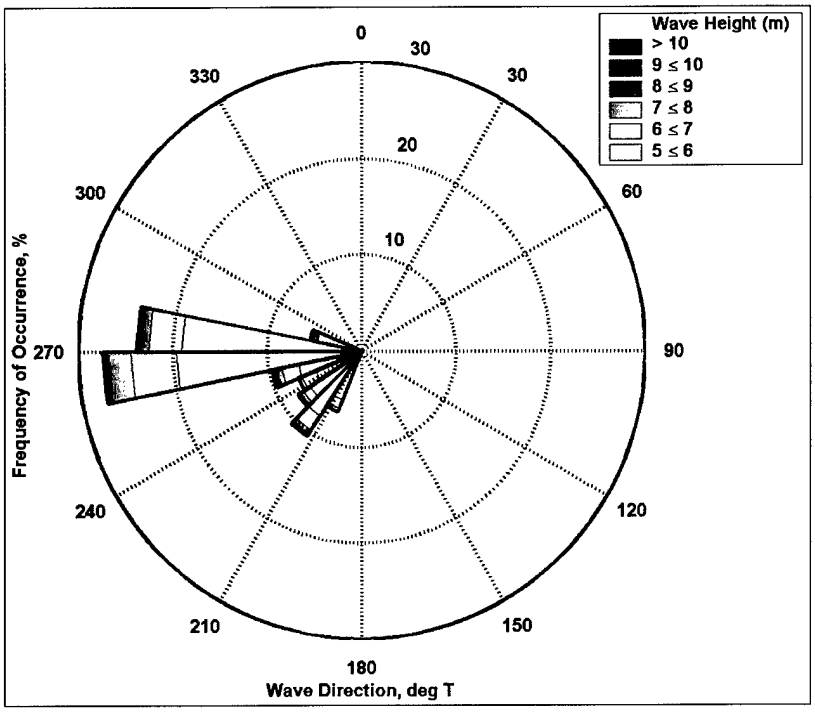

Figure 4-4. Wave rose showing percent frequency of occurrence for waves greater than 5 m only in 11.25-deg bands

Table 4-2
Extreme Significant Wave Height Analysis

Return Period	Washington (NDBC 46005)[1]	Grays Harbor AMS (CDIP buoy 3601)[2]	Grays Harbor POT (CDIP buoy 3601)[2]
2	N/A	7.0	8.0
5	N/A	8.4	8.7
10	12.4	9.2	9.2
25	13.6	10.0	9.6
50	14.3	10.6	10.4
Number of years or storms	22	17	52
Correlation coefficient	0.986	0.986	0.99

[1] Allan and Komar (2002b)
[2] This study

the data from the two buoys. The large difference may reflect the difference in location of the two buoys as influenced by deep-water versus intermediate depth. Lower extreme wave heights might be expected at intermediate depths due to wave breaking.

Interannual variability and long-term trends

Analysis of the NDBC measurements by Allan and Komar (2002b) reveals a statistically significant long-term increase in winter wave height and period over the 20- to 25-year periods of buoy operation, with the largest rates of increase (0.032 m/year) occurring in the Pacific Northwest, corresponding to overall increase of 0.77 m in 24 years. Analysis of the CDIP buoy 3601 measurements over a shorter period at Grays Harbor indicates that the annual mean H_s has been approximately constant at 2.04 m for a 17-year period of record with an average annual standard deviation of approximately 1.0 m (Figure 4-5). In contrast, the annual maximum H_s exhibit a 17 percent increase over the period. Similarly the annual mean T_p is approximately constant at 10.6 sec, whereas the annual maximum T_p increases by approximately 40 percent over the period of record (Figure 4-6).

Allan and Komar attempted to relate the trends in deep-water wave height and period to large-scale climate controls. Results were mixed. The East Pacific Teleconnection Index (EP), a measure of pressure difference between Aleutian Low and Hawaiian High, is related to annual variations in wave heights above and below long-term trends, and to latitudinal variation in the number of storms experienced each winter. However, the EP is not clearly related to actual trends in wave height. The range of climatic variation between El Niño and La Niña, as measured by the Multivariate El Niño/Southern Oscillation (ENSO) Index (MEI), was also found to correlate with wave parameters but at lower latitudes than the Washington coast. The latitude dependence of wave height increases in the North Pacific suggests there may be a linkage with magnitudes, frequencies, and tracks of extratropical storms. For example, Graham and Diaz (2001) found an increase in the frequency and intensity of extreme cyclones in the North Pacific over the last 50 years. Furthermore, Graham and Diaz provide a direct link between increasing extreme wave heights identified by Allan and Komar (2001) and intensities of storms in the North Pacific through analysis of trends in measured extreme surface winds and hindcasts of the generated waves. Their results imply that the progressive increase in wave height extends back at least 50 years. The more vigorous cyclone activity has apparently resulted from increasing upper-tropospheric winds and vertical wind shear over the Central North Pacific. Such changes may be attributable to modulations of El Niño-related teleconnections at decadal and larger scales. Increasing sea surface temperatures in the western tropical Pacific are thought to be the most plausible cause (Graham and Diaz 2001).

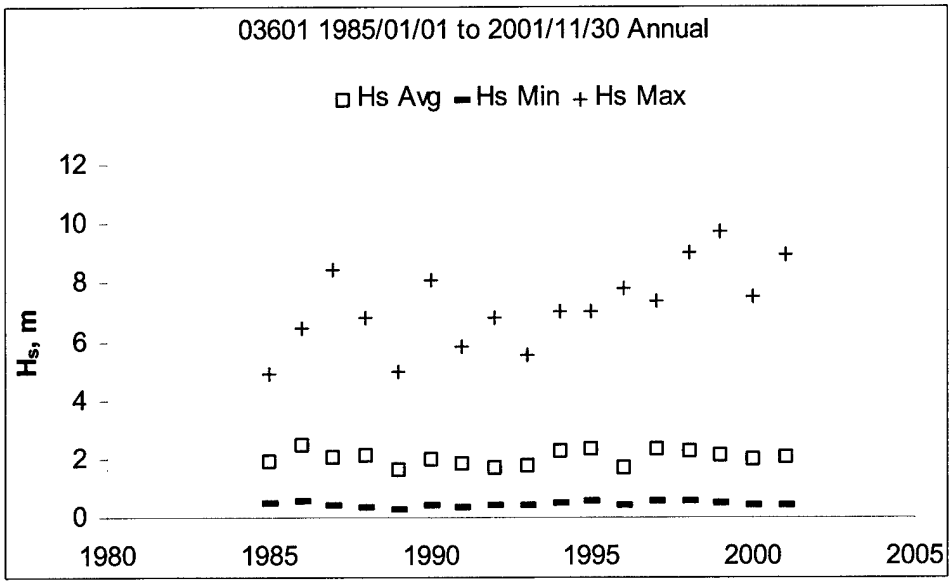

Figure 4-5. Annual wave statistics of CDIP buoy 3601 wave measurements (mean annual H_s, annual maximum H_s, and annual minimum H_s) from 1 January 1985 to 30 November 2001

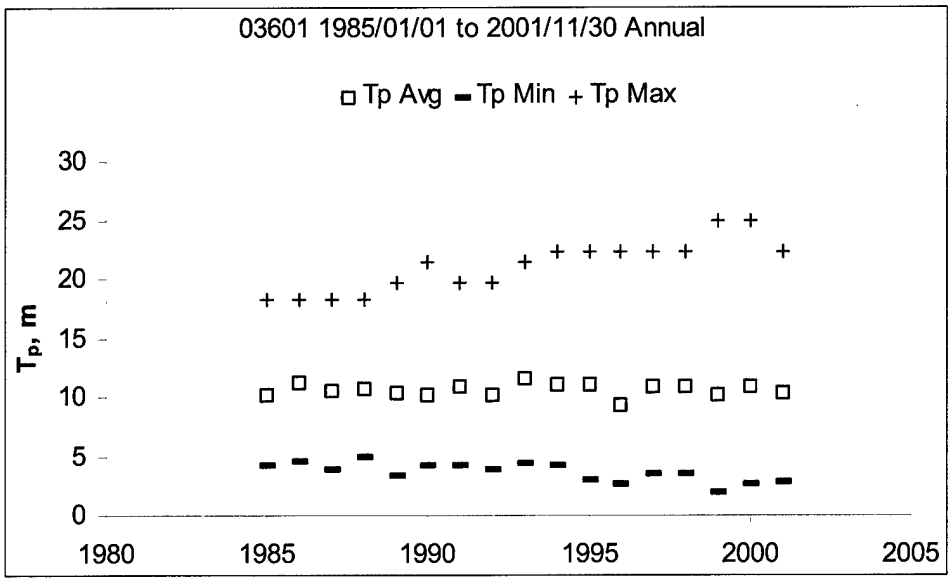

Figure 4-6. Annual wave statistics of CDIP buoy 3601 wave measurements (mean annual T_p, annual maximum T_p, and annual minimum T_p) from 1 January 1985 to 30 November 2001

Wave height and water level anomalies

The variations and trends in deep-water wave heights and periods influence the dynamics of Grays Harbor inlet and adjacent shorelines including the north beach. In particular, water level variation that may be associated with storm surge and set up by breaking waves is a significant factor in beach erosion and may influence the functioning and performance of potential sediment control alternatives at the north jetty.

Figure 4-7 illustrates the strong temporal correlation between the water level anomaly, defined as the difference between the measured water level and predicted water level at Toke Point inside Willapa Bay to the south of Grays Harbor, and H_s measured at the Grays Harbor CDIP buoy 3601. The scatter plot of the same data, shown in Figure 4-8, indicates that water level at Toke Point increases by 0.13 m for every 1-m increase in H_s. For H_s of 8 m, a 1.0-m increase in water level results in a 60-m horizontal shift in the shoreline position at Ocean Shores near the north jetty.

Current and Tide

The current at Grays Harbor is forced by a number of mechanisms, including tidal processes and local, regional, and global meteorological processes. The latter control surface and upper air wind distribution, sea surface temperatures and density distributions, atmospheric pressure variations, and precipitation.

The tide at Grays Harbor is mixed (i.e., having two unequal high and low waters each lunar day), and it exhibits the diurnal inequality typical of the Northwest Pacific coast. At the inlet entrance, the mean diurnal range is 2.6 m, whereas at Aberdeen the mean diurnal range is 3.1 m. The mean spring range near the entrance is approximately 2.8 m. Tidal datum information is shown in Table 2-1. Tidal phase lag is approximately 1 hr for both high and low tides at Aberdeen compared to the ocean tide. Tidal currents dominate the current regime in the estuary, except during high Chehalis River flow when the upper estuary is influenced by its discharge. Nearshore currents near the harbor entrance, driven primarily by wind and waves, are also strongly influenced by tidal discharge in and out of Grays Harbor. The aerial photographs in Figure 4-9 indicate the presence of rip currents in the surf zone north of the north jetty that create high suspended sediment loads in the nearshore that are advected southward past north jetty and into the inlet during periods of west-northwest waves and flood tide. Tidal currents also contribute to wave transformation on the ebb shoal and in the inlet entrance, particularly on ebb tide. Ocean currents outside the influence of estuary tides are driven primarily by winds, deep ocean circulatory currents, and shoaling waves.

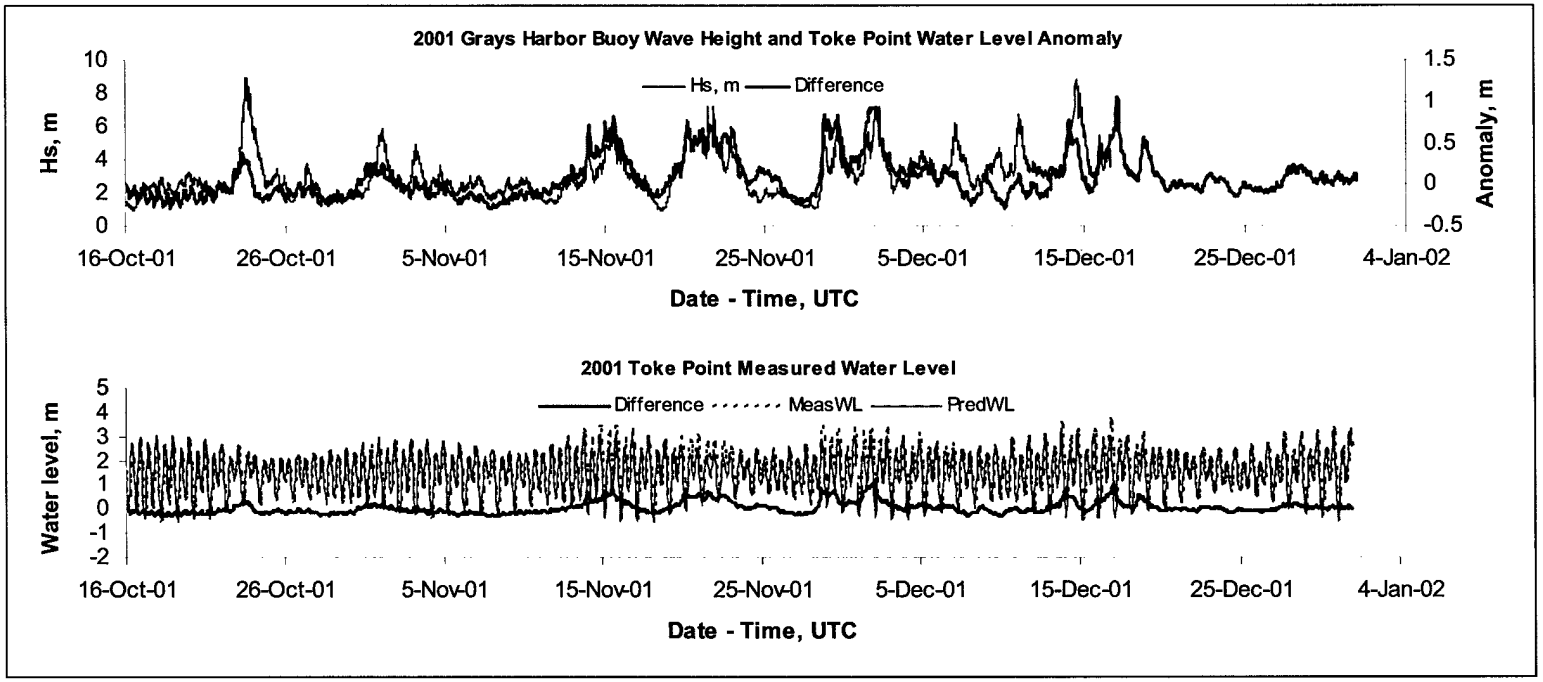

Figure 4-7. Time series of significant wave height at CDIP buoy 3601 and water level anomaly at Toke Point in Willapa Bay (top graph); measured and predicted water levels and water level anomaly at Toke Point (bottom graph) between 16 October 2001 and 4 January 2002

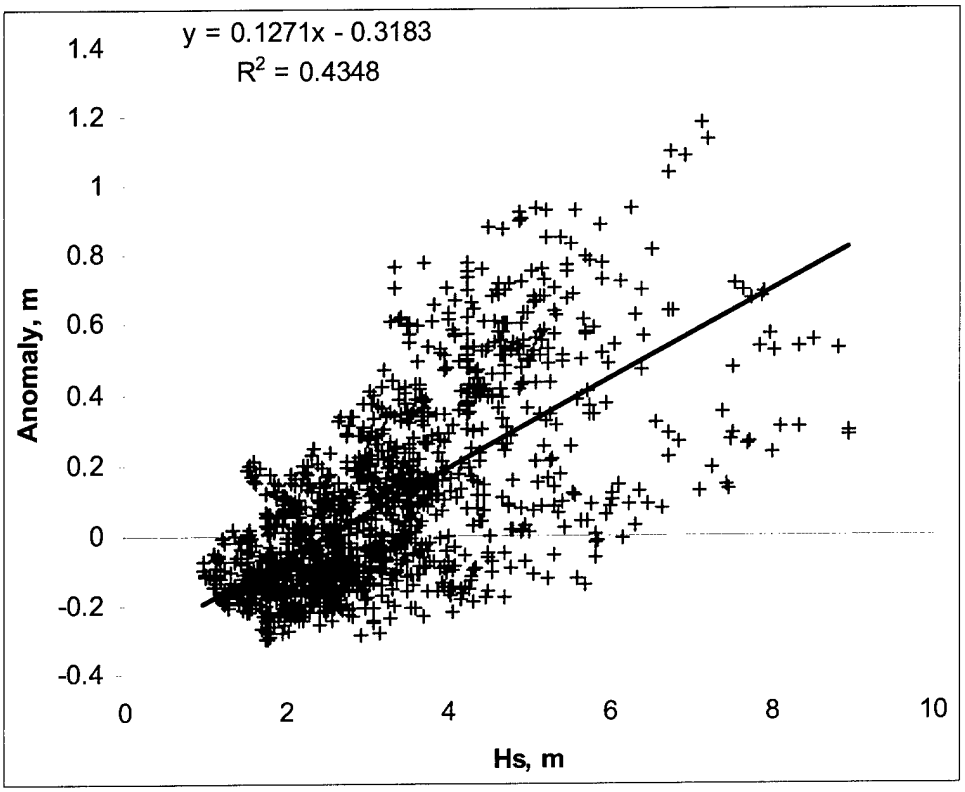

Figure 4-8. Water level anomaly at Toke Point as a function of H_s at CDIP buoy 3601 for 20 October to 16 December 2001

Ocean circulation

Large-scale oceanographic features of the northeast Pacific Ocean have been described by several investigators including Fleming (1955), Tully and Barber (1960), Uda (1963), Dodimede, Favorite, and Hirano (1963), Barnes, Duxbury, and Morse (1972), and Hickey (1979, 1989). The region is influenced by generally weak (5 to 30 cm/sec) large-scale currents (eastern boundary current) with relatively few instabilities that can generate mesoscale eddies and meanders (Hickey 1989); by seasonal variations in the discharge of coastal rivers, of which the Columbia is the major contributor; and by a climate dominated by yearly cyclic changes of the North Pacific High and the Aleutian Low. Coastal currents respond rapidly to local winds and are variable over short periods (days to weeks), but tend to follow seasonal changes in prevailing winds that result in northerly flow in winter and southerly flow in summer.

The Pacific Northwest coastal zone is located at the eastern edge of the region wherein the West Wind Drift divides into the poleward flowing Alaskan Current and the equatorward flowing California Current (Hickey 1989). The general coastal circulation pattern varies with seasonal atmospheric cycles (Anderson and Foster 1979). During the summer, the East Pacific High pressure system migrates

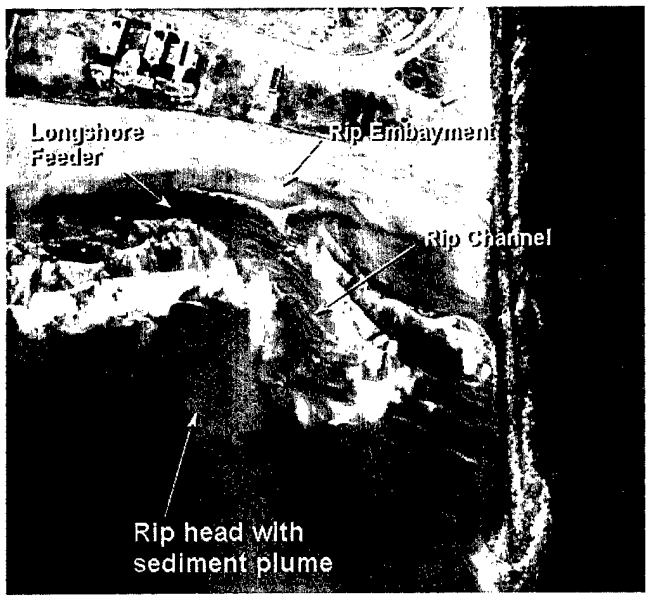

(a) Breaking waves drive southward longshore and rip currents and create high suspended sediment loads in surf zone along Ocean Shores

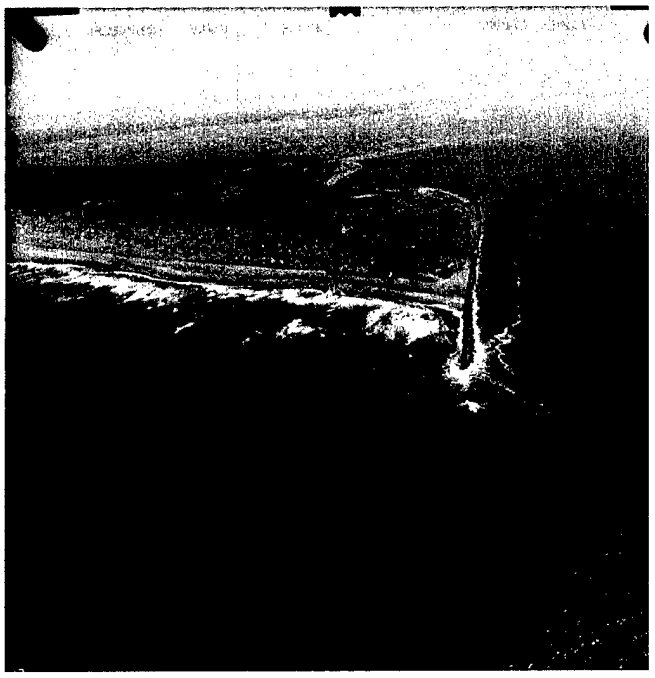

(b) Near the inlet, longshore currents combine with flood tide currents to transport sediment eastward on north side of inlet

Figure 4-9. Aerial photographs illustrating circulation patterns and suspended sediment transport regime typical of summer upwelling conditions and west-northwest waves (Continued)

(c) Suspended sediments entering Grays Harbor on north side of inlet during a flood tide

Figure 4-9. (concluded)

northward from the equatorial region and becomes seasonally stationary off the coasts of California and Oregon. This system generates clockwise winds that blow from the north along the Washington coast and cause surface currents to flow to the southwest (Figure 4-10). The combination of wind stress, ocean density gradients, and Coriolis force creates upwelling of colder, denser bottom water nearshore. The mean current system during the summer generates a vertical circulation pattern of easterly moving bottom water upwelling at the coast and southwesterly moving surface currents.

Hickey (1979) described the seasonal variation of currents comprised by the California Current system, namely, the California Current, the Davidson Current, and the California Undercurrent. The California Current with a typical velocity of 0.1 m/sec and an east-west scale of approximately 1,000 km is strongest during summer (July-August). The velocity maximum appears to be located seaward of the continental shelf at most locations. The California Undercurrent, a jet-like poleward flow with a subsurface maximum, the core of which appears to be confined to the continental slope, also reaches maximum strength during summer.

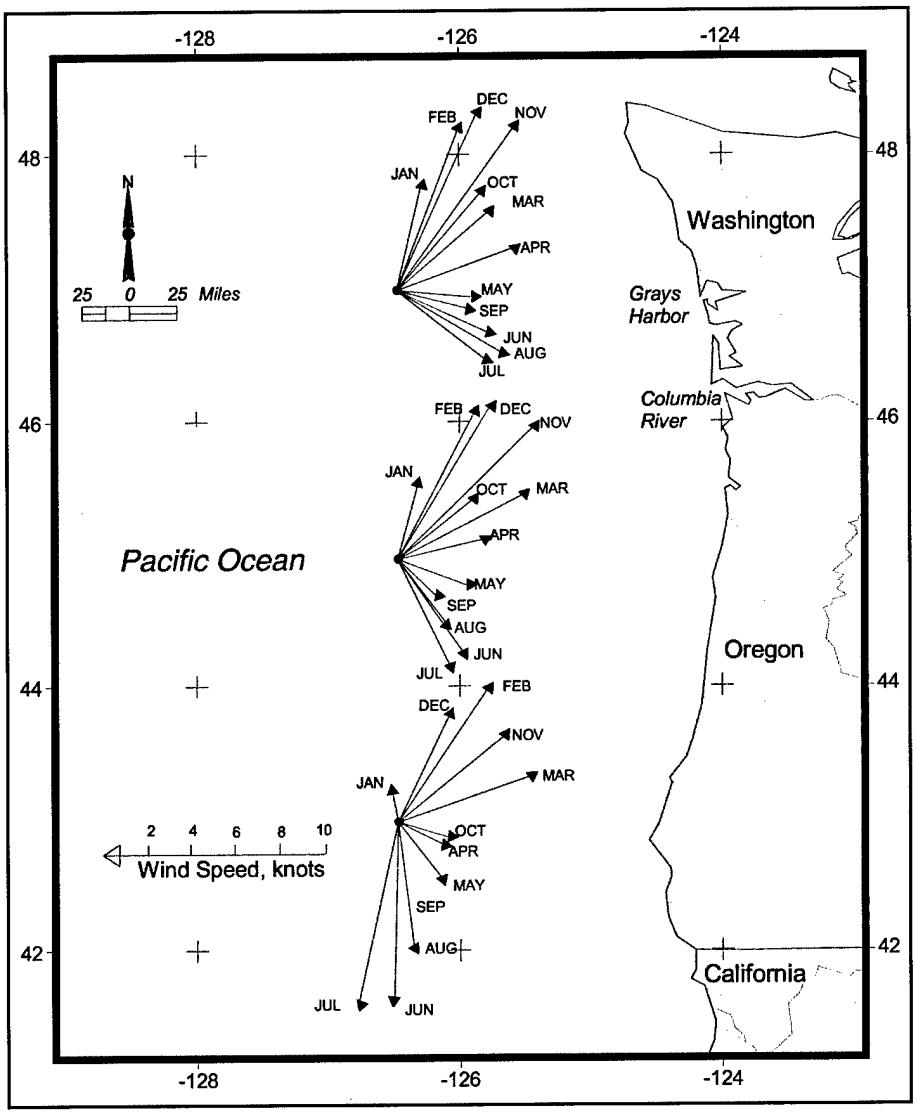

Figure 4-10. Average speed and direction of monthly winds along Washington/Oregon continental shelf (after Duxbury, Morse, and McGary 1966)

During winter, the California Current either moves offshore or is replaced by a pole-ward flow known as the Davidson Current. Also during the winter, the East Pacific High retreats to the equatorial region and low-pressure systems over the Gulf of Alaska (Aleutian Low) dominate the Washington coastal weather migrating west to east across the coast.

Graham and Diaz (2001) describe the life cycle and tracking of North Pacific cyclones: "a typical North Pacific cyclone forms as a wave on the polar front, strengthens, matures, and decays over a period of several days, while traveling several thousand kilometers. During this time, central pressures may fall

20-30 hPa (or more) and then rise again. Individual tracks vary considerably, but most intense lows in the North Pacific form west of the date line between 30 and 40 deg north, tracking first to the east and then curving toward the north as they mature and decay (e.g., Anderson and Gyakum 1989)."

The counterclockwise winds associated with cyclonic activity predominately originate from the south and southwest near the Washington coast. Wind speeds are generally of greater magnitude than those in summer from the north and generate proportionately higher northward flowing surface currents. During the winter, 5 to 8 percent of the wind speeds are between gale-force and storm-force levels. Winds from the south and southwest during winter storms have average speeds of 10 to 20 knots and maximums of 50 to 55 knots (Figure 4-10; Barnes Duxbury, and Morse 1972; Hickey 1989). This meteorological system interrupts the summer density gradient, creating dominant northward surface flow (Davidson Current), with an onshore component, and offshore bottom flow (nearshore downwelling). Storms over the continental shelf intensify the general pattern of circulation. Pressure due to wind setup may be relieved by enhanced downwelling and obliquely seaward bottom flow.

During periods of northerly flow most notably during the winter, coastal currents off Washington State also are influenced by freshwater discharge from the Columbia River. In late summer, the Columbia River accounts for more than 90 percent of the fresh water entering the sea in the region between the Strait of Juan de Fuca and San Francisco Bay. In the winter, this amount decreases to slightly less than 60 percent as a result of the increase in discharge of smaller coastal rivers in response to coastal precipitation and much of the precipitation in the Columbia River basin falling as snow. In winter, the freshwater dilution extends seaward some 50 to 100 km and northward to the Strait of Juan de Fuca (Barnes, Duxbury, and Morse 1972).

Quantitative data on coastal/shelf currents have been obtained from current meters, drogues, and surface floats and indirectly from numerical modeling of coupled ocean-atmospheric circulation. Mean surface speeds reported by Barnes, Duxbury, and Morse (1972) range from 12 cm/sec in summer to 17 cm/sec in winter. Movement of seabed drifters at all seasons is northward at 1 to 2 km/day at depths greater than 40 m, with speeds greater in winter. Hickey (1989) describes and reviews results of analysis of over a decade of measurements including some yearlong current measurements obtained using Aanderaa current meters suspended from taut wire moorings on the continental shelf and slope. Notable were frequent current reversals at most locations and water depths in most seasons. Seasonal signals were largely obscured by large amplitude fluctuations occurring on a scale of several days; such variability is a maximum during winter and a minimum during summer. The principal forcing mechanism for such fluctuations was identified as first mode coastal-trapped waves during summer and local wind stress during winter (Hickey 1989). Transition from poleward winter flow to equatorward spring flow occurs abruptly, whereas the transition from summer to winter flow occurs more gradually during the fall months. According to Hickey, the amplitude of seasonal cycle variations decreases with depth from ~20 cm/sec in the upper water column to ~10 cm/sec in the lower water column on the midshelf. Flow on the inner shelf off Washington was observed to have a greater tendency for poleward flow during summer than flow off the Oregon coast, possibly related to the factor-of-two

decrease in southward wind-driven flow from Oregon to Washington (Landry et al. 1989) as well as the influence of southward flow of the Columbia River plume during summer. Another significant difference is related to the poleward flow of the freshwater Columbia River outflow during winter. This flow is confined to the Washington coast at this time by downwelling circulation. Although flow within the shallow plume is poleward, flow beneath the plume may be equatorward during periods of relaxation of strong southerly winds that typically occur in winter. The general circulation of the Washington and Oregon continental shelf is controlled by large-scale weather systems (Barnes, Duxbury, and Morse 1972). During the summer, winds are generally from the north and northwest at speeds of about 15 knots. As such, littoral currents flow to the south and offshore, and shelf bottom currents flow northward. During the winter, low-pressure systems migrate west to east across the coast, creating winds from the south and southwest with average speeds of 10 to 20 knots and maximums of 50 to 55 knots (Figure 3-2; Barnes, Duxbury, and Morse 1972; Hickey 1989).

Lacy et al. (2001) report measurements of currents profiles, waves, and suspended sediments made with six tripods on the ebb-tidal delta near the 24-m isobath at Grays Harbor in October-December 1999 and May to mid-July 2001. Tidally averaged currents during the fall measurements were directed northward (downwelling) and produced offshore transport of suspended sand. Currents in spring were predominately directed southward (upwelling) except during 2- to 3-day downwelling events. The cross-shore current was directed onshore at mid-depth and offshore close to the bottom, with less offshore transport than during the fall deployment. Northward flowing currents develop at the surface and extend to the seafloor due to an unstratified water column that results from downwelling. The northward dominance of bottom currents during all seasons has been documented by direct current measurements (summarized by Sternberg 1986) and by the movement of seabed drifters (Barnes, Duxbury, and Morse 1972; Hickey 1989).

Tides and inlet circulation

The Grays Harbor estuary has large expanses of tidal flats and numerous channels throughout. Diurnal tidal prism volume for the estuary is 4.8×10^8 cu m (USAED, Seattle, 1989). Spring tide ebb discharges are commonly over 28,000 cu m/sec through the constricted, jettied entrance. Fresh water from river runoff, primarily the Chehalis River, is mixed with seawater in the estuary and forms a low salinity, low density upper layer that moves seaward. Seawater tends to move toward the head of the estuary along the bottom as a high-density current. Vertical mixing of salt water and fresh water is rapid in the estuary, and the estuary is generally well-mixed in the outer harbor and partially mixed in the inner harbor where stratification is at times significant.

The jetties constrict tidal flows between approximately Point Chehalis and Damon Point in the east and the outer bar in the west. The ebb flow has a southwesterly component along the southern half of the entrance, which at times has resulted in scour of a deep channel (greater than 20 m, mllw) along the south jetty. The ebb current extends seaward more than 5,000 m. The flood current is much weaker than the ebb current outside the entrance, except near the jetties. East of the jettied entrance, flood currents become significant across the entrance.

Flood currents are stronger along the north jetty than along the south jetty, while the reverse is true for ebb currents. Outside the influence of the entrance, tidal currents are weak (less than 0.15 m/sec), whereas inside the entrance, peak ebb and flood flows exceed 1 m/sec. Figure 4-11 shows current velocities and patterns in the region of the harbor entrance based on several drogue studies conducted by the Seattle District between 1974 and 1985. Similar patterns have been described based on physical model studies conducted at the U.S. Army Engineer Research and Development Center, Coastal and Hydraulics Laboratory, between September and November 1971, and field measurements by the U.S. Coast and Geodetic Survey.

Seasonal and long-term variability

Considerable research over the past few decades has focused on the character and variability of time-averaged circulation over the North Pacific Ocean. Most analyses reveal a dominant mode of variability associated with fluctuations in the strength, position, and extent of the Aleutian Low (Graham and Diaz 2001). Many studies indicate that much of this variability is related to changes in tropical Pacific sea surface temperatures (SSTs; e.g., Graham et al. 1995). As summarized above, Graham and Diaz (2001) review and describe long-term means and interannual variation of North Pacific winter cyclones. Tracks and formation regions exhibit considerable interannual variability (Anderson and Gyakum 1989), and these changes have significant influence on the marine climate including wave climate and coastal processes (e.g., Seymour et al. 1984; Strange, Graham, and Cayan 1989; Inman and Jenkins 1997; Allan and Komar 2000a), as well as upper-ocean temperature and circulation.

The ENSO defined by warming of equatorial Pacific SSTs is accompanied by a shift in atmospheric pressure across the Pacific and results in unusually high sea levels on the Pacific coast of the continental United States. ENSO events vary in intensity with more intense events occurring on a 4- to-6-year cycle (Michaelson 1989). El Niño in 1982/83 and 1997/98 resulted in significant episodes of beach erosion on the Washington coast when high water levels were accompanied by severe winter storms and downwelling currents. The study by Graham and Diaz (2001) indicates that the frequency and intensity of extreme cyclones over the North Pacific Ocean has increased significantly over the past 50 years, with associated increases in extreme surface winds between 25 and 40 deg north and major changes in cyclone-related circulation patterns in the Gulf of Alaska. More vigorous cyclone activity has apparently resulted from increasing upper-tropospheric winds and vertical wind shear over the central North Pacific. Such changes may be related to ENSO processes at decadal and longer time scales. Increasing SSTs in the western tropical Pacific are suggested as a plausible cause of the observed changes in cyclone-related circulation.

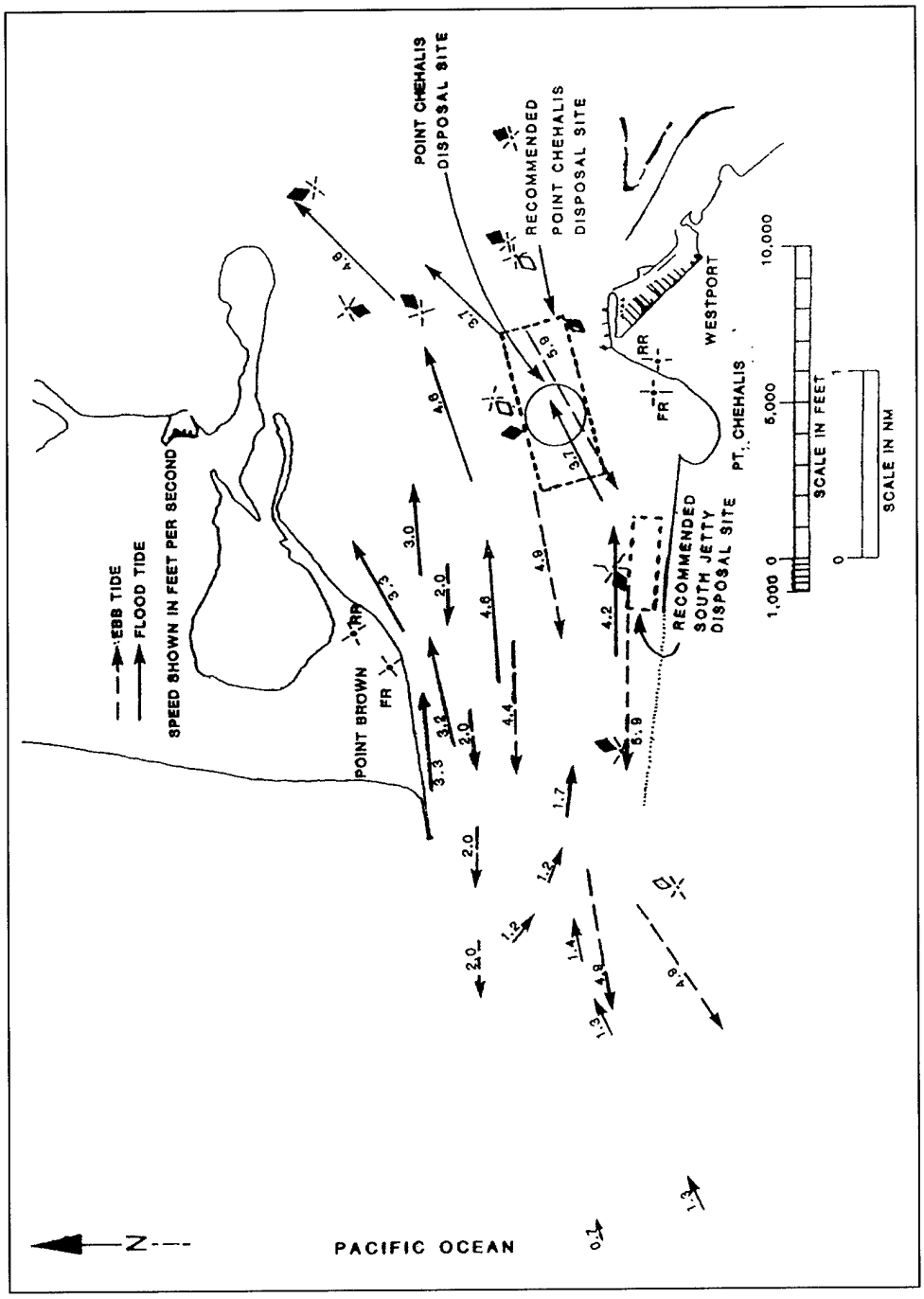

(a) Maximum near-bottom currents as determined by Corps of Engineers Drogue Studies (1974-1981)

Figure 4-11. Currents determined by Corps of Engineers Drogue Studies between 1974–1981 and 1984–1985 (Source: Adapted from USAED, Seattle, 1989) (Continued)

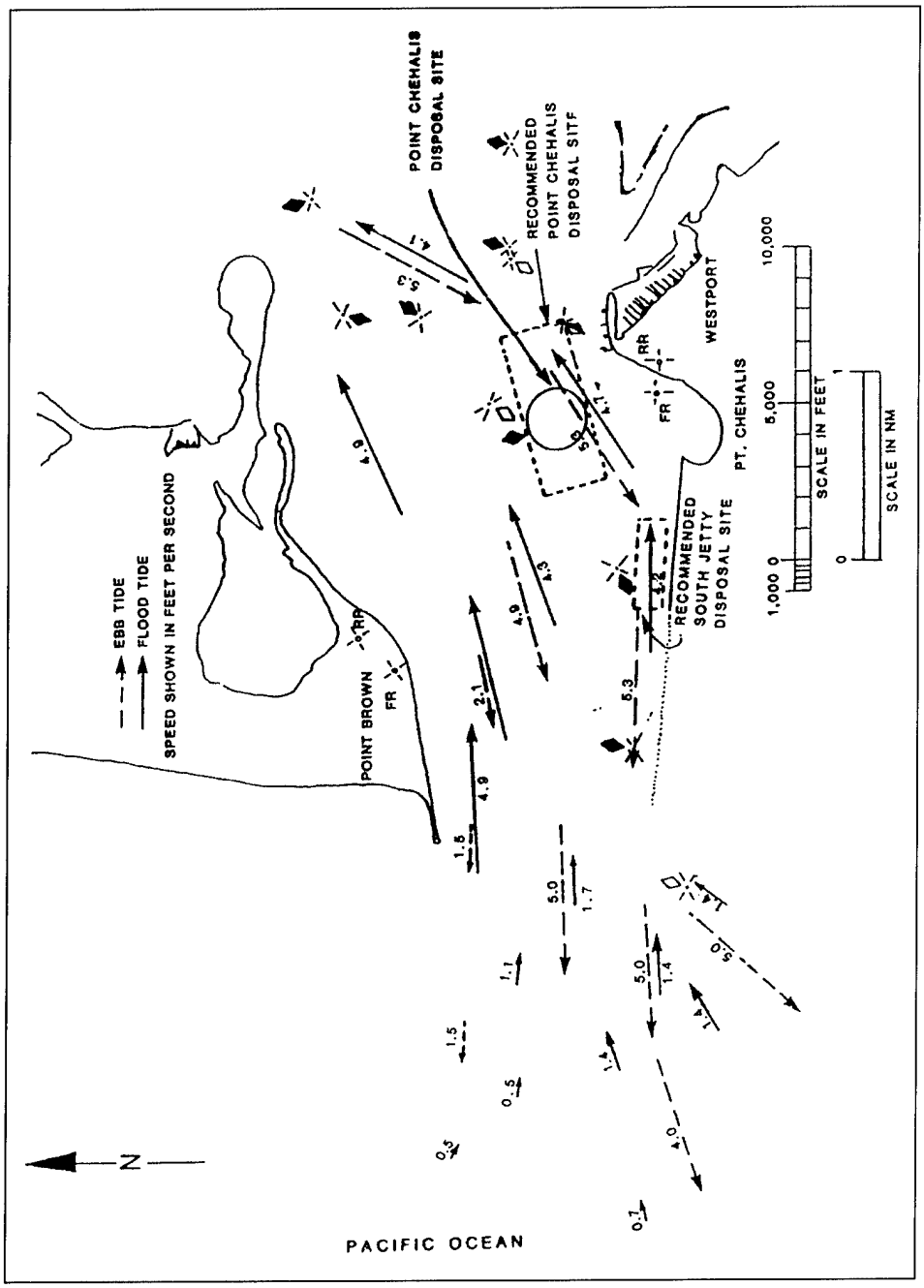

(b) Maximum near-surface currents as determined by Corps of Engineers Drogue Studies (1974-1981)

Figure 4-11. (Continued)

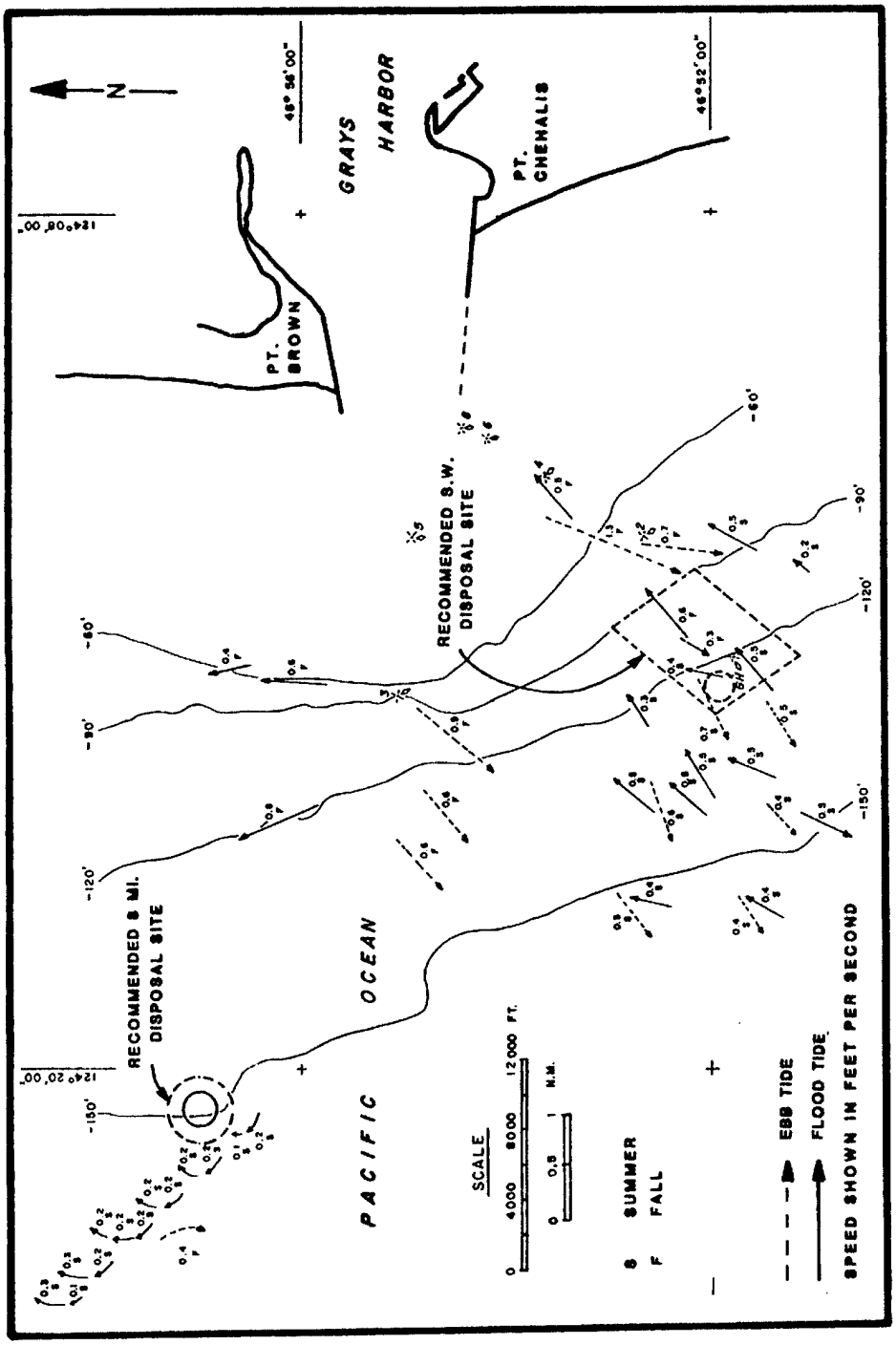

(c) Maximum near-bottom currents as determined by Corps of Engineers Drogue Studies (1984-1985)

Figure 4-11. (Concluded)

The California Current system, at least off California, has interannual as well as seasonal fluctuations (Chelton 1980). These fluctuations also appear to be related to ENSO. During the El Niño, equatorward flow in the California Current is anomalously weak; during La Niña years, equatorward flow in the California Current is anomalously strong.

Sediment Transport

Kachel and Smith (1989) present a comprehensive review and compilation of the current and wave data available for the southern Washington continental shelf prior to the last decade. Their effort was aimed at characterizing typical and extreme sediment transport occurrences in terms of magnitude, duration, and frequency in order to account for the distribution and rates of accumulation and erosion of sediment on the continental shelf. Observations of the resuspension of bottom sediments at mid- to outer-shelf depths during winter storms have been made on the Washington continental shelf by Sternberg and Larsen (1976) and Hickey, Baker, and Kachel (1986). Larsen and Fenton (1974) observed changes in the wave spectrum during sediment transporting events. A typical history for an event off the Washington coast begins with longer period waves (17.5 to 23 sec) of low amplitude followed by successively shorter period waves that first increase and then decrease in height. The typical duration of the sediment transport events at midshelf is 24-32 hr. Drake and Cacchione (1986) observed that substantial increases in suspended sediment that occurred in winter months on the northern California shelf were primarily caused by the coincidence of larger waves (with periods > 12 sec) from distant storms and strong currents associated with local storms. Strong bottom stress due to combined waves and currents is a major factor controlling the distribution of bottom sediments on the shelf.

Application of a sediment transport model by Kachel and Smith (1989) revealed that the most geologically significant transport, in terms of erosion and reworking of bed sediment and volumes or mass transported on the Washington shelf, occurs in storms coincident with large swells, a finding that is consistent with the results of Drake and Cacchione (1986). The effect of extreme transport on the shelf is to remove fine material from the inner shelf and nearshore and southern portion of the Washington shelf and transport it northward and seaward in suspension. Kachel and Smith (1989) further conclude that large storms that leave their mark on the stratigraphic record by eroding and reworking sediment are not the only cause of redistribution of fine sediments northward from the mouth of the Columbia River or of the observed depositional pattern on the shelf. Periods of weaker currents and smaller, shorter storms must contribute significantly to dispersal of fine sediments and silts northward on the midshelf and build up the midshelf silt deposit.

More recently, Sherwood et al. (2001) measured waves, currents, near bottom velocities, and suspended sediments on the ebb delta at Grays Harbor between depths of 10 and 20 m, during two deployments in fall 1999 and spring 2001. During the fall, the primary wave direction shifted from west-northwest to west-southwest; sediment transport was dominated by storm-induced downwelling circulation that transported suspended sediment northward and offshore. Bedload fluxes were shoreward but many times smaller than suspended

load fluxes. During the spring, smaller waves arrived mostly from the west-northwest and sediment transport was dominated by upwelling circulation interrupted by short periods of down welling. Net transport in spring was directed northward at deeper sites and southward at shallower sites. Near-bottom transport was offshore at deeper sites, whereas negligible net cross-shore transport occurred at shallow sites. The bedload contribution to transport was significantly larger in spring relative to the fall and directed onshore. Southward and onshore transport associated with upwelling in spring was associated with beach accretion, whereas the offshore and northward downwelling transport in the fall coincided with beach erosion at Ocean Shores (Ruggiero et al. 2001).

Field Measurements of Coastal Processes

This section presents analysis of time series measurements of waves, currents, and suspended sediment concentrations collected as part of this study during fall 1999 from the inlet and ebb-shoal areas and from the nearshore areas along the north beach during spring 2001.

Measurements of directional waves, currents, sediment in transport, and short-term seabed response in and near the Grays Harbor entrance were made to evaluate the functioning of a proposed shore-parallel submerged spur at north jetty, Grays Harbor. Direct measurements including a suitable range of wave heights, periods, directions, and tidal ranges are required for verification of the numerical and physical models being developed and applied at Grays Harbor to evaluate wave transformation, circulation, and sediment transport. A key to success in modeling is a field measurement program to obtain sufficient information about primary input parameters and evaluating the reasonableness of model results. Calibration and verification data assist in substantially reducing uncertainty of model output so that final results become useful, quantitative approximations. Quantitative estimates of sand transport rates at the Grays Harbor entrance are essential for determining inlet sedimentation and dredging requirements in the navigation channel and to assess existing conditions at the north jetty and along the north beach. The processes controlling sediment transport at the Grays Harbor entrance are complex and are spatially and temporally variable due to the interactions among wave and current boundary layers and the nonlinear variation of sediment transport with respect to forcing. Measurements of near-bottom current and orbital velocities, together with the short-term sediment response, are needed to reduce the uncertainties associated with predictions of sand transport rates. Prior to the present study, data were not available on the near-bed, short-term sediment transport processes and their relationship to forcing by wind, waves, and tides. In particular, no short-term measurements were available with which to evaluate the frequency, intensity, and duration of the alongshore transport of sand at the north beach, the southward bypassing of sediment at north jetty, and east-west fluxes of sediment inside the entrance to Grays Harbor.

Data collection included deployment of: (a) Surf and Inter-tidal Dynamics Sensor Platforms (SIDSEP), (b) High-Energy Sub-Tidal Tripods (HESTT), and (c) vessel-mounted Acoustic Doppler Profiler (ADP) transects of vertical current structure. Each SIDSEP consists of a SonTek Hydra to measure waves, currents, and suspended sediment concentrations (SSC) in the intertidal surf zone on the

north beach and subtidal nearshore along Damon Point. The HESTT were deployed and recovered by an HH-60J helicopter in deeper water near the north jetty and the north beach and consist of ADP and Hydra systems to measure directional waves, current speeds, vertical current structure, and SSC.

In winter and spring 2001, four SIDSEP were deployed near the mllw shoreline along the north beach north of the north jetty. In spring 2001, two HESTT were deployed and recovered by helicopter and several ADP transects together with grab samples of SSC and bottom sediment were obtained near the north jetty. Roving transects of current profiles were obtained using vessel-mounted ADP integrated with a differential GPS and hydrographic survey system from the entrance and inner harbor over two spring tidal cycles in September 2001. In late winter-early spring 2002, instrument arrays were deployed at three locations between the 10- and 12-ft depth contours directly north of the north jetty and at two locations south of Damon Point. Depth values in this chapter are depths below the plane of mllw. Data collection and processing are described in Appendix D, and the HESTT and SIDSEP are described further by Osborne, Hericks, and Kraus (2001).

Measurements from seven tripods equipped with ADP/Hydra systems deployed near the inlet entrance from September to November 1999 were also analyzed (Hericks and Simpson 2000). At approximately the same time, five tripods were deployed by the U.S. Geological Survey (USGS) on the ebb shoal to the north and south of the inlet as part of its 1999 nearshore processes study (Sherwood et al. 2001). Concurrent with the spring 2001 deployments, the USGS deployed five tripod systems on the Grays Harbor ebb shoal to the north and south of the inlet. Figure 4-12 shows the location of instruments deployed in and near Grays Harbor between 1999 and 2002.

Analysis Methods

Waves

Descriptive parameters of surface gravity waves were calculated from time series of water surface elevations (η) using standard spectral analysis and zero-crossing techniques (e.g., Earle, McGehee, Tubman 1995). Descriptive parameters include significant wave height (H_s), spectral significant wave height (H_{m0}), significant wave period (T_s), peak spectral wave period (T_p), average wave period (T_{av}), and mean direction of wave approach at peak frequency (DIR). H_s was determined as $H_{1/3}$, the average of the highest third of the waves, from a zero up-crossing analysis of η. The height H_{m0} was determined using:

$$H_{m0} = 4.0\sqrt{m_0} \tag{4-1}$$

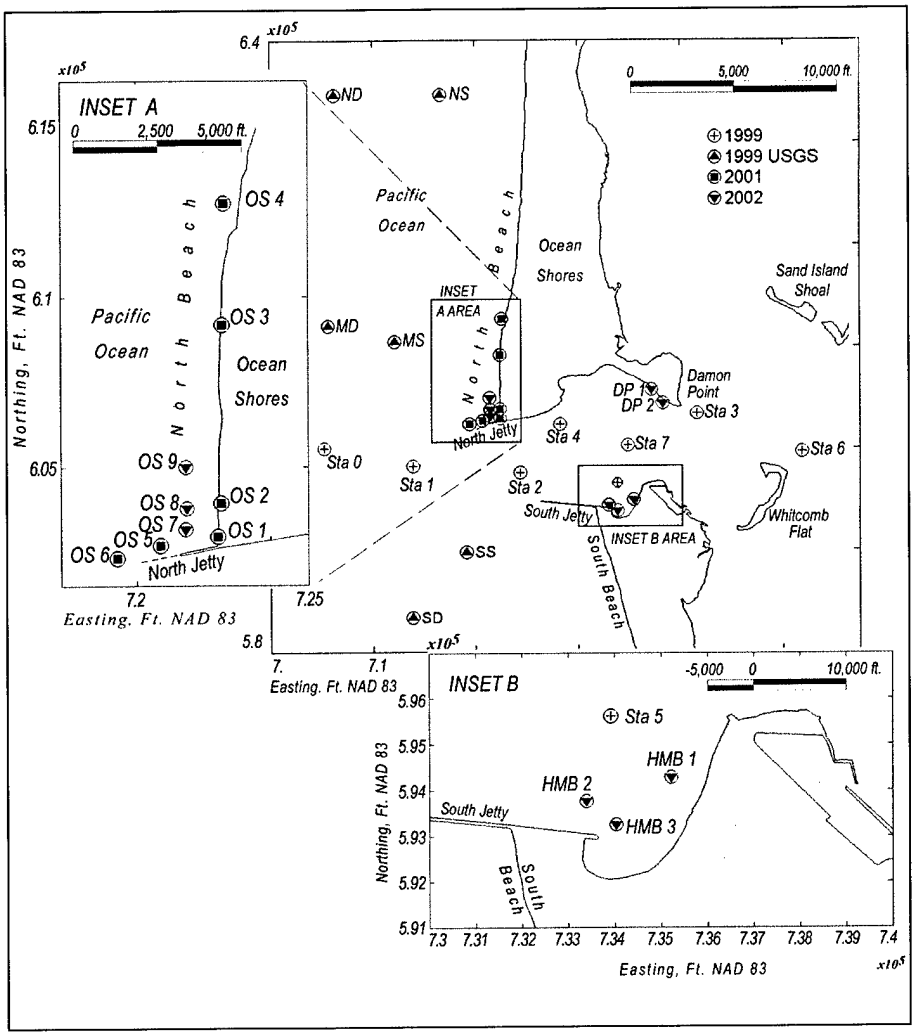

Figure 4-12. Location of instrument deployment in and near Grays Harbor

where m_0 is computed from

$$m_0 = \sum_{n=1}^{N_b} C_{zz}(f_n) df_n \tag{4-2}$$

in which C_{zz} is the nondirectional wave spectrum computed from η, the summation is over all frequency bands centered at f_n, and df_n is the bandwidth. DIR is estimated following the convention of Longuet-Higgins, Cartwright, and Smith (1963) and Earle, McGehee, Tubman (1995) for analysis of pressure-velocity records.

Currents

Near-bottom currents. Instantaneous near-bottom currents from stationary Acoustic-Doppler Velocimeter Ocean (ADVO) measurements were averaged

over a 6-min burst to obtain estimates of local mean currents. Corrections based on linear wave theory, sensor elevation, water depth, and wave number were applied to convert velocities to near-bed wave orbital speeds (e.g., Green and MacDonald 2001).

Current profiles and transects. Stationary measurements of burst-averaged ADP current profiles were bin-averaged to obtain an estimate of the depth-averaged current speeds and directions for direct comparison with numerical circulation model results (Chapter 7). Peak ebb and flood vectors were determined by separating the ebb and flood phases of the current speed time series by zero-crossing analysis.

Profiles of current speed and direction from roving ADP transects obtained at the north jetty and in the inlet were merged with bottom elevation data to produce a cross section of speed and direction relative to distance along the transect. Vertical profiles of speed were depth-averaged from 1 m below the water surface to 0.5 m above bottom. Current direction was first multiplied by the current speed and then averaged to obtain a speed-weighted depth-averaged current direction. Depth-averaged speed and direction vectors were then scaled and plotted as plan-view vectors overlain on a chart of the study area.

Suspended sediments

Instantaneous near-bottom suspended sediment concentrations measured by optical backscatterance sensors (OBS) were averaged over a 17-min burst to obtain estimates of mean near-bed concentration. Time series of individual bursts were also examined to identify relationships to wave forcing. Time series of suspended sediment concentrations were combined with near-bed velocities to compute at-a-point estimates of suspended sediment transport as described below.

Sediment grain size

Relatively small variations in sediment size can result in significant variations in sediment transport potential (e.g., Gailani and Smith 2000). Therefore, appropriate values of sediment size must be defined for calculating transport rates at each measurement location.

Samples of beach sediments were obtained from the beach surface near mllw along the north beach during the deployments and retained for grain size analysis and for OBS calibration. Two grab samples of bottom sediments were obtained from the area near the north jetty, one sample from near tripod sta OS 6 and the other from the south side of the north jetty. Each jetty tripod was equipped with two sediment traps for collecting samples for grain size analysis. Sediment samples were also collected from the streambeds of the Copalis River and Connor Creek upstream from the stream mouths; the two streams deliver suspended sediment and bedload sediment to the north. Beach littoral drift system north of the north jetty. Table 4-3 summarizes grain size statistics for the samples described above.

Table 4-3
Grain Size Statistics

	D_{50} (mm)	Mean grain size, Dmn (mm)	Standard deviation, Dstd (mm)	Skewness	Description		
Top Trap (sta OS 5 & OS 6)	0.207	0.227	0.597	-0.36	Fine sand	Mod sorted	Very skewed, fine
Bottom Trap (sta OS 5 & OS 6)	0.304	0.547	0.259	-0.56	Coarse sand	Poorly sorted	Very skewed, fine
Beach	0.330	0.322	0.696	0.22	Medium sand	Mod well sorted	Skewed, coarse
River	0.177	0.176	0.796	0.00	Fine sand	Very well sorted	Symmetrical
Jetty Grab - sta OS 6	0.195	0.205	0.662	-0.28	Fine sand	Mod well sorted	Skewed, fine
Jetty Grab - South Side	0.390	0.415	0.588	-0.07	Medium sand	Mod sorted	Symmetrical

Sediments from the north beach have a median grain size, D_{50}, of 0.18-0.40 mm. D_{50} is largest near the north jetty and decreases northward (Ruggiero and Voigt 2000). Bottom sediments near the end of the north jetty contain a higher proportion of finer sands than do the beach sediments.

Sediments near the mouth of the Copalis River and Connor Creek have similar size distributions. The narrow distribution of sand sizes, which peaks between 0.125 and 0.250 mm (fine sand), is typical of well-sorted wind-blown sand. The source of this sediment is interpreted to be dunes. Both rivers are actively reworking dune sands prior to delivering the material to the littoral system.

Size distributions of sediment samples from the top traps at the jetty tripods compare well with that of the grab samples of bed sediment taken near sta OS 6. Distributions of sediment from the top traps have a slightly higher percentage of fines, whereas sediment in the bottom traps has a higher percentage of coarse sand and fine gravel. Coarse grains are confined to a discrete layer in the lower trap sample from sta OS 5. The coarse layer is possibly associated with large southwest waves during a storm (14-16 May). The grab sample from the south side of the north jetty also contains a high percentage of coarse sand and fine gravel. Trap sample distributions were used to establish the median grain size for input to sediment transport predictions from the instrument tripods deployed at the jetty as described in the next section. Sediment from the grab sample at sta OS 6 was selected to calibrate the OBS sensors deployed on the jetty tripods. Sediment from beach samples was used to calibrate the OBS sensors deployed on the beach pods.

Bed elevation

The distance from the bed to the SonTek ADVO transducer is recorded at the beginning of each sampling burst. The ADVO acoustically measures the distance to the solid boundary and records a distance when three estimates of boundary positions agree within 1 mm. The measured distance is converted to a relative elevation value referenced to the base of the tripod legs. Negative relative elevations indicate scour below the tripod legs while positive relative elevations indicate net accretion. While each distance measurement is very accurate, changes in frame orientation (instrument pitch and roll) and sinking of the tripod into the sediment as a result of scour can lead to errors in the interpretation of bed elevation change. Relative bed elevation is required as an input to sediment transport algorithms for adjustment of near-bed velocities.

Sediment transport

Quantitative estimates of sand transport rates at Grays Harbor entrance are developed from the wide-area measurements of waves, currents, bed sediment characteristics, and suspended sediment concentrations. Methods listed below were selected for analysis of the north jetty sediment transport conditions during the period of measurements:

a. Bailard's (1981) total load model was applied assuming the velocity field to be represented by the formulations described by Guza and Thornton (1985). The bottom slope is also included in the model. The model is hereafter referred to as "Bailard" (Guza and Thornton 1985).

b. Van Rijn's (1989a, 1989b, 1993) total load model ("van Rijn").

c. Integrated products of at-a-point measurements (e.g., Jaffe, Sternberg, and Sallenger 1984; Osborne and Greenwood 1992a, 1992b). This method is hereafter referred to as the at-a-point measurements method.

Each of the selected methods is based on well-documented techniques and has been verified by both laboratory and field measurements in combined wave and current environments. Each method is different in terms of the simplifying assumptions and representation of transport processes. Each method except the at-a-point measurements method requires estimation of the combined wave and current related shear stresses and current available to transport sediment. The Bailard method and at-a-point measurements method include terms that represent net contributions from waves as well as currents, whereas the van Rijn models applied here include the waves as a mechanism that influences gross transport. In general, most transport occurs near the seabed and bed shear stresses can be better described by using current measurements near the bottom rather than vertically averaged currents, particularly in a stratified regime. Therefore, wherever possible, the near bottom ADVO measurements served as the basis for calculating bed shear stress and friction factors employed in the models. Both the Bailard and van Rijn methods estimate suspended load and bedload separately and then add them to obtain total load. The at-a-point measurements method includes only the suspended load portion of the transport at one point above the bed.

Although the at-a-point measurements are based on measured suspended sand concentration and velocity, they do not provide a record of total transport. The height of OBS sensors above the seabed prevents the kind of measurements required for calculating the near-bed suspended load transport, and the OBS is not capable of measuring the bedload. The at-a-point measurements provide the most direct means of estimating the relative contributions of currents and waves to net transport.

Results

Waves and wave-dominated currents

The joint occurrence of wave height and direction measured at the Grays Harbor CDIP buoy 3601 during the deployments in 1999 and 2001 is shown in Figure 4-13. Table 4-4 provides a summary of statistics for descriptive wave parameters for each deployment. Wave directions measured in May 2001 are representative of the range of wave directions experienced at Grays Harbor, with the majority of waves coming from the west and west-northwest and a smaller number of relatively large waves coming from the southwest. However, the May 2001 observations do not include waves in height classes above 5 m and are representative of summer conditions. Measurements obtained in fall 1999 from the inlet and ebb shoal provide an accurate representation of the transition from summer to winter wave climate with nearly 3 percent of the measured waves being greater than 5 m.

Wave heights in the inlet entrance and on the ebb shoal are also significantly modified by the strength and direction of tidal current. The modifications to wave height and steepness by the tidal current are discussed in the Chapter 7 section on wave modeling.

Spectral analysis of near-bed velocity measurements made during storms reveals that orbital motion associated with surface gravity waves ($T < 25$ sec) contributes the majority of variance to the velocity field on the ebb shoal, the nearshore along the north beach, near north jetty, and in the outer portions of the inlet. At depths as great as 20 m (e.g., sta 0, 1999) short-period surface gravity waves contribute 77 to 92 percent of the total variance in the velocity time series during storms in which H_s exceeds 3 m. The proportion of the total variance associated with infragravity waves ($T > 25$ sec) increases with decreasing depth, particularly within the surf zone and proximity to the shoreline along the north beach, and in the inlet entrance where waves interact with strong tidal currents. At sta 4 (north side of the inlet entrance, depth 10-11 m) for example, short-period waves contribute 54 to 84 percent of the total variance. The variance associated with infragravity waves also grows and decays with increasing and decreasing H_s during storms at all locations on the ebb shoal, the nearshore along the north beach, near the north jetty and in the outer portions of the inlet.

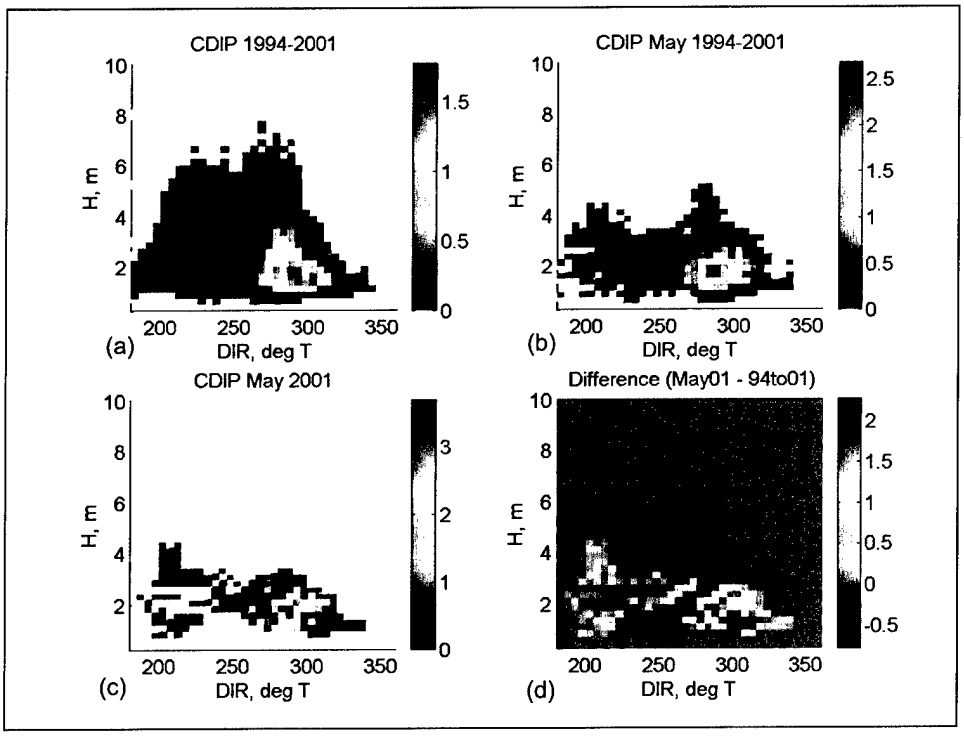

Figure 4-13. Joint occurrence of H_s and (a) DIR measured at Grays Harbor CDIP buoy 3601 for all observations between 1994 and 2001; (b) DIR measured during instrument deployments in fall 1999; (c) DIR measured in spring 2001; and (d) difference between c and a. The color bar represents percent frequency of occurrence

Table 4-4
Summary Statistics of Descriptive Wave Parameters

	1994-2001	1994-2001 (winter averages)	1994-2001 (summer averages)	September-October 1999	November-December 1999	May 2001
H_s, avg	2.1	2.7	1.6	1.9	2.9	1.7
H_s max	9.7	8.8	4.9	7.8	6.0	4.8
Percent Occurrence of H_s > 5 m	2.1	4.4	0.1	2.1	2.9	0
T_p, avg	11	12	9	9.7	12	9
T_p, max	25	21	23	18	22	20
T_p, min	3	3	3	2	4	3
DIR, avg	271	264	279	279	259	274

Figure 4-14 shows time series of h, H_s, and DIR measured concurrently at the Grays Harbor CDIP buoy 3601 and the tripods near the north jetty (sta OS 5 and OS 6) during the spring deployment in 2001. Wave heights, periods, and directions measured at the north jetty correlate well with the offshore buoy measurements in terms of both magnitude and phase. Deviations in wave height between the two series represent the effects of shoaling of smaller waves and depth-limited breaking of the largest waves between the wave buoy at 43 m depth and the north jetty at depths of 7-10 m. Deviations in wave direction between the buoy and the nearshore measurements are caused by refraction of waves from west-northwest induced by nearshore morphology as waves propagate from deep water and by diffraction of waves from west-southwest induced by the presence of the jetty. Local time-varying water depth, controlled by tidal elevation, also causes a small variation in wave height at the north jetty. In contrast, water depth variation associated with the rise and fall of the tide is the major factor controlling the nearshore wave heights measured on the north beach (shown in Figure 4-14).

Average wave orbital velocities, u_0, at the north jetty (sta OS 5) in spring 2001 are shown in Figure 4-15 together with bed shear stress due to waves τ_w and bed shear stress due to combined waves and currents, τ_{cw}. Shear stresses were calculated following the method of Madsen and Wikramanayake (1991). The strong temporal correlation between u_0, τ_w, and τ_{cw} indicates that τ_{cw} is wave-dominated. Near the north jetty, the critical threshold for fine sand is exceeded more than 77 percent of the time by τ_{cw} while the threshold for coarse sand is exceeded 57 percent of the time during the deployment. On the outer ebb shoal, the critical threshold for fine sand is exceeded no more than 27 percent of the time during the fall deployments in 1999, whereas at locations in the inlet entrance, the threshold is exceeded between 40 and 80 percent of the time (Table 4-5).

During storms, strong currents also flow across shore and alongshore, particularly on the ebb shoal, the nearshore along the north beach, near the north jetty, and in the outer portions of the inlet. Burst-averaged current vectors at stations on the ebb shoal and outer entrance are shown in Figure 4-16 during the storm that occurred between 27 October and 2 November 1999, when H_s reached a maximum of 8 m. Waves during the storm arrived predominately from the west-southwest. Currents outside the entrance (sta SS, SD, MD, and ND) and across the entrance (sta 01), have significant offshore (westerly) and northerly components (up to 0.8 m/sec) at the peak of the storm. These strong northwest-directed currents span several tidal cycles and grow and decay synchronously with local wave heights. The measured current patterns indicate that significant quantities of sediment may bypass the entrance during major storms in which waves arrive from the southwest and west-southwest.

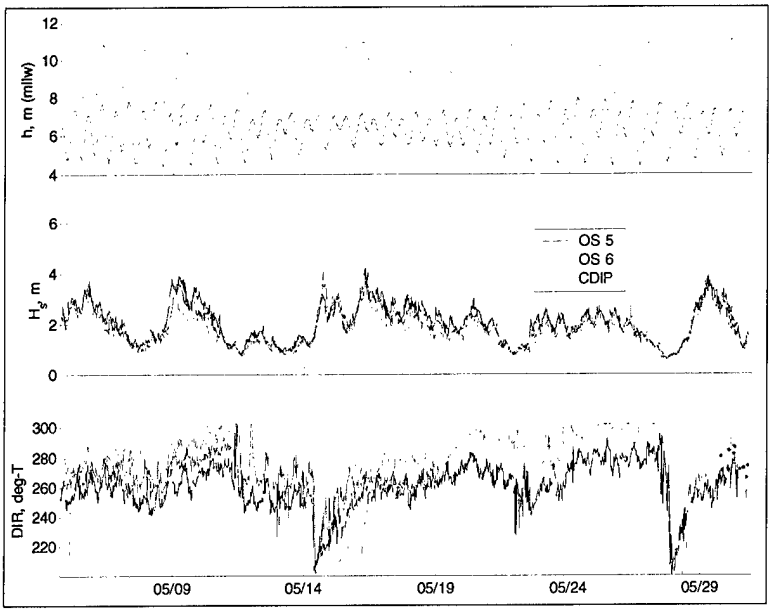

a. Near-bed current vectors

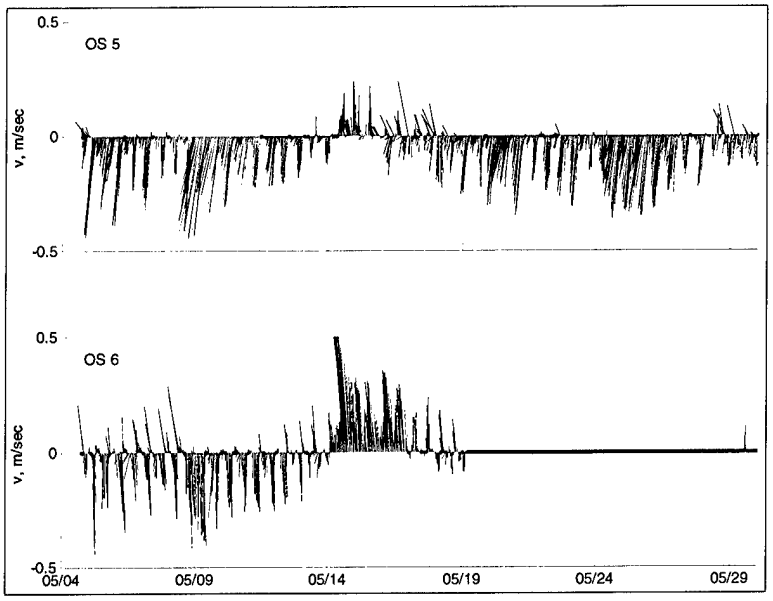

b. Depth-averaged current vectors

Figure 4-14. Time series of h, H_s, DIR. [Note H_s and DIR from CDIP buoy 3601 are also shown in (a)] (Continued)

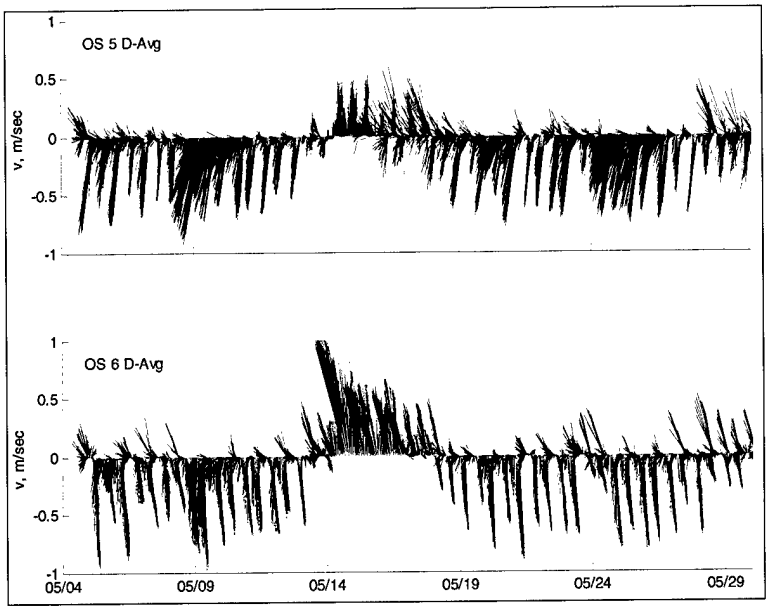

c. Stations OS 5 and OS 6 near north jetty during spring deployment in 2001

Figure 4-14. (Concluded)

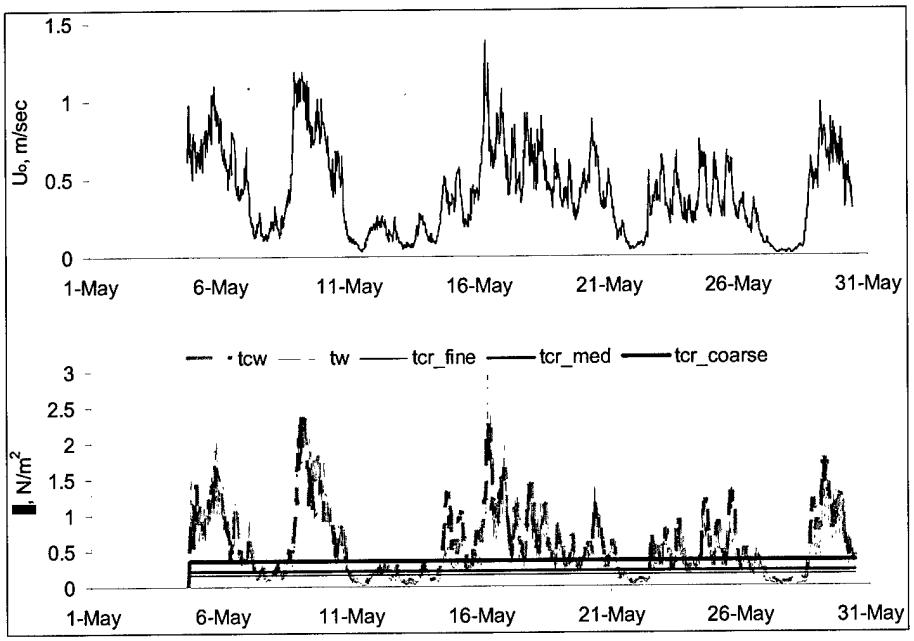

Figure 4-15. Time series of U_0 , τ_{cw}, and τ_w at north jetty (sta OS 5) during spring deployment in May 2001. Also shown is critical threshold shear stress, τ_c, for fine, medium, and coarse sand

Table 4-5
Percentage of Time τ_c Exceeded During Deployment

	Average Depth (m, mllw)	Fine Sand	Medium Sand	Coarse Sand
sta 0	17.6	27	22	13
sta 1	13.3	40	31	17
sta 2	13.5	64	52	26
sta 3	13.7	80	71	50
sta 4	10.4	62	52	37
sta 5	9.6	51	40	25
sta 6	10.0	50	40	19
sta 7	16.8	71	65	48
sta OS 5	7.3	77	72	57
sta OS 6	10.9	64	53	36

Currents in the surf zone along the north beach are complicated by local variations in nearshore bathymetry, by proximity to the north jetty, and by variations in offshore wave height, period, direction, and water depth. Offshore-directed currents predominate near the bed at most locations along the north beach away from the influence of the north jetty (Figure 4-17). Near the north jetty, shoreward-directed currents can occur depending on offshore waves (e.g., sta OS 1 on 7 May 2001). The magnitude of the nearshore current speed varies with h and H_s, as might be expected for a near-bed cross-shore flow in the surf zone. The north component, V_n, is more variable at all four stations. From 7 May 2001 (1740 hours) to 8 May 2001 (1300 hours), the average wave direction was 267 deg (west-southwest), and this produced northwesterly longshore and offshore currents at sta OS 3 and OS 4, but southeasterly (longshore/onshore) flows at sta OS 1 situated directly north of the north jetty (Figure 4-17). Currents at sta OS 2 are predominately northwesterly likely due to the instrument being positioned on the margin of a rip current fed by shoreward flow along the north jetty. The localized circulation near the jetty is often induced by diffraction of waves as they pass the north jetty. From 8 May 2001, at 1300 hours until the end of the deployment, currents at sta OS 3 and OS 4 are southwesterly in response to west-northwest waves.

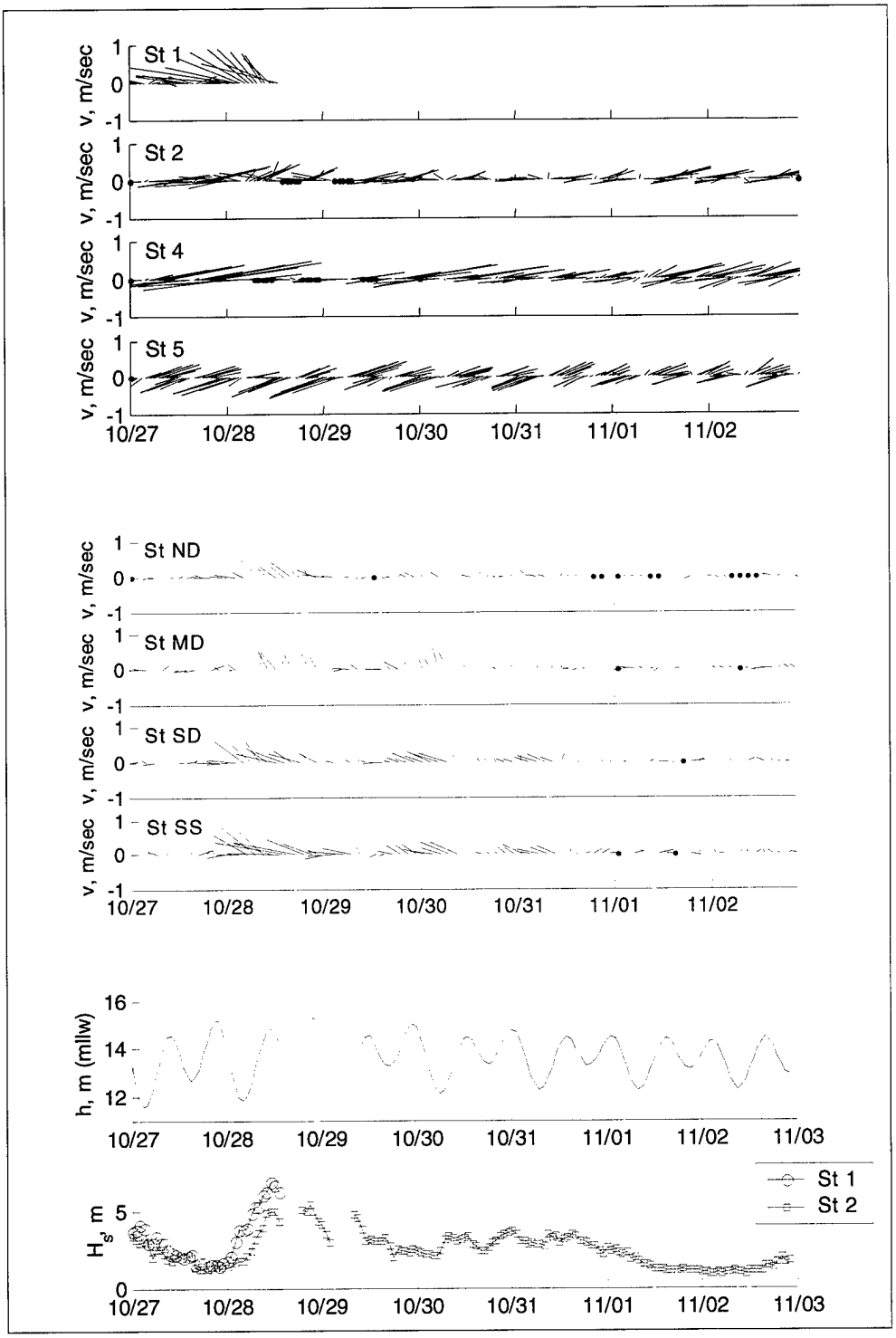

Figure 4-16. Time series of current vectors during storm of 10-27 to 11-03 1999, in inlet entrance (sta 1, 2, 4, 5), ebb shoal (USGS, ND, MD, SD, SS), and h and H_s at sta 1 and 2 inlet entrance stations

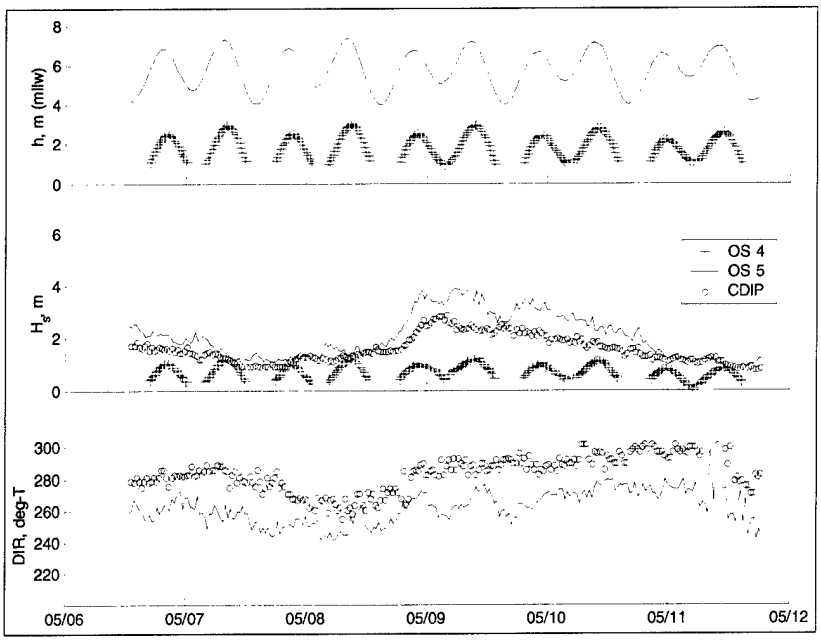

a. Time series of h, H_s, and DIR at sta OS 4 and OS 5 and CDIP buoy 3601

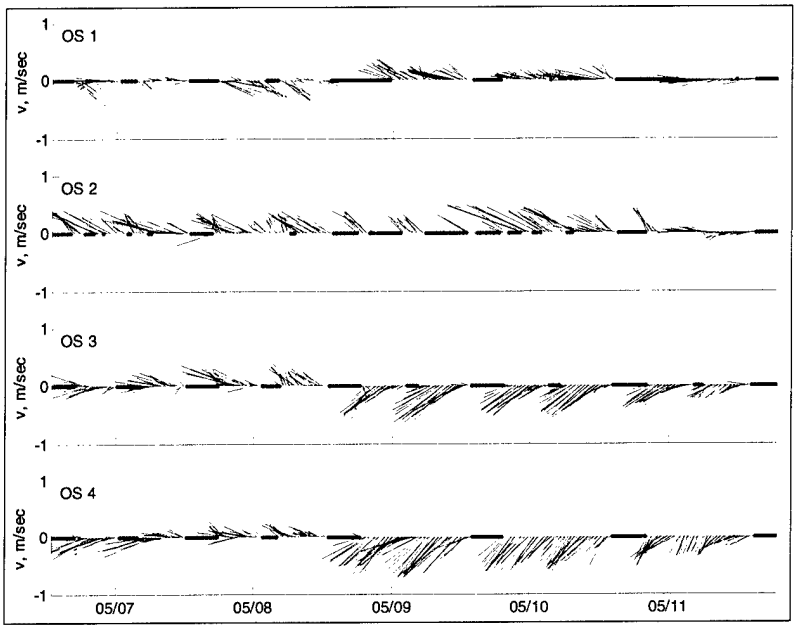

b. Time series of velocity vectors at SIDSEP (sta OS 1 to OS 4)

Figure 4-17. Nearshore measurements during spring 2001 deployment on north beach

Nearshore current direction at locations away from the influence of the jetty varies with offshore wave angle. Figure 4-18 shows time series of the angle of wave approach at CDIP buoy 3601 and current direction at sta OS 4 (4 km north of the north jetty) during May 2001. Between 6 and 7 May 2001, waves approached from the west-northwest (280 deg), and the current direction at sta OS 4 was to the southwest (230 deg). Late on 7 May 2001, the angle of wave approach shifted to the west-southwest (265 deg) and current direction switched to the northwest (315 deg). On 9 May 2001, the angle of wave approach changed back to the west-northwest (285 deg), and the current direction shifted back to the southwest (210 deg). Waves approaching from the southwest yield a northerly longshore current, whereas waves approaching from the northwest result in a southerly longshore current. The exact angle at which this transition occurs is difficult to quantify because the longshore current direction is a function of not only wave angle, but also local depth controlled wave height (position in surf zone), local wind forcing, and beach morphology.

Tides and tidal currents

The speed of tidal currents decreases steeply with distance outside the entrance, except in areas directly seaward of the entrance to a distance of approximately 5 km where the ebb jet dominates the mean current field. Measurements indicate a counterclockwise tidal ellipse at locations outside the inlet (Figure 4-19). Flood currents generally are weak and variable (sta 0 and 1) on the ebb shoal. In contrast, ebb currents are strong and directed offshore due to the concentration of the ebb jet as it exits the inlet.

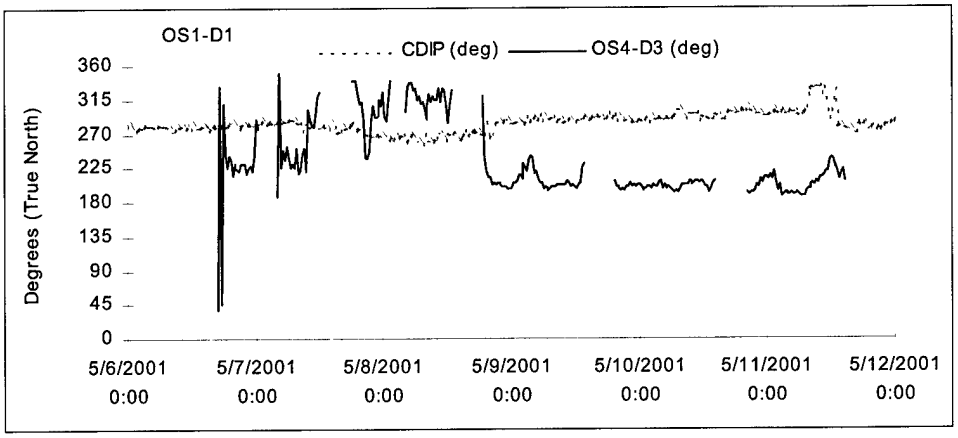

Figure 4-18. Time series of direction of wave approach (α_w) measured at Grays Harbor CDIP buoy 3601 and current direction (α_c) measured at sta OS 4 in May 2001

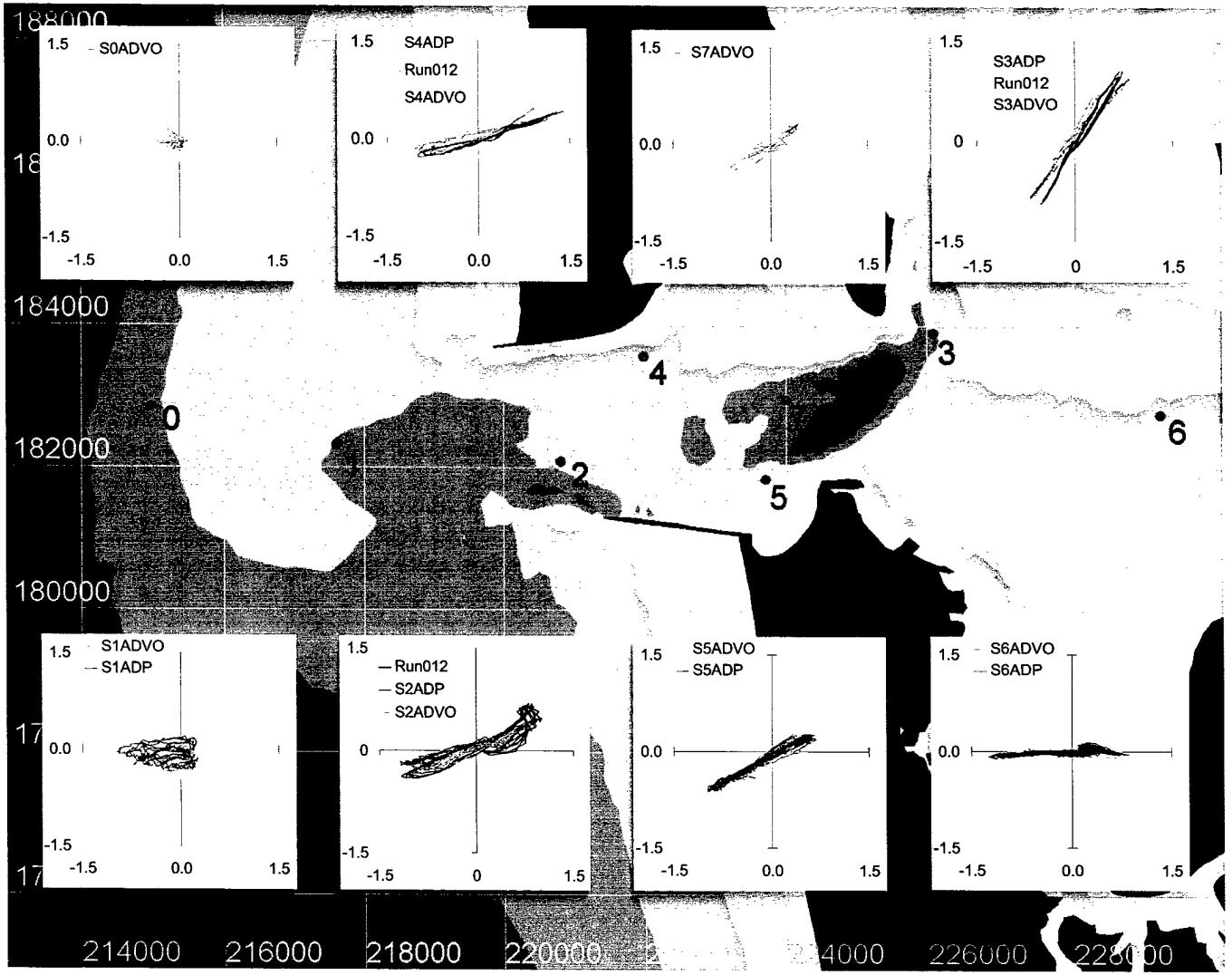

Figure 4-19. Near-bed (ADVO) and depth-averaged (ADP) tidal current ellipses (12-14 September 1999)

Flood current speeds are significant near the jetties. Figure 4-20 shows the average peak ebb and average peak flood vectors at sta OS 5 and OS 6 near the seaward end of the north jetty. Ebb currents are weak in comparison to flood currents at these locations. The patterns indicate convergence (and acceleration) of the flood current as flow is forced to pass over and around the seaward tip of the north jetty to enter Grays Harbor.

Figure 4-21 depicts the vertical and horizontal variation in speed and direction of current flowing past the end of the north jetty at peak flow during flood tide on 12 May 2001. The cross-section corresponds with transect 5 shown in Figure 4-22. The current accelerates up to approximately 1 m/sec over the submerged portion of the north jetty during the flood. Water is forced to flow seaward along the north side of the north jetty through the flood as a result of a separation eddy that occurs at the tip of the jetty. As the flood wanes, the region of westward (seaward) flow expands southward into the entrance channel on the south side of north jetty. Strong southward flows continue past the tip of north jetty following reduction in flood flow on the inlet side of the jetty. Additional figures, showing the horizontal spatial distribution of depth-averaged flow around the north jetty as the flood tide progresses, are included in Appendix D.

Inside the entrance (sta 2, 3, 4, 5, 6, and 7), the strength of tidal forcing increases relative to storm- and wave-driven currents, though wave-orbital motions may dominate the velocity field at locations near the outer inlet (sta 2, 4, and 5), particularly during storms. Peak ebb and flood currents inside the inlet entrance vary mainly with tide range. Inside the inlet, currents are also constrained by inlet bathymetry and the presence of the jetties and tend to flow northeast and southwest on flood and ebb, respectively. At sta 2, in the middle of the entrance between the jetties, near-bottom peak flood and peak ebb speeds are nearly equal. At sta 4, on the north side of the inlet entrance, peak flood speeds are stronger than peak ebb speeds. The opposite is true at sta 5 on the south side of the inlet entrance near Half Moon Bay. Spatial patterns of peak flood and ebb current vectors on a spring tide are shown in Figures 4-23 and 4-24. Appendix D includes additional figures showing spatial current vectors during a spring tide. Measurements support the concept of a separation of the ebb and flood streams to the south and north sides of the inlet, respectively. Strongest currents occur in the deepest portion of the inlet throat off the southeast end of Damon Point. Figure 4-25 depicts the vertical and horizontal variation in speed and direction of current flowing between the tip of Damon Point and Westport during the ebb tide on 18 September. The weakest currents on both ebb and flood occur on the north side of the south jetty to the west of Half Moon Bay.

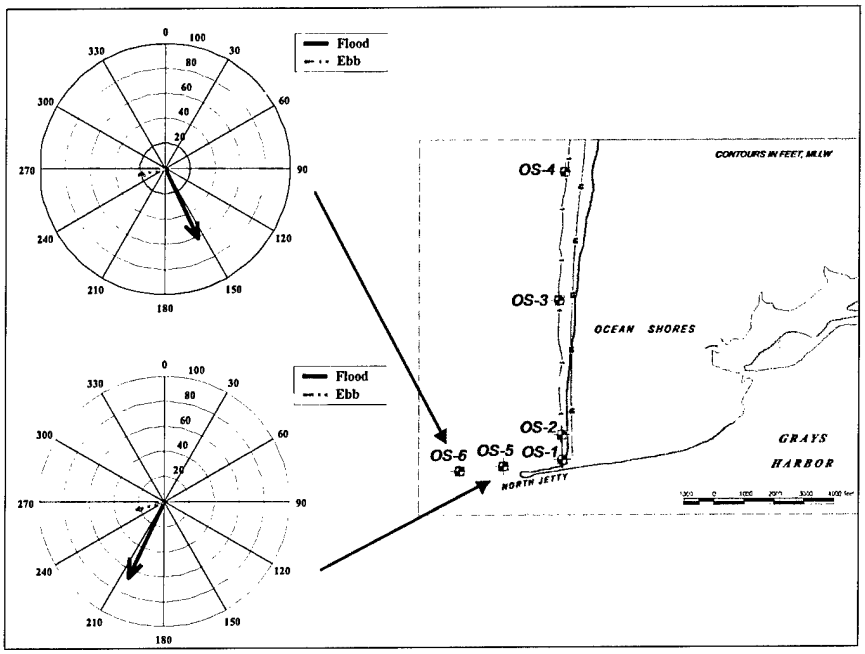

Figure 4-20. Compass plots of average peak flood and average peak ebb velocity vectors. Averaging includes all peak flood and peak ebb vectors between 4 and 30 May 2001

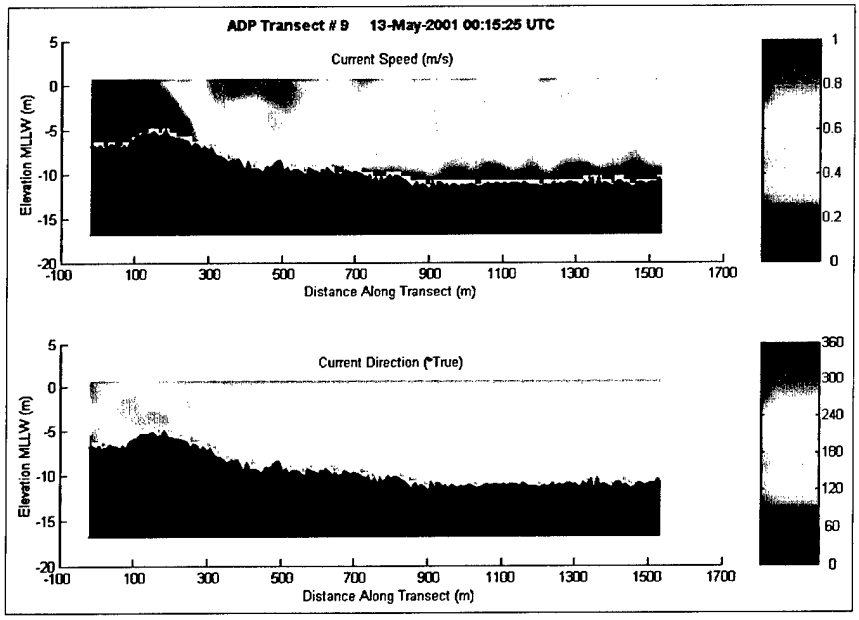

Figure 4-21. View looking south of current speed and direction during 12 May 2001 flood

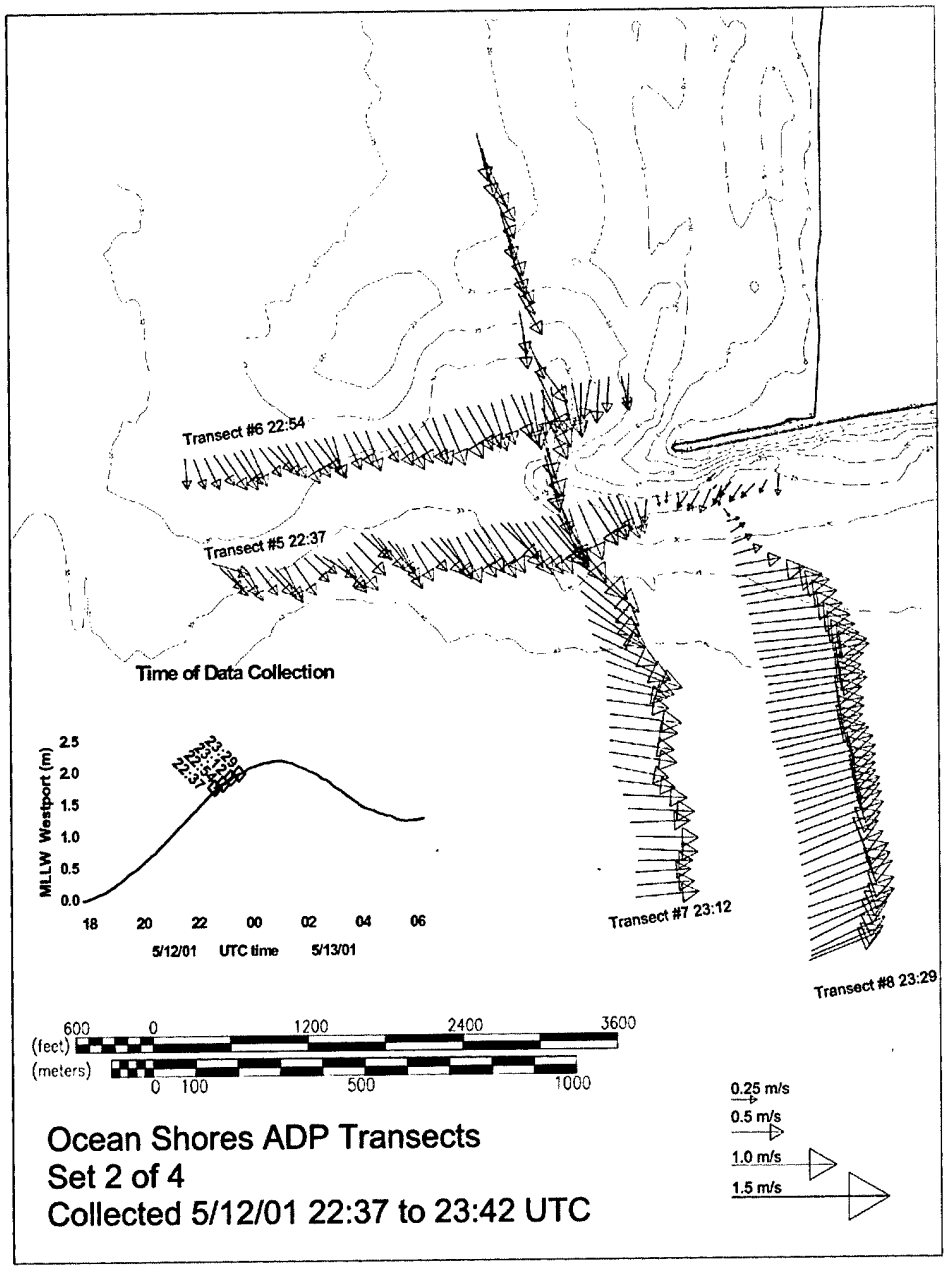

Figure 4-22. Depth-averaged current vectors along ADP transects on 12 May 2001 between 2126 and 2208 UTC

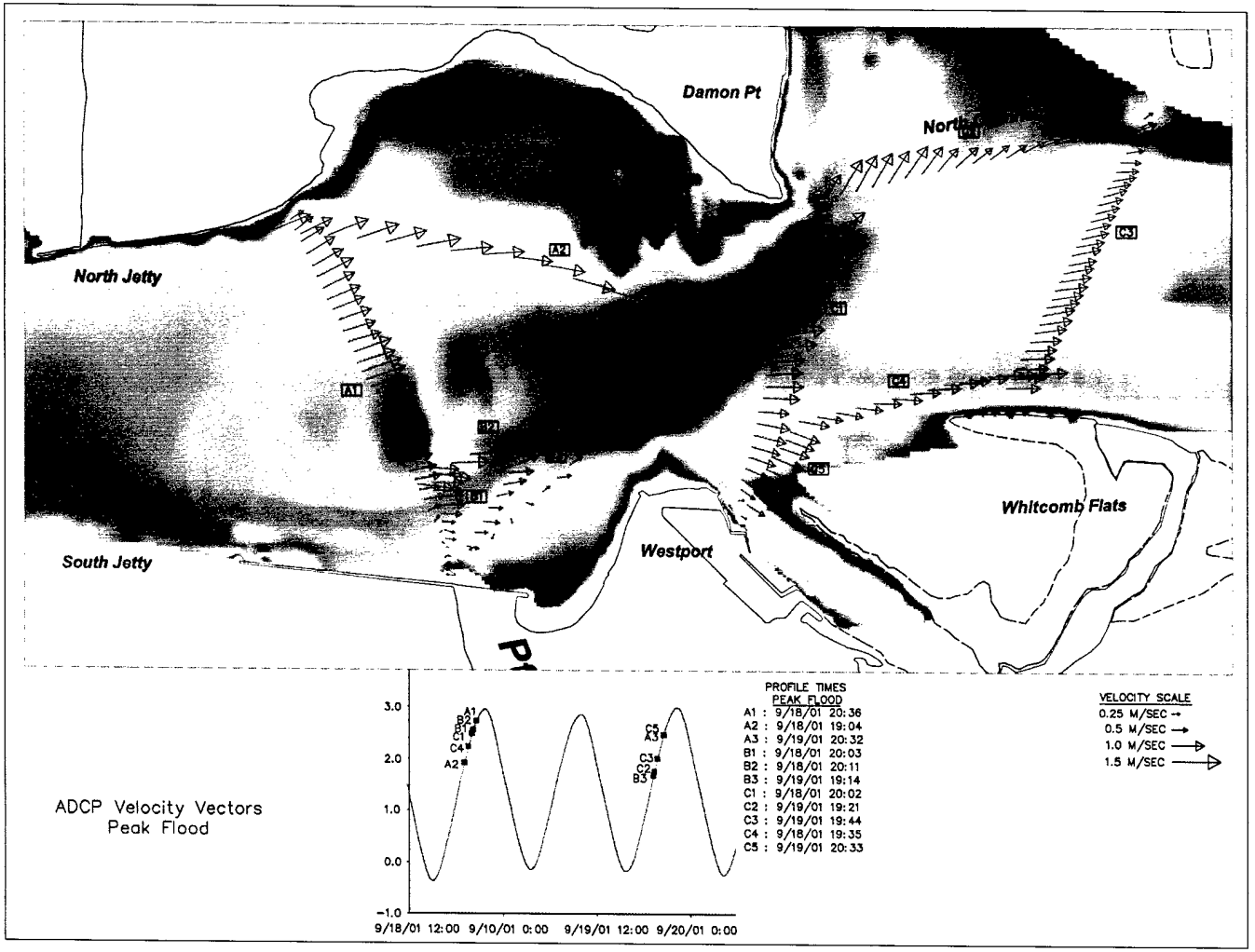

Figure 4-23. Depth-averaged current vectors along ADP transects on 18-20 September 2001 representing peak flood currents during spring tide

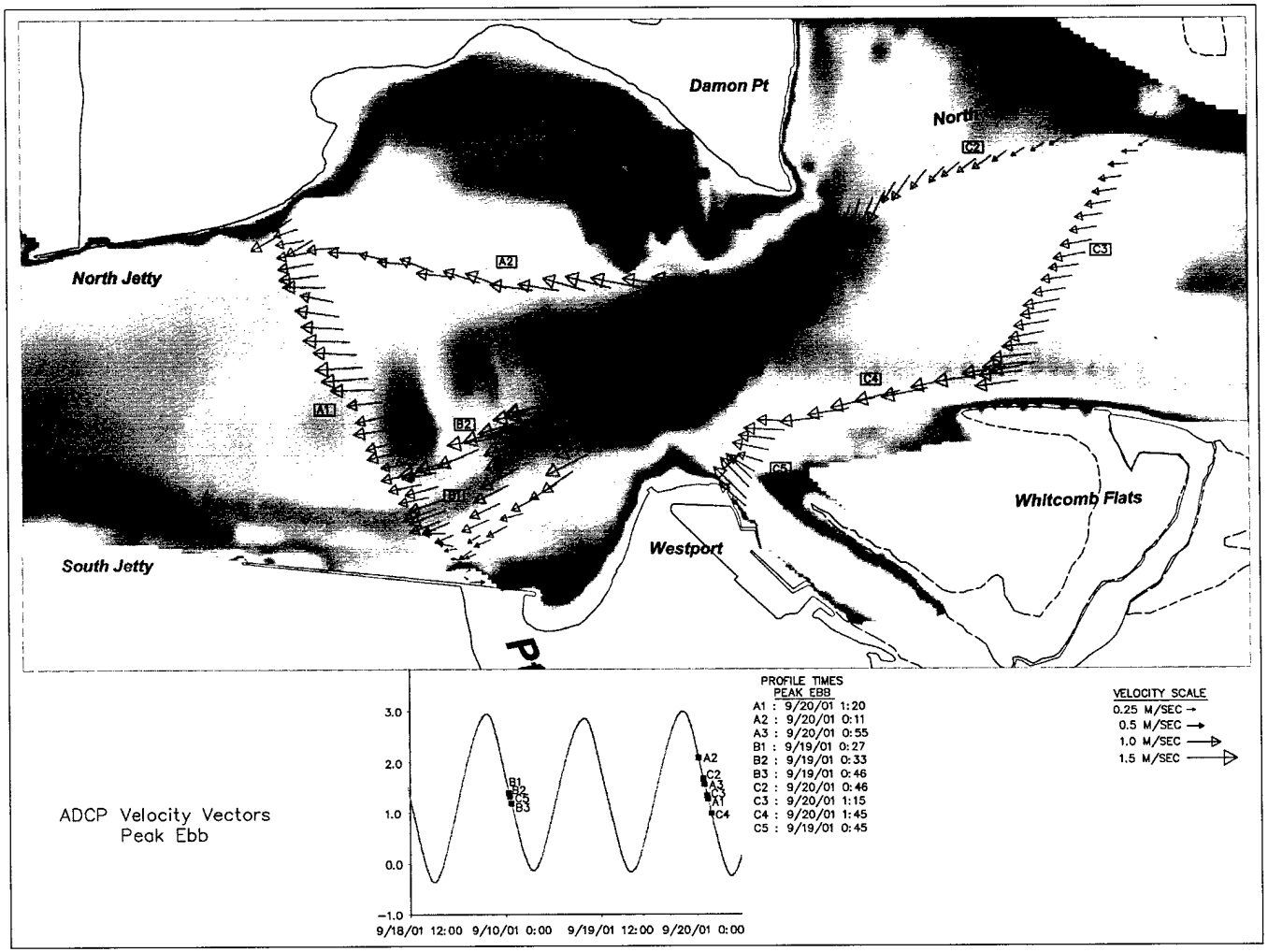

Figure 4-24. Depth-averaged current vectors along ADP transects on 18-20 September 2001 representing peak ebb currents during spring tide

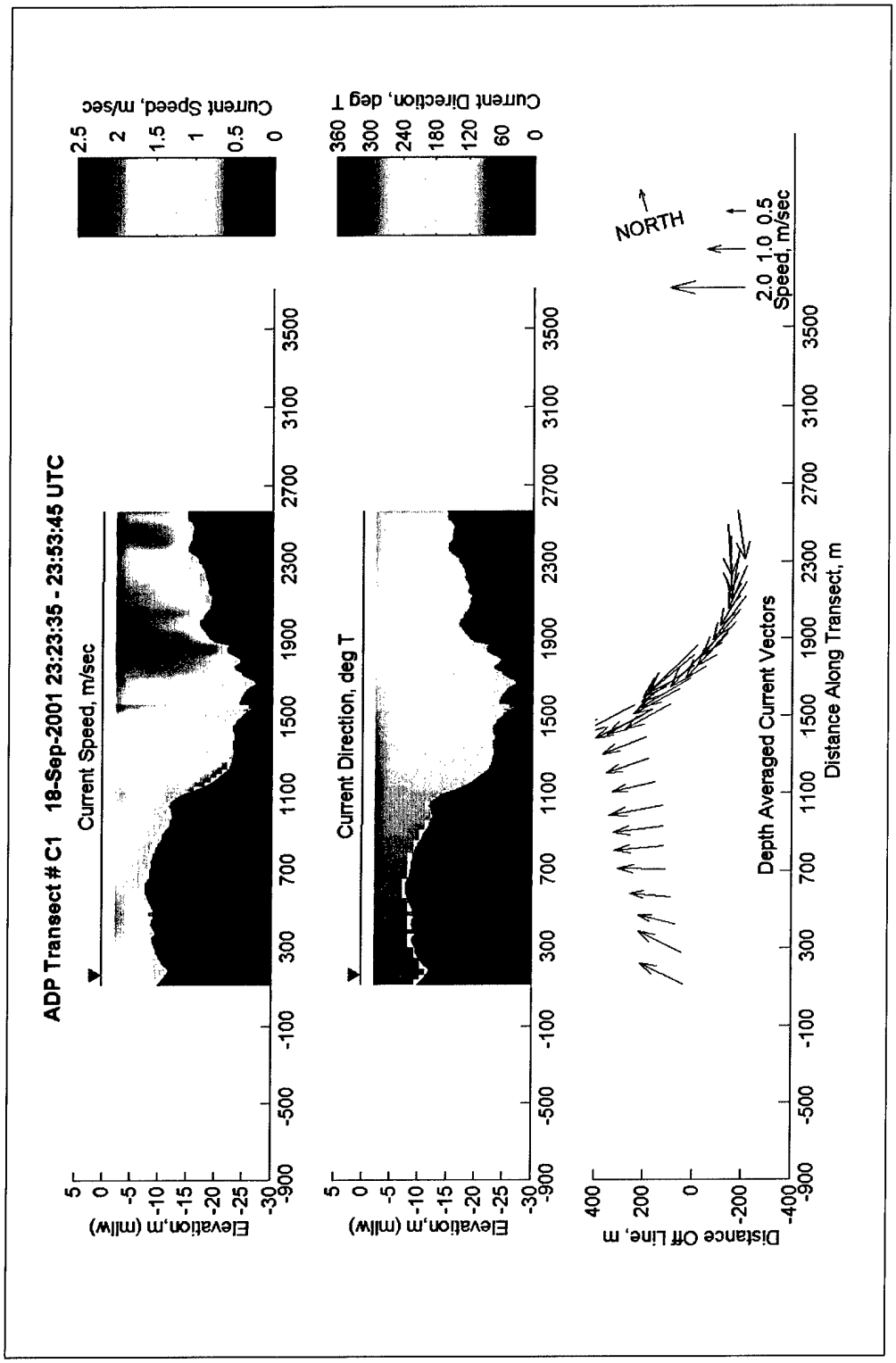

Figure 4-25. View looking west of current speed and direction profiles along ADP transect C1 between Westport and Damon Point on 18 September 2001 during ebb tide

Mixed wave and tide regimes

Areas of the ebb shoal, locations close to the jetties, and locations near the inlet and on shoals in the inlet, may be characterized as mixed-wave and tide regimes.

Time series of depth-averaged current vectors near the north jetty (sta OS 5 and OS 6) are shown in Figure 4-14 during May 2001. At sta OS 5 currents are predominately to the southwest, whereas southeast currents predominate at sta OS 6. Speed and direction are modulated by tidal variation, with flood producing the strongest currents (approximately 1 m/sec). A significant northerly component is evident in the current record during the storm on 14-15 May when southwest waves with maximum H_s of 4.7 m occurred. Time series of current vectors on Damon Point shoal are shown in Figure 4-26.

Time series of current vectors, h, and H_s, measured on Damon Point shoal at sta DP 1 and DP 2 during spring 2002 are shown in Figure 4-26. Currents on Damon Point flow predominately to the southeast (130 to 150 deg). Current speeds are typically in the range of 0.15 to 0.3 m/sec in the nearshore along Damon Point and vary with wave and tidal forcing. Current vector time series reveal a distinct modulation with a 2-week period that coincides with the spring-neap variation of the tide. The lack of a distinct reversal of the tidal current implies that a local recirculation or gyre is associated with the separation of the ebb current as it passes the southeast end of Damon Point. The combined longshore current and tidal current recirculation contributes to a quasi-steady current to the southeast along Damon Point. The presence of swell and breaking waves on the shoal induce high orbital speeds above the threshold of motion for fine and medium sand, ensuring that bed sediment in this area is highly mobile.

Sediment transport

Figure 4-27 illustrates the relationship between burst- and sensor-averaged suspended sediment concentration measured at sta 0, 1, 2, 4, and 5 and the dimensionless skin friction wave Shields parameter, θ_w during 1999. The data follow a similar trend to Green and Black's (1999) relationships for the near bed reference concentration, C_{ref}:

$$C_{ref} = X\rho\theta_w^3 \tag{4-3}$$

where X is an empirical coefficient (approximately 0.005), and ρ_s is sediment density. θ_w is estimated using the skin friction wave friction factor (Madsen and Wikramanayake 1991). The formula significantly overpredicts the measured concentrations; one explanation is that the measurements were made at nominal elevations of 0.6 to 0.9 m above the bed, whereas the empirical coefficient is based on near-bed measurements within a few centimeters of the bed. The relationship confirms that wave-induced bottom stresses contribute to resuspension of sand on the ebb shoal and in the outer inlet.

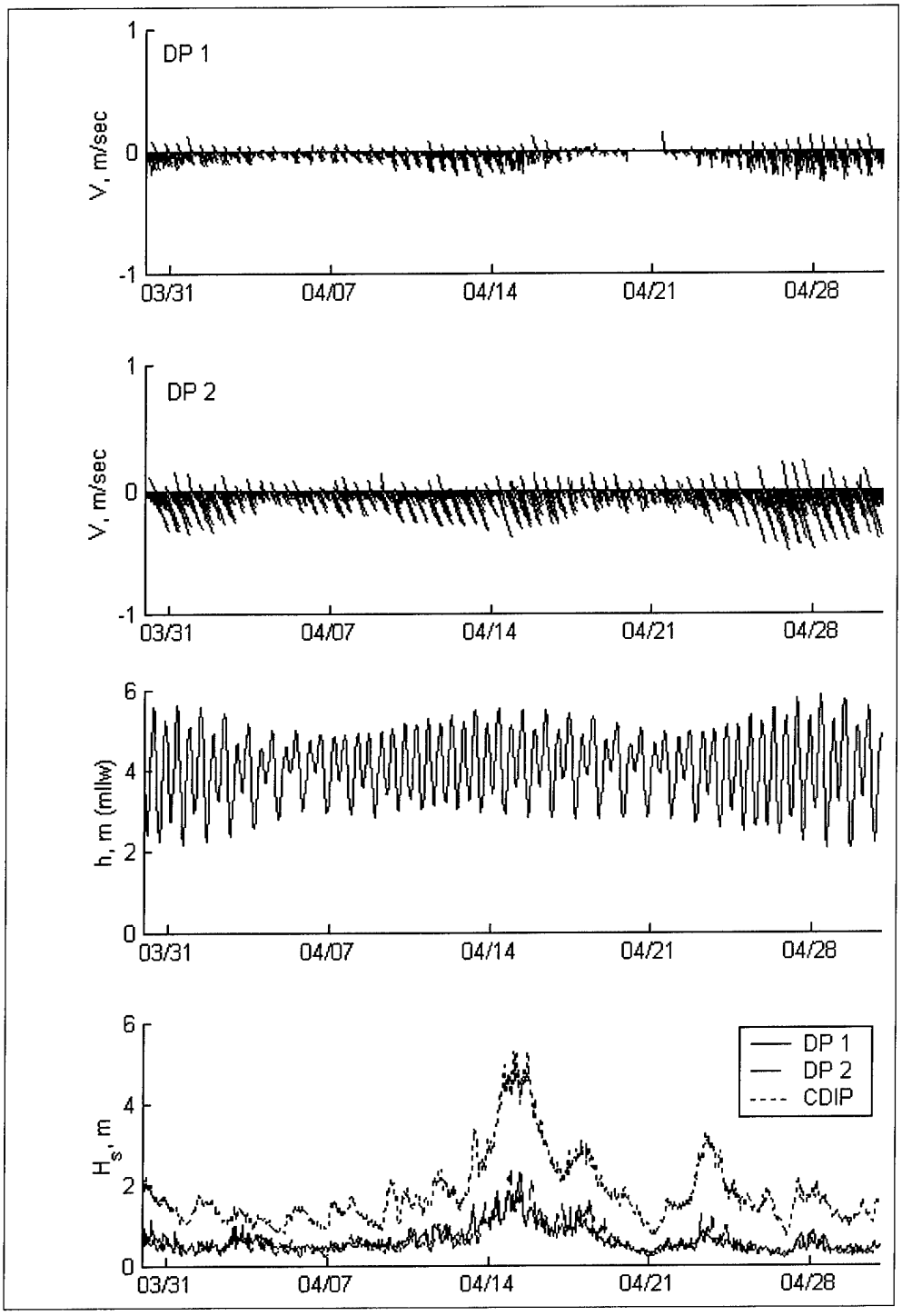

Figure 4-26. Time series of current vectors h and H_s from 29 March 2002 to 2 May 2002 on Damon Point (sta DP 1 and DP 2) and H_s measured at CDIP buoy 3601

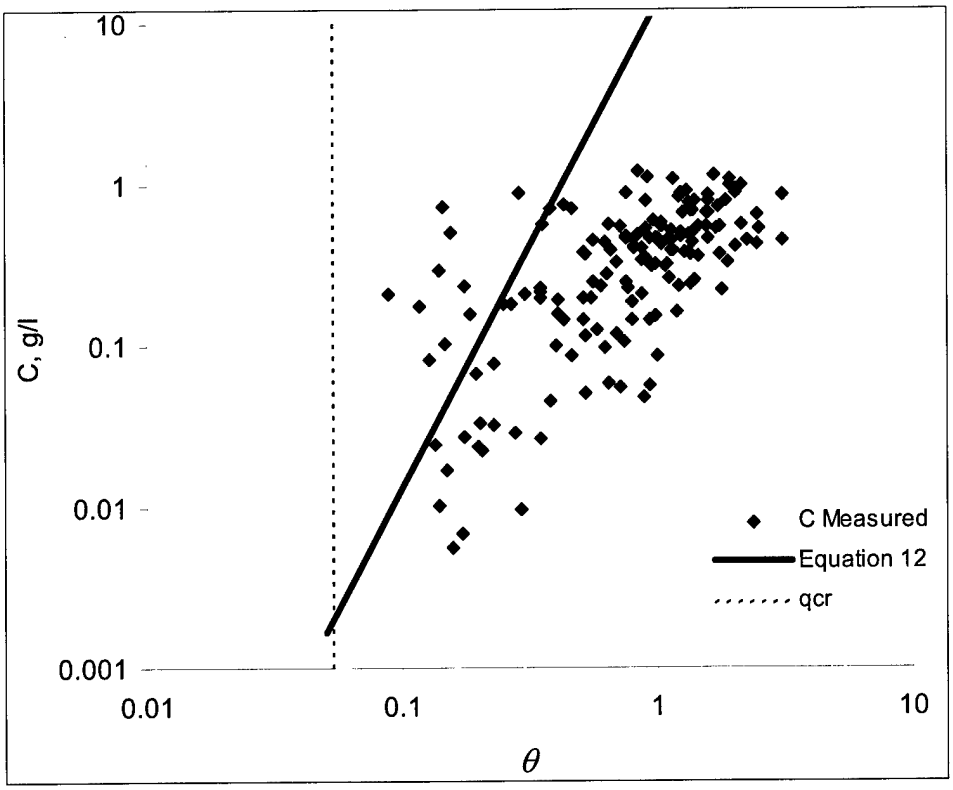

Figure 4-27. Measured near-bed concentration, *C*, and wave Shields parameter, θ_w, the solid line is Green and Black's (1999) equation, and dashed line is critical entrainment threshold for fine sand

Instantaneous point measurements of sediment concentration and velocity were multiplied to estimate the at-a-point suspended sediment flux. The steady and unsteady components of the flux are interpreted as the contributions due to currents and waves, respectively. At sta 0 and 1, outside the entrance on the ebb shoal, measurements indicate that currents dominate the net transport. In general, waves contribute only a small proportion to net transport, based on the at-a-point measurements obtained during the deployments. This may be explained by the fact that the sensors were positioned at relatively high elevations above the sea bed, whereas observations suggest that much greater wave-induced transport may occur very close to the seabed.

Sediment fluxes were also estimated by means of the near-bottom velocity, wave height, period, and direction at each measurement location and applying the van Rijn formula and Bailard formula at each station. The van Rijn formula predicts the sediment concentration and velocity profile and, therefore, permits a comparison with at-a-point field measurements at a given height above the seabed. Figure 4-28 shows a time series of measured and predicted suspended sediment flux due to the current at sta OS 5. The comparison reveals that, in general, the formula predictions are within a factor-of-two of the point measurements; however, discrepancies up to a factor-of-three exist between the

point measurements and the formula predictions. The mean error, $\bar{E}$ (see Chapter 7 for definition of $\bar{E}$), for this comparison is -0.34, indicating the model generally under-predicts the measurements. The relative error, E_{pct} (see Chapter 7 for definition of E_{pct}), is 17.7 percent indicating less than optimal performance, but not poor performance for a practical sediment transport formula (e.g., Davies et al. 2002). Several reasons for the discrepancies may include error in determining the measurement position relative to the seabed, error in the concentration and velocity measurements, and error in the formula predictions. Flux vectors computed with the van Rijn formula and integrated over a 45-day period from mid-October to the end of November 1999 are shown in Figure 4-29. Cumulative flux vectors for this time period range over two orders of magnitude throughout the area of measurement. Fluxes are largest in areas where combined waves and currents are most energetic (inner ebb shoal and outer inlet) and smallest where either combined waves and currents are weaker (greater depths on the outer ebb shoal) or where wave energy is smaller (inner inlet). At locations directly seaward of the inlet entrance, the transport is dominated by the presence of the ebb jet, whereas transport at locations north and south of the inlet is essentially parallel to the coast and directed to the northwest. The northward and offshore transport pattern outside the inlet suggests that the winter wave and current climate promotes sediment moving north to bypass the inlet. Inside the inlet, a moderately strong flood-dominated transport occurs on the north side, while ebb-dominated transport prevails on the south side. Midway between the jetties, the ebb-flood transport is nearly balanced and the net transport is northward due to the prevailing coastal current at this location.

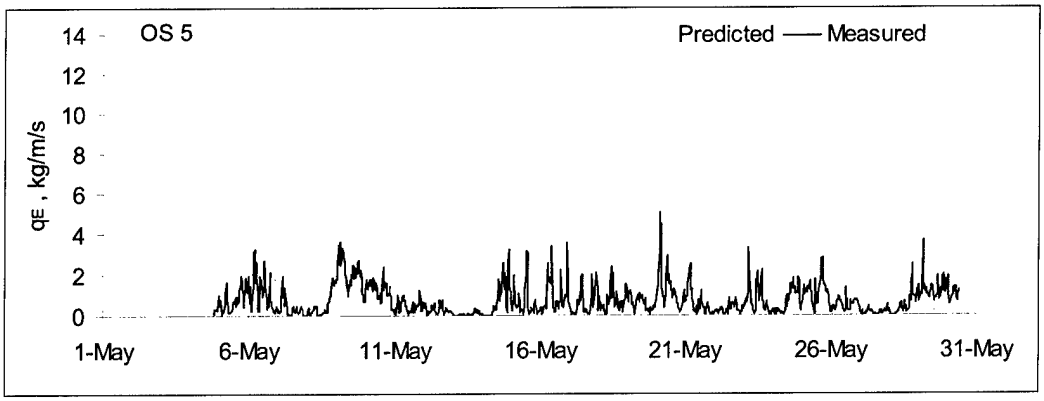

Figure 4-28. Comparison between at-a-point measurements of suspended sediment flux due to current with predicted sediment flux at same elevation using van Rijn formula at sta OS 5

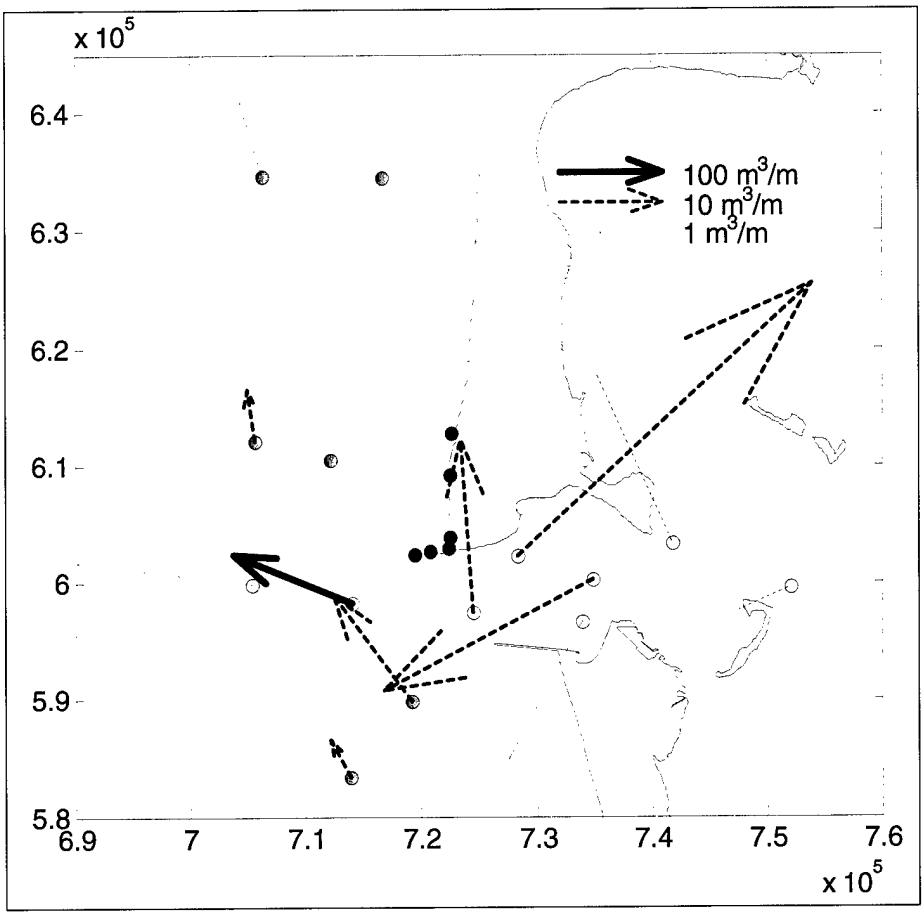

Figure 4-29. Flux vectors computed using van Rijn formula and integrated over a 45-day period from mid-October to end of November 1999. Vector length is scaled to magnitude of flux within a given order of magnitude as indicated by line type

Similarly, sediment fluxes were estimated based upon the directional wave and near-bed velocity measurements obtained near the north jetty during May 2001. Cumulative time series of the north/south transport components for at-a-point computations, Bailard, and van Rijn algorithms at sta OS 5 and OS 6 are shown in Figure 4-30. The at-a-point and van Rijn algorithm estimates suggest net southward transport occurs at both locations, whereas the Bailard algorithm indicates a small net northward flux at sta OS 6 and a large net southward flux at sta OS 5. Spatially averaged estimates for sta OS 5 and OS 6 indicate a net southward volume flux during the month of May. Assuming the transport occurs over a distance of 400 m (the distance separating sta OS 5 and OS 6), the flux estimates indicate a minimum of 30,000 to 60,000 cu m of southward bypassing during May. Further, given that the conditions in May 2001 are representative of the prevailing west-northwest wave climate at the north jetty (Figure 4-12) and assuming between 5 to 8 months of prevailing conditions, the estimates indicate an annual southward bypassing flux of between 200,000 to 500,000 cu m/year.

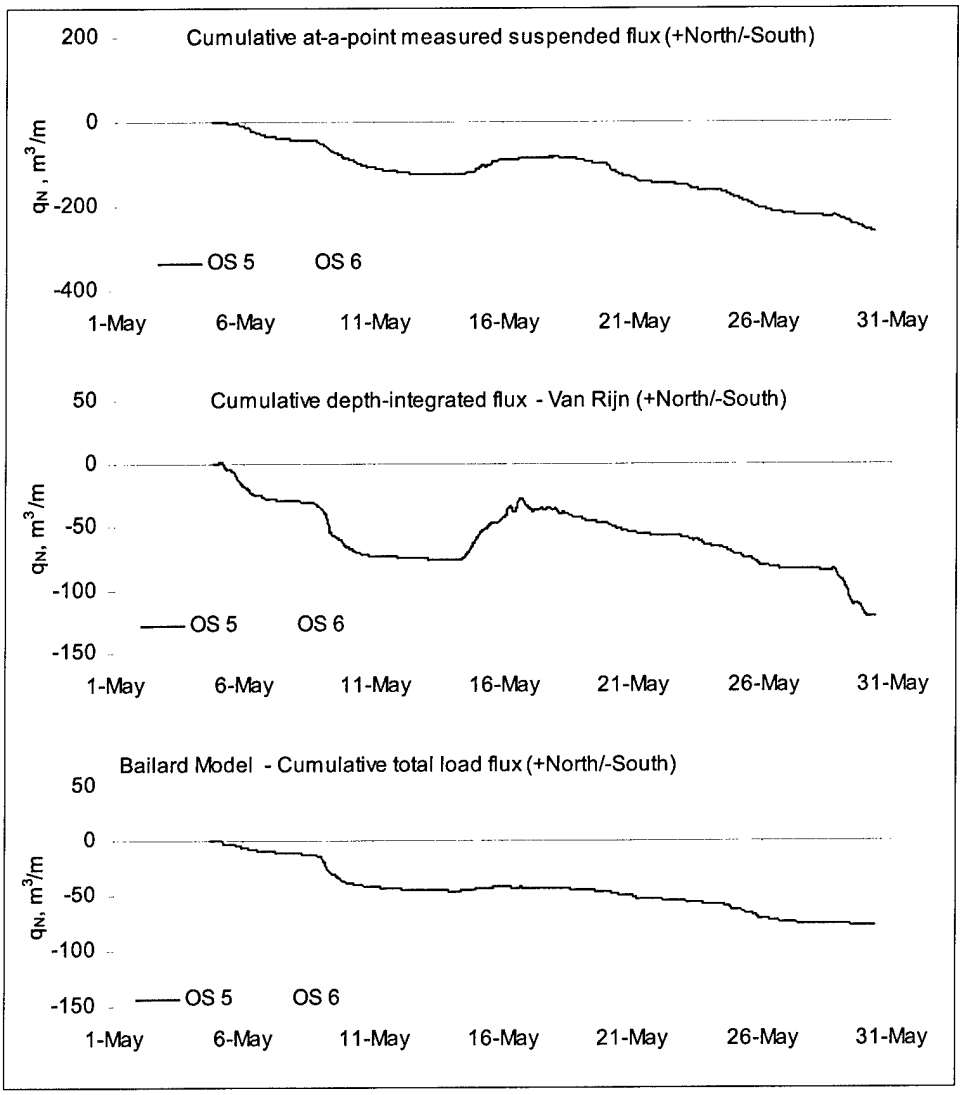

Figure 4-30. Cumulative fluxes computed using at-a-point measurements, van Rijn and Bailard algorithms at sta OS 5 and OS 6 near north jetty – Ocean Shores, during May 2001

Summary

Measurements of waves, currents, and suspended sediment transport in fall 1999, spring 2001, and winter-spring 2002 have captured the seasonality and major characteristics of the wave and sediment transport climate at the entrance to Grays Harbor. Field measurements provide data for verification of numerical model, identification of sediment transport paths, and interpretation of coastal and inlet processes.

The wave climate at Grays Harbor is characterized as energetic. Large waves are responsible for entraining and suspending significant quantities of sand. Near the north jetty, the critical threshold for fine sand was exceeded more than

77 percent of the time while the threshold for coarse sand was exceeded 57 percent of the time during the spring (May 2001 measurements). On the outer ebb shoal, the critical threshold for fine sand was exceeded no more than 27 percent of the time during the fall deployments in 1999, whereas at locations in the inlet entrance, the threshold was exceeded between 40 and 80 percent of the time.

During winter storms and occurrences of waves from the south, southwest, and west-southwest, coastal downwelling circulation promotes northward and offshore transport of sediment along the Washington coast. Measurements at 20 m depth on the ebb shoal indicate cumulative northward transport of approximately 10 cu m/m during a 45-day period during fall 1999. Measurements at 10 m depth indicate a northward flux of 15-20 cu m/m during the same period. At the entrance to Grays Harbor, northward storm-driven currents are diverted seaward by ebb shoal morphology, the south jetty, and ebb-dominated tidal currents on the ebb shoal. Near-bottom currents in 10- to 20-m depth flow to the northwest at up to 0.8 m/sec during storms.

The ebb jet exiting the harbor between the jetties promotes significant offshore transport near the seabed across the inlet. Measurements (and modeling as discussed in Chapter 7) indicate that the speed of tidal currents decreases rapidly with distance outside the entrance, except in the areas directly seaward of the entrance to a distance of approximately 5 km where the ebb jet dominates the mean current field. Since flood tide is relatively weak across the ebb shoal, it is unlikely that significant amounts of sediment enter the inlet during southwest storms except perhaps by some other mechanism such as wave asymmetry. Therefore, most northerly transport is to the northwest and bypasses the inlet entrance. This process may contribute to sedimentation of the bar channel. Sediment that bypasses the south jetty, entrance, and ebb shoal during such storms migrates north. Calculations by Kachel and Smith (1989) and morphological analysis (Chapter 3) suggest much of the sediment transported north along the coast sediment is deposited offshore from Ocean Shores.

In summer, or when waves and swell occur from west-northwest, northwest, or north, waves associate with coastal upwelling circulation and together promote southward and onshore transport of sediment. Wave asymmetry (evidence from co-spectral analysis of measured time series) and upwelling circulation (USGS measurements) deliver sediment to the nearshore zone along Ocean Shores where waves (although often smaller than winter storm waves) are nearly always present and capable of entraining significant quantities of suspended sediment to depths of at least 10 m. West-northwest waves also generate a longshore current directed to the south along the north beach that transports sediment towards the north jetty. Nearshore currents measured along the north beach during summer upwelling are of the order of 0.5 m/sec.

Rip currents are prominent in the area north of the north jetty and may dominate the nearshore circulation within 1,000 m of the jetty. Rips likely serve as a key mechanism delivering sediment to the outer surf zone where coastal currents and the tidal current that accelerate in proximity to the north jetty can carry sediment into the inlet. Currents near the north jetty are dominated by the convergence and acceleration of flood tide as it is forced to flow over and around the submerged end of the jetty to enter the harbor.

Sediment flux estimates indicate a minimum of 30,000 to 60,000 cu m of sediment bypassed the north jetty during May 2001. Southward bypassing flux of suspended sand is well-documented by direct field measurements, bathymetry surveys, and aerial photographs. The May 2001 measurements are considered representative of the prevailing west-northwest waves at the site. The sediment flux calculations based on the field measurements are consistent with calculations made with the calibrated GENESIS model (Chapter 6) within a factor of 2 to 5. Based on these considerations, the measurements indicate an annual southward bypassing flux of 200,000 to 500,000 cu m/year.

Within the inlet, measurements (time series point estimates and spatial roving transects) confirm the inlet circulation patterns of the inlet observed in physical and numerical modeling studies and provide detail at critical areas near the north jetty, Damon Point, and Whitcomb Flat. Flood/ebb dominance on the north/south side of the inlet is confirmed by the roving ADP measurements and point estimates. Ebb flows that trend from northeast to southwest across the inlet from the end of Damon Point have created a deep scour trench and a field of migrating sand waves. A persistent southeast flowing current is present in the nearshore along Damon Point. This current transports sediment toward the distal end of Damon Point and the navigation channel where it may result in channel shoaling. Persistent southeastward transport along Damon Point is consistent with the steady accretion of sediment on Damon Point shoal as documented in Chapter 3.

Inside the inlet, a moderately strong flood-dominated transport occurs on the north side while ebb-dominated transport prevails on the south side. Midway between the jetties (e.g., sta 2 in 1999), the ebb-flood transport is nearly balanced and net transport is northward due to the prevailing coastal current at this location. Waves diminish east of Point Chehalis and Damon Point in the inlet but contribute significantly to entrainment and transport (through wave asymmetry and longshore currents) on the margins of the inlet entrance and on the flanks of spits and shoals (Damon Point, Sand Island Shoal, Whitcomb Flat).

References

Allan, J. C., and Komar, P. D. (2000a). "Spatial and temporal variations in wave climate of the North Pacific," Report to the Oregon Department of Land Conservation and Development, 46 p.

_____. (2000b). "Long-term and climate-related increases in storm wave height in the North Pacific," *EOS Transactions* 47, American Geophysical Union, 561-567.

_____. (2001). "Wave climate change and coastal erosion in the U.S. Pacific Northwest," *Proceedings of the 4th Conference on Ocean Wave Measurement and Analysis, WAVES 2001*, San Francisco, CA, ASCE, 680-690.

_____. (2002a). "The wave climate of the eastern North Pacific: Long-term trends and an El Niño/La Niña dependence," Southwest Washington Coastal Erosion Workshop 2000, G. Gelfenbaum, and G. M. Kaminsky (eds.), Open-File-Report 02-229.

_____. (2002b). "Extreme storms on the Pacific Northwest Coast during the 1997-98 El Niño and 1998-99 La Niña," *Journal of Coastal Research* 18(1), 175-193.

Anderson, W. B., and Foster, A. R. (1979). "QUTR: Desk top survey of the inner continental shelf from Grays Harbor to Destruction Island," Research and Engineering Department, Naval Undersea Warfare Engineering Station, Keyport, WA, p. 102.

Anderson J. R., and Gyakum, J. R. (1989). "A diagnostic study of Pacific basin circulation regimes as determined from extratropical cyclone tracks," *Monthly Weather Review* 117, 2,672-2,686.

Bailard, J. A. (1981). "An energetics total load sediment transport model for a plane sloping beach," *Journal of Geophysical Research* 86, 10,938-10,954.

Barnes, C. A., Duxbury, A. C., and Morse, B. A. (1972). "Circulation and selected properties of the Columbia River effluent at Sea," Chapter 3, A. T. Pruter and D. L. Alverson (eds.), The Columbia River Estuary and Adjacent Ocean Waters: Bioenvironmental Studies, University of Washington Press, Seattle, 41-80.

Chelton, D. B. (1980). "Low frequency sea level variability along the west coast of North America," Ph.D. diss., University of California, San Diego, California, 212 p.

Dodimede, A. J., Favorite, F., and Hirano, T. (1963). "Review of oceanography of the Sub-Arctic Pacific Region," *Bulletin of the International North Pacific Fisheries Commission* 13(2), 195.

Davies, A. G., van Rijn, L. C., Damgaard, J. S., van de Graaff, J., and Ribberink, J. S. (2002). "Intercomparison of research and practical transport models," *Coastal Engineering* 46, 1-23.

Drake, D. E., and Cacchione, D. A. (1986). "Field observations of bed shear stress on sediment resuspension on continental shelves, Alaska and California," *Continental Shelf Research* 6, 415-429.

Duxbury, A. C., Morse, B. A., and McGary, N. (1966). "The Columbia River effluent and its distribution at sea," Department of Oceanography, Technical Report No. 156, Univeristy of Washington, Seattle.

Earle, M. D., McGehee, D., Tubman, M. (1995). "Field wave gaging program, wave data analysis standard," Instruction Report CERC-91-1, Coastal Engineering Research Center, U.S. Army Engineer Waterways Experiment Station, Vicksburg, MS.

Fleming, R. H. (1955). "Review of the oceanography of the Northern Pacific," *International North Pacific Fisheries Commission Bulletin* 2, 1-43.

Gailani, J. Z., and Smith, J. (2000). "Analysis of sediment transport processes," (draft chapter to appear in) Dredged Material Disposal at the Mouth of the Columbia River: Report 2, Technical Report, U.S. Army Engineer Research and Development Center, Vicksburg, MS.

Graham, N. E., Barnett, T. P., Wilde, R., Ponater, M., and Schubert, S. (1995). "On the roles of tropical and midlatitude SSTs in forcing interannual and interdecadal variability in the winter Northern Hemisphere circulation," *Journal of Climate* 7, 1,416-1,441.

Graham, N. E., and Diaz, H. F. (2001). "Evidence for intensification of North Pacific winter cyclones since 1948," *Bulletin of the American Meteorological Society* 82(9), 1,869-1,893.

Green, M. O., and Black, K. P. (1999). "Suspended sediment reference concentration under waves: Field observations and critical analysis of two predictive models," *Coastal Engineering* 38, 115-141.

Green, M. O., and MacDonald, I. T. (2001). "Processes driving estuary infilling by marine sands on an embayed coast," *Marine Geology* 178, 11-37.

Guza, R. T., and Thornton, E. B. (1985). "Velocity moments in nearshore," *Journal of Waterway, Port, Coastal, and Ocean Engineering* 111(2), March, 235-256.

Hemsley, J. M., and Brooks, R. M. (1989). "Waves for coastal design in the United States," *Journal of Coastal Research* 5(4), 639-663.

Hericks, D. B., and Simpson, D. P. (2000). "Grays Harbor estuary physical dynamics study: Final data report," PI Engineering for Offshore and Coastal Technology, Inc.

Hickey, B. M. (1979). The California current system – hypotheses and facts," *Progress in Oceanography* 8, 191-279.

_____. (1989). "Patterns and processes of circulation over the Washington Continental Shelf and Slope," *Coastal Oceanography of Washington and Oregon*, M. R. Landry and B. M. Hickey (eds.), Elsevier Oceanography Series 47, Amsterdam, 41-115.

Hickey, B. M., Baker, E. T., and Kachel, N. B. (1986). "Suspended particle movement in and around Quinault Submarine Canyon," *Marine Geology* 71, 35-85.

Inman, D. L., and Jenkins, S. A. (1997). "Changing wave climate and littoral drift along the California coast," *Proceedings California and the World Ocean '97*, San Diego, CA, ASCE, 538-549.

Jaffe, B. E., Sternberg, R. W., and Sallenger, A. H. (1984). "The role of suspended sediment in shore-normal beach profile change," *Proceedings 19th International Coastal Engineering Conference*, Houston, TX, ASCE, 1,983-1,986.

Kachel, N. B., and Smith, J. D. (1989). "Patterns and processes of circulation over the Washington Continental Shelf and Slope," *Coastal Oceanography of Washington and Oregon*, M. R. Landry and B. M. Hickey (eds.), Elsevier Oceanography Series 47, Amsterdam, 287-348.

Lacy, J., Sherwood, C., Ruggiero, P., Gelfenbaum, G. (2001). "Seasonal changes in nearshore flow and sediment transport near Grays Harbor, Washington," abstract submitted to Eastern Pacific Ocean Conference, Stanford Sierra Camp, CA.

Landry, M. R., Postel, J. R., Peterson, W. K., and Newman, J. (1989). "Broad-scale distributional patterns of hydrographic variables on the Washington/Oregon shelf," *Coastal Oceanography of Washington and Oregon*, M. R. Landry and B. M. Hickey (eds.), Elsevier Oceanography Series 47, Amsterdam, 1-40.

Larsen, L. A., and Fenton, D. (1974). "Open ocean wave studies," Data Report I-73, Vol. 2., Department of Oceanography, University of Washington, Seattle, 560 pp.

Leenknecht, D. A., Szuwalski, A., and Sherlock, A. R. 1992. "Automated Coastal Engineering System," Computer Program, Coastal Engineering Research Center, U.S. Army Engineer Waterways Experiment Station, Vicksburg, MS.

Longuet-Higgins, M. S., Cartwright, D. E., and Smith, N. D. (1963). "Observations of the directional spectrum of sea waves using the motions of a floating buoy," *Ocean Wave Spectra*, Prentice-Hall, Englewood Cliffs, NJ, 111-132.

Madsen, O. S., and Wikramanayake, P. N. (1991). "Simple models for turbulent wave-current bottom boundary layer flow," Dredging Research Program, Contract Report DRP-91-1, Coastal Engineering Research Center, U.S. Army Engineer Waterways Experiment Station, Vicksburg, MS.

Michaelson, J. (1989). "Long-period fluctuations in amplitude and frequency reconstructed from tree-rings," American Geophysical Union, *Geophysical Monograph* 55, 69-74.

Osborne, P .D., and Greenwood, B. (1992a). "Frequency dependent cross-shore suspended sediment transport, 1. A non-barred shoreface," *Marine Geology* 106, 1-24.

_____. (1992b). "Frequency dependent cross-shore suspended sediment transport, 2. A barred shoreface," *Marine Geology* 106, 25-51.

Osborne, P. D., Hericks, D. B., and Kraus, N. C. (2001). "Deployment of oceanographic instruments in high energy environments and near structures," Technical Note ERDC/CHL CHETN -IV-46, U.S. Army Engineer Research and Development Center, Vicksburg, MS, (http://chl.wes.army.mil/library/publications/chetn/pdf/chetn-iv46.pdf).

Ruggiero, P., Kaminsky, G. M., Komar, P. D., and McDougal, W. G. (2001). "Extreme waves and coastal erosion in the Pacific Northwest," *3rd International Symposium on Ocean Wave Measurement and Analysis*, 947-961.

Ruggiero, P., Komar, P. D., McDougal, W. G., and Beach, R. A. (1996). "Extreme water levels, wave runup and coastal erosion," *Proceedings 25th Coastal Engineering Conference*, ASCE, 2,793-2,805.

Ruggiero, P., and Voigt, B. (2000). "Beach Monitoring in the Columbia River Littoral Cell, 1997-2000," Department of Ecology Publication Number 00-06-26, July 2000.

Seymour, R. J., Guza, R. T., O'Reilly, W. C., Castel, D., and Thomas, J. O. (1996). "Coastal data information program: A cooperative program by the U.S. Army Corps of Engineers and the California Department of Boating and Waterways, twentieth annual report, January 1995 through December 1995," Ocean Engineering Research Group, Center for Coastal Studies, December, 218 p.

Seymour, R. J., Strange, R. R., Cayan, D. R., and Nathan, R. A. (1984). "Influence of El Niños on California's wave climate," *Proceedings 19th Coastal Engineering Conference,* ASCE, 577-592.

Sherwood, C. R., Gelfenbaum, G., Howd, P. A., and Palmsten, M. L. (2001). "Sediment transport on a high-energy ebb-tidal delta," *Proceedings Coastal Dynamics '01*, ASCE, 473-482.

Sternberg, R. W. (1986). "Transport and accumulation of river-derived sediments on the Washington continental shelf, U.S.A.," *Journal of Geological Society* 143, London, 945-956.

Sternberg, R. W., and Larsen, L. H. (1976). "Frequency of sediment movement on the Washington Continental Shelf: A note," *Marine Geology* 21, M37-M47.

Strange, R. R., Graham, N. E., and Cayan, D. R. (1989). "Meteorological development of the unusually severe coastal storm during January 16-18, 1988," *Shore and Beach* 57(4), 3-9.

Tillotson, K. J., and Komar, P. D. (1997). "The wave climate of the Pacific Northwest (Oregon and Washington): A comparison of data sources," *Journal of Coastal Research* 13, 440-452.

Tully, J. P., and Barber, F. G. (1960). "An estuarine model of the Sub-Arctic Pacific Ocean, *Journal of the Fisheries Research Board of Canada* 17(1), 91-112.

Uda, M. (1963). "Oceanography of the Sub-Arctic Pacific Ocean," *Journal of Fisheries Research Board of Canada* 20(1), 119-179.

U.S. Army Engineer District, Seattle. (1982). "Appendix D: Engineering design and cost estimates," in Interim Feasibility Report and Final EIS, Grays Harbor, Chehalis, and Hoquiam Rivers, Washington Channel Improvement for Navigation, Seattle, WA, 800 p.

_____. (1989). "Appendix B: Design analysis," in General Design Memorandum and Environmental Impact Statement Supplement: Grays Harbor, Washington, Navigation Improvement Project, Volume 1, TC 202.S42 G72, Seattle, WA.

van Rijn, L. C. (1989a). "Sediment transport, Part I: Bed load transport," *Journal of Hydraulic Engineering* 110(10), 1,431-1,456.

_____. (1989b). "Sediment transport, Part II: Suspended load transport," *Journal of Hydraulic Engineering* 110(11), 1,613-1,641.

_____. (1993). "*Principles of sediment transport in rivers, estuaries and coastal seas.*" Aqua Publications, Amsterdam, The Netherlands.

5 Physical Modeling of North Beach and Jetty[1]

Introduction

In the nearshore environment, incident waves are random and transform by refraction, diffraction, shoaling, and breaking over an irregular bathymetry while interacting with winds, currents, and possibly subaerial or submerged structures. Full representation of such complex interactions is beyond the capabilities of present-day operational numerical models. Physical model experiments conducted at a suitable scale and with attention to boundary conditions can accurately reproduce the wave and current environment in the nearshore regions and near structures. Physical models offer the most accurate means of studying wave-structure interactions and nearshore wave kinematics and dynamics.

To aid in analyzing the performance of the proposed structural alternatives at Grays Harbor, WA, a three-dimensional (3-D) physical model of the north beach (Ocean Shores) and north jetty was constructed to evaluate wave heights, current patterns, and sediment transport in the nearshore north of the north jetty. The physical model was located at the U.S. Army Engineer Research and Development Center, Coastal and Hydraulics Laboratory (CHL). Selected storms from the northwest and from the southwest were reproduced in the model. During the storms, measurements of wave heights and current velocities were taken, and photographic documentation of dye patterns and coal tracer movements was kept.

The physical model was part of a multidisciplinary effort involving field measurement, geomorphic analysis, shoreline response modeling, and wave, current, and sediment transport numerical modeling conducted in this study for the U.S. Army Engineer District, Seattle. These associated studies are documented in other chapters of this report. Coordination was made among the various study components, and visits by the study investigators and local interests were made to the physical model to gain insight into the integrated processes acting at and around the north jetty.

Although waves and currents are quantitatively scaled in a physical model, it is generally not possible to quantitatively scale sediment transport. Instead, sediment transport is divided into the two components of bedload transport and suspended transport. Bedload transport may be qualitatively reproduced in a

[1] Written by Donald L. Ward and Julie A. Cohen, Coastal and Hydraulics Laboratory, U.S. Army Engineer Research and Development Center, Vicksburg, MS.

physical model with coal tracers. Suspended transport is inferred by examining current patterns depicted by dye injected into the water column. Results of such analyses are described here.

Facilities and Equipment

Description of model

To maximize model scale within the space available to construct the model, model limits were set to include only the north half of the entrance to Grays Harbor and extended north from the north jetty for 5,400 ft. Limits of the physical model are depicted in Figure 5-1.

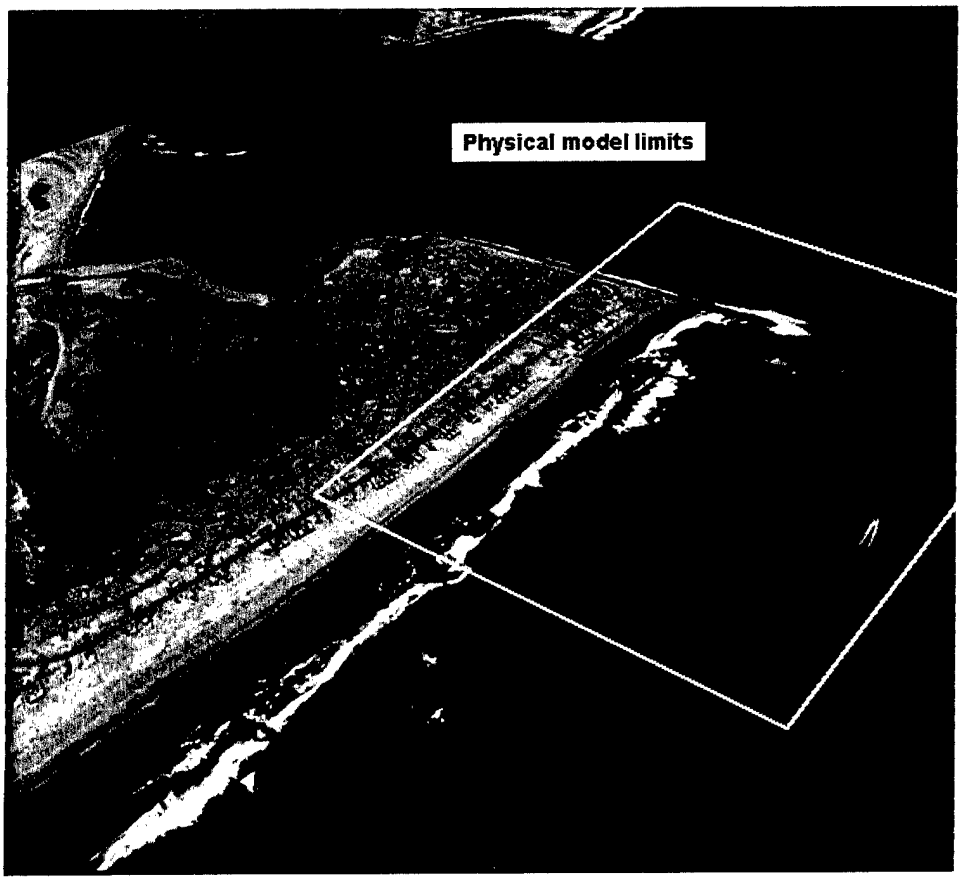

Figure 5-1. Area of prototype reproduced in physical model

The model basin measured 190 ft in north-south orientation and 153 ft in east-west orientation. Bathymetry in the model was molded in concrete to follow the contours of the 1999 field survey conducted by the Seattle District. The molded bathymetry extended seaward to a depth of 30 ft mean lower low water (mllw), then followed a 1:10 (V:H) slope to the basin floor at a depth of 75 ft mllw. The model was constructed at an undistorted scale of 1:75 (model: prototype). Figure 5-2 shows the layout of the physical model built on Froude scaling relationships in which gravity is the primary restoring force to the force of inertia (Hughes 1993). Froude scaling relationships of interest to operation of the Grays Harbor model are listed in Table 5-1. Unless otherwise stated, quantities are expressed as prototype values in this chapter.

Wave and current generation and data acquisition equipment

Storms from the west-northwest were reproduced in the model by a computer-controlled vertical-displacement wedge-type wave generator. The 80-ft-long generator was capable of generating incident spectral waves up to zeroth-order moment[1] or significant wave height[2] of H_s = 6 m and spectral peak period of T_p = 16 sec. The generator was located on the flat bottom of the wave basin and oriented such that waves were propagated at an angle of 289 deg relative to true north. Guide vanes at the ends of the wave generator minimized directional spreading.

The design storm from west-southwest exceeded capabilities of the vertical-displacement wave generator. A Directional Spectral Wave Generator (DSWG) was therefore installed on the flat bottom of the wave basin and oriented such that waves propagating normal to the wave generator would be at an angle of 225 deg. The computer-controlled DSWG consists of 61 independent electric-powered piston-type wave boards. The DSWG is capable of producing waves at an angle of up to 45 deg from normal to the wave board.

Capacitance-type wave gauges measured displacement of the water surface (wave heights), and SonTek™ 2-D Acoustic Doppler Velocimeters (ADVs)[3] (Kraus, Lohrmann, and Cabrera 1994) measured horizontal current velocities. Wave gauges were operated with Jordan controllers and calibrated daily. Velocimeter probes were located as close to the bottom as feasible without touching it. Seed material for the velocimeters was dripped into the water near each probe to improve the signal-to-noise ratio. Measurements were taken by 13 wave gauges during experiments with waves from the west-northwest. Each run with a given storm and water level combination was repeated four times. For each of the four repeat runs, five wave gauges remained in place and eight were repositioned such that water surface elevations were measured at a total of 37 locations. Current velocities were measured at three locations near the jetty and the proposed spur. Locations of wave gauges and velocimeters for the

[1] "Zeroth-order moment wave height" is calculated in the wave frequency domain as four times the square root of the zeroth-order moment of the wave energy spectrum.
[2] "Significant wave height" is the average of the one-third highest waves in the time domain.
[3] NOTE: "velocimeter" in this chapter will refer to Sontek™ 2-D ADV.

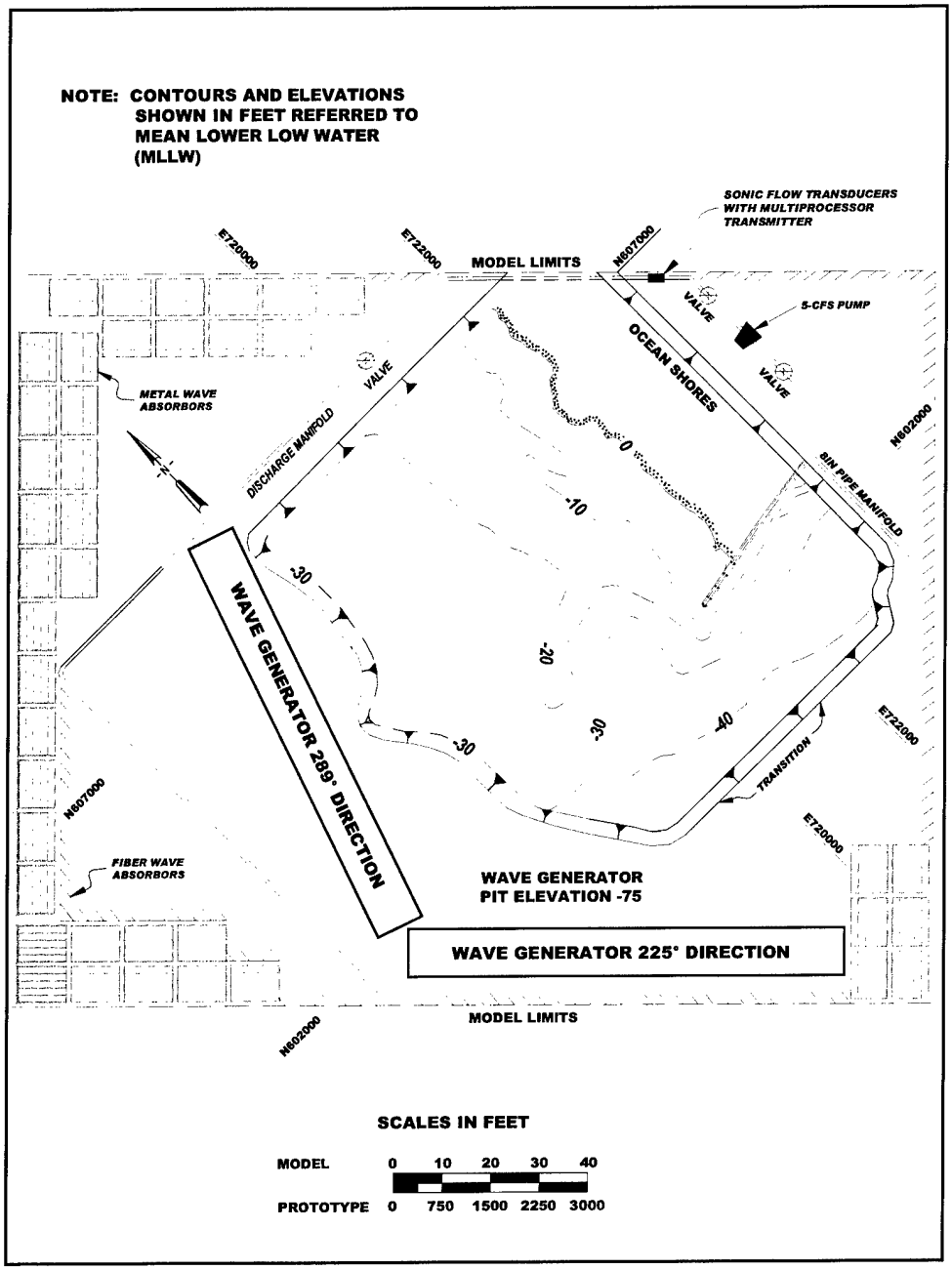

Figure 5-2. Basin layout for physical model

Table 5-1
Froude Scaling Relationships

Characteristic	Dimension	Froude Relationship	Value (model:prototype) Grays Harbor Model
Area	L^2	L^2	1:5,625
Flow Rate	L^3/T	$L^{5/2}$	1:48,714
Length	L	L	1:75
Time	T	$L^{1/2}$	1:8.66
Velocity	L/T	$L^{1/2}$	1:8.66
Volume	L^3	L^3	1:421,875

Note: L represents length and T represents time

west-northwest storms are shown in Figure 5-3. Measurements were taken by 17 wave gauges and 6 velocimeters for waves from the west-southwest. Each storm and water level combination was repeated 4 times with 12 wave gauges being repositioned for each repeat run such that wave rod data were collected from 53 locations for each storm. Locations of wave gauges and velocimeters for west-southwest storms are shown in Figure 5-4. Data from wave gauges and ADVs for all experiments conducted are included in Appendix B.

Tidal flood currents were generated by a 5-cu ft/sec water pump controlled by a gate valve on the return pipe to maintain a 3.1 cu ft/sec flow rate. Intake baffles to the pump were located landward of the model entrance channel to Grays Harbor. Pipes carried the flow to the north side of the model where it was returned to the model via holes cut in the side of the pipe. Guide vanes directed the current from the pipe. Current patterns were controlled by a series of valves along the return pipe, and flow rate in the return pipe was measured with a sonic flow transducer.

Selection of Storms for Model Runs

Figure 5-5 illustrates incident direction and significant height of waves measured during the period 1993 to 1999 at a Coastal Data Information Program (CDIP) buoy sponsored by the Seattle District and located approximately 6 miles offshore of Grays Harbor. Table 5-2 lists wave height and wave period for the most extreme storm recorded from each 22.5-deg direction band, and typical storms and most frequent storms from each direction band. Figure 5-6 illustrates directions of storms with significant wave heights greater than 3 m. The data indicate that the largest storm was from the southwest, and most numerous storms are incident from west and west-northwest. Further information on waves and other oceanographic information at the site are given in Chapter 4.

In consultation with the full study team, storms from the west-northwest and southwest were selected for representation in the physical model. The typical storm with H_s = 5 m and T_p = 13 sec was assigned as the west-northwest design storm. Although the typical storm from the southwest had H_s = 6 m and T_p = 13 sec, a more severe storm was chosen as the design storm for the physical

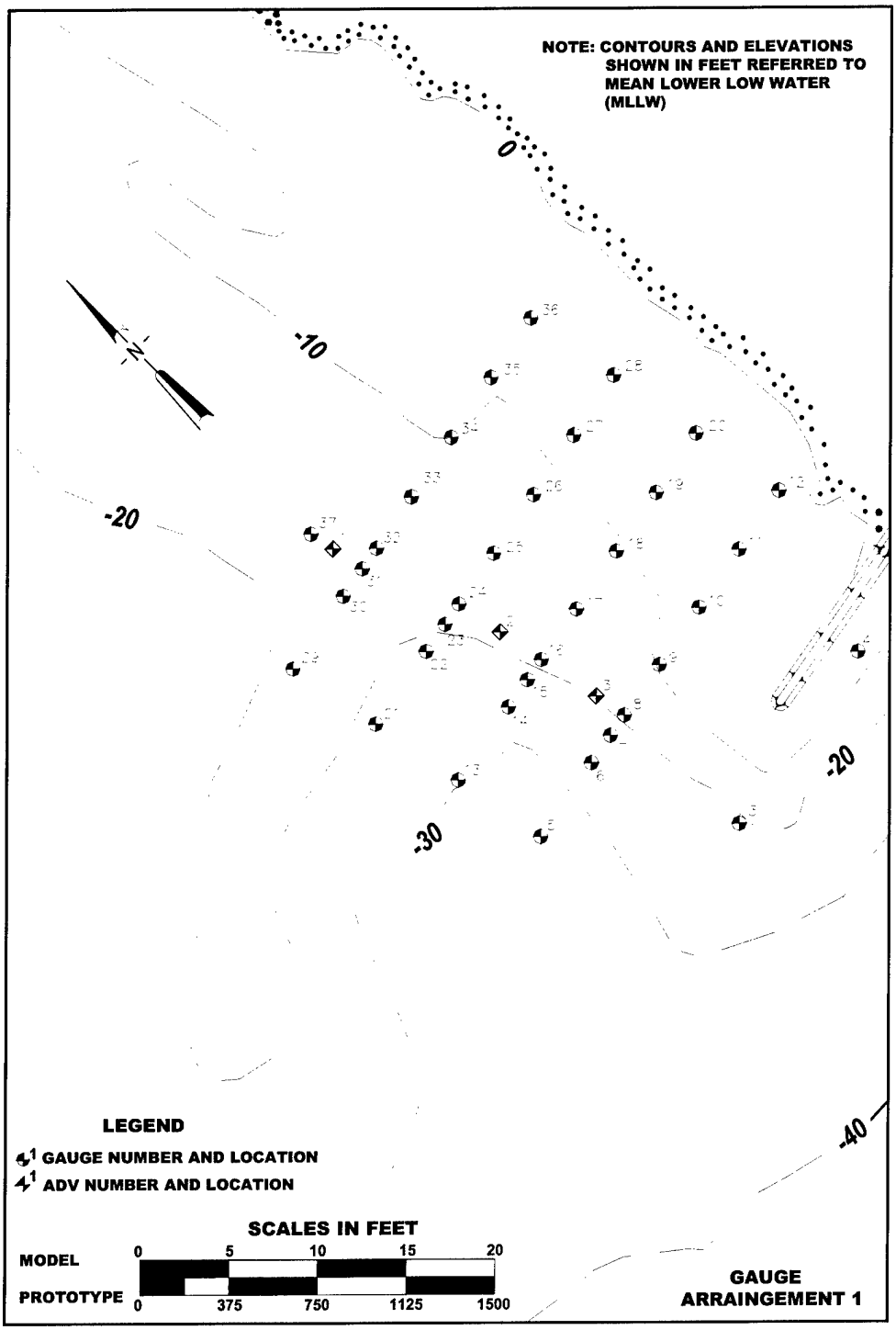

Figure 5-3. Wave gauge and ADV arrangement for waves from west-northwest

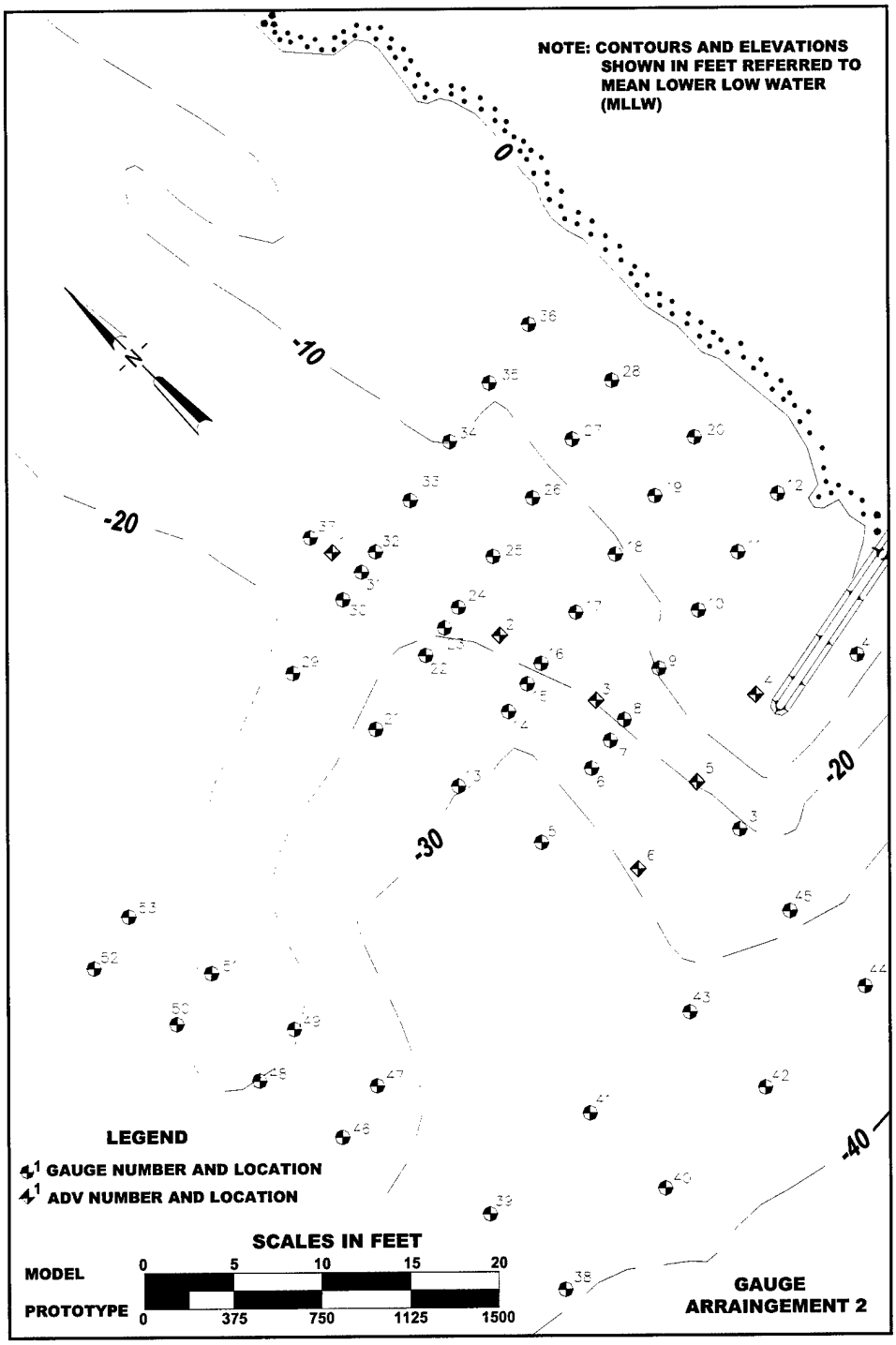

Figure 5-4. Wave gauge and ADV arrangement for waves from southwest

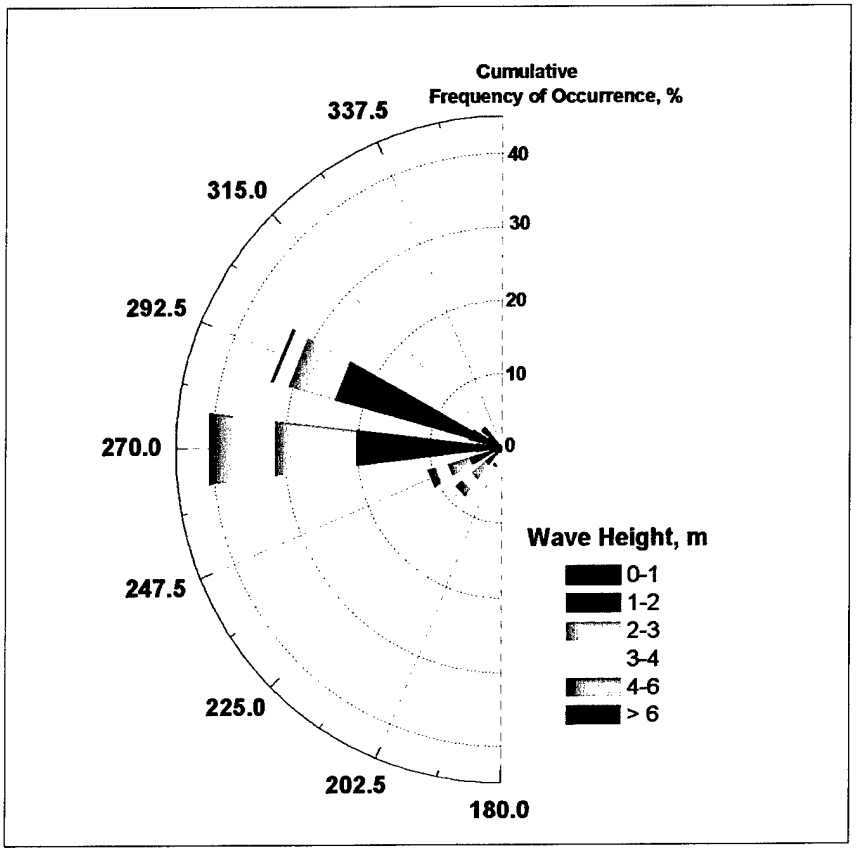

Figure 5-5 Frequency of occurrence of incident waves by height and direction

Table 5-2
Storm Wave Data from CDIP Buoy

		Extreme Storm		Typical Storm		Most Frequent Storm	
Direction	Angle (deg)	Height (m)	Period (sec)	Height (m)	Period (sec)	Height (m)	Period (sec)
Southwest	214-236	9.0	13	6.0	12.76	2.5	8
West-southwest	237-258	8.5	13	6.0	13.65	1.5	8
West	259-280	8.8	18	6.5	16.04	1.5	8
West-northwest	281-303	6.5	15	5.0	13.43	1.5	8

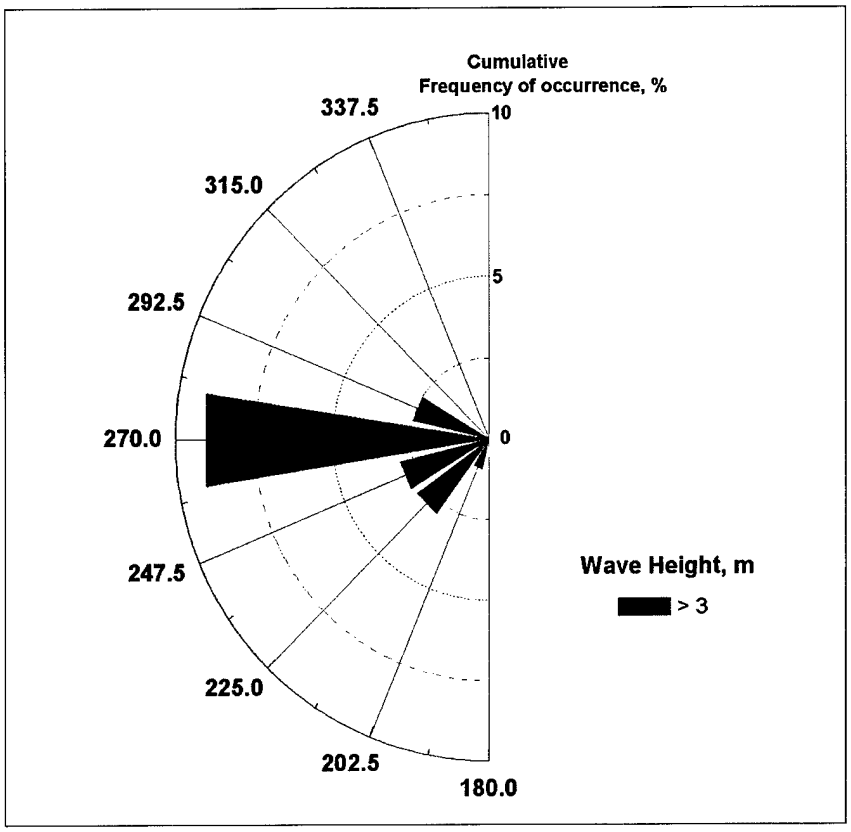

Figure 5-6. Incident direction for storms with significant wave heights greater than or equal to 3 m

model because the most extreme storms occurred between the west and southwest. The southwest design storm was therefore specified as H_s = 6 m and T_p = 16 sec. In addition, less severe storms of H_s = 3 m and T_p = 13 sec, and H_s = 2 m and T_p = 9 sec defined the storms from the west-northwest, and H_s = 3 m and T_p = 12 sec, and H_s = 2 m and T_p = 9 sec were chosen for storms from the southwest.

Table 5-3 lists the wave heights and periods for the physical model runs. Combinations of wave height and period are indicated by their respective numeric values. For example, the entry of 2-m, 9-sec waves implies a generated significant wave height of 2 m with a 9-sec period of peak energy density in prototype values.

Table 5-3
Wave Heights and Periods in Physical Model Experiments

Waves from West-Northwest		Waves from Southwest	
Height (m)	Period (sec)	Height (m)	Period (sec)
2	9	2	9
3	13	3	12
5	13	6	16

Each of the selected storms was reproduced with the numerical model STWAVE, which propagated the storms shoreward to the location of the wave generators in the physical model. Wave height, period, and direction at the location of the wave generator were determined for each storm at each of three water levels: mllw, mean high water (mhw), and mid-tide level (mtl) defined as the arithmetic mean of mean low water and mhw (see Table 2-1 for tide levels).

The circulation pump in the model basin was installed to provide flow in the direction of the flood tide. All model runs at mtl were conducted with full flood current based on a tidal range of 7.2 ft. Additional information on tidal conditions at the site is available in Chapter 4.

Calibration of Physical Model

Calibration of the physical model was required to ensure that currents and incident waves were accurately represented and that interference from the model basin boundaries was minimized. Flow patterns and velocities for the flood tide at mtl were obtained from the numerical model ADCIRC. Velocimeter measurements in the model were compared to the numerical model results (Chapter 7) to aid in setting guide vanes and pipe layout for the circulation system, and adjusting valve settings and size and spacing of openings on the pipe for flow into the physical model.

Wave heights in the physical model were calibrated by comparing measurements from wave gauges in the physical model to output from the numerical model STWAVE (Chapter 7). Guide vanes for the waves were located to minimize directional spreading and ensure wave heights in the vicinity of the north jetty and the north beach were similar to the wave heights predicted by STWAVE.

The physical model was calibrated prior to experiments with the vertical displacement wave generator for storms from the west-northwest and again after the wave generator was replaced with the directional wave generator for storms from the southwest.

Coal Tracer and Dye Studies

Coal tracer studies

Sand movement in the prototype environment includes both suspended sediment transport and bedload transport. Bedload transport may be depicted in a physical model by movement of a tracer material. Natural sand cannot be scaled correctly in the physical model because the scaled grain size would be in the range of clay particles, which are cohesive. Several types of moveable-bed tracer materials are available at CHL. Of the tracer material available at CHL, previous investigations (Giles and Chatham 1974; Bottin and Chatham 1975) indicated that crushed coal tracer provides the best representation of movement of prototype sand in large-scale 3-D models. Coal is lighter than sand and is not

transported identically to sand; therefore, results from a coal tracer study are considered qualitative. Coal tracers have been shown to accurately represent general patterns of transport and to depict areas of accumulation and erosion. Cross-shore movement within the surf zone appears to be biased toward accretion, because accretion of coal tracer on the shoreline was observed in the model during storms that should have produced erosion. Such accretion implies that the coal tracer is behaving as large grain size sand or gravel-sized particles. In addition, coal has to be placed in a quiescent model, and movement of the coal will be observed as soon as the generated waves reach the coal injection lines. It is not possible to run the model long enough to allow the wave-generated currents to reach equilibrium before beginning the coal study. It is expected that some differences will exist between the initial currents generated in the model and the currents that will exist after the model has reached equilibrium. Observations and conclusions regarding coal tracer should be made cautiously, but within these limitations coal tracers are considered a valuable tool for depicting patterns of sediment transport.

The coal tracer studies were conducted with a fine grain coal obtained by sieving containers of ground coal and collecting the coal that passed a 0.4-mm sieve. Specific gravity of the coal was 1.35. The coal was mixed with water to prevent it from floating in surface tension when placed in the model. The coal was injected by hand between two parallel boards to contain the coal during placement on the flooded model. The boards were placed 0.5 ft apart on the model, forming lines of coal that were 37.5-ft-wide prototype. Coal was placed in three lines extending due west from the shoreline and originating 600, 1,500, and 2,250 ft north of the jetty. The injection lines extended approximately 2,400 ft seaward from the mllw line. Two jetty-normal lines were placed between the jetty and the southernmost coal line extending from the shoreline. The most shoreward of the two jetty-normal lines was midway between the shoreline at mllw and the seaward end of the subaerial part of the existing jetty. The second jetty-normal line was placed midway between the subaerial end of the jetty and proposed location of the spur in Alt 2A (sta 165+00).

Removal of the coal after a run is difficult without draining the model. To save time, some runs were conducted by sweeping up the bulk of the coal from the previous run and then laying new injection lines over the remaining coal. Photographs taken before the start of each run depict the lines and any remaining coal in the model to aid in visualizing sediment movement. Figure 5-7 shows location of coal lines at the start of each run.

Photographs depicting movement of the coal were taken with a digital camera connected to a strobe system. The camera was manually operated and recorded the time of each photograph. The camera was located offshore and overhead at state plane coordinates N602175 E7175531 and elevation 2,180 ft (prototype). Photographs taken during the coal runs are contained in Appendix B.

Figure 5-7. Layout of coal tracer lines at start of a run

Dye studies

Dye studies were conducted to allow currents to be depicted in overhead photographs. Dye was injected into the model by hand from a squirt bottle in shore-normal and shore-parallel lines. The dye quickly penetrated the water column and was mixed by waves and currents. Movement of the dye was recorded by photographs taken from the same overhead camera location used in the coal tracer studies. Photographs taken during the dye studies are included in Appendix B.

Web cameras

Two digital cameras were installed over the model and connected to a computer that was transmitted to the world-wide web. The cameras were activated during runs with either coal or dye. Sponsors and interested persons were notified by e-mail prior to making runs that would be broadcast over the web. The camera images could be accessed in real time through a link on the CHL web page.

One of the web cameras was located offshore at state plane coordinates N601225 E7716560 at elevation 1,628 ft. The offshore camera was fixed on a specific view and was not moved during the course of the experiments. All video taken by the offshore camera was recorded and saved in addition to being broadcast. The second camera was mounted onshore in the model at state plane coordinates N602835 E722940 and elevation 1,144 ft. The onshore camera was controlled by a joystick and could be panned or zoomed. Interested parties could contact the model site by telephone and request that the camera be adjusted to more clearly illustrate features of interest.

Description of Alternative Structures in Physical Model

Model layouts for the alternatives are described in this section.

Alternative 1: Existing conditions

The head of the prototype north jetty has been damaged by storms and exists only as a wide, low mound from about sta 161 seaward to approximately sta 171. Shoreward of sta 160, surveys indicate that the jetty has a crest elevation of approximately +18 ft mllw. The jetty intersects north beach around sta 141 and then continues shoreward to the jetty base. The physical model reproduces the remnants of the jetty head at an elevation of -10 ft mllw seaward of sta 161 to 172+50 and extends the jetty shoreward along the entrance to Grays Harbor to sta 135. Between sta 135 and 160, the model jetty was constructed with a 30-ft crest width at elevation +18 ft mllw and 1:2 side slopes. It is assumed that the prototype jetty is reasonably impermeable, and an impervious barrier was placed within the model jetty extending from the shoreline seaward to sta 161.

Because the scale of the jetty is too small to reproduce prototype stability without scale distortion, the subaqueous mound at the tip of the jetty (sta 161 to 172+50) was glued to the model floor to prevent movement of the stones. In the prototype, the submerged stones have become partially buried in the sand, and significant movement of the stones is not expected. Stones in the model jetty were sized by Froude scaling laws to prototype jetty stone, and accounted for differences between model and prototype in stone density and unit weight of water. Froude scaling relationships are given in Table 5-1. Model layout of prototype existing conditions is shown in Figure 5-8.

Alternative 2A: Long rubble mound submerged spur dike

Alternative 2A was modeled as a 1,700-ft-long submerged spur dike perpendicular to the jetty remnants at sta 165. The spur dike was constructed of 3- to 5-ton stone without a core to a crest elevation of -10 ft mllw. Crest width was 33 ft, seaward slope was 1:5 and shore side slope was 1:3. Model layout with Alt 2A is shown in Figure 5-9.

Alternative 2A': Long rubble mound submerged spur dike at sta 162+50

Alternative 2A' was similar to Alt 2A except that the spur dike was moved shoreward 250 ft to sta 162+50. The spur dike was constructed with the same length and cross-section as Alt 2A. Because of the shallower water at the spur 2A' location, crest elevation on Alt 2A' was higher than Alt 2A. Prototype construction of the spur in the shallower water may be a problem. Alternative 2A' is shown in Figure 5-10.

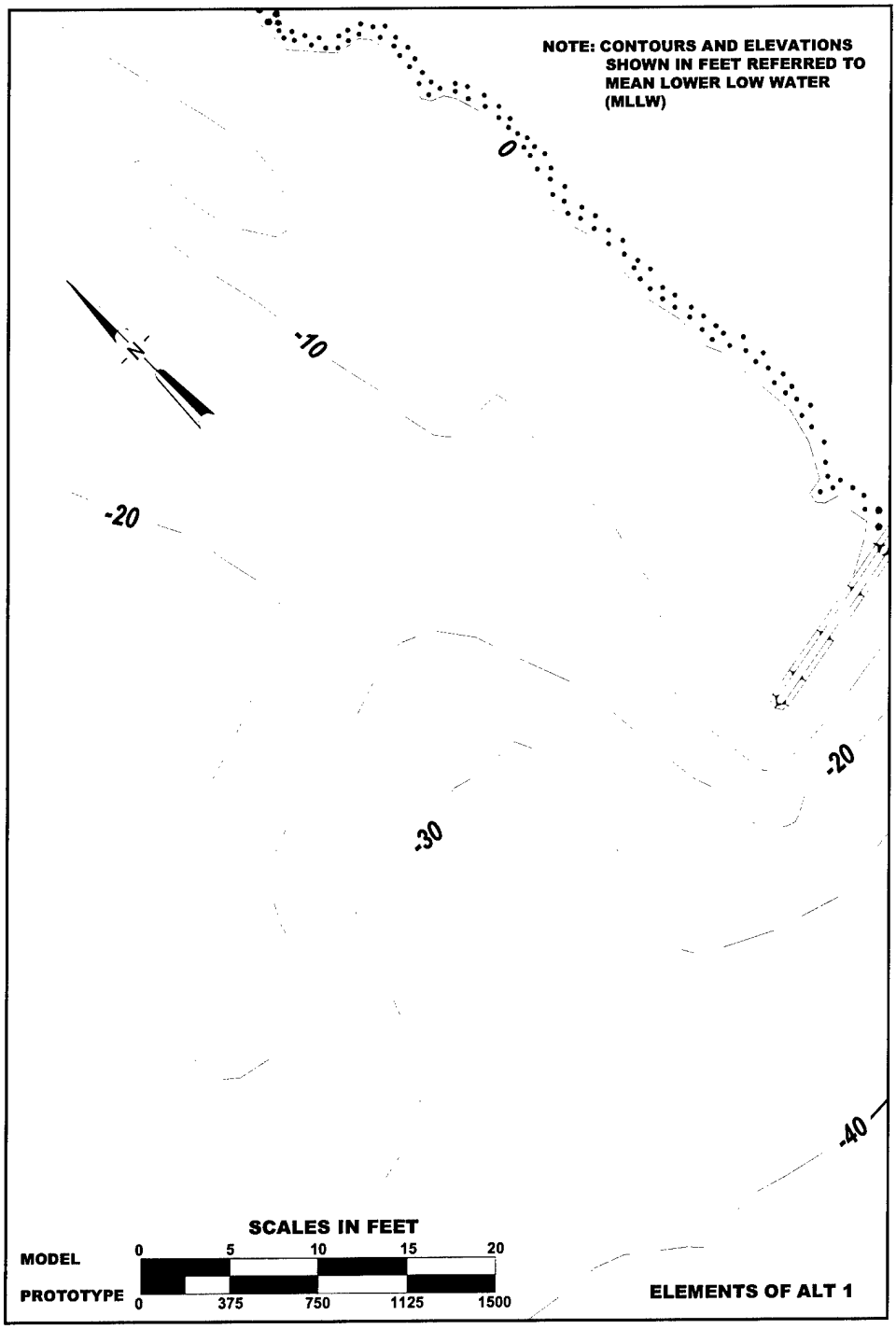

Figure 5-8. Physical model layout of Alt 1

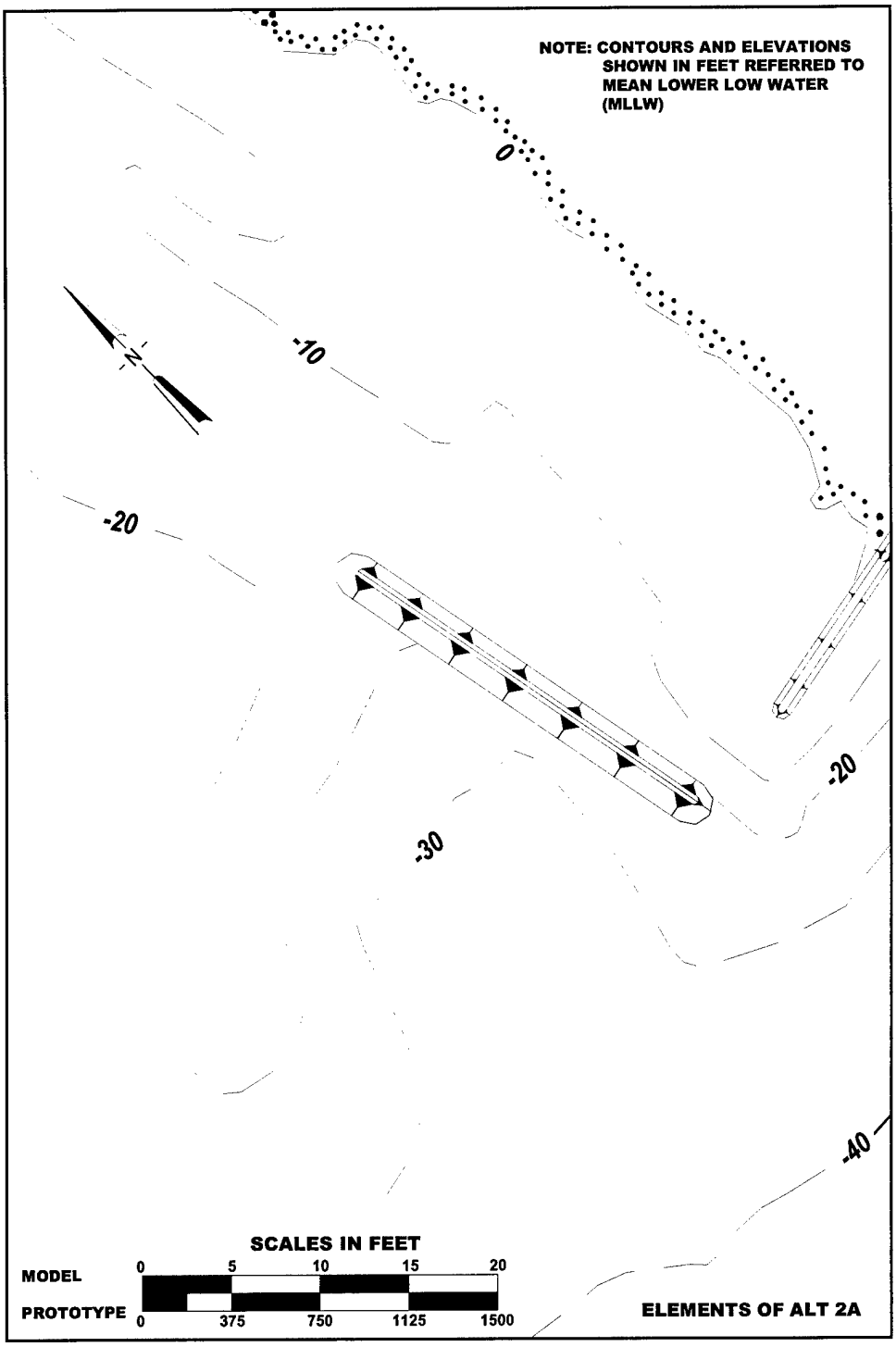

Figure 5-9. Physical model layout of Alt 2A

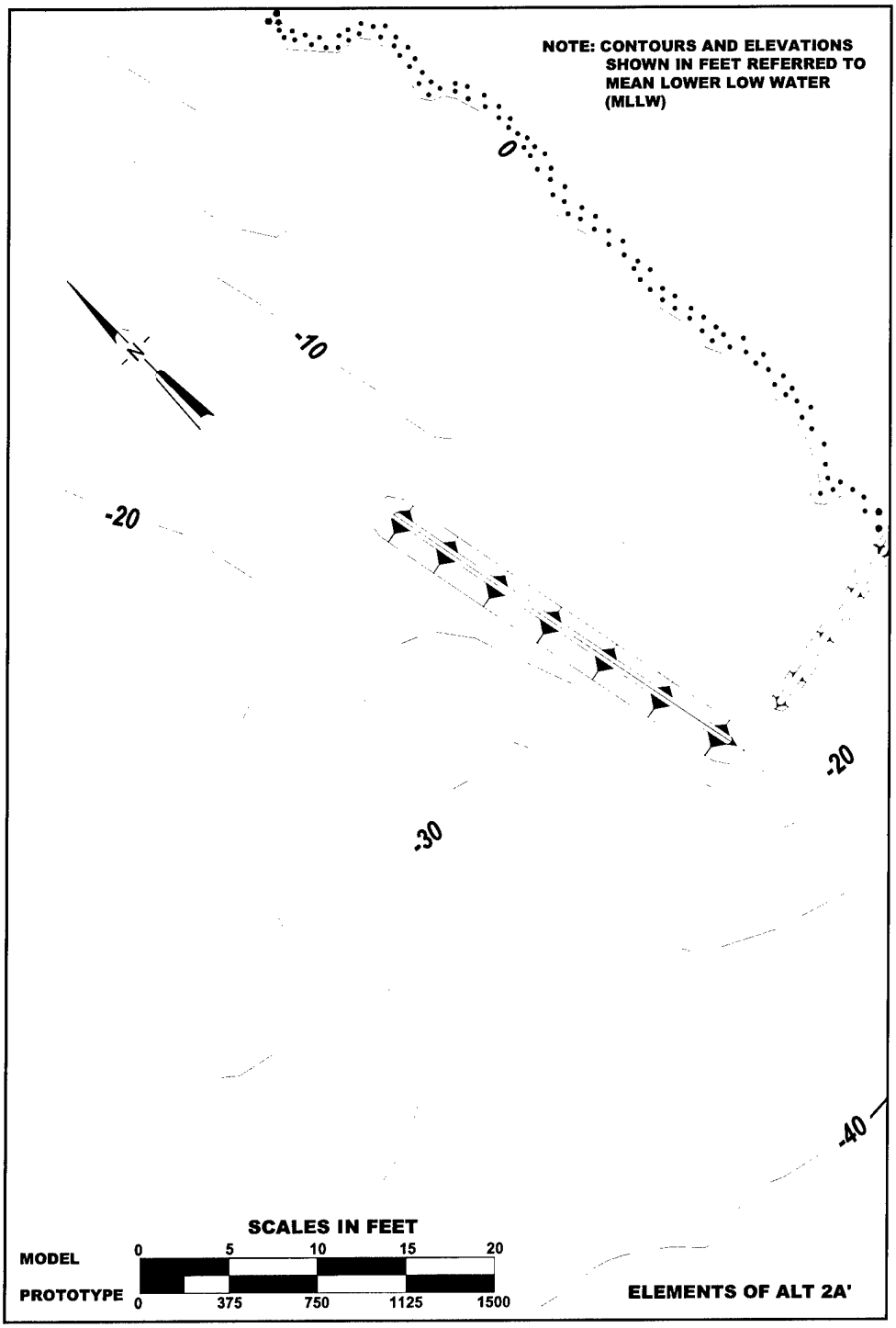

Figure 5-10. Physical model layout of Alt 2A'

Alternative 3B: Full jetty rehabilitation

Alternative 3B did not employ a spur but extended the jetty (subaerially) out to sta 170. Jetty cross section included a crest width of 30 ft at elevation +18 ft mllw and 1:2 side slopes. Alternative 3B is illustrated in Figure 5-11.

Alternative 2A with projected shoreline

The numerical model GENESIS was run as part of this study (Chapter 6) to predict changes in the shoreline that would occur after construction of Alt 2A. The dashed line between the existing shoreline and the -10-ft contour line in Figure 5-12 illustrates the new mllw shoreline determined by GENESIS 5 years after construction of Alt 2A.

Results and Discussion

Storms from west-northwest

General observations. Storms from the west-northwest produced a southbound longshore current that passed the beach adjacent to the north jetty (Ocean Shores) to within a few hundred feet north of the jetty. Dye patterns indicated the current was strongest approximately 800-1,000 ft offshore, with a weaker current 200-300 ft offshore. The longshore current is indicated in Figure 5-13 for Alt 2A with 5-m, 13-sec waves at mhw. The dye was placed as two straight, shore-normal lines.

A circulation pattern is evident near the jetty and is shown in Figures 5-14 through 5-18 for existing conditions with 5-m, 13-sec waves at mhw. A line of dye is placed shore-parallel extending from the jetty north for about 1,000 ft in Figure 5-14. In Figure 5-15, the dye is carried along the shore to the north, then carried seaward in a rip current about 1,500 ft north of the jetty. Offshore at about 1,500 ft, the dye is carried back to the south (Figure 5-16). Near the jetty, the dye pattern splits with a portion of the dye carried back towards shore, completing the gyre, and a portion of the dye continuing south, passing over the submerged jetty remnants and then into the channel (Figure 5-17). In Figure 5-17, an additional line of dye has been placed shore-normal about 1,500 ft north of the jetty, illustrating the longshore current north of the gyre forming near the jetty. The complete gyre is seen in Figure 5-18.

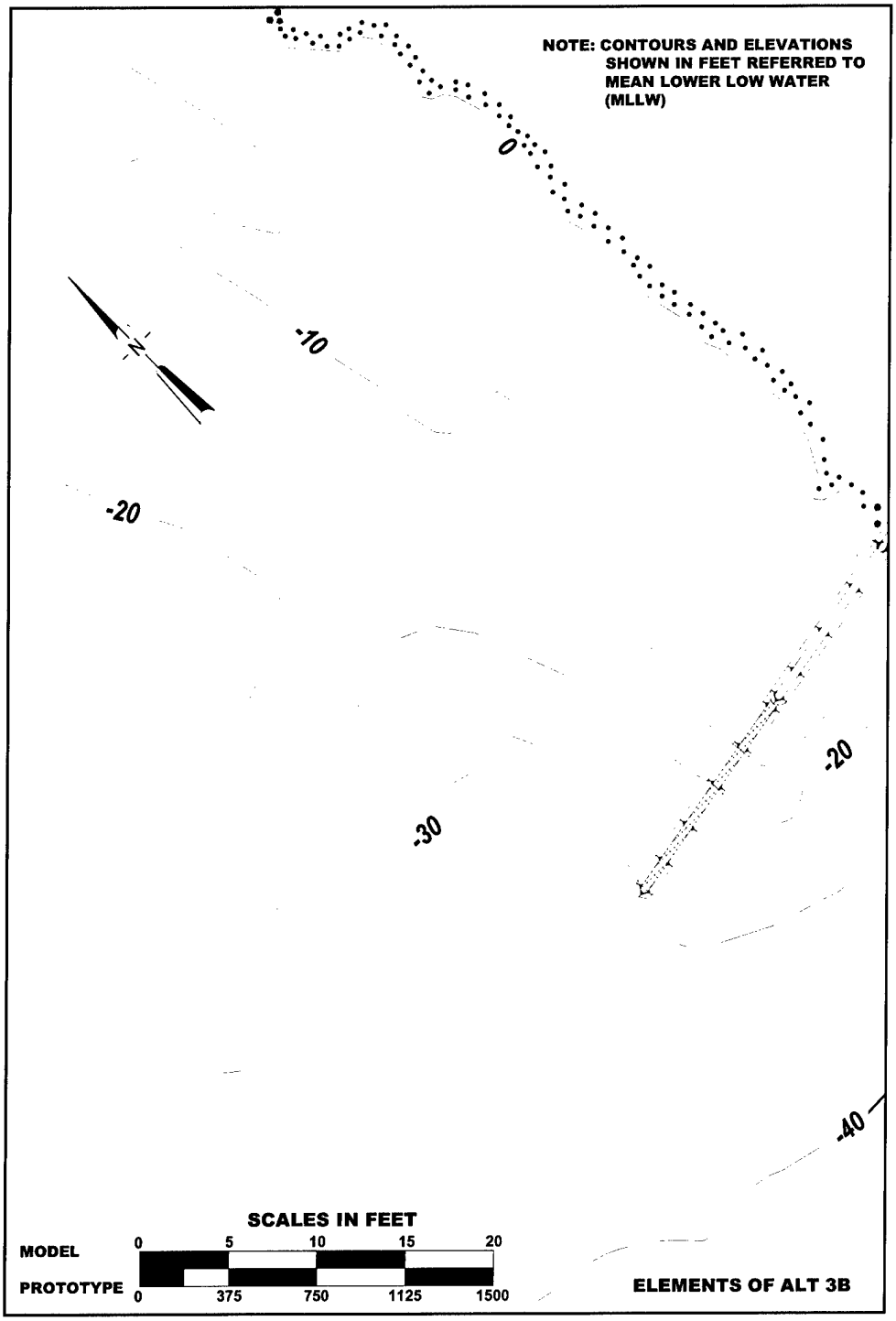

Figure 5-11. Physical model layout of Alt 3B

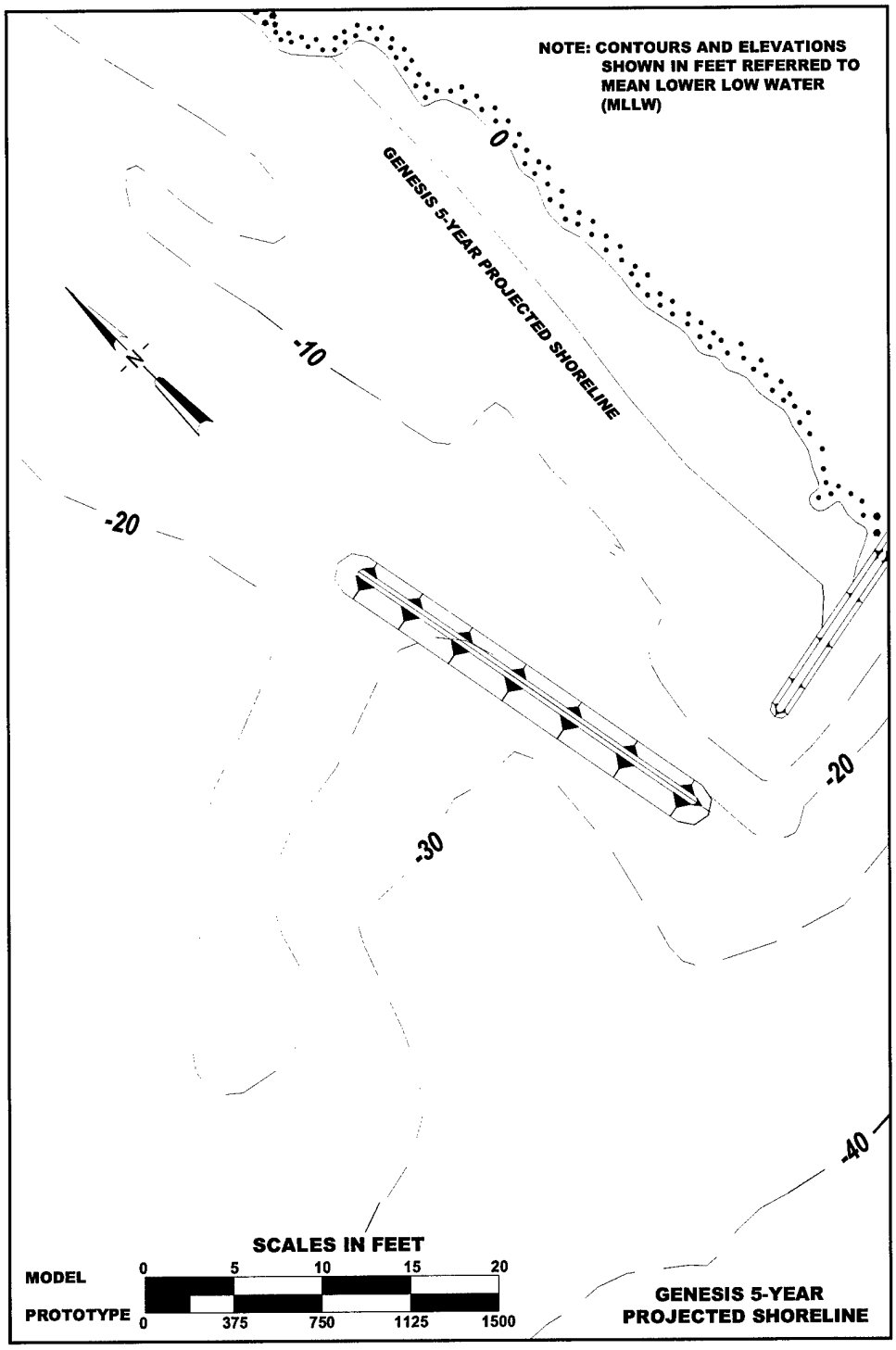

Figure 5-12. Physical model layout of Alt 2A with GENESIS 5-year projected shoreline

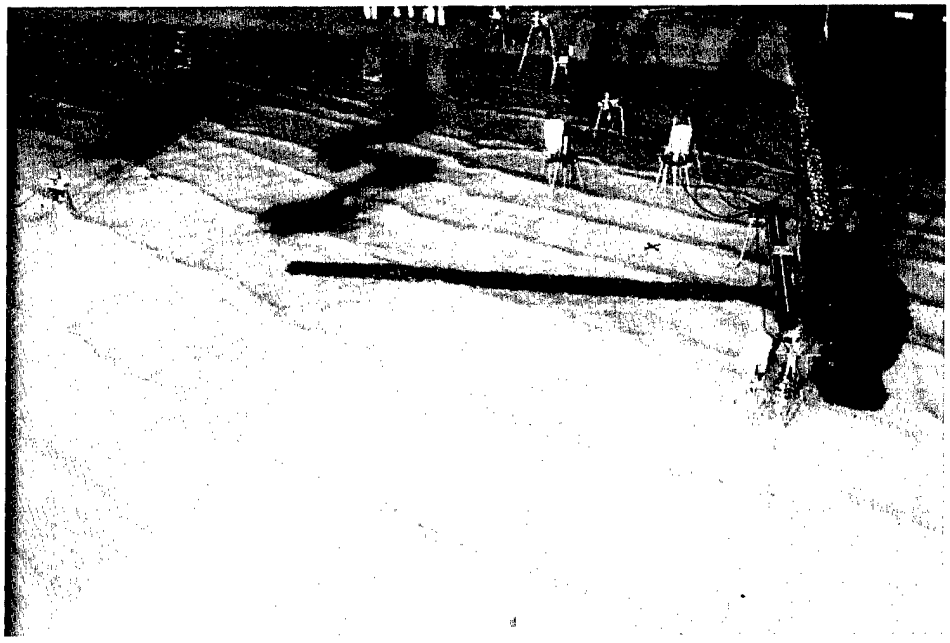

Figure 5-13. Longshore current with Alt 2A and 5-m, 13-sec waves from west-northwest at mhw

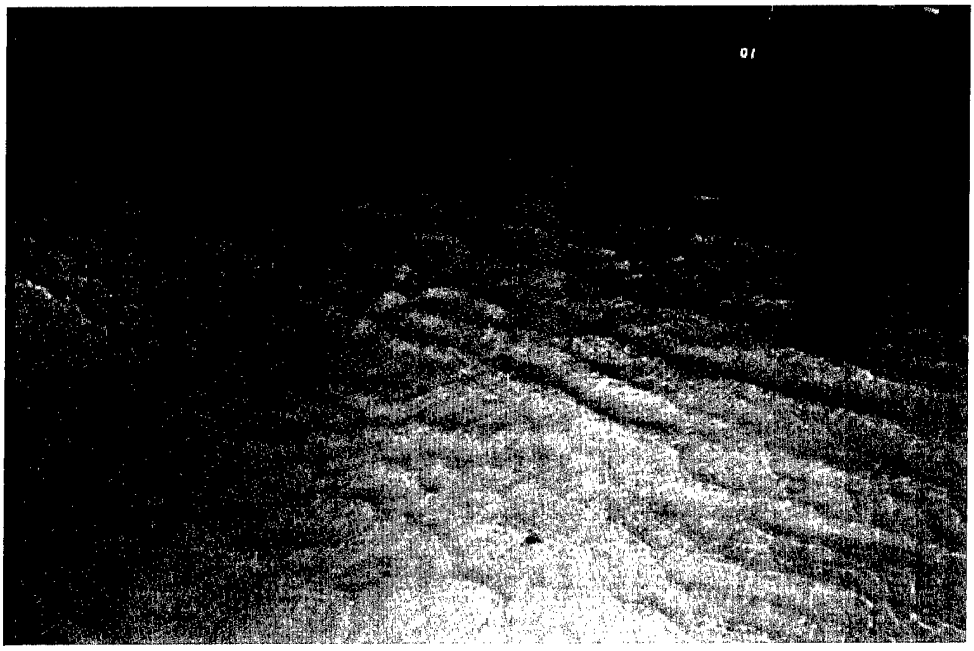

Figure 5-14. Dye placed shore-parallel north of jetty (Alt 1 with 5-m, 13-sec waves from west-northwest at mhw)

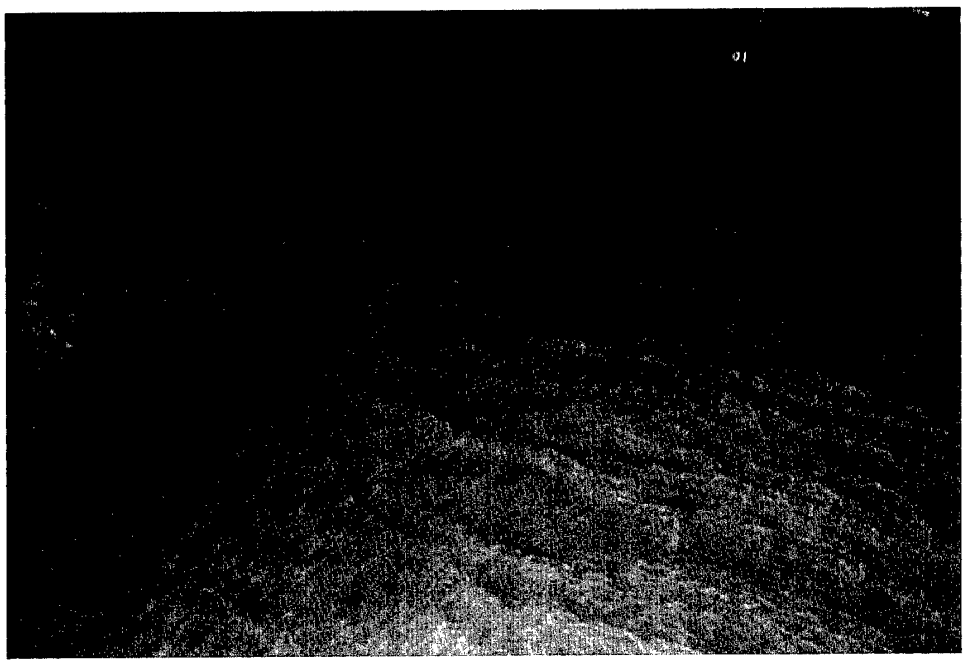

Figure 5-15. Rip current carrying dye seaward (Alt 1 with 5-m, 13-sec waves from west-northwest at mhw)

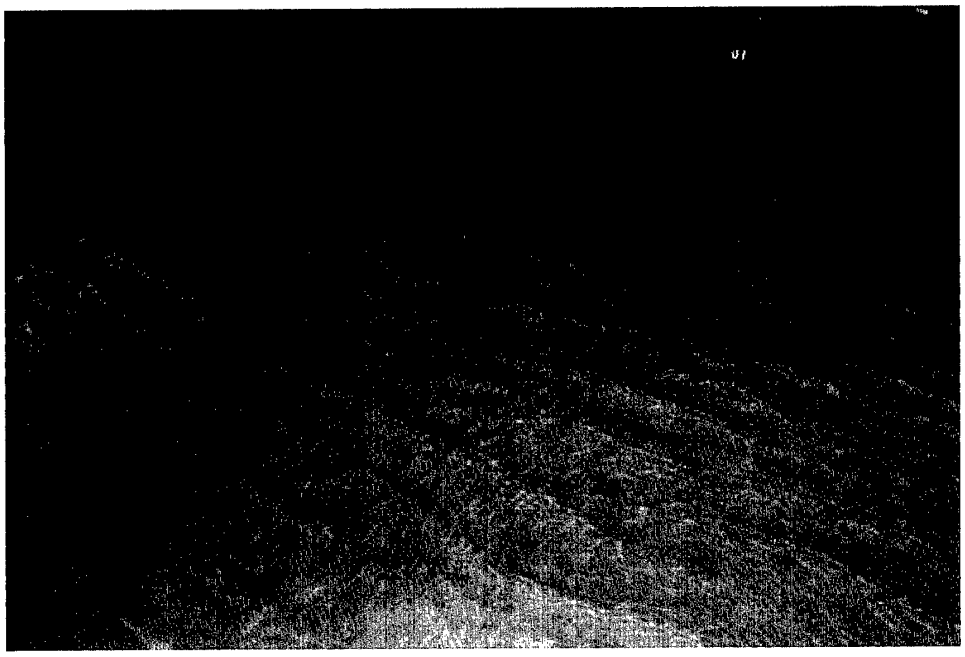

Figure 5-16. At seaward edge of rip current, dye is carried back towards jetty (Alt 1 with 5-m, 13-sec waves from west-northwest at mhw)

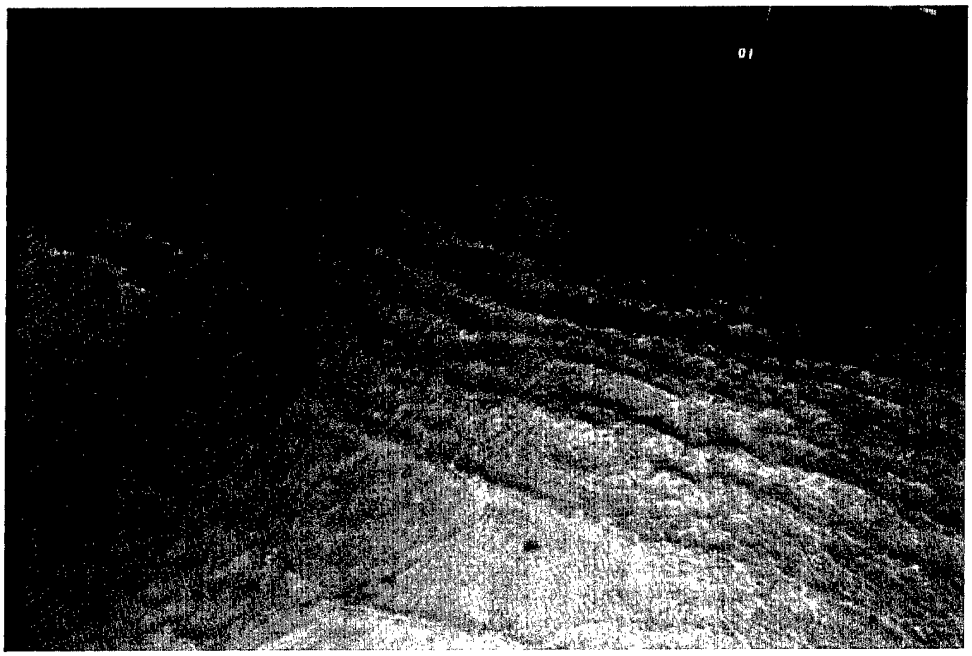

Figure 5-17. Near jetty, dye is carried shoreward completing gyre. An additional line of dye indicates longshore current north of gyre (Alt 1 with 5-m, 13-sec waves from west-northwest at mhw)

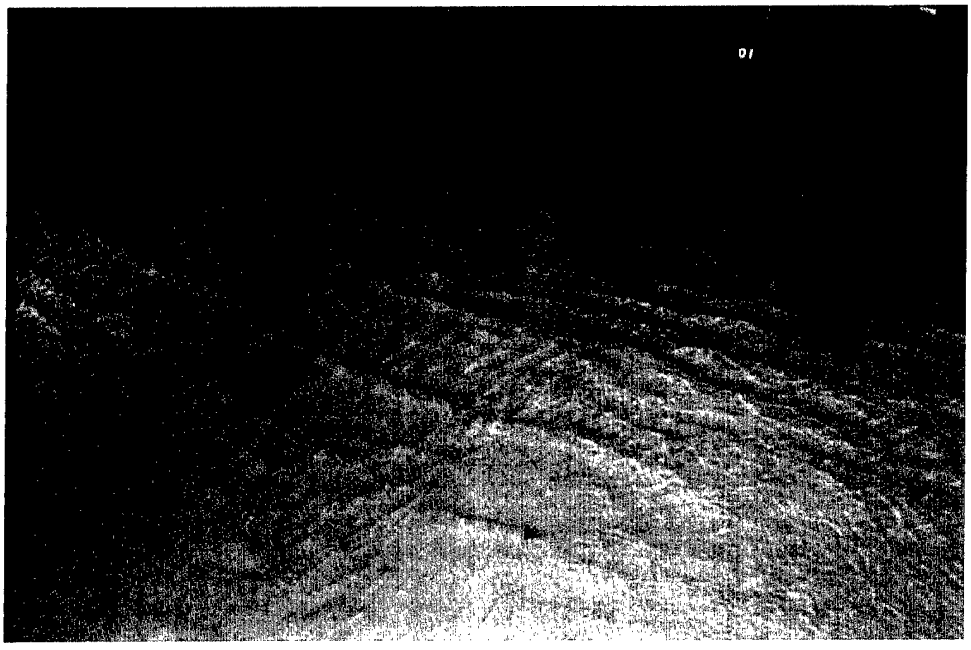

Figure 5-18. Complete counter-clockwise gyre and longshore current north of gyre (Alt 1 with 5-m, 13-sec waves from west-northwest at mhw)

The longshore currents and formation of the gyre were observed for each of the water level, wave height, and wave period combinations studied in the experiments. The gyre and rip current appear to be caused by gradients in local bathymetry. Figure 5-2 includes contour lines for the basin bathymetry in the physical model. The -20 ft mllw contour line indicates a low ridge extending shore-normal at a depth of 10 to 20 ft mllw. For a given wave approaching shore, the part of the wave south of the ridge will remain in deeper water as it propagates over the deeper harbor entrance than the more northern part of the wave in shallower water. The northern part of the wave will approach the shore at an angle towards the south producing a longshore current to the south. Because waves travel faster in deeper water, the southern part of the wave will be incident more towards shore. Aided by diffraction around the low ridge offshore from the jetty, the angle of approach changes until the part of the wave adjacent to the north side of the jetty approaches nearly perpendicular to the shoreline. The shore-normal approach of waves near the jetty produces a shoreward current along the jetty, then establishes a nearshore current to the north. The northbound current near the jetty meets the southbound longshore current, creating a rip current. In the absence of a tidal current, the rip current is located about 1,500 ft north of the jetty. The gyre is formed by the onshore current along the jetty, the northbound current south of the rip current, offshore in the rip current, then south in the longshore current as the rip current dissipates offshore.

Figure 5-19 shows current patterns with 2-m, 9-sec waves at mtl with full flood current. The southerly longshore current is strengthened by the flood tidal current, while there is no change in the northerly current near the jetty. The rip current is pushed south to about 1,000 ft north of the jetty by the stronger longshore current. With 3-m, 13-sec waves from west-northwest at mtl with full flood current (Figure 5-20), the larger waves create a stronger northerly current near the jetty and the rip current is located about 1,250 ft north of the jetty. With 5-m, 13-sec waves (Figure 5-21), the effects of the tidal current are minimal and the rip current is located approximately in the same location as in the absence of the flood current (about 1,500 ft north of jetty).

The coal tracer studies delineated the extent of the gyre and the location of the rip current (Figure 5-22 and Figure 5-23). Although movement of coal tracer in the physical model does not accurately reflect prototype sand movement within the surf zone, the current patterns are accurately depicted. The initial placement pattern of coal lines in the model was shown in Figure 5-7. Figure 5-22 illustrates movement of the coal after being subjected to 5-m, 13-sec waves at mhw. Coal was observed being lifted into suspension by waves and carried around the tip of the subaerial portion of the jetty and entering the inlet under the severe storm waves (Figure 5-22).

Coal was not observed passing around the subaerial jetty tip with the 2-m, 9-sec waves. Formation of the gyre and shoreward transport of the coal north of the gyre was similar for both storms. Figure 5-23 illustrates the gyre for the 2-m, 13-sec waves at mllw.

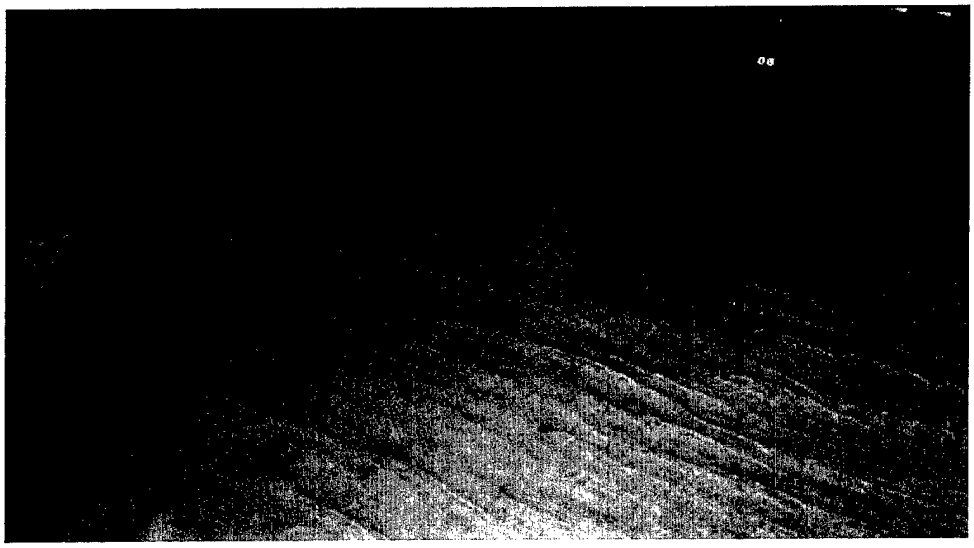

Figure 5-19. Rip current with 2-m, 9-sec waves from west-northwest at mtl with full flood current

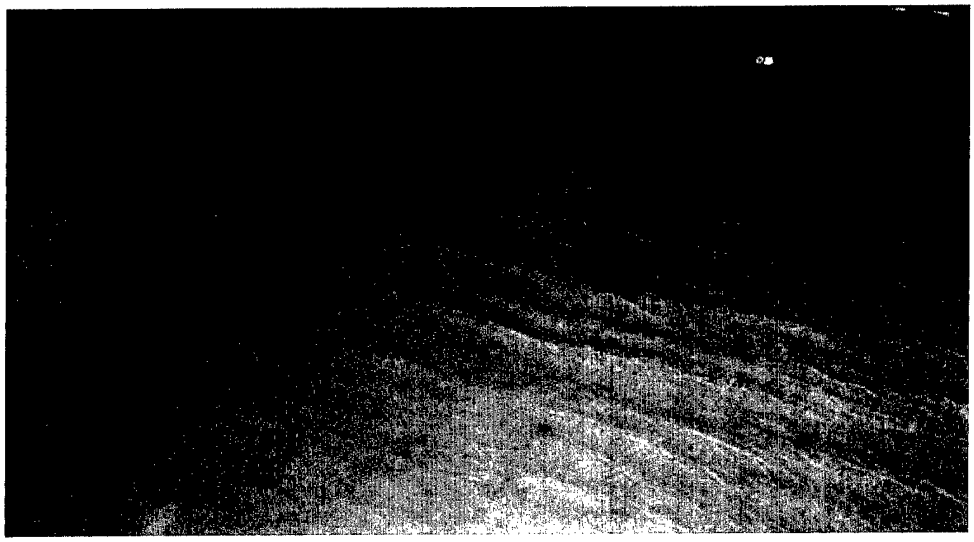

Figure 5-20. Rip current with 3-m, 13-sec waves from west-northwest at mtl with full flood current

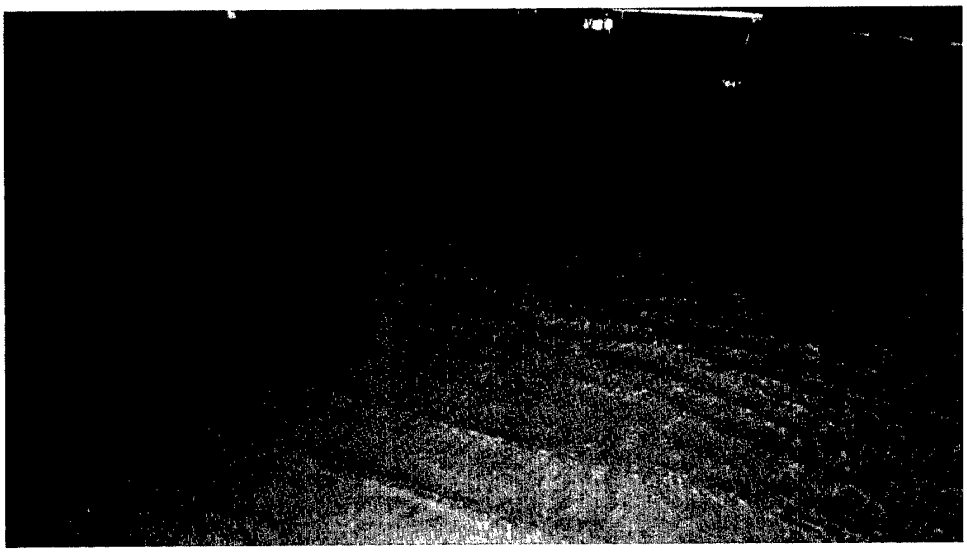

Figure 5-21. Rip current with 5-m, 13-sec waves from west-northwest at mtl with full flood current

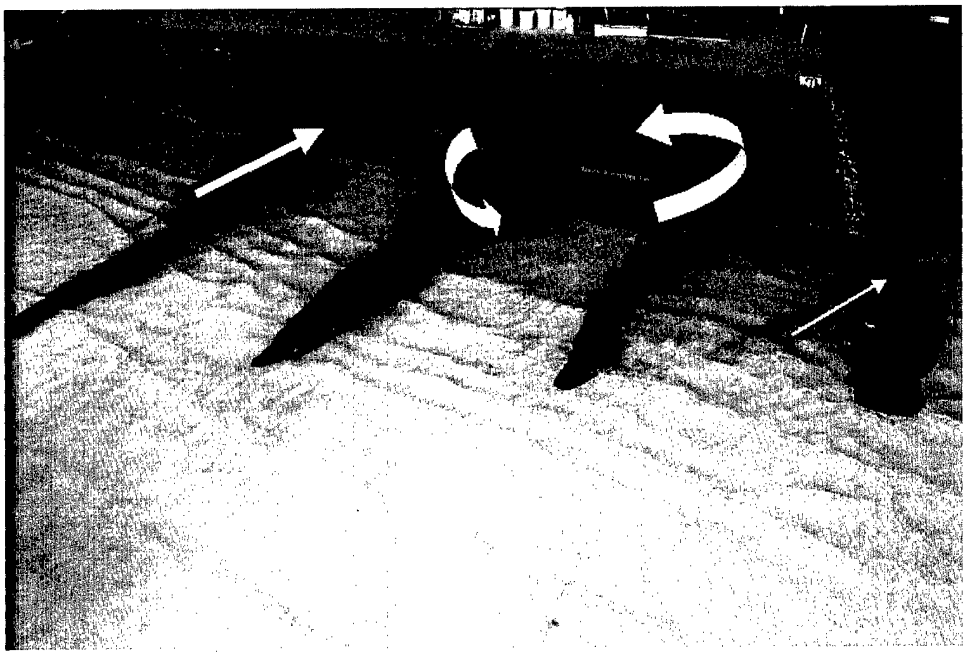

Figure 5-22. Coal patterns of shoreward transport north of gyre, counter-clockwise circulation in gyre, and some coal carried across jetty remnants

Figure 5-23. Coal tracer patterns from mild storm waves at mllw

Coal Tracer Study - Alternative 1: Existing conditions. Coal tracer studies were conducted on the model of existing conditions for 2-m, 9-sec waves and 5-m, 13-sec waves at mllw; 2-m, 9-sec, 3-m, 13-sec, and 5-m, 13-sec waves at mtl with full flood current; and 2-m, 9-sec and 5-m, 13-sec waves at mhw. Four photographs of each water level, wave height, and wave period combination are presented in Appendix B to illustrate sediment transport patterns.

Figure B1 photographs taken were from the coal tracer run at mllw with 2-m, 9-sec waves. After 3 min, 32 sec, the outermost of the jetty-normal lines has moved shoreward. At the intersection of the shoreward jetty-normal line and the southernmost shore-normal line, the coal is moving shore-parallel to the north along the inner edge of the gyre. Movement of the middle portion of the northernmost shore-normal line has begun angling southwards and towards the shore. The movement is more towards the shore than along the shore, indicating transport of the coal is dominated by wave action and that the longshore current is weak. By 6 min, 38 sec, movement of the northernmost shore-normal line towards the shore and south is evident. The central portion of the middle shore-normal line is moving shore-parallel towards the south along the outer edge of the gyre. The outermost of the jetty-normal lines has moved further shoreward and is feeding the coal moving northward on the shoreward side of the gyre. By 9 min, 24 sec, the outermost of the jetty-normal lines is no longer seen. The gyre is well defined by the coal moving northward along the shoreward side of the gyre, movement of the central portion of the middle gyre towards the south, and the shoreward flow along the central portion of the southernmost shore-normal line. The northernmost line is outside the gyre and shows transport shoreward and towards the south. In the corner between the jetty and the shoreline, a small amount of coal from the southern end of the nearshore jetty-normal line is moving in a countercurrent shoreward and southerly.

Figure B2 photographs were taken from the coal tracer run at mllw with 5-m, 13-sec waves. In photograph A of the figure, some coal remains in the model from the previous run and new lines of coal were placed over these remnants. The time stamps in photographs B, C, and D indicate that the increased wave energy is moving the tracer sooner and the patterns are developing more quickly than was observed under the influence of the 2-m, 9-sec waves in Figure B1. Under the 2-m, 9-sec waves, the seaward ends of the shore-normal coal lines show little movement, but movement occurs along the entire length of the coal lines under the 5-m, 13-sec waves indicating sediment transport at greater depths under the larger waves. Angle of the tracer lines on the two northernmost of the shore-normal lines indicates a stronger longshore current. Under the 2-m, 9-sec waves, movement of the outer jetty-normal line was directly towards shore; under the 5-m, 13-sec waves, the movement of the northern half of the line is angled more towards the south. The peak current in the seaward portion of the gyre appears to be approximately the same distance offshore, but the gyre is much larger under the 5-m, 13-sec waves. Movement of coal tracer across the submerged portion of the jetty is observed in photographs B and C of Figure B2, but was not observed with the 2-m, 9-sec waves.

Figure B3 photographs were taken during a run at mtl with 2-m, 9-sec waves and full flood current. Southerly longshore transport is evident along a significant portion of the northernmost shore-normal line of coal, indicating the combined effects of the wave-induced longshore current plus the tidal current. The longshore transport also extends further seaward along the shore-normal lines, as there is movement at the deepest end of the coal lines that was not observed with the 2-m, 9-sec waves at mllw (without the flood current). The gyre does not extend as far to the north as was observed with the 2-m, 9-sec waves at mllw.

Figure B4 photographs were taken during a run at mtl with 3-m, 13-sec waves and full flood current. Movement of coal tracer occurs along the entire length of the shore-normal coal lines, indicating the greater depths affected by the longer 13 sec waves. The longshore current is more pronounced than was observed under 2-m, 9-sec waves at mtl as evidenced by the strong peak in the movement of sediment about halfway out on the northernmost shore-normal line. A lesser peak in the longshore current occurs just seaward of the mllw line. The center of the gyre is in the same approximate location under both the 2-m, 9-sec waves and 3-m, 13-sec waves, but the gyre is larger and extends further seaward from the center under the larger waves.

Figure B5 photographs were taken during a run at mtl with 5-m, 13-sec waves and full flood current. A narrow current directly adjacent to the jetty is evidenced by a fine line of coal along the toe of the submerged portion of the jetty in photograph B. Coal tracer has also been carried across the submerged portion of the jetty as evidenced by the quantity of coal in the channel in photographs B and C. The coal entering the harbor entrance originated from the seaward jetty-normal line of coal. After photograph B, the seaward line of coal has been depleted and the coal along the south side of the jetty is gradually carried away in photographs C and D. Movement of the coal in the outer portion of the shore-normal lines is both shoreward and southward, but with a larger southward component than occurred under the 5-m, 13-sec waves at mllw without the flood current.

Figure B6 photographs were taken during a run at mhw with 2-m, 9-sec waves. The small waves produce less movement of the coal than was observed at mllw. The peak of the longshore current occurs just seaward of the mllw line as evidenced in the northernmost shore-normal line in photograph C. The seaward jetty-normal line is moved directly towards shore with little or no southerly component, and with stronger movement closer to the jetty. Formation of the gyre is indicated by northward shore-parallel movement of sediment seaward of the mllw line on the southernmost shore-normal line, but the gyre appears weak and diffused at this depth. Movement outside the gyre in the middle portion of the northernmost shore-normal line is angled sharply towards shore with only a small southerly component indicating the longshore current is weak at this depth.

Figure B7 photographs were taken during a run at mhw with 5-m, 13-sec waves. The time stamps indicate movement occurs much sooner than under the 2-m, 9-sec waves. Coal tracer movement outside the gyre (northernmost shore-normal line) shows a much stronger southerly component than occurred with the 2-m, 9-sec waves, indicating a stronger longshore current with the larger waves. The large waves carry a significant amount of coal over the submerged portion of the jetty as evidenced by the accumulation of coal along the south side of the jetty. A large quantity of coal is deposited near the shoreline on the north side of the jetty.

Coal Tracer Study - Alternative 2A: 1,500-ft-long jetty-normal submerged spur at sta 165+00. Coal tracer studies with Alt 2A were conducted for 2-m, 9-sec waves and 5-m, 13-sec waves at mllw; 2-m, 9-sec, 3-m, 13-sec, and 5-m, 13-sec waves at mtl with full flood current; and 2-m, 9-sec and 5-m, 13-sec waves at mhw. Four photographs of each water level/wave height/wave period combination are presented to illustrate sediment transport patterns. The incident wave height, period and water level combinations are the same as those run with the model of existing conditions.

Figure B8 photographs were taken during a run at mllw with 2-m, 9-sec waves. Movement of coal tracer shoreward of the spur and near the jetty is considerably slower than observed under existing conditions. Displacement of the seaward jetty-normal coal line at 8 min, 48 sec and 12 min, 46 sec for Alt 2B is similar to the displacement at 6 min, 38 sec and 9 min, 24 sec, respectively, with Alt 1. Northward displacement along the shoreward side of the gyre is also slower with Alt 2A than with Alt 1. The seaward edge of the gyre appears to be closer to shore with Alt 2A than with Alt 1. Movement of coal from the northernmost shore-normal line is unaffected by the spur.

Figure B9 photographs were taken during a run at mllw with 5-m, 13-sec waves. Again, movement of material shoreward of the spur has been slowed relative to movement with Alt 1. Displacement of material from the seaward jetty-normal line at 6 min, 38 sec with Alt 2A is similar to movement at 3 min, 24 sec with Alt 1. Gyre formation is considerably slower with Alt 2A than with Alt 1, and there appears to be less movement of material northward along the shoreline on the north side of the jetty with Alt 2A. Displacement of coal from the northernmost shore-normal line was not altered by the presence of the spur.

Figure B10 photographs were taken during a run at mtl with 2-m, 9-sec waves and full flood current. Northbound movement of tracer shoreward of the

spur is again slower and less pronounced than under similar waves and currents with existing conditions. At 6 min, 14 sec, the northward displacement on the shoreward side of the gyre is similar to the displacement seen at 4 min, 01 sec with existing conditions. Southbound movement on the seaward side of the gyre appears to be similar to movement observed with existing conditions. It appears that the two northernmost shore-normal coal lines are more controlled by the currents for Alt 2A, but the distance traveled by the tracer particles is similar for the same time span. It is likely that less coal was placed on the coal lines prior to the run for Alt 2A than with the existing conditions.

Figure B11 photographs were taken during a run at mtl with 3-m, 13-sec waves and full flood current. There is clearly less displacement shoreward of the spur in Alt 2A than was observed under similar waves and current with existing conditions. Seaward movement from the shoreline on the northern end of the gyre is noticeably reduced in the middle of the shore-normal coal lines with Alt 2A. The presence of the spur has no noticeable effect on the northernmost of the coal lines.

Figure B12 photographs were taken during a run at mtl with 5-m, 13-sec waves and full flood current. After 2 min, 27 sec, the seaward jetty-normal line has moved shoreward slightly, but was completely removed by 1 min, 59 sec with the existing conditions. Displacement shoreward along the south edge of the gyre, northward along the shoreward edge of the gyre, and seaward along the north edge of the gyre is reduced by the presence of the spur. Southerly movement along the seaward edge of the gyre is not significantly reduced due to the presence of the tidal flood current.

Figure B13 photographs were taken during a run at mhw with 2-m, 9-sec waves. Shoreward movement of the jetty-normal coal lines is similar with existing conditions and with the spur. Northward movement of coal near the mllw line from the southernmost coal line indicates a small reduction in the nearshore current with the spur. Otherwise, the spur has little effect on movement of coal tracer for small waves at mhw.

Figure B14 photographs were taken during a run at mhw with 5-m, 13-sec waves. Coal from the outer jetty-normal coal line is carried across the submerged head of the jetty and accumulates on the south side of the jetty under both Alt 1 and Alt 2A. Coal movement is similar between Alt 1 and Alt 2A at mhw.

Dye Studies - Alternative 1: Existing conditions. Dye studies were conducted on experiments with storms from the west-northwest with 2-m, 9-sec waves, 3-m, 13-sec waves, and 5-m, 13-sec waves each at water levels of mllw, mtl, and mhw. Time stamps were not recorded during the dye studies with Alt 1 and waves from the west-northwest. Four photographs from each wave height, wave period, and water level combination are included in Appendix B (Figures B15 through B23) to illustrate the current patterns.

Figure B15 photographs were taken from the dye study at mllw with 2-m, 9-sec waves. Dye was placed in a shore-normal line in the rip current located approximately 1,500 ft north of the jetty and a shore-parallel line between the jetty and the shore-normal line. Dye near the seaward end of the shore-normal line is carried south along the outer edge of the gyre, while the shoreward portion of the line remains stationary. Dye placed along the shoreline is carried

northward to the rip current located approximately 1,500 ft north of the jetty, then carried seaward in the rip current for about 1,000 ft. The dye is then carried south towards the jetty along the seaward edge of the gyre. Part of the dye enters a counterclockwise gyre located between the jetty and the rip current, and the rest of the dye is carried south across the submerged remnants of the jetty head.

Figure B16 photographs were taken from the dye study at mllw with 3-m, 13 sec waves. Dye in the shoreward one-half of the shore-normal dye line remains in the rip current. The seaward half of the shore-normal line is carried south along the outer edge of the gyre until it reaches half the distance from the rip current to the jetty. Some of the dye on the outer edge of the gyre then enters the gyre, and the remainder of the dye is carried south across the submerged remnants of the jetty head and then into the harbor entrance. Dye along the shoreline is carried north to the rip current, then seaward.

Figure B17 photographs were taken from the dye study at mllw with 5-m, 13-sec waves. The rip current is slightly south of the shore-normal dye line. The nearshore portion of the shore-normal dye line is carried south to the rip current, then seaward. The seaward portion of the shore-normal line appears to be carried northward in a weak countercurrent. Dye from the shore-parallel line is carried north to the rip current, then seaward. Along the seaward edge of the gyre, most of the dye is carried south across the submerged remnants of the jetty head and then into the harbor entrance.

Figure B18 photographs were taken from the dye study at mtl with 2-m, 9-sec waves and full flood current. Dye in the seaward portion of the rip current is affected by the tidal current and carried towards the south. Dye in photograph D is beginning to be carried shoreward along the jetty, but appears to be flowing shoreward in a narrower band than occurred at mllw with similar incident waves.

Figure B19 photographs were taken from the dye study at mtl with 3-m, 13-sec waves and full flood current. The shore-normal line was placed north of the rip current. The shoreward half of the line is carried south to the rip current, then seaward. The seaward half of the shore-normal dye line is beyond the rip current and is carried south in the flood tide current.

Figure B20 photographs were taken from the dye study at mtl with 5-m, 13-sec waves and full flood current. The shore-normal dye line is carried south to the rip current, then carried seaward. Unlike the smaller wave heights at mtl, much of the dye from the seaward edge of the gyre is carried shoreward by the southern edge of the gyre, with the remaining dye being carried across the submerged remnants of the jetty head.

Figure B21 photographs were taken from the dye study at mhw with 2-m, 9-sec waves. The shore-normal dye line is north of the rip current. A narrow longshore current near the 0-ft mllw contour line carries dye from the middle of the shore-normal dye line south to the rip current; the dye line is nearly stationary both seaward and shoreward of the longshore current.

Figure B22 photographs were taken from the dye study at mhw with 3-m, 13-sec waves. Dye from the shore-normal line is carried south to the rip current by a narrow longshore current just seaward of the 0-ft mllw contour. Dye from the shore-parallel line is carried north to the rip current.

Figure B23 photographs were taken from the dye study at mhw with 5-m, 13-sec waves. Dye from the shore-normal dye line is carried south to the rip current by a narrow longshore current near the 0-ft mllw contour. The outer portion of the shore-normal dye line is carried south by the second longshore current located further offshore. Much of the dye from the seaward edge of the gyre is carried shoreward in a wide band north of the jetty in the southern edge of the gyre.

Dye Studies - Alternative 2A: 1,500-ft-long jetty-normal submerged spur at sta 165+00. Dye studies for Alt 2A with waves from the west-northwest were conducted at the same wave height, wave period, and water level combinations that were run for the dye studies on Alt 1. Four photographs from each run are presented in Appendix B (Figures B24 through B32) to illustrate the currents in the model. The photographs were taken before time stamps were imprinted on the photographs.

Figure B24 photographs were taken from the dye study at mllw with 2-m, 9-sec waves. Dye in the shoreward one-half of the shore-normal line is carried south until it reaches the rip current, and then is carried seaward. Of the seaward half of the shore-normal dye line, dye shoreward of the jetty is carried in a southerly current into the outer edge of the gyre. Dye near the northern tip of the spur is carried seaward and to the south, but movement is slow. Dye in the outer edge of the gyre separates with part of the dye being carried shoreward along the jetty and part of the dye being carried south across the submerged remnants of the jetty head and into the harbor entrance.

Figure B25 photographs were taken from the dye study at mllw with 3-m, 13-sec waves. The pattern is similar to the run with 2-m, 9-sec waves. Dye movements show the strong southerly current at the seaward end of the rip current entering the gyre, with a weak southerly current over the spur.

Figure B26 photographs were taken from the dye study at mllw with 5-m, 13-sec waves. The gyre is more evident with Alt 2A than with existing conditions and the same incident waves. Currents shoreward of the spur appear to be weaker and more diffuse than with the existing conditions. Much of the dye is carried across the submerged remnants of the jetty head and into the harbor entrance.

Figure B27 photographs were taken from the dye study at mtl with 2-m, 9-sec waves and full flood current. The rip current is located further south near the midpoint of the spur due to the flood current. Southerly flow along the shore north of the rip current and northerly flow along the shore south of the rip current is evident.

Figure B28 photographs were taken from the dye study at mtl with 3-m, 13-sec waves and full flood current. The rip current is further north than with the 2-m, 9 sec waves at mtl, and located about one-quarter of the distance south along the spur. The southerly current on the seaward edge of the gyre is broader and more diffuse than was observed with the existing conditions.

Figure B29 photographs were taken from the dye study at mtl with 5-m, 13-sec waves and full flood current. The rip current is near the northern tip of the spur, which is approximately the same location as observed without the flood

tidal current. Dye in the seaward edge of the gyre appears to be closer to shore with Alt 2A than with existing conditions.

Figure B30 photographs were taken from the dye study at mhw with 2-m, 9-sec waves. Dye at the seaward end of the rip current separates, with part of the dye carried northward and part of the dye carried southward. Little movement of dye along the shoreline south of the rip current is observed. Dye along the shoreline north of the rip current is carried south to the rip current, then seaward.

Figure B31 photographs were taken from the dye study at mhw with 3-m, 13-sec waves. Dye at the seaward end of the rip current is carried to the south along the seaward edge of the gyre; there is no indication of dye being carried to the north as was observed with Alt 2A and 2-m, 9-sec waves at mhw.

Figure B32 photographs were taken from the dye study at mhw with 5-m, 13-sec waves. Current patterns are similar with Alt 1 and Alt 2A at mhw with 5-m, 13-sec waves.

Dye Studies - Alternative 2A': 1,500-ft-long jetty-normal submerged spur at sta 162+50. For Alt 2A', the Alt 2A spur was moved shoreward 250 ft to jetty station 162+50. The cross-section of the spur was the same in Alts 2A and 2A'. Alternative 2A' was constructed in shallower water than Alt 2A; therefore, submerged depth of the structure crest was less than with Alt 2A. Dye studies for Alt 2A' with waves from the west-northwest were conducted at seven of the nine wave height, wave period, and water level combinations that were run for the dye studies on Alt 1 (2-m, 9sec and 5-m, 13 sec waves at mllw; 2-m, 9-sec, 3-m, 13-sec, and 5-m, 13-sec waves at mtl with full flood; 2-m, 9-sec and 5-m, 13-sec waves at mhw). Four photographs from each run are presented in Appendix B (Figures B33 through B39) to illustrate the currents in the model. Time stamps with the photographs are in model units and should be multiplied by 8.66 (Table 5-1) to convert to prototype time.

Figure B33 photographs were taken from a run at mllw with 2-m, 9-sec waves from the west-northwest. Dye was injected as two shore-normal lines north of the northern end of the spur. Dye from the northern dye line is carried south in a narrow nearshore current until it reaches the rip current, and is then carried offshore. Southbound nearshore transport north of the rip current is completely blocked by the rip current. Seaward of the spur, the rip current ends and dye is carried in a weak southerly current.

Figure B34 photographs were taken at mllw with 5-m, 13-sec waves from the west-northwest. Dye from the northern shore-normal line is carried south in a narrow nearshore current to the rip current, and dye is carried north in a countercurrent immediately offshore from the southbound current. Dye carried seaward past the spur is carried southward along the spur, then part of the dye is carried around the tip of the jetty and part of the dye is carried shoreward. There is no discernable gyre.

Figure B35 photographs were taken at mtl with 2-m, 9-sec waves from the west-northwest with full flood current. Dye is carried south in a nearshore current to about 750 ft north of the jetty, then carried seaward along the rip current. The rip current is further south than was observed with 2-m, 9-sec waves at mllw due to the presence of the flood tidal current. At the seaward end of the rip current, most of the dye is carried south across the submerged remnants

of the jetty head, and a small portion of the dye is carried shoreward in a weak gyre.

Figure B36 photographs were taken at mtl with 3-m, 13-sec waves from the west-northwest with full flood current. The rip current is further north than was observed with 2-m, 9-sec waves at mtl, but is further south than was observed with slack tide at mllw. The seaward edge of the gyre is seaward of the spur, and much of the dye moves from the gyre and passes across the submerged remnants of the jetty head.

Figure B37 photographs were taken at mtl with 5-m, 13-sec waves from the west-northwest with full flood current. The rip current is at approximately the same location as at slack tide. With 2-m, 9-sec waves at mtl with flood current (Figure B35), the tidal current carried the dye southward along the shoreline shoreward of the spur about one-half the distance to the jetty. The larger 5-m, 13-sec waves create a stronger current to the north in the gyre that counters the flood current and prevents dye from being carried south along the shoreline shoreward of the spur. Dye is carried south along the spur, then separates with part of the dye being carried across the submerged remnants of the jetty head and part of the dye being carried shoreward in the gyre.

Figure B38 photographs were taken at mhw with 2-m, 9-sec waves from the west-northwest. There is no evidence of a gyre. It appears that the longshore current carried the dye to the south along the shoreline shoreward of the spur most of the way to the jetty. The spur is reducing wave activity shoreward of the spur resulting in a smaller northerly current in a gyre than was observed with either Alt 1 or Alt 2A.

Figure B39 photographs were taken at mhw with 5-m, 13-sec waves from the west-northwest. The 5-m waves create a sufficiently strong northward current in the gyre that the southerly longshore current does not carry dye into the area shoreward of the spur. The gyre appears more diffused than was observed with Alts 1 or 2A.

Dye Studies - Alternative 3B: Full jetty rehabilitation. Alternative 3B repaired the submerged portion of the jetty to sta 170 to a crest elevation of +20 ft, 33-ft crest width, and 1:2 side slopes. The jetty extension was constructed on top of the existing submerged portion of the jetty. Flume layout of Alt 3B is shown in Figure 5-11. Dye studies for Alt 3B with waves from the west-northwest were conducted at seven of the nine wave height, wave period, and water level combinations that were run for the dye studies on Alt 1. These were 2-m, 9-sec and 5-m, 13-sec waves at mllw; 2-m, 9-sec, 3-m, 13-sec, and 5-m, 13-sec waves at mtl with full flood; 2-m, 9-sec and 5-m, 13-sec waves at mhw. Four photographs from each run (Figures B40 through B46) illustrate the currents in the model. Time stamps with the photographs are in model units and should be multiplied by 8.66 (Table 5-1) to convert to prototype time.

Figure B40 photographs were taken from a run at mllw with 2-m, 9-sec waves from the west-northwest. The rip current is at approximately the same location along the shoreline as in Alt 1. The seaward edge of the gyre is located further offshore, resulting in a larger gyre than was observed with either Alt 1 or Alt 2A. With Alts 1 and 2A, the seaward edge of the gyre approaches the jetty slightly seaward of the subaerial jetty head. With Alt 3B, the subaerial jetty head is further offshore, and the seaward edge of the gyre is moved offshore such that

the gyre approaches the jetty near the subaerial jetty head. Near the jetty head the current splits, with part of the dye carried seaward in the gyre and part of the dye being carried around the tip of the jetty and into the harbor entrance.

Figure B41 photographs were taken from a run at mllw with 5-m, 13-sec waves from the west-northwest. The seaward edge of the gyre is at approximately the same location observed with Alts 1 and 2A, rather than being shifted seaward as was observed with the 2-m, 9-sec waves and Alt 3B. After being carried near the jetty head, the current splits, with part of the dye carried towards shore in the gyre and part of the dye carried seaward along the north edge of the jetty and around the jetty head.

Figure B42 photographs were taken from a run at mtl with 2-m, 9-sec waves from the west-northwest and full flood current. Similar to patterns observed with Alt 2A, the rip current is closer to the jetty than was observed without the flood current at mllw. Dye in the seaward edge of the gyre approaches the jetty near the jetty head, then splits, with part of the dye carried shoreward into the gyre and the rest of the dye carried past the jetty head.

Figure B43 photographs were taken during a run at mtl with 3-m, 13-sec waves from the west-northwest and full flood current. Little movement of dye shoreward of the mllw contour is seen other than some spreading. Dye seaward of the mllw contour in the two shore-normal dye lines is carried south to the location of the rip current. The two dye lines merge in the rip current, and the dye is carried seaward, then southward in the seaward edge of the gyre.

Figure B44 photographs were taken during a run at mtl with 5-m, 13-sec waves from the west-northwest with full flood current. Dye patterns are similar to those observed with 3-m, 13-sec waves at mtl except that the currents are faster.

Figure B45 photographs were taken during a run at mhw with 2-m, 9-sec waves from the west-northwest. Dye seaward of the mllw contour is carried south to the location of the rip current, but the rip current appears diffused and weak. After 3 min, 0 sec, dye has not reached the jetty nor been carried shoreward along the south edge of the gyre. After 5 min, 30 sec, dye is carried shoreward in the southern half of the gyre, but movement is diffuse and slow.

Figure B46 photographs were taken during a run at mhw with 5-m, 13-sec waves from the west-northwest. A strong southerly current is seen between the mllw contour and the seaward end of the dye lines. The seaward edge of the gyre is closer to shore than was observed with smaller waves. More dye appears to remain in the gyre rather than being carried around the tip of the jetty than was observed with smaller waves.

Wave heights. Variations in water surface elevation (wave heights) were collected with an array of wave gauges during runs for Alt 1 and 2A with waves from the west-northwest. Significant wave heights and periods of peak energy density calculated from the measured changes in water surface elevation are presented in Appendix B (Tables B1 through B9). Figure 5-3 shows locations of the wave gauges in the model.

Figures B47 through B55 show differences in wave heights between Alts 1 and 2A at each wave gauge. Differences were obtained by subtracting the significant wave height for Alt 1 from the significant wave height for Alt 2A. Therefore, a negative value indicates a smaller wave height for Alt 2A.

With few exceptions, modification of wave height shoreward of the spur in Alt 2A is consistent for each of the wave-height, wave-period, and water-level combinations run. Wave heights directly shoreward of the spur are reduced, with the greatest reductions in wave height occurring at the two gauges near the middle of the spur. Reductions in wave heights were observed at nearly all wave gauges shoreward of the spur with the exception of wave gauges along the north side of the jetty. The three wave gauges placed nearest the shoreline along the north side of the jetty indicate small increases in wave heights with the addition of the spur. It is believed that ponding behind the spur is causing an increase in water surface elevation in the corner between the shoreline and the jetty, resulting in larger wave heights (Browder 1994; Longuet-Higgins 1967).

Reductions in wave heights caused by the spur at different water levels are illustrated in Figures 5-24 through 5-26 for mllw, mtl, and mhw, respectively. At each gauge location shown, the value was obtained by:

$$H_{diff} = \frac{\sum H(\text{Alt 2A})_i - \sum H(\text{Alt 1})_i}{\sum H(\text{Alt 1})_i} 100\% \qquad (5\text{-}1)$$

where H_{diff} = percent difference shown in Figures 5-23 through 5-25, H (Alt 2A) = wave height at the indicated wave gauge for Alt 2A, H (Alt 1) = wave height at the indicated gauge for Alt 1, and the summation over i indicates the sum of measured wave heights with 2-m, 9-sec incident waves plus 3-m, 13-sec incident waves plus 5-m, 13-sec incident waves.

Reductions in wave heights relative to existing conditions due to the presence of the spur are greatest at mllw, and smallest at mhw. As depth increases, the fixed-height spur occupies a smaller percentage of the water column; therefore, the spur has less effect on the hydrodynamic processes. Also, movement in the water column due to a wave decreases with depth; for deeper water, the spur has less influence on wave height. Wave transmission over the spur is further discussed in Chapter 6. At mllw, wave heights along the shoreward toe of the spur are reduced an average of 20 percent, about 15 percent at mtl, and about 10 percent at mhw. Further shoreward, reductions in wave heights with the spur range from about 6 to 12 percent at mllw, 1 to 7 percent at mtl, and 1 to 13 percent at mhw.

Wave height increases near the base of the jetty with the addition of the spur due to ponding and average 14 to 19 percent at mllw, 5 to 13 percent at mtl, and 5 to 7 percent at mhw.

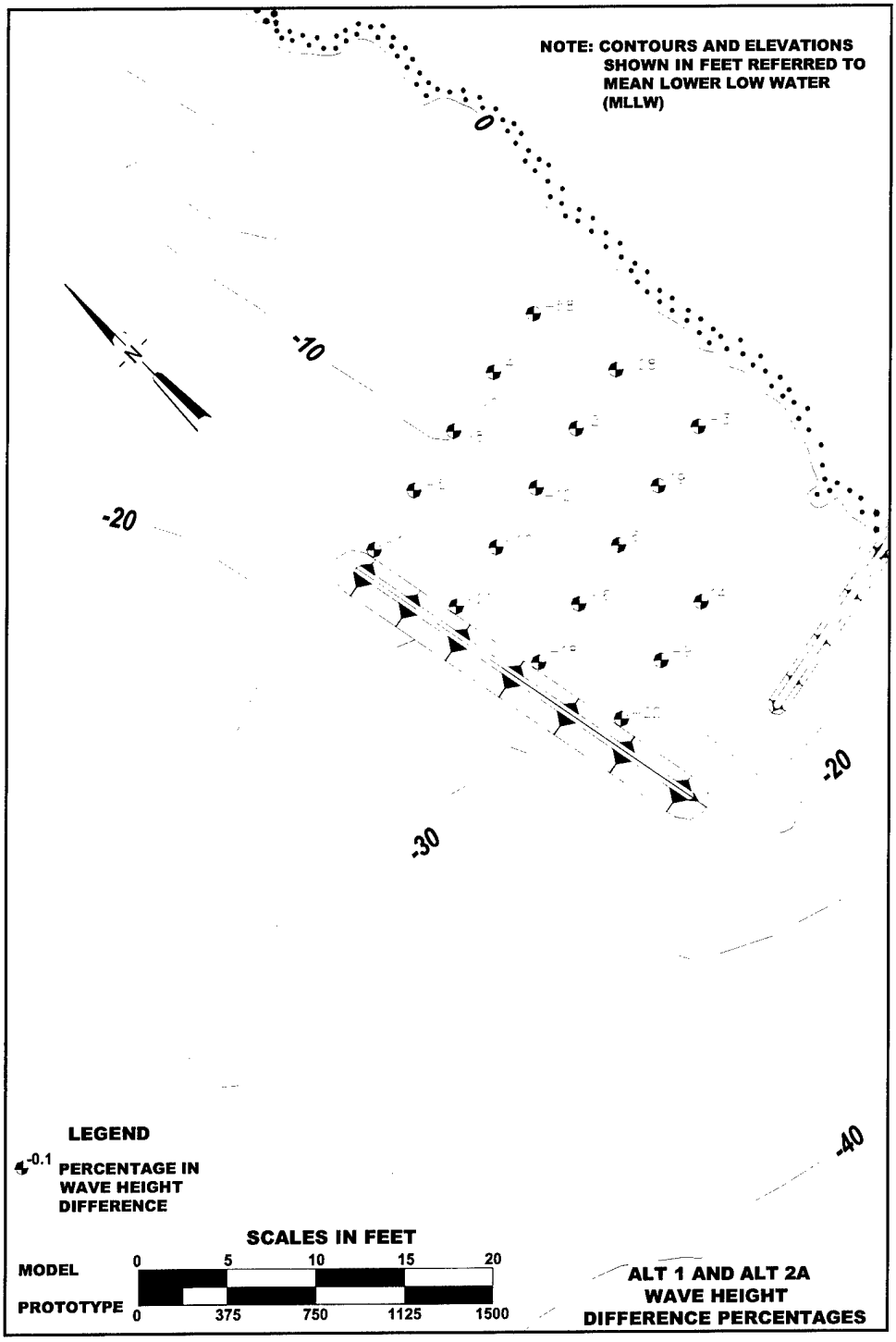

Figure 5-24. Difference in wave heights between Alt 2A and Alt 1 as a percentage of Alt 1 for waves from west-northwest at mllw for wave heights of 2 m, 9 sec; 3 m, 13 sec; and 5 m, 13 sec combined

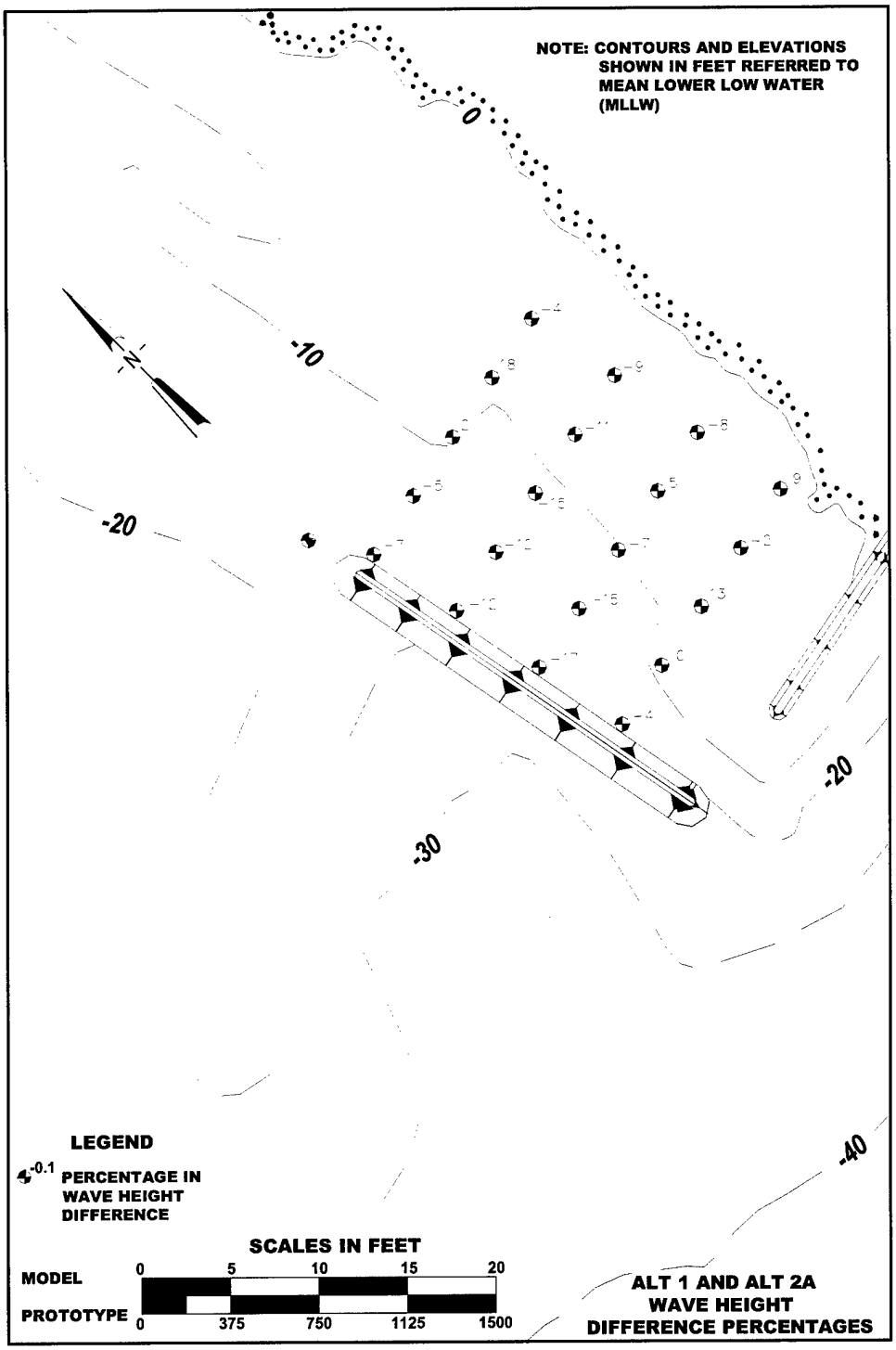

Figure 5-25. Difference in wave heights between Alt 2A and Alt 1 as a percentage of Alt 1 for waves from west-northwest at mtl for wave heights of 2 m, 9 sec; 3 m, 13 sec; and 5 m, 13 sec combined

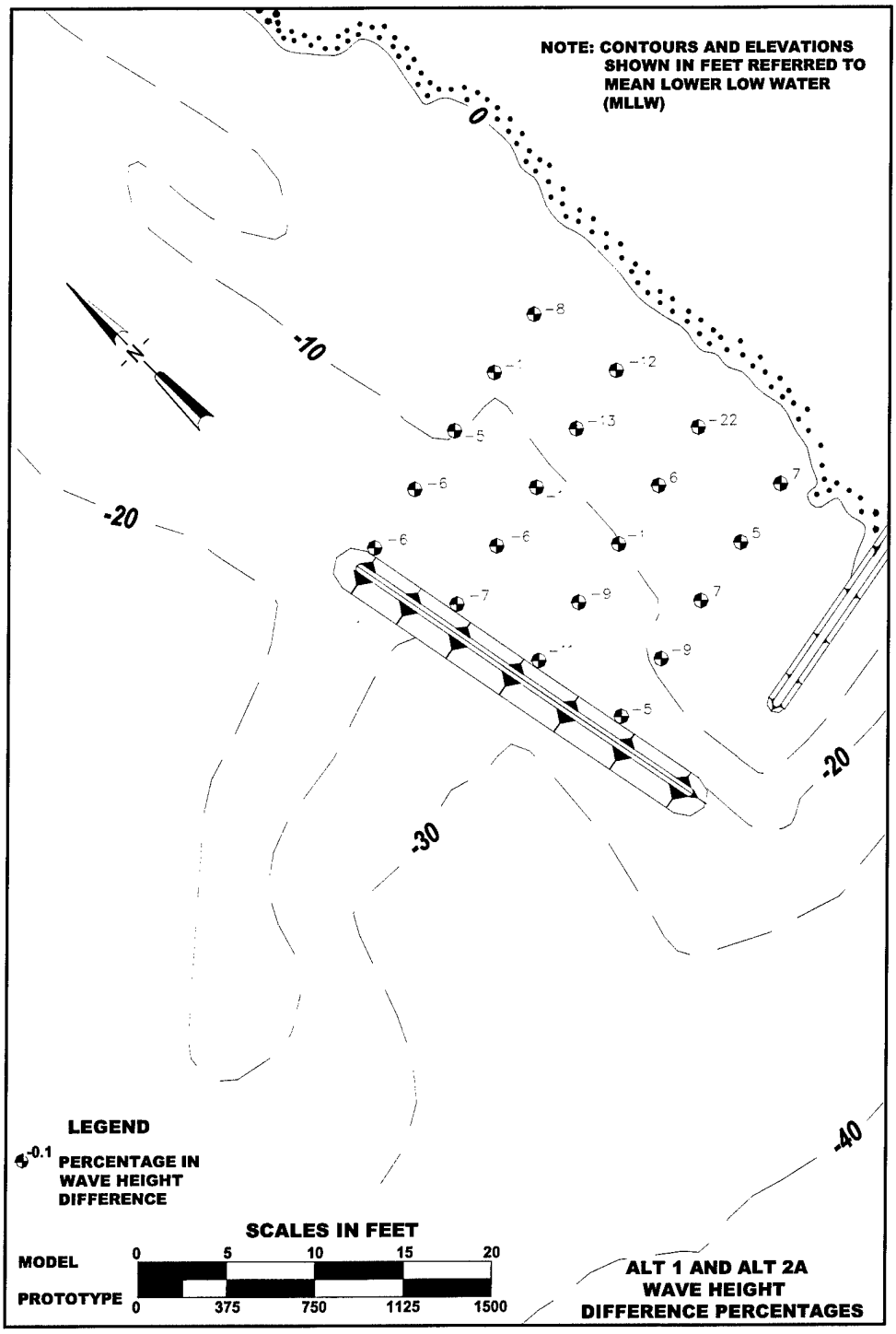

Figure 5-26. Difference in wave heights between Alt 2A and Alt 1 as a percentage of Alt 1 for waves from west-northwest at mhw for wave heights of 2 m, 9 sec; 3 m, 13 sec; and 5 m, 13 sec combined

Current velocities. Current velocities were measured with velocimeters. Influence of the current on sediment transport for the different structural alternatives are best indicated by relative changes in near-bottom velocities. The velocimeters were therefore positioned as close to the bottom as possible without contacting the bottom. Locations of the velocimeters are shown in Figure 5-3 for waves from the west-northwest. Data collected from the velocimeters for Alts 1 and 2A for waves from the west-northwest are included in Appendix B in Tables B10 through B18. Velocities are given in prototype values.

The velocimeters were oriented with the axis of the Alt 2A spur. Data are separated into "southerly" velocities that are parallel to the spur and "offshore" velocities that are perpendicular to the spur. Negative velocities indicate flow either to the north or toward shore. With each data sample, the velocity magnitude was determined, and the average velocity magnitude for the duration of the sampling is included in the tables in Appendix B. Finally, the velocity magnitude was calculated from the average offshore velocity and the average southerly velocity components and included in Appendix B as the magnitude of average velocity.

In general, velocities were reduced after construction of the Alt 2A spur, and the largest reductions were observed with the largest waves. Figure 5-27 shows difference in average velocity magnitude with Alt 2A as a percent of average velocity magnitude with Alt 1 for the sum of measurements with the three storms generated for each of the water levels tested (mllw, mtl, and mhw). Velocity differences were calculated as:

$$AVM_{diff} = \frac{\sum AVM(\text{Alt 2A})_i - \sum AVM(\text{Alt 1})_i}{\sum AVM(\text{Alt 1})_i} 100\% \qquad (5\text{-}2)$$

where AVM_{diff} = percent difference in average velocity magnitude shown in Figure 5-27, AVM (Alt 2A) = average velocity magnitude at the indicated velocity meter for Alt 2A, AVM (Alt 1) = average velocity magnitude at the indicated velocity meter for Alt 1, and the summation over i indicates the sum of calculated average velocity magnitudes with 2-m, 9-sec incident waves plus 3-m, 13-sec incident waves plus 5-m, 13-sec incident waves.

ADV 1 is located off the northern tip of the spur and is not sheltered by the spur from west-northwest waves. Changes in velocities at ADV 1 due to the presence of the spur are minimal. ADVs 2 and 3 are located along the shoreward toe of the spur and bracket the midpoint of the spur length. Greatest reduction in velocity with the spur relative to existing conditions occurred at mllw. At mtl, measured velocities include the flood tidal current.

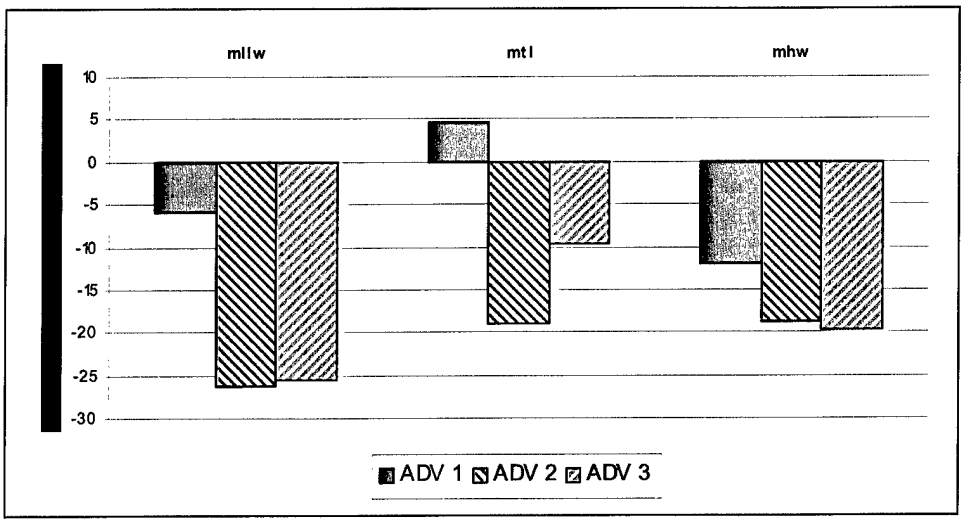

Figure 5-27. Change in average velocity magnitude with Alt 2A relative to Alt 1

Overall agreement is good between the velocities recorded in the physical model and velocities calculated in the numerical model (Chapter 7). Velocities recorded in the physical model are typically smaller than indicated by the numerical model; velocities measured in the physical model were recorded as close to the bottom as possible without distorting the sampling volume, whereas velocities in the numerical model were depth-averaged values. Velocities measured near the bottom (in the boundary layer) are expected to be less than the depth-averaged velocity. Sample measurements taken at mhw with 5-m, 13-sec waves indicated that mid-depth velocities were approximately 15 percent greater than near-bottom velocities. With the Alt 2A spur installed, velocities in the physical model were collected adjacent to the structure toe and recorded differences due to wave-structure interaction that are difficult to replicate in a numerical model. It is also noted that the numerical model results pertain to velocities averaged over a series of runs with different tidal currents; the physical model recorded velocities for one storm, water level, and tidal current at a time. With these differences between the physical model and the numerical model noted, the agreement between the two models is reasonable.

Storms from southwest

General observations. Waves from the southwest generated a longshore current to the north. Figures 5-28 through 5-31 illustrate the general nearshore currents from a run with 3-m, 12-sec waves at mllw. Figure 5-28 illustrates the initial

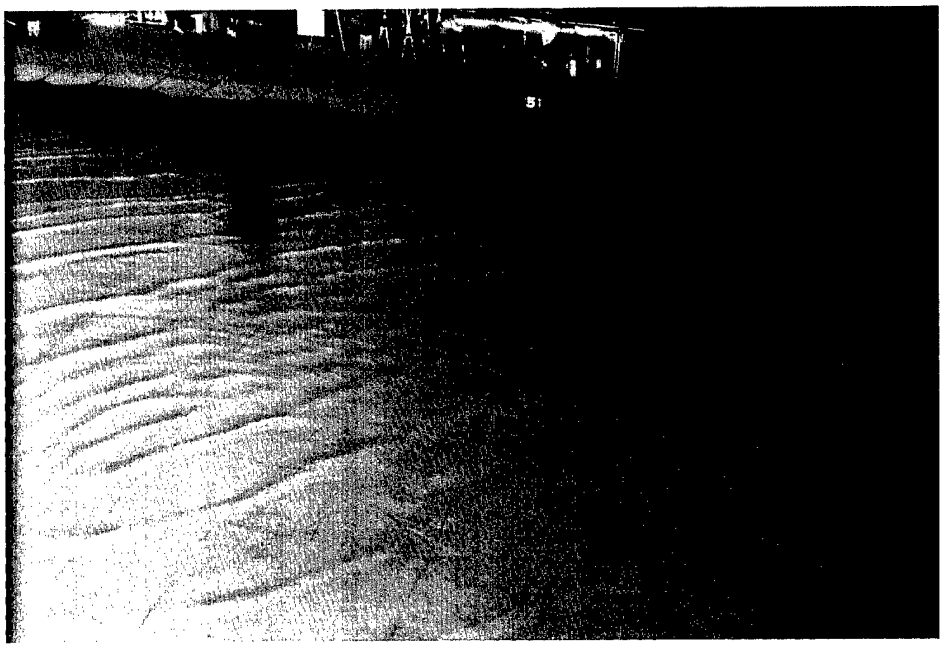

Figure 5-28. Initial placement of dye lines for a run with 3-m, 12-sec waves from southwest at mllw

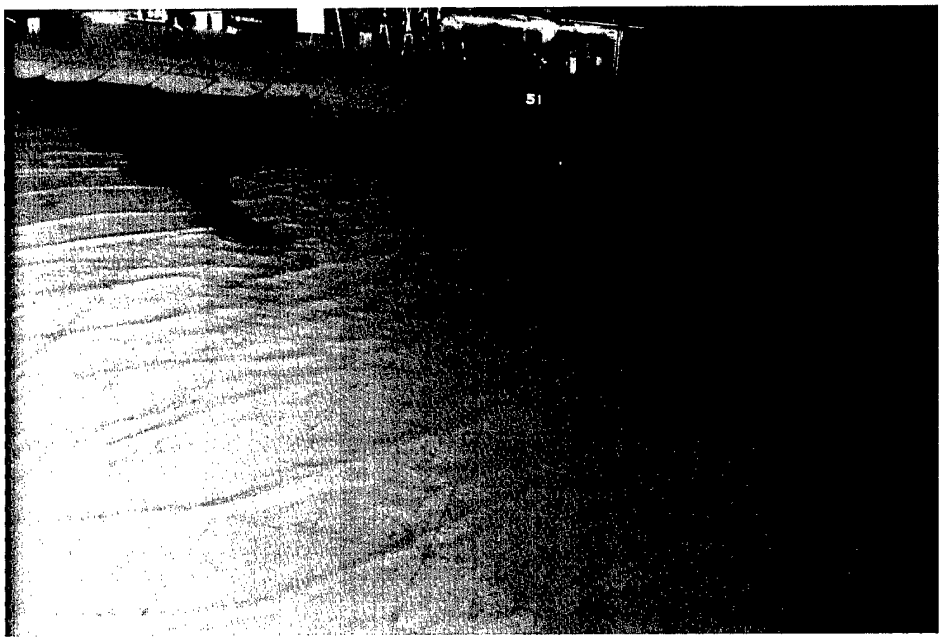

Figure 5-29. Dye pattern with 3-m, 12-sec waves from southwest at mllw taken 2 min, 10 sec (prototype) after Figure 5-28

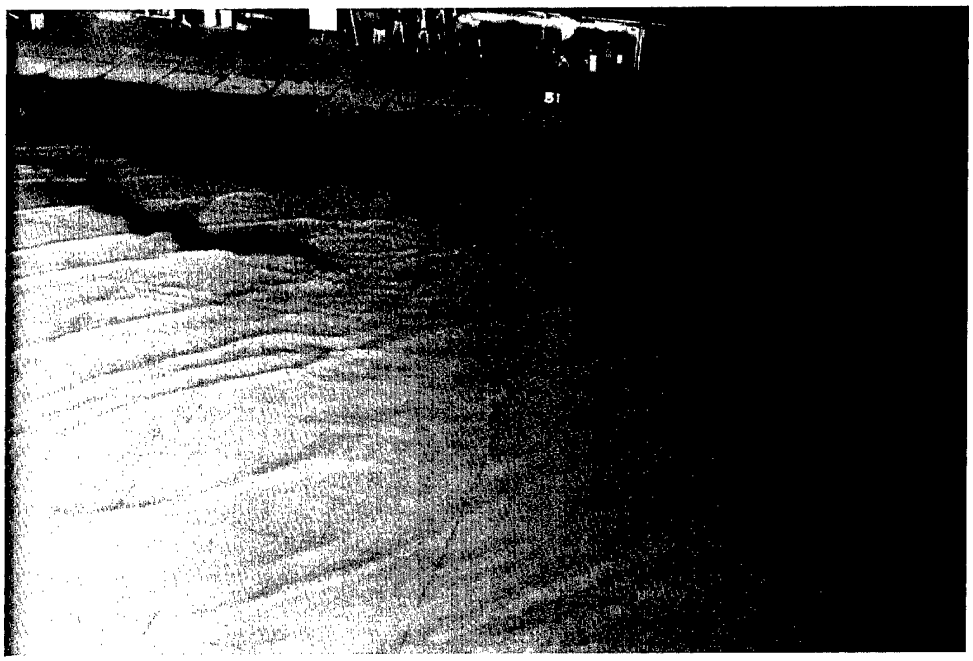

Figure 5-30. Dye pattern with 3-m, 12-sec waves from southwest at mllw taken 8 min, 40 sec (prototype) after Figure 5-28

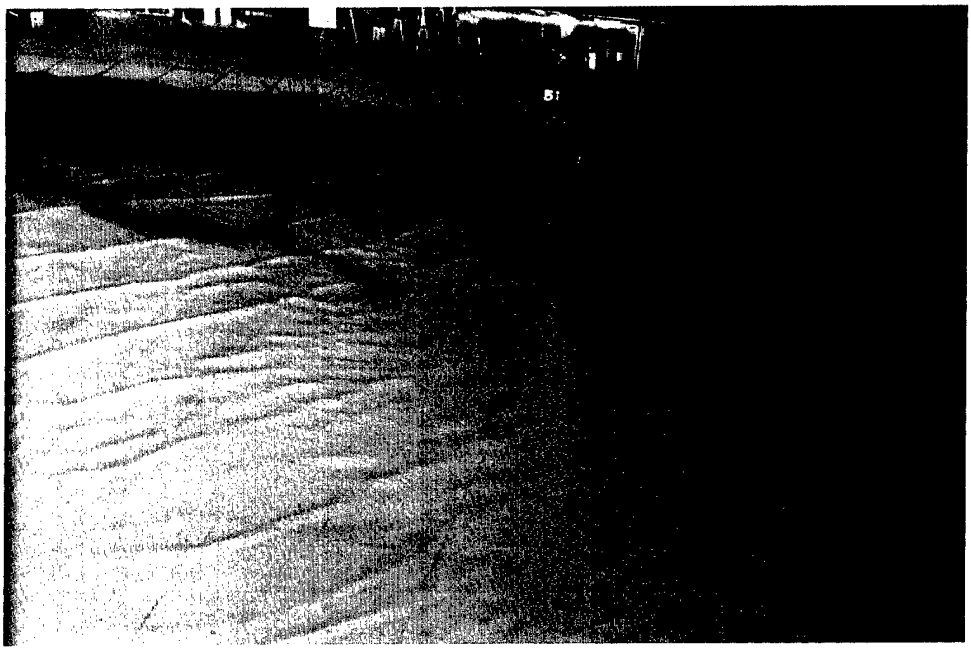

Figure 5-31. Dye pattern with 3-m, 12-sec waves from southwest at mllw taken 13 min (prototype) after Figure 5-28

pattern of dye placement in two shore-normal lines and one shore-parallel line. Dye injected on the shore-normal line along the jetty is carried north and toward the shoreline. The seaward end of the line near the jetty remains stationary, and movement towards the north increases as the dye line approaches shore. Dye in the shore-parallel line remains alongshore and is carried to the north. Displacement of dye to the north near the center of the northern shore-normal line in Figure 5-29 indicates the peak of the longshore current is approximately 100 ft seaward of the mllw contour. The seaward end of the northern shore-normal line remains nearly stationary, but a slow movement to the south in Figures 5-30 and 5-31 indicates the presence of a weak countercurrent offshore. The rip current and the gyre observed with waves from the west-northwest are not seen.

Figures 5-32 and 5-33 were taken with 3-m, 12-sec waves from the southwest at mtl with full flood current. The longshore current nearshore is little altered by the flood-tidal current, but the seaward end of the shore-normal dye line near the jetty is carried south across the submerged remnants of the jetty head.

Dye studies - Alternative 1: Existing conditions. Dye studies with Alt 1 were conducted for 2-m, 9-sec; 3-m, 12-sec; and 6-m, 16-sec waves at water levels of mllw, mtl, and mhw, and included full flood current at mtl. Four photographs of each water level, wave height, and wave period combination are presented in Appendix B to illustrate current patterns. Times listed under each of the four photographs were calculated from the time stamps recorded with the photographs and are in model scale. To convert to prototype scale, the times should be multiplied by 8.66. Model to prototype conversion factors are listed in Table 5-1.

Figure B56 photographs were taken during a run at mllw with 2-m, 9-sec waves. A wave-induced current carries dye north and shoreward from near the subaerial head of the jetty, then northward along the shoreline. Dye adjacent to the submerged portion of the jetty head remains nearly stationary except for the portion near the subaerial head of the jetty. Dye is carried to the south in a weak countercurrent approximately 1,000 ft offshore.

Figure B57 photographs were taken during a run at mllw with 3-m, 12-sec waves. The general pattern is similar to the run with 2-m, 9-sec waves at mllw, except that the longshore current is stronger, and dye is moved shoreward along a longer section of the submerged jetty head, indicating a wider current around the subaerial head of the jetty.

Figure B58 photographs were taken during a run at mllw with 6-m, 16-sec waves. All dye along the submerged jetty head is moved northward and shoreward, indicating the current around the subaerial head of the jetty is wider than with the 2-m, 9-sec or 3-m, 12-sec waves. There is no indication of a southerly countercurrent.

Figure 5-32. Initial placement of dye for a run with 3-m, 12-sec waves from southwest at mtl with full flood current

Figure 5-33. Dye pattern with 3-m, 12-sec waves from southwest at mtl with full flood current taken 8 min 40 sec (prototype) after Figure 5-32

Figure B59 photographs were taken during a run at mtl with 2-m, 9-sec waves and full flood current. The southerly countercurrent observed at mllw with 2-m, 9-sec waves is accelerated by the tidal current, and the longshore current is reduced.

Figure B60 photographs were taken during a run at mtl with 3-m, 12-sec waves and full flood current. Dye near the seaward half of the submerged jetty head is carried by the tidal current to the south across the submerged portion of the jetty. Dye is accumulating in the corner where the beach intercepts the jetty.

Figure B61 photographs were taken during a run at mtl with 6-m, 16-sec waves and full flood current. Dye patterns after 0 min, 58 sec are similar to the patterns observed after 1 min, 14 sec at mtl with 3-m, 12-sec waves, indicating the stronger currents generated by the larger waves. Dye is accumulating in the corner where the beach intersects the jetty.

Figure B62 photographs were taken during a run at mhw with 2-m, 9-sec waves. The countercurrent observed at mllw with 2-m, 9-sec waves is not in evidence. The northern shore-normal line of dye is nearly stationary except for a narrow band along the mllw contour.

Figure B63 photographs were taken during a run at mhw with 3-m, 12-sec waves. Dye from the northern shore-normal line is carried to the north by a longshore current located along the mllw contour and a second current located approximately 1,000 ft offshore. There is little movement of the dye in the northern shore-normal line between these two currents. No dye is carried across the submerged portion of the jetty head, although it is possible that the dye line along the jetty did not extend sufficiently offshore to enter a current flowing south across the submerged portion of the jetty.

Figure B64 photographs were taken during a run at mhw with 6-m, 16-sec waves. A strong longshore current along the mllw contour is carrying the shoreward portion of the northern shore-normal dye line northward, but the seaward end of the dye line is nearly stationary. There is no indication of southerly flow across the submerged portion of the jetty head.

Dye studies - Alternative 2A: 1,500-ft-long jetty-normal submerged spur at sta 165+00. Dye studies for Alt 2A were conducted with the same incident wave height, wave period, and water level combinations that were run with the model of existing conditions (Alt 1). Four photographs of each water level, wave height, and wave period combination are presented in Appendix B to illustrate current patterns.

Figure B65 photographs were taken during a run at mllw with 2-m, 9-sec waves. There is little difference in movement of the dye on the shore-normal dye line closest to the jetty, but dye movement in the more northerly shore-normal dye line is considerably less with Alt 2A.

Figure B66 photographs were taken during a run at mllw with 3-m, 12-sec waves. Dye from the seaward end of the northern shore-normal dye line is carried to the south, while the dye closer to shore is carried to the north. The southerly movement of the seaward end of the line is slower shoreward of Alt 2A than with existing conditions.

Figure B67 photographs were taken during a run at mllw with 6-m, 16-sec waves. There is no southerly movement at the seaward tip of the northern shore-normal dye line. Movement of dye through the southern half of the area shoreward of the spur is similar for Alts 1 and 2A, but movement appears to be slower in the northern half of the area behind Alt 2A than in Alt 1.

Figure B68 photographs were taken during a run at mtl with 2-m, 9-sec waves and full flood current. With Alt 1, the southern shore-normal line of dye moves northward over a wide area from the shoreline out, while the same line with Alt 2A moves northward only in a narrow band near the shore.

Figure B69 photographs were taken during a run at mtl with 3-m, 12-sec waves and full flood current. With Alt 2A, a weak tidal current flows southward shoreward of the spur, while a stronger wave-generated current flows northward along the shoreline. The southerly current is evidenced by the seaward end of the northern shore-normal dye line in Alt 2A and by the seaward end of the southern dye line in Alt 1. The northern shore-normal dye line on Alt 1 is probably too short to extend into the southern flow of the tidal current.

Figure B70 photographs were taken during a run at mtl with 6-m, 16-sec waves and full flood current. With Alt 1, tidal current carries dye south across the submerged portion of the jetty and into the inlet entrance. The southerly transport across the submerged head of the jetty is not observed with Alt 2A, although it is probable that the southerly flow would be observed if the dye extended beyond the spur. It appears that the wave-generated current is sufficiently channeled between the subaerial tip of the jetty and the spur to overcome the weak tidal current adjacent to the submerged head of the jetty. Shoreward of the spur, little movement occurs at the outer end of the northern shore-normal dye line as the wave-generated currents balance the tide-generated currents with Alt 2A. With Alt 1, the wave-generated currents dominated, and the dye was moved in a northerly direction.

Figure B71 photographs were taken during a run at mhw with 2-m, 9-sec waves. A small countercurrent exists shoreward of the northern end of the spur with Alt 2A that is not observed with Alt 1, and there appears to be more accumulation of dye near the junction of the jetty and the shoreline with Alt 2A, but the observed differences in currents between Alt 2A and Alt 1 are minor.

Figure B72 photographs were take during a run at mhw with 3-m, 12-sec waves. No differences are observed, indicating that the presence of the spur does little to modify current patterns under small waves at high water.

Figure B73 photographs were taken during a run at mhw with 6-m, 16-sec waves. Dye movement with Alt 2A from the northern shore-normal dye line indicates a strong current adjacent to the shore and a strong current offshore near the end of the dye line, but the current is weak in the middle of the line. The same pattern is observed with Alt 1 except that the dye line does not extend seaward of the area where the current is very weak. Changes to tidal and wave-generated currents due to the presence of the spur appear to be minimal at high water.

Wave heights. Variations in water surface elevation (wave height) were collected with an array of wave gauges during runs for Alts 1, 2A, and 3B with waves from the southwest. Significant wave heights and periods of peak energy density calculated from the measured changes in water surface elevation are presented in Appendix B (Tables B19 through B27). Locations of the wave gauges in the model are shown in Figure 5-4.

Figures B74 through B82 show differences in wave heights between Alts 1 and 2A at each wave gauge. Differences were obtained by subtracting the significant wave height for Alt 1 from the significant wave height for Alt 2A. Therefore, a negative value indicates a smaller wave height for Alt 2A. Greatest reductions in wave heights with construction of the spur were typically at the three southernmost wave gauges along the shoreward toe of the spur.

Reductions in wave heights caused by the Alt 2A spur at different water levels are illustrated in Figures 5-34 through 5-36 for mllw, mtl, and mhw, respectively. At each gauge location shown, the value was obtained by Equation 5-1 with the exception that the summation over *i* indicates the sum of measured wave heights with 2-m, 9-sec incident waves plus 3-m, 12-sec incident waves plus 6-m, 16-sec incident waves.

Figures B83 through B91 show differences in wave heights between Alt 1 and Alt 3B at each wave gauge. Differences were obtained by subtracting the significant wave height for Alt 1 from the significant wave height for Alt 3B. Therefore, a negative value indicates a smaller wave height with Alt 3B.

With the rehabilitation of the jetty to its full length (Alt 3B), wave heights within about 1,500 ft north of the jetty were typically reduced by 0.1 to 0.3 m. The exception was wave gauges closest to the jetty near jetty station 165+00 (location of Alt 2A spur) (wave gauges 6 through 9), which recorded reductions in wave heights on the order of 1.0 m. Wave heights for Alt 3B were smaller than for Alt 1, but greater than for Alt 2A.

Reductions in wave heights caused by rehabilitation of the jetty (Alt 3B) at different water levels are illustrated in Figures 5-37 through 5-39 for mllw, mtl, and mhw, respectively. At each gauge location shown, the value was obtained by Equation 5-1 with the exception that the summation over *i* indicates the sum of measured wave heights with 2-m, 9-sec incident waves plus 3-m, 12-sec incident waves plus 6-m, 16-sec incident waves.

Current velocities. Current velocities were measured with velocimeters positioned as close to the bottom as possible without contacting the bottom. Locations of the velocimeters were shown in Figure 5-4 for waves from the southwest. Data collected from the velocimeters for Alts 1, A, and 3B for waves from the southwest are included in Appendix B in Tables B28 through B36. Velocities are given in prototype values.

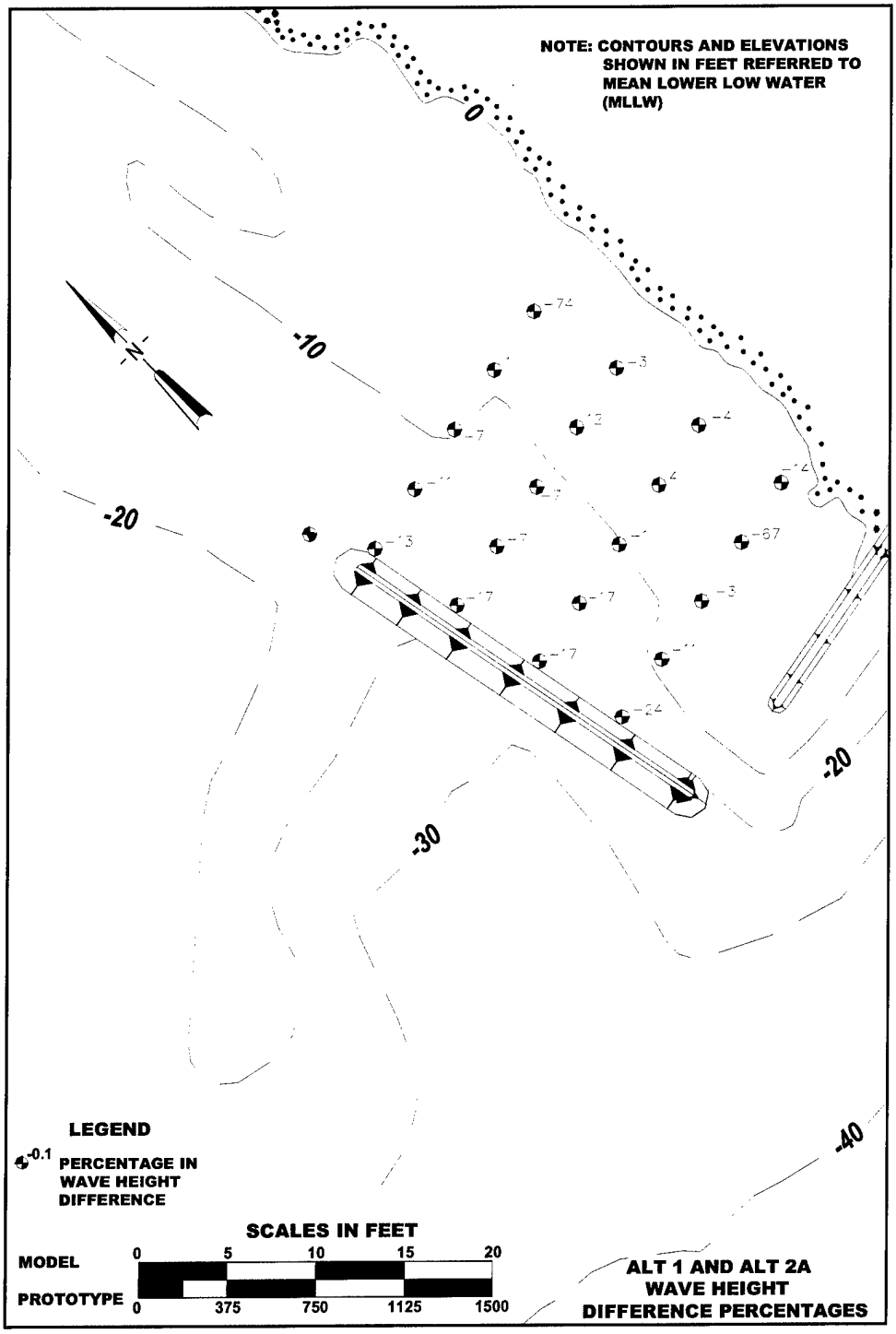

Figure 5-34. Difference in wave heights between Alt 2A and Alt 1 as a percentage of Alt 1 for waves from southwest at mllw for wave heights of 2 m, 9 sec; 3 m, 12 sec; and 6 m, 16 sec combined

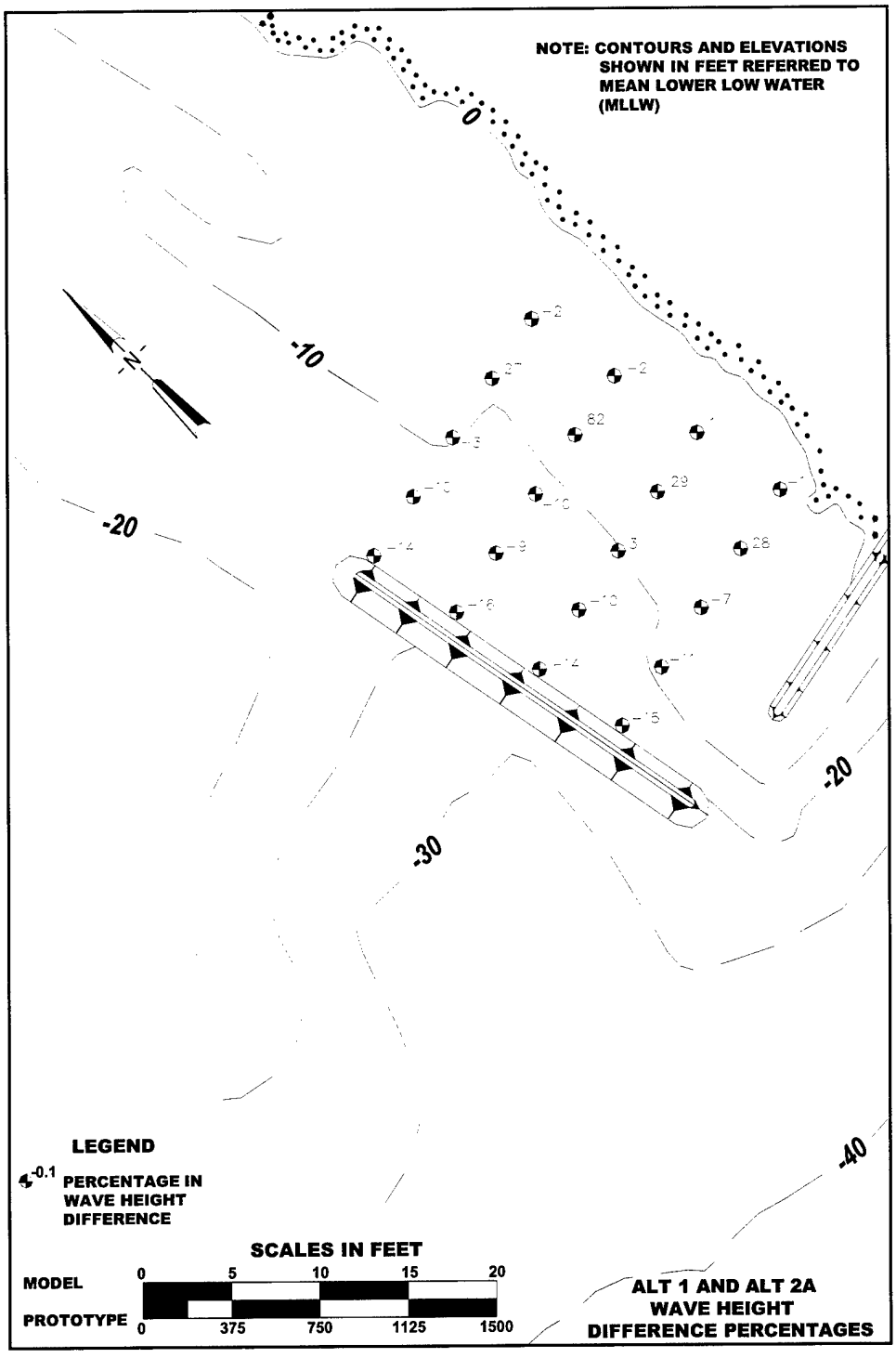

Figure 5-35. Difference in wave heights between Alt 2A and Alt 1 as a percentage of Alt 1 for waves from southwest at mtl for wave heights of 2 m, 9 sec; 3 m, 12 sec; and 6 m, 16 sec combined

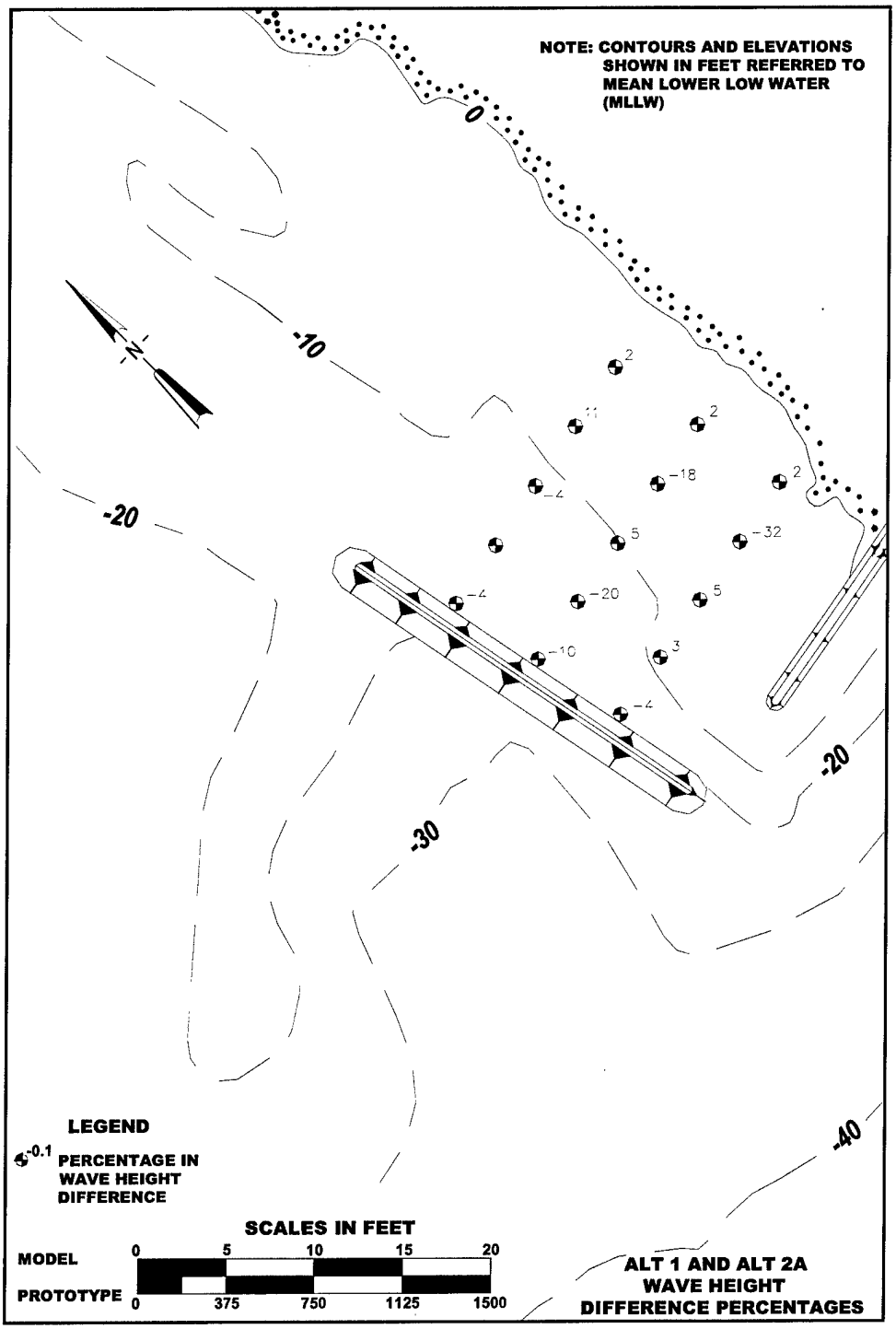

Figure 5-36. Difference in wave heights between Alt 2A and Alt 1 as a percentage of Alt 1 for waves from southwest at mhw for wave heights of 2 m, 9 sec; 3 m, 12 sec; and 6 m, 16 sec combined

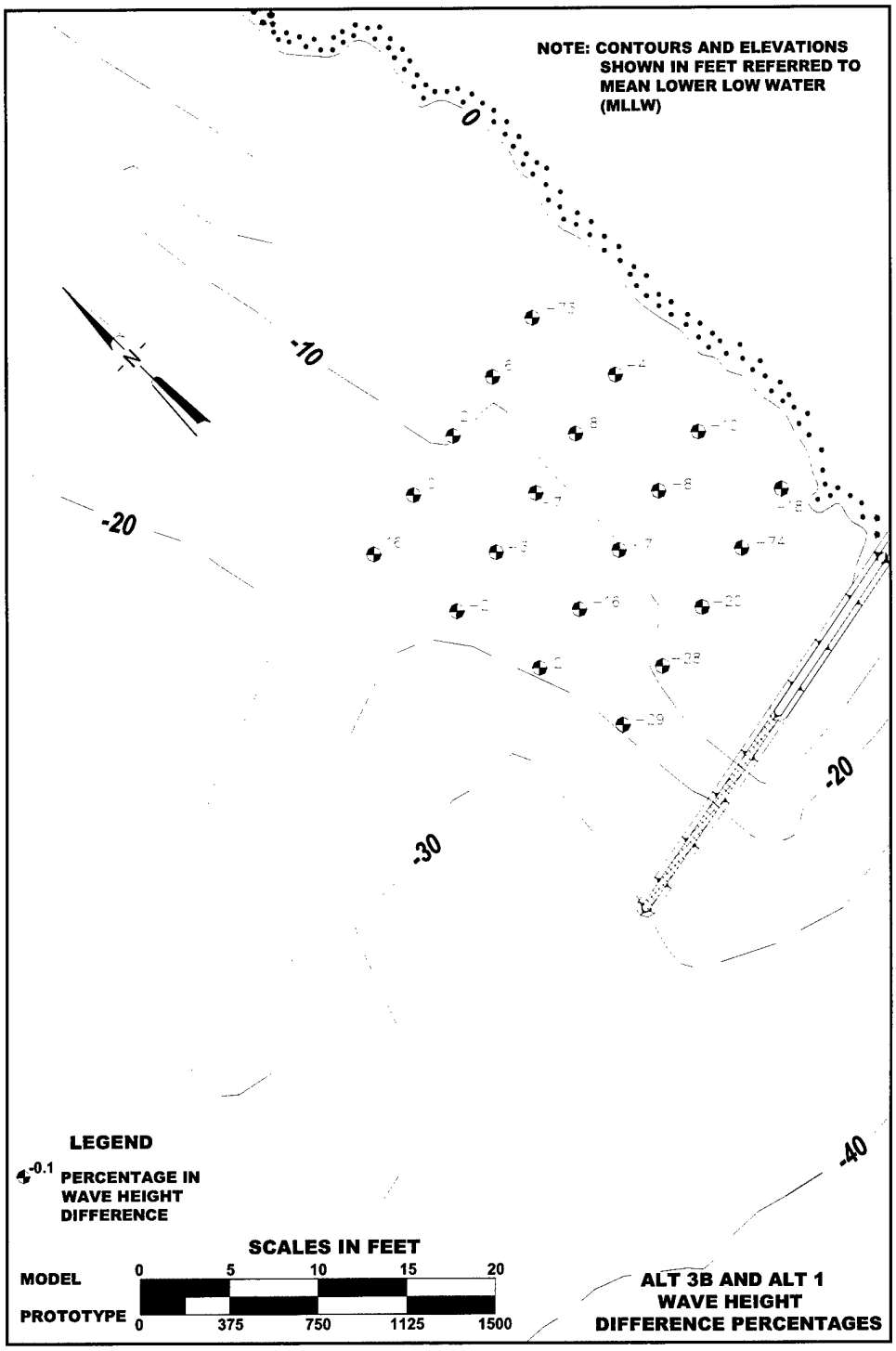

Figure 5-37. Difference in wave heights between Alt 3B and Alt 1 as a percentage of Alt 1 for waves from southwest at mllw for wave heights of 2 m, 9 sec; 3 m, 12 sec; 6 m, 16 sec combined

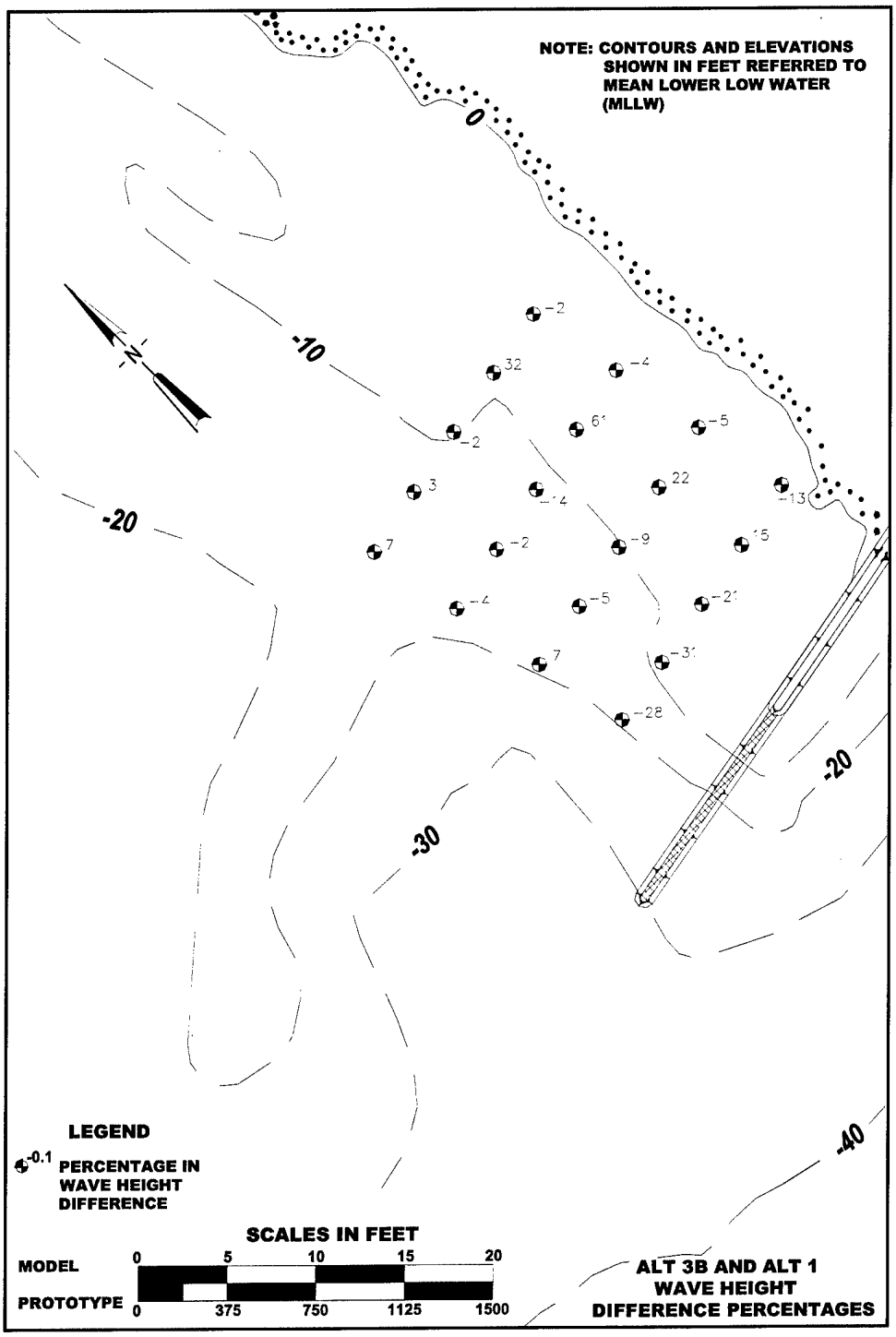

Figure 5-38. Difference in wave heights between Alt 3B and Alt 1 as a percentage of Alt 1 for waves from southwest at mtl for wave heights of 2 m, 9 sec; 3 m, 12 sec; 6 m, 16 sec combined

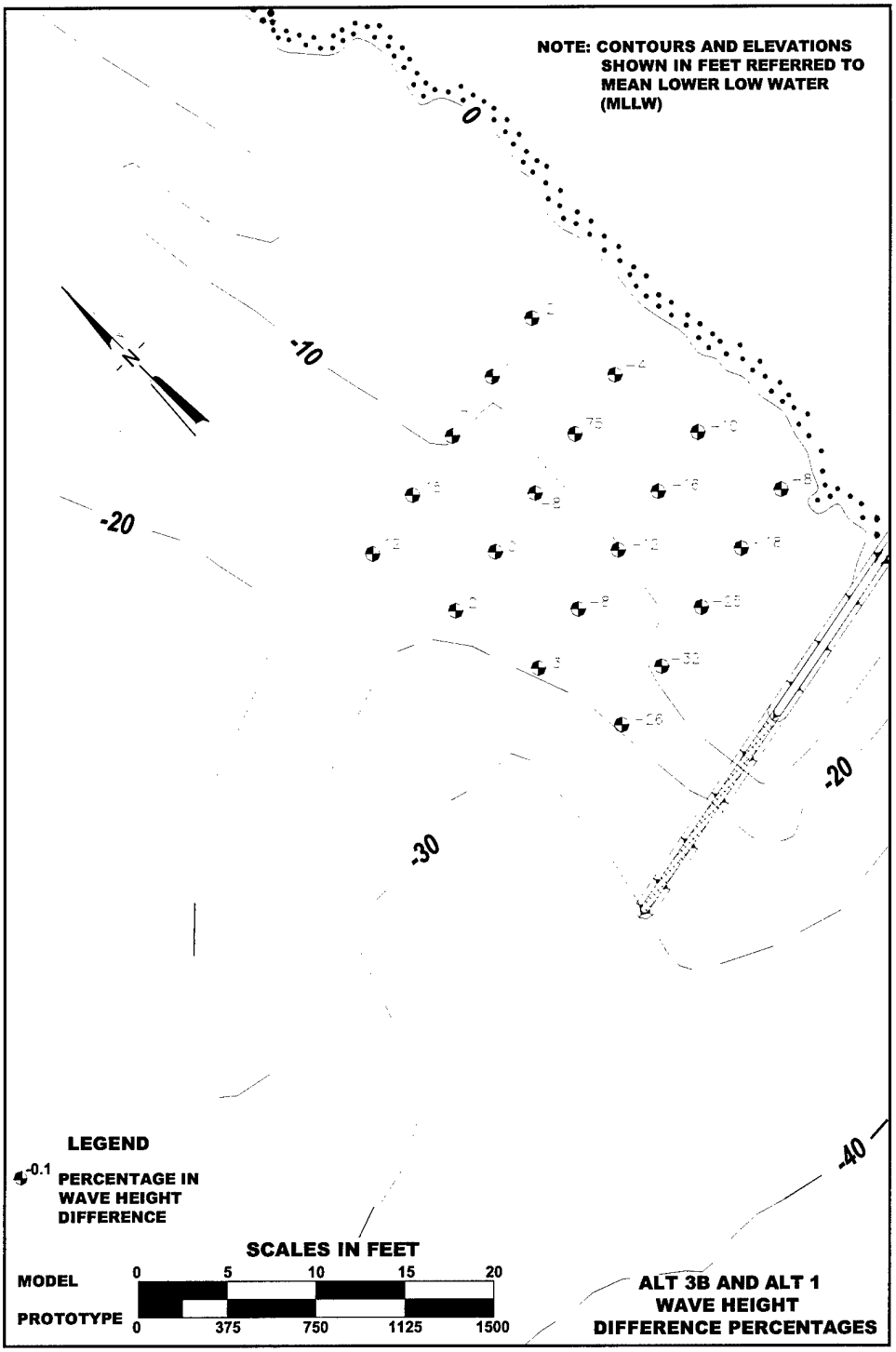

Figure 5-39. Difference in wave heights between Alt 3B and Alt 1 as a percentage of Alt 1 for waves from southwest at mhw for wave heights of 2 m, 9 sec; 3 m, 12 sec; 6 m, 16 sec combined

Changes in current velocities with the addition of Alt 2A and Alt 3B are summarized in Figures 5-40 and 5-41, respectively. Velocity differences were calculated by Equation 5-2 except the summation over *i* includes 2-m, 9-sec waves plus 3-m, 12-sec waves plus 6-m, 16-sec waves.

Alternative 2A with GENESIS 5-year projected shoreline

The shoreline will respond to the presence of the submerged spur, as discussed in Chapter 6. Location of the shoreline 5 years after the spur is built was estimated with the numerical model GENESIS. The GENESIS 5-year projected shoreline was installed in the model by surveying the location of the projected mllw shoreline. Sand was placed in the model to raise the bottom elevation along the projected shoreline from the depth with existing bathymetry to mllw. Shoreward of the predicted shoreline, the beach was built up by maintaining a constant thickness of sand from the shoreline to the dunes in the existing model. The thickness of sand along the predicted shoreline varied with changes in the existing bathymetry. Effort was made to maintain the thickness at the location of each template used in the original construction of the model and to average the differences between the templates. Seaward of the projected shoreline, the sand layer was tapered to meet the existing bathymetry shoreward of the location of the spur. The seaward edge of the sand layer was tapered shoreward to intersect the existing shoreline approximately 2,500 ft north of the jetty. After the sand was placed, concrete mortar was spread over the surface of the sand, wetted, and smoothed with a wooden float to match the surface roughness of the rest of the model.

Storms from west-northwest. The vertical displacement wave generator was returned to the wave basin at the conclusion of all experiments with storms from the southwest. Due to time constraints, the circulation system could not be positioned at the exact location as for previous runs from the west-northwest. Therefore, the runs from the west-northwest were conducted only with slack tide at mllw and mhw. Wave heights and periods included 2-m, 9-sec waves; 3-m, 13-sec waves; and 5-m, 13-sec waves.

Storms from west-northwest dye studies. Figure B92 photographs were taken during a run at mllw with 2-m, 9-sec waves. The rip current is evident in Photograph B. In Photograph C, the longshore current and the rest of the gyre are seen. The gyre is smaller than was observed with the same incident waves and existing shoreline, and movement of the dye is slower.

Figure B93 photographs were taken during a run at mllw with 3-m, 13-sec waves. The northern edge of the gyre is further south than was observed with the existing shoreline, and the gyre is smaller. Some of the dye along the shoreline is carried north to the rip current, but it is not carried seaward in the rip as far as was observed with the existing shoreline.

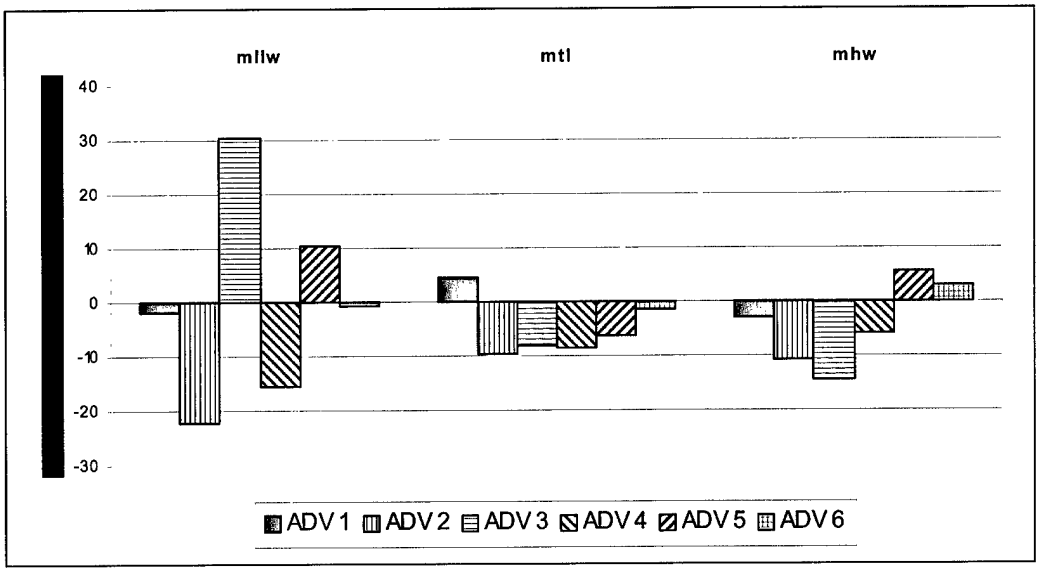

Figure 5-40. Velocity differences with Alt 2A relative to Alt 1 for 2-m, 9-sec waves; 3-m, 12-sec waves; and 6-m, 16-sec waves combined

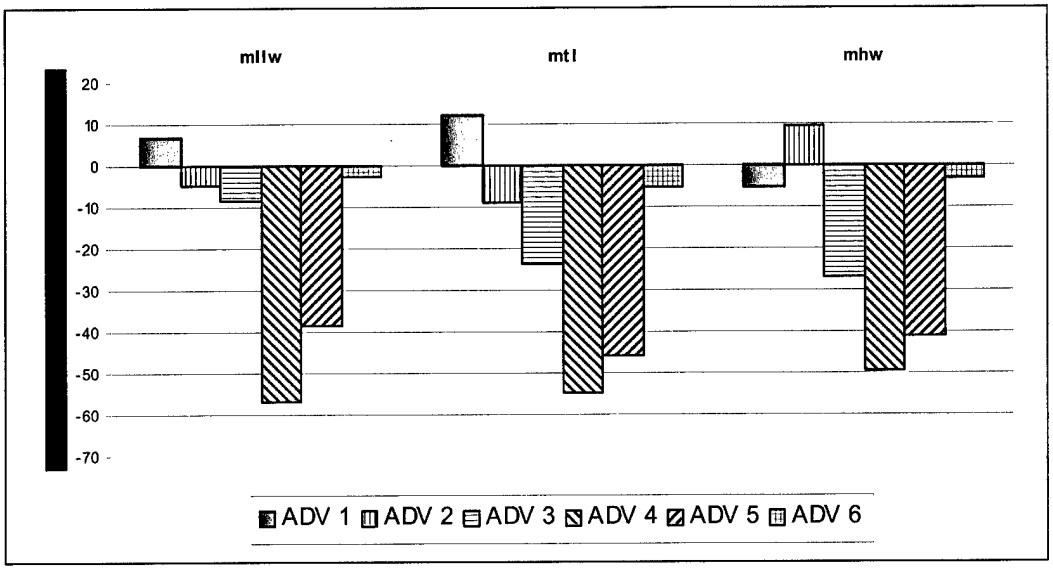

Figure 5-41. Velocity differences with Alt 3B relative to Alt 1 for 2-m, 9-sec waves; 3-m, 12-sec waves; and 6-m, 16-sec waves combined

Figure B94 photographs were taken during a run at mllw with 5-m, 13-sec waves. The dye is carried into a small gyre in the corner where the jetty intersects the shoreline. The rip current observed with the existing shoreline near the northern tip of the spur is not seen.

Figure B95 photographs were taken during a run at mhw with 2-m, 9-sec waves. The gyre is larger than was observed at mllw with 2-m, 9-sec waves, but smaller than was observed with the existing shoreline.

Figure B96 photographs were taken during a run at mhw with 3-m, 13-sec waves. A weak gyre is seen, but it is diffuse and not well-defined.

Figure B97 photographs were taken during a run at mhw with 5-m, 13-sec waves. Little movement is observed for dye injected along the north side of the subaerial portion of the jetty. The gyre is much smaller than was observed with the existing shoreline. All dye movement shoreward of the spur is slower than with the existing shoreline.

Storms from west-northwest wave heights. The wave board on the wave generator was replaced with a larger wave board prior to runs with the 5-year projected shoreline. With the same wave generation signal developed for the smaller wave board, the larger wave board generated larger incident waves. There was no noticeable change in wave heights for the 2-m, 9 sec waves, but the 3-m, 13-sec waves and the 5-m, 13-sec generated wave heights increased between 10 and 20 percent. Wave gauges 1 and 2 were located directly in front of and at the same depth as the wave generator and measured the generated wave heights.

Changes in water surface elevation (wave heights) were measured at the four wave gauges located nearest the spur on the shoreward side (gauges 9, 17, 25, and 33), in addition to gauges 1 and 2. Wave heights and periods calculated from data collected by the wave gauges are given in Tables B37 through B39 for runs at mllw and Tables B40 through B42 for runs at mhw.

Wave heights behind the spur were adjusted by the average difference in wave height at gauges 1 and 2 for runs with the old wave board and runs with the new wave board. At mllw and 5-m, 13-sec waves, wave heights at gauges 1 and 2 with the 5-year projected shoreline (new wave board) were 9 percent larger than with the same wave generation signal and the existing shoreline (previous wave board). Wave heights behind the spur with the 5-year projected shoreline were therefore reduced 9 percent. Differences between wave heights with the existing shoreline and the adjusted wave heights with the 5-year projected shoreline were less than 5 percent at mhw and less than 10 percent at mllw. In Figure 5-42, wave heights at gauges 9, 17, 25, and 33 were averaged and plotted to illustrate the difference between existing conditions and adjusted wave heights with the 5-year projected shoreline. Adjusted wave heights with the 5-year projected shoreline were equal to or less than wave heights with the existing shoreline, with the exception of the 2-m, 9-sec waves at mhw (4 percent larger with 5-year projected shoreline).

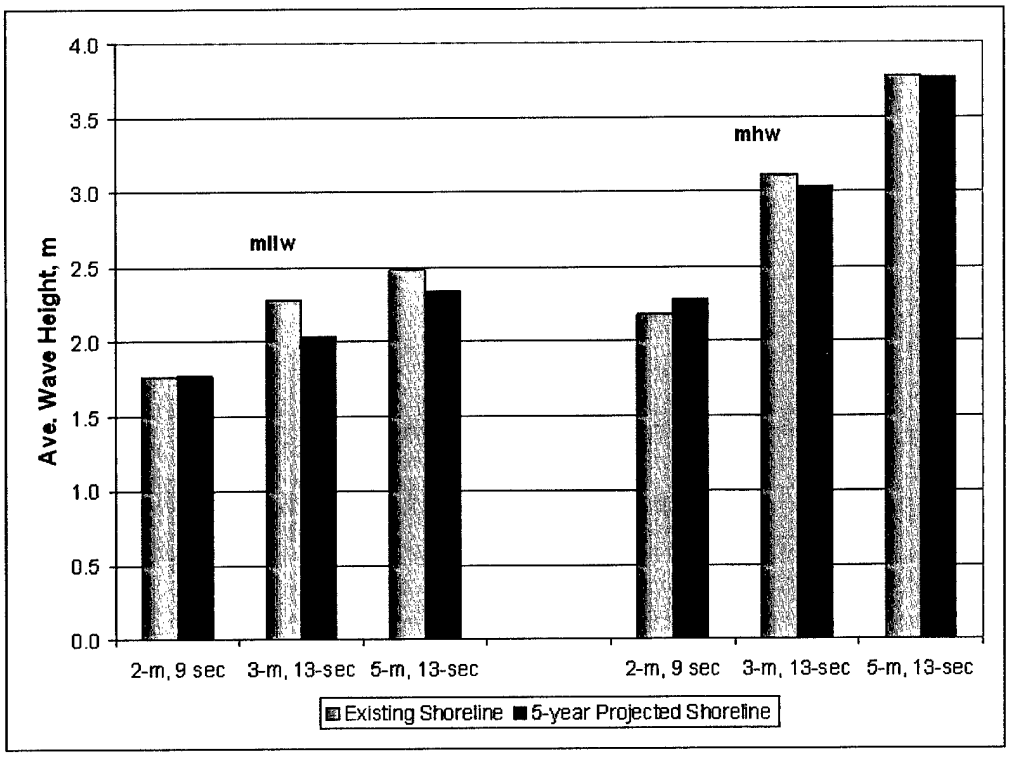

Figure 5-42. Average wave heights shoreward of spur with existing shoreline and 5-year projected shoreline for waves from west-northwest

Storms from west-northwest current velocities. Current velocities were measured with ADVs 2 and 3 near the midpoint of the spur on the shoreward side, and ADV 4 shoreward of the spur and alongside the jetty. Locations of the ADVs are shown in Figure 5-3. Velocity measurements are given in Tables B43 through B45 for runs at mllw and Tables B46 through B48 for runs at mhw.

Storms from southwest. The GENESIS 5-year projected shoreline was installed in the model at the conclusion of experiments with waves from the southwest on the existing shoreline. Incident waves were generated with the same wave generator for tests with the existing shoreline and the 5-year projected shoreline; therefore, there was no need to adjust wave heights as was required with storms from the west-northwest. Studies with Alt 2A and the 5-year projected shoreline were conducted with the same wave height, wave period, and water level combinations that were run with the model of existing conditions (Alt 1) and the model of Alt 2A with the existing shoreline.

Storms from southwest dye studies. Figure B98 photographs were taken during a run at mllw with 2-m, 9-sec waves. A small amount of dye is crossing around the tip of the subaerial portion of the jetty and entering the harbor. Dye movement is much slower than was observed with Alt 2A and the existing shoreline. Dye is carried along the shoreline from the jetty to the north until it reaches the area of the rip current observed with existing conditions (approximately 1,500 ft north of the jetty). Dye in the rip current is carried seaward almost to the end of the spur, then is carried north and back towards the shore. Dye along the jetty is carried shoreward and slowly to the north.

Figure B99 photographs were taken during a run at mllw with 3-m, 12-sec waves. Dye is being carried south across the submerged portion of the jetty head and into the inlet. The longshore current north of the jetty is carrying the dye to the north, and there is no indication of the rip current.

Figure B100 photographs were taken during a run at mllw with 6-m, 16-sec waves. There is no dye movement across the submerged head of the jetty, and no indication of a rip current. Dye is carried shoreward and very slowly to the north along the spur, and to the north much more rapidly near shore. With Alt 2A and the existing shoreline, most of the dye from the shore-normal dye line along the jetty has been carried to shore within 0 min 30 sec. With Alt 2A and the 5-year projected shoreline, much of the dye remains as far seaward as the spur after 0 min 45 sec.

Figure B101 photographs were taken during a run at mtl with 2-m, 9-sec waves and full flood current. Part of the dye from the shore-normal line along the jetty is carried shoreward to the north; the rest of the dye in the outer portion of the line is carried south across the submerged portion of the jetty head. The longshore current carries the dye north along the shoreline, and there is a southerly tidal current seaward of the spur. Dye patterns at 2-m, 9-sec waves at mtl with the existing shoreline indicated the presence of a rip current located approximately 1,500 ft north of the jetty; the rip current is not evident with the projected shoreline.

Figure B102 photographs were taken during a run at mtl with 3-m, 12-sec waves and full flood current. The longshore current is evidenced both with the existing shoreline and the 5-year projected shoreline, but the current is stronger shoreward of the spur with the existing shoreline. Not evident in the few photographs included in B102 is a southerly flow offshore of the spur due to the tidal current. The southerly flow is near the seaward toe of the spur with the existing shoreline, but between 500 and 1,000 ft further offshore with the 5-year projected shoreline.

Figure B103 photographs were taken during a run at mtl with 6-m, 16-sec waves and full flood current. The dye is being carried to the north more quickly shoreward of the spur with the existing shoreline than with the 5-year projected shoreline; otherwise, no significant differences between the two shorelines are noted.

Figure B104 photographs were taken during a run at mhw with 2-m, 9-sec waves. A weak southerly flow across the submerged head of the jetty exists with the 5-year projected shoreline that is not evident with the existing shoreline, and dye appears to be accumulating near the intersection of the shoreline and the north jetty with the 5-year projected shoreline.

Figure B105 photographs were taken during a run at mhw with 3-m, 12-sec waves. The dye line across the spur with the 5-year projected shoreline is nearly stationary, while the dye is moved quickly shoreward and northward with the existing shoreline. For both the existing and projected shorelines, the dye indicates a quiescent area near the intersection of the shoreline and the jetty. The longshore current is clearly stronger with the existing shoreline.

Figure B106 photographs were taken during a run at mhw with 6-m, 16 sec waves. Dye near the intersection of the shoreline and the jetty is carried north along the shoreline with the 5-year projected shoreline, but appears to remain in a quiescent area with the existing shoreline. There is a slight northward current along the shoreward toe of the spur with the 5-year projected shoreline that is not seen with the existing shoreline.

Storms from southwest wave heights. Changes in water surface elevation (wave heights) were collected during experiments with the GENESIS 5-year projected shoreline at two wave gauges (wave gauges 1 and 2) located directly in front of the wave generator to ensure consistency in the wave generation, and at four gauges located shoreward of the spur (wave gauges 9, 17, 25, and 33). Data files from the 3-m, 12-sec wave runs at mllw and 6-m, 16-sec wave runs at mllw were corrupt, and the wave height data could not be retrieved. Wave heights measured during experiments with the projected shoreline are presented in Tables B49 through B55.

Figures B107 through B113 show differences in wave heights at four wave gauge locations shoreward of the spur measured for Alt 2A with the existing shoreline compared to Alt 2A with the 5-year projected shoreline. Wave height differences indicated in Figures B107 through B113 are in meters at prototype scale. A negative value indicates that the wave height was smaller for the projected shoreline than for the existing shoreline. Data files from the 3-m, 12-sec waves at mllw and 6-m, 16-sec waves at mllw were corrupt, and the wave height data could not be retrieved. Wave height differences for all other wave height, wave period, and water level combinations tested are included in Figures B107 through B113. In nearly all runs, wave heights either showed no change or were smaller with the projected shoreline.

For 2-m, 9-sec waves at mllw, measured wave heights shoreward of the spur with the 5-year projected shoreline range from 1.12 m to 1.69 m (Table B49), or approximately a 20 percent reduction in wave height due to the change in shoreline. Average reduction in wave height in comparison to the existing shoreline is more than 0.4 m (Figure B107).

At mtl, with flood current, a large reduction in wave height was recorded at the third wave gauge north of the jetty (wave gauge 25), with smaller reductions in wave heights at the other three gauges. For example, for 2-m, 9-sec waves the reduction at gauge 25 is 0.8 m, while the other three gauges average 0.2 m (Figure B108). For 3-m, 12-sec waves, the reduction at gauge 25 is 1.0 m, while the other three gauges average 0.3 m (Figure B109). For 6-m, 16-sec waves, the reduction is 1.2 m, while the other three gauges average just 0.2 m (Figure B110).

At mhw, little change in wave height was measured for the projected shoreline configuration for the 2-m, 9-sec waves. Gauge 25 recorded a 0.2-m increase in wave height; gauge 9 measured a 0.2-m decrease in wave height; and

there was no change recorded at gauge 17 (Figure B111). With 3-m, 12-sec waves and 6-m, 16-sec waves (Figures B112 and B113, respectively), gauge 25 again recorded reductions in wave height of a meter or more, with only minor changes recorded at the other three gauges.

In Figure 5-43, wave heights at the four gauges located directly shoreward of the spur (gauges 9, 17, 25, and 33) were averaged to illustrate differences in wave height with existing shoreline and with the 5-year projected shoreline.

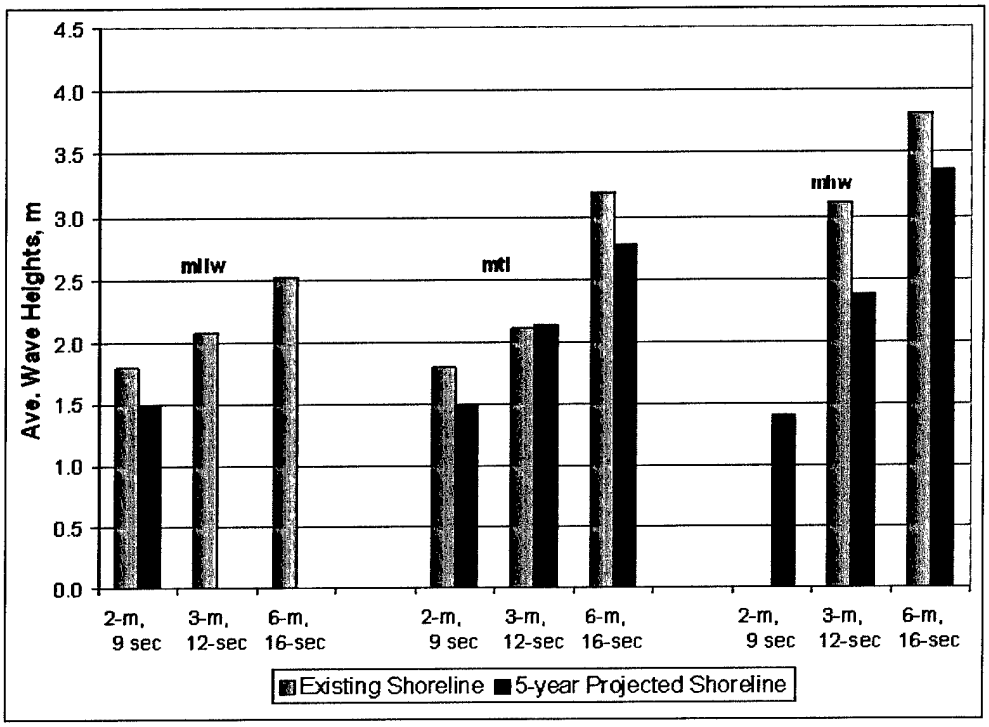

Figure 5-43. Average wave heights shoreward of spur with existing shoreline and 5-year projected shoreline for waves from southwest

Storms from southwest current velocities. Current velocities were measured with ADVs 2 and 3 near the midpoint of the spur on the shoreward side, and with ADV 4 located shoreward of the spur and alongside the jetty. Figure 5-4 shows locations of the ADVs. Velocity measurements are given in Tables B56 through B58 for runs at mllw, Tables B59 through B61 for runs at mtl, and Tables B62 through B64 for runs at mhw.

Summary

Results of the physical model study indicate that Alt 2A (long spur 1,500 ft) and Alt 3B (short jetty) will be effective in reducing wave heights and current velocities north of the north jetty at Grays Harbor. The reduction in wave heights

and currents will promote sediment accumulation in the nearshore north of the jetty. Although accumulation of sediment is indicated for both Alt 2A and Alt 3B, dye patterns indicate that Alt 3B will accumulate sediment in a larger area than Alt 2A, and a larger total accumulation is expected for Alt 3B.

Waves from the west-northwest produce a longshore current flowing to the south. Local bathymetric changes near the jetty change the angle of the incident waves such that waves along the jetty approach nearly shore-normal and generate a longshore current flowing to the north. Where the northward flowing current meets the southward flowing longshore current, a rip current is produced. The rip current is approximately 1,500 ft north of the jetty at slack tide. During flood tide, the southward flowing longshore current is augmented by the flood tidal current, and the rip current is pushed further south towards the jetty. Currents flowing shoreward along the jetty, north along the shoreline, seaward in the rip current, then southward back towards the jetty create a gyre bounded by the jetty and adjacent shore.

A southerly longshore current north of the rip current, the rip current, and the gyre were observed in the dye studies and the coal tracer studies at each wave height, wave period, and water level combination and with each alternative structural configuration tested. The rip current has also been observed at the prototype site.

After construction of Alt 2A, wave heights were reduced relative to existing conditions (Alt 1) over most of the area shoreward of the spur. Wave heights increased slightly in the corner where the jetty intersects the shoreline, implying some amount of water ponding caused by the Alt 2A spur. Current velocities along the spur were reduced relative to existing conditions. Reductions in wave heights and reductions in velocities along the spur (with the addition of the spur) are consistent with results from the numerical model study reported in Chapter 7.

With storms from the west-northwest, time stamps in the coal tracer study indicate patterns of sediment movement are similar with existing conditions and with Alt 2A spur, but movement of the tracer material is slower shoreward of the Alt 2A spur. Reduction in movement of the tracer was most noticeable in the gyre shoreward of the spur near the corner where the jetty intersects the shoreline. The presence of the spur did little to modify movement of coal injected in the line located north of the northern tip of the spur.

The combination of lower wave heights, reduced current velocities, and slower movement of bedload tracer material with Alt 2A relative to Alt 1 indicates that sediment will be deposited behind the spur and cause the shoreline to accrete.

After construction of Alt 3B, the gyre appeared larger and more diffuse in the dye study than with Alt 1 or Alt 2A. The rip current remained in approximately the same location, but the seaward edge of the gyre was displaced further offshore. The dye patterns indicated that deposition of sediment would occur north of the jetty, causing the shoreline to accrete, and that the depositional area would be larger than with Alt 2A.

Storms from the southwest produce a longshore current flowing to the north. The rip current and gyre observed with storms from the west-northwest were not seen. Currents crossing the submerged remnants of the jetty head moved

shoreward and northward, creating a small area in the corner where the jetty intersects the shoreline that was either quiescent or contained a small clockwise counter-current.

After construction of Alt 2A, wave heights north of the jetty were reduced, with the greatest reductions along the spur. Current velocities generally decreased along the jetty and the spur, although an increase in velocity was observed at mllw at one velocimeter located near the base of the spur. The increase in velocity was localized and confirmed in the numerical model reported in Chapter 7.

Wave heights north of the jetty after construction of Alt 3B were less than for Alt 1, but greater than for Alt 2A for similar incident waves. Reductions in wave heights were greatest in the shadow zone north of the jetty. Current velocities were generally lower than with Alt 2A or Alt 1.

The numerical model GENESIS provided an estimate of shoreline advance behind the Alt 2A spur (Chapter 6). For storms from the west-northwest and the southwest, studies conducted with Alt 2A and the GENESIS 5-year projected shoreline indicate wave heights and currents will be further reduced shoreward of the spur as the beach accretes.

There was no evidence of increased current velocities between the shoreline and the spur with the 5-year projected shoreline due to channeling or the reduction in cross-sectional area between the shoreline and the spur.

References

Bottin, R. R., Jr., and Chatham, C. E., Jr. (1975). "Design for wave protection, flood control, and prevention of shoaling, Cattaraugus Creek Harbor, New York, hydraulic model investigation," Technical Report H-75-18, Hydraulics Laboratory, U.S. Army Engineer Waterways Experiment Station, Vicksburg, MS.

Browder, A. E. (1994). "Performance of narrow-crested submerged breakwaters," M.S. thesis, Department of Civil and Coastal Engineering, University of Florida, Gainesville, FL, 106 p.

Giles, M. L., and Chatham, C. E., Jr. (1974). "Remedial plans for prevention of harbor shoaling, Port Orford, Oregon, hydraulic model investigation," Technical Report H-74-4, Hydraulics Laboratory, U.S. Army Engineer Waterways Experiment Station, Vicksburg, MS.

Hughes, S. A. (1993). *Physical models and laboratory techniques in coastal engineering*, Advanced Series on Ocean Engineering, Vol 7, World Scientific Publishing, River Edge, NJ.

Kraus, N. C., Lohrmann, A., and Cabrera, R. (1994). "New acoustic meter for measuring 3-D laboratory flows," *Journal of Hydraulic Engineering* 120(3), 406-412.

Longuet-Higgins, M. S. (1967). "On the wave-induced difference in mean sea level between the two sides of a submerged breakwater," *Journal of Marine Research* 2(2), 148-153.

6 Longshore Sand Transport and Shoreline Change Modeling[1]

This chapter describes the evolution of the shoreline and the longshore sediment transport on the beaches north of Grays Harbor, WA, during the past 25 years. An enhanced version of the shoreline change model GENESIS (Hanson and Kraus 1989) was calibrated and verified based upon data from the site from the 1970s to the 1990s. The calibrated model was applied to estimate the existing longshore transport rates and to evaluate the longshore transport and shoreline change obtained in response to the various structural alternatives, including jetty rehabilitation and construction of a submerged jetty spur.

Model Overview

The GENESIS model has been applied to numerous engineering projects and has demonstrated favorable capability to predict long-term shoreline change. GENESIS was designed to simulate long-term shoreline change produced by temporal and spatial differences in the longshore sand transport at coastal engineering projects. The beach profile is assumed to remain in a state of quasi-equilibrium over the long term. The advance or recession of the beach is realized as a seaward or landward translation of the entire profile so that only one point of the profile, taken as the shoreline, is required to model the evolution of a sandy coast. Cross-shore processes are assumed to average out over a sufficiently long simulation interval, and shoreline change produced by cross-shore sand transport is represented as sediment sources or sinks. Beach nourishment is represented in GENESIS as an advance of shoreline position.

Cross-shore processes are more significant at Grays Harbor than at most beaches adjacent to inlets. Littoral feeding from the deflation and onshore movement of the ebb shoal and rip currents that transport sediment past the tip of the jetty are cross-shore processes that influence shoreline evolution at the project site. Pope (1991) discusses ebb shoal evolution at various sites where jetties have been constructed or extended. GENESIS does not simulate these

[1] Written by Ty V. Wamsley, Coastal and Hydraulics Laboratory, U.S. Army Engineer Research and Development Center, Vicksburg, MS.

processes directly, and they must be summarized and represented in the model as a sand source or sink. Therefore, calculated shoreline position must be interpreted with caution, and results are mainly intended to compare shoreline responses due to changes in longshore transport rates among the studied alternatives. A focus of the model output analysis is to compare the alternative's ability to alter the southward transport of sand and modify shoreline change.

In GENESIS, the transport rate is represented as a function of breaking wave height and direction. An internal wave transformation model computes the breaking wave field along the modeled shoreline, including wave diffraction in the lee of coastal structures such as the north jetty and the proposed spur. The resulting breaking wave quantities are used to compute the transport volumes that drive the changes in the shoreline plan form. The governing equation for the longshore sand transport rate Q is (Kraus and Harikai 1983):

$$Q = (H^2 C_g)_b \left(a_1 \sin 2\alpha - a_2 \cos\alpha \frac{\partial H}{\partial x} \right)_b \tag{6-1}$$

where

H = wave height

C_g = wave group speed

α = angle of waves to the shoreline

b = denotes the wave breaker position

a_1, a_2 = nondimensional parameters

x = position on x-axis, which is oriented parallel to the trend of the coast

The first term is the classical Coastal Engineering Research Center (CERC) equation for calculating longshore sand transport. The second term accounts for the longshore current and sand transport associated with a gradient in wave height (Ozasa and Brampton 1980; Kraus and Harikai 1983). The model requires two empirical coefficients, K_1 and K_2, which serve as calibration coefficients and are contained in a_1 and a_2 as:

$$a_1 = \frac{K_1}{16(\rho_s / \rho - 1)(1-p)(1.416)^{5/2}}$$
$$a_2 = \frac{K_2}{8(\rho_s / \rho - 1)(1-p)\tan\beta(1.416)^{7/2}} \tag{6-2}$$

where

ρ_s = density of sand (taken to be 2,650 kg/cu m for quartz sand)

ρ = density of water (taken to be 1,030 kg/cu m for seawater)

p = porosity of sand on the bed (taken to be 0.4)

$\tan\beta$ = average bottom slope from the shoreline to the depth of active longshore sand transport

The factors involving 1.416 convert from significant wave height to root-mean-square (rms) wave height. The coefficients K_1 and K_2 are determined during a calibration procedure by reproducing measured changes in shoreline position over a given time interval.

The original version of GENESIS did not represent longshore transport produced by tidal flows and local wind. The north jetty project site at Grays Harbor is adjacent to an inlet where tidal currents could contribute to the longshore sand transport. Therefore, an enhanced GENESIS model, called GENESIS-T was applied (Wamsley and Hanson 2002). GENESIS-T (Hanson and Kraus 2000) is being developed under funding provided by the U.S. Army Corps of Engineers' Coastal Inlets Research Program. It calculates the longshore sand transport rate by means of an extended version of the Bagnold (1963) formula. Equation 6-1 can be modified (Hanson and Kraus 2000) to explicitly represent a longshore current as:

$$Q = a_3 (H^2 C_g)_b \cos\alpha_b \frac{v_l}{u_m} \tag{6-3}$$

where

a_3 = nondimensional coefficient

v_l = average longshore current in the surf zone from all sources

u_m = maximum wave-induced near-bottom horizontal velocity

It is therefore possible to estimate the longshore transport and shoreline change originating from multiple sources of a longshore current. GENESIS-T converts the computed breaking wave parameters to a wave driven longshore current velocity. A tidal or wind driven current (or both) can be read from a file and superimposed on the wave-generated current before the associated sand transport rate is calculated. Tidal and/or wind currents input to the model represent the average across the surf zone and are produced externally (Hanson and Kraus 2000).

In addition to multiple sources of longshore current, GENESIS-T also introduces the application of a regional offshore contour shape (Hanson and Kraus 1993). Standard GENESIS calculates the offshore contour orientation, upon which the incoming waves are refracted, as a smoothed rendering of shoreline orientation. This methodology does not adequately represent local bathymetric features, such as the ebb shoal at Grays Harbor. Even if an external wave model is run to provide nearshore wave information, the wave station reference line may need to be placed where irregular bathymetric features exist,

and introduction of the regional offshore contours allows a more accurate representation of wave refraction from the station line to the point of breaking. An offshore contour was specified for the present project to account for the influence of the ebb shoal morphology and will be discussed in the Waves section later in this chapter.

Boundary conditions

GENESIS-T requires appropriate boundary conditions at the lateral boundaries. Inappropriate boundary conditions may dominate the solution on the interior of the grid. GENESIS-T currently allows for pinned-beach, moving, or gated boundaries. A pinned-beach boundary represents a shore with no longshore transport gradient at the boundary, and the shoreline position at the boundary, therefore, does not move. A moving boundary represents a historical shoreline change rate so that the final simulated shoreline position corresponds with a known measured shoreline position. The transport rate across the boundary is computed based on the required shoreline movement. Both the pinned-beach and moving boundary conditions should be located far away from the project to assure that the specified transport values at the boundary are not affected by the project changes, or vice versa.

The gated boundary condition may be specified if a structure such as a groin or jetty is located on an end of the calculation grid. The action of the groin or jetty located on the boundary is formulated in terms of the amount of sand that can pass the structure through the combined actions of sand bypassing and sand transmission. A permeability factor in the GENESIS set up describes sand transmission over, through, and landward of a shore-connected structure such as a jetty. The north jetty was assumed to be impermeable.

Sand bypassing is represented by introducing a bypassing factor. The bypassing factor is a function of the water depth at the tip of the structure and a computed depth of longshore transport. The present version of GENESIS-T computes the depth at the tip of a structure based upon the equilibrium profile shape deduced by Dean (1977) and the distance from the shoreline to the structure tip. Changes in structure tip depth due to tidal variation were not considered in GENESIS-T and this may be problematic where there is a large tidal range, such as at Grays Harbor. Therefore, the GENESIS-T bypassing algorithm was modified for the Grays Harbor project to include changes in tide level. A file with water level changes from mtl derived from the Westport tidal gage updates the calculated depth of the structure tip to calculate bypassed sand volume.

The existing gated boundary condition couples the computation of the bypassing factor and the longshore transport rate at the boundary. The coupled formulation is appropriate if the structure is a groin or shore-attached breakwater, but may produce unrealistic results for a jetty because of the discontinuity of shoreline position at a tidal inlet. Therefore, a new jetty-gated boundary condition was developed for this project. The jetty-gated boundary decouples the computation of the bypassing factor and the longshore transport rate at the cell wall adjacent to the jetty. The introduction of this boundary condition allowed for more accurate simulations at the Grays Harbor jettied inlet.

Breakwaters in GENESIS-T

The focus of the present study is to evaluate the performance of a submerged jetty spur in comparison to the performances of other alternatives, including the existing condition, for controlling the southward bypassing of sediment at the north jetty. The spur is readily modeled in GENESIS-T as a detached breakwater. Detached breakwaters are defined in GENESIS-T by specifying the location of the structure tips and a transmission coefficient. The structures may vary in length and orientation.

Structures such as breakwaters and jetties modify the waves around them and alter the response of the shoreline in their lee. Accurate calculation of waves transforming under combined diffraction, refraction, and shoaling is necessary for realistic predictions of shoreline change near structures. Goda, Takayama, and Suzuki (1978) developed methods for calculating diffraction of random waves that are implemented in GENESIS-T. The details of application of the methods to calculate wave breaking produced by combined diffraction, refraction, and shoaling in GENESIS-T are given by Kraus (1981, 1982, 1984, 1988).

The accurate calculation of wave transformation at a detached breakwater requires knowledge about wave transmission at the structure. Wave transmission refers to the propagation of waves over and through a breakwater and is described in the modeling system by a transmission coefficient, K_t. The present version of GENESIS-T allows for a single K_t value to be assigned to each detached breakwater. Wave transmission is a leading parameter determining the response of the shoreline to a detached breakwater (Hanson, Kraus, and Nakashima 1989; Hanson and Kraus 1990), and careful consideration must be given in selecting an appropriate K_t value.

Time-dependent wave transmission coefficient

Wave transmission properties of a structure can vary significantly depending on structure configuration and composition. Wave transmission properties also vary over different time scales as controlled by tidal variations and changes in the incident waves (see Figure 6-1 for notation). The large tidal range and seasonality of the wave climate at Grays Harbor necessitated the development of a time-dependent wave transmission coefficient. GENESIS-T was modified to compute K_t using the Ahrens (2001) dominant-mode approach. Ahrens defines the total transmission coefficient as:

$$K_t = \sqrt{(K_t)_{\text{thru}}^2 + (K_t)_{\text{over}}^2} \tag{6-4}$$

where $(K_t)_{\text{thru}}$ = transmission coefficient associated with wave energy transmitting through the structure and $(K_t)_{\text{over}}$ = transmission coefficient associated with overtopping or transmission over the crest of a submerged breakwater. The expression for $(K_t)_{\text{thru}}$ is:

$$(K_t)_{\text{thru}} = 1.0/(1.0 + f_{\text{thru}}) \tag{6-5}$$

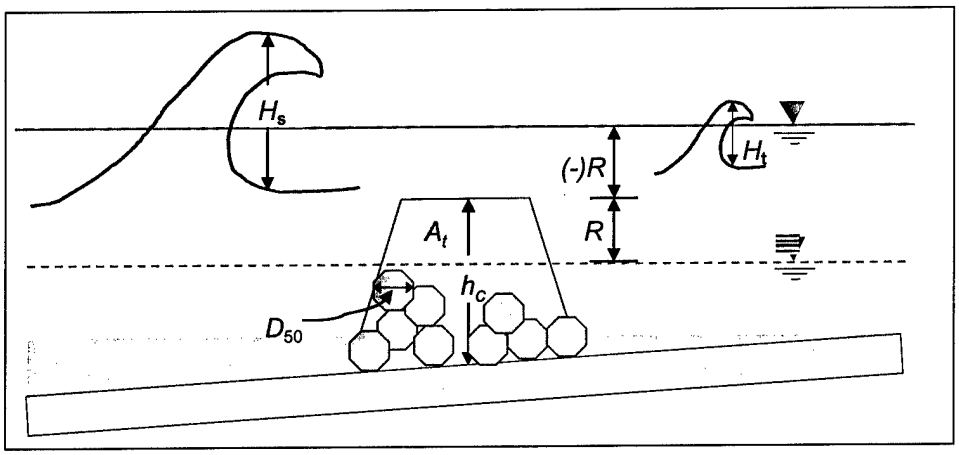

Figure 6-1. Notation for wave transmission predictive formulas

where

$$f_{\text{thru}} = \left(\frac{H_i}{D_{50}}\right)^{0.982} \exp\left[0.433 + 2.35\left(\frac{A_t}{L_o h_c}\right)\right] \tag{6-6}$$

with

H_i = significant incident wave height

D_{50} = nominal stone diameter

A_t = total cross-sectional area of the breakwater

h_c = crest height of the breakwater

L_o = deepwater wavelength

The expression for $(K_t)_{\text{over}}$ is analogous to Equation 6-5 and the formulation for f_{over} depends on whether the structure is submerged or surface piercing. For a submerged structure, such as the proposed spur at Grays Harbor, the equation for f_{over} is:

$$f_{\text{over}} = \exp\left[-0.646 + 0.631\frac{R}{H_i} + 0.00137\frac{A_t}{D_{50}^2}\right] \tag{6-7}$$

where R = structure freeboard.

GENESIS-T computes the transmission coefficient at each time step to represent the influence of the incident wave and water level. Water level is read from an external file derived from the Westport tide gage data. The user specifies the geometric properties (crest height and width, slopes on seaward and landward sides, and median rock size) of the structure. The calculated K_t will have a strong influence on the wave field behind and adjacent to the structure as it influences wave transmission and diffraction.

The applicability of the Ahrens equation to the proposed Grays Harbor spur was assessed by comparing the equation predictions of wave transmission to data from numerical and physical models of the Grays Harbor spur. Pacific International Engineering (PIE)[2] simulated wave transformation over the proposed spur with the fully nonlinear 1-D Boussinesq wave model of Wei et al. (1995). Simulations were run for nine storms (H_i= 4, 6, 8 m; T_p= 10, 15, 20 sec; shape of offshore spectrum approximated using JONSWAP, γ = 3.3) at mean lower low water (mllw) and mean higher high water (mhhw). The Ahrens equation predictions are compared to the numerical model in Figure 6-2. The root-mean-square error (RMSE) between the measured and predicted values is also given in Figure 6-2. Wave transmission data were collected at three locations along the spur for three different offshore wave combinations (H_i = 2,3,5 m; T_p = 9,13,13 sec) in the three-dimensional (3-D) physical model of the Grays Harbor site. The physical model is described in Chapter 5. Each wave condition was run at mllw, mean sea level (msl), and mean high water (mhw). The transmission data collected at the three measurement locations along the spur were averaged and are compared to calculated values using the Ahrens equation in Figure 6-2. As Figure 6-2 shows, Ahrens' equation predictions compare well to both the numerical and physical model results with a RMSE of 0.1 or less.

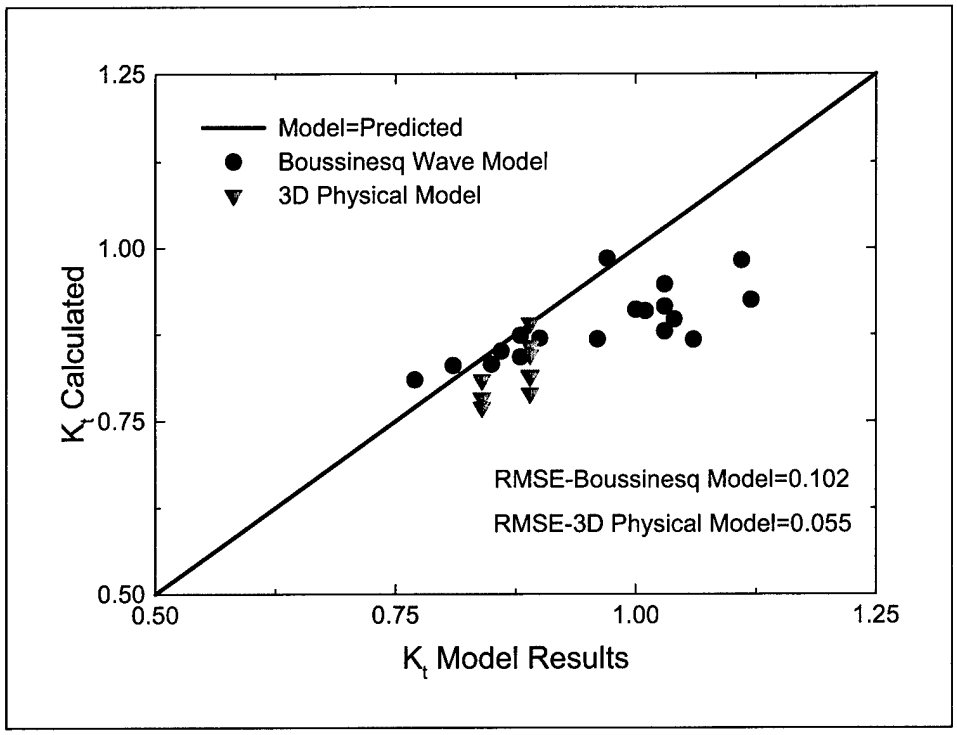

Figure 6-2. Transmission coefficient calculations

[2] Personal communication, Dr. Philip Osborne, PIE, May 2001.

Waves

The original GENESIS calculates the transport rate as a function of breaking wave height and direction. GENESIS-T includes the influence of currents originating from other sources, but these play a secondary role because of the energetic wave climate at Grays Harbor. The breaking wave-induced transport contribution dominates the transport rate calculation and accurate representations of the offshore wave input and the nearshore wave transformation are necessary for the shoreline change model.

Offshore wave data are input to the model at a fixed time interval and can be obtained from either a hindcast calculation or from wave gauge measurements. Data derived from the Grays Harbor Coastal Data Information Program (CDIP) buoy were accessed for this study. The buoy is a Datawell Directional Buoy that measures wave height, direction, and period. Directional wave data have been available since the latter part of 1993. Small gaps in the wave data record that occurred during buoy downtime were filled correlating with wave measurements from a wave gauge offshore the mouth of the Columbia River. Statistical analysis was performed on the complete wave record to develop a representative offshore wave time series to drive the GENESIS-T model.

Representative offshore wave time series

The GENESIS-T model for Grays Harbor was calibrated to reproduce shoreline change observed between September 1976 and August 1985. The model was verified by reference to shoreline change observed between September 1985 and August 1995. Offshore wave data for the entire calibration/verification periods were not available, and a representative wave climate had to be derived from the existing record. For long simulation periods for which wave data are not available, GENESIS-T allows for a shorter wave data file to be repeated. The shorter wave record must represent the typical wave climate because the wave data forces the model multiple times over a single simulation period. If a year of unusually high or low wave energy is included in the shortened record, multiple forcing by the atypical waves may bias model calibration, and procedures were implemented to examine this.

Typical years in the available wave record were determined by a statistical analysis scoring system established by Gravens, Scheffner, and Hubertz (1989). The wave record for each year was divided into eight angle bands (Table 6-1). The number of waves and the average significant wave height in each of the eight angle bands were computed for each year. The 6-year (1994-1999) average and standard deviation for the number of waves and the average wave height in each angle band were then computed. Values formed as the average plus and minus the standard deviation were then computed to give a representative tolerance. The number of waves and the average wave height for each year-angle band combination were compared to the representative tolerance. Each year of the record was assigned a point for values within the tolerance.

Table 6-1
Selection of Representative Wave Time Series

Angle Band	1 191.25 deg		2 213.75 deg		3 236.25 deg		4 258.75 deg		5 281.25 deg		6 303.75 deg		7 326.25 deg		8 348.75 deg		Normalized Potential Transport			
Year	No. of Event	Avg H (m)	No. of Event	Avg H (m)	No. of Event	Avg H (m)	No. of Event	Avg H (m)	No. of Event	Avg H (m)	No. of Event	Avg H (m)	No. of Event	Avg H (m)	No. of Event	Avg H (m)	South	North	Net	Gross
1994	19	2.15	99	3.03	247	2.69	654	2.25	1301	2.17	244	1.46	356	1.24	0	NA	0.30	0.50	0.20	0.8
1995	25	2.21	146	2.94	306	2.70	807	2.11	1141	2.03	479	1.40	16	1.18	0	NA	0.22	0.64	0.42	0.86
1996	47	1.79	170	2.45	335	2.21	599	2.19	1206	2.07	560	1.46	10	1.37	1	0.91	0.27	0.46	0.19	0.73
1997	35	2.72	191	2.78	325	2.36	755	2.17	1261	2.15	335	1.77	17	1.95	0	NA	0.32	0.67	0.35	0.99
1998	26	2.03	146	3.13	288	2.81	601	2.82	1391	2.14	457	1.52	11	1.19	0	NA	0.27	0.87	0.60	1.14
1999	47	3.34	167	3.93	217	3.20	646	2.58	1406	2.10	413	1.57	17	1.25	7	1.06	0.35	1.09	0.74	1.44
Avg	33	2.37	153	3.04	286	2.66	677	2.35	1284	2.11	415	1.53	71	1.36	1	0.99	0.29	0.71	0.42	1.00
SD	12	0.56	31	0.50	46	0.35	85	0.28	104	0.05	112	0.13	140	0.30	3	0.11	0.05	0.24	0.22	0.25
Avg +SD	45	2.93	184	3.54	332	3.01	762	2.63	1388	2.16	527	1.66	211	1.66	4	1.10	0.34	0.95	0.64	1.25
Avg -SD	21	1.81	122	2.54	240	2.31	592	2.07	1180	2.06	303	1.40	-68	1.06	-2	0.88	0.24	0.47	0.20	0.75

Summary

Year	1994	1995	1996	1997	1998	1999
Points	18	19	12	20	21	9

A normalized potential transport was also computed for each year of the record using SEDTRAN (Gravens and Kraus 1991). SEDTRAN is a program that computes potential longshore sand transport rates using the longshore energy flux with input from a wave time series. The transport was normalized by the average gross transport rate for the years of record. The 6-year average and standard deviations of the normalized potential south-directed, north-directed, net, and gross transport were computed and a representative tolerance defined for each category as described above. Each year of the record was assigned two points for each transport category that fell within the tolerance. The points were summed for each year and the results are given in Table 6-1. There was a clear distinction with 4 years having similar high point totals and 2 years with a significantly lower score. The years with the highest scores were deemed representative of the overall wave climate and used to drive the shoreline change model.

STWAVE modeling

The accuracy of shoreline change modeling calculations is improved with better estimates of breaking wave height and direction. The breaking wave pattern is determined by the offshore wave parameters (wave height, period, and direction) and the bathymetry over which the waves propagate. A nearshore wave transformation simulation was performed with the steady-state spectral wave model STWAVE (STeady-state spectral WAVE model) (Resio 1988; Smith, Sherlock, and Resio 2001). The wave model extends from approximately 3.7 miles south of the north jetty to about 10.9 miles to the north in the alongshore direction and 8.6 miles in the cross-shore direction. The large domain ensures that the influence of the ebb-shoal bathymetry is considered in the nearshore wave transformation. The individual grid cells are 82 ft by 82 ft. The grid was created with the 1999 bathymetry.

Wave transformation simulations performed by STWAVE and similar full wave models are time consuming, and it is not practical to run the external wave model for each offshore wave. A time-saving technique was implemented in which the offshore waves were divided into height, period, and direction bands. The band limits are given in Table 6-2. Dividing the offshore wave time series in this manner resulted in 238 waves to be simulated by STWAVE. STWAVE requires that the incident wave spectra be specified as energy density as a function of frequency and direction. An incident spectrum was specified from the wave height, period, and direction of each of the 238 incident waves by applying a parametric spectral shape together with a directional spreading function. A TMA shallow water spectrum description (Bouws et al. 1985) and a $\cos^{nn} \alpha$ directional distribution function, where *nn* is an even power and α is the angular deviation from the spectral peak wave direction, were applied. The parameters controlling frequency and directional spreading were set in accordance with guidelines established in the STWAVE user's manual (Smith, Sherlock, and Resio 2001).

Table 6-2
Wave Band Limits

Height Bands (m)	Period Bands (sec)	Direction Bands (deg)
0.0 – 1.0	0 – 5	180 – 210
1.0 – 1.5	5 – 7	210 – 240
1.5 – 2.0	7 – 9	240 – 255
2.0 – 2.5	9 – 11	255 – 270
2.5 – 3.0	11 – 13	270 – 285
3.0 – 4.0	13 – 15	285 – 300
4.0 – 5.0	15 – 17	300 – 330
5.0 – 6.0	> 17	330 – 360
> 6.0	-	-

STWAVE transforms the waves from the offshore boundary across the nearshore bathymetry. The results are saved at a station reference line that runs along the 33 ft depth contour relative to msl. The wave parameters saved at the station line are then transformed by GENESIS-T from the reference depth contour to the breaking point. The station line must be located seaward of breaking point but as near to shore as possible to utilize the wave model transformation capabilities. At Grays Harbor, because waves break on the ebb shoal, the station line had to be located where the ebb-shoal depth contours still influence wave refraction. To ensure that the GENESIS-T transformation to breaking accounted for the ebb-shoal bathymetry, an offshore contour representing the morphology in the vicinity of the reference line was specified. A sensitivity analysis to assess the influence of including the offshore contour capability of GENESIS-T found that it was necessary for the predictive capability of the model. The results demonstrate the improvements possible through specifying the offshore contour in GENESIS-T for modeling shoreline response of the beach located near an inlet.

Tidal Currents

Tidal currents may be a nonnegligible contributing factor to the overall sand transport rate if a project site is located adjacent to an inlet. The large tidal prism at Grays Harbor produces tidal currents that should be considered in longshore transport rate calculations. GENESIS-T incorporates tidal currents by reading velocities from an external file and superimposing them on a wave-generated current computed from the breaking-wave parameters. GENESIS-T does not calculate the current produced from the tide. These currents, represented by an average through the surf zone, must be obtained externally and are specified for each calculation cell wall at each tidal current time step.

A time series of tidal currents at Grays Harbor was estimated from the ADvanced CIRulation (ADCIRC) model of the Grays Harbor estuary and adjacent beaches. ADCIRC is a multidimensional, depth-integrated finite-element hydrodynamic circulation model (Luettich, Westerink, and Scheffner 1992). Application of ADCIRC is described in Chapter 7.

To obtain the current velocities to be used by GENESIS-T, the ADCIRC model was forced with tidal constituents on the ocean boundary for a 28-day period. Tidal current velocities were saved at a 2-hr time step. The velocities were interpolated onto a rectilinear grid within the Surface-water Modeling System (Brigham Young University Engineering Computer Graphics Laboratory 1997). The y-axis of the rectilinear grid was directed offshore, and the x-axis was oriented along the general trend of the shoreline and coincided with the GENESIS-T calculation domain.

The interpolated ADCIRC results at each grid cell were recorded in their x and y components. GENESIS-T requires a representative shore-parallel current be obtained at each GENESIS cell wall. Therefore, shore-parallel velocities were resolved from the ADCIRC velocity components and then averaged across the surf zone for each tidal current time step. The results for the 28-day tidal cycle were saved in a file and accessed by GENESIS-T at the specified time step. The 28-day record is repeated during simulations.

A sensitivity analysis to assess the influence of the tidal currents found that they had relatively little effect on the longshore transport and shoreline evolution at Grays Harbor. The influence of the tidal currents was evident only as minor changes in transport and shoreline predictions within about 0.5 mile of the jetty, indicating that the large Pacific coast waves dominate the longshore processes.

Cross-shore Transport Processes

Cross-shore processes transport large volumes of sand on to and off of the beaches adjacent to Grays Harbor. Littoral feeding from the ebb shoal and rip currents that transport sand seaward of the jetty tip must be included when modeling the evolution of the shoreline.

Littoral feeding

Since the construction of the jetties at the entrance to Grays Harbor, shoreline change on the adjacent beaches has been governed by sediment supply from the ebb tidal shoal (Kaminsky et al. 1999a). The onshore transport of sand is represented as a sediment source by the GENESIS-T shoreline change model. Kraus and Harikai (1983) developed a phenomenological methodology to qualitatively describe the spatial distribution of onshore sand transport near an inlet, and this approach was applied for the present study. The feeding rate is distributed over approximately 3 miles, is greatest adjacent to the jetty, and decreases with increasing distance north of the jetty. The sediment pathways defined in the sediment budget developed in Chapter 3 qualitatively supports this distribution. A sensitivity analysis was performed on the spatial distribution of the onshore transport and the shoreline simulation results were insensitive to reasonable changes in the distribution.

The volume of onshore transport has decreased with time as the flanks of the ebb shoal deflate in response to increased peak tidal velocities resulting from construction of the jetties at the turn of the century. Therefore, volume estimates must be made for both the 1976 to 1985 calibration period and the 1985 to 1995 verification period to simulate the reduced contribution from the ebb shoal.

Kaminsky, Buijsman, and Ruggiero (2000) developed an integrated sediment budget for the entire Columbia River littoral cell from analysis of bathymetric, topographic, and shoreline data from the 1950s to 1995. The quantitative sediment budget included a net 1 million cu m/year (approximately 1.3 million cu yd/year) sediment gain on the north beach from the Grays Harbor ebb shoal/inlet complex. The actual feeding rate from the ebb shoal is presumably higher as southbound sediment bypasses the north jetty and exits the north beach cell. However, because the 1976 to 1985 period falls near the end of the time period analyzed by Kaminsky, Buijsman, and Ruggiero (2000), a feeding rate of 1.3 million cu yd/year was deemed reasonable as a first approximation and implemented following the methodology of Kraus and Harikai (1983) for the 1976 to 1985 model calibration period.

The littoral feeding for the 1985 to 1995 simulation was initially based on the detailed sediment budget for the Grays Harbor entrance presented in Chapter 3. The budget was based on bathymetric change from 1987 to 2001 and included approximately 1,100,000 cu yd/year of littoral feeding to the north beach from the ebb shoal. The period 1985 to 1995 was simulated by input of this onshore transport rate with a distribution identical to that for the calibration period.

Rip current transport

Rip currents are a major component of the surf zone circulation and often a dominant mechanism for offshore transport of water and sand. Quantification of the sand transport in rip currents was expected to be required to achieve reliable prediction of shoreline evolution at Grays Harbor, as a persistent rip current has been observed near the north jetty. The rip current contributes to shoreline recession and influences the volume of sand that bypasses the north jetty and enters the inlet.

Prediction of rip current transport in time and space is difficult, as discussed in Appendix C. A comprehensive description of a rip current and its predicted modification of the adjacent shoreline require the ability to identify its location, size, strength, and persistence. A laboratory study of the rip near the north jetty was performed in the 3-D physical model described in Chapter 5 to determine if the necessary characteristics of the rip could be estimated with a reasonable amount of certainty. The rip current signal was found to be persistent but complex. Assuming an average rate loss throughout the year was determined to be reasonable given the available information and state of knowledge about sediment transport in a rip current.

The GENESIS-T model represents the volume of sand lost from the system due to the rip current as a sediment sink near the north jetty. The volume of sand lost due to the rip was assumed to be constant in time and space and estimated from results of the sediment budget work presented in Chapter 3. The sediment budget estimate of the average annual volume of sand bypassing the north jetty is 400,000 cu yd. This value includes both the cross-shore rip transport and sand that is carried around the jetty tip by longshore currents and sand that bypasses the end of the jetty due to longshore sand transport only. Preliminary GENESIS-T model simulations were made to estimate the longshore component of the bypassing sediment. Based on these preliminary runs, the longshore component

of bypassing was estimated to be approximately 75,000 cu yd/year. The remaining 325,000 cu yd/year was assumed to result from rip current transport.

The volume of rip transport is assumed to be related to the south-directed longshore transport rate near the jetty. Because the average annual southbound transport at the jetty has not changed since 1976 (see the Longshore Sand Transport section later in this chapter), the 325,000-cu yd/year estimate of rip transport was specified for both the calibration and verification simulations. The sensitivity of the model to circulation patterns around the rip current was assessed by varying the distribution of cross-shore transport both temporally and spatially based on COASTL results presented in Chapter 7. A small rip embayment formed at the rip location, but overall shoreline trends did not change.

Model Configuration

Spatial domain

The first step in configuring the model is to establish a shoreline coordinate system. The shoreline trend must be determined and a longshore (x) axis drawn parallel to the trend. The orientation of the x-axis for the Grays Harbor model was determined from regional maps to have an azimuth of 2 deg. The x-axis extended north from its origin at Washington State Plane 83 coordinates 725,423 ft east and 602,705 ft north. The shore-normal (y) axis is directed offshore to create a right-hand system. The grid spacing (dx) was specified at 82 ft.

The objective of the GENESIS-T model is to assess the existing longshore transport regime near the north jetty and evaluate whether the construction of a submerged spur or a jetty rehabilitation will produce beneficial changes in longshore transport rates. The model must therefore extend far enough to include the area in which transport rates are altered by the proposed structure at the project site. Preliminary model runs were made with and without a 1,500 ft submerged spur located near the jetty terminus. Preliminary model runs indicated that the proposed spur will influence the longshore transport and resulting shoreline changes about 2.5 miles north of the north jetty. The right lateral boundary (north boundary) is modeled by specifying the moving boundary condition. A moving boundary condition should be located away from the project to assure that boundary effects do not influence the project area. Therefore, the right boundary was placed 1.2 miles north of the project area, 3.7 miles from the north jetty. The left lateral boundary (south boundary) is located at the north jetty and modeled by specifying the jetty-gated boundary. Based on local site maps, the seaward terminus of the jetty was set 3,700 ft from the GENESIS-T origin.

Shoreline position data were obtained from the Washington Department of Ecology (WDOE). The WDOE developed accurate shoreline maps of the southwest Washington coast with systematic procedures and consistent methodologies as discussed in Kaminsky et al. (1999b). The shoreline position data were referenced to the GENESIS-T longshore baseline and values

interpolated to longshore grid points using a cubic interpolation. Spatial domains were created from shoreline data for the years 1976, 1985, 1995, and 2000.

Additional input parameters

The vertical extent of beach profile movement, defined by the average berm height and depth of closure, is a fundamental quantity in determining shoreline change in a one-line model such as GENESIS-T. The average berm height was set at 9.8 ft and was determined from beach profile analysis. The depth of closure is more difficult to define and estimate. Hallermeier (1978, 1981) has given an expression for calculating a depth, d, which defines the seaward boundary of the zone where significant longshore transport takes place:

$$d = 2.28H_s - 68.5(H_s^2 / gT_s^2) \tag{6-8}$$

where

H_s = significant nearshore wave height

g = acceleration due to gravity

T_s = wave period of the significant waves

Following Kraus and Harakai (1983), Equation 6-8 was adopted to compute a representative depth of closure at Grays Harbor. A frequency distribution of the depth of active transport calculated with Equation 6-8, based upon nearshore wave data from the STWAVE simulation, is shown in Figure 6-3. The distribution has a mean of 17 ft and a mode of 6.9 ft. The depth ranges from zero to 40 ft account for nearly 98 percent of the total wave population and 40 ft was applied for the depth of closure.

The longshore transport parameters, K_1 and K_2, are determined by model calibration. The transport parameter K_1 controls the time scale of the simulated shoreline change and the magnitude of the longshore sand transport rate. A K_1 value of 0.1 was selected for the Grays Harbor project to optimize the shoreline calibration. This K_1 value also gave a reasonable gross transport rate based on local knowledge and compares well with the morphologic analysis in Chapter 3. The transport parameter K_2 controls in part the longshore sand transport generated by a longshore gradient in breaking wave height. The value of K_2 is typically 0.5 to 1.0 times that of K_1. The shoreline calibration was optimized using a K_2 of 0.075.

GENESIS-T requires that the median sediment grain size d_{50} also be included as an input parameter. The d_{50} is input to the Dean (1977) equilibrium profile formula to compute the depth at the tip of a structure. The depth at the tip and a computed depth of longshore transport control the volume of sand bypassing the structure. Profiles were analyzed near the north jetty to estimate the d_{50} required

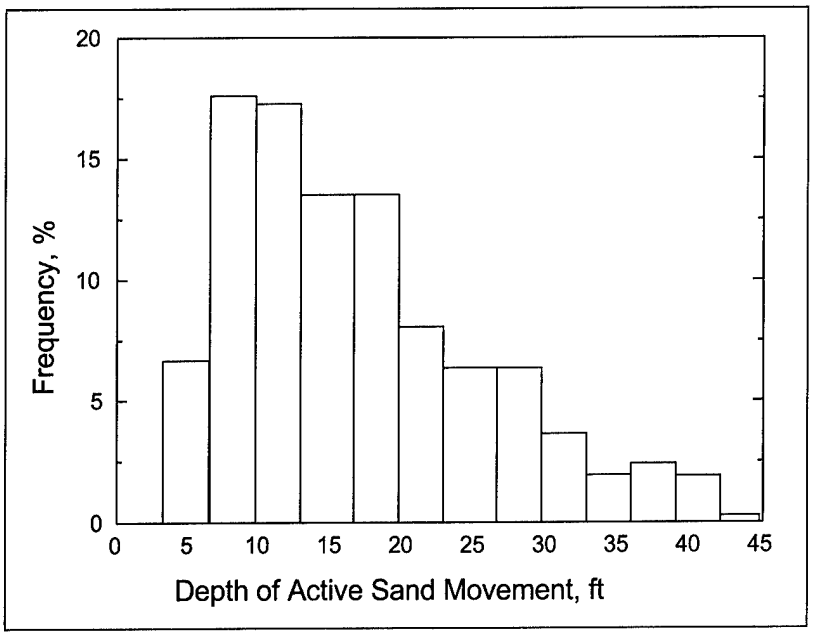

Figure 6-3. Frequency distribution of depth of active sand movement

to obtain a reasonable depth at the seaward end of the jetty. The profile analysis indicated that d_{50} of 0.18 mm was appropriate. The WDOE collected sand samples along the southwest Washington coast and determined the sand grain size using a sieve analysis. The WDOE reports that the grain size near the Grays Harbor north jetty is approximately 0.22 mm, and the grain size farther north is about 0.16 mm (Ruggiero and Voigt 2000). A d_{50} of 0.18 mm from profile analysis is consistent with the grain size data.

Model Calibration

Model calibration is the procedure of reproducing changes in measured shoreline position over a certain time interval. The calibrated model is verified by applying it to reproduce changes measured over a time interval different from the calibration interval. Successful verification indicates that the model predictions are independent of the calibration period.

The accuracy of the model is assessed qualitatively by comparing the measured and predicted shoreline plan forms. A quantitative measure of the model's predictive capability is the calibration and verification error. The calibration and verification error is the spatially averaged absolute difference between measured and predicted shoreline positions. The GENESIS-T model was calibrated by comparison to the change in measured shoreline positions from September 1976 to August 1985 and verified by simulating shoreline change from September 1985 to August 1995.

Calibration (1976 to 1985)

September 1976 to August 1985 was a period of shoreline advance along the entire modeled domain. The average shoreline advance within 3.7 miles of the north jetty was 150 ft for this period. The shoreline advance was consistent alongshore with slightly greater advance experienced with increasing distance north of the jetty.

A summary of input values for the 1976 to 1985 period simulation is given in Table 6-3 and the resulting shoreline prediction is plotted with the measured 1985 shoreline in Figure 6-4. The K_1 value of 0.1 was selected by optimizing the model prediction while maintaining reasonable gross transport rates. Likewise, K_2 was varied to optimize the model prediction. The predicted shoreline compares well with the measured shoreline. The shoreline change trends are reproduced well and the average absolute difference from the August 1985 shoreline is 31 ft.

Table 6-3
Summary of Model Input

Input	Value
Calibration coefficient, K_1	0.1
Calibration coefficient, K_2	0.075
Median grain size, d_{50}	0.18 mm
Closure depth	40 ft
Average berm height	9.8 ft
Average annual cross-shore feeding	1.3 million cu yd
Average annual rip transport	325,000 cu yd

The volume predicted to bypass the jetty via longshore transport only is about 45,000 cu yd/year. The total volume lost to the inlet, including the 325,000 cu yd/year representing the rip current and modeled as a sediment sink, is therefore about 370,000 cu yd/year. The net contribution from the inlet to the north beach is approximately 930,000 cu yd/year (1.3 million less 370,000 cu yd/year). Kaminsky, Buijsman, and Ruggiero (2000) estimated that the average net contribution from the inlet to the north beach from the 1950s to 1995 was about 1.3 million cu yd/year. Because the calibration period (1976-1985) covers the middle to latter part of the period analyzed by Kaminsky, the 930,000 cu yd/year appears reasonable. Based on the shoreline predictions and the reasonableness of the assumed cross-shore rates, the calibrated model estimates of the longshore sand transport regime are considered acceptable.

Verification (1985 to 1995)

From September 1985 to August 1995 the shoreline receded an average of 100 ft within 1 mile of the north jetty. The shoreline was relatively stable farther to the north, experiencing an average shoreline advance of about 1 ft/year over the 10-year period.

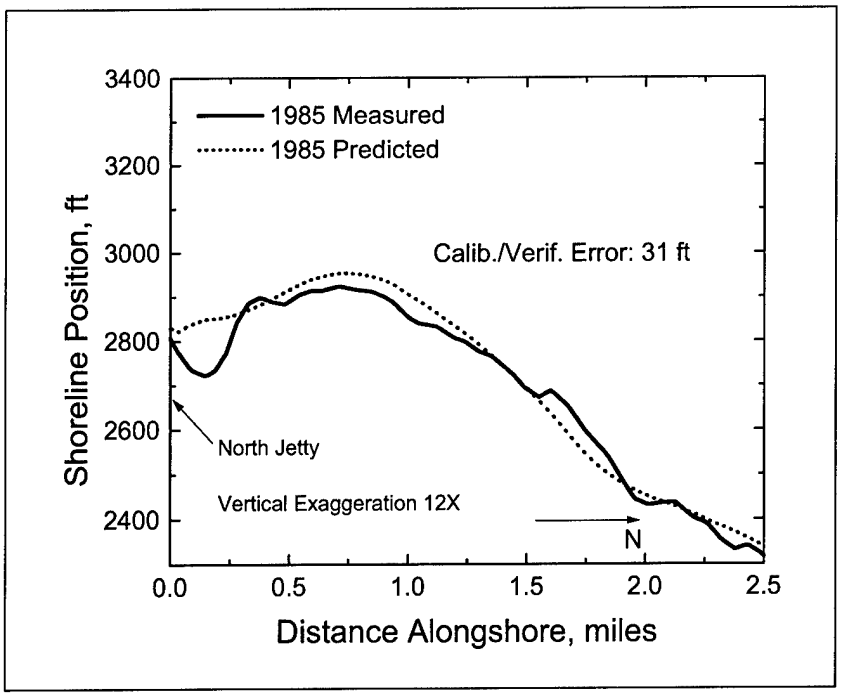

Figure 6-4. Measured and predicted 1985 shorelines

The calibrated model was run to predict shoreline change from 1985 to 1995. All calibrated model inputs were unchanged, except for the littoral feeding from the ebb shoal. The volume of onshore transport was changed to represent the decreasing sediment supply from the deflating ebb shoal. The onshore transport volume was set at 1,100,000 cu yd/year in accordance with the 1987 to 2001 sediment budget presented in Chapter 3 and the model predicted too much accretion. Reducing the onshore transport by about 200,000 cu yd/year optimized results. The predicted 1995 shoreline modeled with a littoral feeding rate of 900,000 cu yd/year is plotted with the measured shoreline in Figure 6-5. The measured and predicted shorelines compare well with an average absolute difference from the measured 1995 shoreline of only 22 ft. The 900,000 cu yd/year feeding rate reflects a reduction in volume from the calibration period, as expected, and is within 20 percent of the sediment budget results presented in Chapter 3. The model accurately reproduced the 1995 shoreline with a reasonable feeding rate, and the GENESIS-T model verification is considered acceptable.

Existing condition (Alt 1)

The existing longshore transport was evaluated by performing a 5-year simulation forced by the representative waves with the calibrated GENESIS-T model and an initial shoreline measured in 2000. All calibrated model input was left unchanged with the onshore feeding rate varied ±25 percent from 900,000 cu yd/year. Feeding rates in this range are reasonable according to the sediment budget developed in Chapter 3. The 5-year predicted shorelines are plotted with the initial shoreline in Figure 6-6. The initial measured shoreline is characterized by large shoreline undulations, which are smoothed by the model.

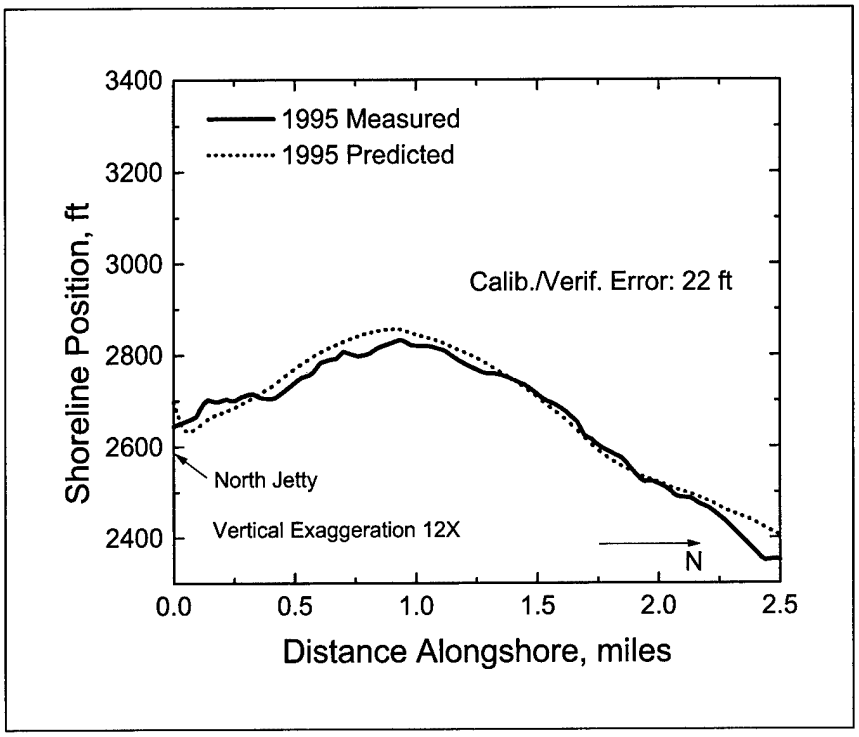

Figure 6-5. Measured and predicted 1995 shorelines

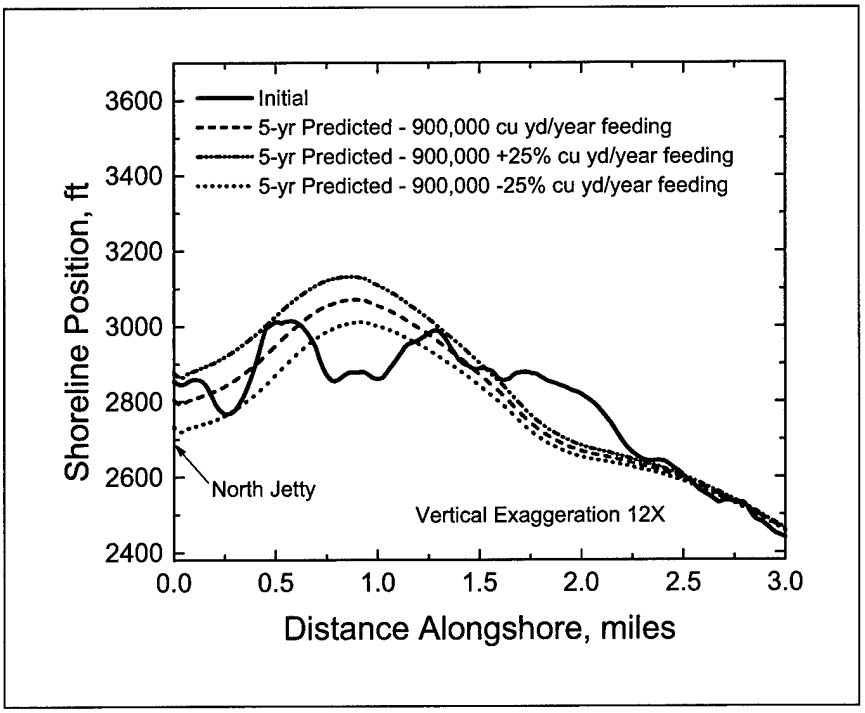

Figure 6-6. Existing condition 5-year predicted shorelines for various onshore feeding rates

However, the predicted shoreline is generally stable. There is a zone of beach accretion 0.75 to 1 mile north of the jetty and an area of shoreline recession predicted at 1.75 to 2 miles north of the jetty. The results should be interpreted with caution, as there is considerable uncertainty regarding the magnitude of future littoral feeding rates from the ebb shoal.

Longshore Sand Transport

The GENESIS-T model was calibrated and verified for the purpose of estimating the existing longshore sand transport rates and assessing the changes in longshore sand transport created by the introduction of various structural alternatives. This section discusses the evolution of the longshore transport regime since 1976 and estimates of the existing longshore sand transport.

The gross transport rate is the sum of longshore sand transport rate in both directions. The GENESIS-T model estimates gross transport rates of 1 to 2 million cu yd/year. The net transport rate is the difference between the rates of north- and south-directed sediment flow. The estimated average annual net longshore transport rate for three different time periods are plotted in Figure 6-7. Positive values of net transport denote north-directed transport and negative values are south directed. The predominant direction of longshore transport is to the north with a reversal to the south within 2,000 ft of the jetty.

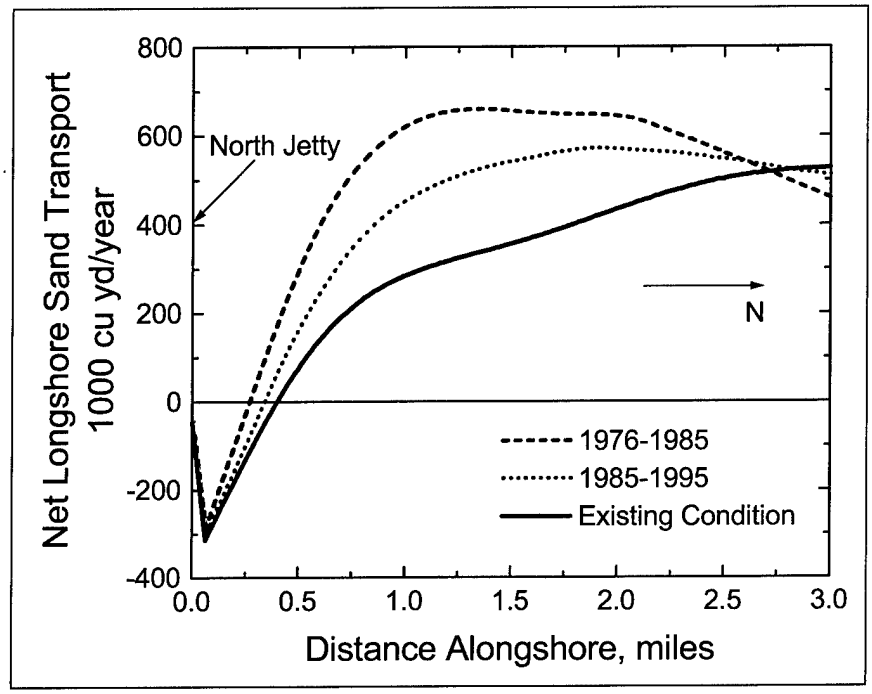

Figure 6-7. Net longshore sand transport

The gradient in the net longshore transport rate governs shoreline change associated with longshore processes only. A positive gradient indicates erosion, and a negative gradient yields accretion. The gradient in the average net longshore sand transport from 1975 to 1985 indicates erosion within 1 mile of the jetty, stabilizes 1 to 2 miles from the jetty, and then transitions to a potential accretionary longshore transport regime at distances greater than 2 miles north of the jetty. The average net longshore transport rate gradients from 1985 to 1995 indicate a reduced potential for erosion within 1 mile of the jetty and less potential for accretion at distances greater than 2 miles north of the jetty.

The estimates of the existing net longshore transport suggest a continued reduction in the potential for erosion within 1 mile of the jetty. The potential for accretion 2 miles north of the jetty has transitioned to a slightly erosive transport gradient that stabilizes near 3 miles north of the jetty. The implication of this transport regime is that, although the dependency of the beach on the littoral feeding from the ebb shoal seems to have reduced over time, the beach will continue to require the cross-shore feeding from the ebb shoal to maintain its present position near the jetty. Also, the accretion experienced at distances 2 to 3 miles from the jetty is not predicted to continue. Based on this analysis, a reduction in cross-shore feeding will result in either shoreline recession or less shoreline advance within approximately 3 miles of the jetty.

The sand that enters the inlet from the north beach originates as south-directed transport that bypasses the north jetty. The estimated average annual south-directed transport rate for calibration, verification, and existing-condition time periods is plotted in Figure 6-8. The southbound transport is greatest near the jetty and decreases with increasing distance from the jetty. The average annual southbound transport within 0.25 miles of the jetty is essentially unchanged since 1976. The maximum south-directed transport rate is approximately 925,000 cu yd/year and occurs at the jetty. South-directed transport rates have generally increased between 0.25 and 2.5 miles from 1976 to the present. The southbound rate becomes relatively stable at about 275,000 cu yd/year 2.5 miles north of the jetty.

The south-directed volumes shown in Figure 6-8 are the potential rates approaching the jetty. The actual volume of longshore sand transport predicted to bypass the jetty for each of the three simulations is about 45,000 cu yd/year. Therefore, based on the sediment budget estimate of sand bypassing the jetty each year presented in Chapter 3 and the calibration results presented above, the GENESIS-T model predicts that just over 10 percent of the bypassed volume is attributable solely to longshore processes. The remainder results from cross-shore processes that sweep sediments offshore that can then be carried around the north jetty by the longshore current.

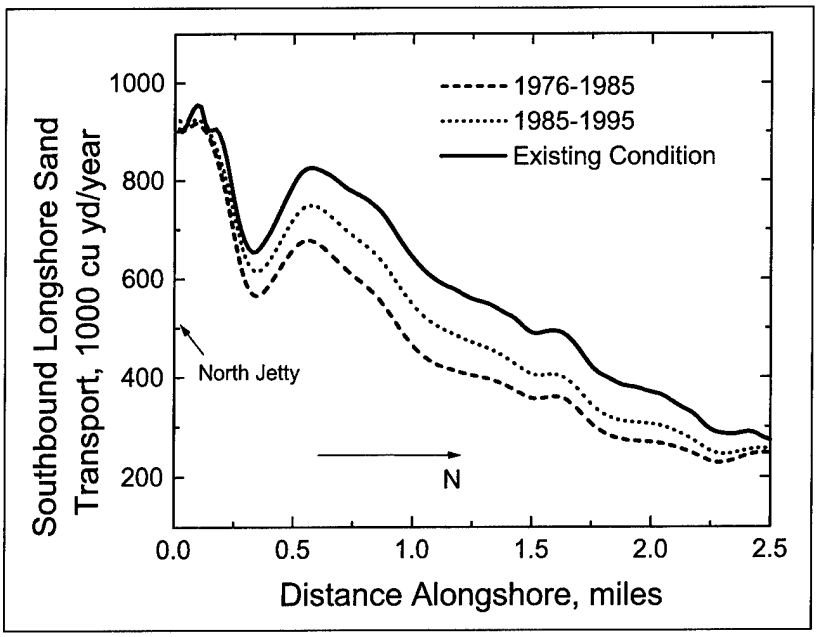

Figure 6-8. Southbound longshore sand transport

Results and Sensitivity Analysis

Having estimated the existing longshore transport, the calibrated GENESIS-T model can be applied to evaluate various alternatives for reducing sediment bypassing and shoreline recession. Both 5- and 30-year simulations were run to assess the short- and long-term changes induced by each alternative. The longshore sand transport results from Alt 1 (existing condition) were provided in the Longshore Sand Transport section earlier.

The purpose of each proposed alternative is to reduce sand bypassing the north jetty and to reduce erosion adjacent to the jetty. Because GENESIS-T does not directly model cross-shore processes, each configuration is evaluated based on the transport and shoreline changes associated with alterations of the longshore processes. The results are presented relative to Alt 1. Changes in the shoreline position, net transport rate, and south-directed sand transport rate were evaluated. A positive change in shoreline position indicates increased accretion or reduced erosion relative to Alt 1. A negative change is indicative of reduced shoreline advance or increased recession. The sensitivity of the results to changes in wave energy and direction were also analyzed.

Overall, model results indicate that structural alternatives create subtle changes in shoreline position. Based on an analysis of topographic data collected by the WDOE from 1997 to 2001, the seasonal variability of the north beach shoreline is 70 to 200 ft. The shoreline position change predicted by the model for each alternative is generally within this range of variability. The greatest change in both shoreline position and computed transport rates for all alternatives is within 0.5 mile of the north jetty. The computed change in transport rates at distances greater than 0.5 mile north of the jetty are less than 10 percent. Although these changes are discussed to illustrate trends in the results, the

magnitude of change is within the uncertainty of the model and the changes are not considered significant. The influence of each structural alternative is therefore considered to be limited to within 0.5 mile of the north jetty.

Spur configuration (Alts 2A and 2B)

The construction of a submerged rubble mound spur has been proposed as an alternative for reducing channel sedimentation and coastal erosion at the Grays Harbor north jetty. Two spur configurations were evaluated. The first, Alt 2A, is a long (approximately 1,500 ft) submerged spur with a -10 ft mllw crest height, a 30-ft crest width, seaward side slope of 1:5 and a landward side slope of 1:3. The proposed location is at north jetty sta 165+00 where the average toe depth is approximately 26 ft. The proposed rubble mound structure has a broad gradation with a median rock size of about 3 ft. Alt 2B is identical to Alt 2A except that the length has been shortened to 800 ft.

The submerged spur was modeled in GENESIS-T as a detached breakwater. The tips of the submerged spur were specified in the model at approximately 4,150 ft from and oriented parallel to the GENESIS-T x-axis. The transmission coefficient was computed at each time step based on the structure geometry, incident waves, and water levels.

A 5-year simulation was made with the calibrated GENESIS-T model and compared to a 5-year Alt 1 simulation to evaluate the short-term changes caused by the introduction of a spur. A plot of the relative short-term change in shoreline position caused by the spur is given in Figure 6-9. The longshore extent of the shoreline benefit appears to be independent of spur length. Both the long and short spurs produce a shoreline benefit within approximately 0.5 mile of the jetty and negative shoreline changes from that point to about 2.5 miles north of the jetty. The cross-shore extent of the changes, however, is different for each alternative. Alt 2A resulted in positive shoreline change in the lee of the spur relative to Alt 1, with a maximum change of 265 ft versus a positive change of 170 ft for Alt 2B. A corresponding increase in negative shoreline change occurred north of the spur for Alt 2A. The maximum negative change in shoreline position relative to Alt 1 was approximately -75 ft about 1 mile from the jetty for Alt 2A and was -40 ft at 0.9 mile from the jetty for Alt 2B. Minimal change in shoreline position is predicted at distances greater than 2.5 miles north of the jetty for both spur alternatives.

The net longshore transport with the spur in place is compared to the Alt 1 results in Figure 6-10. The spur reduces the transport gradient within about 1 mile of the jetty suggesting that, although there is a reduced reliance on cross-shore sand feeding, continued feeding from the ebb shoal is required for beach stability. The short-term percent change in the estimated average annual south-directed transport rate relative to Alt 1 is plotted in Figure 6-11. The introduction of the spur results in increased potential southbound transport, particularly near the northern tip of the structure. Patterns of sediment transport similar to Alt 2A

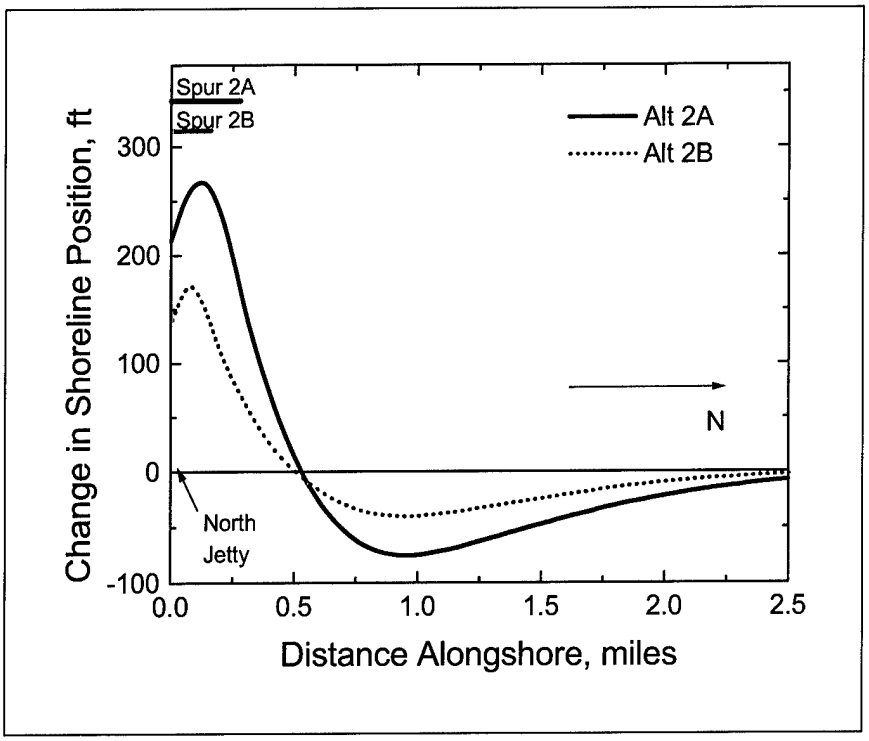

Figure 6-9. Short-term change in shoreline position relative to Alt 1

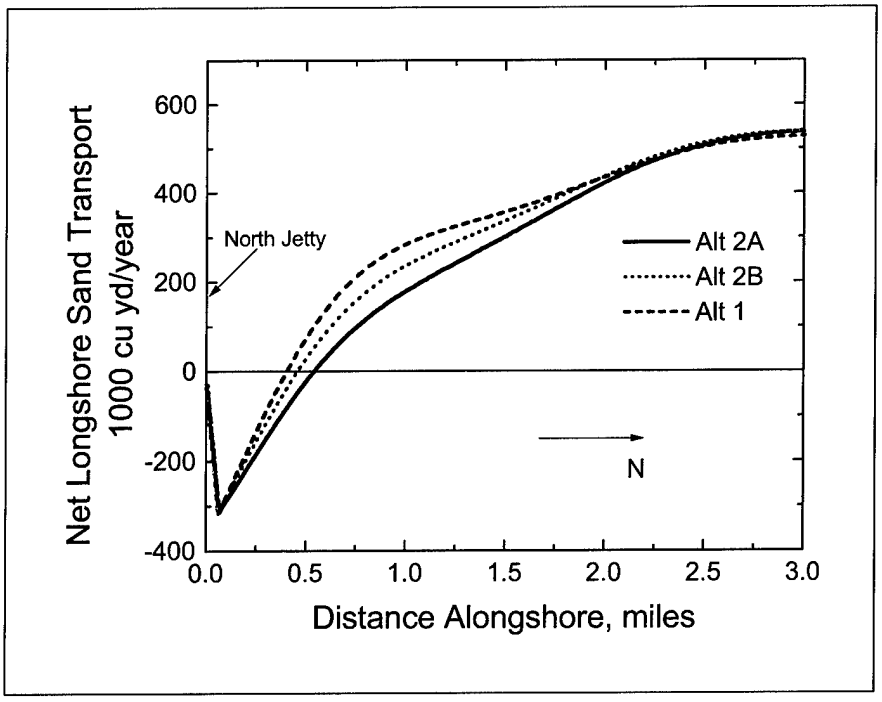

Figure 6-10. Net longshore sand transport

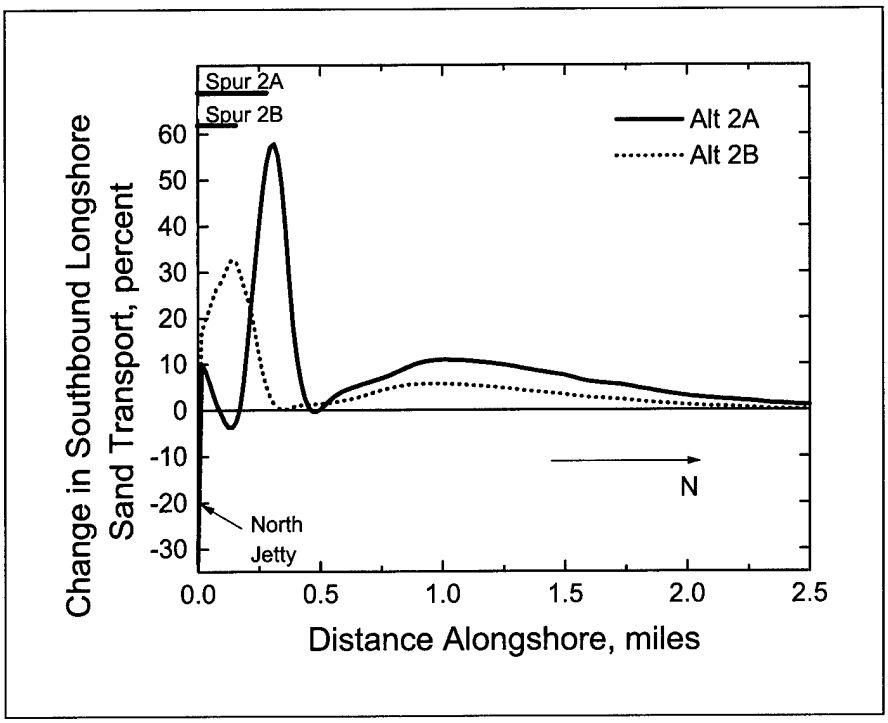

Figure 6-11. Short-term percent change in south-directed transport relative to Alt 1

were obtained by Zyserman and Johnson (2002). They applied a quasi-3-D model of flow and sediment transport with a morphologic update scheme to simulate planform development behind surface-piercing detached breakwaters. ADCIRC results presented in Chapter 7 also indicate an increase in south-directed flow across a majority of the surf zone with the spur in place.

The average increase in potential southbound longshore transport within 0.5 miles of the jetty is approximately 17 percent for Alt 2A and 13 percent for Alt 2B. At distances greater than 0.5 mile, the change in the south-directed transport rate is less than 10 percent for both alternatives.

Model predictions of south-directed transport near the spur were found to be sensitive to the K_1 calibration value. Although general trends in the predicted shoreline response to the spur change subtly with K_1, the predicted south-directed transport may reverse for certain wave conditions with a small increase in K_1 values near a threshold value between 0.1 and 0.11. The transport reversal is a consequence of the balance between the K_2 term and the K_1 term in Equation 6-1 in an area greatly influenced by diffraction. The change can be abrupt due to the discretization of the nearshore wave field. The short-term percent change in southbound transport relative to Alt 1 for K_1 values approximately equal to or greater than 0.11 is represented by the plot in Figure 6-12 and shows a reversal from the changes in Figure 6-11 (K_1=0.1). The average decrease in potential southbound longshore transport within 0.5 mile of the jetty is approximately 13 percent for Alt 2A and 6 percent for Alt 2B. At distances greater than 0.5 mile, the change in the south-directed transport rate is less than 5 percent for both alternatives.

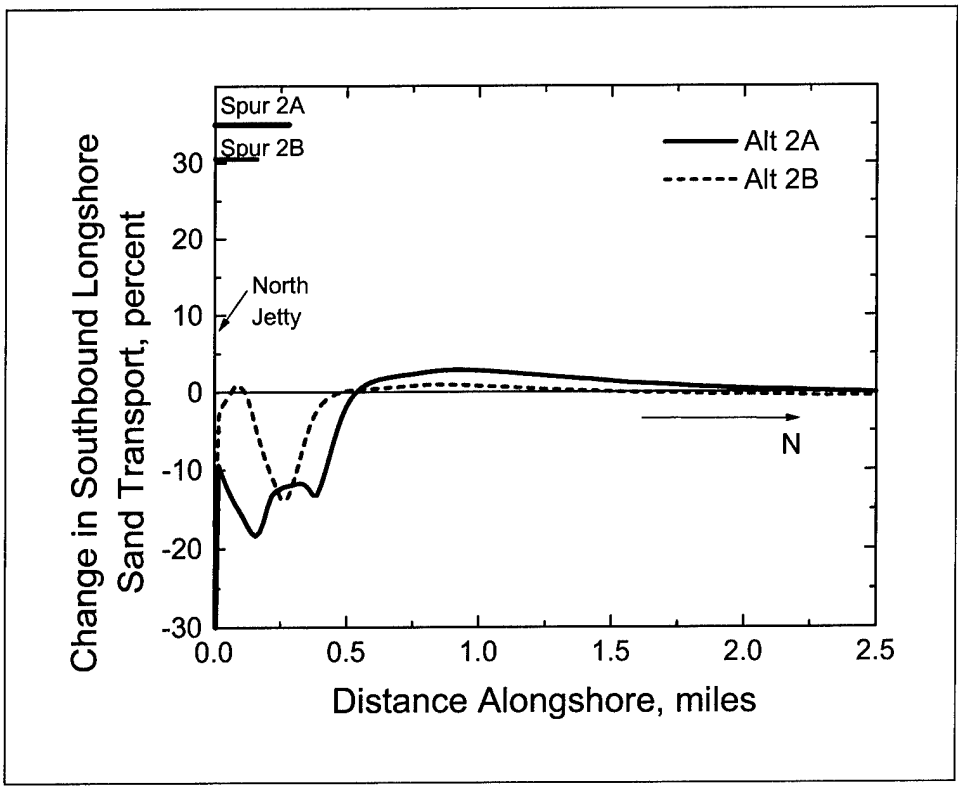

Figure 6-12. Short-term percent change in south-directed transport relative to Alt 1 for K_1 value equal to 0.11

For both spurs, the wave diffraction alters wave angle and drives greater volumes of sand behind the spur, where it is then impounded at the jetty. Although the south-directed transport approaching the jetty may be increased due to changes in wave angle, volume of bypassed sand, which is controlled in the model by wave height at the jetty, is reduced due to reduced wave heights in the lee of the spur. The bypassing rate resulting only from longshore processes is reduced by about 33 percent for both Alt 2A and Alt 2B from 45,000 cu yd/year to about 30,000 cu yd/year. The GENESIS-T model is not capable of estimating the change in the volume of bypassed sand that is associated with the cross-shore rip current. However, an increase in the south-directed longshore transport may supply additional sediment to the rip that could then be carried out and around the jetty tip. The overall effectiveness of the spur at reducing sand entering the inlet depends, therefore, on its functioning to alter the cross-shore flow and its sand trapping capability. Bypassing calculations that consider longshore and cross-shore processes are presented in Chapters 7 and 8.

A 30-year simulation was run to determine the long-term results of spur construction. Figure 6-13 is a plot of the long-term change in shoreline position relative to Alt 1. The results are similar to those for the short-term simulation with the longshore extent of shoreline benefit of spur construction again independent of spur length. The cross-shore extent of change is greater for Alt 2A. The 30-year simulation shows a positive change in shoreline position both in the lee of the spur and north of the spur relative to the short-term simulations.

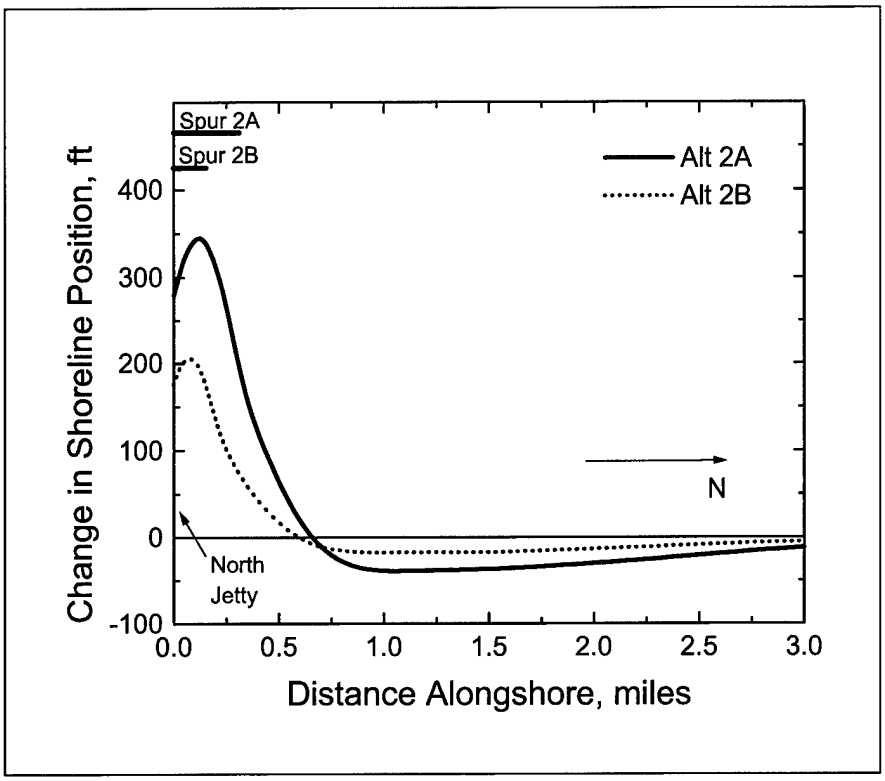

Figure 6-13. Long-term change in shoreline position relative to Alt 1

The average annual transport rate over the last 4 years of the 30-year simulation was computed for each alternative to determine the long-term influence of the spur on longshore transport. The long-term percent change in southbound transport is similar to the short-term change for both spur alternatives. The average estimated bypassing volume over the last 4 years of the 30-year simulation for the existing condition was about 47,000 cu yd/year. The bypassed volume for both spur alternatives over that same time period is reduced by about 15 percent versus Alt 1.

Jetty rehabilitation (Alts 3A and 3B)

The north jetty is currently about 1,600 ft shorter than the authorized length. Rehabilitating the jetty to its authorized length is a second alternative for reducing channel sedimentation and coastal erosion. Two rehabilitation alternatives were evaluated with the calibrated GENESIS-T model. The first, Alt 3A, is a partial rehabilitation from sta 160+00 to sta 165+00. Alt 3B proposes a full rehabilitation to sta 170+00.

A 5-year simulation was run relative to Alt 1 applying the calibrated GENESIS-T model to evaluate the short-term shoreline and longshore transport changes caused by jetty rehabilitation. A plot of the relative short-term change in shoreline positions is given in Figure 6-14. The change in shoreline position is similar to the changes induced by the spur configurations with positive shoreline position change relative to Alt 1 within about 0.5 mile of the jetty. Alt 3A has

a maximum change of 140 ft, and the full rehabilitation (Alt 3B) produces a shoreline that is located as much as 250 ft seaward of Alt 1. At distances between about 0.5 and 2.5 miles north of the jetty, shoreline change relative to Alt 1 is negative, with the maximum occurring about 0.75 mile north of the jetty for both alternatives. The maximum negative change in shoreline position relative to Alt 1 is -30 ft for Alt 3A and -55 ft for Alt 3B.

The change in shoreline position relative to Alt 1 after 30 years is plotted in Figure 6-15. The cross-shore extent of relative shoreline advance adjacent to the jetty is similar to the short-term results. The changes to the north are reduced when compared to the short-term simulations.

The net longshore transport for both rehabilitation alternatives is similar to the existing condition results shown in Figure 6-10. The relative percent change in south-directed transport is given in Figure 6-16. The results for Alt 3A and Alt 3B are similar. At distances greater than about 0.5 mile north of the jetty, the change in south-directed transport is generally less than 5 percent. Within 750 ft of the jetty, the potential for southbound transport is increased to a maximum of 16 percent for Alt 3A and 22 percent for Alt 3B. The average relative percent increase in south-directed transport within 750 ft of the jetty is 7.5 percent for both Alt 3A and Alt 3B. From 750 ft to about 0.5 mile north of the jetty, the potential for south-directed transport is reduced. The short-term results are representative of the change in southbound transport after 30 years.

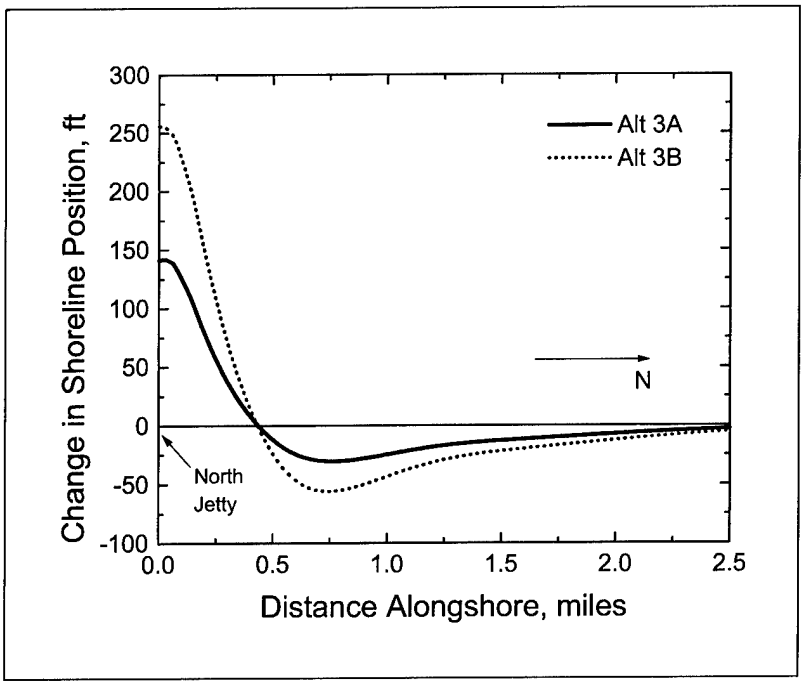

Figure 6-14. Short-term change in shoreline position relative to Alt 1

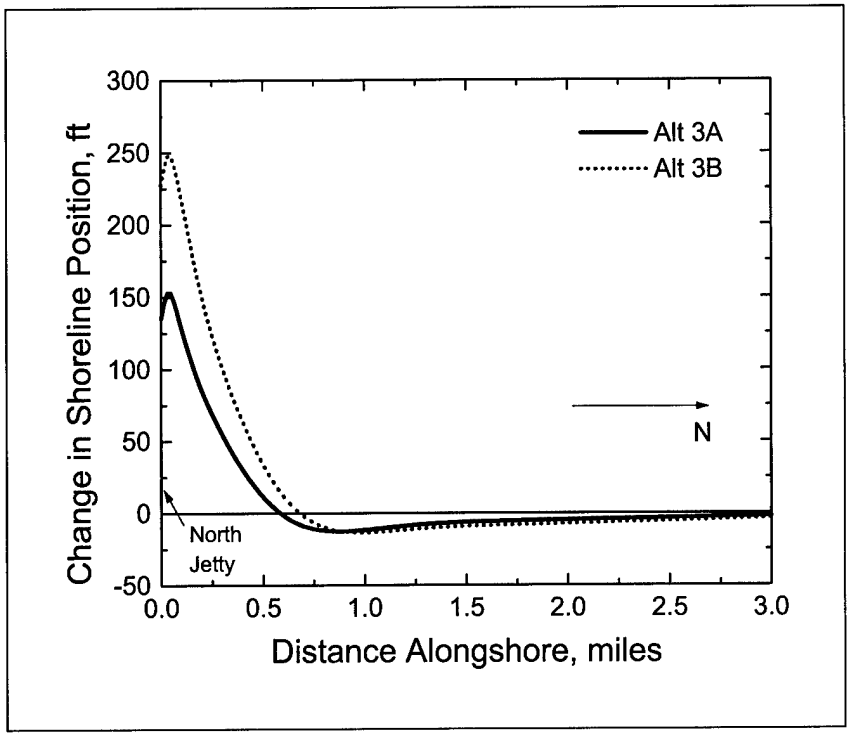

Figure 6-15. Long-term change in shoreline position relative to Alt 1

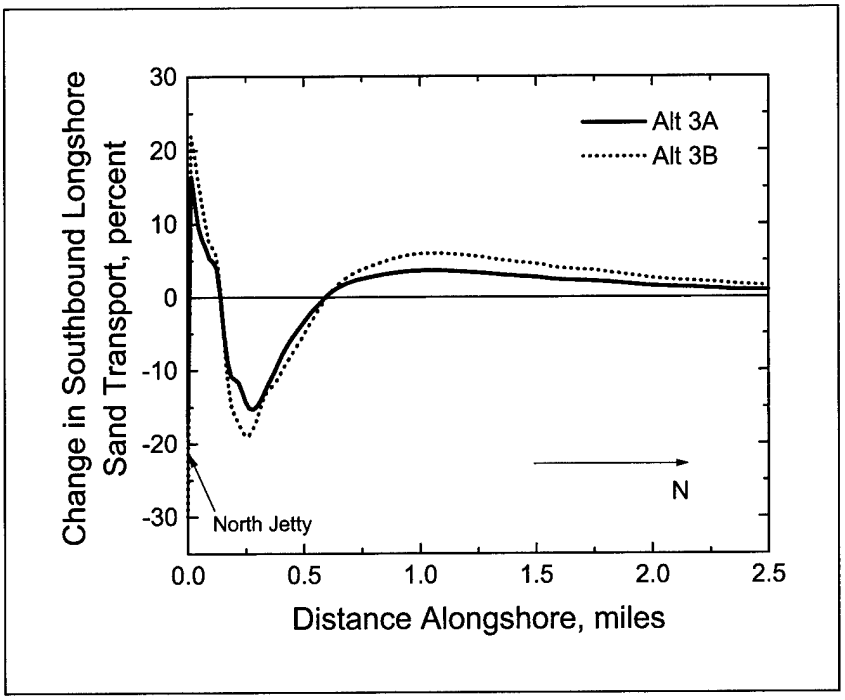

Figure 6-16. Short-term percent change in south-directed transport relative to Alt 1

Rehabilitating the jetty extends the emergent portion farther seaward and helps reduce bypassing. The model predicts that Alt 3A and Alt 3B will reduce bypassing attributable only to longshore processes by about 17 and 30 percent, respectively. The model does not represent the bypassing that was simulated as a cross-shore sink. It is reasonable, however, to assume that extension of the jetty farther seaward would trap a portion of the sediment carried seaward by the rip and further reduce the volume of bypassed sediment.

Combination structure (Alt 4)

Alternative 4 is a combination of Alt 3A and Alt 2B. The short- and long-term relative change in shoreline positions are plotted in Figure 6-17. Positive shoreline position change is predicted adjacent to the jetty with a corresponding negative change in shoreline position relative to Alt 1 farther north. The cross-shore extent of the negative shoreline change is reduced for the long-term simulation.

The net longshore transport is similar to that of Alt 2B in Figure 6-10. The relative change in short-term south-directed longshore sand transport is plotted in Figure 6-18 and is representative of the long-term change. Similar to Alt 2A and Alt 2B, the southbound transport is sensitive to K_1. The average relative change in southbound transport within 0.5 mile of the jetty is bounded by an approximately 11 percent increase and 10 percent decrease. The model predicts that Alt 4 will reduce sediment bypassing the north jetty attributable to longshore processes by only 50 percent relative to Alt 1.

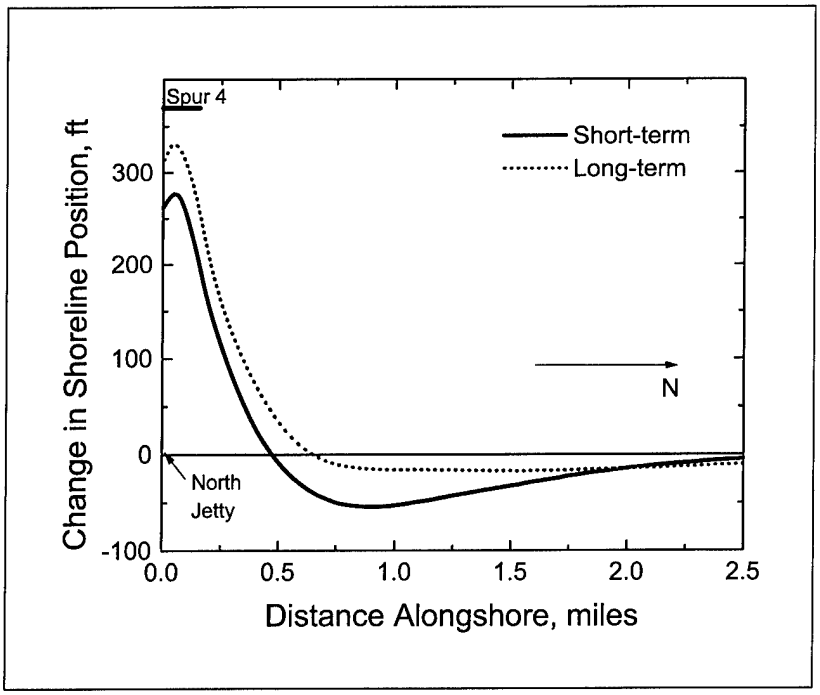

Figure 6-17. Short- and long-term changes in shoreline position for Alt 4 relative to Alt 1

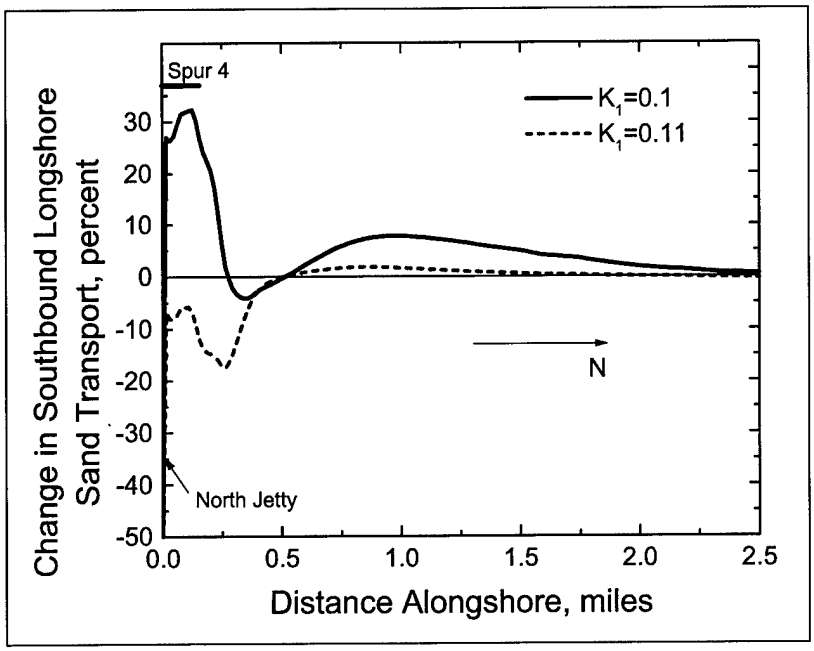

Figure 6-18. Short-term percent change in south-directed longshore transport for Alt 4 relative to Alt 1 for different values of K_1

Sensitivity analysis

An analysis was performed to assess the sensitivity of the shoreline and longshore transport response to changes in wave height and direction. GENESIS-T simulations for each alternative were driven with the modified incident wave cases listed in Table 6-4. The purpose is to understand how each structural alternative responds to changes in the incident waves and the consequences of those changes on the longshore processes. To isolate the sensitivity of results due solely to the structural alternative, the change relative to Alt 1 for each alternative and wave case was evaluated and discussed relative to the change obtained with the representative wave condition.

Table 6-4
Incident Wave Cases for Sensitivity Analysis

Wave Case	Description
REP	Representative waves
WAV1	Increase the REP wave heights by 10 percent
WAV2	Decrease the REP wave heights by 10 percent
WAV3	Adjust the REP wave angle such that waves approach from a 5 deg more southerly direction
WAV4	Adjust the REP wave angle such that waves approach from a 5 deg more northerly direction

A plot of the relative change in shoreline positions over a 5-year simulation of Alt 2A is given in Figure 6-19 for each wave case. Overall, the system response is similar for all wave cases. The cross-shore extent of shoreline change varies depending on the wave case. The system is more sensitive to increases in wave height (WAV1) and a rotation of wave propagation such that waves approach from a more northerly direction (WAV4) than it is to a reduction in wave height (WAV2) or to waves approaching from a more southerly direction (WAV3). Incident wave cases WAV1 and WAV4 transport greater volumes of sand to the south, and it is impounded at the jetty behind the spur. The spur holds the additional volume of sand, advancing the shoreline in the lee of the structure relative to the REP wave case. Because greater sand volume is held behind the spur, a reduced volume is available farther to the north and increased shoreline recession is obtained at that location relative to the REP wave case. The system appears to be comparatively insensitive to moderate decreases in wave height and waves that come from a more southerly direction. These waves tend to reduce the south-directed transport and sand supply to the area behind the spur is decreased. Wave diffraction around the spur regulates northbound transport behind the structure and a similar volume of sand is retained for the WAV2 and WAV3 cases as is for the REP case, resulting in comparatively little relative shoreline position change.

The relative change in shoreline positions over a 5-year simulation of Alt 2B is plotted in Figure 6-20 for each wave case. The overall system response is again similar for all wave cases. Similar to Alt 2A, the Alt 2B spur retains sand, advancing the shoreline in the lee of the structure relative to the REP wave case. A smaller volume is retained behind the spur relative to Alt 2A because the Alt 2B spur is shorter and produces less wave diffraction and wave sheltering.

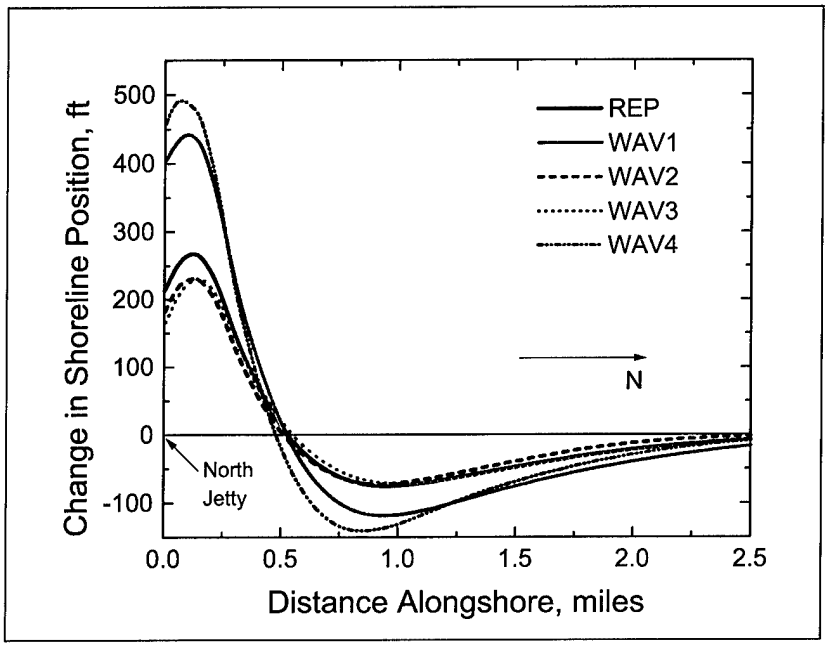

Figure 6-19. Change in shoreline position for Alt 2A relative to Alt 1 for various wave cases

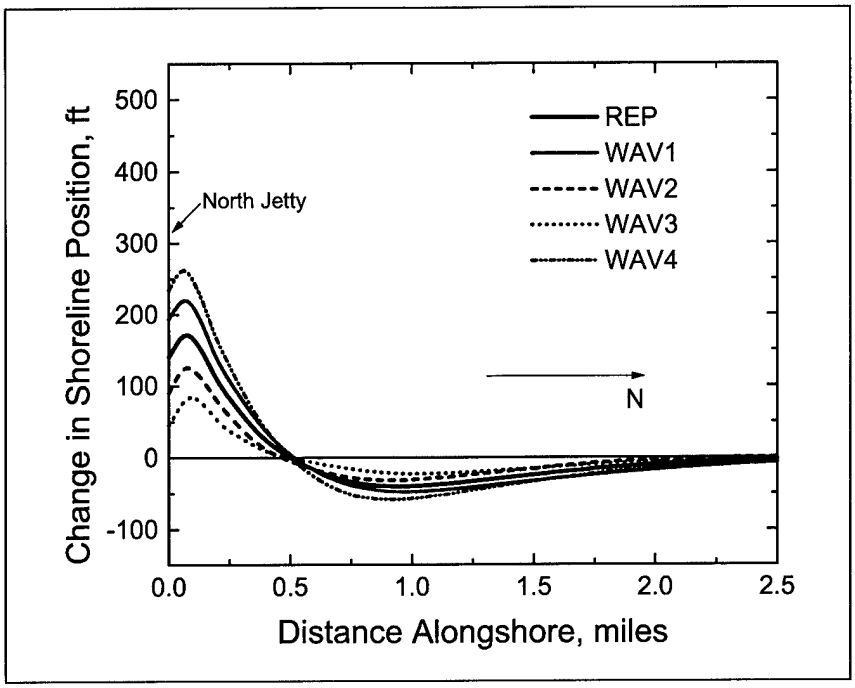

Figure 6-20. Change in shoreline position for Alt 2B relative to Alt 1 for various wave cases

The jetty rehabilitation alternatives Alt 3A and Alt 3B respond in a similar manner to changes in incident wave cases. The responses differ only in that the cross-shore extent of the changes for Alt 3A are less than those obtained for Alt 3B. A plot of the change in shoreline positions of Alt 3B relative to Alt 1 over a 5-year simulation is shown in Figure 6-21 for each wave case and is representative of the changes for Alt 3A. The overall system response is similar for the various wave cases. The shoreline response to the jetty rehabilitation is insensitive to changes in wave height. Adjusting the wave angle alters the diffraction pattern of the jetty and does produce changes in the shoreline response. Rotating the direction of wave propagation such that waves approach from a 5 deg more southerly direction (WAV3) results in greater shoreline advance relative to Alt 1 when compared to the REP waves. This change in wave angle enlarges the zone of wave diffraction relative to REP, which reduces transport away from the jetty. Waves that approach from 5 deg more northerly directions have a smaller diffraction zone than the REP wave case when the waves propagate from the south, promoting greater transport to the north away from the jetty. The result is shoreline change relative to Alt 1 that is comparatively less than the change for the REP wave case.

The overall response of the shoreline to Alt 4 is similar for all wave cases and the other alternatives. A plot of the change in shoreline positions relative to Alt 1 over a 5-year simulation of Alt 4 is given in Figure 6-22 for each wave case. The sensitivity of Alt 4 to changes in wave height (wave cases WAV1 and WAV2) is similar to the sensitivity of Alt 2B. This is expected because the response of the jetty rehabilitation alternatives does not change with changes in wave height. Alt 4 is the least sensitive structural alternative to changes in wave

direction. If the wave angle is adjusted so that waves approach from a more southerly direction (WAV3), less sand is impounded at the jetty by waves that approach from the north and less is therefore retained by the spur. The extended jetty and more oblique wave angle produce greater wave diffraction, however, which reduces sand transport from behind the spur when waves approach from the south and the shoreline change relative to the REP wave case is reduced. If the wave angle is adjusted so that waves approach from a more northerly direction (WAV4), waves that approach from the north impound a greater volume at the jetty and a portion is held by the spur. For waves that approach from the south, the change in wave angle shrinks the diffraction zone, promoting transport away from the jetty relative to the REP wave case. The result is less shoreline change relative to Alt 1 when compared to the REP wave case.

In summary, the overall response of each structural alternative is similar for all wave cases. Changes in the incident wave height and direction alter only the cross-shore extent of the shoreline changes relative to Alt 1. If additional volumes of sand are transported to the south, Alt 2A and Alt 2B retain a portion of that additional volume in the lee of the spur. Alt 3A and Alt 3B are less sensitive to changes in the incident waves than are the spur alternatives. Alt 4 is the least sensitive alternative to changes in the wave environment.

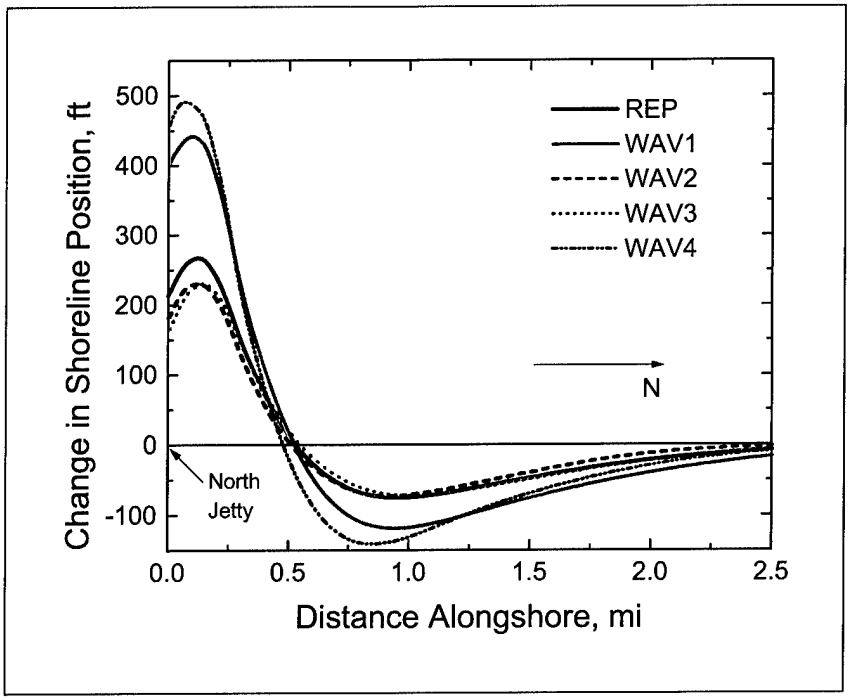

Figure 6-21. Change in shoreline position for Alt 3B relative to Alt 1 for various wave cases

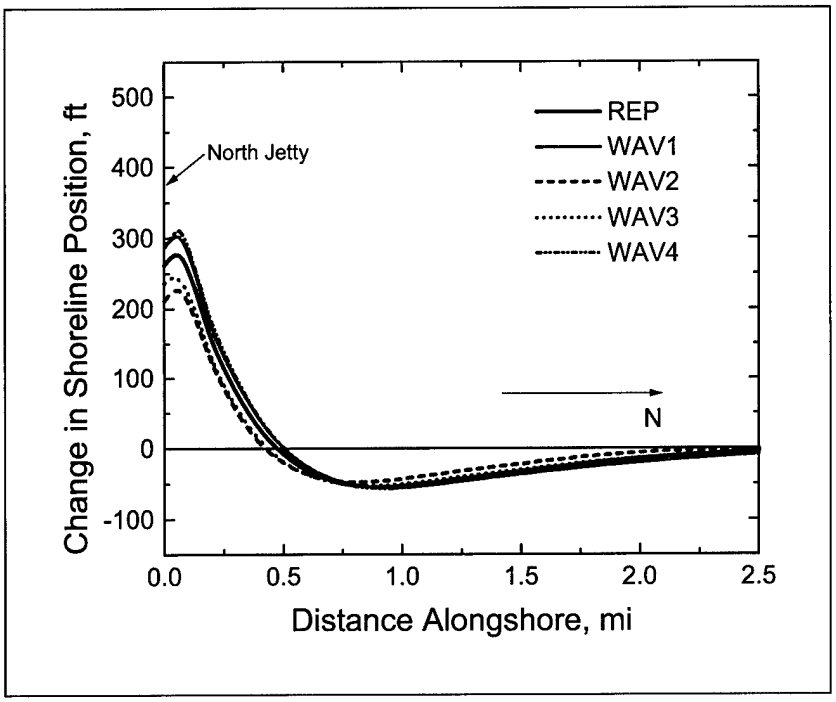

Figure 6-22. Change in shoreline position for Alt 4 relative to Alt 1 for various wave cases

Discussion

The energetic wave climate at Grays Harbor transports large volumes of sand to the north in winter and to the south in summer. A schematic of the sediment pathways and transport rates is given in Figure 6-23. The gross transport rate estimate is approximately 1 to 2 million cu yd/year within 3 miles of the jetty. The predominant direction of transport is to the north with a reversal to the south within 2,000 ft of the north jetty. The net north-directed transport increases from the reversal point and levels off 3 miles from the jetty to approximately 500,000 cu yd/year (approximately 800,000 cu yd/year to the north and 300,000 cu yd/year to the south). Directly adjacent to the jetty, the south-directed transport reaches 900,000 cu yd/year, and the net longshore transport is approximately 200,000 cu yd/year to the south. This gradient in transport promotes a sediment deficit at the beach north of Grays Harbor. The deficit has been satisfied in modern time by cross-shore transport of material supplied to the beaches from the ebb shoal. The sand supplied from the deflating ebb shoal has decreased over time. The model indicates that the sand supplied from the ebb shoal averaged about 1.3 million cu yd/year from 1976-1985 and reduced to an average of 900,000 cu yd/year from 1985 to 1995. An estimated 370,000 cu yd of sand is lost from the beach to the inlet each year as sediment is transported offshore by rip currents and then carried around the jetty by the longshore current. The model indicates that approximately 85-90 percent of the volume bypassing the jetty is attributable to rip currents that carry sediment seaward of the jetty tip.

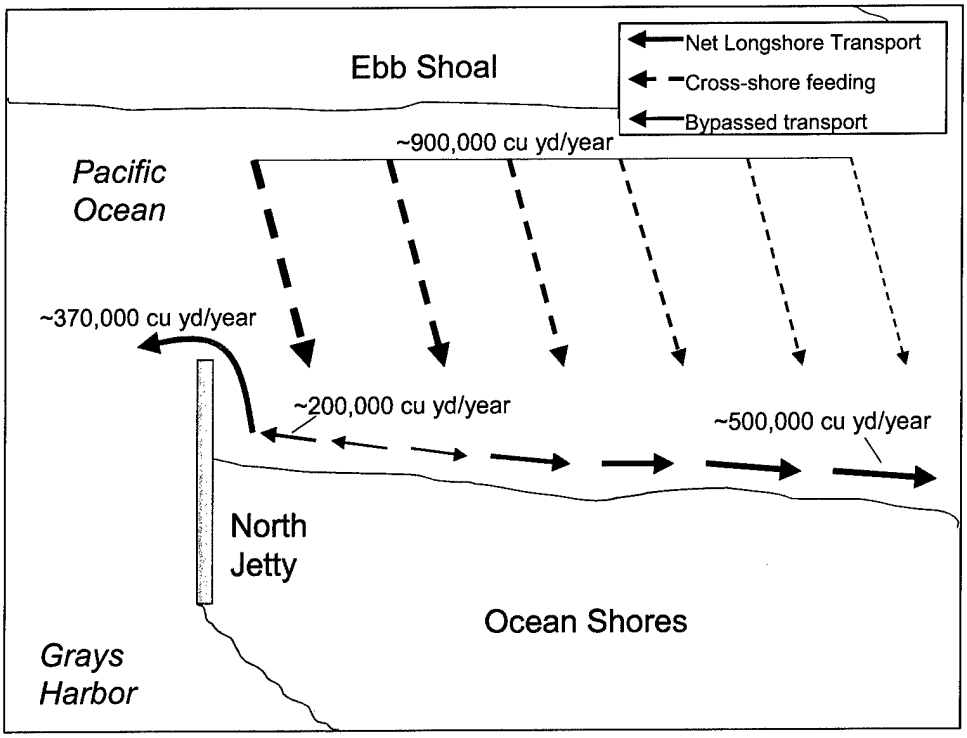

Figure 6-23. Schematic of sediment pathways and transport volumes

The recently developed GENESIS-T model was applied to evaluate five structural alternatives to determine if they reduced the potential for both sand bypassing the north jetty and shoreline erosion adjacent to the jetty. Each structural alternative was evaluated by comparing the results relative to the existing or "no-project" condition (Alt 1) and assumes no changes occur in the cross-shore processes. Therefore, the GENESIS-T analysis only considers changes in the longshore processes induced by each structure. The model results indicate that all of the proposed structural alternatives produce greater than 10 percent change in the longshore transport rate only within 0.5 mile of the jetty. Changes in transport of 10 percent or less are within the uncertainty of the model and are not considered significant. Therefore, the influence of all the alternatives is considered to be limited to within 0.5 mile of the north jetty.

The model predicts that approximately 10-15 percent of the sediment that bypasses the north jetty is attributable to longshore transport. All the evaluated structural alternatives reduced the bypassing relative to the existing condition attributable only to longshore transport. The spur alternatives (Alt 2A and Alt 2B) reduce bypassing by 33 percent, Alt 3A by 17 percent, Alt 3B by 30 percent, and Alt 4 by 50 percent. The volume of sand bypassing the north jetty and entering the inlet is primarily governed by cross-shore flow in rip currents at the jetty. An increase in south-directed transport may supply additional sediment to the rips that can then be carried seaward and transported around the jetty tip. The average percent change in south-directed transport within 2,000 ft of the jetty relative to Alt 1 is between a 20 percent increase and 15 percent reduction for the alternatives that include a spur (Alt 2A, Alt 2B, and Alt 4).

There is only a small change (a 5 percent reduction) in the average south-directed transport within 2,000 ft of the jetty for the jetty rehabilitation alternatives. The average was computed within 2,000 ft because that is the area in where rip currents are commonly observed near the jetty, and transport changes in this area may result in changes to the bypassed sand volume. An assessment of the overall effectiveness of the spur at reducing sand entering the inlet must consider its functioning to alter cross-shore flow. Analysis of the changes in cross-shore flow induced by the spur was conducted in associated studies with the physical model and other numerical models and the results are presented in Chapters 5, 7, and 8. Estimates of changes in bypassing that consider cross-shore flows are given in Chapters 7 and 8.

The shoreline response is similar for all five structural alternatives. Each alternative tends to promote beach accretion relative to Alt 1 adjacent to the jetty. The shoreline response for the various alternatives only differed in the cross-shore extent of the shoreline changes. The larger structures (Alt 2A and Alt 3B) and the combination structure (Alt 4) create the greatest change, with maximum changes in shoreline position relative to Alt 1 of approximately 250 ft. The smaller structures (Alt 2B and Alt 3A) also produce shoreline advance relative to Alt 1 with maximum advance of approximately 150 ft. The relative shoreline advance is greatest at the jetty and tapers off to the north. The predicted shoreline change is on the order of the measured 70 to 200 ft of seasonal and interannual shoreline variability. Therefore, the shoreline changes produced by any of the alternatives may be subtle when considering the natural variability in the system.

References

Ahrens, J. P. (2001). "Wave transmission over and through rubble-mound breakwaters," Contract Report submitted to the Coastal and Hydraulics Laboratory, U.S. Army Engineer Research and Development Center, Vicksburg, MS.

Bagnold, R. A. (1963). "Mechanics of marine sedimentation," in *The Sea,* Vol 3, Interscience, M. N. Hill (ed.), New York, 507-528.

Bouws, E., Gunther, H., Rosenthal, W., and Vincent, C. L. (1985). "Similarity of the wind wave spectrum in finite depth waves; 1. Spectral form," *Journal of Geophysical Research* 90(C1), 975-986.

Brigham Young University Engineering Computer Graphics Laboratory. (1997). "Surface-water modeling system reference manual," Brigham Young University, Provo, UT. (http://hlnet.wes.army.mil/software/sms/doc.htp)

Dean, R. G. (1977). "Equilibrium beach profiles: U.S. Atlantic and Gulf coasts," Ocean Engineering Report No. 12, Department of Civil Engineering, University of Delaware, Newark, DE.

Goda, Y., Takayama, T., and Suzuki, Y. (1978). "Diffraction diagrams for directional random waves," *Proceedings 16th Coastal Engineering Conference,* American Society of Civil Engineers (ASCE), 628-650.

Gravens, M. B., and Kraus, N. C. (1991). "Genesis: Generalized model for simulating shoreline change, Report 2: Workbook and system user's manual," Technical Report CERC-89-19, Coastal Engineering Research Center, U.S. Army Engineer Waterways Experiment Station, Vicksburg, MS.

Gravens, M. B., Scheffner, N. W., and Hubertz, J. M. (1989). "Coastal processes from Asbury Park to Manasquan, New Jersey," Miscellaneous Paper CERC-89-11, Coastal Engineering Research Center, U.S. Army Engineer Waterways Experiment Station, Vicksburg, MS.

Hallermeier, R. J. (1978). "Uses for a calculated limit depth to beach erosion," *Proceedings 16th Coastal Engineering Conference,* ASCE, 1493-1512.

Hallermeier, R. J. (1981). "A profile zonation for seasonal sand beaches from wave climate," *Coastal Engineering* 4, 253-277.

Hanson, H., and Kraus, N. C. (1989). "GENESIS: Generalized model for simulating shoreline change, Report 1: Technical reference," Technical Report CERC-89-19, Coastal Engineering Research Center, U.S. Army Engineer Waterways Experiment Station, Vicksburg, MS.

_____. (1990). "Shoreline response to a single transmissive detached breakwater," *Proceedings 22nd Coastal Engineering Conference*, ASCE, 2,034-2,046.

_____. (1993). "Offshore bathymetry and time step in shoreline response numerical models," *Large-Scale Coastal Behavior '93*, U.S. Geological Survey, Open-File Report 93-381, 58-60.

_____. (2000). "Representation of tombolos and sediment transport by tidal current in the GENESIS model," *Proceedings 13th National Conference on Beach Preservation Technology*, Florida Shore and Beach Preservation Association, 64-80.

Hanson, H., Kraus, N. C., and Nakashima, L. D. (1989). "Shoreline change behind transmissive detached breakwaters," *Proceedings Coastal Zone '89*, ASCE, 568-582.

Kaminsky, G. M., Buijsman, M., Gelfenbaum, G., Ruggiero, P., Jol, H. M., Gibbs, A. E., and Peterson, C. D. (1999a). "Synthesizing geological observations and processes-response data for modeling coastal change at management scale," *Proceedings of Coastal Sediments '99*, ASCE, 1,660-1,675.

Kaminsky, G. M., Daniels, R. C., Huxford, R., McCandless, D., and Ruggiero, P. (1999b). "Mapping erosion hazards in Pacific County, Washington," *Journal of Coastal Research,* Special Issue 28.

Kaminsky, G. M., Buijsman, M. C., and Ruggiero, P. (2000). "Predicting shoreline change at decadal scale in the Pacific Northwest, USA," *Proceedings 27th Coastal Engineering Conference*, ASCE, 2,400-2,413.

Kraus, N. C. (1981). "One-line development and simulation for Oarai Beach," NERC Report No. 13, Cooperative Research of Surf Zone Dynamics, Part 3: Beaches Near Breakwaters and Rocky Coasts, Nearshore Environment Research Center, Tokyo, Japan, 155-192.

_____. (1982). "Pragmatic calculation of the breaking wave height and wave angle behind structures," *Proceedings 29th Japanese Coastal Engineering Conference,* Japan Society of Civil Engineers, 295-299 (in Japanese).

_____. (1984). "Estimate of breaking wave height behind structures," *Journal of Waterway, Port, Coastal, and Ocean Engineering* 110(2), 276-282.

_____. (1988). "Part IV: Prediction models of shoreline change," Chapter 2, Wave Model, in *Nearshore Dynamics and Coastal Processes: Theory, Measurement, and Predictive Models,* K. Horikawa (ed.), University of Tokyo Press, Tokyo, Japan, 324-328.

Kraus, N. C., and Harikai, S. (1983). "Numerical model of the shoreline change at Oarai Beach," *Coastal Engineering* 7(1), 1-28.

Luettich, R. A., Westerink, J. J., and Scheffner, N. W. (1992). "ADCIRC: An advanced three-dimensional circulation model for shelves, coasts, and estuaries, Report 1: Theory and methodology of ADCIRC-2DD1 and ADCIRC-3DL," Technical Report DRP-92-6, U.S. Army Engineer Waterways Experiment Station, Vicksburg, MS.

Ozasa, H., and Brampton, A. H. (1980). "Mathematical modeling of beaches backed by seawalls," *Coastal Engineering* 4(1), 47-64.

Pope, J. (1991). "Ebb delta and shoreline response to inlet stabilization, examples from the southeast Atlantic coast," *Proceedings Coastal Zone '91,* ASCE, 643-654.

Resio, D. T. (1988). "A steady-state wave model for coastal applications," *Proceedings 21st Coastal Engineering Conference,* ASCE, 929-940.

Ruggiero, P., and Voigt, B. (2000). "Beach monitoring in the Columbia River littoral cell, 1997-2000," Publication No. 00-06-26, Coastal Monitoring & Analysis Program, Washington Department of Ecology, Olympia, WA.

Smith, J. M., Sherlock, A. R., and Resio, D. T. (2001). "STWAVE: Steady-state spectral wave model user's manual for STWAVE version 3.0," ERDC/CHL SR-01-1, Coastal and Hydraulics Laboratory, U.S. Army Engineer Research and Development Center, Vicksburg, MS.

Wamsley, T. V., and Hanson, H. (2002). "Evaluation of proposed submerged jetty spur on shoreline evolution, Grays Harbor, Washington," *Proceedings 28th International Coastal Engineering Conference,* Vol. 3, World Scientific, 2,625-2,637.

Wei, G., Kirby, J. T., Grilli, S. T., and Subramanya, R. (1995). "A fully nonlinear Boussinesq model for surface waves, I: Highly nonlinear, unsteady waves," *Journal of Fluid Mechanics* 294, 71-92.

Zyserman, J. A., and Johnson, H. K. (2002). "Modelling morphological processes in the vicinity of shore-parallel breakwaters," *Coastal Engineering* 45, 261-284.

7 Wave, Circulation, and Sediment Transport Modeling[1]

Wave, circulation, and sediment transport models were established and calibrated for the Grays Harbor, WA, area and then applied in the present study. This chapter first describes the wave and circulation models and their implementation at Grays Harbor, followed by discussion and interpretation of model calculations. The wave and circulation models provide input for forcing sediment transport models. Linkage of the tidal circulation and wave models within the Surface-water Modeling System (SMS) (Zundel, Cialone, and Moreland 2002) framework provides the capability of simulating tidal and wave-induced currents for the Grays Harbor entrance and is described in this chapter. Five project alternatives as defined in Chapter 1 are evaluated based on changes to the tidal and wave-induced currents. Topics contained in this chapter include a general description of the study area, previous model studies, hydrodynamic model description, wave model description, grid development, model calibration, linkage of the wave and circulation models, sediment transport pathway calculations, and application of the models to evaluate project alternatives.

Sediment transport is evaluated by two methods in this study. In the first, a Lagrangian sediment transport model, PSed (Davies, Serrer, and Watson 2000) was applied to the simulated currents from the wave and current model to identify sediment mobility and particle paths between the north jetty, Grays Harbor inlet, and the navigation channel for appropriate sediment size distributions. The second method analyzes localized sediment transport rates, bypassing rates, and pathways at the north jetty, as described in Chapter 8.

Circulation model results obtained from the combined wave and current interaction within the Steering Module are contained in Appendix E. The governing equations for all models described in this chapter are contained in Appendix H.

[1] Written by Mary A. Cialone, U.S. Army Engineer Research and Development Center, Coastal and Hydraulics Laboratory, Vicksburg, MS; and Michael H. Davies and Philip D. Osborne, Pacific International Engineering, PLLC, Seattle, WA.

Oceanographic Setting of Grays Harbor

The oceanographic and nearshore setting at Grays Harbor is fully described in Chapter 4 and is reviewed here to summarize the processes that contribute to the hydrodynamics and sediment transport in this area.

Water movement in Grays Harbor is driven by tide, wind, waves, and freshwater inflows. Continental shelf processes, such as the Columbia River freshwater plume and upwelling (Sternberg 1986; Landry et al. 1989; Hickey 1989) modify flow and transport inside Grays Harbor. Columbia River freshwater inflow and upwelling are not represented in this modeling effort because these processes are secondary to tide, wind, and wave-generated currents. Episodic events such as winter storms and processes related to El Niño can also modify the circulation, thereby changing sediment transport processes. Specific storms are included in the circulation model calibration process.

Tides

Diurnal and semidiurnal constituents are the dominant contributors to tidal motion in Grays Harbor Bay. The primary constituents forcing the bay are M_2, K_1, S_2, O_1, SA, N_2, and P_1, in order of largest to smallest amplitude. The M_2 tidal constituent is dominant, being 2.5 times greater than the K_1 constituent at Aberdeen on the northeast side of Grays Harbor Bay. Table 7-1 lists tidal constituent amplitudes for water level at Aberdeen, Toke Point (Willapa Bay), and Neah Bay (Straits of Juan de Fuca) as calculated by the National Ocean Service (NOS), National Oceanic and Atmospheric Administration (NOAA).

Tidal data computed at gauges located in Grays Harbor are listed in Table 7-2. Values are referenced to local mean lower low water (mllw). Tidal range is defined as the difference in height between consecutive higher high and lower low water levels. At Westport, the mean tide range is 2.2 m, and the spring tide range is 2.8 m. At Aberdeen the mean tide range is 2.4 m, and the spring tide range is 3.1 m. The tide range increases from the entrance to the upper reaches of the bay because of the constriction (or funneling) as the tidal wave propagates into the bay.

Local wind and freshwater inflow

Meteorological data for the Washington coast near Grays Harbor were extracted from the NOAA National Centers for Environmental Prediction (NCEP) database (Shea et al. 1994). This database contains wind speeds and directions, at 6-hr intervals, having a spatial resolution of about 1.9 deg in latitude and longitude. Subsequent processing interpolated these winds onto a Gaussian grid having a spatial resolution of 0.25 deg. Winds were also interpolated in time, yielding hourly wind fields. Winds for this region usually propagate from north to northwest during May through September and from south to southwest during October through April. Strong winds, around 5 m/sec, are observed from November through February in normal fair-weather conditions. Because of the large tidal range of Grays Harbor, water levels are not greatly influenced by local fair-weather winds.

Table 7-1
Tidal Constituent Amplitudes at Aberdeen, Toke Point, and Neah Bay, m*

Constituent	Aberdeen	Toke Point	Neah Bay
M_2	1.12	0.98	0.79
S_2	0.29	0.26	0.23
N_2	0.23	0.20	0.17
K_1	0.44	0.43	0.50
M_4	0.05	0.02	0.01
O_1	0.27	0.26	0.31
M_6	0.04	0.01	0.01
MK_3	0.01	---	0.02
S_4	0.01	---	---
MN_4	0.02	0.01	0.01
NU_2	0.05	0.05	0.03
S_6	---	---	---
MU_2	0.03	0.01	0.02
$2N_2$	0.03	0.02	0.02
OO_1	0.01	0.01	0.02
LAM_2	0.02	0.01	0.01
S_1	0.01	0.01	0.02
M_1	0.02	0.02	0.02
J_1	0.02	0.02	0.03
M_m	---	---	---
SSA	0.05	---	0.02
SA	0.26	0.15	0.14
MSF	---	---	---
MF	---	0.02	---
RHO	0.01	0.01	0.01
Q_1	0.05	0.05	0.06
T_2	0.02	0.02	0.01
R_2	0.02	---	---
$2Q_1$	0.01	0.01	0.01
P_1	0.13	0.13	0.16
$2SM_2$	0.01	---	---
M_3	0.01	---	---
L_2	0.05	0.03	0.01
$2MK_3$	0.02	-----	0.01
K_2	0.08	0.07	0.06
M_8	0.01	---	---
MS_4	0.03	0.01	0.01

*Source: NOS http://www.opsd.nos.noaa.gov.

Table 7-2
Tidal Datums for Willapa Tide Gauges, m*

Datum	Westport	Point Brown	Aberdeen	Cosmopolis
Highest observed water level	3.4	3.5	4.2	3.8
mhhw	2.8	2.9	3.1	3.3
mhw	2.6	2.6	2.8	3.1
mtl	1.5	1.5	1.6	1.8
mlw	0.4	0.4	0.4	0.5
mllw	0.0	0.0	0.0	0.0
Lowest observed water level	-0.7	-0.7	-1.0	-0.9

*Source: (NOS http://www.opsd.nos.noaa.gov).
Note: mhhw = mean higher high water, mhw = mean high water, mtl = mean tide level, mlw = mean low water, mllw = mean lower low water.

Grays Harbor has one of the largest tidal prisms in the United States (5.5×10^8 m^3) (Johnson 1973). Freshwater inflow from the Chehalis River varies between 3 cu m/sec during the low flow months and 300 cu m/sec during the high flow months (U.S. Geological Survey [USGS] web site) (Figure 7-1). Because freshwater inflow represents less than 2 percent of the tidal prism, it was not considered in this application.

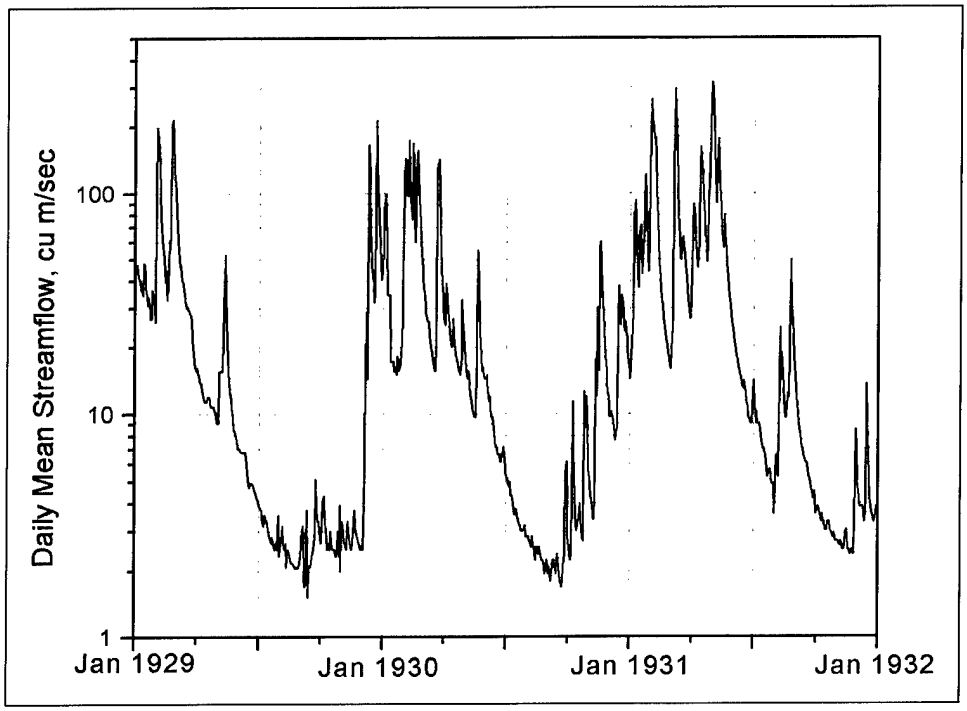

Figure 7-1. Mean daily stream flow for Chehalis River, WA (USGS 12023500)

Tidal Circulation Model

Water-surface elevation and currents were calculated by applying the hydrodynamic model Advanced CIRCulation (ADCIRC) (Luettich, Westerink, and Scheffner 1992). ADCIRC is a 2-D, depth-integrated, finite-element hydrodynamic model. It was developed with the capability of operating over a wide range of element sizes. This flexibility in grid resolution over the computational domain allows for fine resolution in the project area and coarse resolution in areas distant from the region of interest. Grid flexibility is a central operational factor to this project because the evaluation of structural alternatives requires the ability to resolve these structures in the large model domain.

Model attributes include the following capabilities:

a. Simulating tidal circulation and storm-surge propagation over large computational domains while simultaneously providing high resolution in areas of complex shoreline configuration and bathymetry. The targeted areas of interest include continental shelves, nearshore areas, and estuaries.

b. Representing all pertinent physics of the two-dimensional equations of motion. These include tidal potential, Coriolis, and all nonlinear terms of the governing equations.

c. Providing accurate and efficient computations over time periods ranging from months to years.

In two dimensions, the model is formulated with the depth-averaged shallow water equations for conservation of mass and momentum. The formulation requires that the water is incompressible and that hydrostatic pressure conditions exist. Applying standard quadratic parameterization for bottom stress and neglecting baroclinic terms and lateral diffusion/dispersion effects, a set of conservation equations in primitive, nonconservative form, are incorporated in the model. If the wave field changes slowly in time, the radiation stress gradients can be included in the momentum balance (Luettich, Westernik, and Scheffner 1992; Westerink et al. 1994; Luettich and Westerink 1999). Appendix H contains the ADCIRC governing equations.

ADCIRC Mesh Development

For hydrodynamic model simulations, the Grays Harbor study area was defined by means of an unstructured grid composed of triangular elements (Figure 7-2). The computational grid encompassed a regional area extending from 40.8 to 51.2°N and 130.5 to 122.7°W and contains 30,254 nodes and 58,231 elements. Lowest resolution was specified offshore in the Pacific Ocean, and highest resolution was specified at Grays Harbor and the surf zone for a 12-km stretch north of the north jetty. Element sizes ranged from more than 60 km in the open ocean to 25 m near the north jetty. Figure 7-2 shows the grid for the entire Grays Harbor, Figure 7-3 shows a regional view of the grid that illustrates the variation in resolution over a portion of the domain, and Figure 7-4 shows grid detail for Grays Harbor.

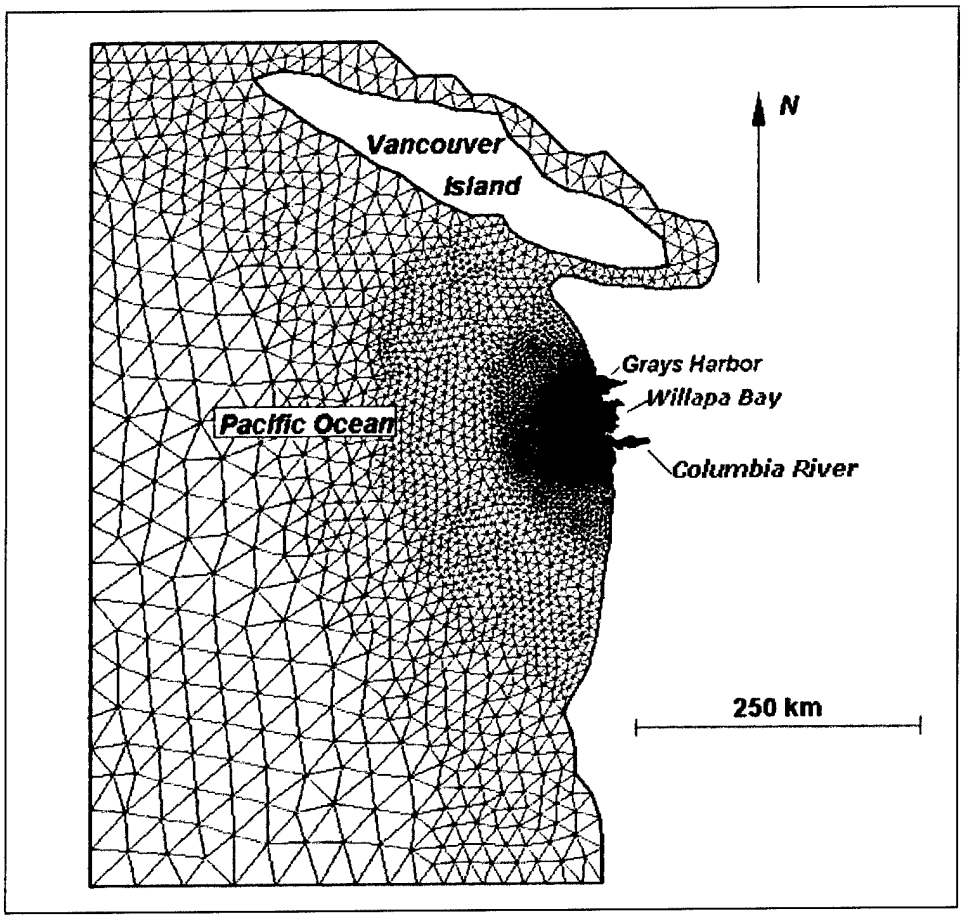

Figure 7-2. ADCIRC grid for Grays Harbor application

Shoreline data were obtained from the NOAA Medium Resolution Shoreline Database, which is composed of shoreline position information digitized from NOAA navigation charts. Although this shoreline does not represent the most recent shoreline position, the bathymetry indicates 1999 conditions, and model simulations were, therefore, for 1999 conditions. Water depths were specified at the vertices (referred to as nodes) of the triangles that compose the grid. Bathymetry data for the grid domain were obtained from several sources. NOS bathymetry data were supplied to represent the Pacific Ocean. Within Grays Harbor, high-density bathymetry data were obtained from the Seattle District. These data were collected in 1999, as described in Chapter 4. Regions of Grays Harbor not covered by the 1999 surveys have bathymetry applied from NOS navigation charts and survey data obtained from GEODAS (GEOphysical DAta System), an interactive database management system developed by the National Geophysical Data Center (NGDC) for assimilation, storage, and retrieval of geophysical data. Figure 7-5 shows bathymetry contours of Grays Harbor calculated from the composite data, and Figure 7-6 shows detail of bathymetry in the entrance. Tidal-flat elevations were estimated from NOS charts. Typical tidal-flat elevation specified in the grid is 0.5-1.5 m below mean tide level (mtl).

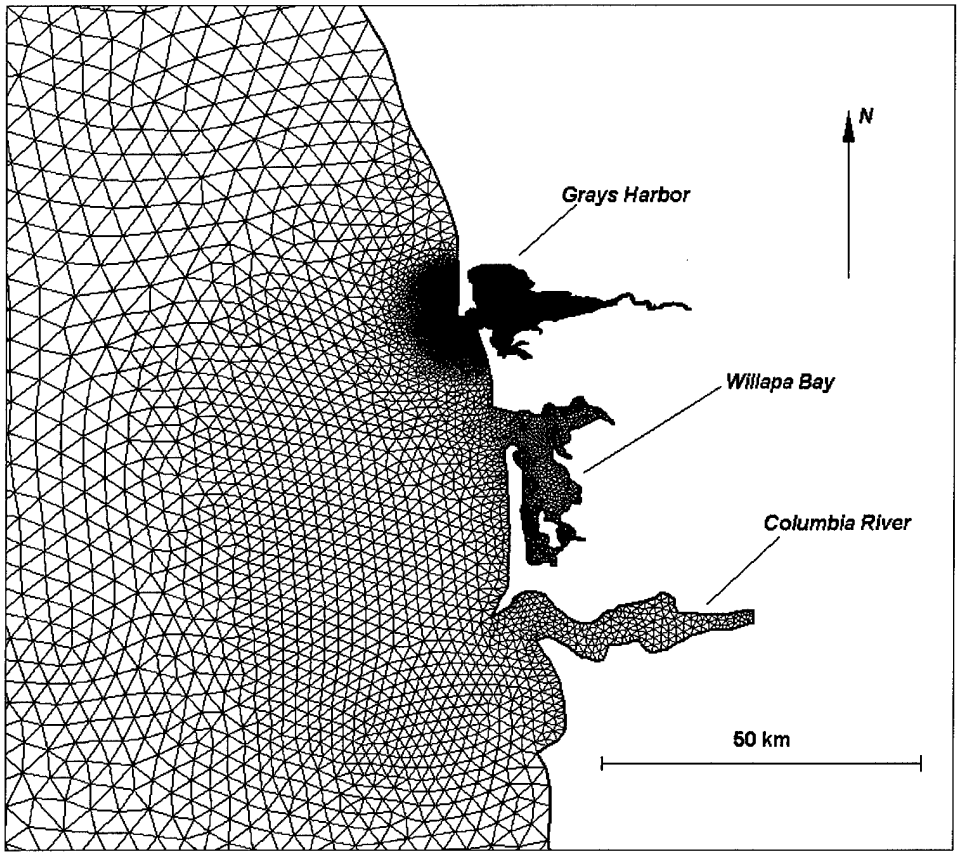

Figure 7-3. Regional view of ADCIRC grid showing variation in resolution

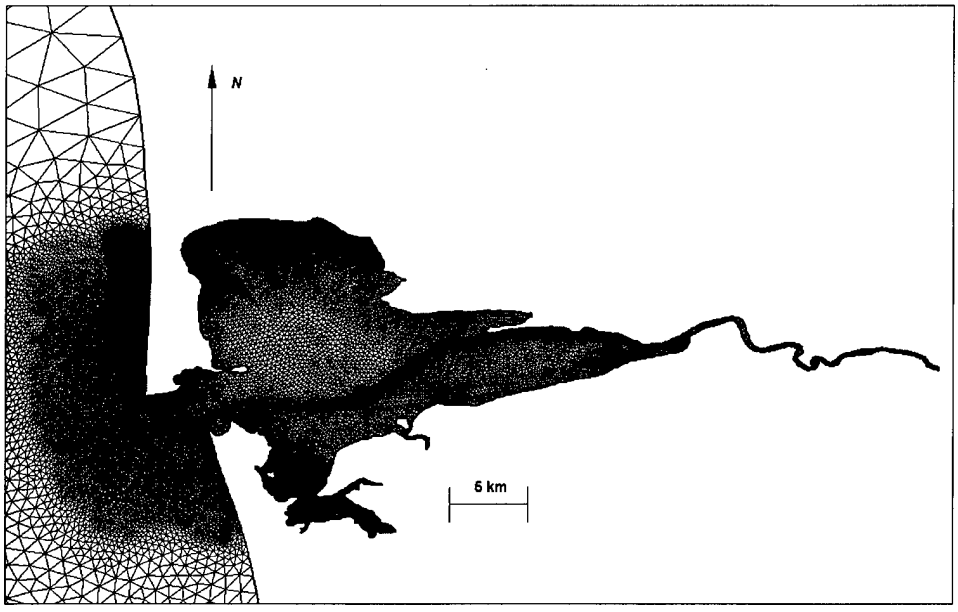

Figure 7-4. Detail of ADCIRC grid for Grays Harbor

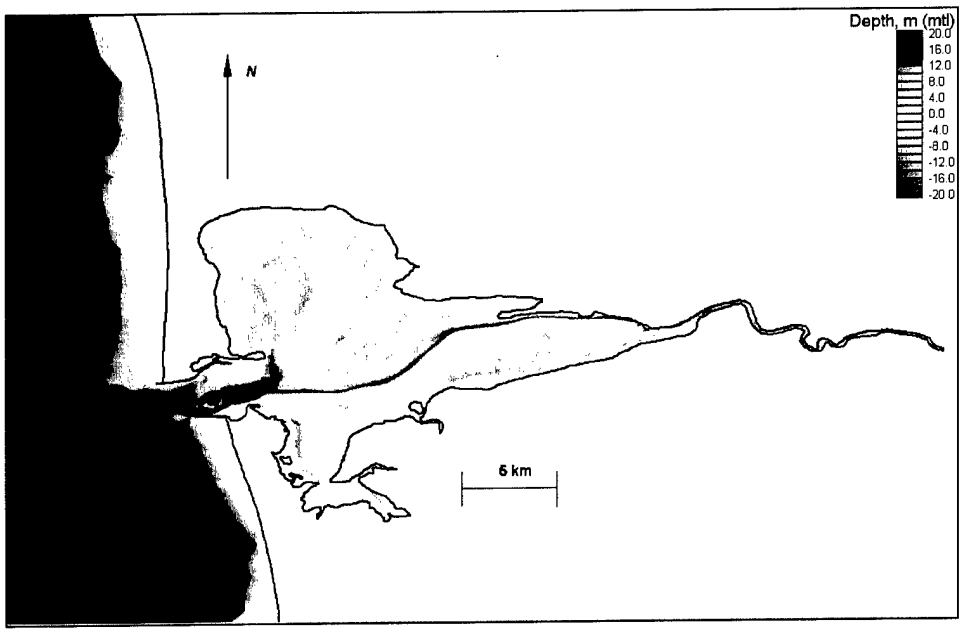

Figure 7-5. Grays Harbor Bay bathymetric contours from 1999 data

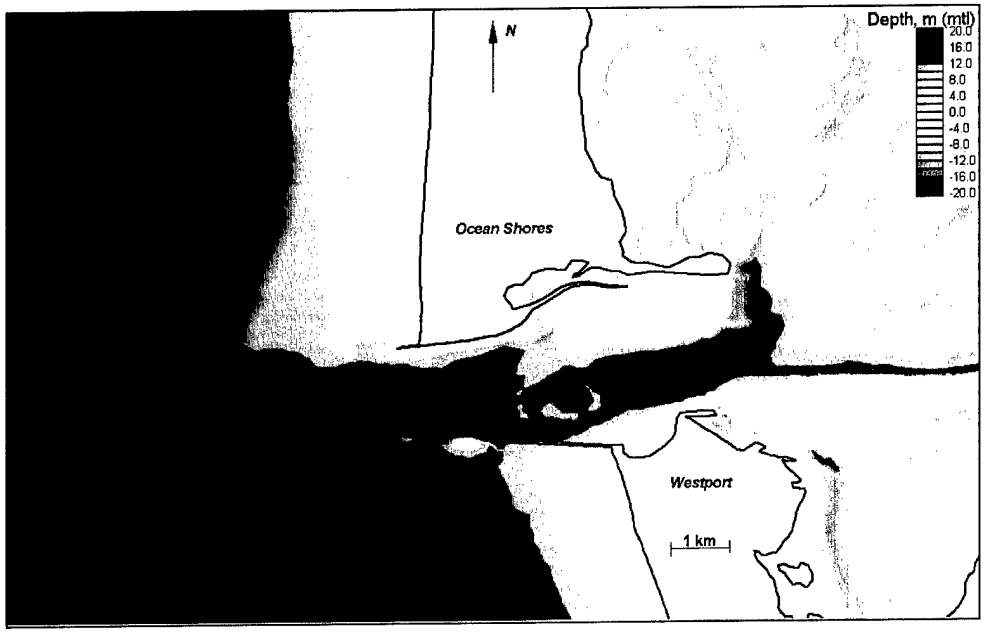

Figure 7-6. Grays Harbor entrance bathymetric contours from 1999 data. (Although this shoreline does not represent most recent shoreline position, bathymetry indicates 1999 conditions, and model simulations were, therefore, for 1999 conditions)

ADCIRC Model Calibration

Calibration of a hydrodynamic model such as ADCIRC is performed to ensure that the model can adequately predict hydrodynamic conditions in a given study area. Model accuracy depends upon the reliable solution of the governing equations, accuracy of the boundary and forcing conditions, representation of the study area geometry (bathymetry and shoreline position), and the values of certain basic parameters. A satisfactory comparison between calculations and measurements in the calibration procedure provides confidence that the model adequately replicates hydrodynamic processes in the study area.

For this study, calibration of the circulation model was accomplished by comparison of water surface elevation and current model calculations to measurements made at several locations within the Grays Harbor entrance and bay. (As described in Chapter 4, wave, water level, and current data were collected over a 2-month interval in 1999.) The calibration simulation was made for the time period corresponding to the first month of field data collection. The model was forced with tidal constituents from the LeProvost et al. (1994) tidal constituent database starting on 10 September 1999. Eight constituents (K_1, O_1, M_2, N_2, S_2, K_2, P_1, and Q_1) were selected for the free surface, tidal forcing boundary condition. NCEP wind data obtained from NOAA were also applied.

In the calibration process, it was essential to simulate the significant flooding and drying that occurs on the tidal flats of Grays Harbor, North Bay, and South Bay with each tidal cycle to ensure that the resulting hydrodynamics would be accurately modeled. In very shallow water such as the tidal flats in Grays Harbor, the application of hybrid friction is useful because the expression for hybrid friction becomes highly dissipative as water depth becomes small. Hybrid friction is calculated as a base friction value that increases exponentially as the water depth becomes shallower than a minimum threshold. User-specified parameters govern the behavior of the friction factor in deep and shallow water. Setting the shallow water parameter to 1/3 gives a Manning friction law type of behavior. For this calibration, an optimum value of bottom friction was specified as 0.003 with a minimum threshold of 1.0, asymptotic approach of 10, and friction factor increase of 0.333. A 30-day simulation with a 1.5-sec time-step was made, and model results at the measurements station locations were recorded every 15 min.

Comparison of Measured and Calculated Water Level and Current

Verification of the circulation model was conducted by comparison of water level and current calculations to measurements at monitoring stations located within the study area. As part of this study (Chapter 4), water level recording stations were located at (a) Westport, (b) South Bay, (c) North Bay, and (d) Aberdeen (Figure 7-7). Velocity recording stations located in the inlet entrance are shown in Figure 7-8. Three error calculations were made to quantify the comparisons: the mean error, root-mean-square (rms) error, and percent error. The mean error $\bar{E}$ is the arithmetic average of the difference between the calculated and measured value:

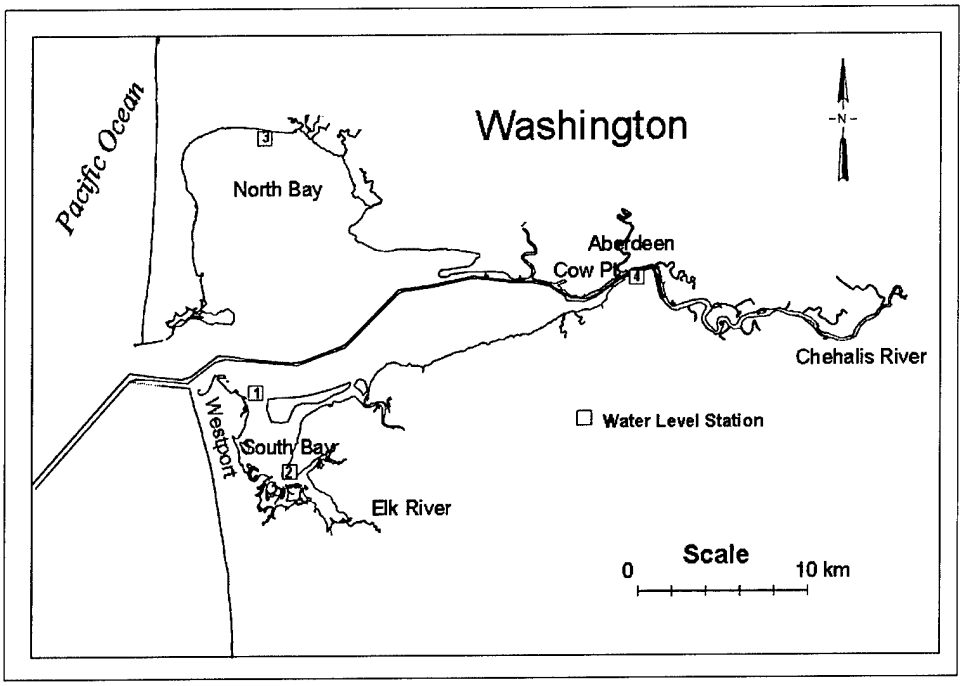

Figure 7-7. Water level measurement locations

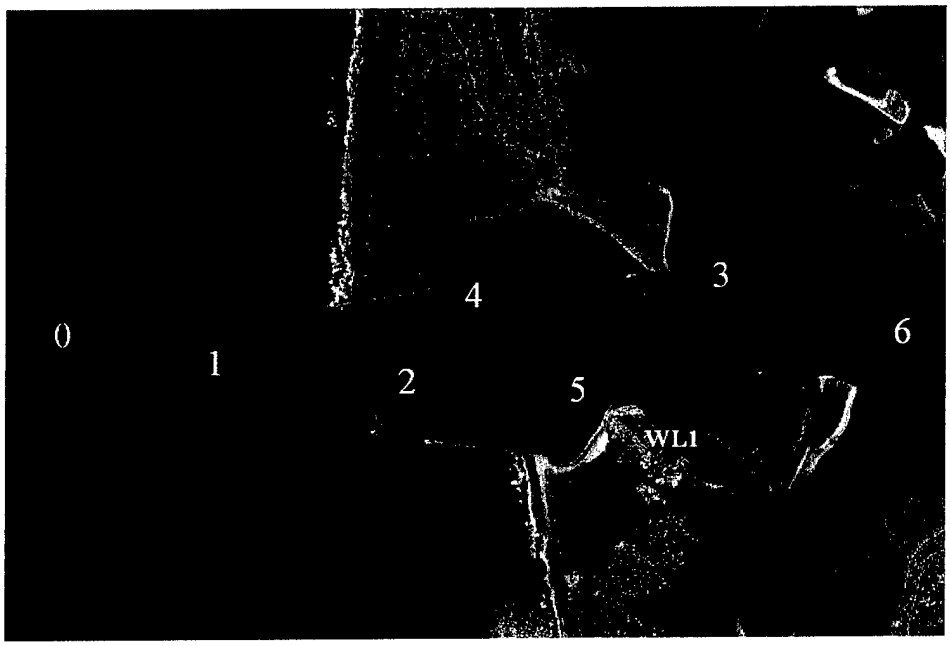

Figure 7-8. Current measurement locations

$$\overline{E} = \frac{\sum_{i=1}^{n} (\chi_{calc,i} - \chi_{meas,i})}{N} \tag{7-1}$$

where χ_{calc} is the calculated value of a variable, χ_{meas} is the measured value of a variable χ, and N is the number of points. A positive value of the mean error indicates that, on average, the calculated values overpredict the measurements, whereas a negative value indicates that the calculated values underpredict the measurements.

The rms error E_{rms} provides an absolute measure of error without regard to over- or underprediction. The rms error is given by:

$$E_{rms} = \sqrt{\frac{\sum_{i=1}^{N} (\chi_{calc,i} - \chi_{meas,i})^2}{N}} \tag{7-2}$$

Percent error E_{pct} is defined in terms of the rms error as:

$$E_{pct} = 100 \frac{E_{rms}}{R} \tag{7-3}$$

where R = representative range for values of the variable χ. For percent error calculations of water level, the difference between mean higher high water (mhhw) and mllw (diurnal tide range) at each station is taken as R. Percent error values of less than 10 are considered acceptable. For current speed, R was computed from the maximum range of current magnitude values measured at each station.

Validation of the circulation model was made for the first month of field data collection (11 September 1999 – 11 October 1999). Field measurements indicate that tidal elevation measurements at sta 1 and 2 have a similar response, with a spring tide range for this time period of approximately 3.3 m. (This is 0.5 m larger than the average spring tide range of 2.8 m.) Water level measurements at sta 3 show less variation in minimum elevation and a smaller spring range, likely due to the numerous tidal flats. Water level measurements at sta 4 show amplification of the tide to a maximum 3.6-m range. Validation of the circulation model for the first month of 1999 field data collection shows calculated tidal elevations compare well with measurements around the periphery of the bay at sta 1 through 4 (Table 7-3 and Figures 7-9 through 7-12), with the maximum error being 5.8 percent. Underprediction of the maximum low water elevations at sta 3 may be attributed to slight misrepresentation of tidal flats in this region. Bathymetric conditions of the tidal flats were represented by information from existing navigation charts and the GEODAS database and may not fully represent 1999 bathymetric conditions and/or not have sufficient accuracy.

Table 7-3
Wave Model Validation for Tide Stations 1 Through 4

Station	E_{rms}, m	Mean Error, m	Range, m	Percent Error
Tide 1	0.12	0.05	3.32	3.5
Tide 2	0.13	0.05	3.39	3.9
Tide 3	0.17	0.04	2.93	5.8
Tide 4	0.13	0.00	3.78	3.4

Field measurements of currents indicate sta 3 and 4, located on the north side of the inlet, have stronger flood than ebb currents, and sta 2 and 5, on the south side, have stronger ebb than flood current. Station 1 is in a region that is dominated by the ebb jet and influenced by the current generated by breaking waves. Comparison of calculated and measured currents indicates good agreement at velocity sta 2 through 6 (Table 7-4 and Figures 7-13 through 7-24) with a maximum error of 9.6 percent. This inlet throat area is tide-dominated, and such results can be expected. Station 1, however, shows less agreement (13.9 percent). Calculated and measured currents are in phase and show good agreement of peak flood current magnitudes, but ebb current magnitudes are underpredicted. Wave-induced currents in this region are significant; hence improved current calculation requires dynamic linking of the wave and circulation models. (In this study, the wave and circulation models were subsequently linked and results were compared to field data at two locations. It is recommended that circulation model calibration at an inlet entrance be accomplished within the SMS Steering Module to account for wave-induced currents.)

Table 7-4
Current Model Validation for Velocity Stations 1 Through 6

Station	E_{rms}, m/sec	Mean Error, m/sec	Range, m/sec	Percent Error
Velocity 1	0.21	-0.15	1.49	13.9
Velocity 2	0.11	0.03	1.37	8.0
Velocity 3	0.11	0.04	1.31	8.5
Velocity 4	0.12	0.02	1.65	7.1
Velocity 5	0.11	0.0	1.24	8.7
Velocity 6	0.12	-0.051	1.26	9.6

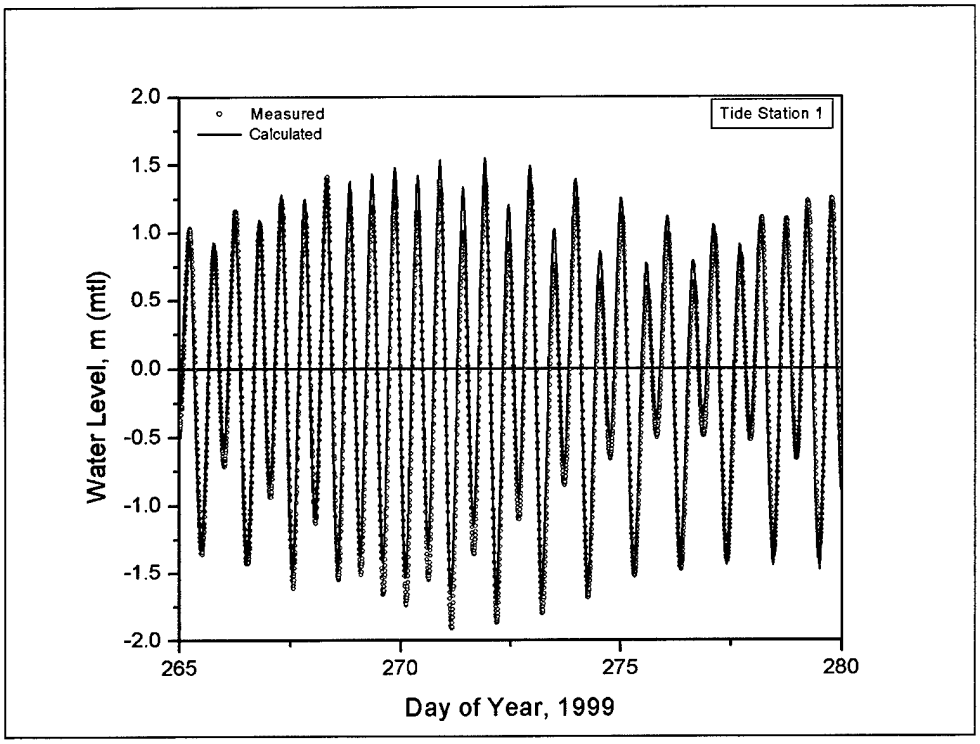

Figure 7-9. Measured and calculated water level time series at tide sta 1

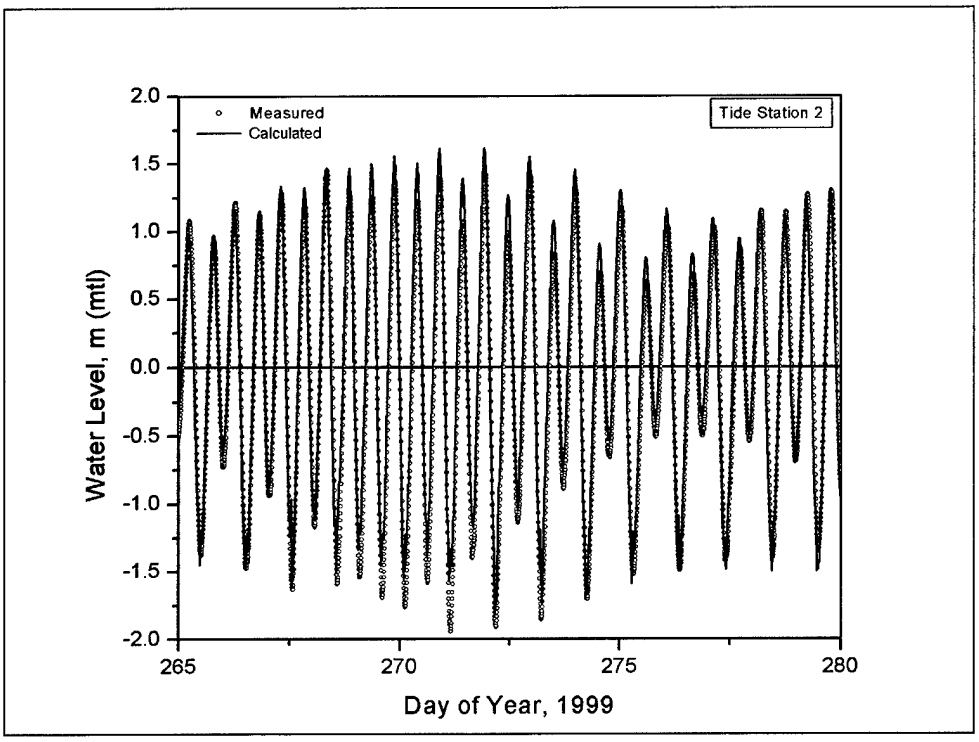

Figure 7-10. Measured and calculated water level time series at tide sta 2

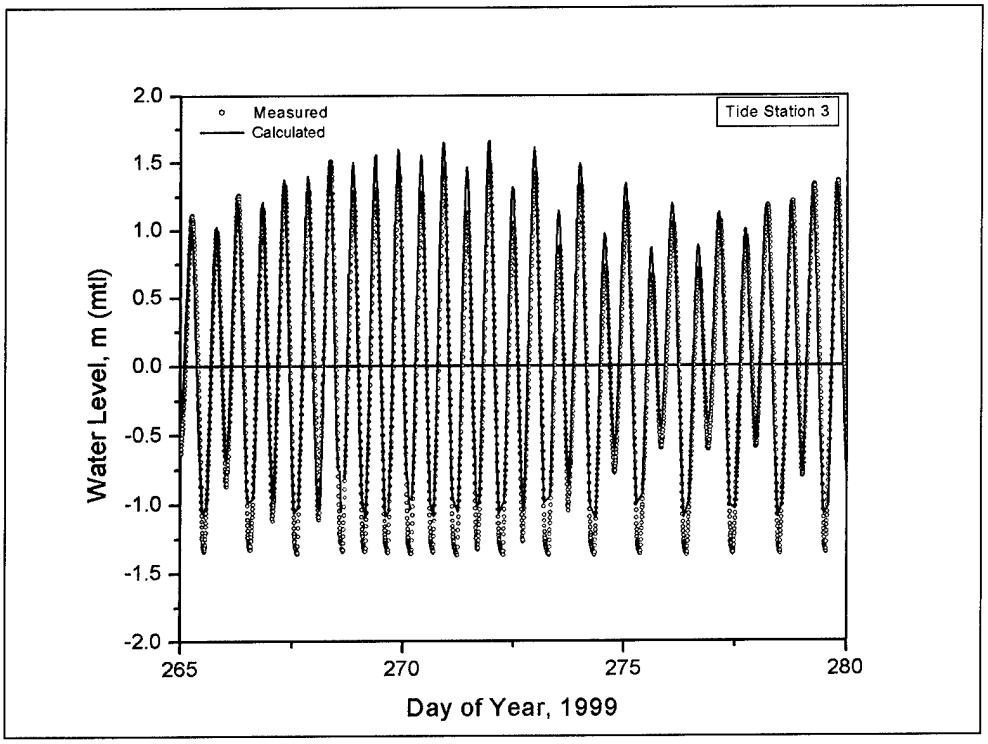

Figure 7-11. Measured and calculated water level time series at tide sta 3

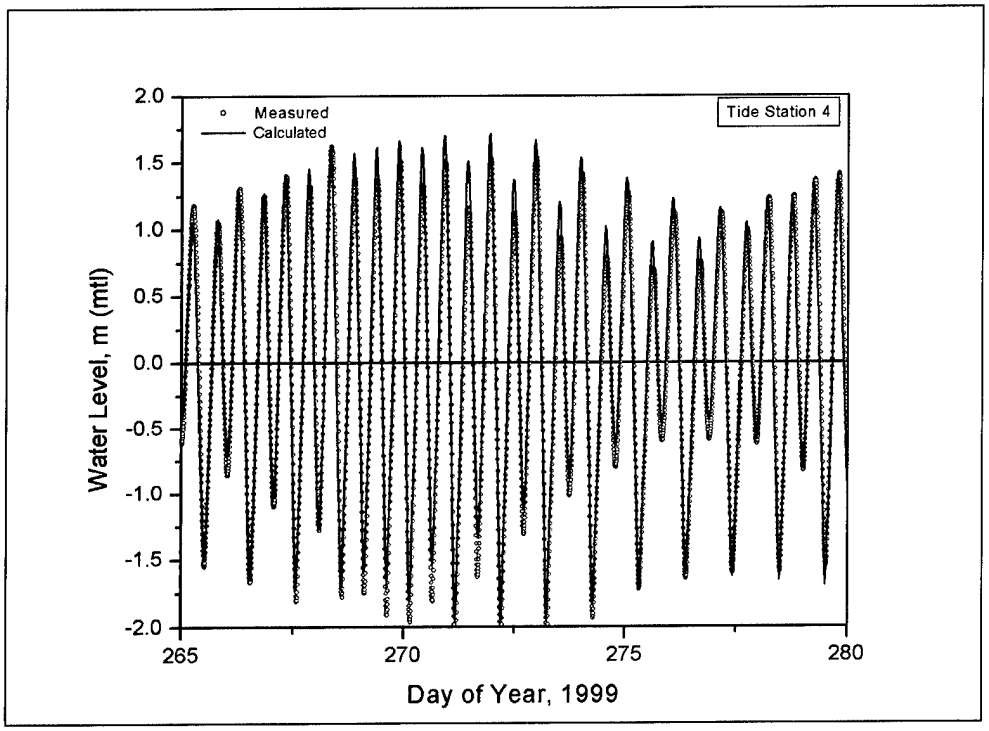

Figure 7-12. Measured and calculated water level time series at tide sta 4

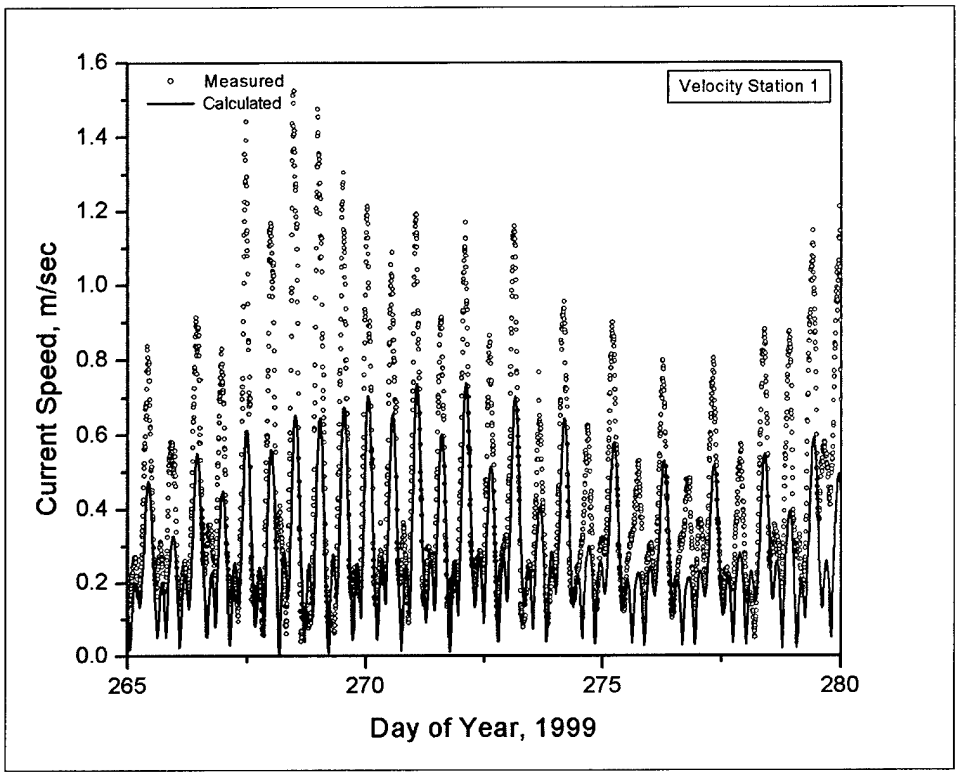

Figure 7-13. Measured and calculated current speed at velocity sta 1 for 15-day period

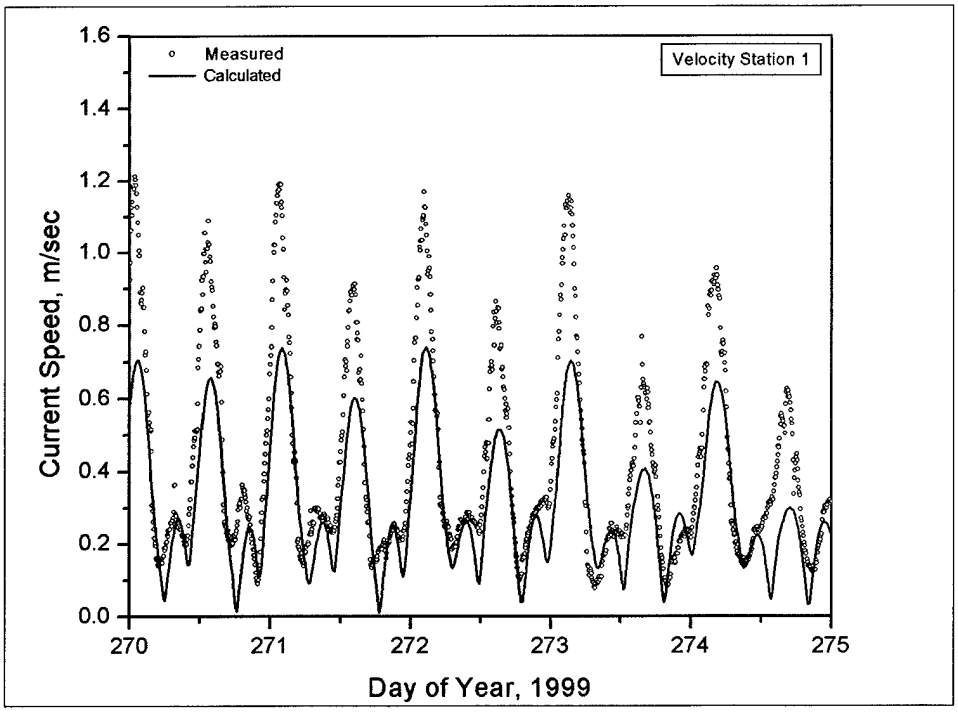

Figure 7-14. Measured and calculated current speed at velocity sta 1 for 5-day period

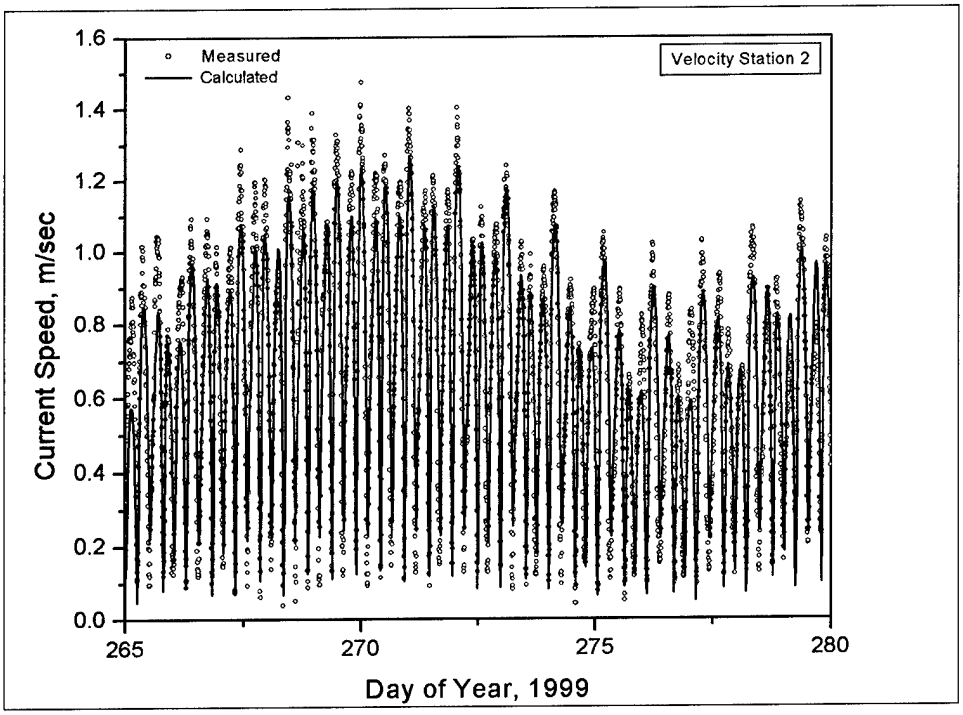

Figure 7-15. Measured and calculated current speed at velocity sta 2 for 15-day period

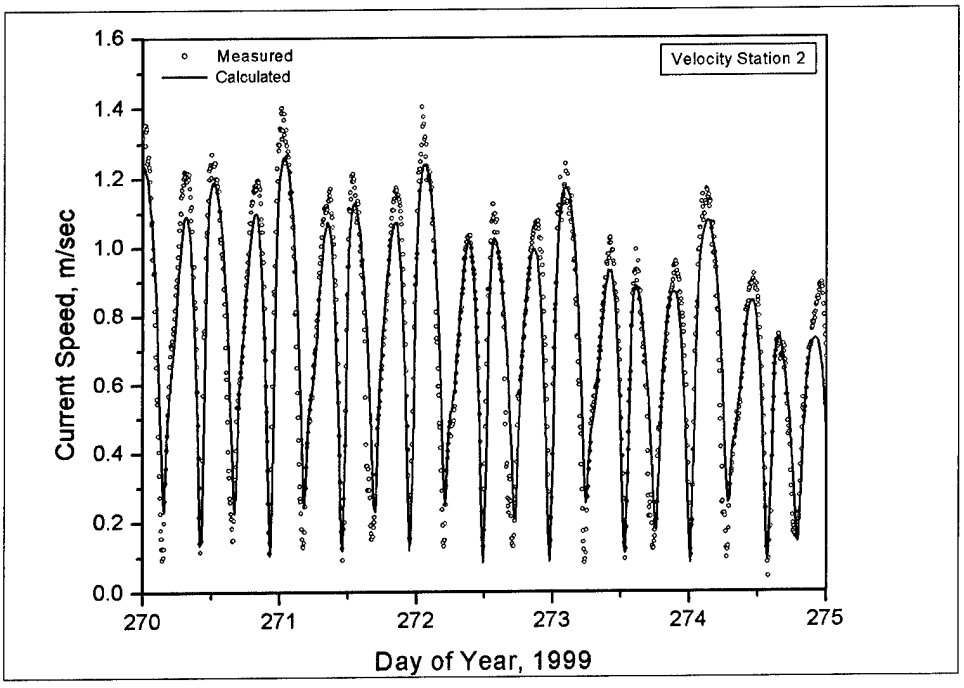

Figure 7-16. Measured and calculated current speed at velocity sta 2 for 5-day period

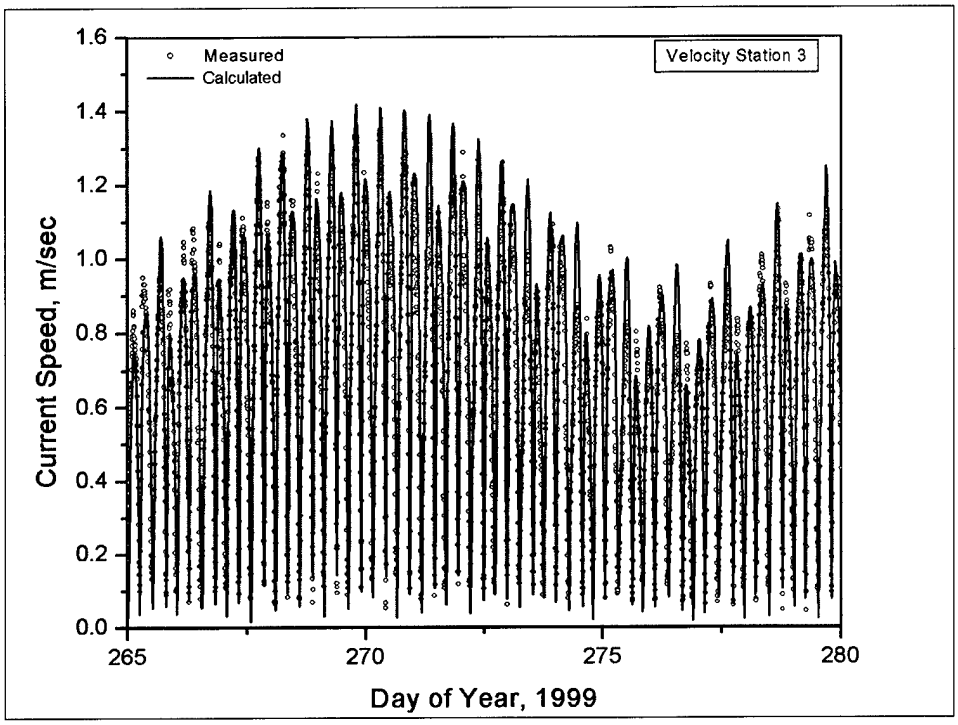

Figure 7-17. Measured and calculated current speed at velocity sta 3 for 15-day period

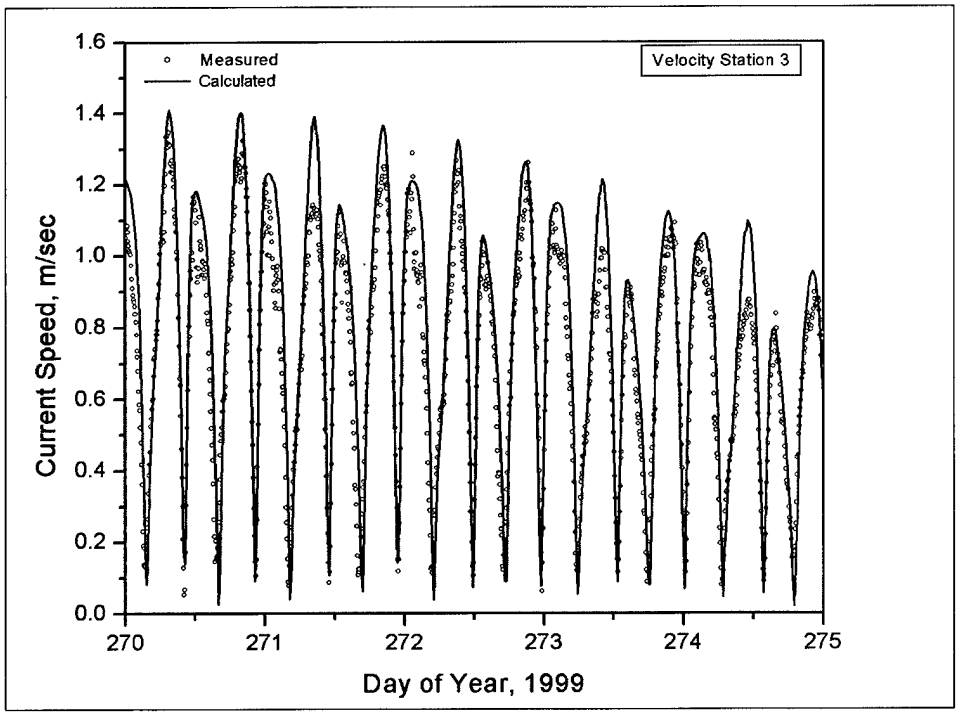

Figure 7-18. Measured and calculated current speed at velocity sta 3 for 5-day period

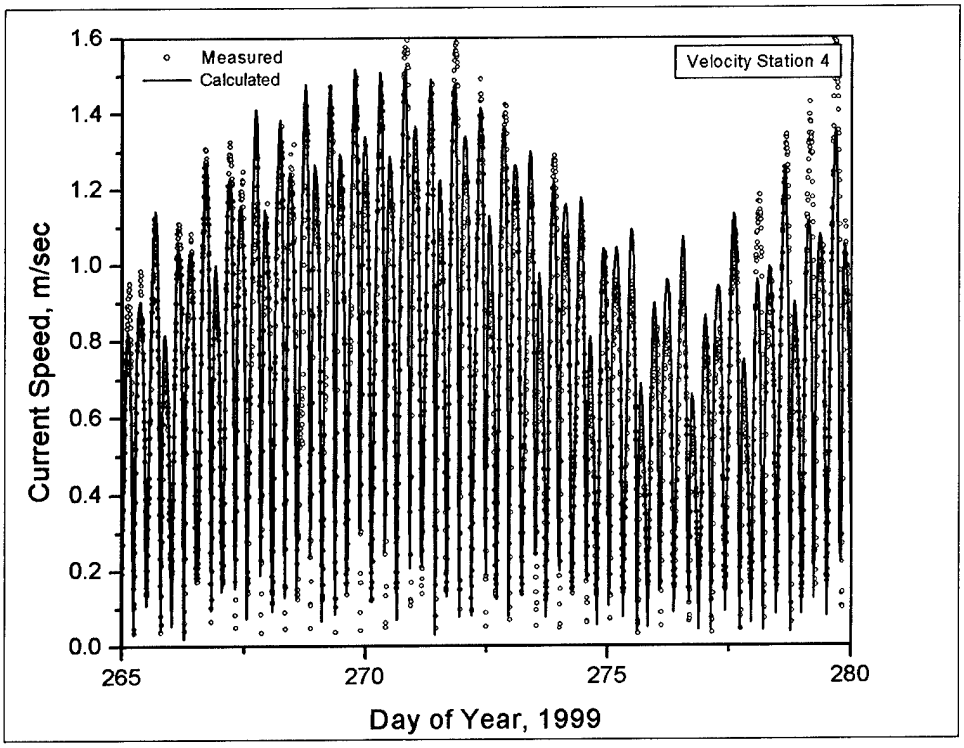

Figure 7-19. Measured and calculated current speed at velocity sta 4 for 15-day period

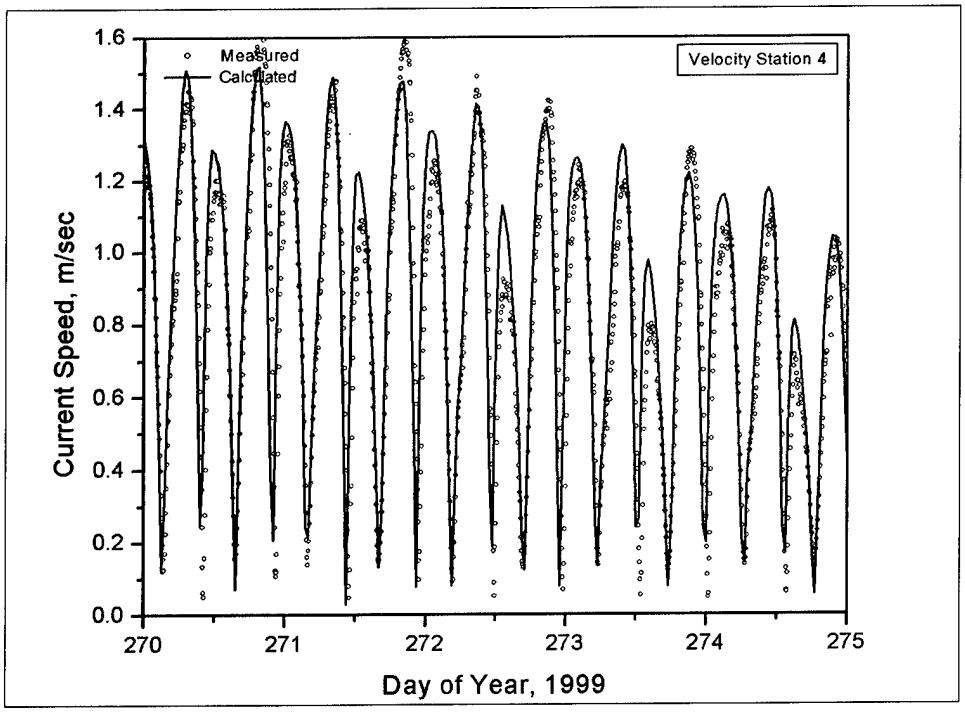

Figure 7-20. Measured and calculated current speed at velocity sta 4 for 5-day period

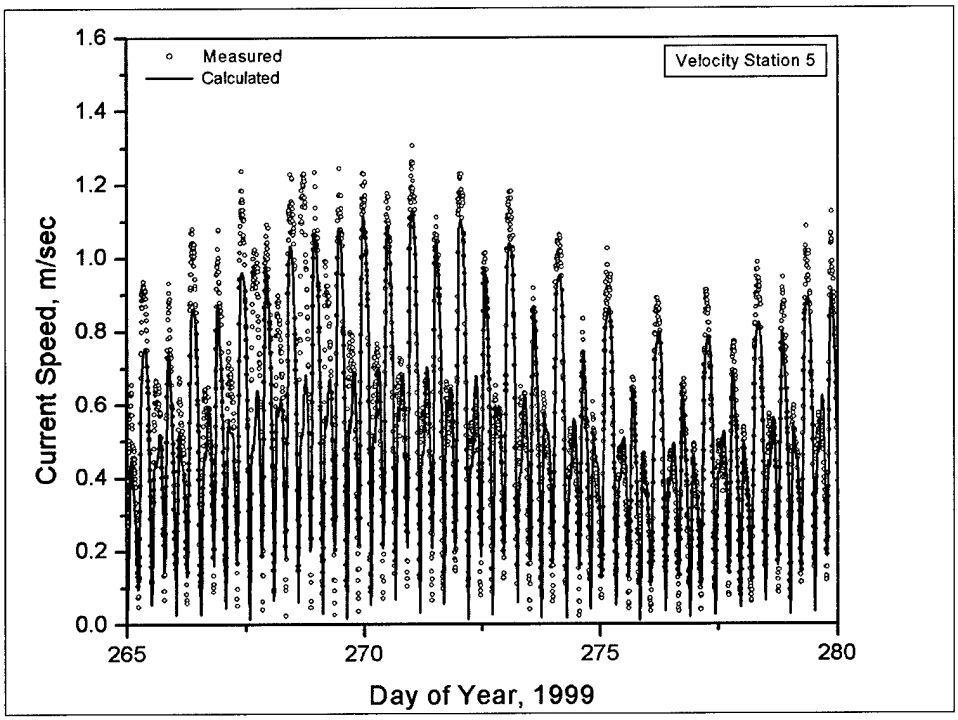

Figure 7-21. Measured and calculated current speed at velocity sta 5 for 15-day period

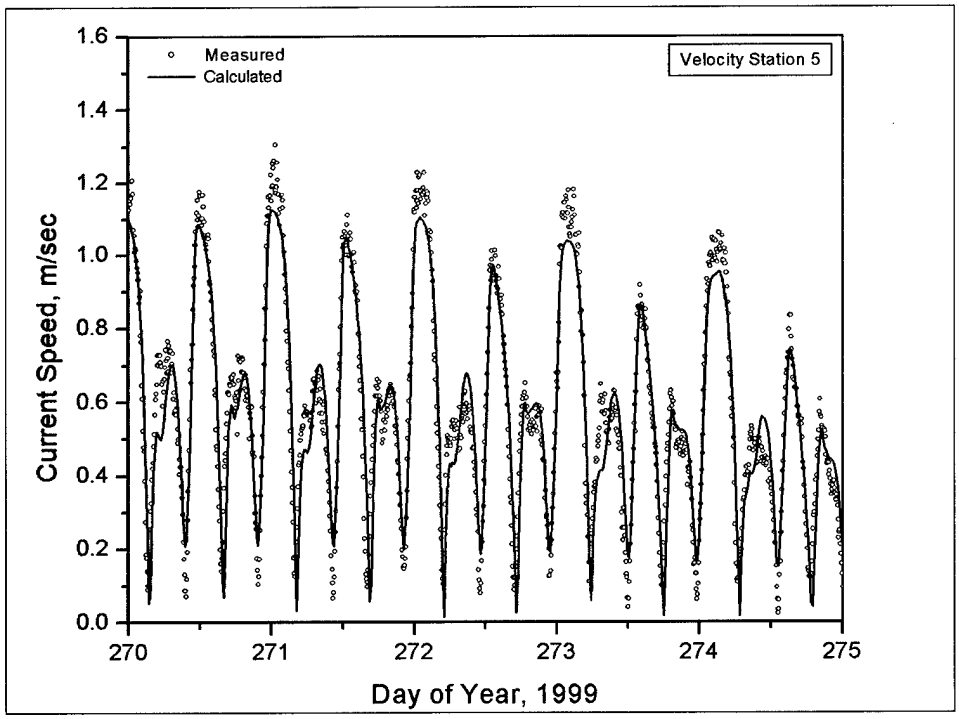

Figure 7-22. Measured and calculated current speed at velocity sta 5 for 5-day period

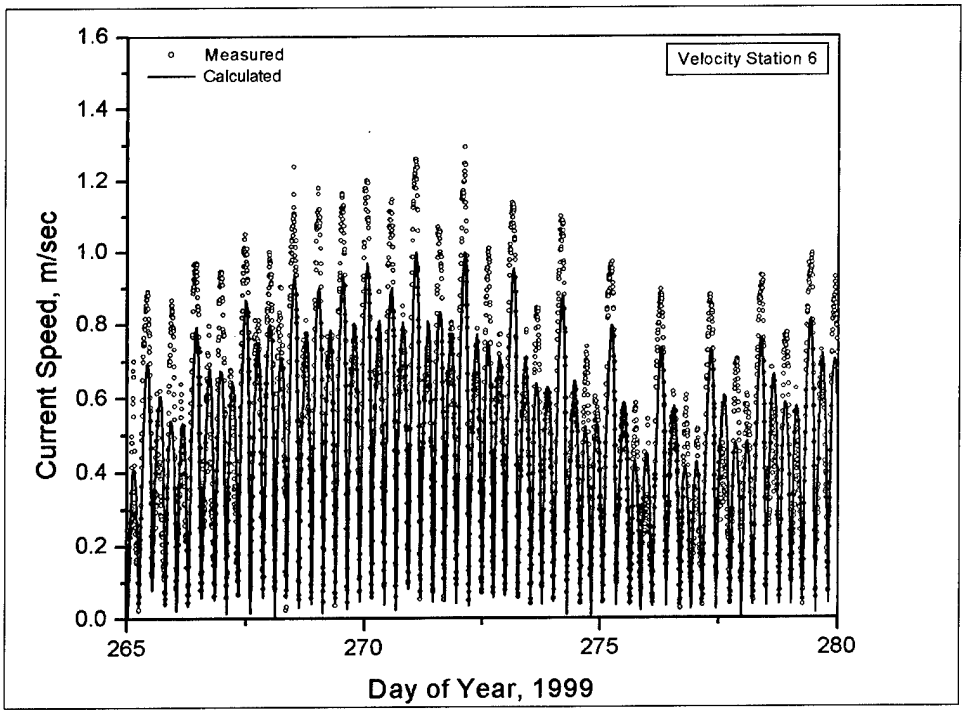

Figure 7-23. Measured and calculated current speed at velocity sta 6 for 15-day period

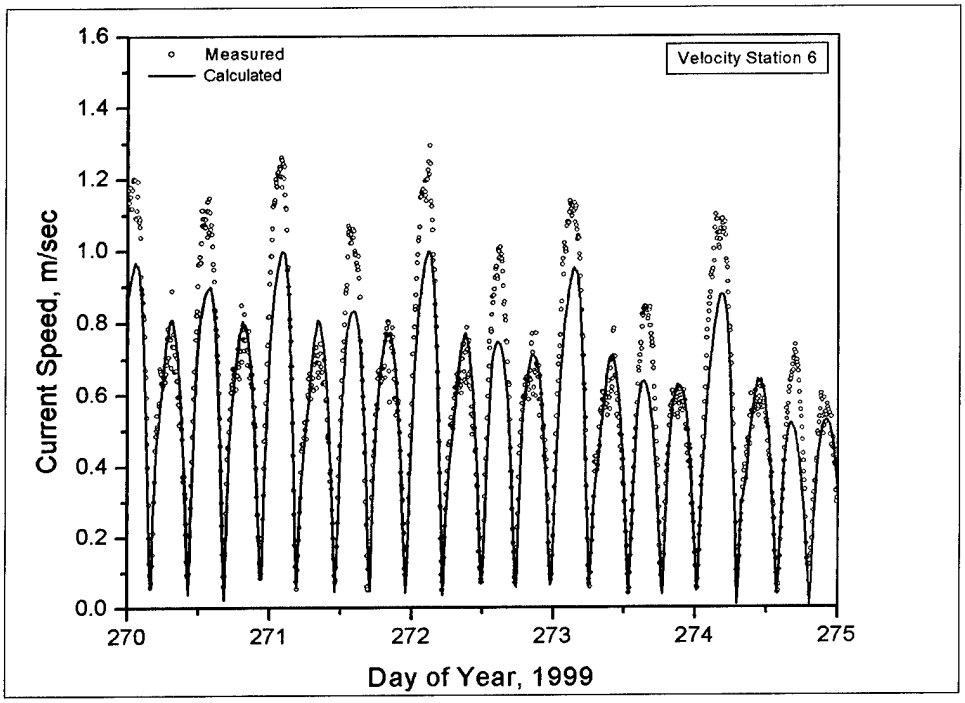

Figure 7-24. Measured and calculated current speed at velocity sta 6 for 5-day period

Wave Transformation Model

The STeady-state spectral WAVE model (STWAVE) (Resio 1987; Smith, Sherlock, and Resio 2001) computes nearshore wind-wave growth and propagation and was operated to transform waves at and around the Grays Harbor entrance as part of the evaluation of project alternatives. STWAVE numerically solves the steady-state conservation of spectral action balance along backward-traced wave rays. Assumptions underlying STWAVE are as follows:

a. Mild bottom slope and negligible wave reflection.

b. Spatially homogeneous offshore wave conditions.

c. Steady waves, currents, and winds.

d. Linear refraction and shoaling.

e. Depth-uniform current.

f. Negligible bottom friction.

STWAVE is a half-plane model, meaning that only waves propagating toward the coast are represented. Waves reflected from the coast or waves generated by winds blowing offshore are neglected. Wave breaking in the surf zone limits the maximum wave height based on the local water depth (ratio of maximum zero moment wave height to water depth cannot exceed 0.64) and wave steepness. STWAVE is a finite-difference model and calculates wave spectra on a rectangular grid with square grid cells. The model outputs zero-moment wave height, peak wave period, mean wave direction, radiation stress gradients (at all grid points), and two-dimensional spectra at selected grid points.

STWAVE input requirements and optional inputs are as follows:

a. Bathymetry grid (including shoreline position, grid dimensions, and grid resolution).

b. Incident frequency-direction wave spectrum on the offshore grid boundary.

c. Current field (optional).

d. Tide elevation, wind speed, and wind direction (optional).

STWAVE was run within the SMS Steering Module to compute wave-generated currents and water levels within ADCIRC. Linkage of the models is presented in a subsequent section.

Bathymetry grid

The wave model requires a computational bathymetric grid to transform waves from the offshore boundary to the nearshore. The grid was generated with the SMS Cartesian grid generator applied to digital bathymetry. (The SMS was applied to transform the ADCIRC bathymetry to the STWAVE domain; therefore, the same data sources described in the ADCIRC grid development section were selected to develop the STWAVE grid.) The grid origin (southwest corner of the grid) is located at the Washington South state plane coordinate x = 214,774.8 m and y = 166,560.8 m. The grid was oriented at 350 deg (rotated

10 deg counter-clockwise from True North). The STWAVE grid resolution was 50 m for the original calibration simulations, with 341 cells across the shore and 588 cells along the shore. The offshore boundary is at the Grays Harbor National Data Buoy Center (NDBC) buoy at a depth of 41 m. The existing condition bathymetry and STWAVE nearshore grid are shown in Figure 7-25. Depths are given in meters relative to mtl.

Input wave spectra

Input wave spectra are the primary forcing mechanism for the wave model. The input spectra represent the distribution of wave energy with respect to frequency and direction. For this project, one-dimensional frequency spectra from the Grays Harbor buoy (supported by the Seattle District) were obtained for the time period corresponding to the field data collection time period. Two-dimensional (2-D) spectra were generated from the one-dimensional spectra by applying a $\cos^{nn}(\alpha-\alpha_m)$ directional distribution, where α is the component wave direction, and α_m is the peak wave direction. Values of *nn* that generated the representative spectra are given as a function of peak period T_p in Table 7-5 (Thompson et al. 1996).

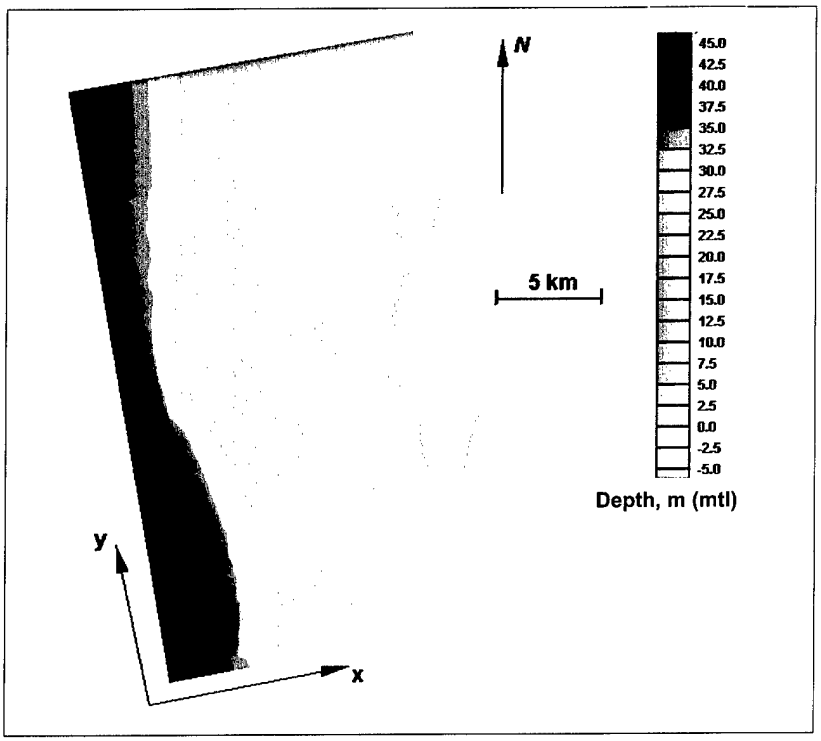

Figure 7-25. STWAVE existing condition bathymetry grid

Table 7-5 Values of *nn* Defining Representative Spectra					
T_p, sec	≤10	14	15	18	20
nn	4	16	18	26	30

Tide

Tide elevation is applied in STWAVE as constant water depth change over the entire grid. Within the Grays Harbor domain, the tide elevation varies spatially, but the influence of this variation on wave transformation is relatively small (and is on the order of wind and wave setup, which are neglected). Tide elevation for wave runs was specified from the Westport water level measurements. Because the grid depths are specified relative to mtl, tide fluctuations were correspondingly specified relative to mtl.

Wave Model Validation

STWAVE simulations of the entire first month (11 September – 14 October 1999) of the 2-month period of field data collection (11 September – 17 November 1999) were accomplished by driving the model with the Coastal Data Information Program (CDIP) Grays Harbor buoy wave spectra at 3-hr intervals for the data collection period. The buoy is located at 46°51.47'N latitude and 124°14.64'W longitude, approximately 9 km southwest of the entrance to Grays Harbor in a depth of 40-42 m. One-dimensional frequency spectra from the Datawell Directional buoy at Grays Harbor (03601) were obtained from the CDIP web site. The theoretical directional spread as in Table 7-5 was applied to the frequency spectra to create 2-D spectra for input to the STWAVE model. The number of spectra was reduced to one every 3 hr to limit the number of model simulations. The 2-D spectra were rotated 10 deg west of north to correspond with the grid orientation. Tide elevation data from water level sta 1 (WL1 in Figure 7-8) were included to adjust bathymetry for each 3-hr time period. These bathymetric changes were incorporated to account for water level (and depth) fluctuations due to the tide. Wave-current interaction was not included in the simulations.

Model validation with the field data showed good correlation. A preliminary comparison of wave height at seven wave gauge locations (sta 0 through 6 in Figure 7-8) to the model results at these locations is given in Figures 7-26 though 7-32. The wave height attenuates little from sta 0 to sta 2 because wave breaking was minor. The stations in the inlet entrance demonstrate a reduced wave height because breaking and diffraction occur. All stations show some evidence of tidal influence, with the most predominant influence at the interior stations (sta 3 and 6). The difference between wave height produced in the model and prototype wave height shows that model results are generally within 0.5 m of the prototype. It is noted that uncertainty in the buoy measurements is on the order of ±5 percent for wave height, ±1 sec for wave period, and ±10 deg for wave direction.

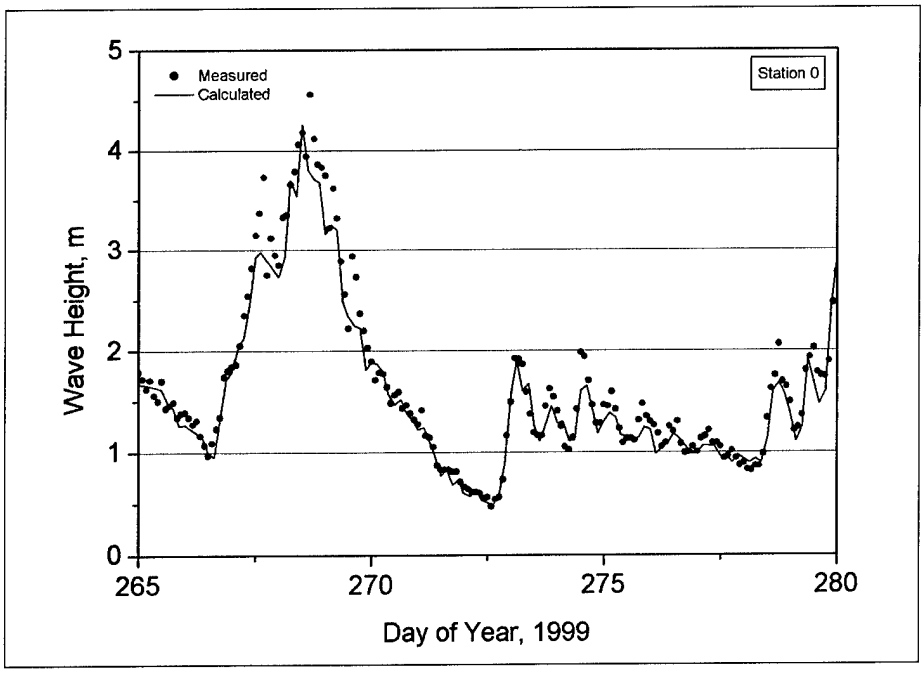

Figure 7-26. Measured and calculated wave height at sta 0

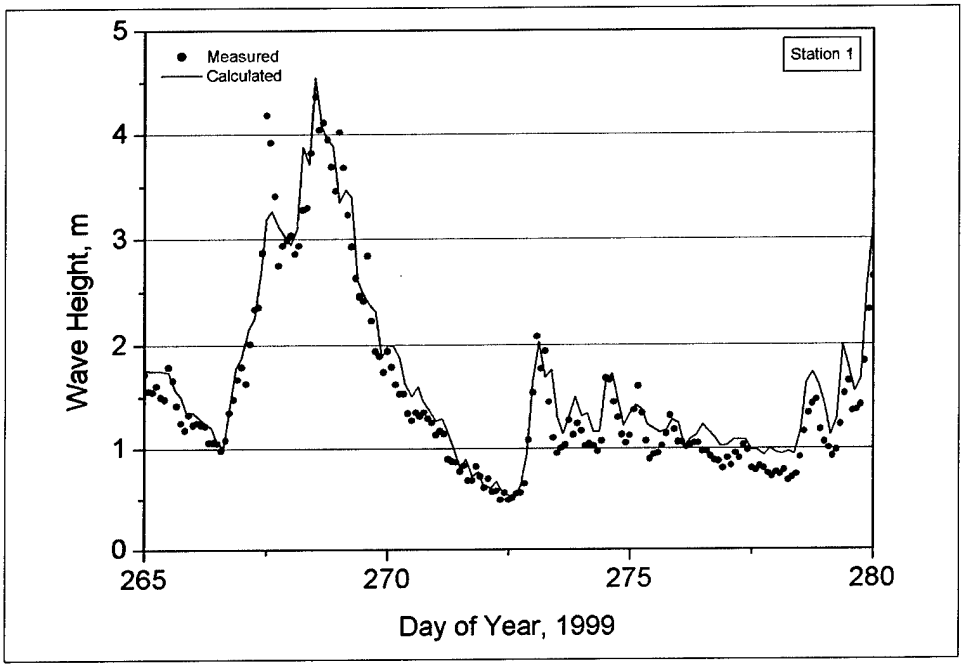

Figure 7-27. Measured and calculated wave height at sta 1

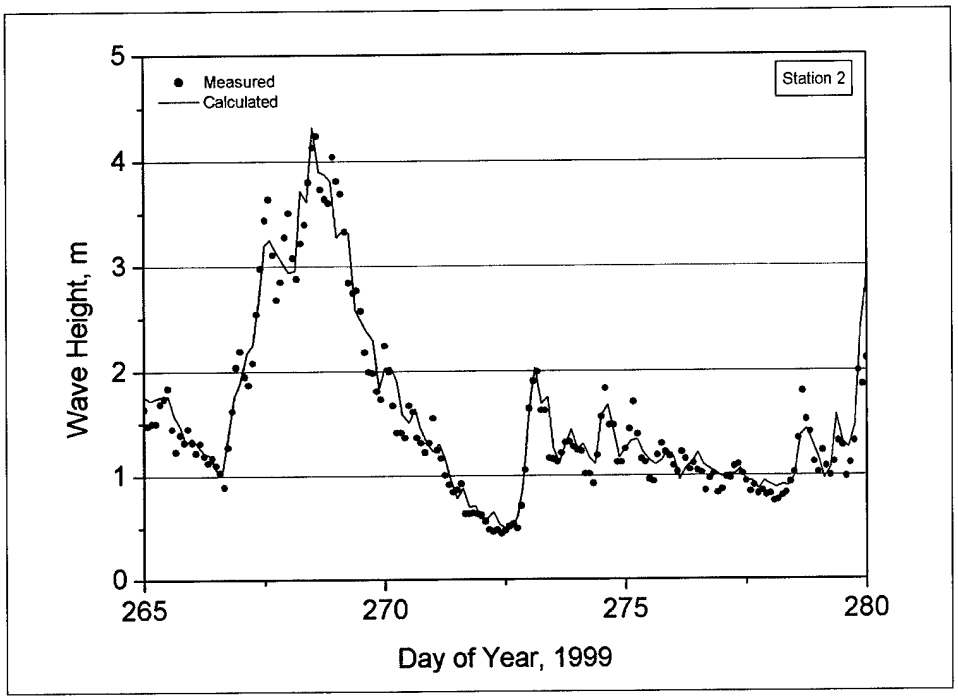

Figure 7-28. Measured and calculated wave height at sta 2

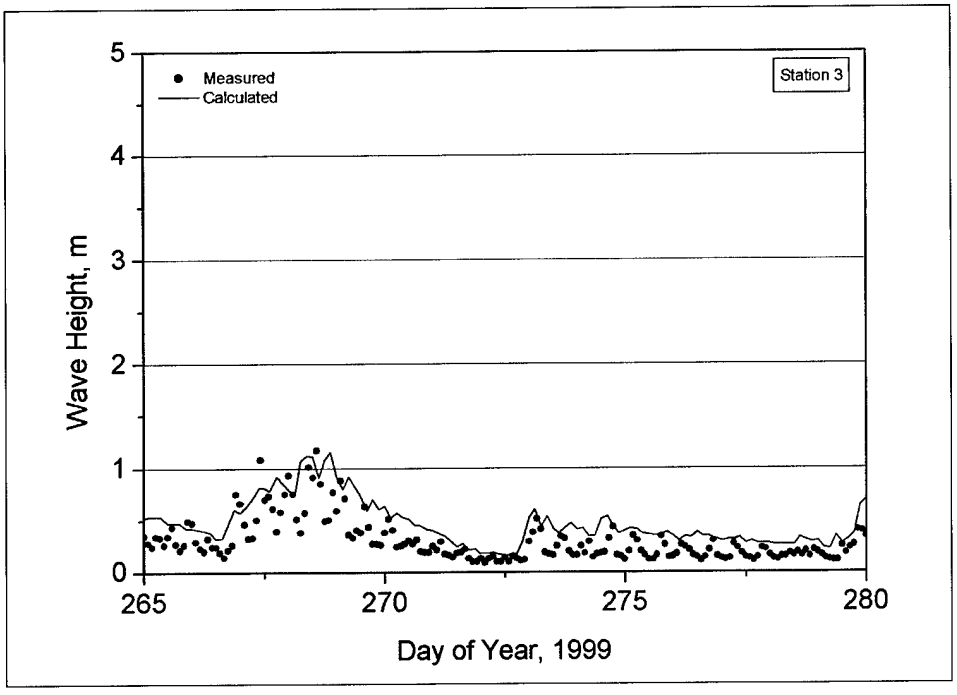

Figure 7-29. Measured and calculated wave height at sta 3

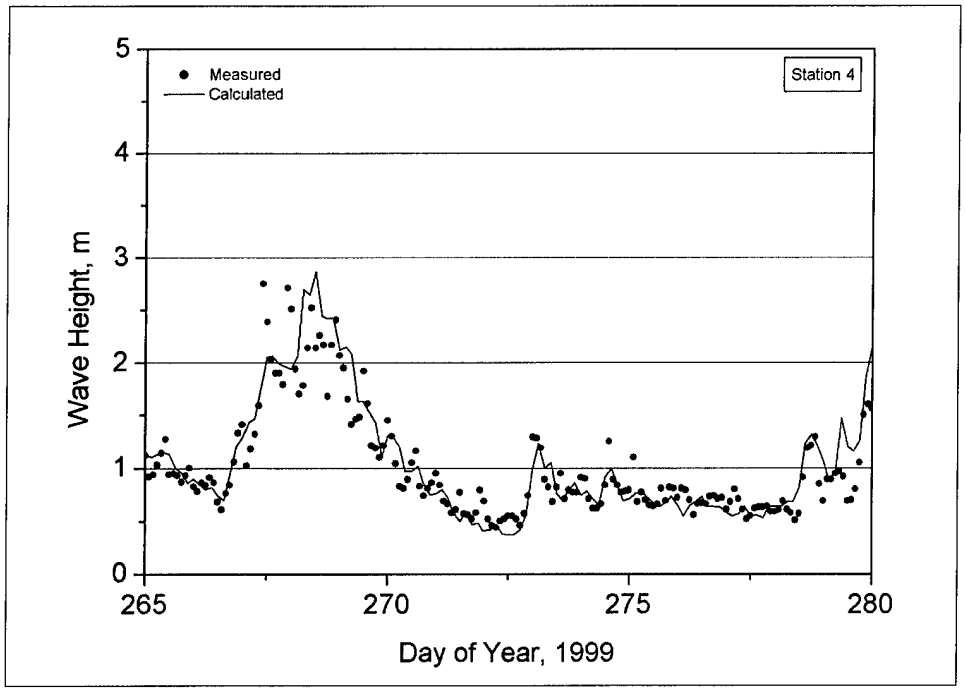

Figure 7-30. Measured and calculated wave height at sta 4

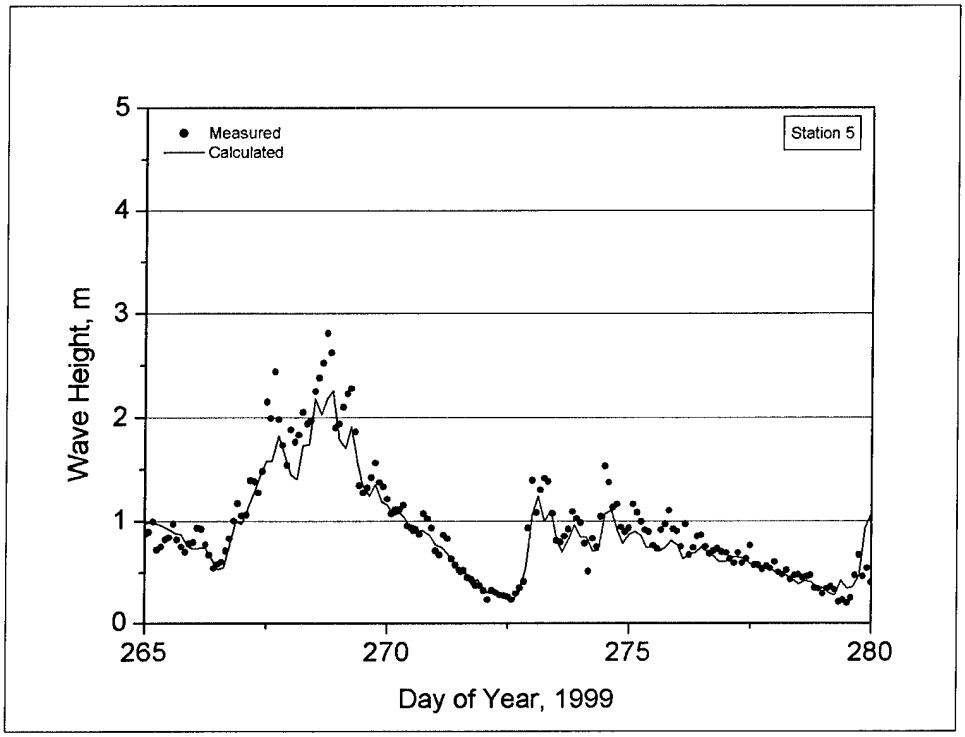

Figure 7-31. Measured and calculated wave height at sta 5

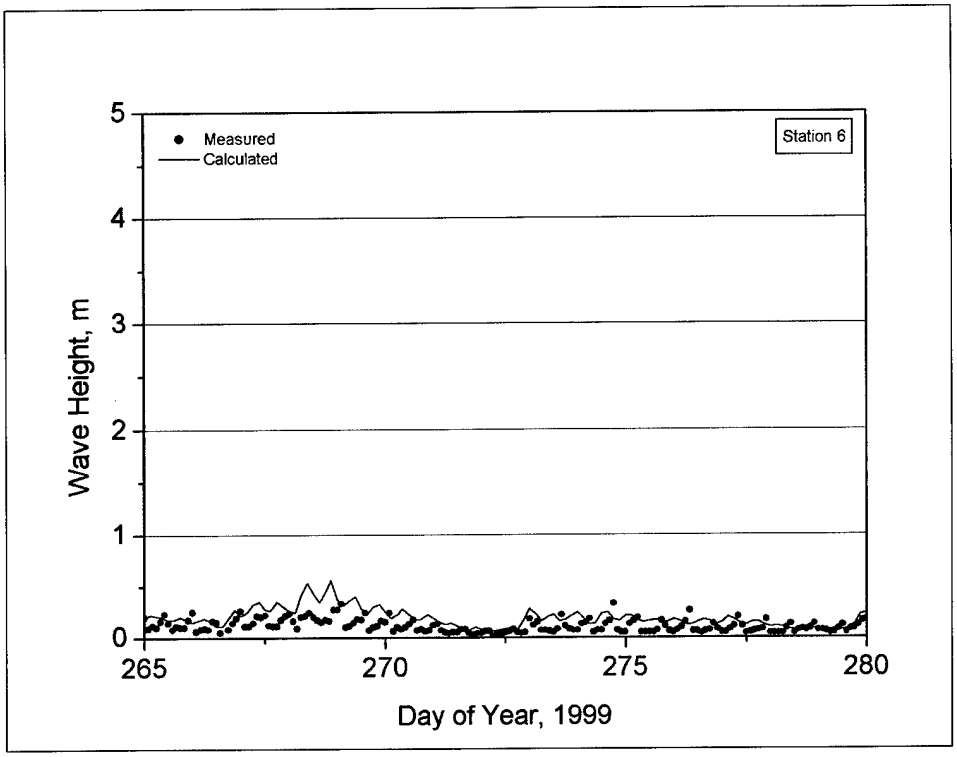

Figure 7-32. Measured and calculated wave height at sta 6

Linkage of Wave and Circulation Models in SMS

The SMS is a pre- and post-processor developed for operating various numerical hydrodynamic models (Zundel 2002). The SMS software package allows users to create and edit meshes and grids, setup and save model input files, run numerical model simulations, and view model solutions. The Steering Module was developed within SMS by the Coastal Inlets Research Program (Holliday, McNair, and Kraus 2003) to automate repetitive user tasks and required data sharing between circulation and wave propagation numerical models (Zundel, Cialone, and Moreland 2002). At present, the Steering Module couples ADCIRC and STWAVE, as well as M2D (Militello 1998; Militello and Zundel 2003) and STWAVE. Future work will couple other U.S. Army Corps of Engineers (USACE) circulation and wave models via the Steering Module.

The Steering Module facilitates input and output sharing, as well as interpolation, between ADCIRC and STWAVE. ADCIRC can be forced by input of the wave radiation stresses produced by STWAVE, in addition to the tidal- and wind-induced currents. The current fields computed by ADCIRC can serve as input to STWAVE to simulate wave transformation on a current. For this project, SMS linked the wave and hydrodynamic models to examine wave-induced currents near the north jetty. For this application, after sensitivity testing, one-way passing from STWAVE to ADCIRC was selected to calculate the contribution of waves to the current (Cialone et al. 2002).

2001 Calibration of Linked Models

Linkage of wave and circulation models was accomplished within the SMS Steering Module. Calibration of the linked models was made for a time period when surf zone field data were available for comparison. As described in Chapter 4, wave, current, suspended sediment concentration, and water level measurements were made near the north jetty tip in May 2001 with several instruments (Acoustic Doppler Profiler [ADP], Acoustic Doppler Velocimeter-Ocean [ADVO] and two Optical Backscatterance [OBS] turbidity sensors) mounted on tripods (sta OS 5 and OS 6 in Figure 4-12) (Osborne, Hericks, and Kraus 2002). Bathymetry data collected by the Seattle District for the Grays Harbor region were available for this time interval. Wave and circulation model grids described previously were revised in the areas where data were available. Wave information was obtained from the CDIP buoy, wind information was obtained from NCEP, and tidal constituents were generated with the LeProvost et al. (1994) database. The linked model calibration run was for a 9-day period (8-16 May 2001) with the wave model input updated every 3 hr.

Comparisons of circulation model current component results to field data collected at sta OS 5 and OS 6 were made, and plots of the first 3 days of the simulation and measurements are shown in Figures 7-33 through 7-36. Measurements at sta OS 5 indicate predominantly southwestward currents (Figures 7-33 and 7-34). The predicted magnitude and phase of the southward and westward velocity components compare well to the measurements; however, low magnitude flow reversals to the northeast in the model calculations are not indicated in the measurements. (Examination of model results in this region indicates the presence of a large eddy near the gauge location, which could account for some of the difference. In addition, there may be other regional-scale ocean phenomena that are not modeled with sufficient accuracy for a limited model domain. Measurements at sta OS 6 indicate predominantly southeastward and westward currents that are modeled fairly well with the SMS Steering Module, except for the prediction of short periods of low magnitude, flow reversal to the northwest (Figures 7-35 and 7-36). The east-west component is modeled well in magnitude and phase. The north-south component is in phase, but underpredicted in magnitude.

Simulation of Alternatives

Numerical simulations of the hydrodynamics associated with the existing condition and project alternatives were made by operating the ADCIRC and STWAVE models within the SMS Steering Module. Five structural alternatives were individually included in the numerical simulations, and the resulting hydrodynamic conditions were compared to those produced for the existing condition. All Steering Module simulations were for 5 days with one wave condition applied continuously. Initially, two tide ranges, two wave conditions, and five alternatives (20 model input configurations) were simulated along with the four existing condition configurations (two tide ranges and two wave

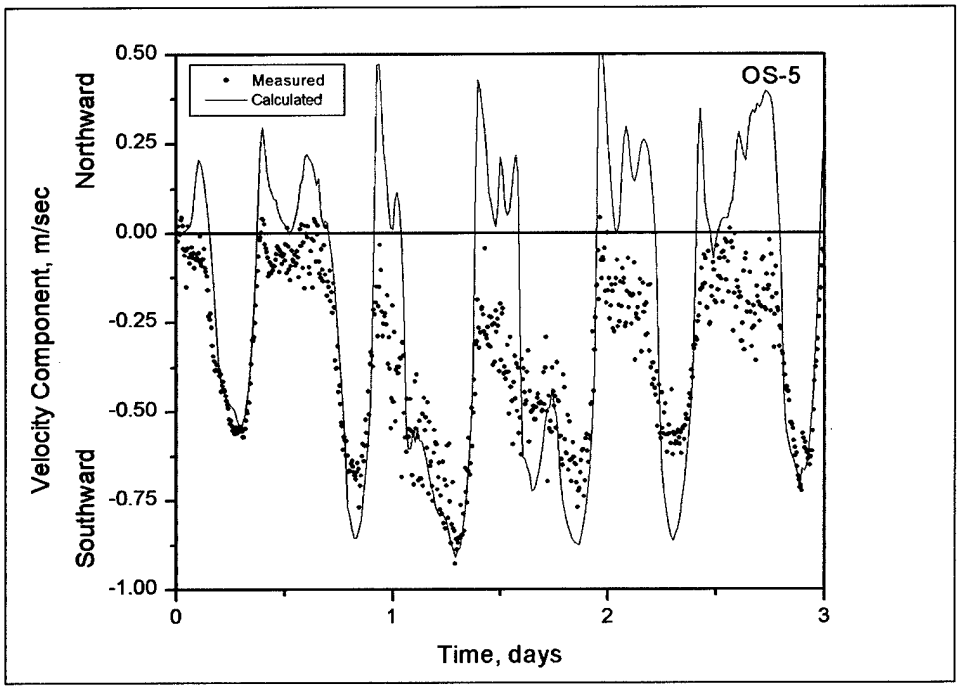

Figure 7-33. Measured and calculated north-south velocity component at sta OS 5

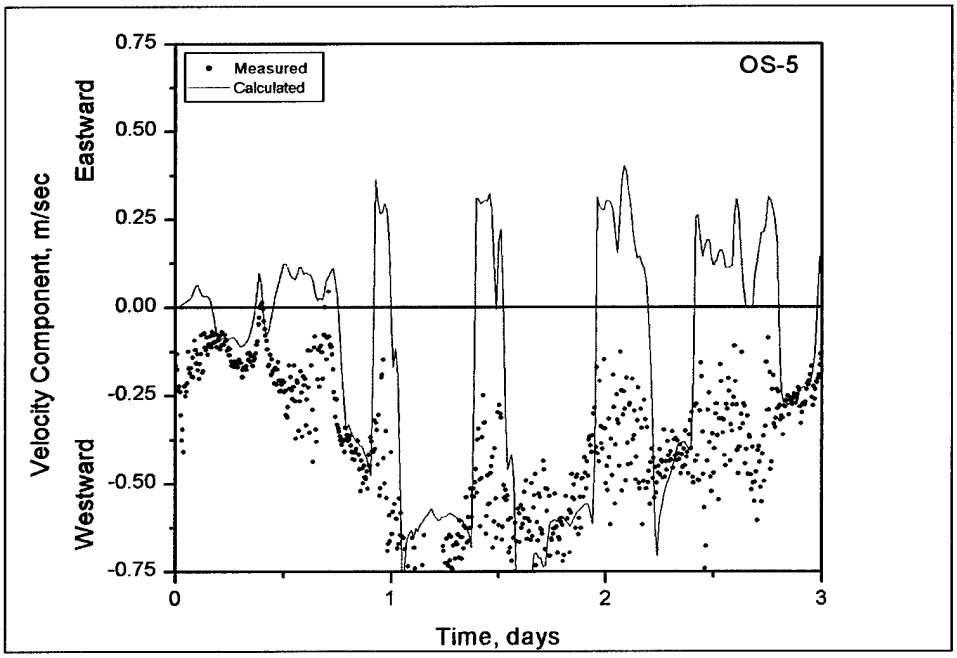

Figure 7-34. Measured and calculated east-west velocity component at sta OS 5

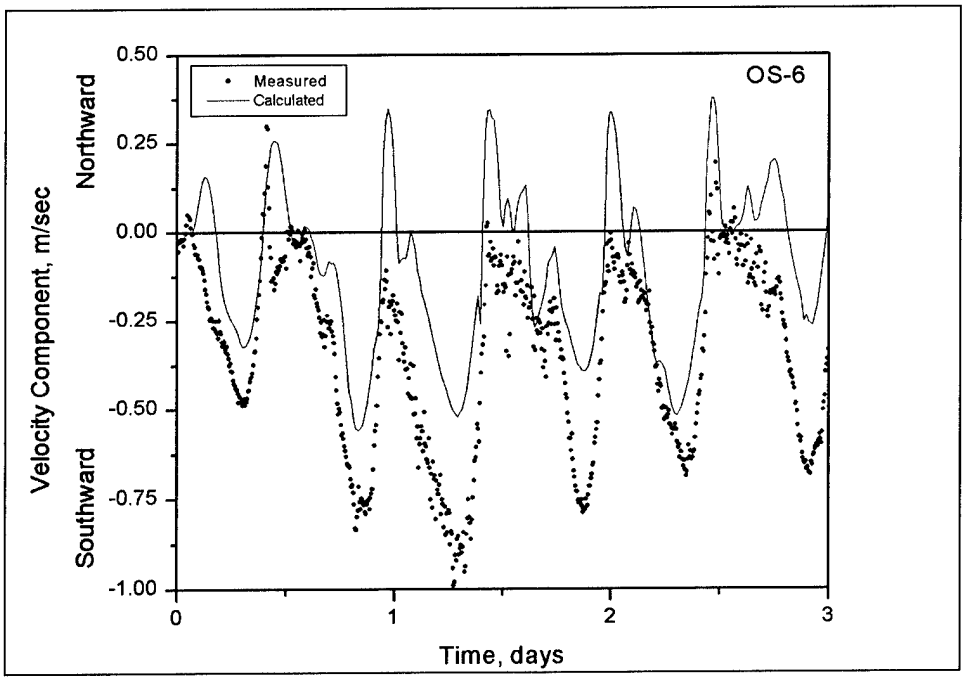

Figure 7-35. Measured and calculated north-south velocity component at sta OS 6

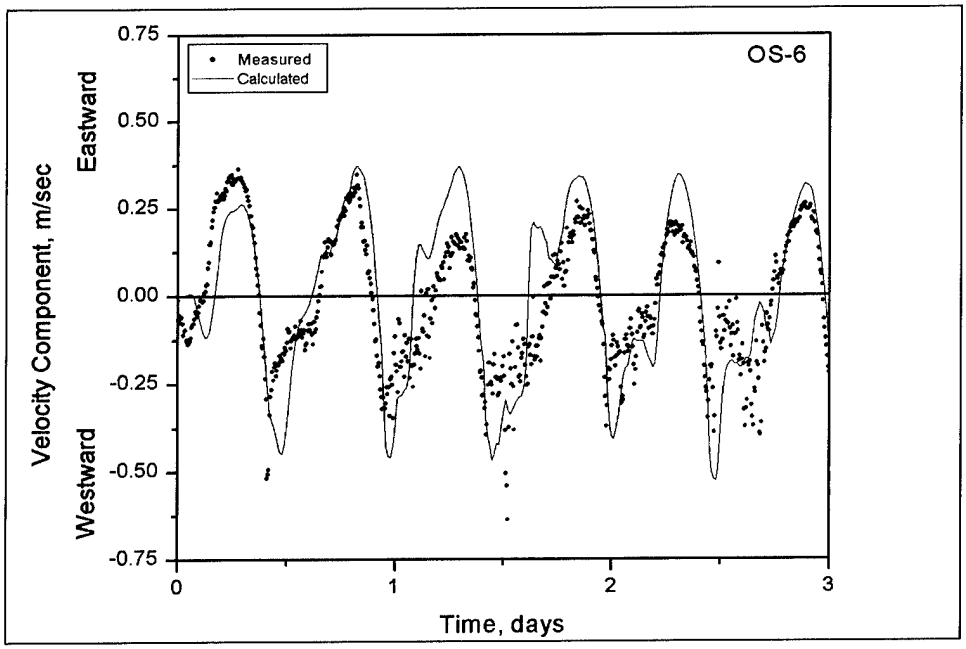

Figure 7-36. Measured and calculated east-west velocity component at sta OS 6

conditions) for a total of 24 configurations. Simulation times were selected to include a spring or neap tide condition. A 5-m, 13-sec, west-northwest wave and a 6-m, 14-sec, west-southwest wave were selected to represent moderate storm conditions. These simulations are referred to as Runs 104 through 127 (Table 7-6). Figures 7-37 to 7-42 show the existing condition bathymetry and structural alternative bathymetries. Note that the spur alternatives represent a submerged structure with an elevation 4.54 m below mtl. The jetty rehabilitation alternatives are considered 4.6 to 4.7 m above mtl and were modeled as land cells.

Analysis of the initial 24 simulations encompassed an examination of peak flood and peak ebb plan view maps, statistical comparisons of mean currents at 16 grid node locations (Figure 7-43), velocity component time-series comparisons, mean current maps, and global differences in current magnitude for each project alternative compared to the existing condition.

Plan view maps

Peak flood and ebb plan view maps were created for all 66 simulations and are presented in Appendix E. For discussion, Figures 7-44 through 7-59 also show plan view maps for the first four existing condition simulations (Runs 104-107) at peak flood and peak ebb. Note that the ADCIRC grid was finely resolved at and around the north jetty project site. Coarser grid resolution at the south jetty and at Westport may not have represented all possible wave-induced currents and eddies in these areas. The coarse resolution enabled efficient calculation of the overall circulation pattern through the inlet while enabling computation of detailed hydrodynamics in the project area. Evaluation of project alternatives in the Ocean Shores and the north jetty region was accomplished with this approach. Circulation patterns at the south jetty and Westport in these figures should not be consulted for design.

Figures 7-44 and 7-45 show flood tide conditions with a west-northwest wave and spring tide forcing (Run 104). The strong southbound longshore current in the Ocean Shores region and flood tide conditions combine to strengthen the current near the north jetty tip to approximately 3 m/sec. The longshore current is approximately 1.3-1.7 m/sec. Currents in the inlet throat are also 1.3-1.7 m/sec at peak flood, with the stronger flood current running along the north side of the inlet. Figures 7-46 and 7-47 show ebb tide conditions with a west-northwest wave and spring tidal forcing (Run 104). The ebb jet is deflected to the south upon exiting the inlet throat due to the southbound longshore current. Currents at the north jetty tip are strongest, and currents along the inlet side of the north jetty remain flooding within a 150-m band south of the north jetty.

Figures 7-48 and 7-49 show flood tide conditions with a west-southwest wave and spring tide forcing (Run 105). West-southwest waves induce a longshore current directed to the north, but there is a flow reversal within 500 m north of the north jetty, resulting in a southbound current. Flow around the north jetty tip is to the south, and a strong flood current along the inlet side of the north

Table 7-6
Steering Module Simulations

Run	Alternative	Tide	Wave Direction	Wave Condition
104	Existing	Spring	west-northwest	5-m, 13-sec
105	Existing	Spring	west-southwest	6-m, 14-sec
106	Existing	Neap	west-northwest	5-m, 13-sec
107	Existing	Neap	west-southwest	6-m, 14-sec
108	Alt 2A	Spring	west-northwest	5-m, 13-sec
109	Alt 2A	Spring	west-southwest	6-m, 14-sec
110	Alt 2A	Neap	west-northwest	5-m, 13-sec
111	Alt 2A	Neap	west-southwest	6-m, 14-sec
112	Alt 2B	Spring	west-northwest	5-m, 13-sec
113	Alt 2B	Spring	west-southwest	6-m, 14-sec
114	Alt 2B	Neap	west-northwest	5-m, 13-sec
115	Alt 2B	Neap	west-southwest	6-m, 14-sec
116	Alt 3A	Spring	west-northwest	5-m, 13-sec
117	Alt 3A	Spring	west-southwest	6-m, 14-sec
118	Alt 3A	Neap	west-northwest	5-m, 13-sec
119	Alt 3A	Neap	west-southwest	6-m, 14-sec
120	Alt 3B	Spring	west-northwest	5-m, 13-sec
121	Alt 3B	Spring	west-southwest	6-m, 14-sec
122	Alt 3B	Neap	west-northwest	5-m, 13-sec
123	Alt 3B	Neap	west-southwest	6-m, 14-sec
124	Alt 4A	Spring	west-northwest	5-m, 13-sec
125	Alt 4A	Spring	west-southwest	6-m, 14-sec
126	Alt 4A	Neap	west-northwest	5-m, 13-sec
127	Alt 4A	Neap	west-southwest	6-m, 14-sec
128	Existing	Spring	west	2.5-m, 10-sec
129	Alt 2A	Spring	west	2.5-m, 10-sec
130	Alt 2B	Spring	west	2.5-m, 10-sec
131	Alt3A	Spring	west	2.5-m, 10-sec
132	Alt 3B	Spring	west	2.5-m, 10-sec
133	Alt 4A	Spring	west	2.5-m, 10-sec
134	Existing	Spring	west-northwest	5-year shoreline
135	Alt 2A	Spring	west-northwest	5-year shoreline
136	Alt 2B	Spring	west-northwest	5-year shoreline
137	Alt3A	Spring	west-northwest	5-year shoreline
138	Alt 3B	Spring	west-northwest	5-year shoreline
139	Alt 4A	Spring	west-northwest	5-year shoreline

(Continued)

Table 7-6 (Concluded)

Run	Alternative	Tide	Wave Direction	Wave Condition
140	Existing	Spring	west	5-year shoreline
141	Alt 2A	Spring	west	5-year shoreline
142	Alt 2B	Spring	west	5-year shoreline
143	Alt3A	Spring	west	5-year shoreline
144	Alt 3B	Spring	west	5-year shoreline
145	Alt 4A	Spring	west	5-year shoreline
146	Existing	Spring	west-southwest	5-year shoreline
147	Alt 2A	Spring	west-southwest	5-year shoreline
148	Alt 2B	Spring	west-southwest	5-year shoreline
149	Alt3A	Spring	west-southwest	5-year shoreline
150	Alt 3B	Spring	west-southwest	5-year shoreline
151	Alt 4A	Spring	west-southwest	5-year shoreline
152	Existing	Spring	west-northwest	30-year shoreline
153	Alt 2A	Spring	west-northwest	30-year shoreline
154	Alt 2B	Spring	west-northwest	30-year shoreline
155	Alt3A	Spring	west-northwest	30-year shoreline
156	Alt 3B	Spring	west-northwest	30-year shoreline
157	Alt 4A	Spring	west-northwest	30-year shoreline
158	Existing	Spring	west	30-year shoreline
159	Alt 2A	Spring	west	30-year shoreline
160	Alt 2B	Spring	west	30-year shoreline
161	Alt3A	Spring	west	30-year shoreline
162	Alt 3B	Spring	west	30-year shoreline
163	Alt 4A	Spring	west	30-year shoreline
164	Existing	Spring	west-southwest	30-year shoreline
165	Alt 2A	Spring	west-southwest	30-year shoreline
166	Alt 2B	Spring	west-southwest	30-year shoreline
167	Alt3A	Spring	west-southwest	30-year shoreline
168	Alt 3B	Spring	west-southwest	30-year shoreline
169	Alt 4A	Spring	west-southwest	30-year shoreline

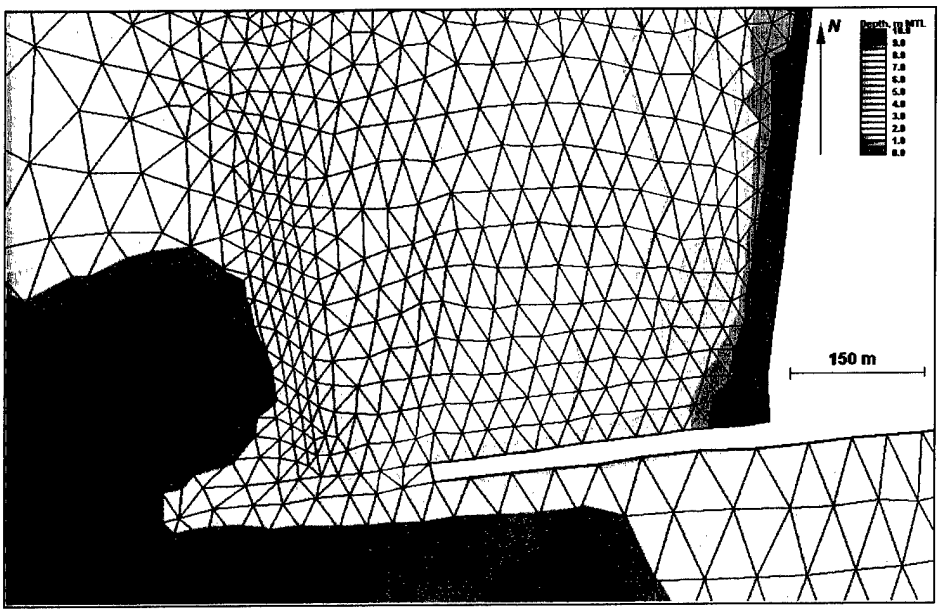

Figure 7-37. Existing condition bathymetry

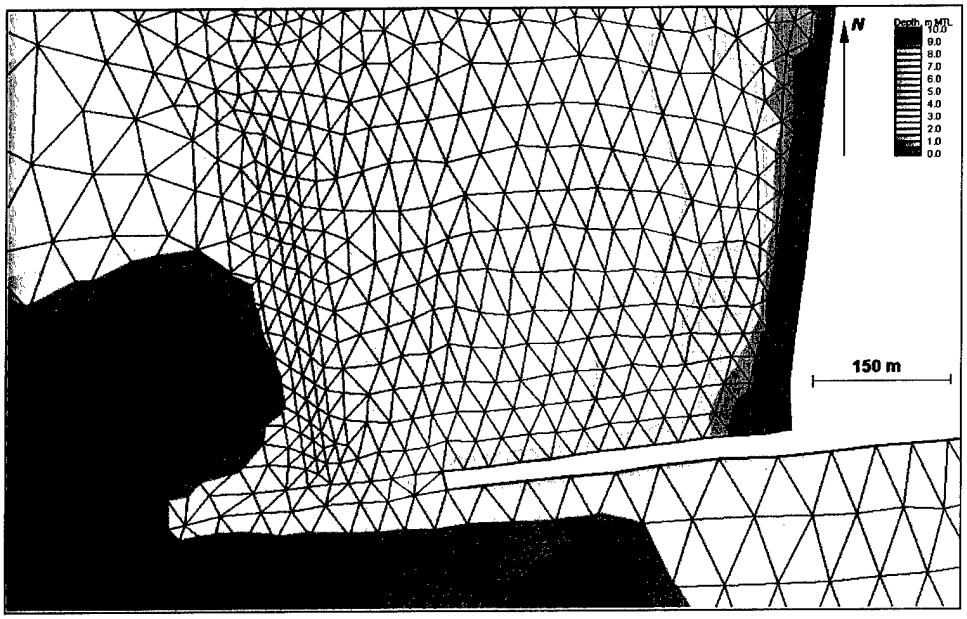

Figure 7-38. Alternative 2A bathymetry

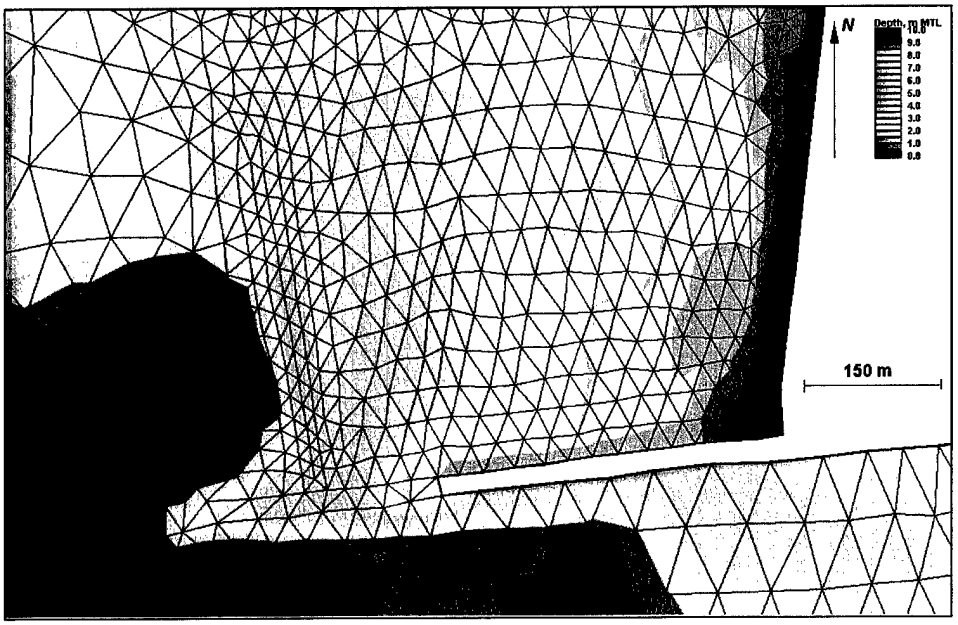

Figure 7-39. Alternative 2B bathymetry

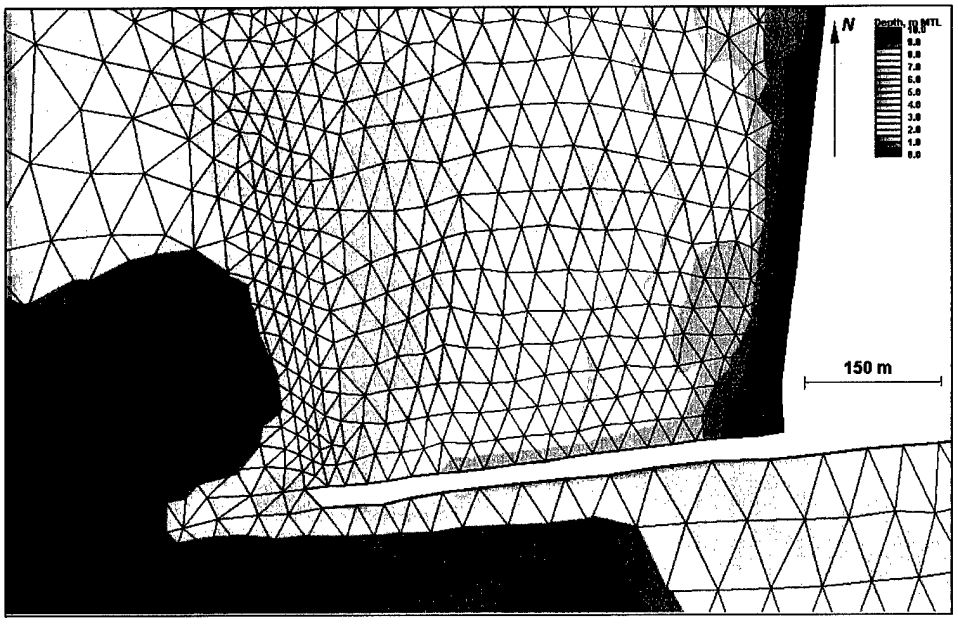

Figure 7-40. Alternative 3A bathymetry

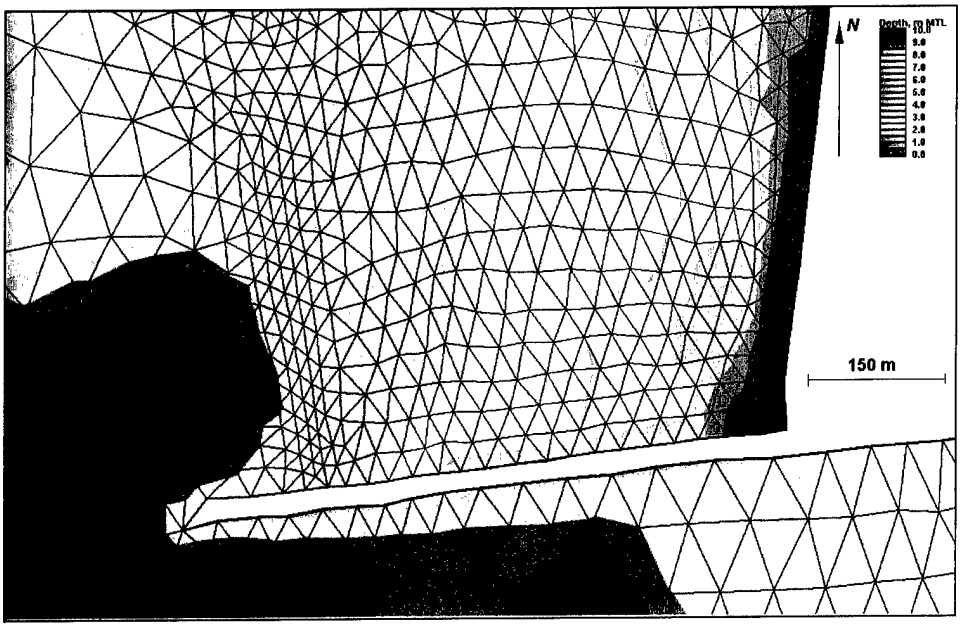

Figure7-41. Alternative 3B bathymetry

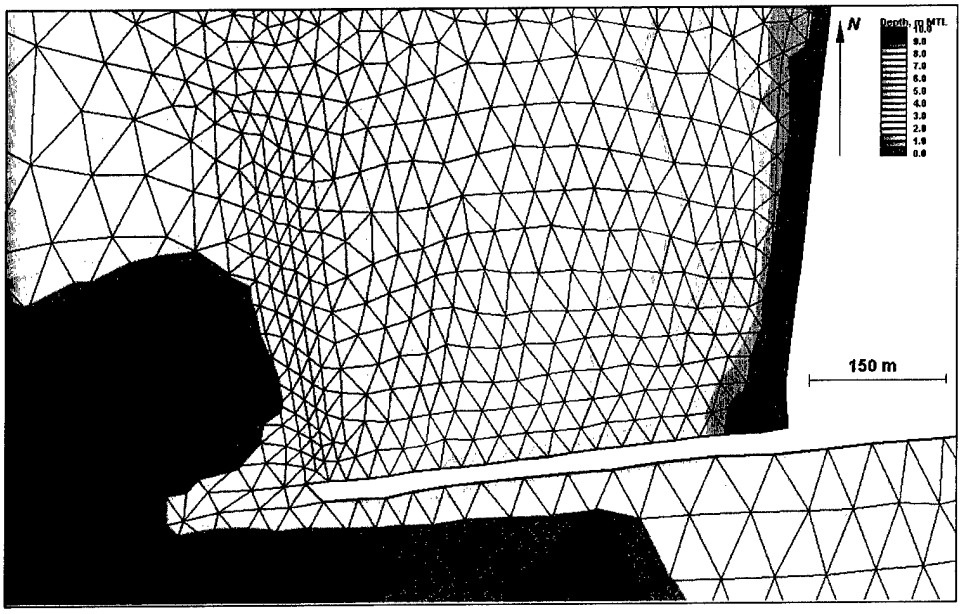

Figure 7-42. Alternative 4A bathymetry

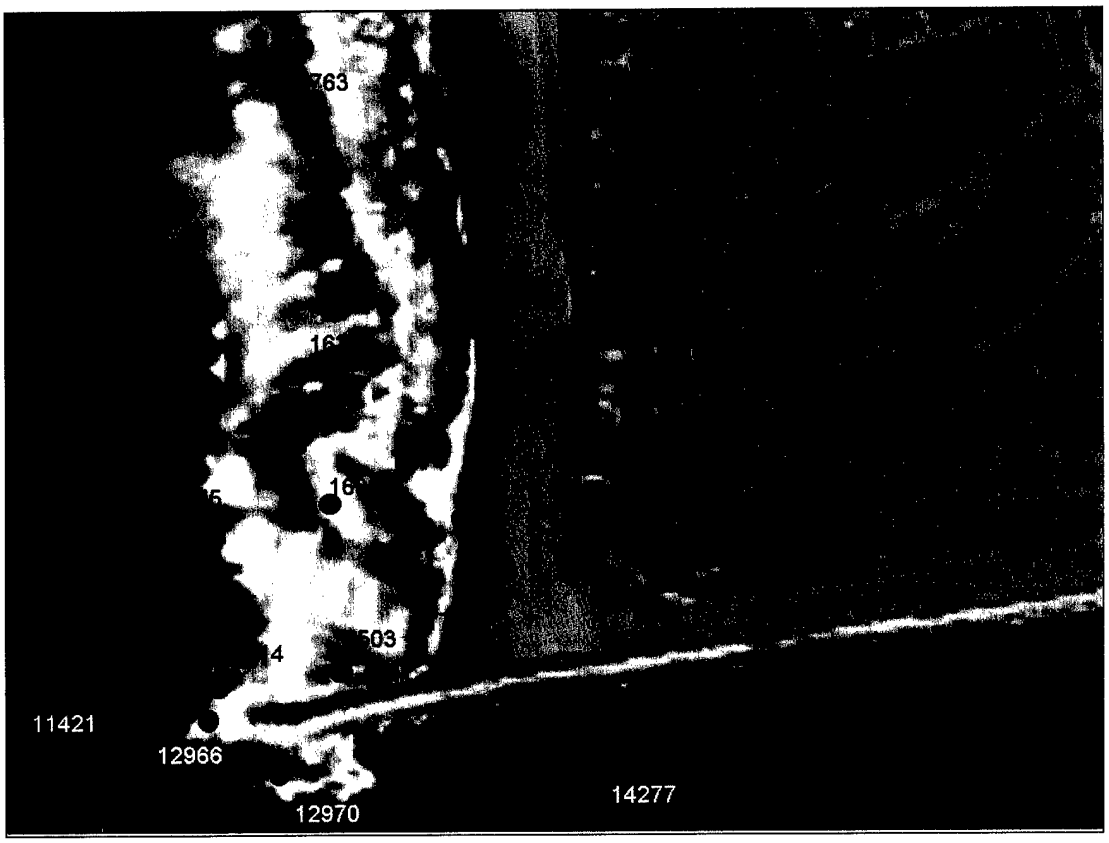

Figure 7-43. ADCIRC grid node locations for statistical analysis

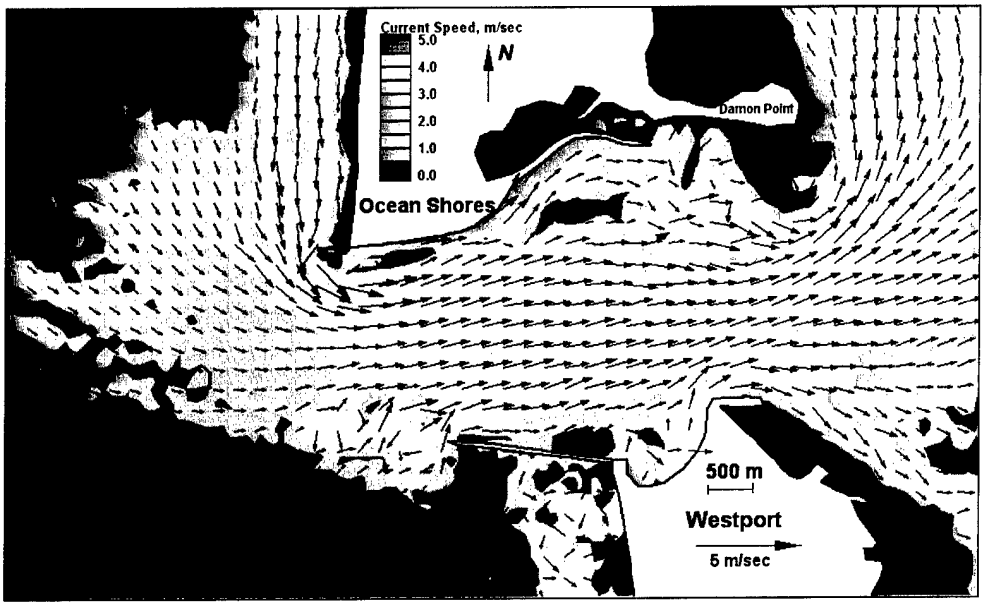

Figure 7-44. Run 104 (west-northwest, spring tide), inlet view of flood tide

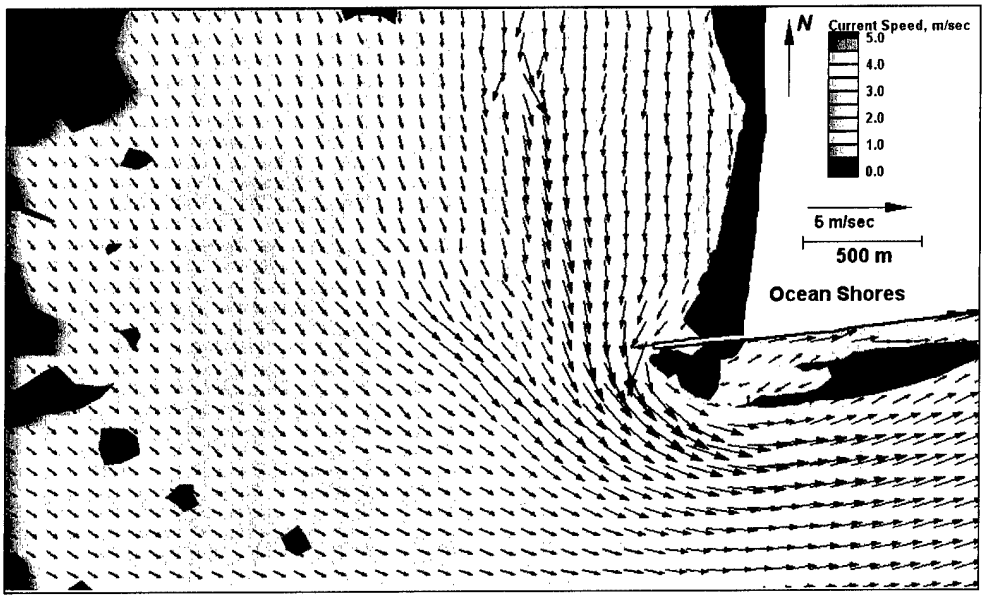

Figure 7-45. Run 104 (west-northwest, spring tide), north jetty view of flood tide

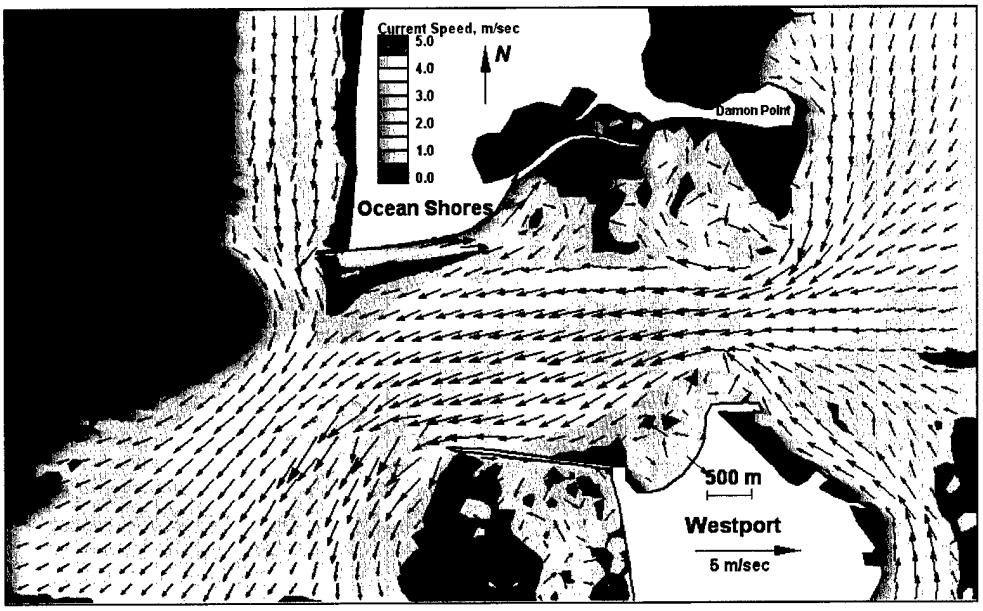

Figure 7-46. Run 104 (west-northwest, spring tide), inlet view of ebb tide

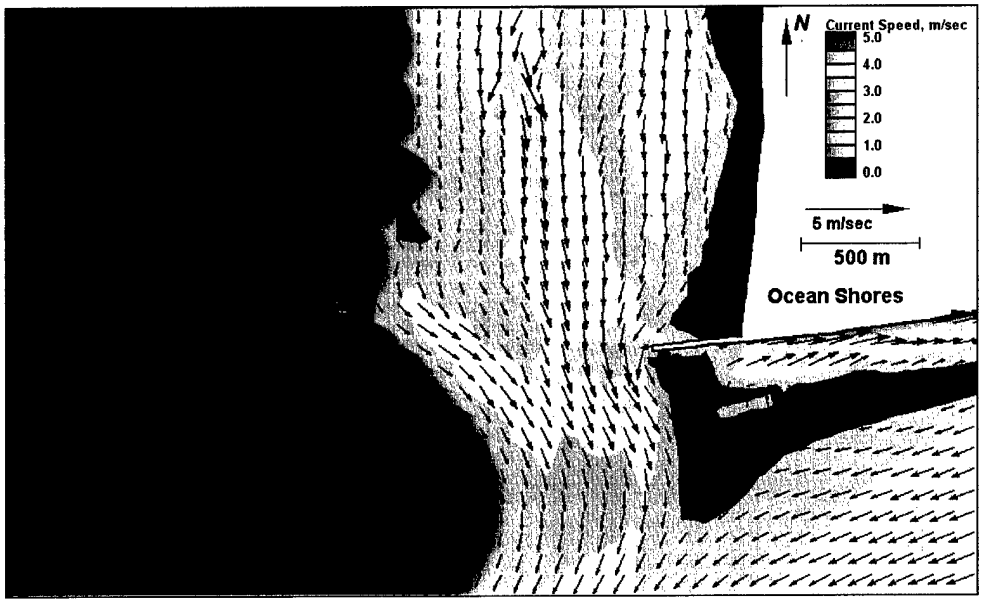

Figure 7-47. Run 104 (west-northwest, spring tide), north jetty view of ebb tide

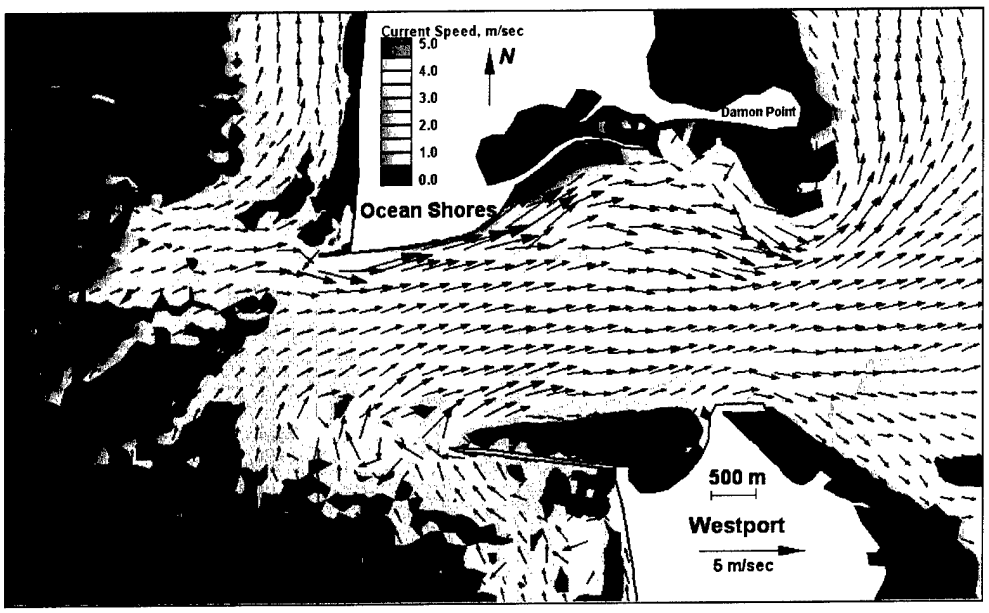

Figure 7-48. Run 105 (west-southwest, spring tide), inlet view of flood tide

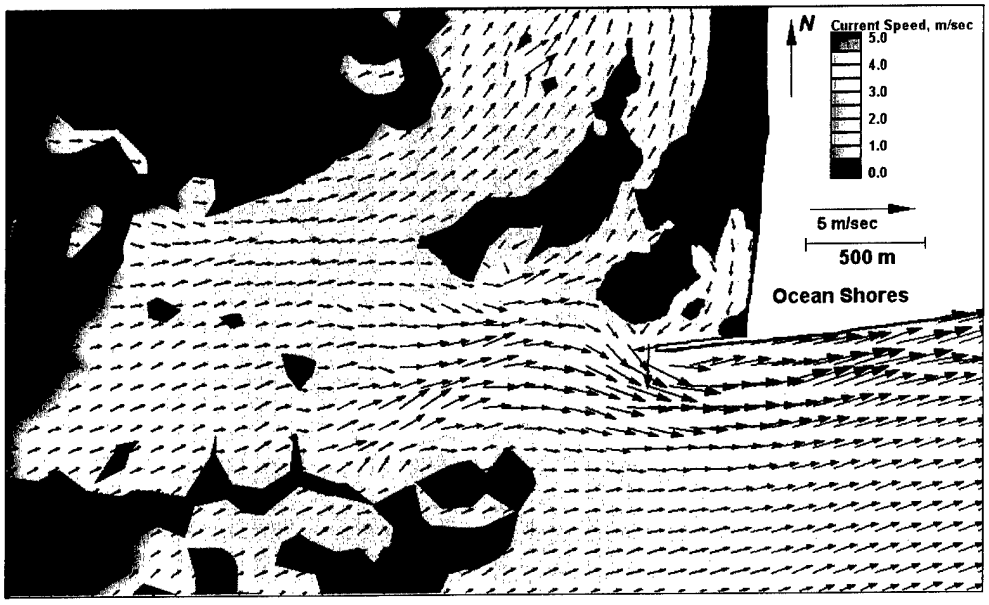

Figure 7-49. Run 105 (west-southwest, spring tide), north jetty view of flood tide

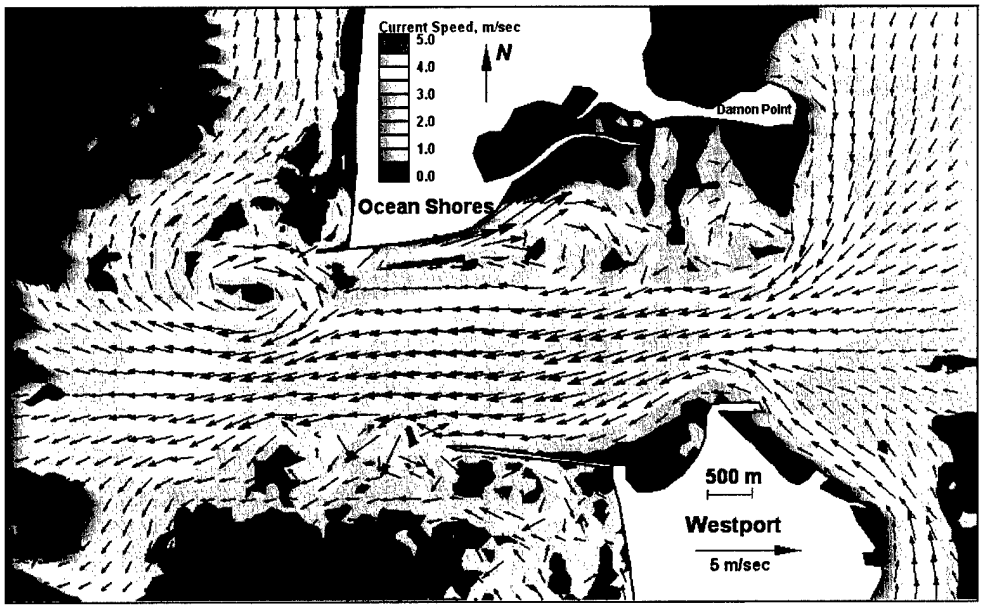

Figure 7-50. Run 105 (west-southwest, spring tide), inlet view of ebb tide

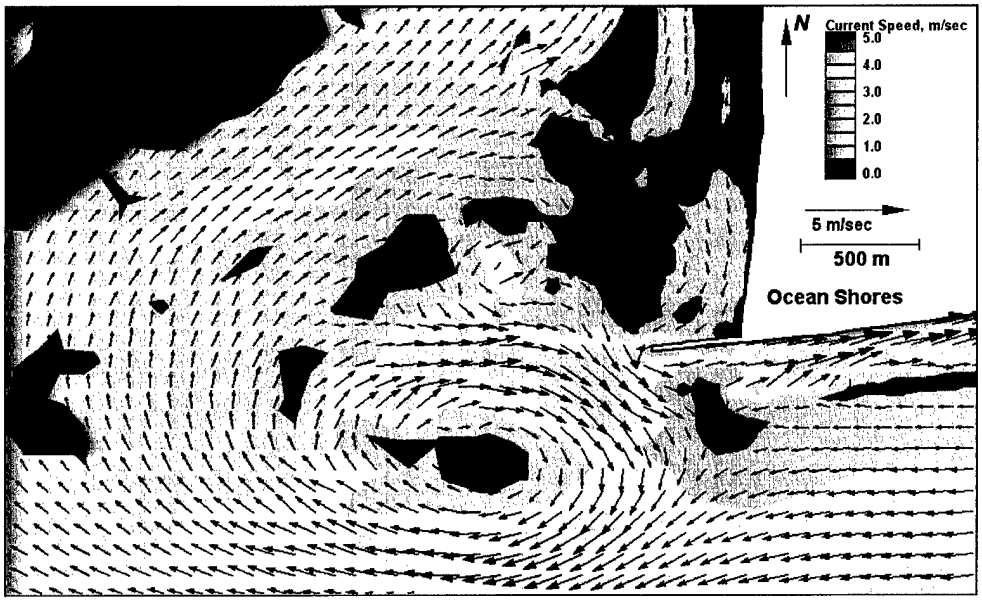

Figure 7-51. Run 105 (west-southwest, spring tide), north jetty view of ebb tide

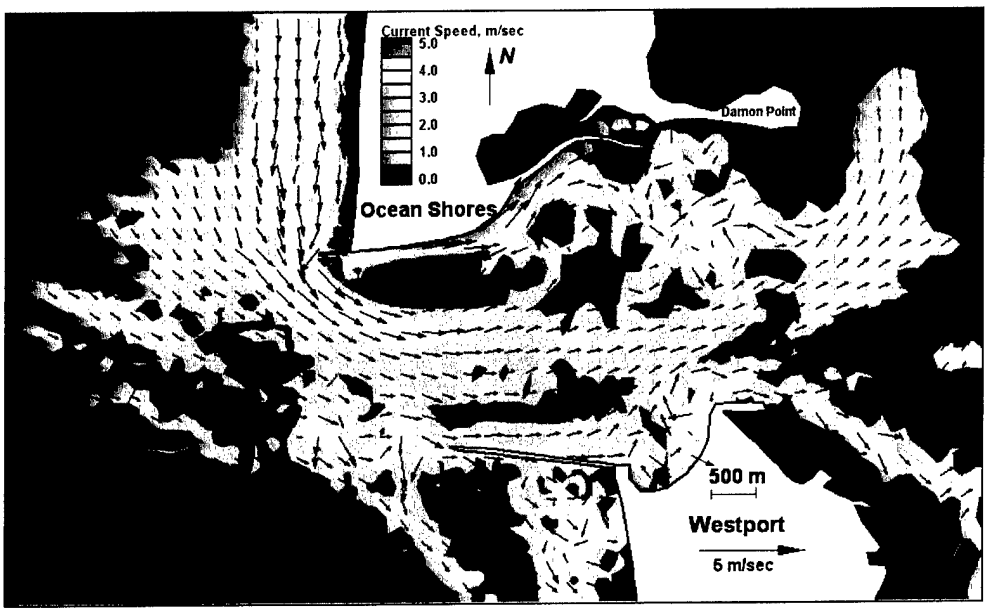

Figure 7-52. Run 106 (west-northwest, neap tide), inlet view of flood tide

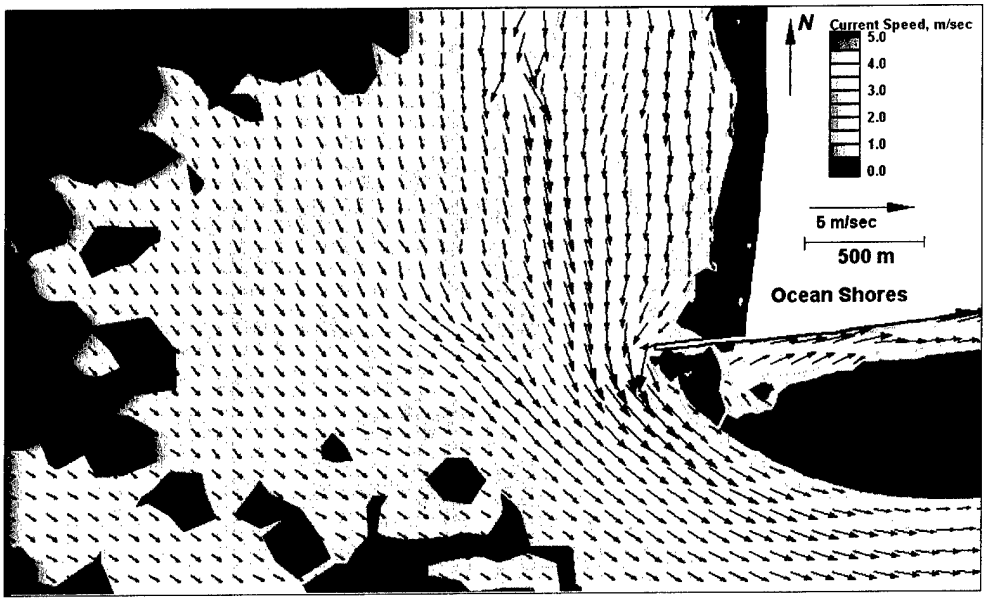

Figure 7-53. Run 106 (west-northwest, neap tide), north jetty view of flood tide

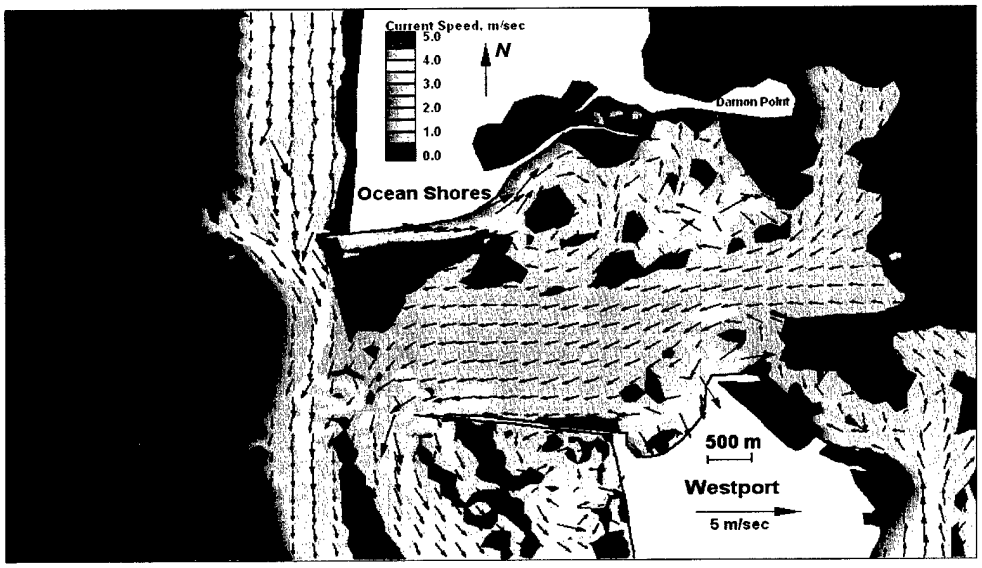

Figure 7-54. Run 106 (west-northwest, neap tide), inlet view of ebb tide

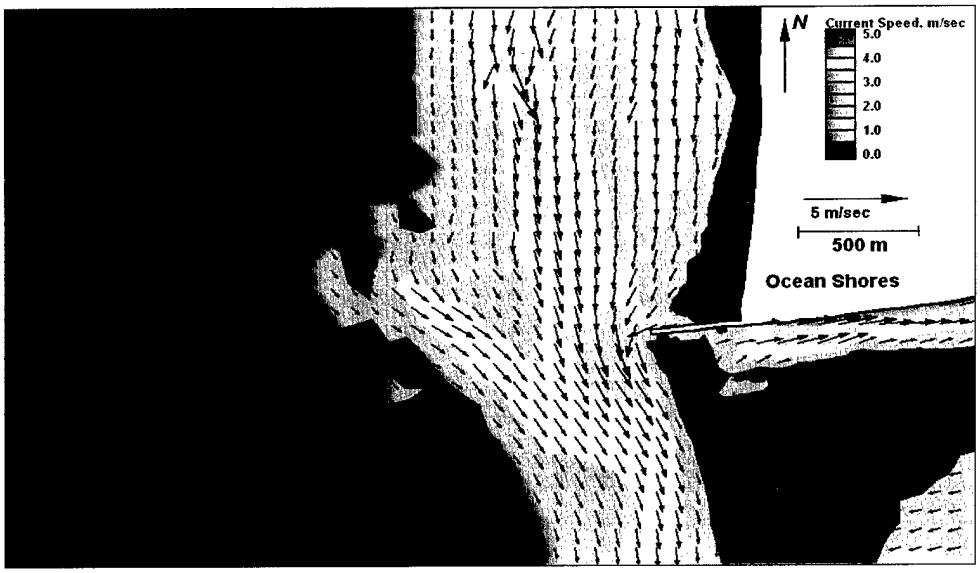

Figure 7-55. Run 106 (west-northwest, neap tide), north jetty view of ebb tide

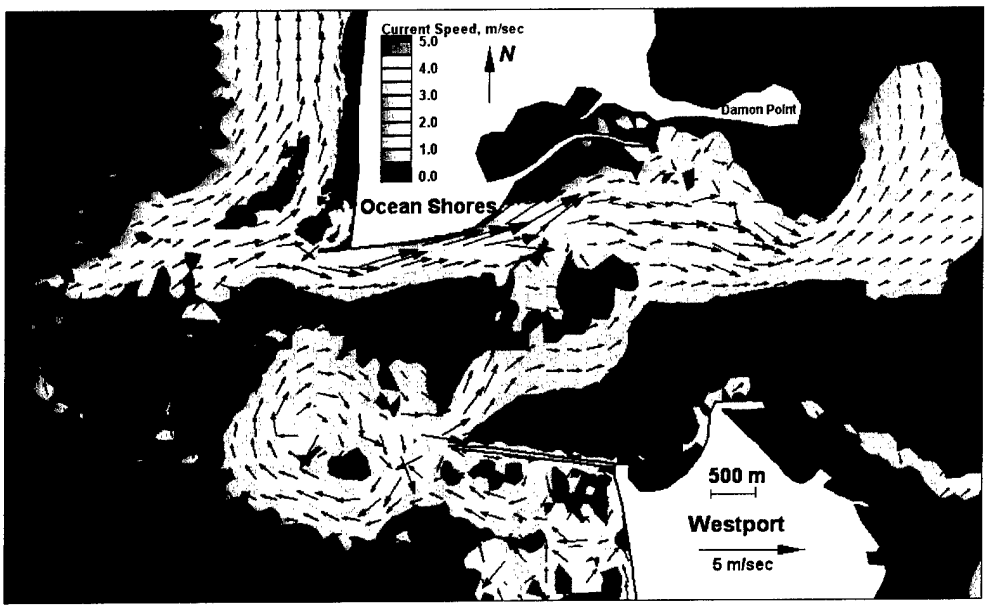

Figure 7-56. Run 107 (west-southwest, neap tide), inlet view of flood tide

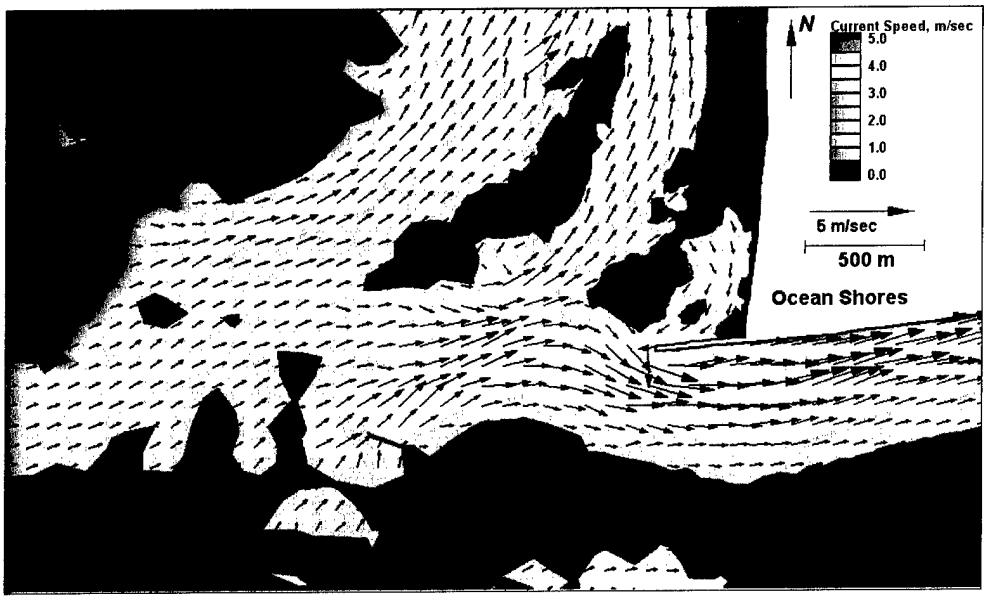

Figure 7-57. Run 107 (west-southwest, neap tide), north jetty view of flood tide

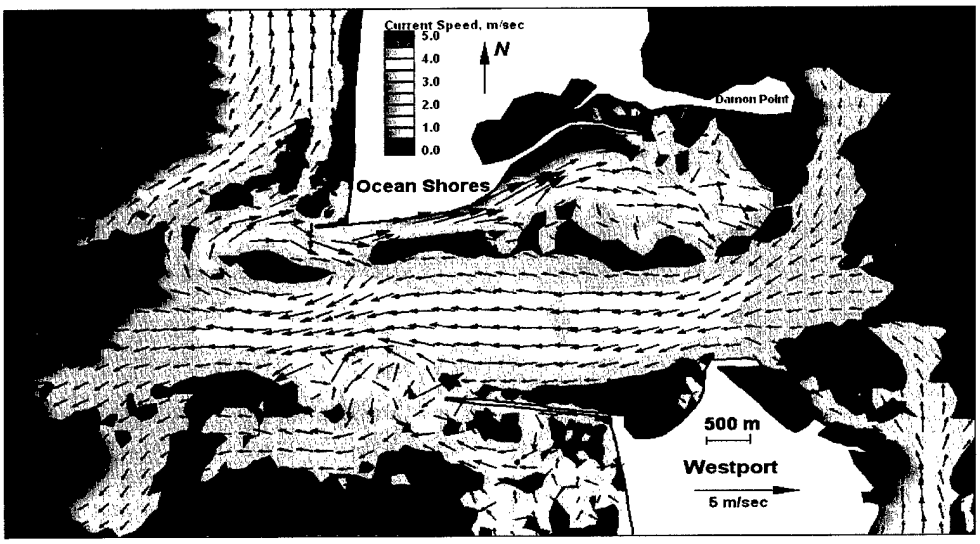

Figure 7-58. Run 107 (west-southwest, neap tide), inlet view of ebb tide

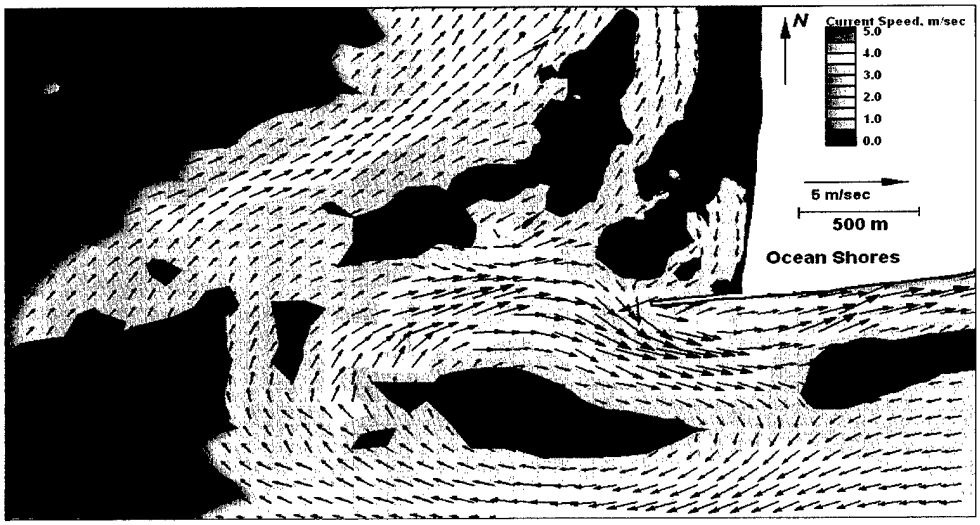

Figure 7-59. Run 107 (west-southwest, neap tide), north jetty view of ebb tide

jetty is generated by the combined tide and wave condition. Figures 7-50 and 7-51 show ebb tide conditions with a west-southwest wave and spring tide forcing (Run 105). The ebb jet and northbound longshore current interact to create a large, clockwise gyre near the north jetty. The ebb jet is directed to the west under the influence of west-southwest waves (as compared to the ebb jet being deflected to the south by west-northwest waves).

Figures 7-52 and 7-53 show flood tide conditions with a west-northwest wave and neap tide forcing (Run 106). As with spring tide forcing, the flood current around the north jetty tip is approximately 3 m/sec, and the longshore current near Ocean Shores generally ranges between 1.3-1.7 m/sec, whereas the flood current in the inlet throat is less than observed for spring tide condition (0.5-0.9 m/sec). This region is least influenced by the combination of waves and currents and is dominated by tidal currents, hence the reduction in current magnitude from spring to neap conditions. Figures 7-54 and 7-55 show ebb tide conditions with a west-northwest wave and neap tide forcing (Run 106). Currents in the inlet are weaker than for spring tide (0.7-0.9 m/sec), and the weakened ebb jet merges with the southbound longshore current. Currents around the north jetty are strongest, and the longshore current near Ocean Shores is similar to the spring tide condition simulation (Run 104). The longshore current across the inlet mouth is directed due south because of the weakened ebb jet and, therefore, creates a stronger longshore current along the Westport surf zone than the spring tide condition simulation (Run 104).

Figures 7-56 and 7-57 show flood tide conditions with a west-southwest wave and neap tide forcing (Run 107). The longshore current at Ocean Shores is slightly stronger than the longshore current observed for spring tide conditions (Run 105). Currents in the inlet throat are concentrated along the north jetty, influenced by the west-southwest direction of wave approach. Generally, flood tidal currents are weak (0.5 m/sec) in the inlet throat. Figures 7-58 and 7-59 show ebb tide conditions with a west-southwest wave and neap tide forcing (Run 107). Ebb currents in the inlet throat are 1.3-1.7 m/sec, less than spring tide ebb currents, but sufficient to create an ebb jet beyond the jetties. The ebb jet and northbound longshore current interact to create an elongated, clockwise gyre near the north jetty.

Statistical analysis at selected locations

Statistical analysis of the velocity time-series was performed at 16 ADCIRC node locations (Figure 7-43). These locations were selected based on their proximity to the existing and proposed structural alternatives. The northernmost three points are located approximately 1 km north of the north jetty. The second and third northernmost sets of points are approximately 500 and 250 m north of the north jetty, respectively, and were selected because they are near the end of Alt 2A (Long Spur) and in the lee of the structure, respectively. The remaining points were selected because of their proximity to the north jetty and jetty rehabilitation alternatives.

In the analysis of each 5-day Steering Module time-series, the first day of the simulation was not included because the simulations had a 1-day ramp period (where forcing conditions are gradually increased to full forcing over a selected time period). Analysis of the remaining 4 days (eight tidal cycles) showed

consistent response for each tidal cycle, indicating periodicity. Therefore, four tidal cycles or approximately 2 days (approximately the start of Day 2 through the start of Day 4) were selected as representative of the simulation and statistics were computed for this time period. Table 7-7 lists the mean current components computed for the 16 node locations for each simulation. A positive value indicates a northward mean current, and a negative value indicates a southward mean current for the *V* velocity component. A positive value indicates an eastward mean current, and a negative value indicates a westward mean current for the *U* velocity component.

Mean current maps for the 16 node locations are also given for each simulation in Figures 7-60 through 7-83. The figures provide a visual representation of the information contained in Table 7-7. Table 7-8 compiles the difference between the mean for a given alternative and the mean for the corresponding existing condition. For example, Runs 108, 112, 116, 120, and 124 are compared to Run 104 because each is for west-northwest, spring tide conditions. For the *U*-component of velocity at a given node, positive values indicate an increase in eastbound or reduction in westbound mean current, and negative values indicate a reduction in eastbound or increase in westbound mean current caused by the structural alternative. For the *V*-component of velocity at a given node, positive values indicate an increase in northbound current or a reduction in southbound current, and negative values indicate a reduction in northbound or increase in southbound mean current caused by the alternative.

The statistical summaries of the velocity components at 16 selected nodes show that the strongest southbound current occurs near the jetty tip at Node 12966, regardless of the direction of wave approach. The interaction of tidal and wave-induced currents close to the north jetty tip (at Node 12966) shows the modeled west-northwest wave conditions produce southbound currents, and modeled west-southwest wave conditions also produce southbound currents. West-southwest waves induce a current to the north, but there is a flow reversal within 500 m north of the north jetty resulting in a southbound mean current as recorded at eight of the nine nodes north of the north jetty.

The maximum eastbound current is a function of wave approach. West-southwest waves lead to the strongest eastbound current in the inlet at Node 14277. West-northwest waves have the strongest eastbound current off the north jetty at Node 11421 for existing and spur alternatives and at the jetty tip (Nodes 12966 and 13614) for the jetty rehabilitation alternatives. Maximum changes for the 16 nodes generally occur near the jetty tip. The jetty rehabilitation alternatives block and deflect current and reduce currents dramatically in the immediate vicinity of the structural alternatives.

Analysis of Ocean Shores nodes. Analysis of the nine nodes north of the north jetty was divided according to the response to wave approach and structural alternative as follows:

a. Alternatives 2A/2B and west-northwest waves.

b. Altternatives 2A/2B and west-southwest waves.

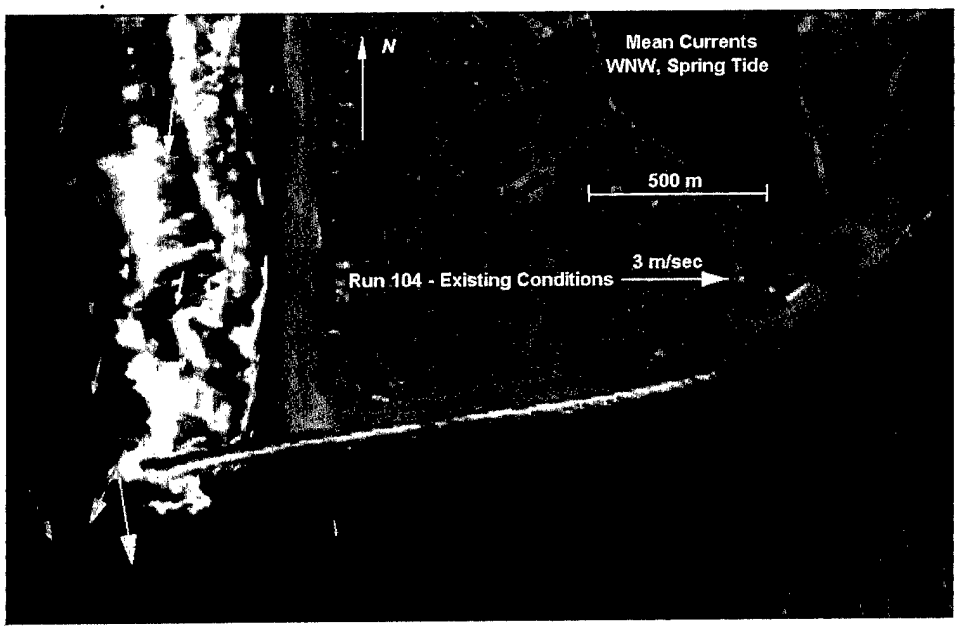

Figure 7-60. Mean currents for Run 104 (existing, west-northwest waves, spring tide)

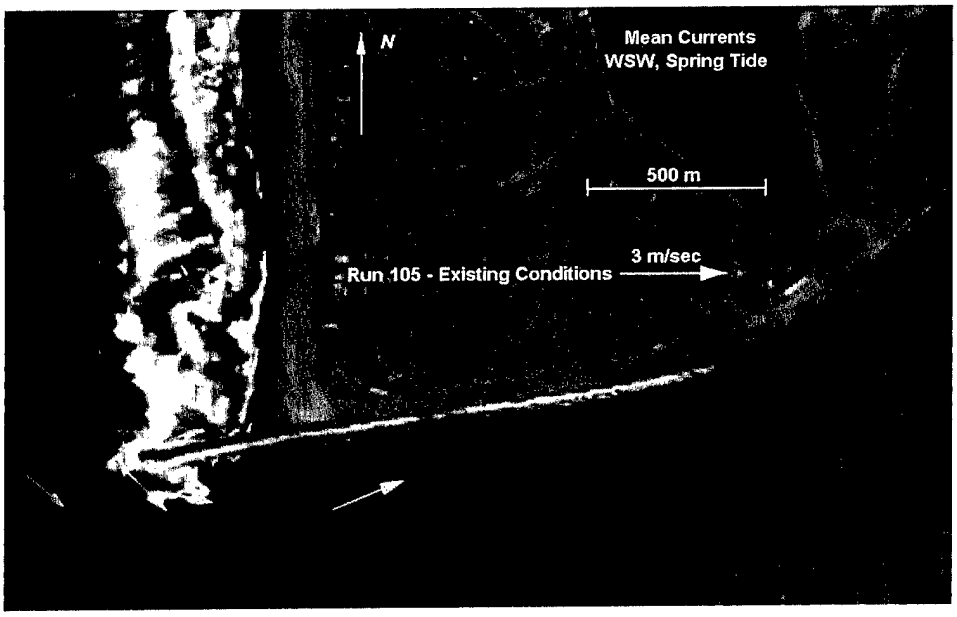

Figure 7-61. Mean currents for Run 105 (existing, west-southwest waves, spring tide)

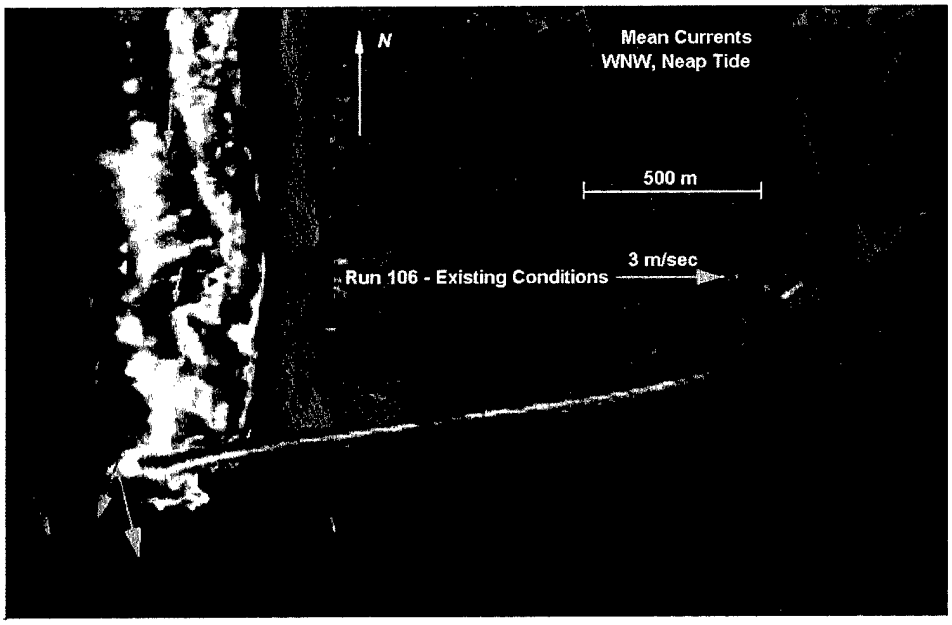

Figure 7-62. Mean currents for Run 106 (existing, west-northwest waves, neap tide)

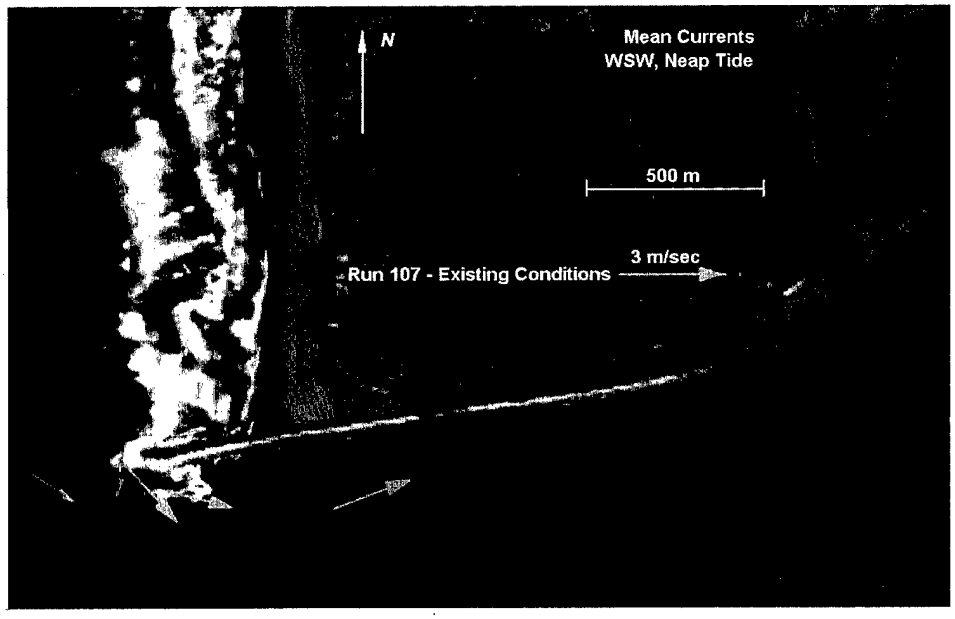

Figure 7-63. Mean currents for Run 107 (existing, west-southwest waves, neap tide)

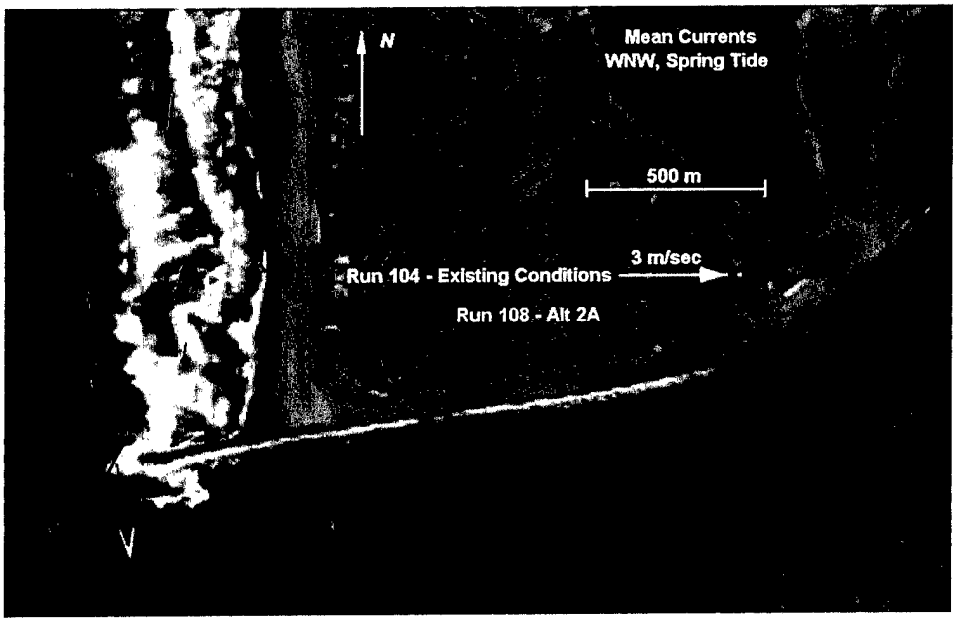

Figure 7-64. Mean currents for existing (Run 104) versus Alt 2A (Run 108)

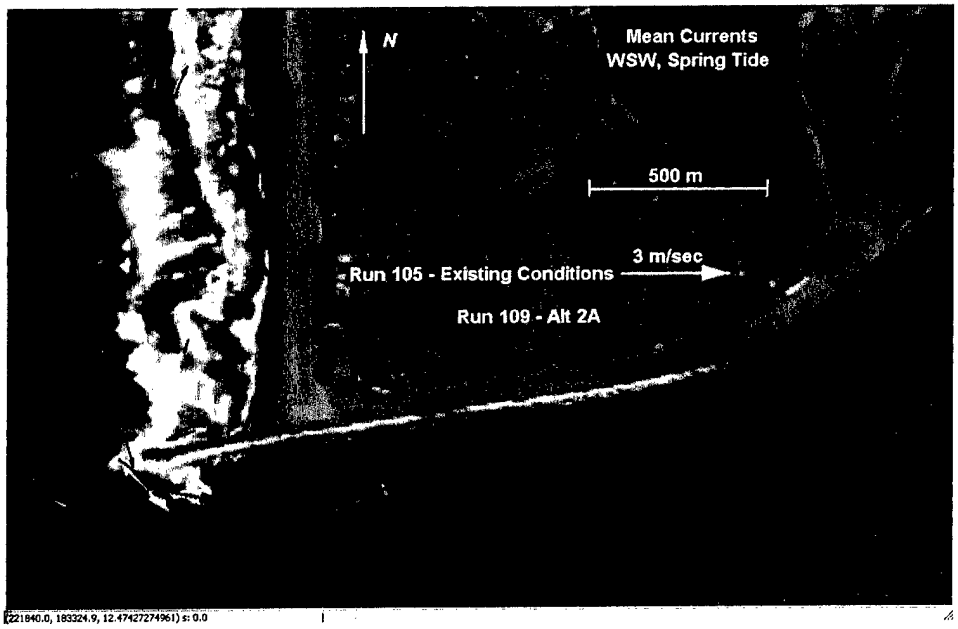

Figure 7-65. Mean currents for existing (Run 105) versus Alt 2A (Run 109)

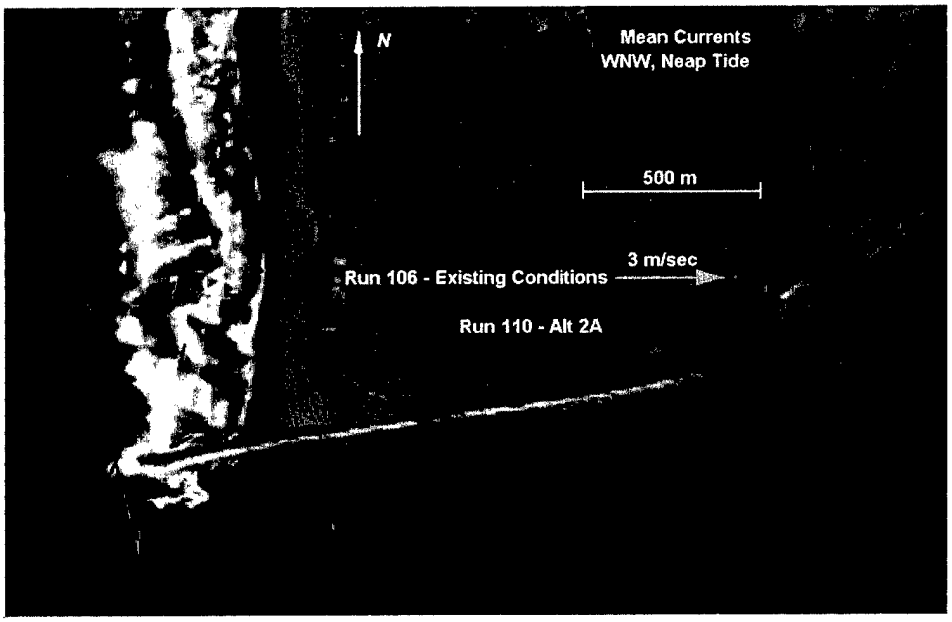

Figure 7-66. Mean currents for existing (Run 106) versus Alt 2A (Run 110)

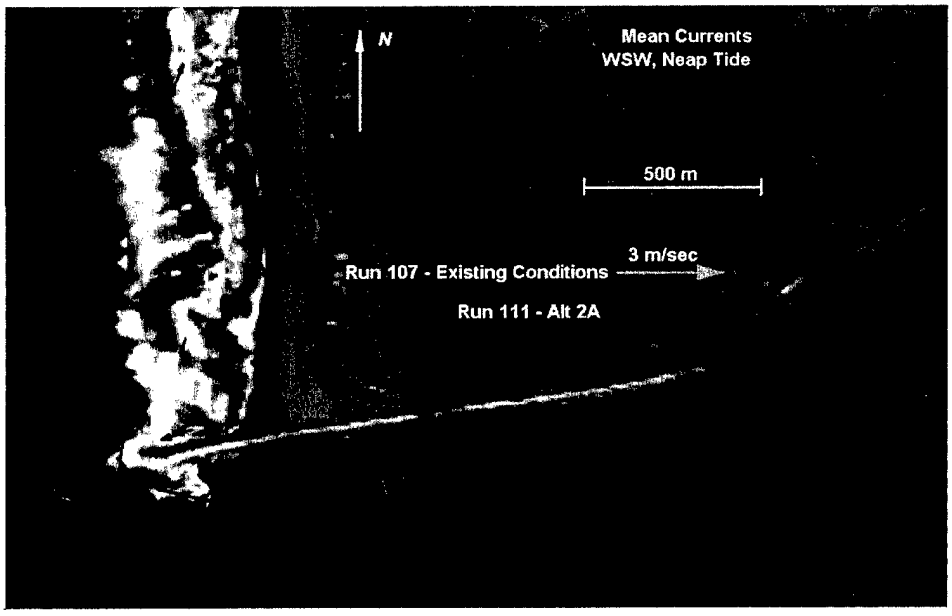

Figure 7-67. Mean currents for existing (Run 107) versus Alt 2A (Run 111)

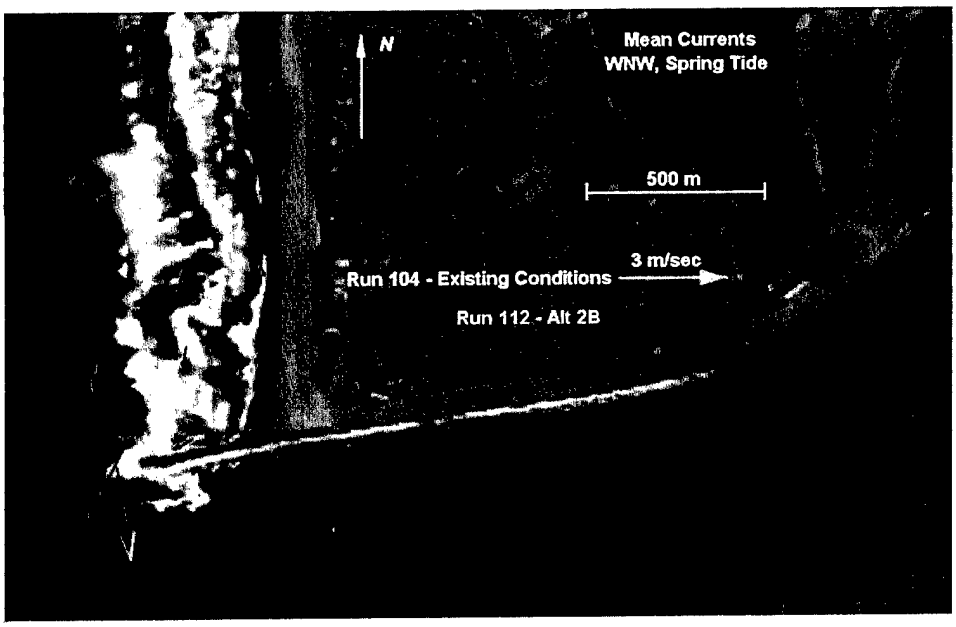

Figure 7-68. Mean currents for existing (Run 104) versus Alt 2B (Run 112)

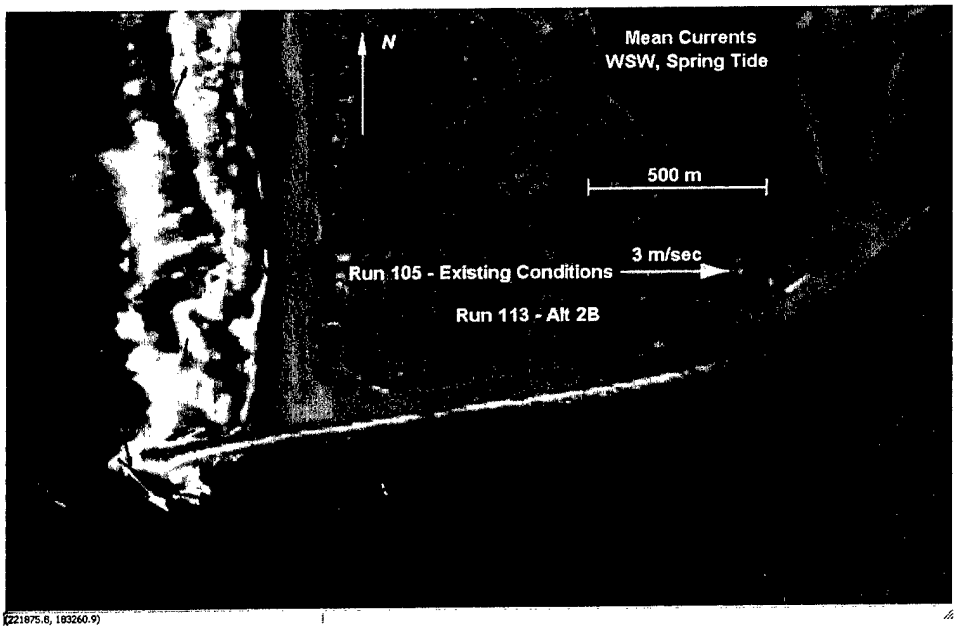

Figure 7-69. Mean currents for existing (Run 105) versus Alt 2B (Run 113)

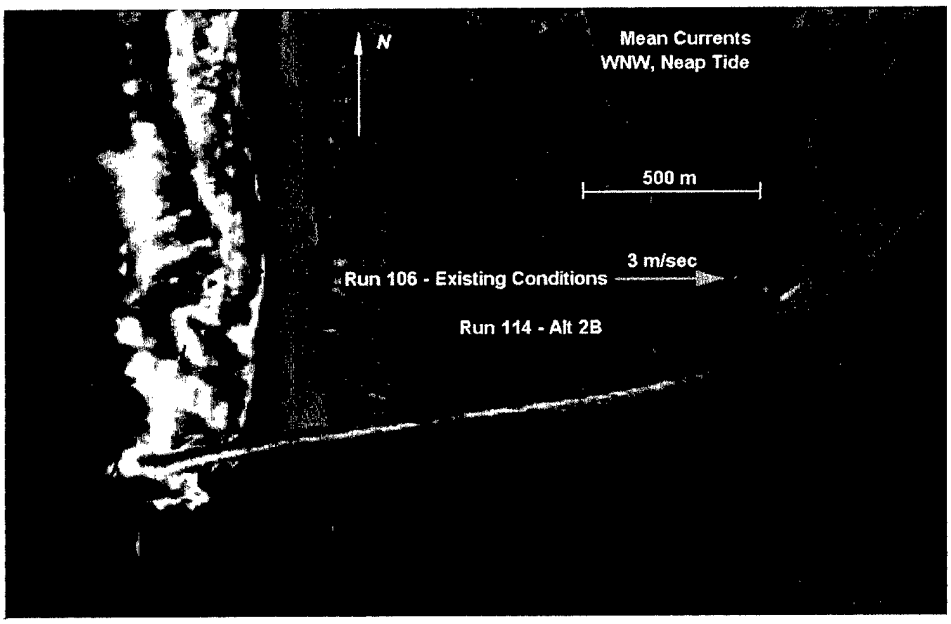

Figure 7-70. Mean currents for existing (Run 106) versus Alt 2B (Run 114)

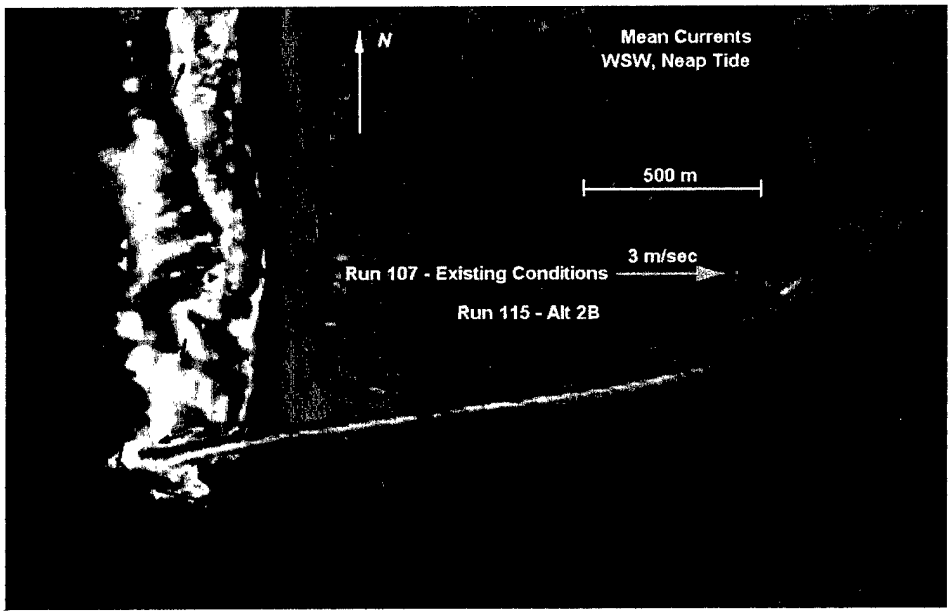

Figure 7-71. Mean currents for existing (Run 107) versus Alt 2B (Run 115)

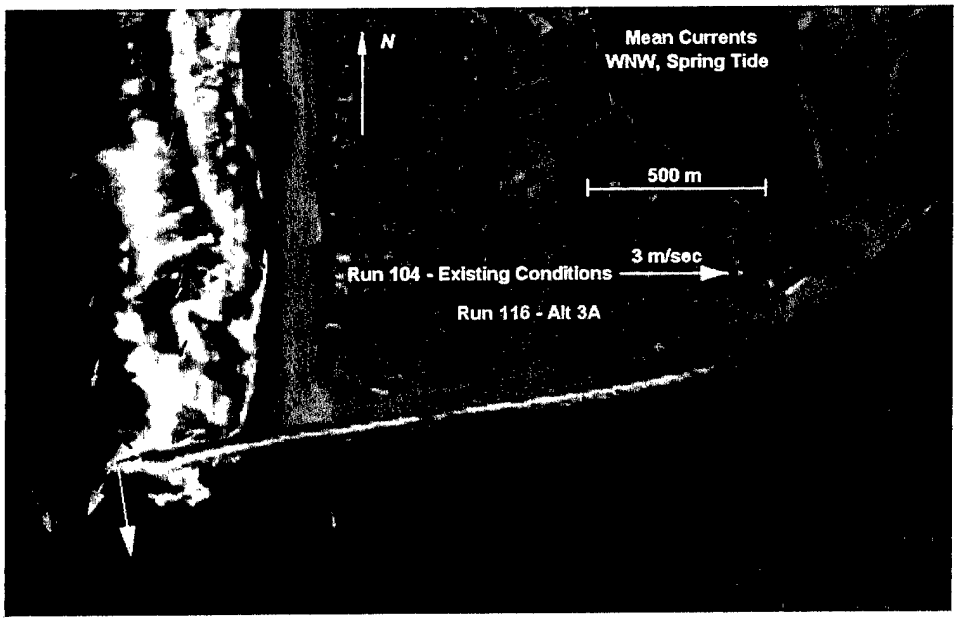

Figure 7-72. Mean currents for existing (Run 104) versus Alt 3A (Run 116)

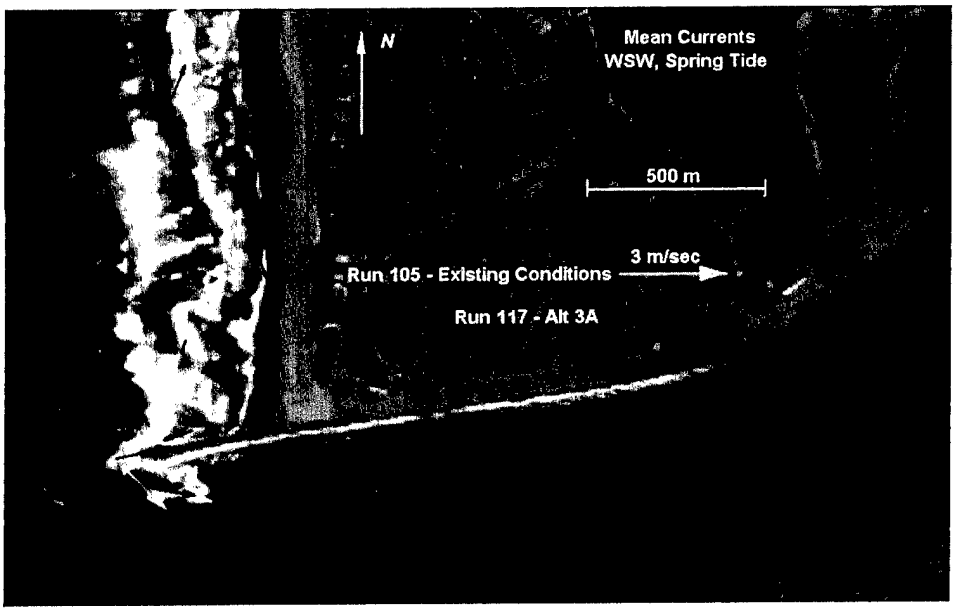

Figure 7-73. Mean currents for existing (Run 105) versus Alt 3A (Run 117)

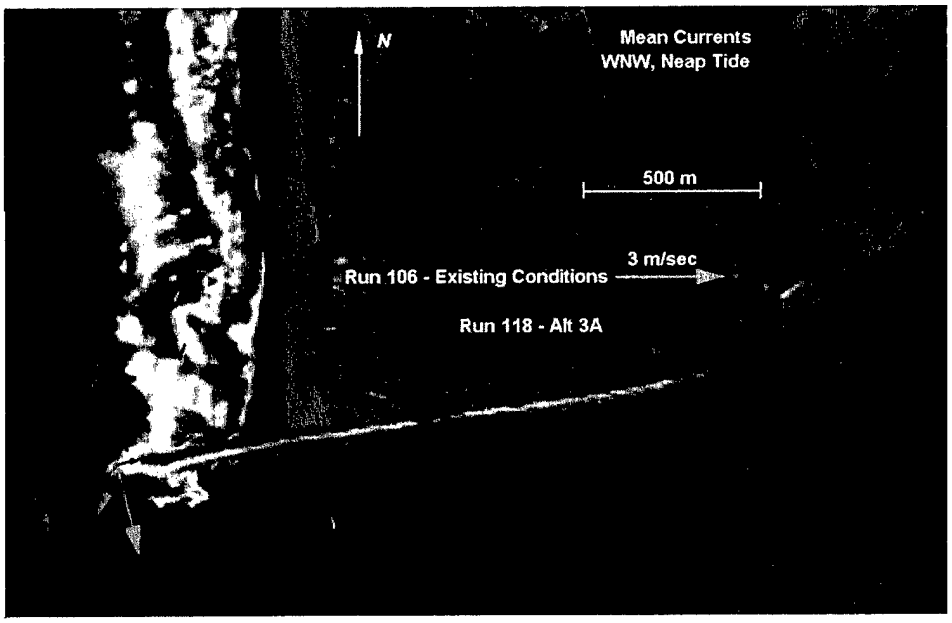

Figure 7-74. Mean currents for existing (Run 106) versus Alt 3A (Run 118)

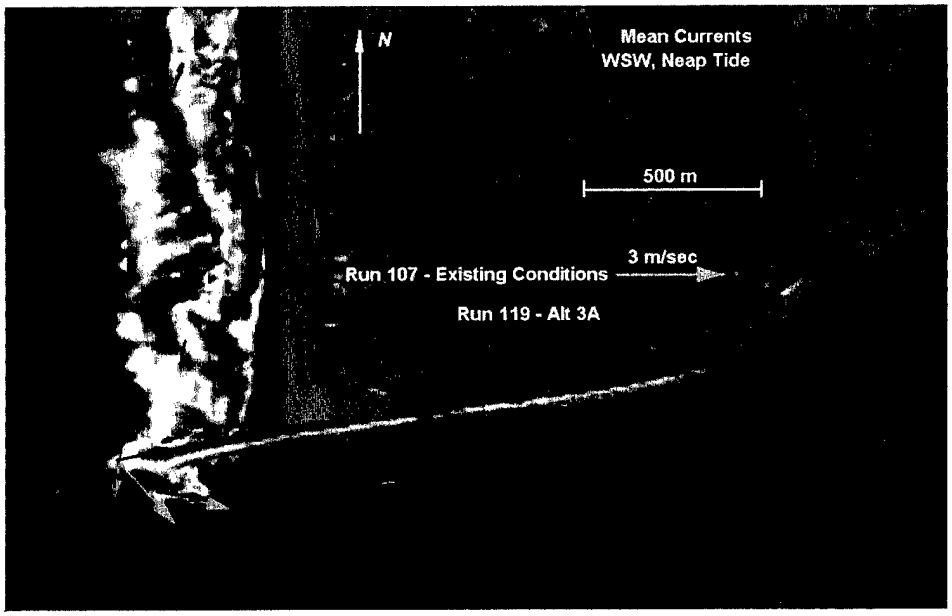

Figure 7-75. Mean currents for existing (Run 107) versus Alt 3A (Run 119)

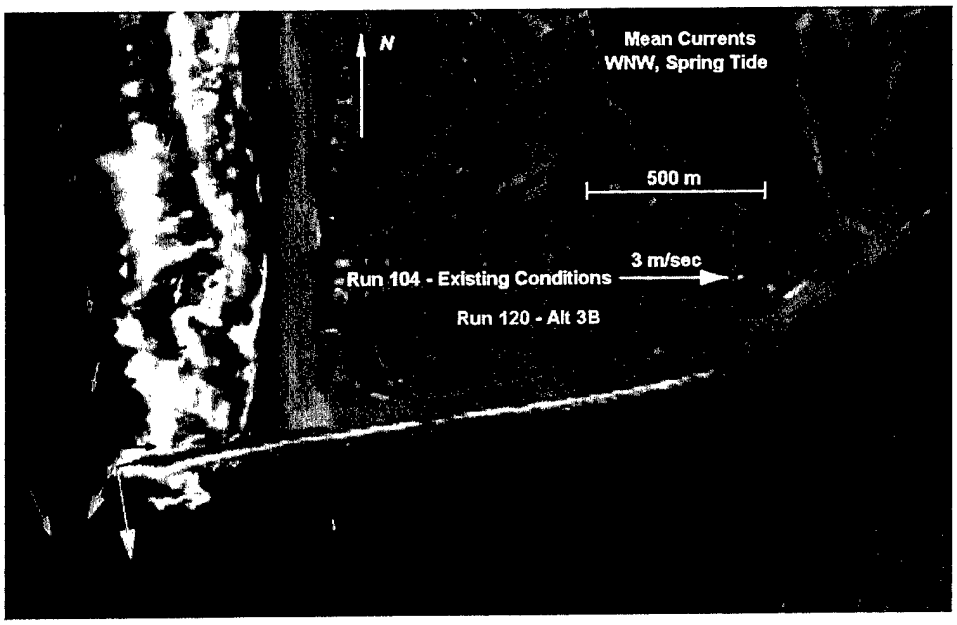

Figure 7-76. Mean currents for existing (Run 104) versus Alt 3B (Run 120)

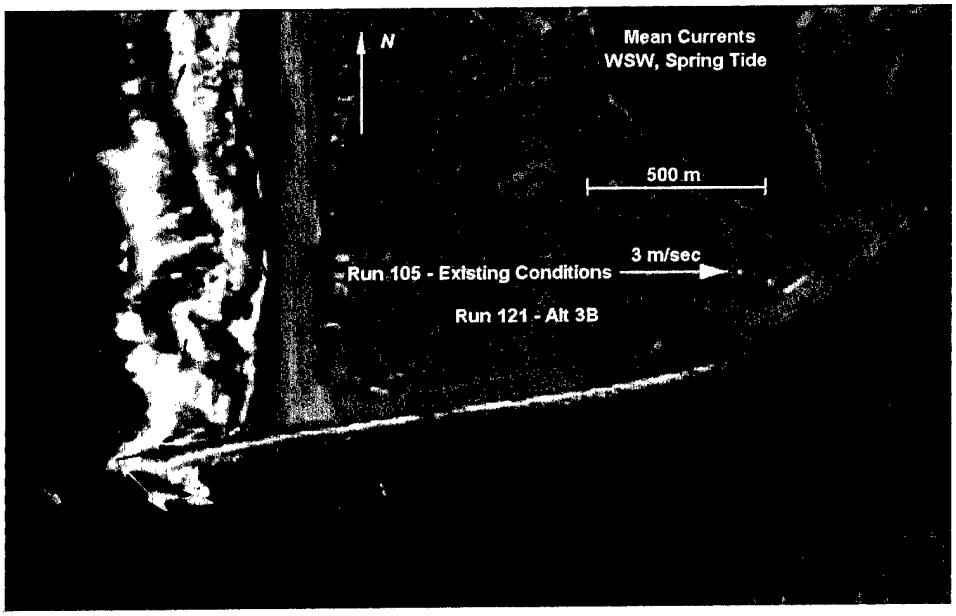

Figure 7-77. Mean currents for existing (Run 105) versus Alt 3B (Run 121)

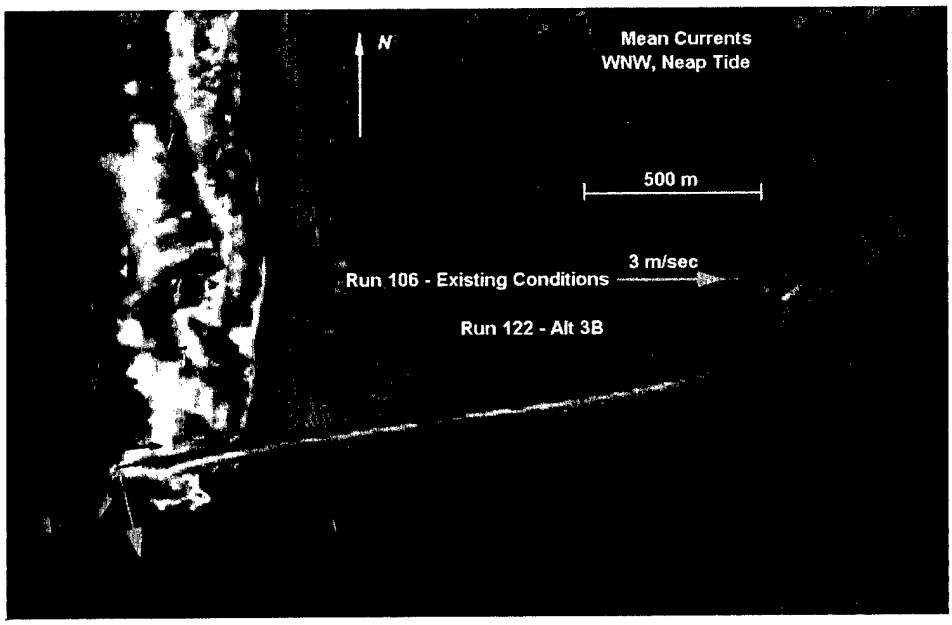

Figure 7-78. Mean currents for existing (Run 106) versus Alt 3B (Run 122)

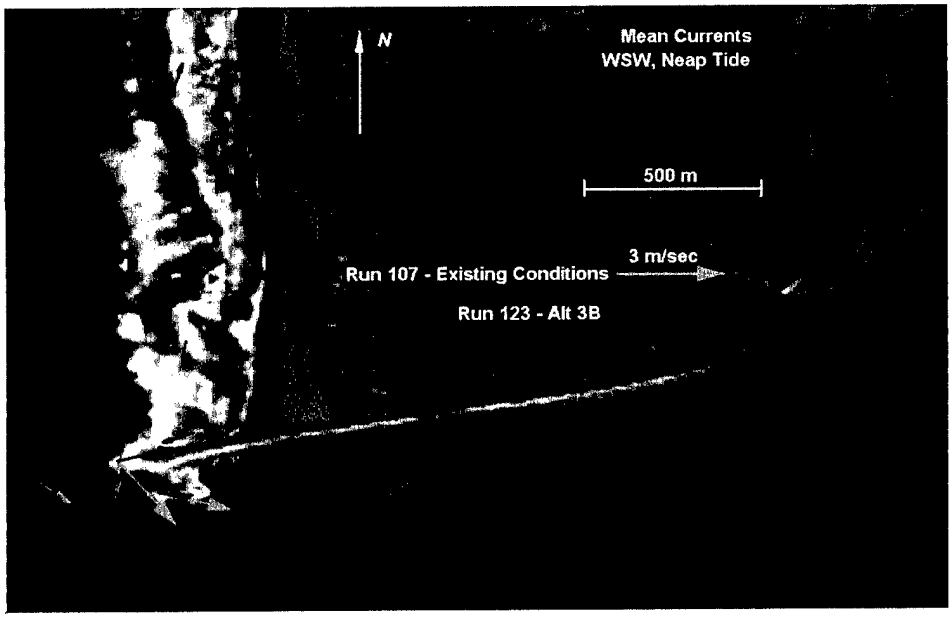

Figure 7-79. Mean currents for existing (Run 107) versus Alt 3B (Run 123)

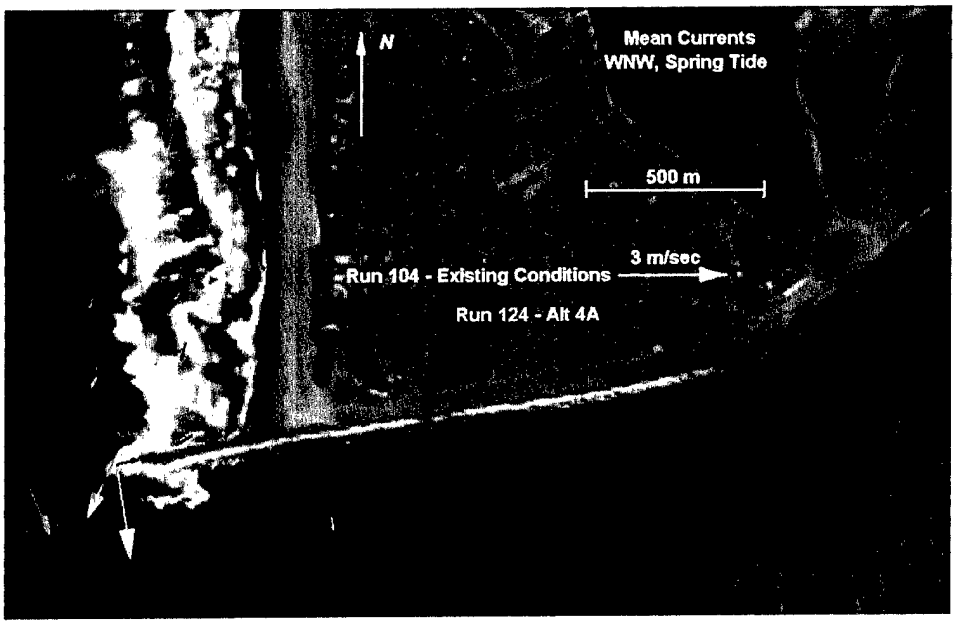

Figure 7-80. Mean currents for existing (Run 104) versus Alt 4A (Run 124)

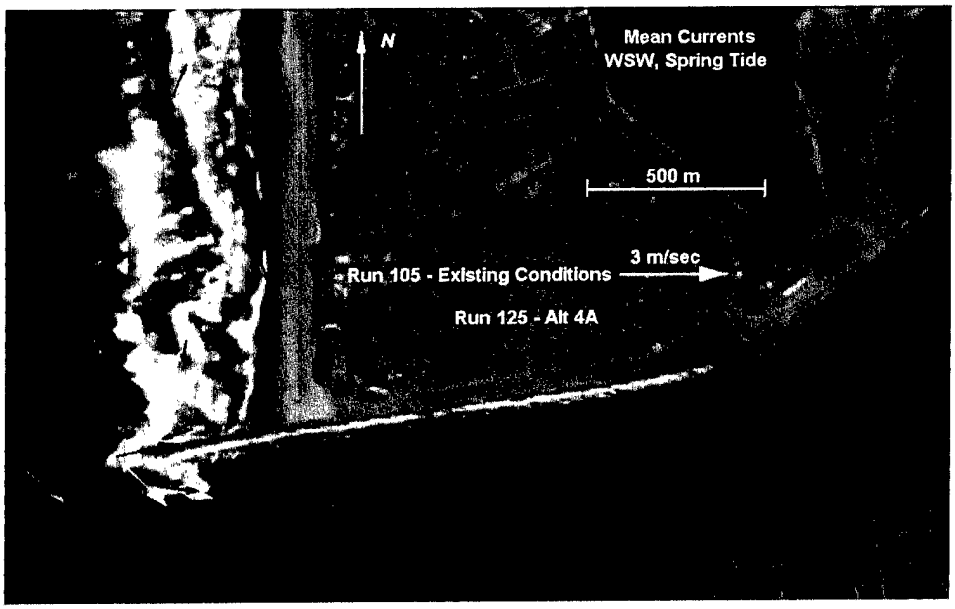

Figure 7-81. Mean currents for existing (Run 105) versus Alt 4A (Run 125)

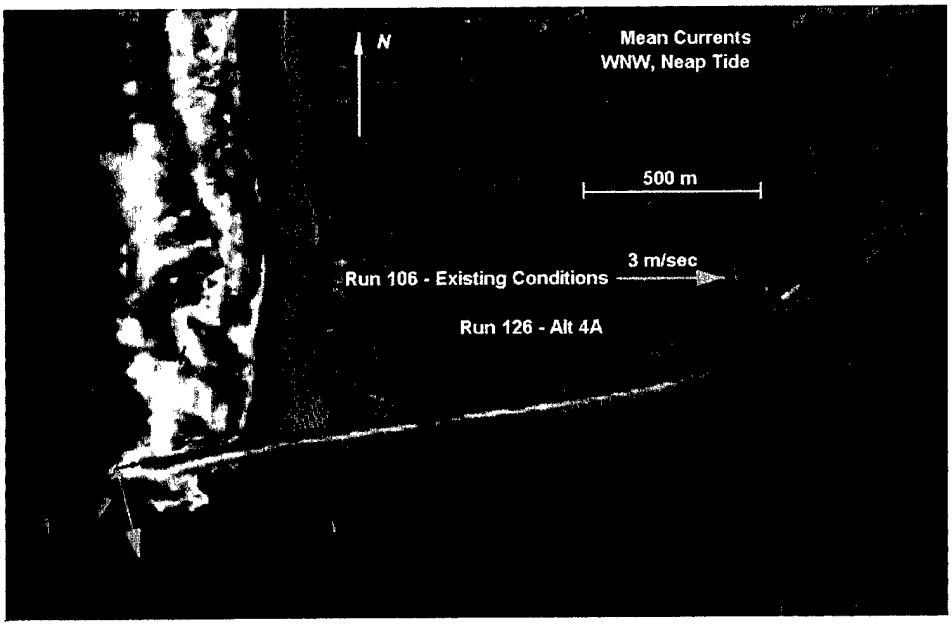

Figure 7-82. Mean currents for existing (Run 106) versus Alt 4A (Run 126)

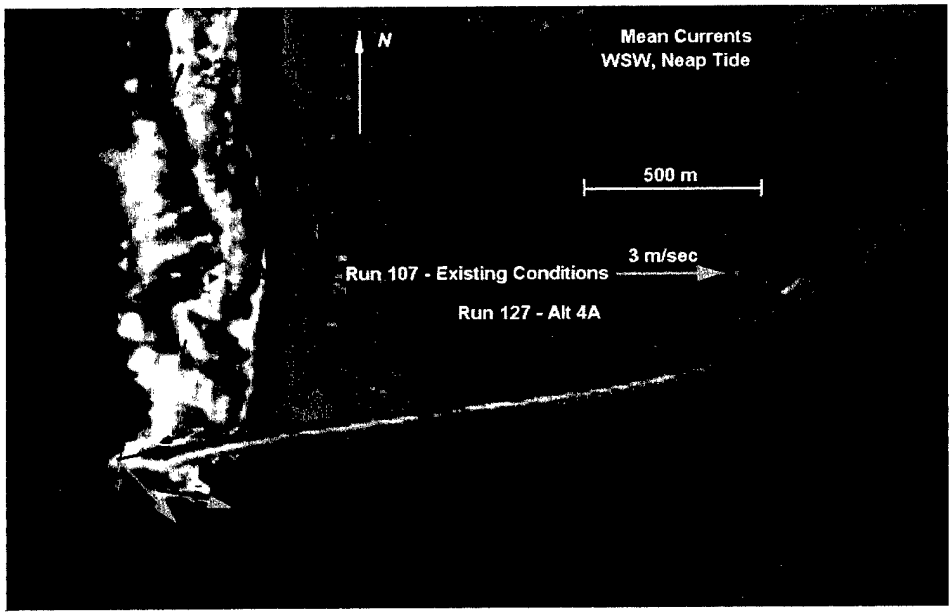

Figure 7-83. Mean currents for existing (Run 107) versus Alt 4A (Run 127)

Table 7-7
Mean Currents at Select Node Locations, m/sec

Node	Run 104 (Existing)	Run 105 (Existing)	Run 106 (Existing)	Run 107 (Existing)	Run 108 (Alt 2A)	Run 109 (Alt 2A)	Run 110 (Alt 2A)	Run 111 (Alt 2A)	Run 112 (Alt 2B)	Run 113 (Alt 2B)	Run 114 (Alt 2B)	Run 115 (Alt 2B)	Run 116 (Alt 3A)
u17188	-0.04	-0.06	-0.06	-0.08	-0.04	-0.07	-0.06	-0.08	-0.04	-0.07	-0.06	-0.09	-0.03
v17188	-0.16	-0.25	-0.23	-0.37	-0.16	-0.25	-0.23	-0.37	-0.16	-0.25	-0.23	-0.38	-0.15
u15503	-0.53	-0.76	-0.52	-0.83	-0.56	-0.72	-0.56	-0.85	-0.52	-0.72	-0.52	-0.88	-0.41
v15503	-0.28	-0.26	-0.28	-0.29	-0.29	-0.23	-0.29	-0.29	-0.28	-0.24	-0.28	-0.3	-0.19
u13614	-0.95	0.05	-0.7	-0.23	-0.98	0.23	-0.81	-0.19	-0.94	0.19	-0.76	-0.28	0.23
v13614	-2.00	-1.00	-1.96	-1.62	-1.97	-0.78	-1.92	-1.62	-2.01	-0.76	-1.96	-1.54	-0.16
u12966	0.41	1.42	0.63	1.64	0.33	1.53	0.46	1.65	0.33	1.56	0.48	1.62	0.60
v12966	-2.60	-1.41	-2.51	-1.79	-2.24	-1.21	-2.21	-1.82	-2.29	-1.18	-2.26	-1.74	0.11
u12970	-0.12	1.58	-0.16	2.05	-0.24	1.69	-0.25	2.18	-0.22	1.69	-0.23	2.09	-0.31
v12970	-0.09	-0.35	-0.11	-0.51	-0.01	-0.31	-0.02	-0.52	-0.02	-0.31	-0.03	-0.5	0.20
u14277	0.07	1.98	0.11	2.20	0.14	2.08	0.21	2.27	0.13	2.11	0.19	2.22	0.33
v14277	-0.41	0.78	-0.42	0.79	-0.41	0.78	-0.41	0.79	-0.41	0.77	-0.41	0.78	-0.44
u18006	0.14	0.19	0.12	0.19	0.15	0.20	0.12	0.2	0.15	0.19	0.12	0.20	0.12
v18006	-0.24	-0.42	-0.18	-0.48	-0.26	-0.45	-0.2	-0.55	-0.25	-0.43	-0.19	-0.54	-0.17
u16330	-0.17	0.13	-0.16	0.17	-0.15	0.12	-0.14	0.21	-0.16	0.13	-0.15	0.21	-0.22
v16330	-0.92	-0.26	-0.93	-0.23	-0.95	-0.35	-0.96	-0.35	-0.92	-0.3	-0.94	-0.34	-0.81
u13589	0.12	0.42	0.11	0.40	0.16	0.32	0.15	0.33	0.12	0.40	0.11	0.49	0.05
v13589	-1.06	0.24	-1.06	0.42	-0.99	0.45	-0.99	0.70	-1.03	0.30	-1.03	0.45	-0.94
u18257	-0.01	-0.01	-0.01	0.00	-0.01	-0.01	-0.01	-0.01	-0.01	0.00	-0.01	0.00	-0.01
v18257	-0.18	-0.01	-0.06	0.00	-0.18	-0.04	-0.06	-0.02	-0.17	0.01	-0.06	0.01	-0.16
u15763	-0.15	0.31	-0.10	0.29	-0.15	0.34	-0.09	0.32	-0.15	0.33	-0.1	0.33	-0.16
v15763	-1.51	0.78	-1.49	0.78	-1.51	0.73	-1.49	0.73	-1.50	0.77	-1.48	0.79	-1.45
u13251	-0.26	0.28	-0.25	0.29	-0.27	0.29	-0.26	0.30	-0.26	0.28	-0.26	0.32	-0.29
v13251	-0.9	0.11	-0.89	0.18	-0.89	0.14	-0.88	0.22	-0.89	0.10	-0.89	0.19	-0.85
u11421	0.70	1.08	0.69	1.27	0.67	1.11	0.66	1.34	0.68	1.11	0.67	1.30	0.45
v11421	-1.55	-0.95	-1.57	-0.83	-1.55	-0.88	-1.57	-0.79	-1.56	-0.87	-1.59	-0.83	-1.73
u18283	-0.03	-0.06	-0.03	-0.06	-0.03	-0.06	-0.03	-0.07	-0.03	-0.06	-0.03	-0.06	-0.03
v18283	-0.17	-0.49	-0.16	-0.56	-0.17	-0.51	-0.16	-0.60	-0.18	-0.52	-0.17	-0.61	-0.13
u16336	-0.1	-0.06	-0.09	-0.05	-0.09	-0.12	-0.08	-0.11	-0.10	-0.07	-0.08	-0.05	-0.16
v16336	-0.58	-0.39	-0.58	-0.43	-0.64	-0.39	-0.65	-0.52	-0.6	-0.41	-0.6	-0.59	-0.41
u14255	-0.21	0.01	-0.21	0.11	-0.17	-0.06	-0.16	0.08	-0.14	-0.15	-0.14	-0.09	-0.38
v14255	-1.04	-0.11	-1.04	0.02	-0.91	-0.06	-0.92	0.03	-0.99	0.00	-0.98	0.06	-0.91

(Continued)

Note: a positive (+) u-component indicates an eastbound mean current; a negative (-) u-components indicate a westbound mean current; a positive (+) v-component indicates a northbound mean current; and a negative (-) v-component indicates a southtbound mean current.

Table 7-7 (Concluded)

Node	Run 117 (Alt 3A)	Run 118 (Alt 3A)	Run 119 (Alt 3A)	Run 120 (Alt 3B)	Run 121 (Alt 3B)	Run 122 (Alt 3B)	Run 123 (Alt 3B)	Run 124 (Alt 4A)	Run 125 (Alt 4A)	Run 126 (Alt 4A)	Run 127 (Alt 4A)
u17188	-0.06	-0.05	-0.07	-0.02	-0.07	-0.05	-0.07	-0.03	-0.07	-0.05	-0.09
v17188	-0.25	-0.22	-0.37	-0.16	-0.25	-0.25	-0.37	-0.15	-0.26	-0.22	-0.37
u15503	-0.76	-0.44	-0.81	-0.03	-0.79	-0.1	-0.81	-0.45	-0.81	-0.44	-0.85
v15503	-0.26	-0.23	-0.28	-0.03	-0.29	-0.02	-0.29	-0.24	-0.29	-0.25	-0.3
u13614	-0.56	0.14	-0.75	0.91	-1.14	1.06	-1.14	-0.61	-0.95	-0.65	-1.12
v13614	-0.25	-0.15	-0.31	-0.01	-0.48	0.03	-0.47	-0.4	-0.34	-0.4	-0.42
u12966	1.63	0.6	1.57	0.68	1.75	0.66	1.68	0.6	1.71	0.60	1.60
v12966	0.3	0.11	0.29	0.12	0.32	0.12	0.31	0.11	0.31	0.11	0.29
u12970	1.09	-0.28	1.39	-0.15	0.90	-0.13	0.92	-0.3	1.15	-0.28	1.46
v12970	-0.19	0.19	-0.21	0.19	-0.13	0.19	-0.15	0.19	-0.16	0.19	-0.21
u14277	1.97	0.44	2.16	0.42	2.08	0.56	2.08	0.33	2.00	0.44	2.20
v14277	0.74	-0.39	0.77	-0.41	0.78	-0.37	0.78	-0.44	0.73	-0.39	0.78
u18006	0.2	0.09	0.20	0.08	0.21	0.05	0.20	0.13	0.21	0.1	0.21
v18006	-0.45	-0.11	-0.52	-0.07	-0.49	-0.03	-0.54	-0.2	-0.51	-0.14	-0.57
u16330	0.11	-0.21	0.18	-0.31	0.17	-0.28	0.18	-0.19	0.19	-0.19	0.23
v16330	-0.28	-0.82	-0.27	-0.67	-0.31	-0.67	-0.29	-0.84	-0.37	-0.85	-0.33
u13589	0.37	0.03	0.39	-0.05	0.46	-0.06	0.39	0.07	0.42	0.05	0.41
v13589	0.38	-0.93	0.46	-0.83	0.27	-0.83	0.43	-0.93	0.43	-0.92	0.56
u18257	0	-0.01	0.00	-0.01	0.00	-0.01	-0.01	-0.01	0.00	-0.01	-0.01
v18257	0.01	-0.06	0.00	-0.16	0.02	-0.06	-0.02	-0.16	0.01	-0.06	-0.01
u15763	0.33	-0.11	0.31	-0.17	0.34	-0.13	0.32	-0.16	0.36	-0.11	0.32
v15763	0.78	-1.42	0.79	-1.37	0.82	-1.35	0.80	-1.45	0.78	-1.43	0.79
u13251	0.29	-0.29	0.30	-0.32	0.30	-0.32	0.32	-0.29	0.31	-0.28	0.30
v13251	0.2	-0.84	0.26	-0.81	0.22	-0.8	0.37	-0.85	0.21	-0.84	0.25
u11421	0.98	0.41	1.24	0.47	1.28	0.38	1.58	0.45	0.96	0.40	1.32
v11421	-0.84	-1.74	-0.94	-2.16	-1.43	-2.11	-1.38	-1.74	-0.82	-1.74	-0.94
u18283	-0.06	-0.02	-0.07	-0.03	-0.07	-0.02	-0.07	-0.03	-0.07	-0.02	-0.07
v18283	-0.5	-0.12	-0.57	-0.18	-0.53	-0.16	-0.57	-0.14	-0.55	-0.13	-0.61
u16336	-0.08	-0.13	-0.07	-0.27	-0.07	-0.24	-0.09	-0.12	-0.09	-0.1	-0.09
v16336	-0.4	-0.41	-0.47	-0.08	-0.5	-0.1	-0.5	-0.48	-0.55	-0.47	-0.59
u14255	-0.06	-0.37	-0.02	-0.59	0.04	-0.59	0.01	-0.25	-0.06	-0.26	-0.06
v14255	0.08	-0.9	0.11	-0.9	0.02	-0.88	0.17	-0.85	0.26	-0.84	0.39

Note: a positive (+) u-component indicates an eastbound mean current; a negative (-) u-components indicate a westbound mean current; a positive (+) v-component indicates a northbound mean current; and a negative (-) v-component indicates a southtbound mean current.

Table 7-8
Difference in Current Magnitude Between Alternatives and Existing Condition, m/sec

Node	108-104 (Alt 2A-Ex)	112-104 (Alt 2B-Ex)	116-104 (Alt 3A-Ex)	120-104 (Alt 3B-Ex)	124-104 (Alt 4A-Ex)	109-105 (Alt 2A-Ex)	113-105 (Alt 2B-Ex)	117-105 (Alt 3A-Ex)	121-105 (Alt 3B-Ex)	125-105 (Alt 4A-Ex)
u17188	0.00	0.00	0.01	0.01	0.01	0.00	-0.01	0.00	0.00	0.00
v17188	0.00	0.00	0.00	0.00	0.01	0.00	0.00	0.00	0.00	0.00
u15503	-0.04	0.00	0.11	0.5	0.08	0.04	0.04	0.00	-0.03	-0.05
v15503	-0.01	0.00	0.09	0.25	0.04	0.03	0.02	-0.01	-0.03	-0.03
u13614	-0.03	0.01	1.18	1.86	0.34	0.18	0.14	-0.6	-1.18	-1.00
v13614	0.04	-0.01	1.84	2.00	1.6	0.22	0.24	0.75	0.51	0.65
u12966	-0.08	-0.08	0.19	0.27	0.19	0.10	0.14	0.2	0.33	0.28
v12966	0.36	0.30	2.71	2.72	2.71	0.20	0.22	1.7	1.73	1.72
u12970	-0.13	-0.11	-0.19	-0.03	-0.18	0.11	0.11	-0.48	-0.68	-0.43
v12970	0.08	0.07	0.29	0.28	0.28	0.04	0.04	0.15	0.22	0.19
u14277	0.07	0.06	0.26	0.35	0.26	0.10	0.13	-0.02	0.1	0.01
v14277	0.00	0.00	-0.02	0.00	-0.02	0.00	-0.01	-0.04	0.00	-0.05
u18006	0.01	0.00	-0.02	-0.06	-0.01	0.00	0.00	0.00	0.01	0.02
v18006	-0.02	-0.01	0.07	0.17	0.04	-0.04	-0.01	-0.03	-0.07	-0.1
u16330	0.02	0.01	-0.05	-0.13	-0.02	0.00	0.00	-0.02	0.05	0.07
v16330	-0.03	-0.01	0.11	0.25	0.08	-0.09	-0.04	-0.02	-0.06	-0.11
u13589	0.04	0.00	-0.08	-0.18	-0.06	-0.1	-0.02	-0.05	0.05	0.00
v13589	0.07	0.03	0.12	0.23	0.13	0.21	0.06	0.14	0.03	0.19
u18257	0.00	0.00	0.00	0.00	0.00	0.00	0.00	0.00	0.01	0.01
v18257	0.00	0.00	0.01	0.02	0.01	-0.03	0.02	0.02	0.03	0.02
u15763	0.00	0.00	-0.01	-0.02	-0.01	0.03	0.02	0.02	0.03	0.05
v15763	0.00	0.00	0.06	0.13	0.06	-0.04	0.00	0.00	0.04	0.01
u13251	0.00	0.00	-0.03	-0.06	-0.03	0.01	0.00	0.00	0.02	0.02
v13251	0.01	0.01	0.05	0.09	0.05	0.03	-0.02	0.09	0.11	0.1
u11421	-0.03	-0.02	-0.25	-0.23	-0.25	0.03	0.03	-0.10	0.20	-0.12
v11421	0.00	-0.01	-0.18	-0.61	-0.18	0.06	0.08	0.11	-0.48	0.12
u18283	0.00	0.00	0.00	0.00	0.00	0.00	0.00	0.00	-0.01	-0.01
v18283	0.00	-0.01	0.05	-0.01	0.03	-0.02	-0.03	-0.01	-0.04	-0.06
u16336	0.01	0.01	-0.06	-0.17	-0.01	-0.06	0.00	-0.01	0	-0.03
v16336	-0.07	-0.03	0.17	0.49	0.09	0.00	-0.03	-0.02	-0.11	-0.16
u14255	0.05	0.07	-0.17	-0.38	-0.04	-0.07	-0.16	-0.07	0.03	-0.08
v14255	0.13	0.06	0.13	0.14	0.19	0.05	0.11	0.19	0.13	0.37

(Continued)

Note: For eastbound mean current, a positive (+) difference indicates an increase in the eastbound mean current; a negative difference (-) indicates a decrease in the eastbound mean current. For westbound mean current, a positive (+) difference indicates a decrease in the westbound mean current; a negative difference (-) indicates an increase in the westbound mean current.
For northbound mean current, a positive (+) difference indicates an increase in the northbound mean current; a negative difference (-) indicates a decrease in the northbound mean current. For southbound mean currents, a positive (+) difference indicates a decrease in the southbound mean current; a negative difference (-) indicates an increase in the southbound mean current.
"Ex" denotes Existing condition.

Table 7-8 (Continued)

Node	110-106 (Alt 2A-Ex)	114-106 (Alt 2B-Ex)	118-106 (Alt 3A-Ex)	122-106 (Alt 3B-Ex)	126-106 (Alt 4A-Ex)	111-107 (Alt 2A-Ex)	115-107 (Alt 2B-Ex)	119-107 (Alt 3A-Ex)	123-107 (Alt 3B-Ex)	127-107 (Alt 4A-Ex)
u17188	0.00	0.00	0.01	0.00	0.01	0.00	-0.01	0.01	0.01	0.00
v17188	0.00	0.00	0.01	-0.01	0.01	-0.01	-0.01	0.00	0.00	0.00
u15503	-0.04	0.00	0.08	0.42	0.08	-0.01	-0.05	0.02	0.03	-0.02
v15503	-0.01	0.00	0.05	0.26	0.03	0.00	-0.01	0.01	0.00	-0.01
u13614	-0.12	-0.06	0.83	1.75	0.05	0.04	-0.05	-0.52	-0.92	-0.89
v13614	0.03	0.00	1.8	1.98	1.56	0.00	0.08	1.31	1.14	1.2
u12966	-0.18	-0.15	-0.04	0.02	-0.03	0.00	-0.03	-0.08	0.04	-0.04
v12966	0.30	0.26	2.62	2.63	2.62	-0.02	0.05	2.08	2.1	2.09
u12970	-0.09	-0.08	-0.12	0.02	-0.12	0.13	0.04	-0.66	-1.13	-0.59
v12970	0.09	0.08	0.30	0.30	0.30	-0.01	0.01	0.30	0.36	0.30
u14277	0.10	0.08	0.33	0.45	0.33	0.08	0.02	-0.04	-0.12	0.00
v14277	0.01	0.00	0.03	0.04	0.03	0.00	-0.01	-0.02	-0.01	-0.01
u18006	0.00	0.00	-0.03	-0.07	-0.02	0.01	0.01	0.01	0.01	0.02
v18006	-0.02	-0.01	0.07	0.16	0.05	-0.07	-0.06	-0.04	-0.06	-0.09
u16330	0.02	0.01	-0.05	-0.12	-0.02	0.04	0.05	0.01	0.01	0.06
v16330	-0.03	-0.01	0.11	0.27	0.08	-0.12	-0.11	-0.03	-0.06	-0.1
u13589	0.04	0.00	-0.08	-0.17	-0.06	-0.07	0.09	-0.01	-0.01	0.01
v13589	0.07	0.03	0.13	0.23	0.14	0.28	0.03	0.04	0.01	0.14
u18257	0.00	0.00	0.00	0.00	0.00	-0.01	0.00	0.00	0.00	0.00
v18257	0.00	0.00	0.00	0.01	0.00	-0.02	0.01	0.00	-0.02	-0.02
u15763	0.00	0.00	-0.01	-0.03	-0.01	0.03	0.04	0.02	0.04	0.04
v15763	0.00	0.00	0.07	0.14	0.06	-0.05	0.02	0.02	0.02	0.02
u13251	0.00	0.00	-0.03	-0.07	-0.03	0.01	0.02	0.01	0.03	0.00
v13251	0.01	0.01	0.05	0.10	0.05	0.04	0.01	0.08	0.19	0.07
u11421	-0.03	-0.02	-0.28	-0.31	-0.29	0.07	0.03	-0.02	0.31	0.05
v11421	0.00	-0.01	-0.16	-0.53	-0.16	0.04	0.00	-0.11	-0.55	-0.1
u18283	0.00	0.00	0.00	0.00	0.00	0.00	0.00	0.00	-0.01	-0.01
v18283	0.00	0.00	0.04	0.00	0.03	-0.04	-0.05	-0.01	-0.01	-0.05
u16336	0.01	0.00	-0.04	-0.15	-0.02	-0.06	-0.01	-0.03	-0.04	-0.05
v16336	-0.07	-0.03	0.17	0.48	0.1	-0.09	-0.16	-0.04	-0.07	-0.16
u14255	0.05	0.07	-0.16	-0.38	-0.05	-0.03	-0.20	-0.13	-0.10	-0.17
v14255	0.12	0.06	0.14	0.16	0.20	0.00	0.03	0.09	0.15	0.37

Note: For eastbound mean current, a positive (+) difference indicates an increase in the eastbound mean current; a negative difference (-) indicates a decrease in the eastbound mean current. For westbound mean current, a positive (+) difference indicates a decrease in the westbound mean current; a negative difference (-) indicates an increase in the westbound mean current.
For northbound mean current, a positive (+) difference indicates an increase in the northbound mean current; a negative difference (-) indicates a decrease in the northbound mean current. For southbound mean current, a positive (+) difference indicates a decrease in the southbound mean current; a negative difference (-) indicates an increase in the southbound mean current.
"Ex" denotes Existing condition.

c. Alternatives 3A/3B/4A and west-northwest waves.

d. Alternatives 3A/3B/4A and west-southwest waves.

Alternatives 2A, 2B, and west-northwest waves. Analysis of current at the nine nodes located landward of Alt 2A and 2B shows that, for west-northwest waves, the seaward-most nodes (closest to the spur structure) experience a decrease in southward mean current (0.03-0.13 m/sec), whereas nodes closer to land (16330, 16336, 15503, and 18006) experience a small increase in southerly directed current (0.01-0.07 m/sec). (It will be shown that the main area landward of the spur experiences an increase in southward current for west-northwest waves.) The east-west mean current shows westerly directed flows for the southern six nodes and easterly and westerly flows for the northern three nodes. The spur structures increase the eastbound and decrease the westbound current at the northern three nodes and increase the westbound current at the southern three nodes. The middle nodes experience a decrease in westbound current.

Alternatives 2A, 2B, and west-southwest waves. For west-southwest waves, changes in southward current are similar as for west-northwest waves with a few exceptions. Node 13589 (which has a northward mean current in the presence of west-southwest waves) experiences an increased northward current with the spur alternatives. At Node 15503, the southward mean current decreases, and at Node 18283 the southward mean current increases. (It will be shown that the main area landward of the spur experiences an increase in southward currents with west-southwest waves. Alternatives 2A and 2B cause greater change in southbound mean currents for west-southwest waves than for west-northwest waves. The northward current, north of the spur location, experiences an increase in northward current for these conditions.) The east-west mean currents show easterly directed mean currents at the seaward-most and northern nodes (13614, 14255, 13589, 16330, and 18006) and westerly currents at the remaining nodes (15503, 17188, 16336, and 18283). The spur structures decrease the eastbound current at the northern three nodes and increase the eastbound and decrease the westbound current at the southern nodes. This trend is opposite to the east-west changes caused by Alt 2A and 2B for west-northwest waves.

Alternatives 3A, 3B, 4A, and west-northwest waves. For west-northwest waves and Alt 3A, 3B, and 4A, all nodes experience a decrease in southbound current except 11421, 18283 (for Alt 3B), and 16336 (for Alt 3A). Node 11421 is located near the tip of the rehabilitated jetty and experiences an increased southerly current as is expected. (It will be shown that the main area landward of the jetty experiences a decrease in southward currents with west-northwest waves.) The east-west mean current has a westerly directed mean at all nodes except 13589 and 18006. The jetty structures decrease the eastbound and increase the westbound current at the northern three nodes and decrease the westbound current at the southern nodes. This trend is opposite to the east-west changes caused by Alt 2A and 2B for west-northwest waves.

Alternatives 3A, 3B, 4A, and west-southwest waves. The response for west-southwest waves and Alt 3A, 3B, and 4A is different than the response to west-northwest waves because nine nodes are now located in the lee of the west-southwest wave approach. Node 13589 (as well as nodes 13251 and 15763) has a northerly directed mean current that increases with Alt 3A, 3B, and 4A. The

southerly directed current increases for the middle and shoreward-most nodes (16339, 16336, 15503, 18006, and 18283) and decreases for Nodes 13614 and 14255. (It will be shown that the main area landward of the jetty experiences an increase in southward and northward currents with west-southwest waves.) The east-west mean current shows an easterly directed flow at the seaward-most and northern nodes (13614, 14255, 13589, 16330, and 18006) and westerly mean flow at the remaining nodes (15503, 17188, 16336, and 18283). The shorter jetty structure (Alt 3A) decreases the eastbound current at the northern three nodes and decreases the eastbound current at the southern nodes. The longer jetty structure (Alt 3B) increases the eastbound current at the northern three nodes and increases the westbound current at the southern nodes, similar or the response to the spur alternatives and west-northwest waves. In summary, the jetty alternatives produce greater changes in mean current than the spur alternatives.

Time series of velocity components

Time series plots of velocity components at the 16 node locations were completed for the 24 Steering Module simulations (Appendix E). Each plot compares the current component for the existing condition to all corresponding project alternatives. For example, Runs 108 (Alt 2A), 112 (Alt 2B), 116 (Alt 3A), 120 (Alt 3B), and 124 (Alt 4A) are compared to Run 104 (Existing) because each is for west-northwest, spring tide conditions. Time series plots for Node 11421 (near the terminus of the Alt 3B jetty rehabilitation) are shown in Figures 7-84 through 7-91 for discussion. Southeasterly currents are prevalent at this location for the four modeled wave conditions. The spur-only alternatives (Alt 2A and 2B) cause little-to-no change in velocity components at Node 11421, whereas the jetty rehabilitation (Alt 3A and 3B) and spur-plus-jetty alternative (Alt 4A) increase (0.2-0.6 m/sec) the southbound and decrease (0.2-0.3m/sec) the eastbound current at Node 11421 for west-northwest waves. For west-southwest waves, again the spur alternatives cause little change in velocity components at 11421. For Alt 3A and 4A, west-southwest-spring tide time series plots at Node 11421 show the influence of a gyre passing near the north jetty during ebb tide (Figures 7-62 and 7-63). For these alternatives, there is an increase in southbound current during flood tide and short bursts of increased northbound current as the gyre passes this node location. Alternative 3B causes an increased southbound (0.5-0.6 m/sec) current and increased eastbound (0.2-0.3 m/sec) current for west-southwest waves.

Global difference plan view maps

Node-to-node statistical comparisons of simulation results are informative for examining the magnitude of change at selected points caused by the structural alternatives. These data were presented and discussed in the previous section. Another method of evaluating the structural alternatives is to examine an overview or plan view difference map that shows the general pattern of change produced by the various structural alternatives. These change maps are discussed in this section.

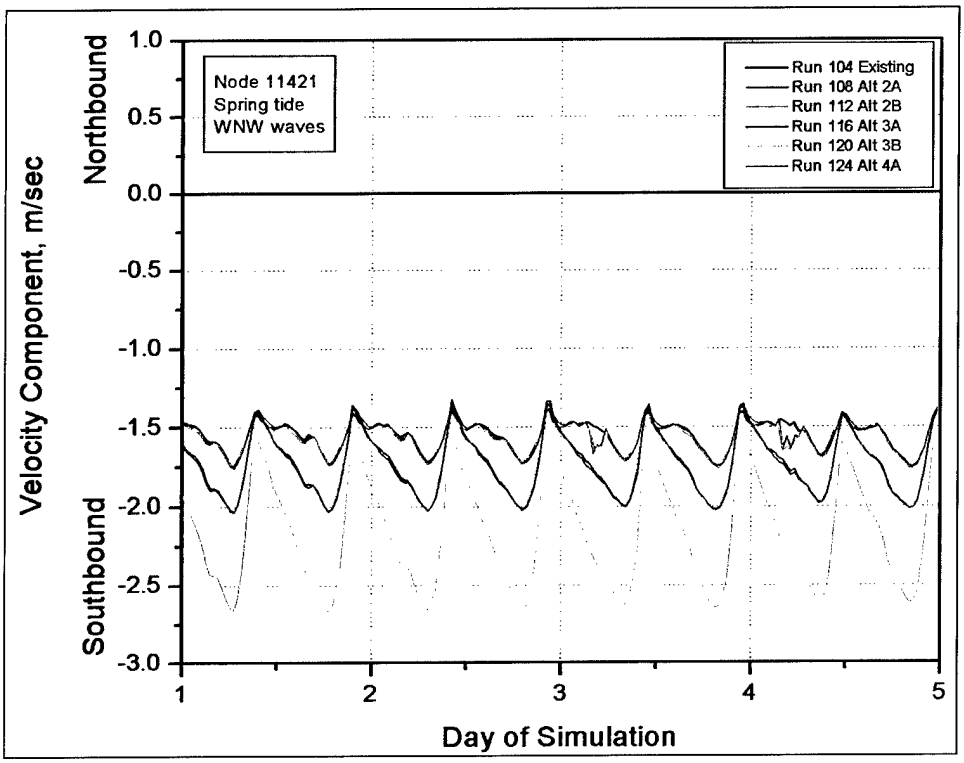

Figure 7-84. Time series of north-south velocity component at node 11421 for spring tide and west-northwest waves

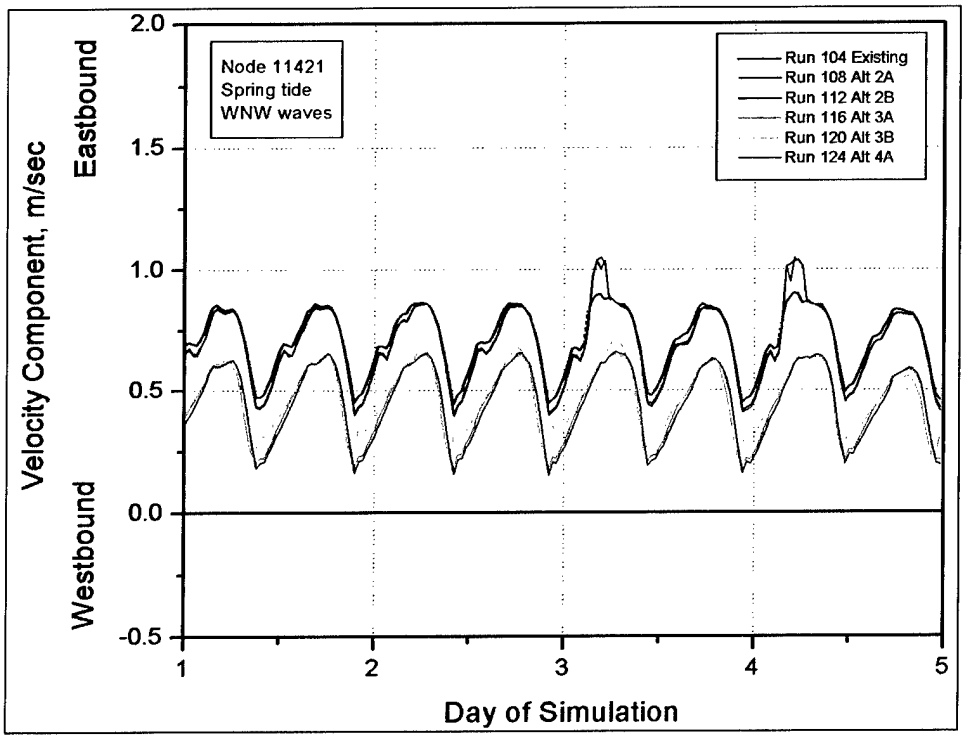

Figure 7-85. Time series of east-west velocity component at node 11421 for spring tide and west-northwest waves

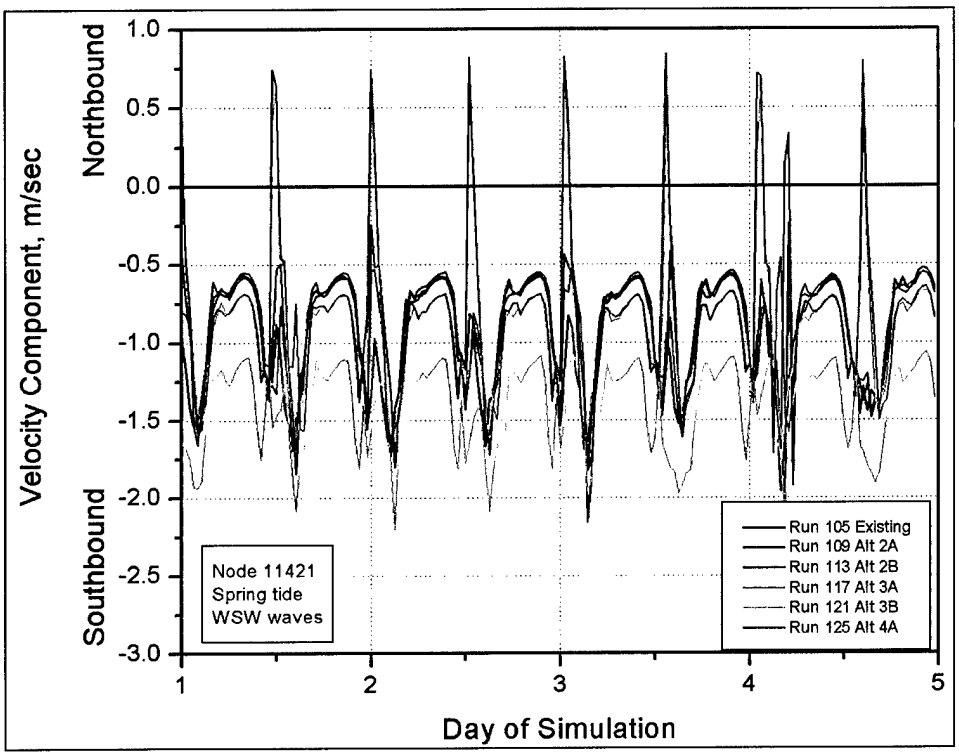

Figure 7-86. Time series of north-south velocity component at node 11421 for spring tide and west-southwest waves

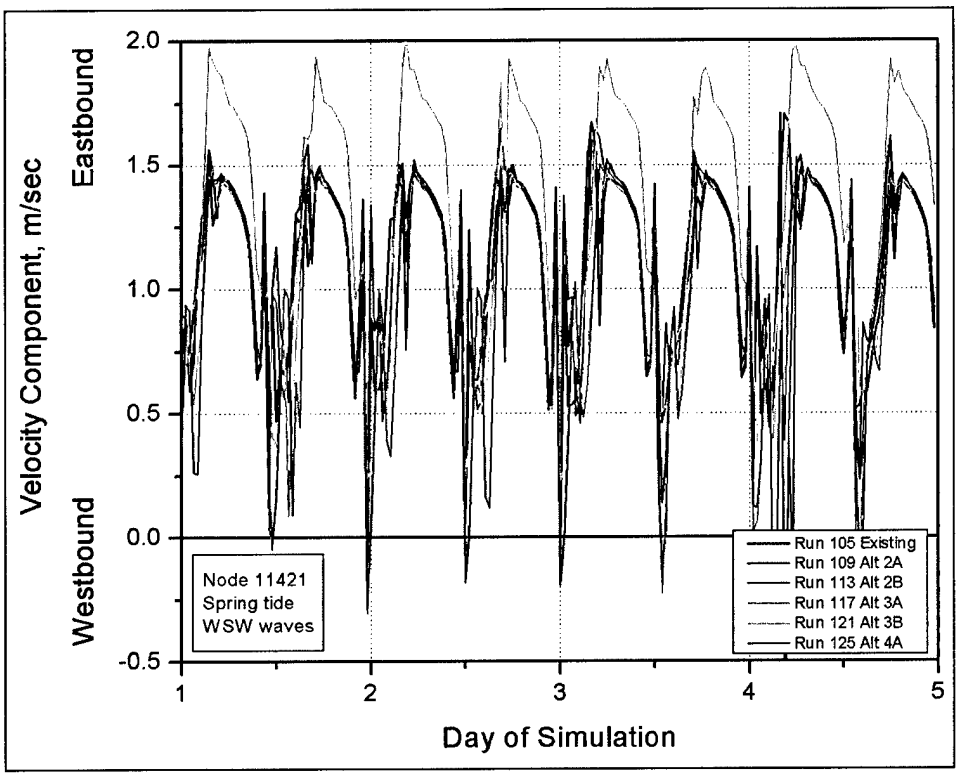

Figure 7-87. Time series of east-west velocity component at node 11421 for spring tide and west-southwest waves

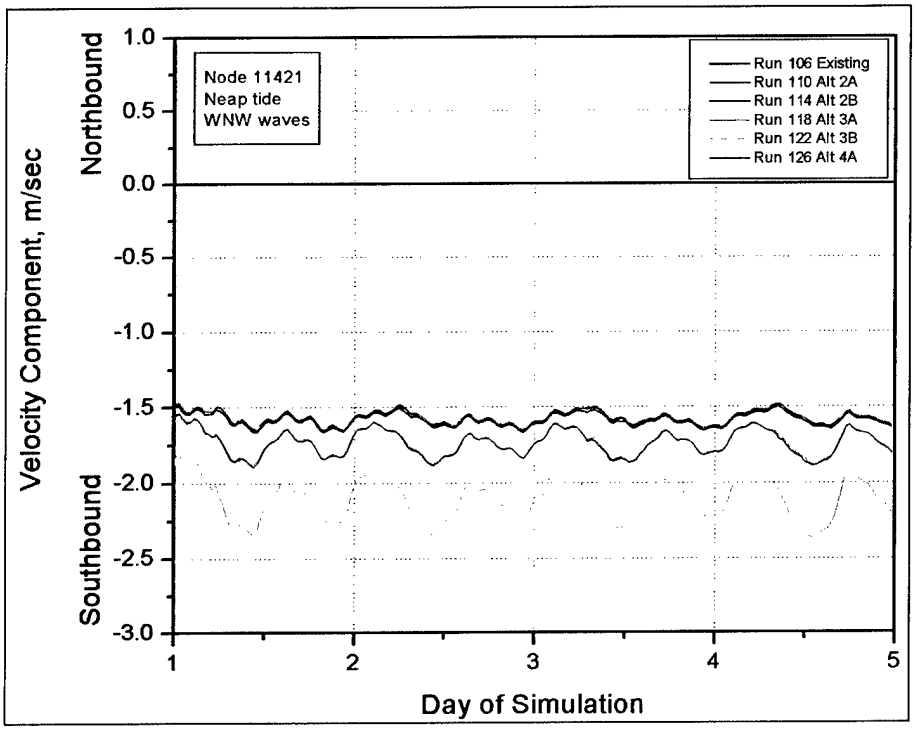

Figure 7-88. Time series of north-south velocity component at node 11421 for neap tide and west-northwest waves

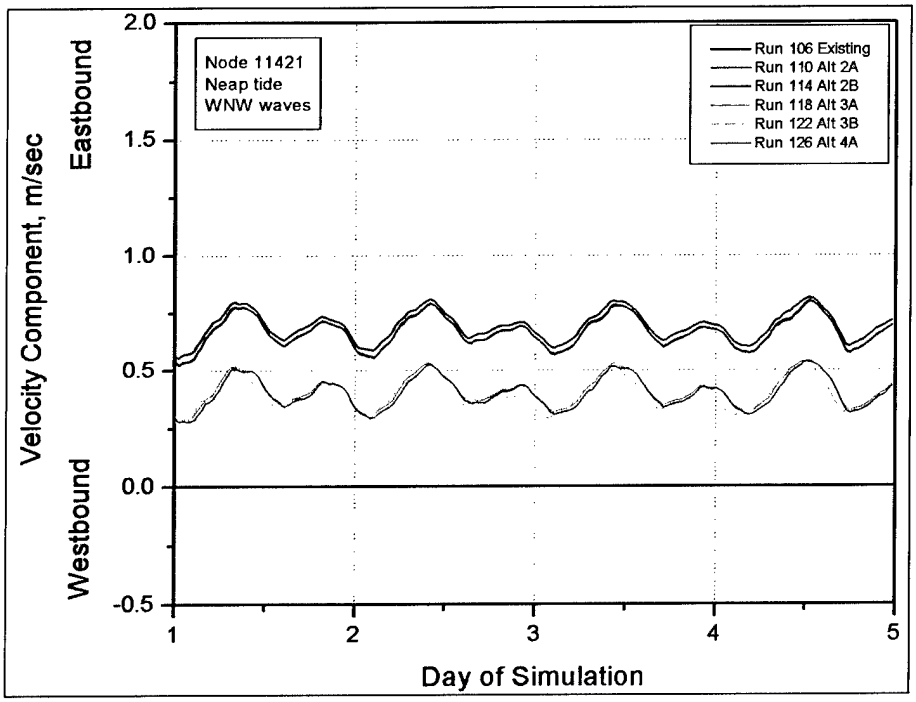

Figure 7-89. Time series of east-west velocity component at node 11421 for neap tide and west-northwest waves

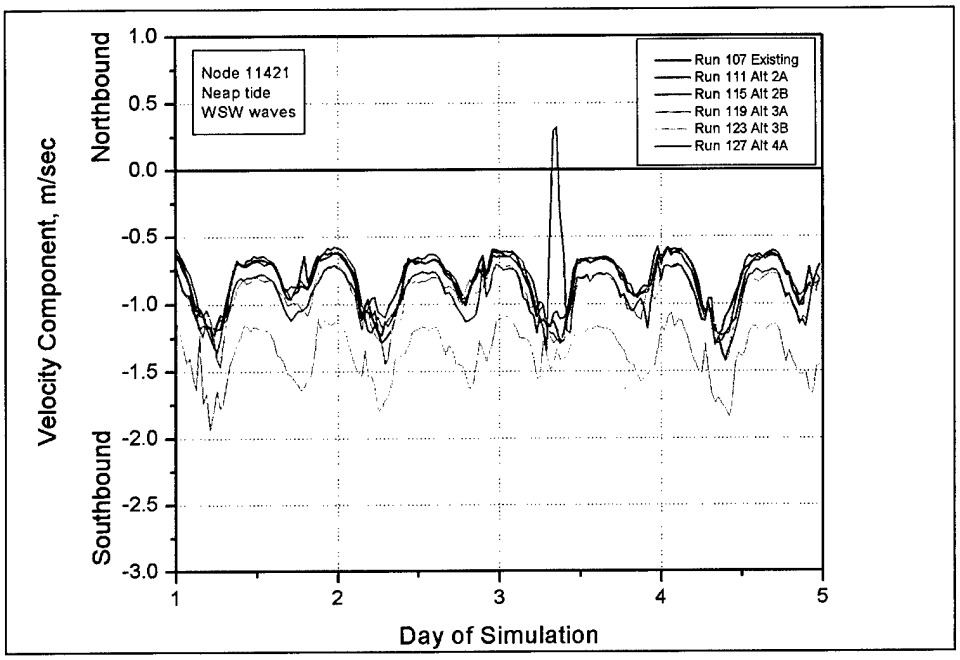

Figure 7-90. Time series of north-south velocity component at node 11421 for neap tide and west-southwest waves

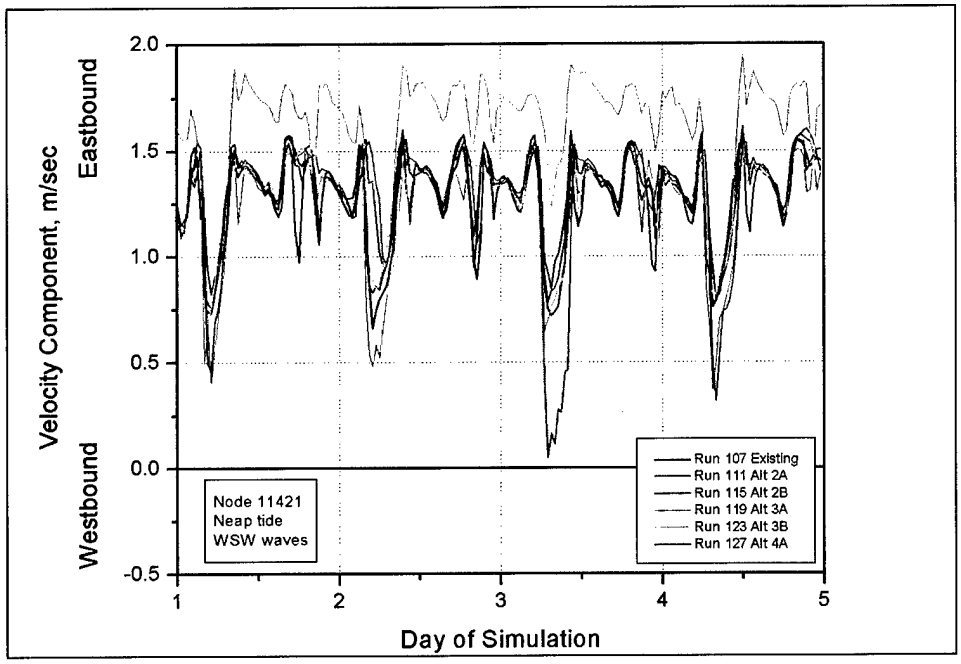

Figure 7-91. Time series of east-west velocity component at node 11421 for neap tide and west-southwest waves

Difference maps were created for each alternative compared to the corresponding existing condition. For example, Runs 108, 112, 116, 120, and 124 are compared to Run 104 because each is for west-northwest, spring tide conditions (Figures 7-92 through 7-101). Red and yellow color contours indicate a large to moderate increase in current magnitude, respectively. Blue and light blue contours indicate a large to moderate decrease in current magnitude, respectively. The vectors do not indicate differences, but represent current vectors for the project alternative. Difference maps at peak flood and peak ebb for each alternative are given in Appendix E. Figures 7-92 to 7-101 show difference maps for all west-northwest, spring tide cases for discussion purposes. Figures 7-92 through 7-95 show that changes in current magnitude produced by the spur alternatives (Alts 2A and 2B) and west-northwest waves are small but measurable, and are limited to the surf zone and a narrow band near the spur structure. There is an increase in current magnitude (to the south) shoreward of the spur structure for at least 1 km north of the jetty. For west-southwest waves, there is also an increased current magnitude to the north, north of the reversal point (Appendix E). The current at the structure location and continuing around the north jetty into the inlet is reduced. However, the current along the inlet side of the north jetty is slightly increased, which may promote scour because there would be less material transported around the jetty tip. Small changes in current magnitude may or may not be sufficiently significant to change sediment transport in areas of strong currents, but small changes in current magnitude in areas of somewhat weaker current, such as in the inner surf zone, may serve to initiate sediment transport. This phenomenon is investigated with the sediment transport models.

Figures 7-96 through 7-101 show that the jetty rehabilitation alternatives (Alts 3A, 3B, and 4A) and west-northwest waves cause a reduction in current magnitude at the jetty rehabilitation location and the area south of the structure, and a corresponding increase in current magnitude further seaward where the current is deflected. The surf zone north of the north jetty shows a reduction in southbound current with Alts 3A, 3B, and 4A and west-northwest waves. Appendix E shows that, with west-southwest waves, Alts 3A, 3B, and 4A increase southbound currents in the surf zone and shadow zone north of the jetty. Alt 3B also causes currents along the inlet side of the north jetty to increase for west-northwest waves (Figure 7-98 and 7-99). The increase is less pronounced for west-southwest waves.

Alternatives 2A and 2B difference maps for west-southwest waves and spring tide (Runs 109 and 113 compared to 105) show larger changes in current magnitude near the spur structure and in the area landward of the structure than was caused by the west-northwest waves (Appendix E). Alternatives 3A (Run 117) and 3B (Run 121) with west-southwest waves show the greatest changes in the gyre, near the jetty, and in the longshore current magnitude 500 m north of the north jetty. West-southwest waves and Alts 3A, 3B, and 4A increase southbound currents in the surf zone and shadow zone north of the jetty and increase northbound currents further north (beyond 500 m north of the jetty). Difference maps for west-northwest and west-southwest neap tide show similar patterns as spring tide, but the changes are more extensive in scale and greater in magnitude.

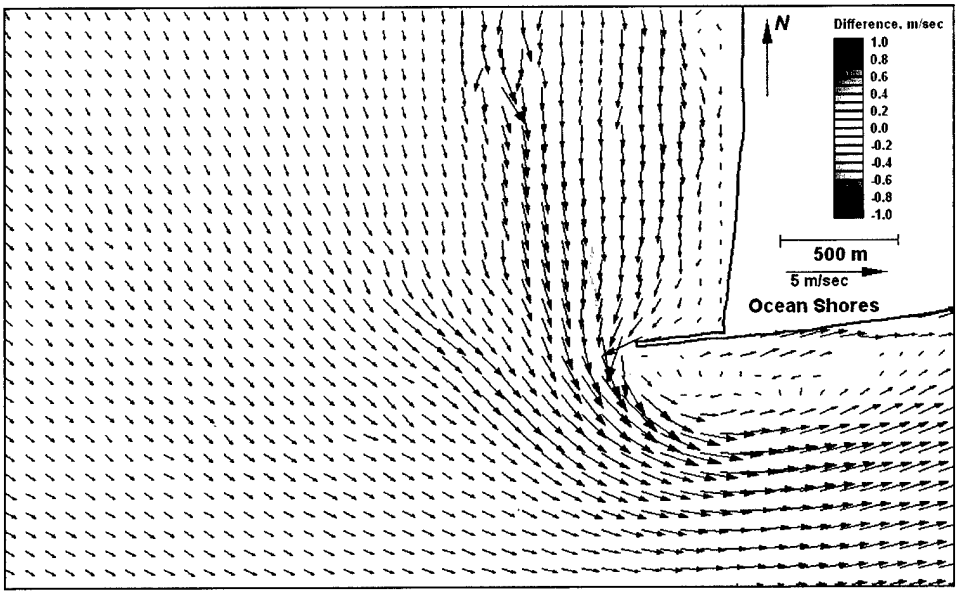

Figure 7-92. Difference map Alt 2A – existing (Run 108 – Run 104) for peak flood

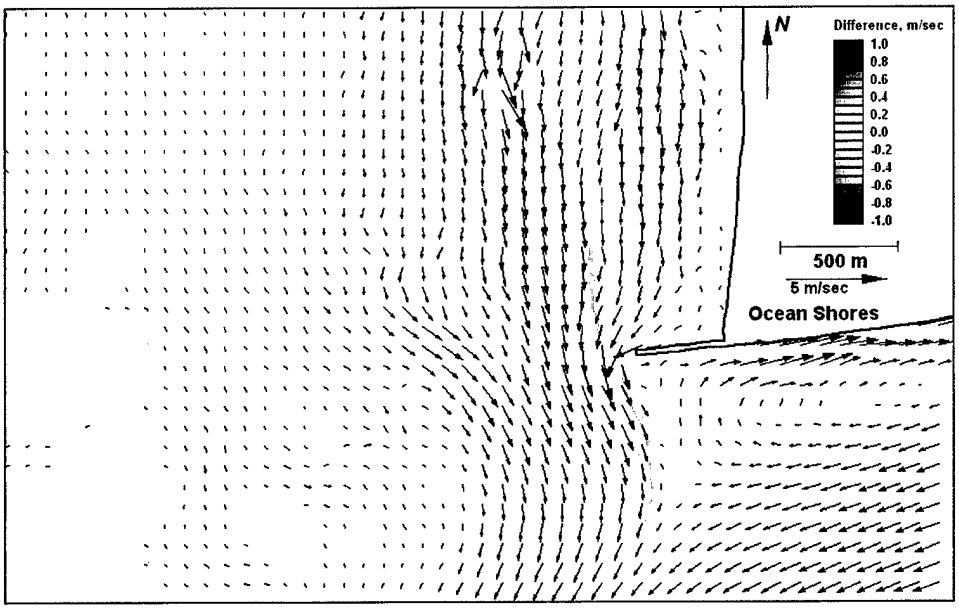

Figure 7-93. Difference map Alt 2A – existing (Run 108 – Run 104) for peak ebb

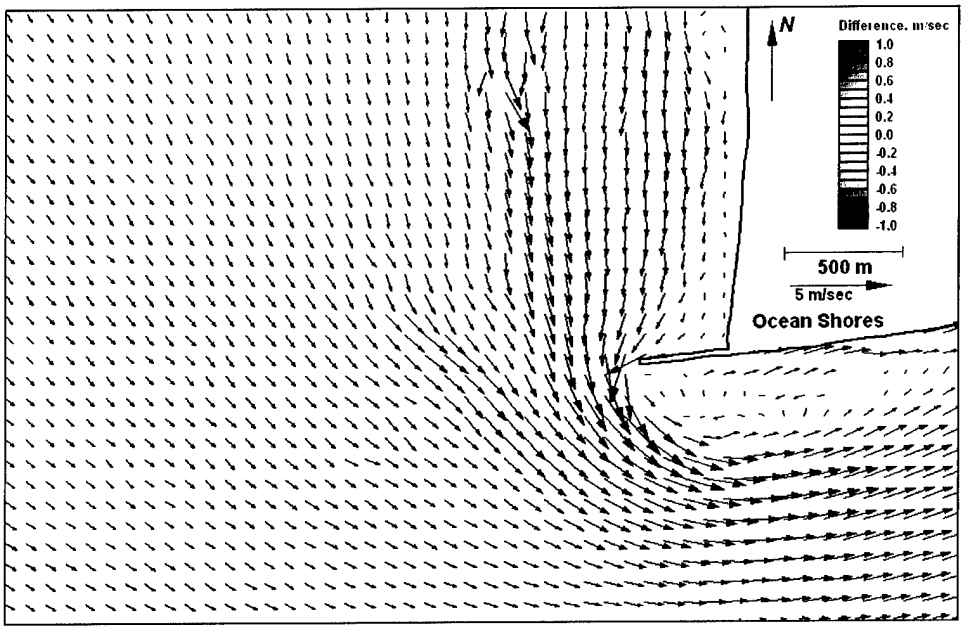

Figure 7-94. Difference map Alt 2B – existing (Run 112 – Run 104) for peak flood

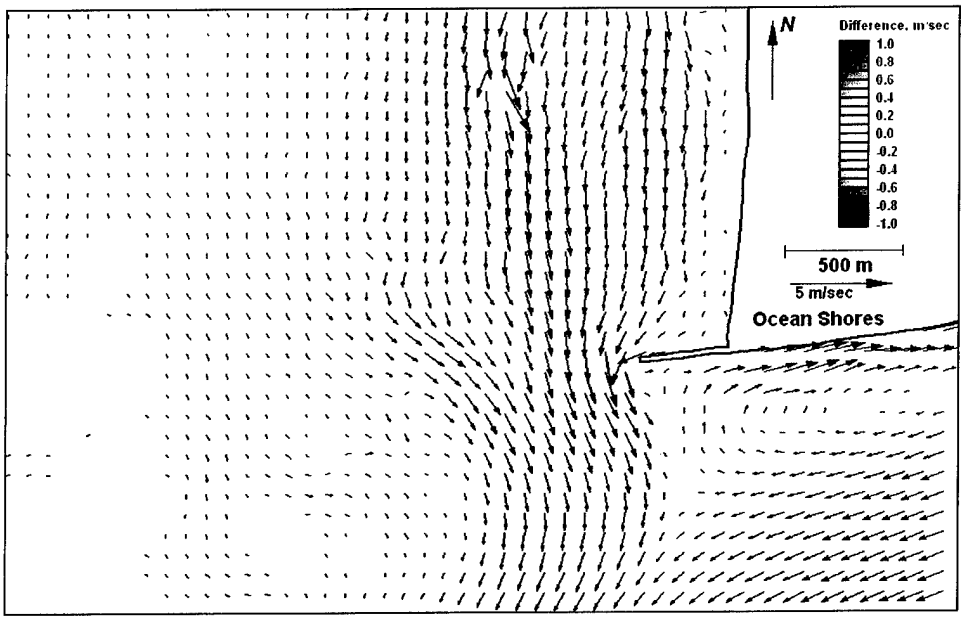

Figure 7-95. Difference map Alt 2B – existing (Run 112 – Run 104) for peak ebb

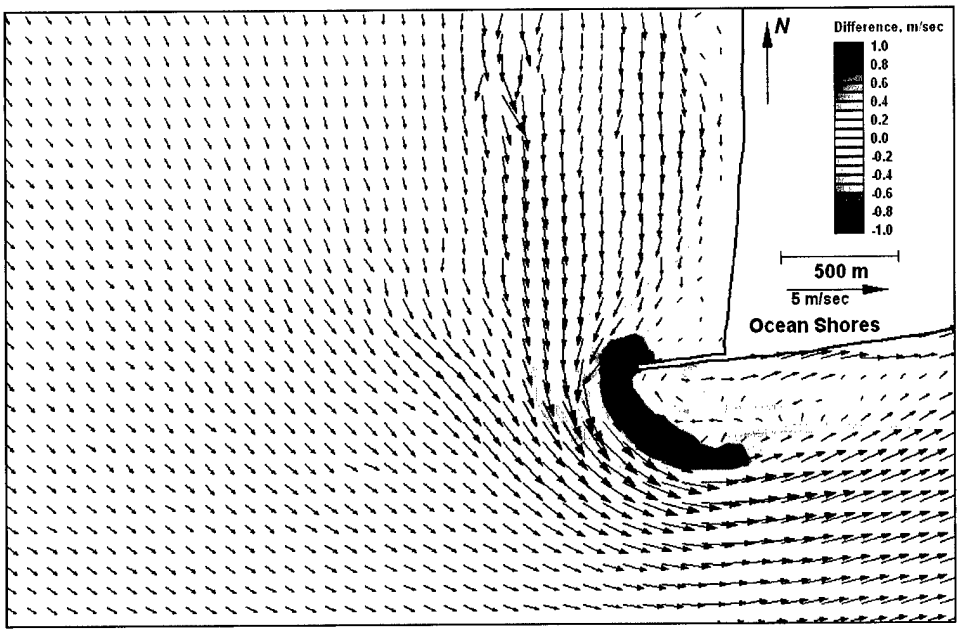

Figure 7-96. Difference map Alt 3A – existing (Run 116 – Run 104) for peak flood

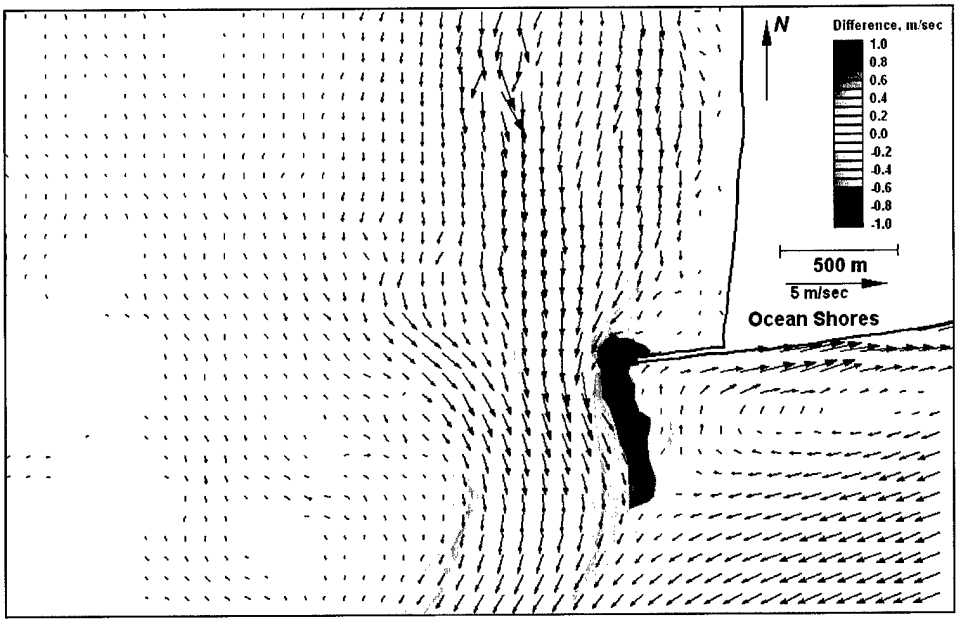

Figure 7-97. Difference map Alt 3A – existing (Run 116 – Run 104) for peak ebb

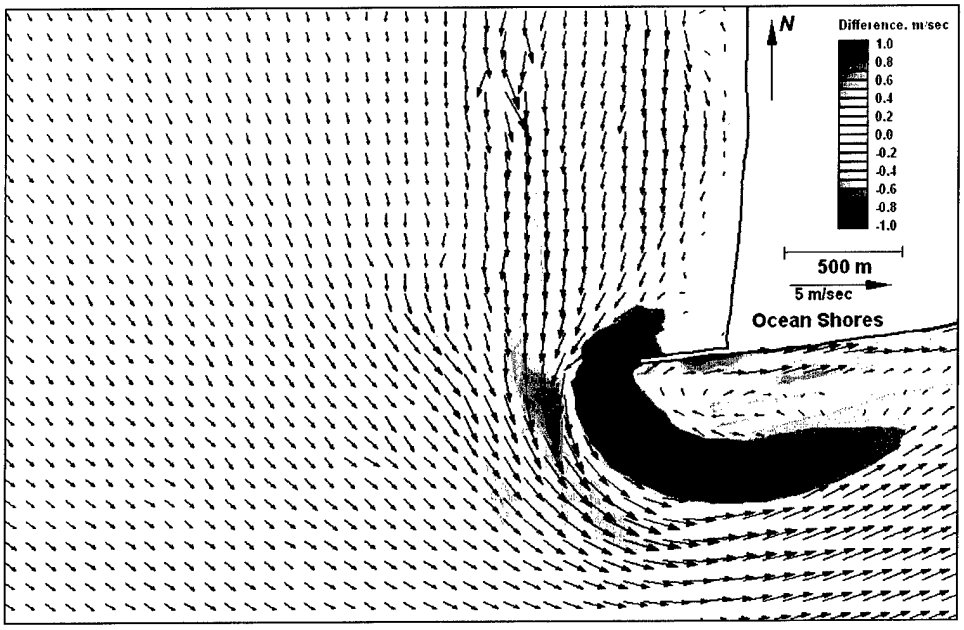

Figure 7-98. Difference map Alt 3B – existing (Run 120 – Run 104) for peak flood

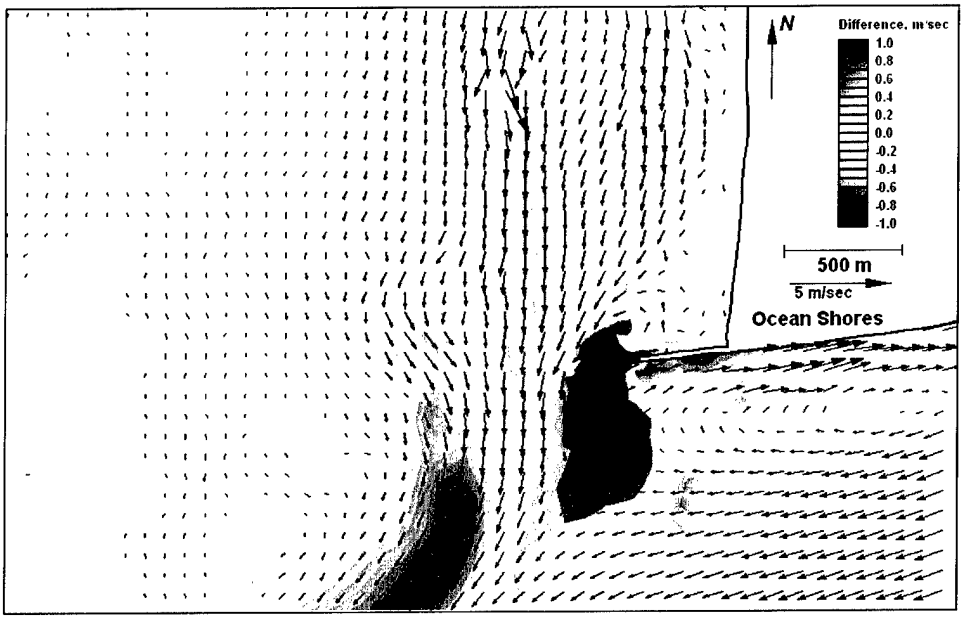

Figure 7-99. Difference map Alt 3B – existing (Run 120 – Run 104) for peak ebb

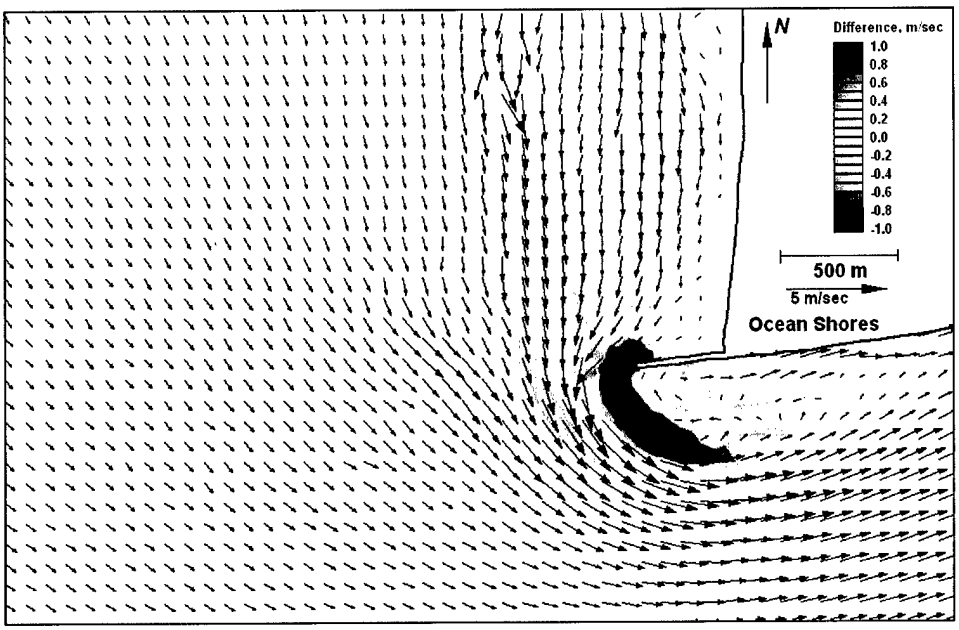

Figure 7-100. Difference map Alt 4A – existing (Run 124 – Run 104) for peak flood

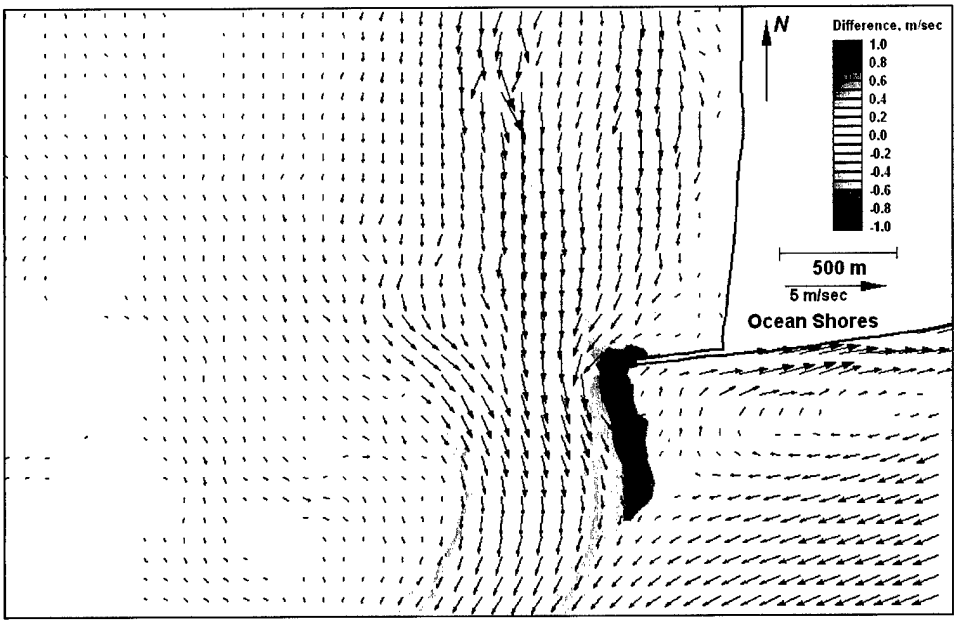

Figure 7-101. Difference map Alt 4A – existing (Run 124 – Run 104) for peak ebb

Westerly waves

After completion of data analysis for the 24 simulations, denoted Run 104 through 127, an examination of the response of structural alternatives to a typical westerly wave was made to augment the evaluation process. A 5-day spring tide simulation with the inclusion of 2.5-m, 10-sec westerly waves was conducted for the existing condition and the five structural alternatives (Runs 128-133 in Table 7-6). Appendix E shows the resulting plan view current patterns, global difference maps, and time series plots for these cases. Plan view current patterns for the existing condition shows that the longshore current is weak, and small gyres are prevalent north of the north jetty on flood and ebb tide. A rip current is observed 400 m north of the north jetty on ebb tide (Figures 7-102 and 7-103).

The current at the north jetty tip is directed southward during flood tide and northeastward during ebb tide and are noticeably weaker than the current at the jetty tip for west-northwest or west-southwest storm waves. The flood current in the inlet throat is directed slightly to the northeast, and the ebb current is directed slightly to the southwest. Note that normally incident waves can still drive a longshore current due to the longshore gradient in wave height.

Time series generated for the westerly wave simulations at the 16 node locations show that the longshore current components are approximately 0.5 m/sec or less in the surf zone, north of the north jetty (Appendix E). In contrast to the southerly current at Nodes 16330 and 16336 for west-northwest and west-southwest waves, the time series indicate that, with waves from the west, a westerly (rip) current is present at these locations. The north-south current component at the jetty tip (Node 12966) is weaker than with the west-northwest or west-southwest storm wave conditions.

A comparison of the time series for the existing condition with westerly waves and the structural alternatives with westerly waves are also given in Appendix E. Changes caused by the structural alternatives that are evident in the time series are at Nodes 15503, 13614, and 13589. The current components for Node 15503 (adjacent to the jetty) indicate that Alt 3B causes an increase to the southwest. The southern component changes from approximately 0.12 to 0.28 m/sec and the westerly component changes from approximately 0.19 to 0.52 m/sec. That is, Alt 3B increases the strength of the offshore-directed current near the jetty. At Node 13614, Alt 2A causes the northeast velocity to be directed more southward by reducing the east-west component and Alt 3A, 3B, and 4A cause the velocity to be directed more east-west by reducing the north-south component. The time series at Node 13589 shows that Alt 2A increases the northbound and decreases the eastbound velocity component at that location.

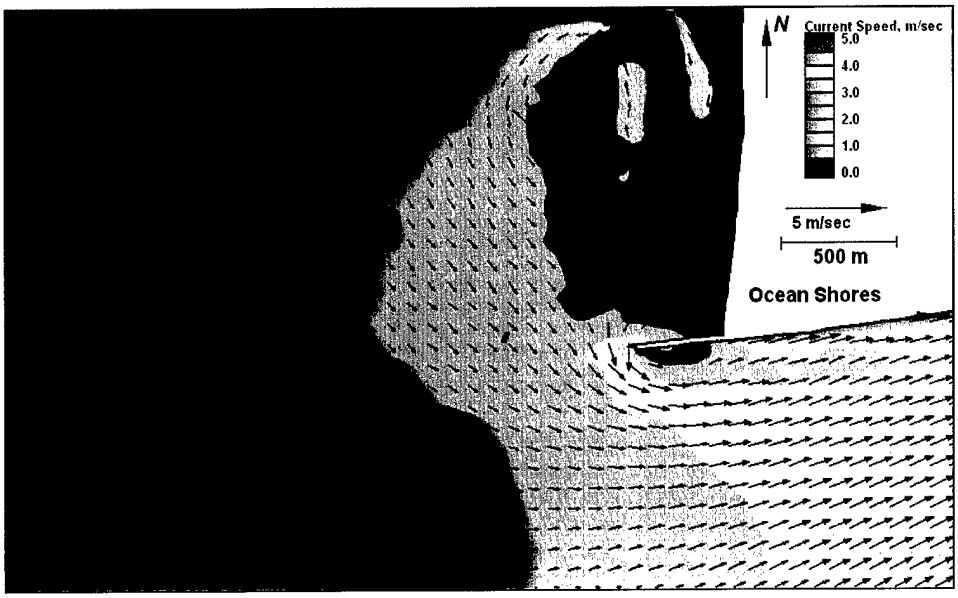

Figure 7-102. Run 128 (existing, west, spring tide) north jetty view of flood tide

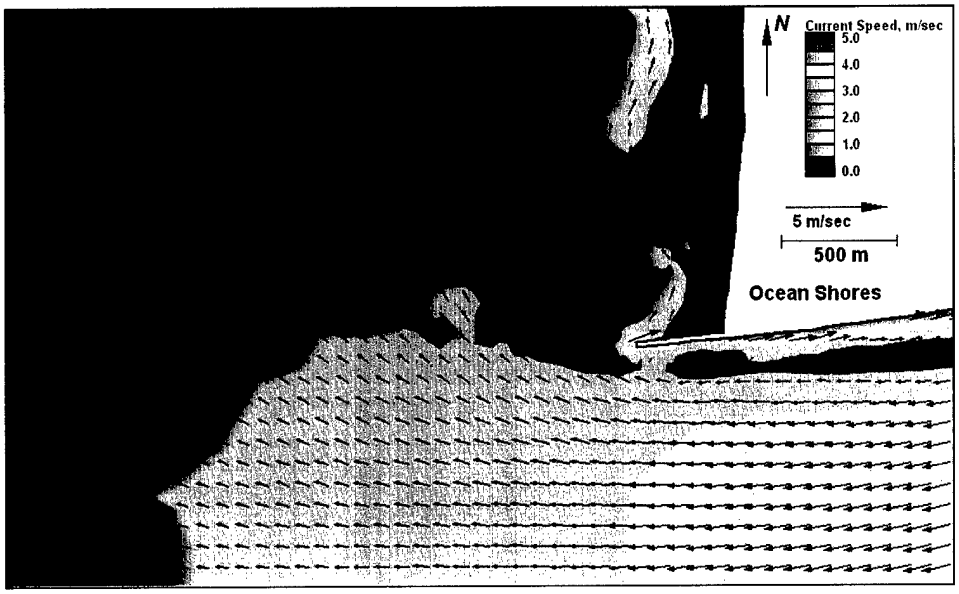

Figure 7-103. Run 128 (existing, west, spring tide) north jetty view of ebb tide

Statistical analysis summaries of the westerly wave condition simulation for existing bathymetric conditions (Run 128) and five structural alternatives (Runs 129-133) are listed in Table 7-9. Mean current components and the difference between alternatives and existing condition mean current components are calculated in the same manner as was applied to the first 24 simulations. The tabulated mean currents confirm the weak longshore current observed in the plan view ebb and flood current maps (Figures 7-102 and 7-103). The nine nodes shoreward of the spur location have southbound mean currents of 0.11 to 0.53 m/sec, except for Nodes 13589 and 16336 that have northbound mean current. The east-west mean current components range from 0.19 m/sec to the west at Node 15503 to 0.46 m/sec to the east at Node 13614. The nine nodes do not follow a trend or pattern in east-west mean currents. This is further indication of the presence of rips or gyres with the westerly wave condition.

Alternatives 2A/2B and westerly waves. With the spur alternatives in place and westerly waves, there is an increase in southbound current of 0.04 to 0.34 m/sec, an increase in westerly current of 0.21 m/sec and decrease in easterly current of 0.24 m/sec at the southern three nodes, and an increase in the easterly current and decrease in westerly mean current at two of the three northern nodes. This trend is similar to the response of west-northwest waves to Alt 2A/2B. Node 13589 near the northern end of the spur changes from northeasterly directed currents for the existing condition to slightly west of north-directed currents for Alt 2A. The mean northward component increases 0.33 m/sec.

Alternatives 3A, 3B, 4A, and westerly waves. The response of currents to westerly waves and Alt 3A, 3B, and 4A shows an increase in southbound current at the shoreward six nodes and a decrease in southbound and increase in northbound mean current at the seaward three nodes. The northern three nodes show an increase in eastward and decrease in westward current and the southern six nodes show an increase in westward and decrease in eastward mean current. This trend is similar to the response of west-southwest waves to Alt 3B.

Difference maps were generated by comparing the current pattern at peak flood and peak ebb for each structural alternative to the corresponding existing-condition current pattern (Appendix E). All alternatives indicate an increase in southbound current shoreward of the spur location for westerly waves. Changes are stronger on ebb than flood. Comparison of each alternative to the existing condition current pattern is as follows:

a. At peak flood, Alt 2A shows a more defined, increased southward current close to the shoreline and along the inlet side of the north jetty. Alternative 2A also shows a more defined, stronger southward current close to the shoreline at peak ebb, an area of reduced current landward of the spur, increased northward and southward currents seaward of the spur, increased currents along the inlet side of the north jetty, and reduced current approximately 100 m south of the north jetty.

Table 7-9
Mean Currents for Westerly Waves and Difference in Mean Currents Between Alternatives and Existing Condition

Node	Run 128 (Existing)	Run 129 (Alt 2A)	Run 130 (Alt 2B)	Run 131 (Alt 3A)	Run 132 (Alt 3B)	Run 133 (Alt 4A)	Differences				
							129-128	130-128	131-128	132-128	133-128
U17188	-0.03	-0.03	-0.04	-0.04	-0.04	-0.04	0.00	-0.01	-0.01	-0.01	-0.01
V17188	-0.16	-0.17	-0.17	-0.17	-0.18	-0.17	-0.01	-0.01	-0.02	-0.02	-0.02
U15503	-0.19	-0.41	-0.21	-0.43	-0.52	-0.4	-0.21	-0.01	-0.24	-0.33	-0.21
V15503	-0.12	-0.21	-0.12	-0.21	-0.28	-0.19	-0.08	0.01	-0.08	-0.15	-0.07
U13614	0.46	0.22	0.44	0.19	-0.33	0.21	-0.24	-0.02	-0.28	-0.8	-0.26
V13614	-0.53	-0.88	-0.54	0.02	-0.15	0.06	-0.34	0	0.55	0.38	0.59
U12966	0.92	0.81	0.85	0	0	0	-0.1	-0.06	-0.92	-0.92	-0.92
V12966	-0.54	-1.09	-0.59	0	0	0	-0.55	-0.04	0.54	0.54	0.54
U12970	0.28	0.54	0.28	0.24	0.21	0.23	0.26	0.01	-0.04	-0.07	-0.04
V12970	0.1	0.04	0.11	0.12	0.13	0.13	-0.06	0	0.02	0.02	0.02
U14277	0.27	0.39	0.29	0.12	0.12	0.11	0.12	0.01	-0.15	-0.15	-0.16
V14277	0.02	0.02	0.02	0.06	0.06	0.06	0.00	0	0.04	0.04	0.04
U18006	0.16	0.19	0.16	0.18	0.2	0.18	0.03	0.00	0.02	0.03	0.02
V18006	-0.11	-0.25	-0.11	-0.21	-0.27	-0.22	-0.14	0.00	-0.1	-0.16	-0.11
U16330	-0.17	-0.12	-0.18	-0.12	-0.03	-0.15	0.06	-0.01	0.05	0.14	0.02
V16330	-0.15	-0.35	-0.17	-0.28	-0.24	-0.33	-0.2	-0.02	-0.13	-0.09	-0.19
U13589	0.11	-0.06	0.08	0.17	0.22	0.14	-0.17	-0.02	0.07	0.12	0.03
V13589	0.12	0.44	0.14	0.17	0.13	0.25	0.33	0.03	0.05	0.02	0.13
U18257	-0.02	-0.02	-0.02	-0.02	-0.02	-0.02	0	0.00	0	0.00	0
V18257	-0.08	-0.11	-0.08	-0.09	-0.08	-0.09	-0.03	0	-0.01	0	-0.01
U15763	0.15	0.2	0.16	0.17	0.16	0.2	0.05	0.01	0.02	0.01	0.04
V15763	0.32	0.33	0.32	0.36	0.38	0.36	0.01	0.00	0.04	0.06	0.04
U13251	0.1	0.15	0.12	0.12	0.11	0.14	0.05	0.02	0.02	0.01	0.04
V13251	0.08	0.1	0.1	0.07	0.06	0.11	0.02	0.02	0	-0.02	0.04
U11421	0.13	0.23	0.15	0.18	0.35	0.18	0.1	0.02	0.05	0.22	0.05
V11421	-0.12	-0.23	-0.09	-0.2	-0.36	-0.18	-0.11	0.03	-0.08	-0.24	-0.06
U18283	-0.06	-0.07	-0.05	-0.07	-0.06	-0.07	-0.01	0	-0.01	0	-0.01
V18283	-0.15	-0.19	-0.17	-0.2	-0.32	-0.19	-0.04	-0.03	-0.05	-0.17	-0.04
U16336	-0.12	-0.27	-0.09	-0.23	-0.12	-0.21	-0.16	0.03	-0.11	0.0	-0.09
V16336	0.03	-0.15	0.04	-0.15	-0.28	-0.15	-0.18	0.01	-0.19	-0.31	-0.19
U14255	0.00	0.14	-0.1	-0.16	0.06	-0.22	0.14	-0.1	-0.16	0.06	-0.22
V14255	-0.2	-0.14	-0.08	-0.1	-0.06	0.07	0.06	0.12	0.1	0.13	0.27

Note: A positive (+) u-component indicates an eastbound mean current; a negative (-) u-components indicate a westbound mean current, a positive (+) v-component indicates a northbound mean current, and a negative (-) v-component indicates a southbound mean current.
For eastbound mean current, a positive (+) difference indicates an increase in the eastbound mean current; a negative difference (-) indicates a decrease in the eastbound mean current. For westbound mean current, a positive (+) difference indicates a decrease in the westbound mean current; a negative difference (-) indicates an increase in the westbound mean current.
For northbound mean current, a positive (+) difference indicates an increase in the northbound mean current; a negative difference (-) indicates a decrease in the northbound mean current. For southbound mean current, a positive (+) difference indicates a decrease in the southbound mean current; a negative difference (-) indicates an increase in the southbound mean current.

b. Alternative 2B has a similar response pattern as Alt 2A, but the magnitude of change is smaller for Alt 2B.

c. The changes in current caused by Alt 3A at peak flood are concentrated near the structural alternative (short jetty) location. There is a reduction in current magnitude at the structure location and a corresponding increase in current magnitude seaward of the structure location. At peak ebb, the southward longshore current at Ocean Shores increases with Alt 3A, and a rip current 300 m north of the north jetty is observed. A northward longshore current observed 500 m north of the north jetty increases in magnitude for a 100-m stretch across the surf zone close to shore and decreases for a 100-m stretch further seaward. Current magnitudes at the structure location are reduced.

d. Alternative 3B (full jetty rehabilitation) has a similar response pattern to Alt 3A, but the magnitude of change is larger for Alt 3B, and the rip current location is closer to the north jetty for Alt 3B.

e. Alternative 4A has a similar response pattern to Alt 3A, but the magnitude of change is slightly larger for Alt 4A shoreward of the spur location.

Simulations with 5-Year and 30-Year Shoreline

Steering Module simulations of future conditions were accomplished by inclusion of the GENESIS-predicted shoreline position (Chapter 6) after 5 and 30 years for the existing condition and 5 project alternatives, resulting in 12 bathymetric grids for ADCIRC and STWAVE. Bathymetric adjustments landward of a future (5 or 30 years) shoreline position were linearly sloped from an existing ADCIRC node elevation to the future condition (new) shoreline position. Bathymetric adjustments seaward of a future shoreline position were dependent upon grid resolution seaward of the new shoreline position and the beach profile at that location. Adjustment to water depths transitioned from the new shoreline position to the original beach profile.

Simulations of the 5-year shoreline and spring tide conditions with west-northwest (Runs 134-139), west (Runs 140-145), and west-southwest (Runs 146-151) waves were made for the existing condition and each project alternative. Simulations of the 30-year shoreline and spring tide conditions with west-northwest (Runs 152-157), west (Runs 158-163), and west-southwest (Runs 164-169) waves were also run for the existing condition and each project alternative. Analysis of the simulations included an examination of peak flood and peak ebb plan view maps and global differences in current magnitude for each project alternative compared to the existing condition (Appendix E).

Simulation of 5-year shoreline

5-year shoreline and west-northwest waves. Runs 134 through 139 include the 5-year shoreline position, spring tide, and west-northwest waves for the existing condition and five project alternatives. Similar to the original shoreline position simulation (Run 108), Alt 2A for the 5-year shoreline simulation (Run 135) increases the southbound current shoreward of the spur and

decreases currents at the spur location. The increase in current magnitude close to the jetty tip is larger for the 5-year shoreline Alt 2A simulation (Run 135 – Run 134) than the original Alt 2A simulation (Run 108 – Run 104). However, the spatial extent of change is smaller. Changes in currents caused by Alt 2B (Run 136 – Run 134) are similar to Alt 2A (Run 135 – Run 134), but the magnitude and spatial extent are smaller. Alternative 2B current changes with the 5-year shoreline (Run 136 – Run 134) compared to changes in the current with the original shoreline Alt 2B simulation (Run 112 – Run 104) show a smaller spatial extent.

Similar to the original shoreline position simulation (Run 116), Alt 3A for the 5-year shoreline simulation (Run 137) decreases the southbound current landward of the spur and around the jetty tip. Alternative 3B (Run 138) causes the same pattern of change as Alt 3A, but with a greater magnitude of change. The Alt 3B changes in current with the 5-year shoreline (Run 138 – Run 134) compared to the changes with the original shoreline (Run 120 – Run 104) show similar patterns of change, but smaller magnitudes and extent of change with the 5-year shoreline. Changes in current caused by Alt 4A are similar to Alt 3A.

5-year shoreline and west waves. Runs 140 through 145 include the 5-year shoreline position, spring tide, and westerly waves for existing bathymetric conditions and the five project alternatives. The current change trends for the 5-year shoreline position for each alternative (Runs 141 through 145) compared to the existing condition simulation (Run 140) are similar to the original changes caused by each project alternative (Runs 129-133 compared to 128) (see previous section). Comparing changes in current magnitude caused by Alt 2A for the 5-year shoreline simulation (Run 141 vs. 140) to the changes caused by Alt 2A for the original shoreline position (Run 129 vs. 128) shows a smaller change in current magnitude for the 5-year shoreline simulation, but the trend is similar. Alternative 2B shows a small southbound increase and a large northbound increase for the 5-year shoreline simulation (Run 142-140) compared to the original simulation (Run 130-128). Alternatives 3A and 3B current changes with the 5-year shoreline (Run 143 and 144 vs. Run 140) compared to the current changes with the original shoreline Alt 3A and 3B simulations (Run 131 and 132 vs. Run 128) show similar patterns, but with greater decrease in current magnitude at the jetty tip for the 5-year shoreline simulation. The 5-year shoreline simulation of Alt 3A shows a more defined rip current on ebb (Run 143 ebb, Figures E-160 and E-330) than the original shoreline position simulation of Alt 3A (Run 131 ebb, Figure E-113 and E-290). Changes in current caused by Alt 4A are similar to Alt 3A.

5-year shoreline and west-southwest waves. Runs 146 through 151 include the 5-year shoreline position, spring tide, and west-southwest waves for existing bathymetric conditions and the five project alternatives. The results of the west-southwest simulations were more interesting than the west-northwest and westerly results because a notable difference was observed between the 5-year shoreline simulations and the original shoreline position simulations for this direction. The original west-southwest simulation (Run 105) shows longshore current to the north with a reversal (southward) current in the first 500 m north of the north jetty. The 5-year shoreline simulation with west-southwest waves (Run 146) shows longshore current to the north developing closer to the north jetty and a much smaller area of low magnitude, southward currents. It is

therefore difficult to compare changes in current magnitude caused by Alt 2A for the 5-year shoreline simulation (Run 147 vs. 146) to the changes caused by Alt 2A for the original shoreline position (Run 109 vs. 105).

Comparing Alt 2A (Run 147) to the 5-year existing condition simulation (Run 146) shows an increase in northbound current shoreward of the spur and a decrease in northbound current further north of the spur location, and a shift in the eddy location causing an increase in current magnitude on the inlet side of the north jetty. Comparing Alt 2B (Run 148) to the 5-year existing condition simulation (Run 146) shows an increase in southbound current near the north jetty. That is, the Alt 2B spur appears to create a sheltered area, and diffraction around the spur tip causes a southbound current. Comparing Alt 3A, 3B, and 4A for the 5-year shoreline simulation (Runs 149 through Run 151) currents to the 5-year existing-condition simulation (Run 146) current shows an increase in northbound current with the jetty alternatives, a shift in the gyre position, a decrease in current magnitude at the jetty tip, and an increase in current magnitude south of the north jetty. Results for Alt 3A, 3B, and 4A are similar to the existing shoreline simulation results, with the exception of the decreased or eliminated flow reversal near the north jetty for most of the 5-year shoreline simulations.

Simulation of 30-year shoreline

30-year shoreline and west-northwest waves. Runs 152 through 157 include the 30-year shoreline position, spring tide, and west-northwest waves for the existing condition and five project alternatives. Results look similar to the 5-year shoreline simulations, with one minor exception. Simulation of Alt 2B with the 30-year shoreline (Run 154) compared to the 30-year shoreline for the existing condition (Run 152) shows a greater reduction in flood current in the inlet than the 5-year shoreline simulation (Run 136 vs. Run 134).

30-year shoreline and westerly waves. Runs 158 through 163 include the 30-year shoreline position, spring tide, and westerly waves for the existing condition and five project alternatives. Results look similar to the 5-year shoreline simulations.

30-year shoreline and west-southwest waves. Runs 164 through 169 include the 30-year shoreline position, spring tide, and WEST-SOUTHWEST waves for the existing condition and five project alternatives. Results look similar to the 5-year shoreline simulations.

Comparison to Physical Model

Calculations from the tidal circulation model (ADCIRC) were compared with velocity measurements in the physical model for similar wave and current conditions. In the physical model, the sampling volume for the current velocity was placed close to the bottom because of interest in bed load transport (transport of coal powder, Chapter 5). In contrast, depth-averaged velocities are calculated in ADCIRC, implying a possible positive offset, with the numerically calculated (point measurement) values expected to be slightly larger than those in the physical model (average-volume, near-bottom measurement). Other

considerations when calculating mean currents for the physical and numerical simulations were the length of each simulation and the temporal variation of tides in numerical model simulations versus a steady, flood current in the physical model simulations.

Velocity measurements for the long spur (Alt 2A) for 5-m, 13-sec west-northwest waves at mtl (Table B-15) were compared with mean currents from ADCIRC-STWAVE numerical simulation Run 104 (Table 7-7). Both the physical and numerical simulations were for the existing condition. Physical model current measurement locations were at the north end of the spur (Acoustic Doppler Velocimeter (ADV 1) and at two points bracketing the midpoint of the spur length (ADV 2 and ADV 3, respectively), although the spur was not present for the comparison simulation. Mean currents measured in the physical model for the existing condition were compared with numerical model Run 104 mean currents near the spur (Node 13589) and at the midpoint of the spur (Node 14255). Node 13589 is closest to ADV 1 and Node 14255 is closest to ADV 2.

Physical model measurements show currents at ADV 1 and ADV 2 directed to the southeast. The easterly component at both gages is 0.29 m/sec, and the southerly component ranges from 0.88 to 1.10 m/sec, scaled to prototype. Numerical model mean currents at Nodes 13589 and 14255 are directed to the southeast and southwest, respectively. Numerical model mean currents show a smaller east-west component by -0.21 to 0.12 m/sec than the physical model east-west component. The predominant (southerly) component of mean velocity is 1.04 to 1.06 m/sec. Magnitudes of the mean velocity measured in the physical model were 0.93 to 1.14 m/sec, which bracket the numerical model mean magnitudes of 1.06 and 1.07 m/sec.

Velocity measurements in the physical model taken shoreward of the spur for 5-m, 13-sec west-northwest waves at mtl (Table B-15) were also compared to mean currents from ADCIRC-STWAVE numerical simulation Run 108 (Table 7-7). Both the physical and numerical simulations were for Alt 2A. Comparison locations were at the same locations described in the preceding paragraphs. The physical model measurements show the current at ADV 1 and ADV 2 to the southeast. The easterly component increases to 0.37 to 0.41 m/sec and the southerly component decreases to 0.79 to 0.82 m/sec compared to the existing-condition simulation. Numerical model mean currents at Nodes 13589 and 14255 are to the southeast and southwest, respectively. The mean current calculated with the numerical models has a smaller east-west component of -0.17 to 0.16 m/sec than the physical model east-west component. The predominant (southerly) component of mean velocity decreases to 0.91 to 0.99 m/sec compared with the existing condition simulation. The magnitude of the mean velocity measured in the physical model is 0.89 to 0.90 m/sec, which is close to the numerical model mean magnitudes of 0.93 and 1.00 m/sec. Both the physical and numerical model current measurements show a reduction in southbound current at the spur location.

In summary, mean currents in the numerical and physical models are consistent for west-northwest waves, despite the somewhat different representative measurement (near-bottom velocity for the physical model; depth-averaged velocity for the numerical model). In addition, the numerical model includes temporal variation of the tide, whereas the physical model includes only

a flood current. Consistency between the numerical and physical models generates confidence in the evaluation of project alternatives.

Analysis of Predicted Sediment Transport Pathways at Grays Harbor

This section describes application of the Lagrangian sediment transport model, PSed (Davies, Serrer, and Watson 2000) to ADCIRC-STWAVE Steering Module simulations of combined wave and tidal currents in Grays Harbor. The analysis has two objectives: simulate and analyze sediment pathways in the estuary and identify changes in sediment pathways in response to project alternatives.

Model Description – PSed

PSed is a Lagrangian sediment transport model developed at the Canadian Hydraulics Centre of the National Research Council of Canada. In the model, sediment entrainment, mobility, advection, and deposition are predicted in a particle-based approach. The model accepts steady and unsteady flow fields on a finite element grid as input. Bathymetry, free surface elevation, and currents are input to PSed from a variety of finite element hydrodynamic simulation models, including ADCIRC. Other optional inputs include sediment grain-size maps or bed roughness maps. Sediment sources are user-defined as either point sources or line sources. Point sources can release sediment at a constant, user-specified rate or at a time-varying rate defined by the user or released at a rate controlled by a time series input file. Line sources allow an even rate of release of parcels from random locations along a user-defined line or transect. A flow-chart for PSed is provided in Figure 7-104.

Sediment mobility is the propensity for sediment to be in motion under given flow conditions. Mathematically, it is the ratio of the shear stress exerted by the flow field on the sediment to the critical shear stress for the inception of sediment motion. An overview of the calculation is provided in Appendix H.

Sediment released into the flow field is characterized by grain size distribution, grain density, and fall velocity. PSed operates as a quasi-3-D sediment transport model. Sediment particles released into the flow field are first assessed to determine their mobility; if mobile and resting on the bed, sediment is advected vertically and horizontally by the flow field at a rate proportional to the potential sediment transport rate at that location in space and time. Dispersion in the model is treated as a random-walk process. Local instantaneous calculations are made of bed shear, sediment mobility, and bedform development. The local time series of sediment mobility was used to define the sediment parcel release rates for all point sources. A constant release rate was specified for all line sources.

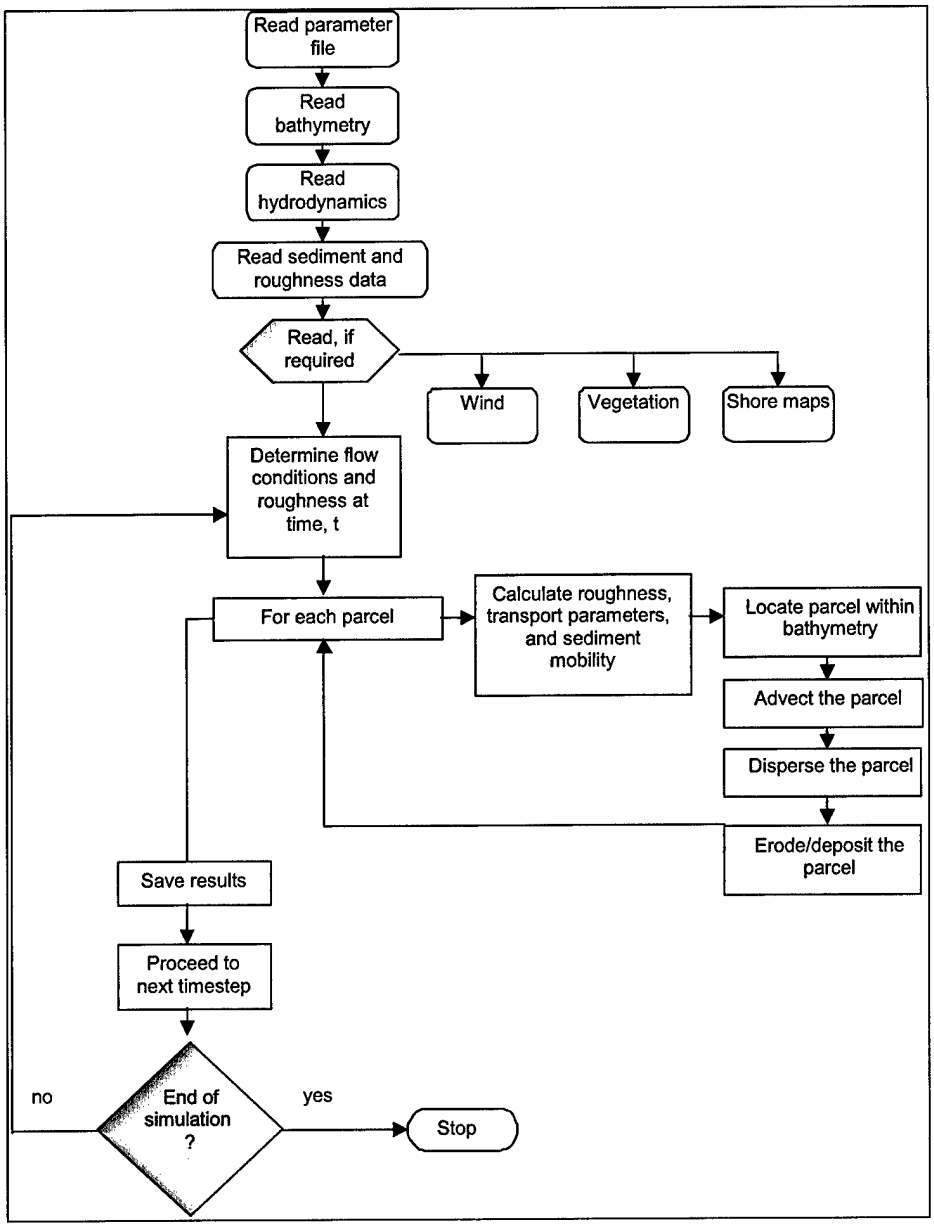

Figure 7-104. Flowchart for PSed calculation

Circulation Patterns and Sediment Pathways

Grain-size map

The investigation of sediment pathways in the estuary required development of a grain-size map. A grain-size map for Grays Harbor was developed from Beverage and Swecker (1969) and USACE (1977). The map shown in Figure 7-105 specifies three sediment classes: silt in the upper estuary (D_{35}=0.05 mm), sand throughout the lower estuary, on the ebb shoal, and along the shores (D_{35}=0.3 mm), and coarse sand to fine gravel in the inlet (D_{35} = 1.0 mm).

Sediment sources

Four sources of sediment to the inlet were investigated:

a. Sediment moving southward into the estuary bypassing the north jetty.

b. Sediment moving northward into the estuary bypassing the south jetty.

c. Reworking of sediment within the estuary.

d. Reworking of sediment on the ebb shoal.

For sediment entering the estuary from the north and south, and for sediment reworked on the ebb shoal, parcels of sand were released along a line source in each case. Within the estuary, sediment parcels were released from 22 point sources. The coordinates of the line source locations are listed in Table 7-10, and the point source locations are listed in Table 7-11 and shown graphically in Figure 7-106. PSed simulations were run with a medium-sand size distribution (D_{35} = 0.3 mm) placed at each location.

Catchment analysis

PSed output consists of sediment parcel locations as a function of time. Each sediment parcel has attributes such as elevation above the bed, grain size, mobility, and critical shear stress, and these can be output as well. The resulting sediment pathways simulations can be viewed as an animated sediment field or as single frames of parcel locations that can be extracted and plotted. Several of these plots are presented in the following section. Catchment areas or simulated sediment traps can also be defined, and the PSed results can be summarized by the number of sediment parcels accumulated within a trap as a function of time. For Grays Harbor, seven sediment catchment areas were defined for the PSed analysis (Figure 7-107).

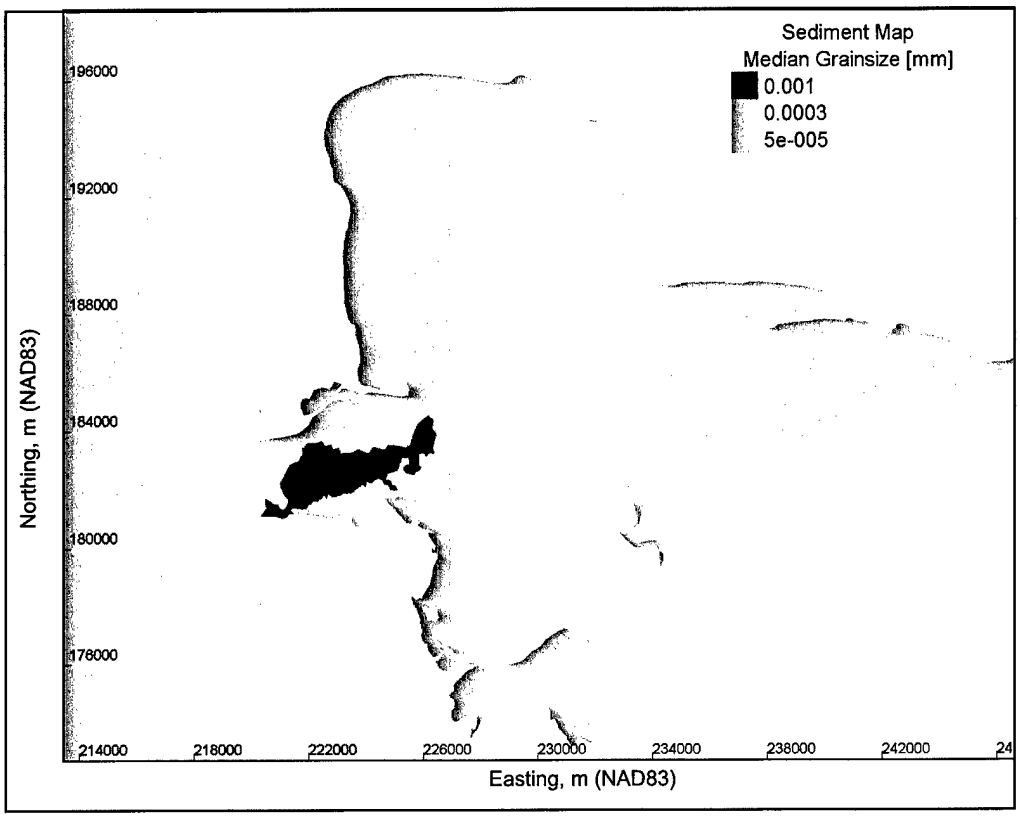

Figure 7-105. Grain size map for PSed simulations

Table 7-10
Endpoints of Line Sources of Sediment for PSed Analysis of Pathways

Location	Parcels	Easting	Northing	Easting	Northing
North beach	100,000	220339	186042	219220	186140
South beach	120,000	223753	178382	222543	178162
Ebb shoal	100,000	216162	179209	217455	178401

Washington State Plane South 4602, m; North American Datum 1983 (NAD83).

Table 7-11
Point Sources of Sediment for PSed Analysis of Pathways

Location	Easting, m (NAD83)	Northing, m (NAD83)
1	223318	193505
2	228715	193154
3	230900	192560
4	240613	191319
5	235999	188918
6	232519	187650
7	229848	187434
8	224883	187326
9	227096	186867
10	226745	185842
11	247170	184250
12	223318	183009
13	228715	185869
14	230900	186409
15	240613	186490
16	235999	188162
17	232519	179744
18	229848	183279
19	224883	187380
20	227096	187029
21	226745	186490
22		

Washington State Plane South 4602.

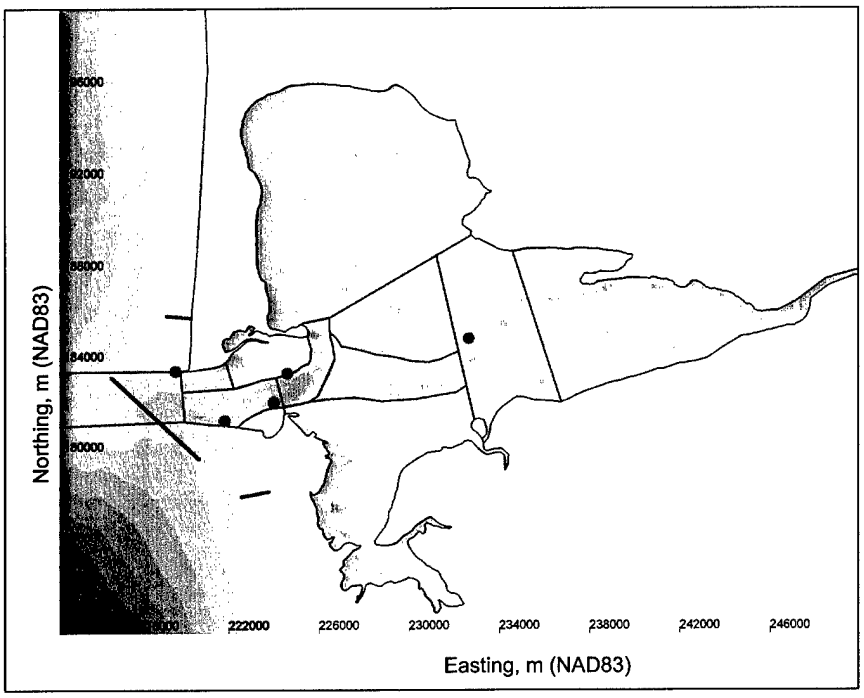

Figure 7-106. Point sources releasing sediment within estuary. Blue lines show location of line sources, red points show individual point sources, and yellow squares show distributed 22 sources for inner estuary

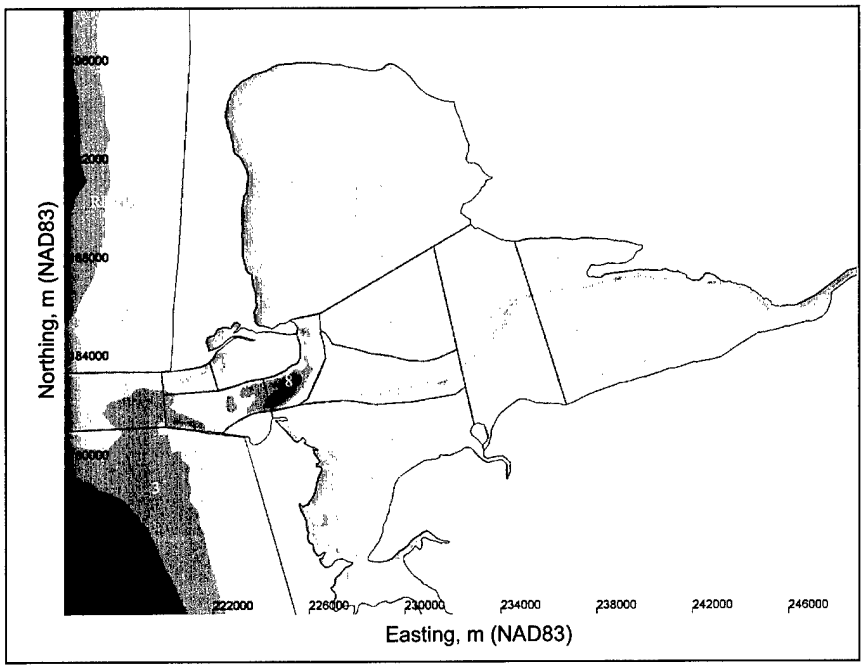

Figure 7-107. Catchment areas for sediment trap analysis

The total number of parcels found within each catchment area (or sediment trap) is then tabulated and compared with similar results for other project alternatives. The results of this sediment trap analysis are presented as the percentage of the total number of sediment particles introduced into the flow field contained within each catchment area at the end of a 5-day hydrodynamic simulation. Final trap content is taken as the average trap content calculated over the last 6 hr of the simulation. Catchment areas were amalgamated into three groups: Reaches 1 through 3 form the offshore area; Reaches 4 through 8 form the inlet area, and Reaches 9 through 14 form the inner estuary area.

Tidal forcing

Time series of water surface elevation for the spring and neap tide conditions are shown in Figure 7-108 and Figure 7-109, respectively. For PSed simulations driven by these ADCIRC runs, sediment simulations were started 17.5 hr into the run so as to omit the first tidal cycle during which time the circulation model is ramping up. The spring tide runs were analyzed for the time interval 17.5 to 116.5 hr (forming eight tidal cycles). PSed analysis on the neap tide runs also was conducted over an integer number of fully developed tidal cycles, in this case from 17.5 to 119.5 hr.

Table 7-12 summarizes the ADCIRC/STWAVE runs used in the PSed analysis. Although analysis was run on all conditions, only runs with waves from the WEST-SOUTHWEST are reported here because they relate most directly to bypassing of sand at the north jetty.

Existing Condition

Sediment mobility maps

Figure 77-110 shows the temporal average of sediment mobility in the estuary for D_{50}=0.3 mm. This average was computed for the interval between 17.5 and 116 hr in Run 104, eight tidal cycles. This map shows that, for waves from the west-northwest, there is a strong average mobility toward the south, particularly at the tip of the north jetty. Wave-driven currents force a strong residual mobility along the south face of the north jetty. However, because of the circulation patterns and eddying that occur at the tip of the north jetty, there is no strong mobility path between the tip of the north jetty and the longshore current running along the south edge of the north jetty. Sediment mobility vectors directly to the south of the tip of the north jetty tend to point toward the south and southwest, suggesting that bypassing sediment will be carried past the jetty to an area where tidal flows, not wave-driven flows, will control their fate.

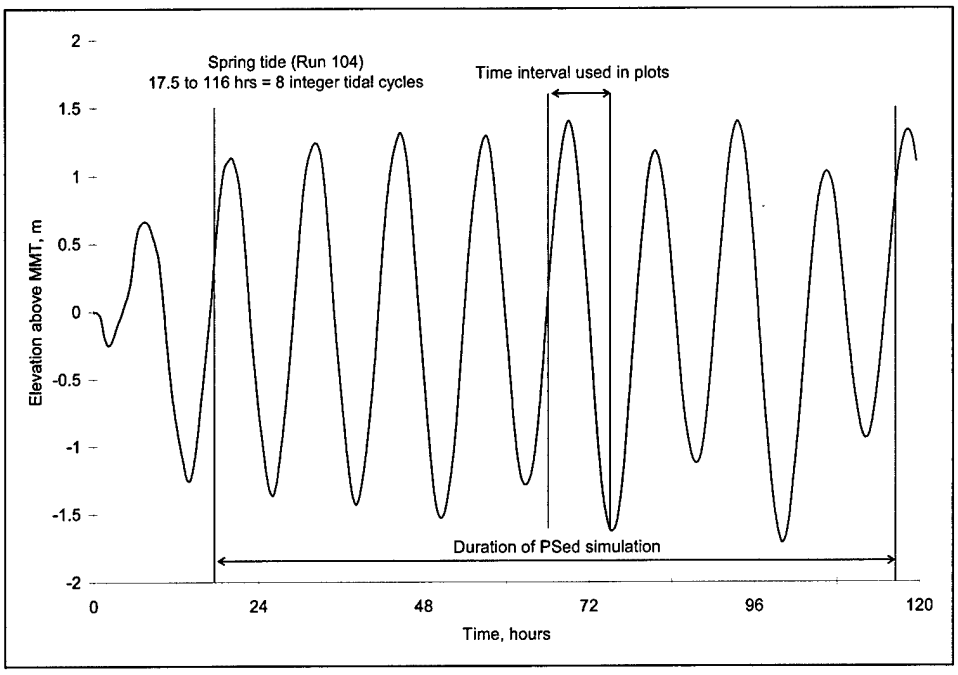

Figure 7-108. Offshore water surface time series, spring tide (Run 104)

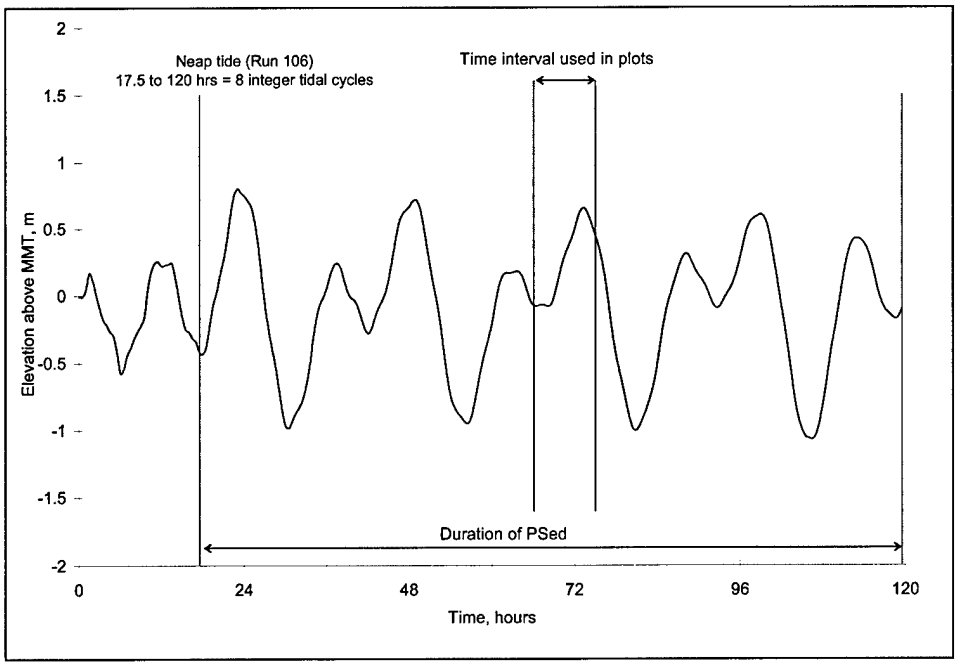

Figure 7-109. Offshore water surface time series, neap tide (Run 106)

Table 7-12
ADCIRC/STWAVE Runs Input to PSed Analysis

Alternative	Wave Direction	Tide	Run
Existing	west-northwest	Spring	104
	west-southwest	Spring	105
	west-northwest	Neap	106
	west-southwest	Neap	107
2a	west-northwest	Spring	108
	west-southwest	Spring	109
	west-northwest	Neap	110
	west-southwest	Neap	111
2b	west-northwest	Spring	112
	west-southwest	Spring	113
	west-northwest	Neap	114
	west-southwest	Neap	115
3a	west-northwest	Spring	116
	west-southwest	Spring	117
	west-northwest	Neap	118
	west-southwest	Neap	119
3b	west-northwest	Spring	120
	west-southwest	Spring	121
	west-northwest	Neap	122
	west-southwest	Neap	123
4a	west-northwest	Spring	124
	west-southwest	Spring	125
	west-northwest	Neap	126
	west-southwest	Neap	127

North jetty

Figure 7-111 shows sediment parcel locations at peak flood and at peak ebb for sediment originating from a shore-normal transect at Ocean Shores beach. There are two main sediment pathways for sediment originating from the north. Some sediment passing the north jetty is transported directly to the south and slightly offshore, finally being deposited on the ebb shoal. The flood tide carries sediment into the estuary past Damon Point, where it can be deposited and redistributed through the estuary. Sediment deposited on the ebb shoal is occasionally remobilized and transported into the estuary on the flood, but the net transport of this sediment is typically toward the ebb shoal.

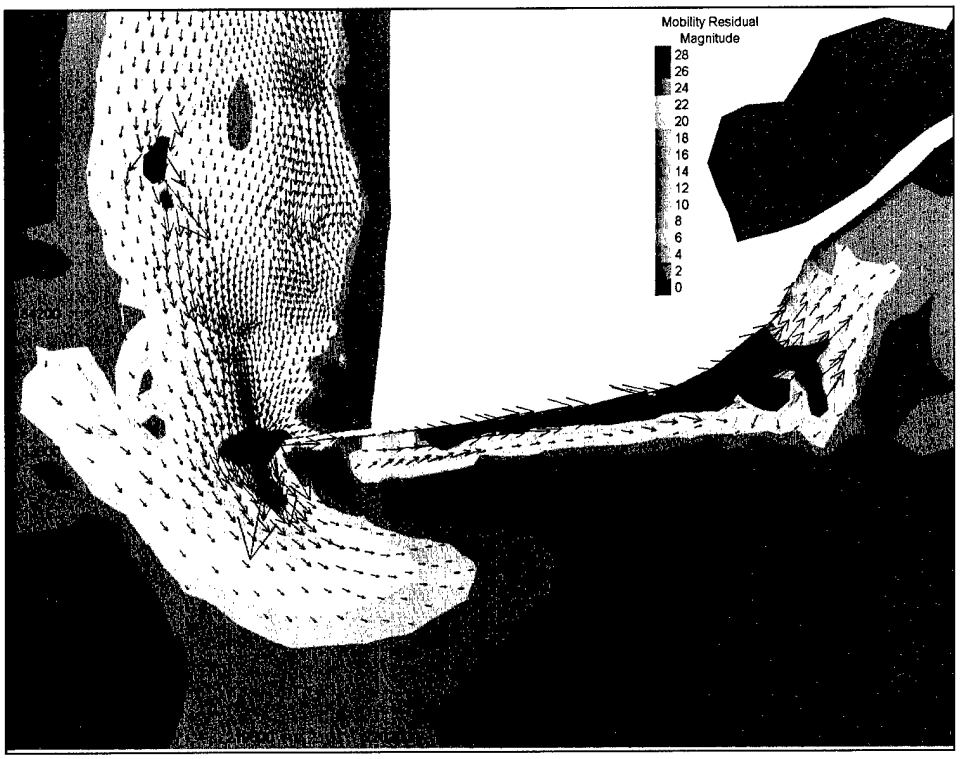

Figure 7-110. Temporally averaged (residual) sediment mobility for 0.3-mm sand (Run 104)

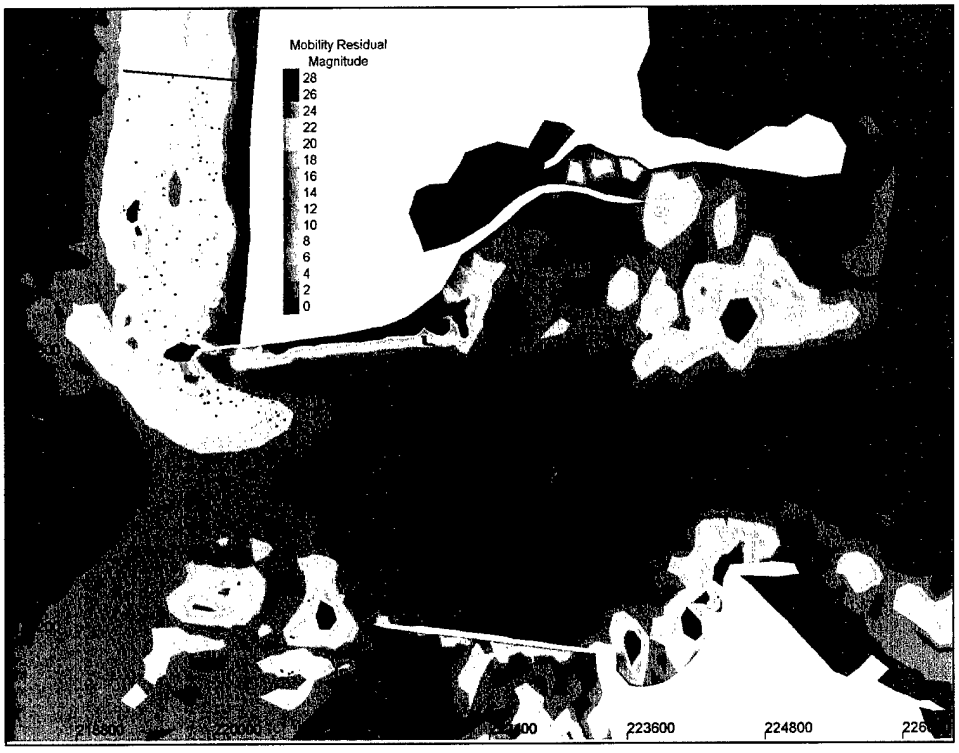

Figure 7-111. Sediment parcel locations during flood tide for Run 104 superimposed on a contour map of residual mobility

Figure 7-111 shows that, during flood tide, sediment transported into the estuary does not reach a point that is sufficiently far north to enter the strong sediment transport zone that extends to the south side of the inlet and south jetty. The result is that the sediment pathways from the simulations do not indicate any significant sediment transport from the north jetty to the distal tip of Damon Point.

The longshore current running along the south face of the north jetty is strong and well-defined along the western half of the north jetty (Figure 7-112). From this point eastward, however, the current becomes less well-defined (Figure 7-113). Although STWAVE simulations extend as far as Damon Point, the resolution of the ADCIRC grid decreases in this area, and the longshore current is unresolved. The logical sediment pathway here is for a longshore current to continue in the nearshore along Damon Point as confirmed by the field measurements (Chapter 4). Sediment reaching the southeast tip of Damon Point is subsequently carried by tidal action farther into the estuary on flood and out toward the ebb shoal on ebb tide. The complete pathway from the north jetty to Damon Point is not well-defined in these simulations; however, the fate of sediment that has been transported to Damon Point can be examined by placing a sediment source at Damon Point.

Figures 7-114 through 7-118 show the final sediment parcel locations after 5 days of simulation for various sites throughout the study area. These figures illustrate that all sediment sources can contribute to deposition in the inner estuary and along the navigation channel.

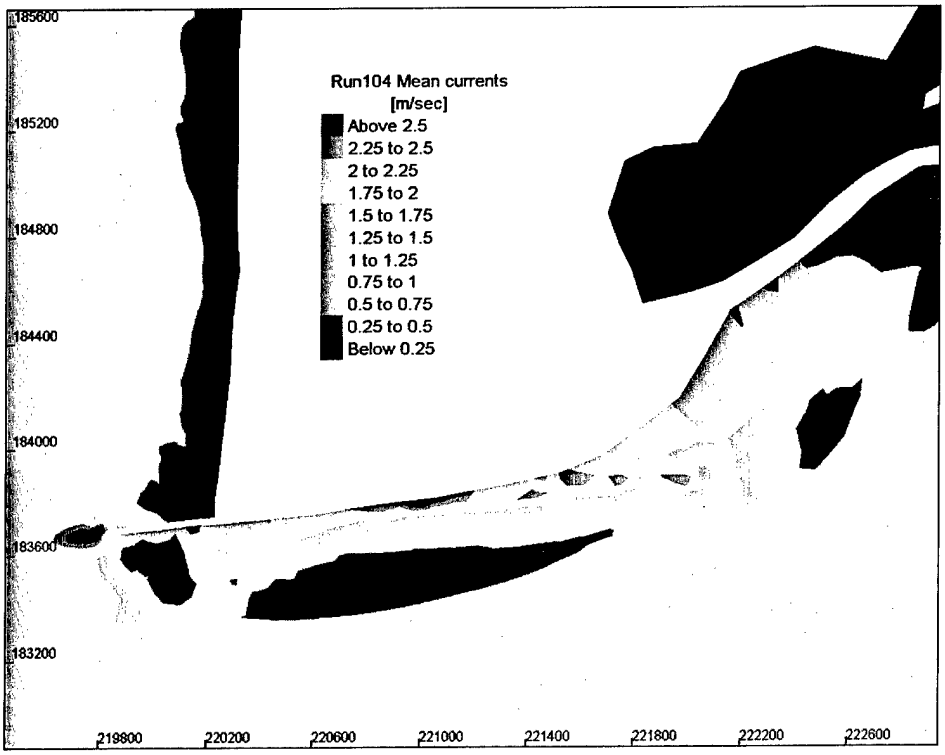

Figure 7-112. Mean currents for Run 104 (8 tidal cycles from 17.5 to 116 hr)

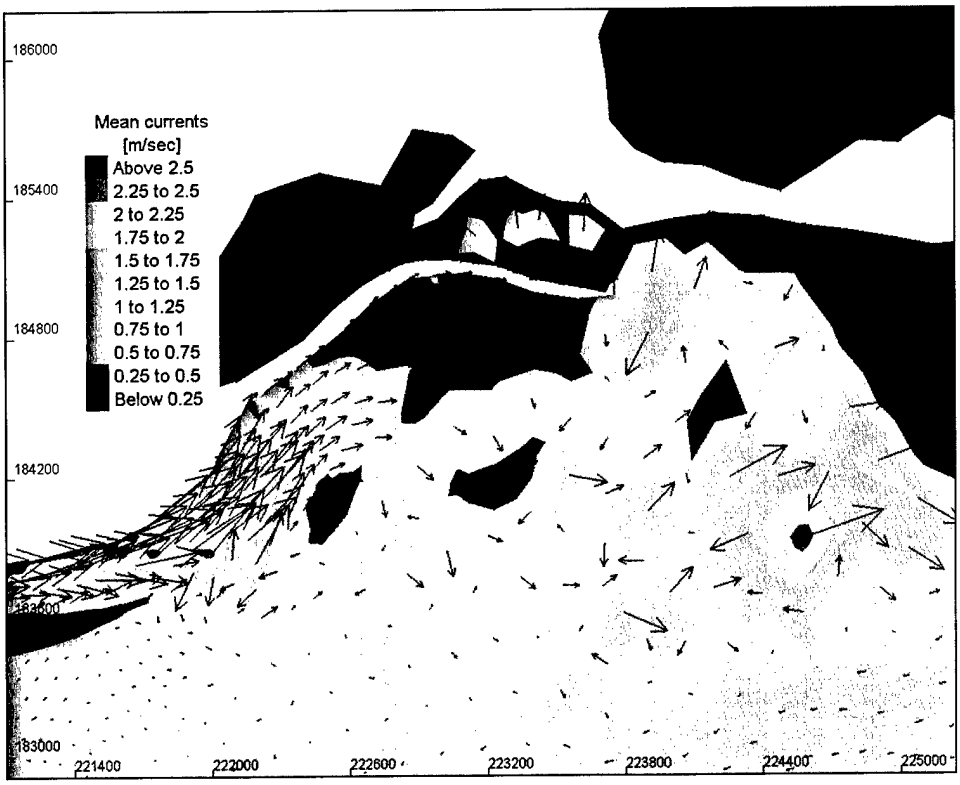

Figure 7-113. Mean current vectors for Run 104 (8 tidal cycles 17.5 to 116 hr)

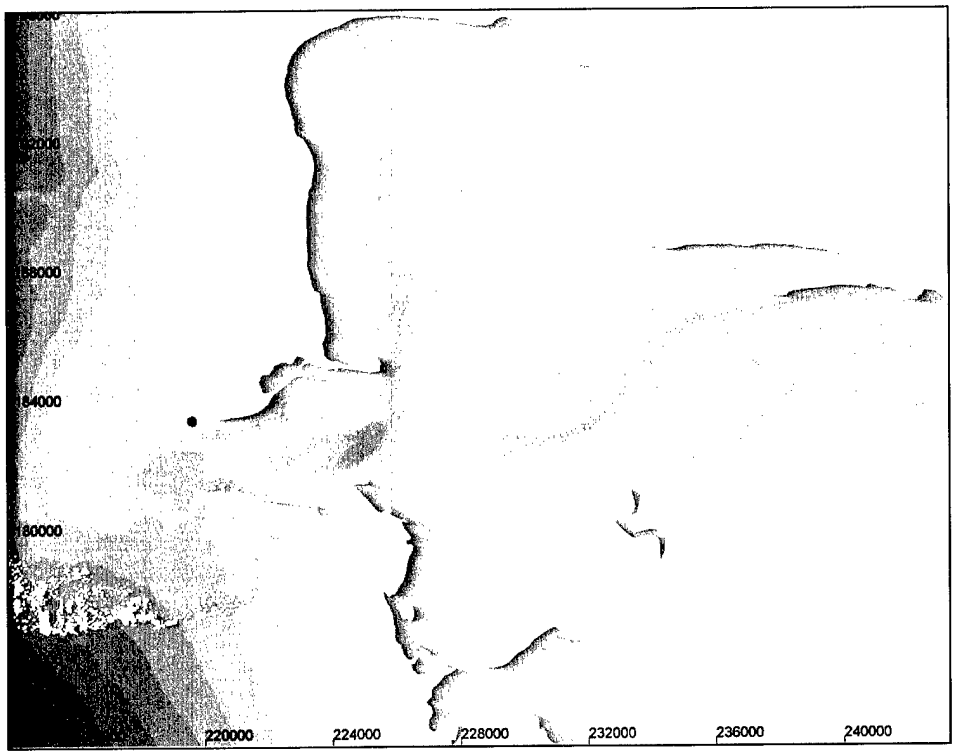

Figure 7-114. Final sediment parcel locations for Run 104, sand source at north jetty

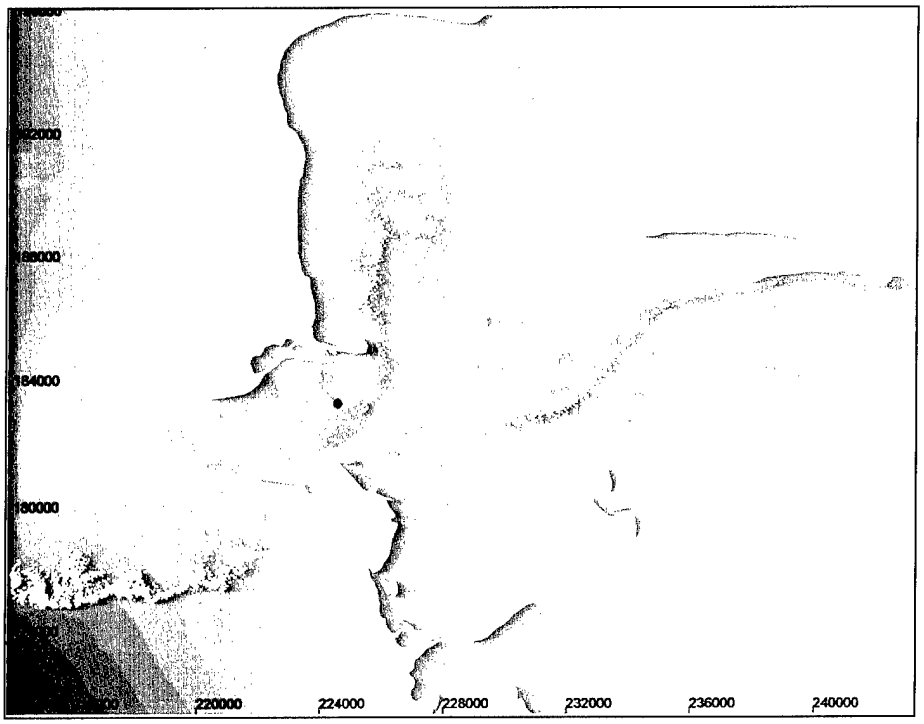

Figure 7-115. Final sediment parcel locations for Run 104, sand source at Damon Point

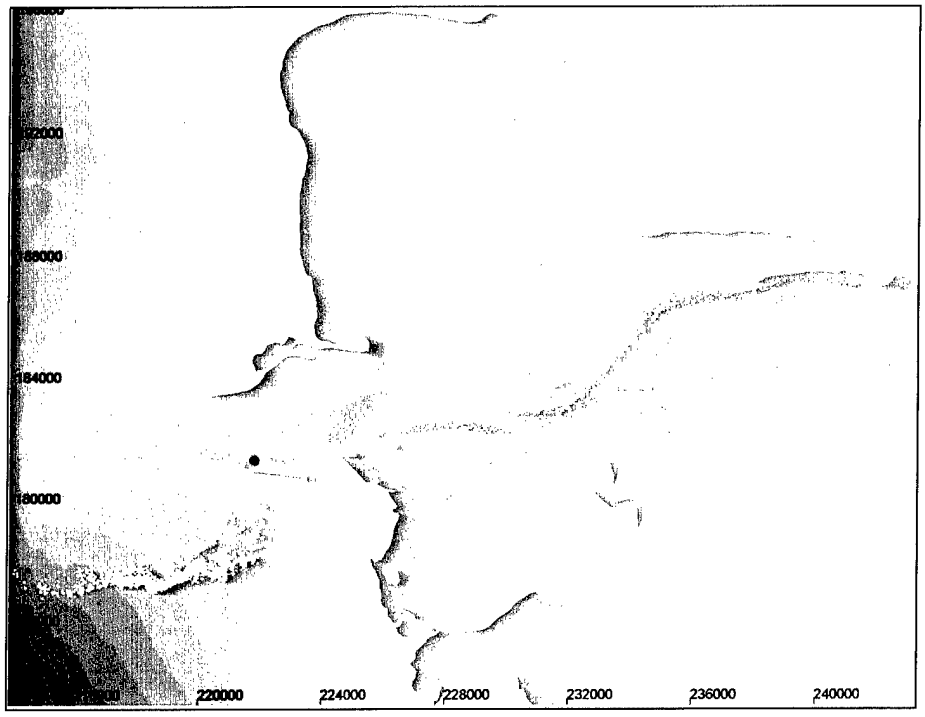

Figure 7-116. Final sediment parcel locations for Run 104, sand source at south jetty

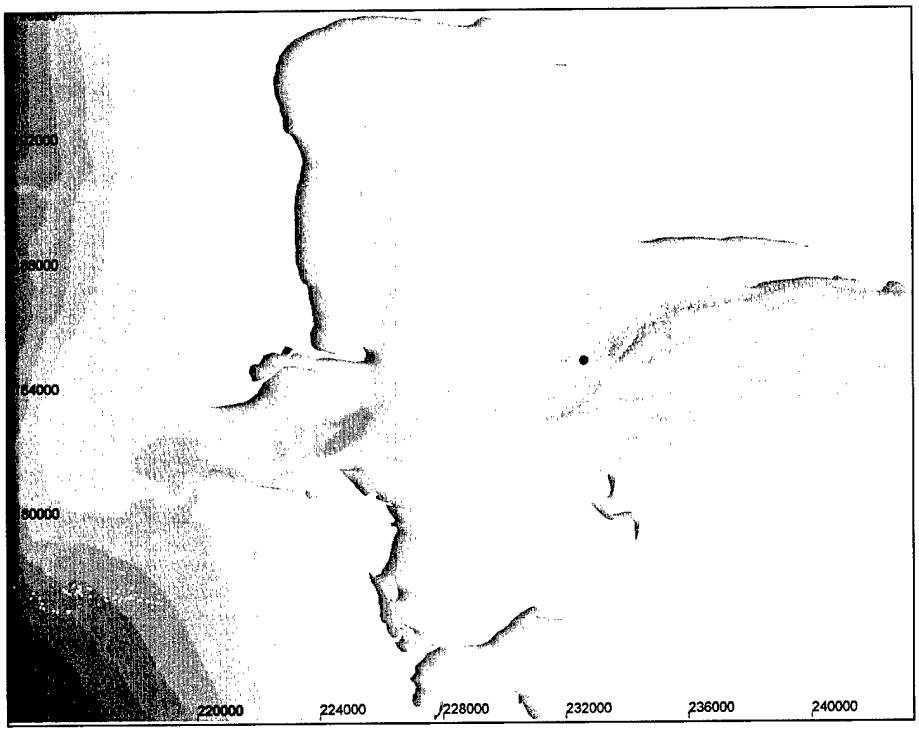

Figure 7-117. Final sediment parcel locations for Run 104, sand source at lower reach

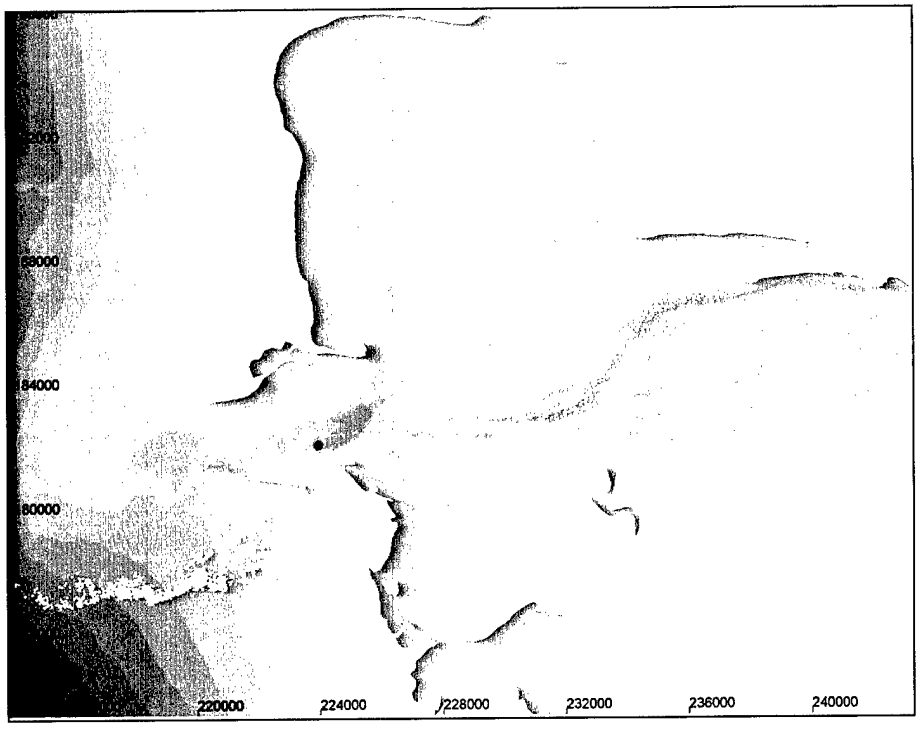

Figure 7-118. Final sediment parcel locations for Run 104 with sand source at Point Chehalis

Inner estuary

A series of 22 point sources (red circles) served to represent sediment sources located within the estuary (Table 7-11, Figure 7-119). Figure 7-119 illustrates the fine-grain parcel locations at the end of 5 days of simulation. Sediment within the estuary tends to remain inside the estuary with a significant portion (53 percent) being deposited in Reaches 13 and 14 (as defined in Figure 7-107). This observation is consistent with Figure 3-9, which shows the distribution of marine, riverine, and mixed sediments in the estuary. That is, riverine sediment within the estuary will remain in the Chelis River reaches and the upper portion of North Bay.

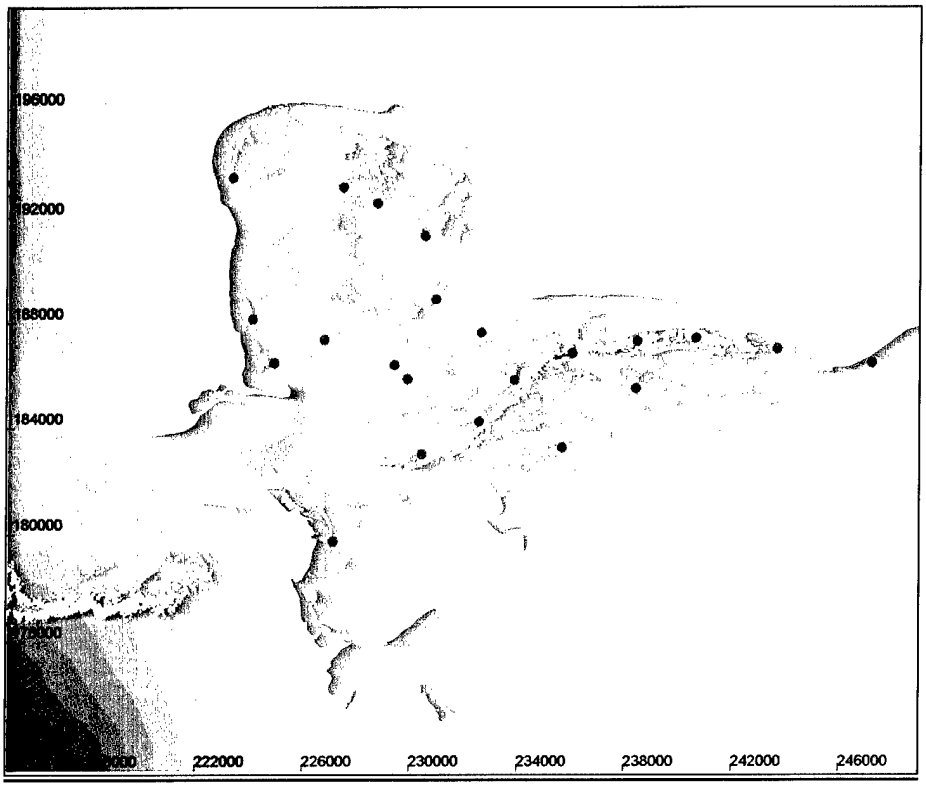

Figure 7-119. Sand pathways at end of 5-day simulation for sources within estuary, Run 104 (spring tide, waves H_s = 5 m, T_p = 13 sec from west-northwest)

Sediment trap analysis

The sediment pathways observed during PSed modeling can be summarized in tabular form in terms of the percentage of the overall number of parcels in the simulation that accumulated in each reach for each source (Table 7-13). Analysis shows that 25 percent of the sediment released at the south jetty during waves from the west-northwest enter the inner estuary as compared to only 10 percent of the sediment released at the north jetty. For sediment released at Damon

Point, 41 percent is moved offshore, whereas 21 percent enter the inner estuary. For sediment released at the lower reach location, however, 91 percent remains in the inner estuary. These results are likely to be compromised by the circulation patterns simulated between the north jetty and Damon Point. Improvement in grid resolution and bathymetry would be required, as well as additional analysis to resolve the currents and pathways more accurately.

Table 7-13
Sediment Trap Results for Simulations with Run 104 Hydrodynamics

	Percentage of Total Parcels Ending in Reaches		
Source Point	Offshore (R1 to R3)	Inlet (R4 to R8)	Estuary (R9 to R14)
North jetty	77.1	12.5	10.4
South jetty	65.4	9.7	25.0
Damon Point	41.0	38.0	21.1
Lower reach	8.0	0.9	91.2
Point Chehalis	58.7	6.8	34.6

Evaluation of Alternatives

Run 106 provides a reference condition for waves from the west-northwest on a neap tide, from which comparisons can be made between the existing condition and various project alternatives. In most plots that follow (Figures 7-120 through 7-125), sediment pathways are indistinguishable and they are best analyzed statistically. The cases where a clearly visible difference in sediment pathway simulations exists are discussed in the following paragraphs.

Analysis of the ADCIRC and STWAVE velocity fields reported that the spur alternatives (Alt 2A, Alt 2B) increased eastward current velocities in the area to the south of the north jetty. Figure 7-120 shows PSed sediment pathway simulations for Runs 106 and 110 (Alt 2A). This simulation suggests that there is no appreciable difference in the path taken by sediment bypassing the north jetty with Alt 2A (blue) in comparison to the existing condition (red). In these figures, it is evident that sediment released at the north jetty is transported toward the southeast, and sediment plumes for the existing and Alt 2A conditions are identical.

The results for the shorter spur alternative (Alt 2B) are shown in Figure 7-121. The long spur showed no appreciable influence on sediment pathways near the north jetty, and the same can be concluded for the shorter spur.

The jetty rehabilitation alternatives cause a more southward flow of sediment beyond the tip of the north jetty (Figure 7-122). Sediment in the Alt 3A simulation (blue) has more of a tendency to bypass the inlet than does sediment under the existing condition (red). With the Alt 3A jetty rehabilitation in place, the plume is carried as far into the inlet as for the existing condition, and the Alt 3A simulation shows a stronger tendency for sediment to bypass the inlet.

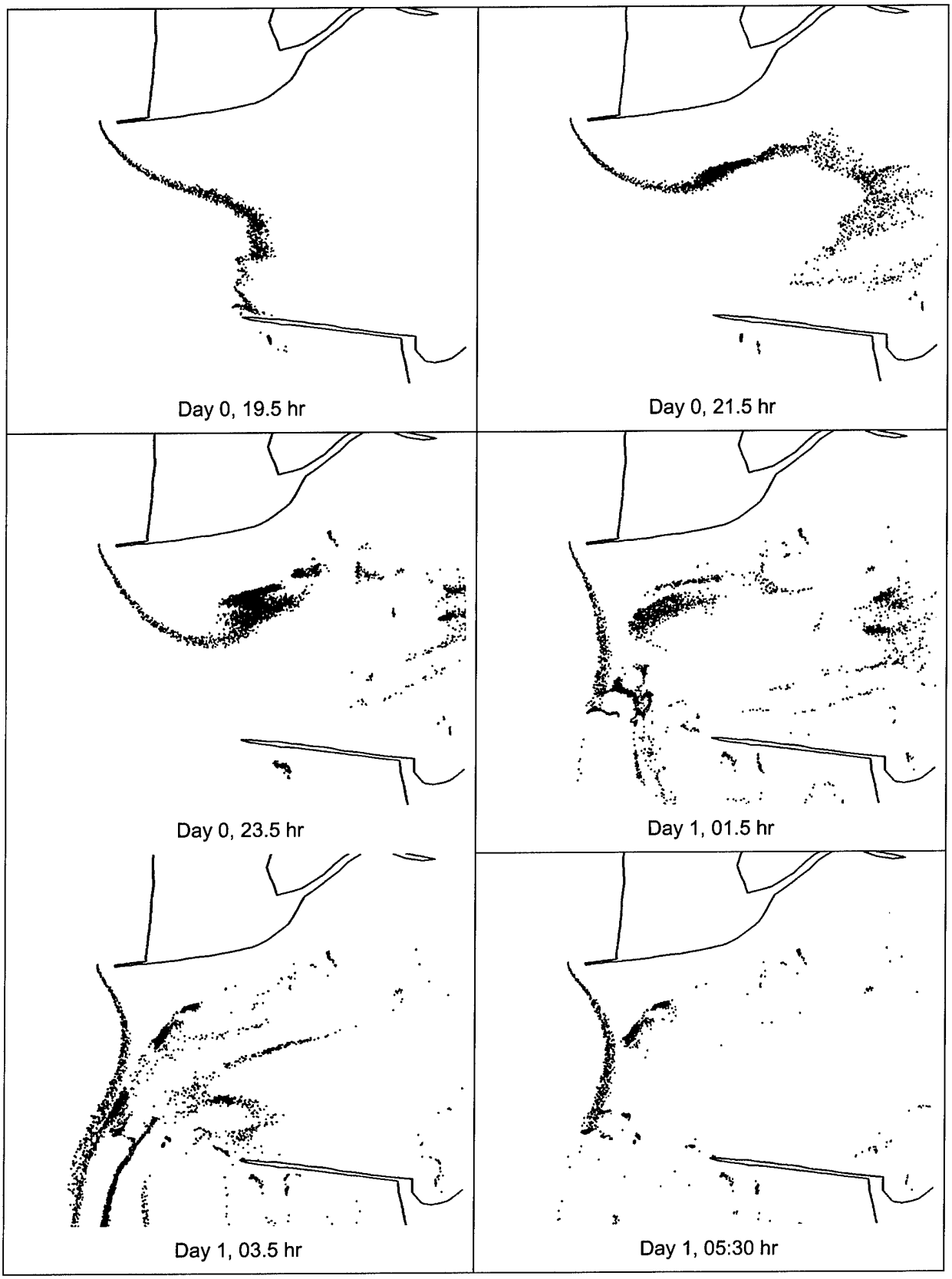

Figure 7-120. Comparison of sediment pathways at north jetty for existing condition (red) and Alt 2A (blue) for west-northwest waves on a neap tide (Runs 106 and 110, respectively)

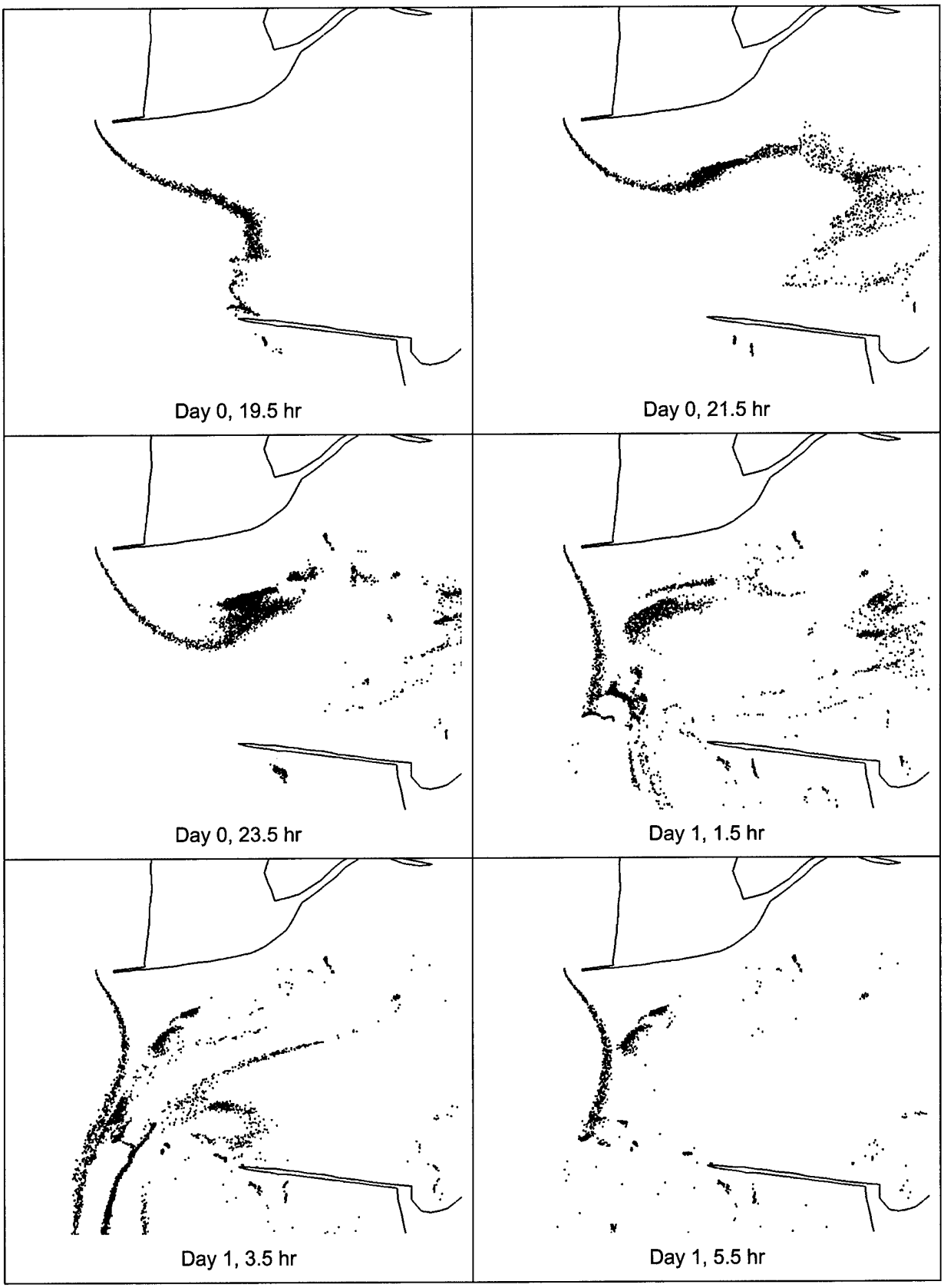

Figure 7-121. Comparison of sediment pathways at north jetty for existing condition (red) and Alt 2B (blue) for west-northwest waves on a neap tide (Runs 110 and 114, respectively)

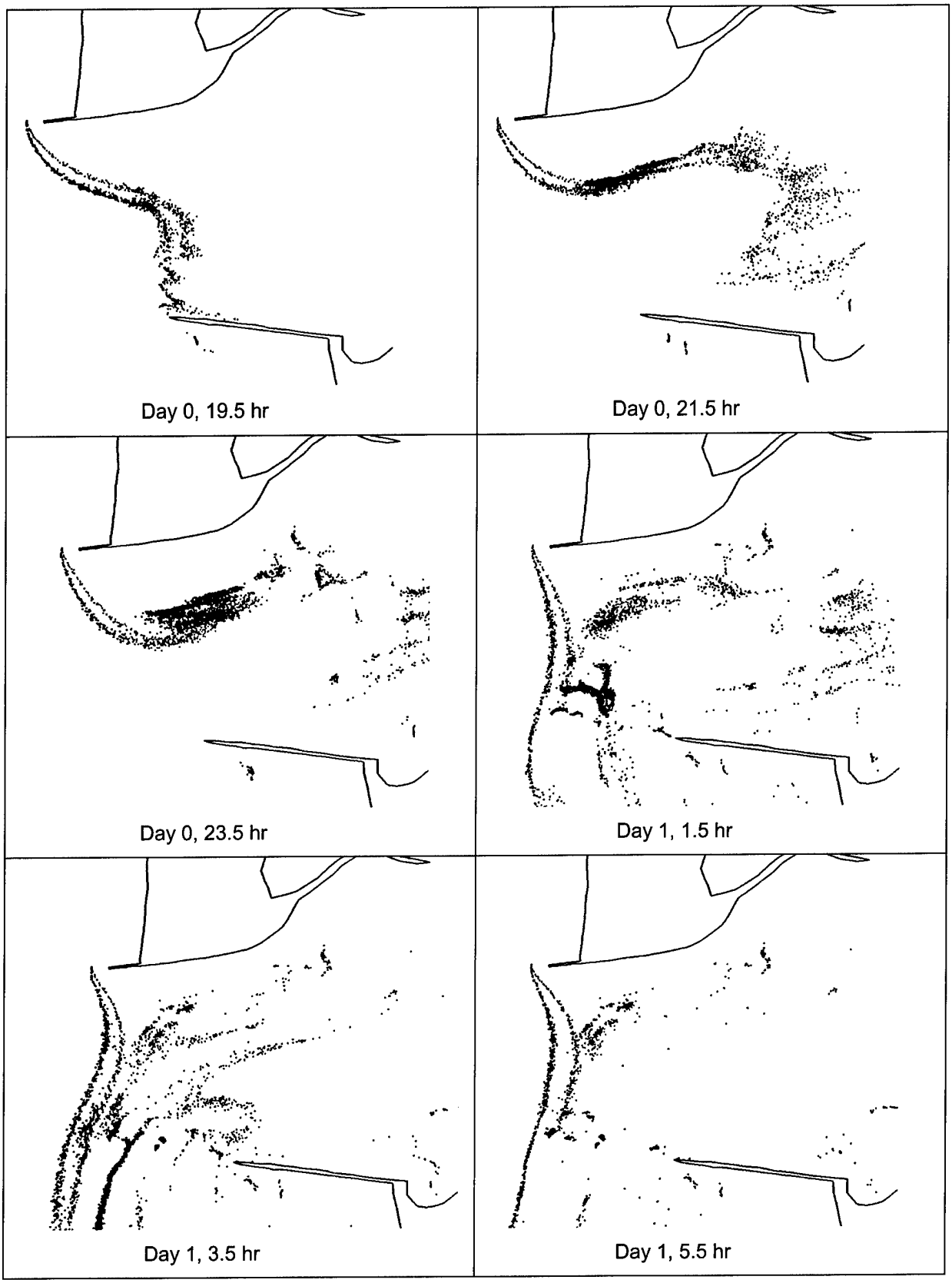

Figure 7-122. Comparison of sediment pathways at north jetty for existing condition (red) and Alt 3A (blue) for west-northwest waves on a neap tide (Runs 106 and 118, respectively)

Figure 7-123 shows that sediment in the Alt 3B simulation (blue) move more slowly past the tip of the jetty (see frames Day 0, 19.5 hr, and Day 0, 21.5 hr). The sediment would settle from suspension at this location during slack water. As the flood tide progresses, the sediment is then remobilized and transported into the estuary. The path of sediment for Alt 3B (e.g., at Day 1, 1.5 hr) is closer to the north edge of the channel, leading directly to Damon Point. This suggests that schemes which reduce the sediment transport rate at the tip of the jetty would create a greater tendency for bypassing sediments to be transported to Damon Point because they encourage bypassing sediment to remain on the north side of the inlet where they can be carried eastward on the flood. This analysis is based on a single point source and may be sensitive to the location of that sediment source.

The sediment pathways for Alt 4 are shown in Figure 7-124. These patterns are essentially identical to those for Alt 3A, suggesting that the jetty rehabilitation, not the short spur, is the controlling factor in defining the sediment pathway for Alt 4.

Figure 7-125 shows a comparison of the sediment pathways predicted for each alternative 12.5 hr after the start of release of sediment (i.e., at Day 1 at 5.5 hr). In each of these plots, the existing condition is shown in red. For sediment released at the tip of the north jetty, this figure shows the following:

a. Negligible influence of either spur (Alt 2A, Alt 2B) on the pathways.

b. Increased bypassing caused by the short jetty rehabilitation (Alt 3A).

c. Tendency for sediment accumulation during slack water and ebb just south of the jetty tip for the longer jetty rehabilitation (Alt 3B).

Similarity between sediment paths for the combined short spur – short jetty rehabilitation (Alt 4) and the short jetty rehabilitation alone (Alt 3A).

Results of the sediment trap analysis are compiled in Table 7-14 for a point source released at the north jetty. Table 7-15 compiles the results of a similar analysis for a line source of sediment released along the beach just north of the north jetty. Comparison indicates that the sediment trap statistics are not sensitive to source location. Almost 80 percent of the sediment bypassing the north jetty (at this one point-source location) moves to the offshore region, 10 to 20 percent move to the inlet, and 5 to 10 percent move to the inner estuary. This analysis indicates that the spur alternatives (Alt 2A, Alt 2B) cause a 5 to 7 percent increase in sediment entering the estuary (Reaches 9 through 14) whereas the two jetty rehabilitation alternatives (Alt 3A, Alt 4) cause a 2 percent reduction in sediment entering the estuary. The Alt 3B simulation results did not have the same duration as the other runs and, as such, could not be included in this analysis.

Summary

In this chapter, the effectiveness of five structural alternatives at modifying current patterns and sediment transport at Grays Harbor was evaluated by numerical simulations of tidal and wave-induced currents and sediment movement. The circulation model simulations, including the wave contributions, were input to drive a Lagrangian sediment transport model to identify sediment pathways and changes in pathways in response to the project alternatives.

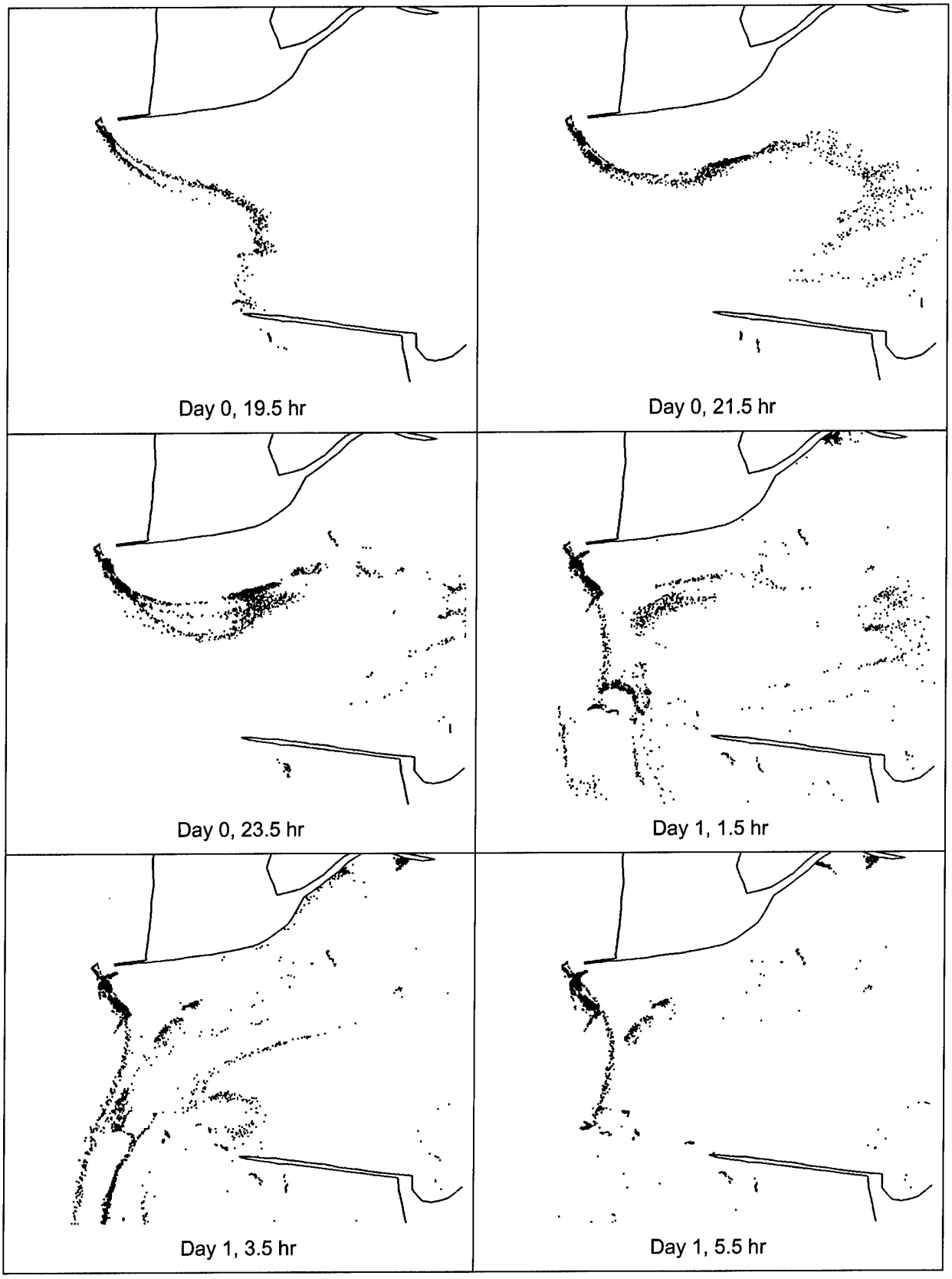

Figure 7-123. Comparison of sediment pathways at north jetty for existing condition (red) and Alt 3B (blue) for west-northwest waves on a neap tide (Runs 106 and 122, respectively)

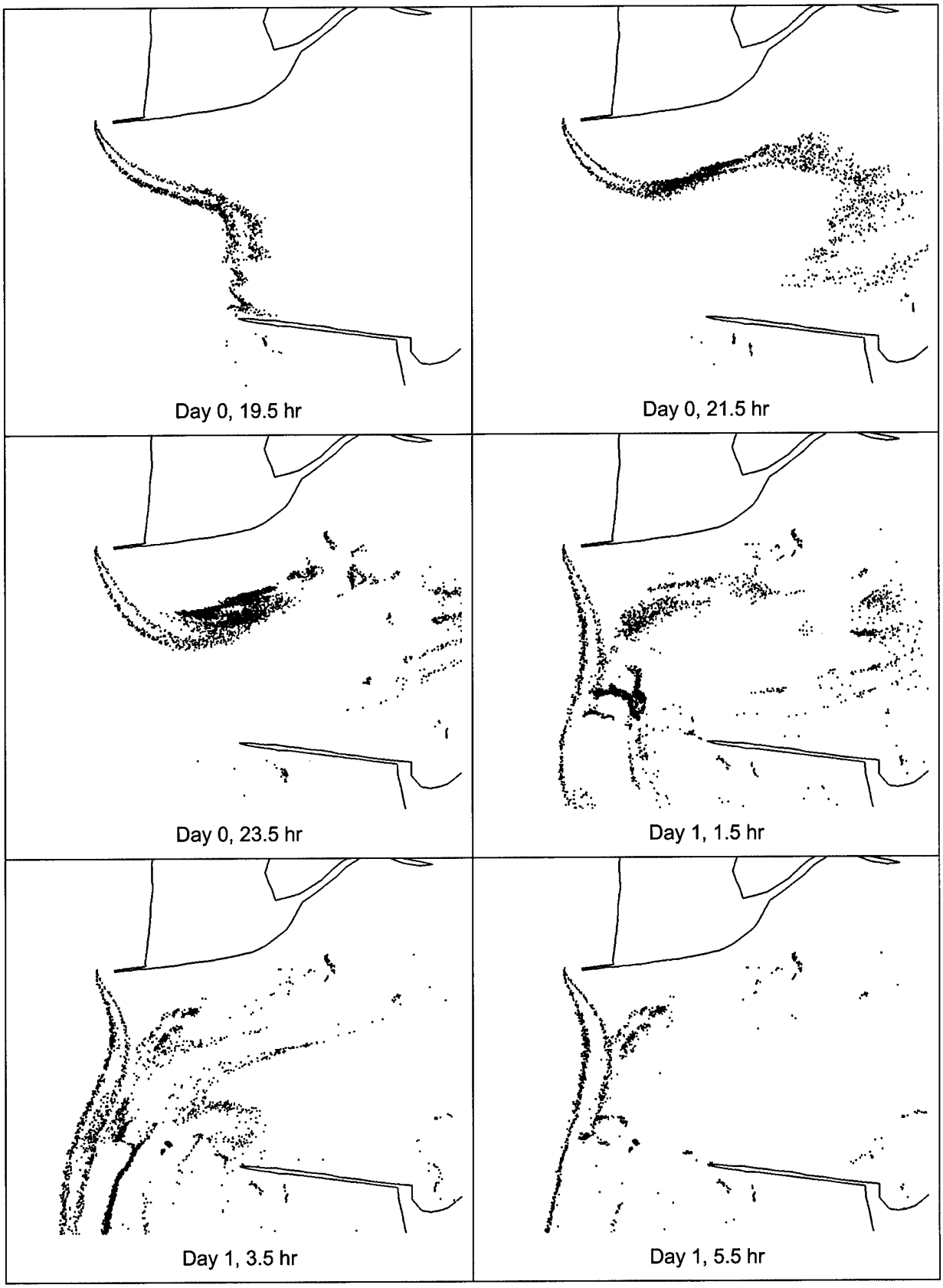

Figure 7-124. Comparison of sediment pathways at north jetty for existing condition (red) and Alt 4 (blue) for west-northwest waves on a neap tide (Runs 106 and 126, respectively)

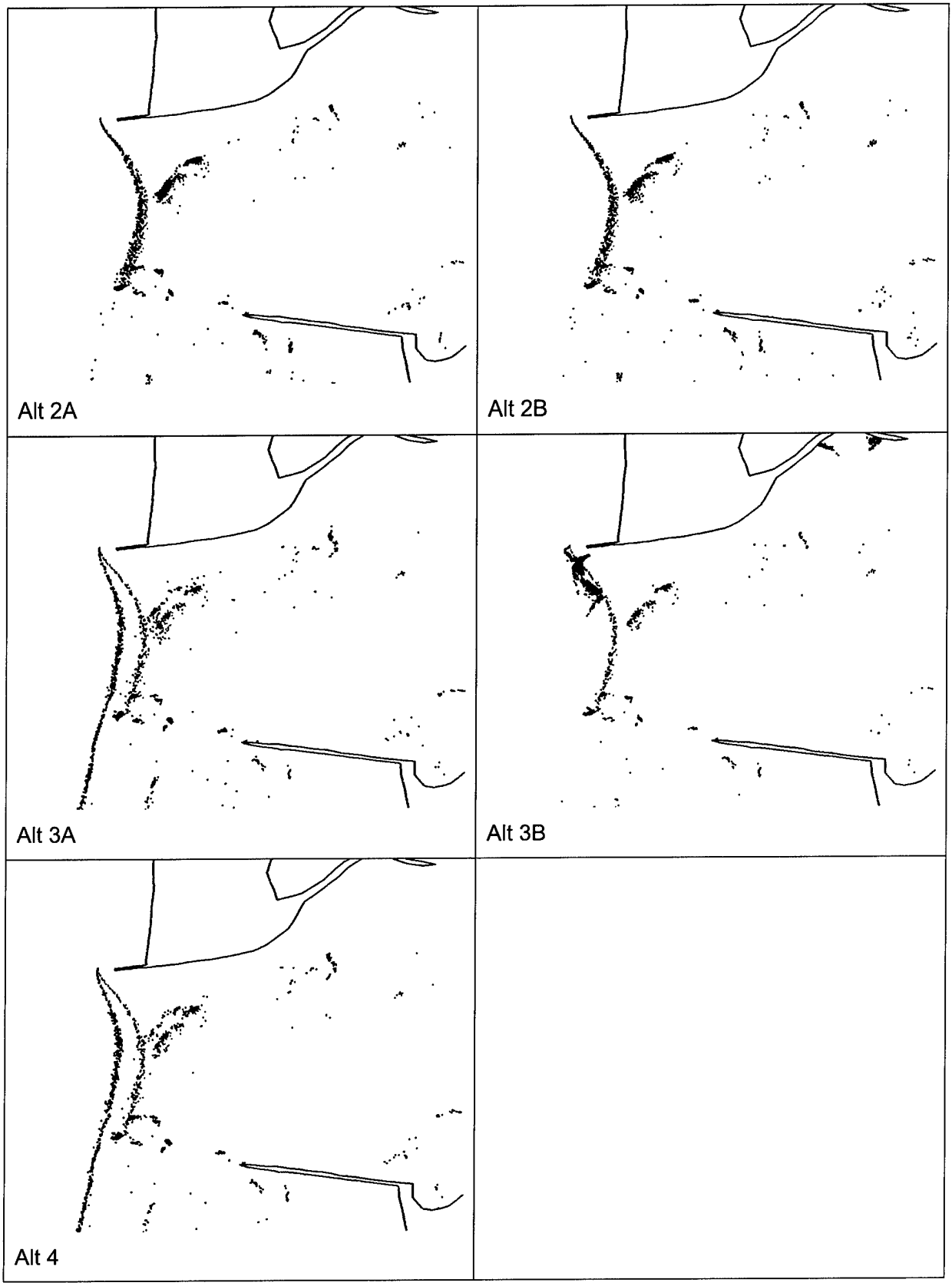

Figure 7-125. Comparison of sediment pathways at Day 1, 5.5 hr for all project alternatives against existing condition (red) for neap tide with waves from west-northwest

Table 7-14
Sediment Trap Results for a Point Source at North Jetty

Run Number	Percentage of Total Parcels Ending in Reaches		
	Offshore (Reach 1 to 3)	Inlet (Reach 4 to 8)	Estuary (Reach 9 to 14)
104 (Existing condition)	80.4	12.9	6.7
108 (Alt 2A)	76.9	10.7	12.5
112 (Alt 2B)	78.0	10.3	11.7
116 (Alt 3A)	77.0	18.0	5.0
120 (Alt 3B)	N/A	N/A	N/A
124 (Alt 4A)	76.6	18.7	4.6

Table 7-15
Sediment Trap Results for a Line Source North of North Jetty

Run Number	Percentage of Total Parcels Ending in Reaches		
	Offshore (Reach 1 to 3)	Inlet (Reach 4 to 8)	Estuary (Reach 9 to 14)
104 (Existing condition)	78.4	16.2	5.5
108 (Alt 2A)	77.8	10.0	12.2
112 (Alt 2B)	78.1	9.7	12.2
116 (Alt 3A)	80.9	14.8	4.3
120 (Alt 3B)	N/A	N/A	N/A
124 (Alt 4A)	80.6	15.5	4.0

The ability of the wave and circulation models to predict waves and currents at Grays Harbor was evaluated by comparing model results to field data collected at Grays Harbor and to physical model measurements near the north jetty. Verification of the tidal circulation model was made for the first month of field data collection (10 September 99 – 10 October 99). Calculated tidal elevations compared well with measurements around the periphery of the bay, with the maximum error being 5.8 percent. Underprediction of the maximum low water elevations at one station (sta 3) was attributed to slight misrepresentation of tidal flats in this region.

Comparison of calculated and measured currents indicated good agreement at velocity sta 2 through 6 with a maximum error of 9.6 percent. The inlet throat area is tide-dominated, and such results can be expected. Station 1, however, showed less agreement (13.9 percent). Calculated and measured currents were in phase and showed good agreement of peak flood current magnitudes, but ebb current magnitudes were underpredicted. Wave-induced currents in this region are significant; hence improved current calculation required dynamic linking of the wave and circulation models. The wave and circulation models were then linked for a shorter time period (due to the computational intensity of the linked models) and results were compared to field data at two locations.

Wave model validation with the field data showed good correlation. The difference between wave height produced in the model and prototype wave

height showed that model results are generally within 0.5 m of the prototype. It is noted that uncertainty in the buoy measurements is on the order of ±5 percent for wave height, ±1 sec for wave period, and ±10 deg for wave direction.

Calculations from ADCIRC were also compared to velocity measurements in the physical model for similar wave and current conditions. In the physical model, the sampling volume for the current velocity was placed close to the bottom because of interest in bed load transport. In contrast, depth-averaged velocities are calculated in ADCIRC, implying a possible positive offset with the numerically calculated (point measurement) values being expected to be slightly larger than those in the physical model (average-volume, near-bottom measurement). However, other considerations in calculating mean currents for the physical and numerical simulations were the length of each simulation and the temporal variation of tides in the numerical model simulations versus a steady, flood current in the physical model simulations. Mean currents in the numerical and physical models are consistent for west-northwest waves, despite the somewhat different representative measurement (near-bottom velocity for the physical model; depth-averaged velocity for the numerical model), which generates confidence in applying the models to evaluate project alternatives.

With the numerical modeling tools calibrated for existing conditions, five structural alternatives were simulated with a set of tide and wave conditions. The effectiveness of the project alternatives was evaluated by five methods. Analysis of the initial 24 circulation model simulations involved examination of peak flood and peak ebb plan view maps, statistical comparisons of mean currents at 16 grid node locations, comparisons of velocity component time series, maps of mean current, and global differences in current magnitude for each project alternative compared to the existing condition.

The overall current patterns for the project site showed a strong southward current around the north jetty tip. Simulations of combined tidal and wave-induced currents demonstrated that the current at the tip can exceed 2.5 m/sec to the south, and the longshore current is in the range of 1.3 to 1.7 m/sec for moderate storm (5-6 m) waves. (Field measurements indicate 1.0 m/sec currents 150 m north of the jetty tip, but flow convergence would be expected to accelerate flow as the jetty tip is approached. Longshore current measurements were on the order of 0.6 to 0.8 m/sec for 4-m waves. Smaller measured longshore current magnitudes can be attributed to smaller measured wave heights and the location of the field measurements in the extreme nearshore region.) west-southwest waves induce a longshore current to the north, but there is a flow reversal within 500 m north of the north jetty, resulting in a southbound current for this wave condition as well. Simulations show that the ebb jet at Grays Harbor can be deflected to the south or north upon exiting the inlet throat if a strong longshore current is present.

Statistical comparisons of the mean current at selected points and of the global difference maps for the existing condition and project alternatives indicate that the largest changes in current magnitude are localized to the vicinity of the structural alternatives. The spur alternatives cause a minor decrease in the southerly directed current at their location and a minor increase in current magnitude shoreward of the spur. Mean current maps show that the spur does not alter the cross-shore currents, except at Node 13589 (near the spur tip). The mean current at this location is directed more northward with the spur in place. That is, the spur structure causes currents to sweep further north.

Jetty alternatives produce greater changes in mean current than the spur alternatives because they are directly in the path of the maximum current. There is a minor decrease in current magnitude in the shadow of the jetty and major changes in current magnitude at the jetty rehabilitation location. The maximum current for the existing condition occurs near Node 12966 and exceeds 2.5 m/sec, whereas the maximum current for the jetty rehabilitation alternative occurs near Node 11421 and is 1.3 to 1.8 m/sec for Alt 3A and 1.9 to 2.2 m/sec for Alt 3B. Therefore, the maximum current is shifted seaward but is reduced in magnitude. The jetty rehabilitation alternatives increase offshore-directed flow along the jetty and create an offshore sweeping effect on the general flow in the first 250 m north of the jetty. The combination alternative (Alt 4A) behaves similar to Alt 3A.

In summary, the structural alternatives produce a minor perturbation to the overall circulation within 1 to 2 km of the north jetty at Grays Harbor. Changes in current magnitude may be large, local to the structural alternative, and usually indicate a shift in the location of maximum flow.

The PSed analysis examined sediment pathways associated with the hydrodynamics predicted by the ADCIRC and STWAVE simulations. The Lagrangian analysis revealed some of the possible pathways for sediment transported from the north and south beaches to enter the inner estuary, by which alterations in pathways for the various proposed project alternatives could be estimated.

The PSed simulations of sediment pathways estimated that 10 percent of the sediment bypassing the north jetty moves to the inner estuary under the existing conditions based on a 5-day simulation of wave and tidal conditions (Table 7-13). The sediment budget developed in Chapter 3 for the 1954/56 to 1987 time period shows a similar pattern, that sediment reaching north beach from offshore is transported south around the jetty and into the entrance area. Then flood currents and wave-induced currents transport this bypassed sediment toward Damon Point, where a portion is deposited in a large subaqueous spit to the south and west of the tip of the spit.

Both the PSed analysis and the sediment budget analysis indicate the presence of a sediment pathway between the north jetty and Damon Point. The sediment budget analysis found that, for the period 1954/56 to 1987, approximately 400,000 cu yd/year of sediment bypasses the north jetty and 479,000 cu yd/year accumulates at Damon Point. Based upon long-term net transport rates from the sediment budget work, it could be concluded that 100 percent of sediment bypassing the north jetty arrives in the vicinity of Damon Point. In comparison, the PSed simulations based on the ADCIRC simulations indicate that only 10 percent of the bypassing sediment arrives in the vicinity of Damon Point and the remainder is deposited offshore. This discrepancy may be attributed to differences in hydrodynamics between the 5-day simulation used in the PSed simulations and the long-term patterns of sediment transport between 1954/56 and 1987. It could also be due to limited resolution of wave-driven circulation along the south side of the north jetty in the ADCIRC simulations and the failure of PSed to fully include wave-driven transport processes. Another possible reason for this discrepancy is that the net sediment transport rates developed in Chapter 3 do not reflect the short-term (i.e., 5-day time-scale simulated in the ADCIRC-PSed analysis), fine-scale transport patterns that occur between the north jetty and Damon Point. The key point in the PSed analysis is that it shows a pathway for sediments from the north jetty to

Damon Point and allows comparison of the relative responses of the system to the various structural alternatives on this sediment pathway.

The proposed jetty rehabilitation alternatives were predicted to cause an overall decrease in sediment entering the inner estuary, whereas the spur alternatives were predicted to increase sediment entry to the inner estuary. The PSed analysis has also shown that the longer jetty rehabilitation (Alt 3B) could increase the transport of sediment along the south face of the north jetty because of increased deposition to the south of the jetty during slack water which, when remobilized during the flood, is carried along the south face of the jetty. However, this is not apparent in the overall sediment trap statistics.

The sediment pathway analysis depends upon the input hydrodynamic conditions. Limited resolution of the longshore currents between the north jetty and Damon Point may lead to an underestimation of the strength of the sediment pathway between the tip of the north jetty and the distal end of Damon Point. It is possible that the sediments bypassing the north jetty follow a more direct path to Damon Point than has been shown by these simulations.

References

Beverage, J., and Swecker, M. (1969). "Estuarine studies in upper Grays Harbor, Washington," U.S. Geological Survey Water Supply Paper 1873-B, Reston, VA, 90 pp.

Cialone, M. A., Militello, A., Brown, M. E., and Kraus, N. C. (2002). "Coupling of wave and circulation numerical models at Grays Harbor Entrance, Washington, USA," *Proceedings 28th Coastal Engineering Conference,* World Scientific, 1,279-1,291.

Davies, M. H., Serrer, M., and Watson, D. A. W. (2000). "PSed 2000 – A Lagrangian sediment transport model," Preliminary Technical Report HYD-TR-051, Canadian Hydraulics Centre, National Research Council, Canada, 41 pp.

Hickey, B. M. (1989). "Patterns and processes of circulation over the Washington continental shelf and slope circulation," *Coastal Oceanography of Washington and Oregon*, Chapter 2, M. R. Landry and B. M. Hickey (ed.), Elsevier Oceanography Series, Amsterdam, 41-115.

Holliday, B. W., McNair, E. C., and Kraus, N. C. (2003). "The U.S. Army Corps of Engineers' Coastal Inlets Research Program," *Proceedings Dredging '02*, ASCE, Reston, VA.

Johnson, J. W. (1973). "Characteristics and behavior of Pacific Coast tidal inlets,"*Journal of Waterways, Harbors, and Coastal Engineering Division* 99(WW3), New York, NY, 325-339.

Landry, M. R., Postel, J. R., Peterson, W. K., and Newman, J. (1989). "Broad-scale distributional patterns of hydrographic variables on the Washington/Oregon shelf," *Coastal Oceanography of Washington and Oregon*, Chapter 2, M. R. Landry and B. M. Hickey (ed.), Elsevier Oceanography Series, Amsterdam, 1-40.

LeProvost, C., Genco, M. L., Lyard, F., Vincent, P., and Canceill, P. (1994). "Spectroscopy of the world tides from a hydrodynamic finite element model," *Journal of Geophysical Research* 99(C12), 777-797.

Luettich, R. A., Westerink, J. J., and Scheffner, N. W. (1992). "ADCIRC: An advanced three-dimensional circulation model for shelves, coasts, and estuaries; Report 1, Theory and methodology of ADCIRC-2DDI and ADCIRC-3DL," Technical Report DRP-92-6, U.S. Army Engineer Waterways Experiment Station, Vicksburg, MS.

Luettich, R. A., Jr., and Westerink, J. J. (1999). "Implementation of the wave radiation stress gradient as a forcing for the ADCIRC hydrodynamic model: Upgrades and documentation for ADCIRC version 34.12," Contractors Report, Department of the Army, U.S. Army Engineer Waterways Experiment Station, Vicksburg, MS, May 1999, 9 pp.

Militello, A. (1998). "Hydrodynamics of wind-dominated, shallow embayments," Ph.D diss., Division of Marine and Environmental Systems, Florida Institute of Technology, Melbourne, FL.

Militello, A., and Zundel, A. K. 2003. "Two-dimensional circulation model M2D: Report 1, technical documentation and user's guide," Coastal Inlets Research Program, Technical Report ERDC-CHL-TR-03-xx, U.S. Army Engineer Research and Development Center, Vicksburg, MS (in preparation).

Osborne, P. D., Hericks, D. B., and Kraus, N. C. (2002). "Deployment of oceanographic instruments in high-energy environments and near structures," Technical Note ERDC/CHL CHETN IV-46, U.S. Army Engineer Research and Development Center, Vicksburg, MS.

Resio, D. T. (1987). "Shallow-water waves, Report I: Theory," *Journal of Waterway, Port, Coastal, and Ocean Engineering* 113(3), 264-281.

Shea, D. J., Worley, S. J., Stern, I. R., and Hoar, T. J. (1994). An introduction to atmospheric and oceanographic datasets, NCAR Technical Note NCAR/TN-404+IA, Boulder, CO, 132 pp.

Smith, J. M., Sherlock, A. R., and Resio, D.T. (2001). STWAVE: Steady-state spectral wave Model User's Manual for STWAVE Version 3.0, Instruction Report ERDC/CHL IR-01-1, U.S. Army Engineer Research and Development Center, Coastal and Hydraulics Laboratory, Vicksburg, MS.

Sternberg, R. W. (1986). "Transport and accumulation of river-derived sediment on the Washington continental shelf, USA," *Journal of the Geological Society, London* 143, 945-956.

Thompson, E. F., Hadley, L. L., Brandon, W. A., McGehee, D. D., and Hubertz, J. M. (1996). "Wave response of Kahului Harbor, Maui, Hawaii," Technical Report CERC-96-11, U.S. Army Engineer Waterways Experiment Station, Vicksburg, MS.

USACE. (1977). "Maintenance dredging and the environment of Grays Harbor, Washington, summary report," prepared for the U.S. Army Engineer District, Seattle, by the State of Washington Department of Ecology in conformance with contract DACW67-74-C-0086, 102 p.

Westerink, J. J., Blain, C. A., Luettich, R. A., Jr., and Scheffner, N. W. (1994). "ADCIRC: An advanced three-dimensional circulation model for shelves coasts and estuaries, Report 2: Users manual for ADCIRC-2DDI," Dredging Research Program Technical Report DRP-92-6, U.S. Army Engineer Waterways Experiment Station, Vicksburg, MS, 156 p.

Zundel, A. K. (2002). "Surface-water modeling system reference manual, Version 8.0," EMRLTN-SMS-2002-1, Environmental Modeling Research Laboratory, Brigham Young University, Provo, UT, April 2002.

Zundel, A. K., Cialone, M. A., and Moreland, T. J. (2002). "SMS steering module for coupling waves and currents, 1: ADCIRC and STWAVE," Technical Note ERDC/CHL CHETN IV-41, U.S. Army Engineer Research and Development Center, Vicksburg, MS.

8 Annualized Circulation and Sediment Bypassing at North Jetty[1]

An annualized representation of the local circulation, sediment transport, and southward bypassing of sediment at the north jetty was developed and applied to evaluate five project alternatives. This chapter describes the combined wave and current circulation model and its implementation at the north jetty. Sediment transport potential by waves and currents is also computed using the waves and currents predicted by the circulation model. Potential sediment transport rates from a large number of combinations of wave and current parameters are reduced to estimate the annual sediment transport potential at the north jetty. The sediment transport potentials are combined with a Lagrangian sediment transport model to evaluate the potential southward bypassing of sediment and the changes associated with the alternatives.

Annualized Circulation at North Jetty

The ADCIRC and STWAVE Steering Module simulations (Chapter 7) describe the time-varying tide- and wave-induced circulation patterns over the entire study area. These wide-area Steering Module simulations provide good resolution of the tidal cycle variations in circulation for a limited number of combinations of wave height, period, and direction. Representation of the average annual circulation patterns at the north jetty requires simulation of a large number and broad range of discrete combinations of wave heights, periods, and directions as well as water levels, tide phases, and bathymetries that can be weighted according to their probability of occurrence. Evaluation of the detailed wave- and tide-induced circulation patterns at the north jetty for a broad range of inputs is more efficiently handled with a small-domain model focused on the area of interest.

The CoastL model (MacDonald 1998) is applied to simulate the circulation at the north jetty for existing conditions and for the various project alternatives for five different bathymetries. The purpose of the CoastL analysis is to provide a

[1] Written by Neil J. MacDonald, Michael H. Davies, and Philip D. Osborne of Pacific International Engineering, PLLC.

representation of the annual wave-induced circulation at the north jetty for comparison of the alternatives. Also, the detailed circulation patterns are required for the evaluation of sediment transport potential and southward sediment bypassing of the north jetty to derive representation of the southward sediment bypassing for each alternative. Sediment response is addressed through analysis of changes in mean currents, in potential sediment transport, and by means of Lagrangian techniques to predict the changes in sediment pathways and the rate at which Lagrangian sediment parcels bypass the north jetty.

Steady-state tide-induced currents corresponding to high water slack, peak flood, peak ebb, and low water slack were included in the CoastL simulations. A range of wave heights, periods, and directions was selected that, in a discrete manner, represent the annual wave climate at the north jetty. The frequency of occurrence of each wave parameter combination was determined from the Coastal Data Information Program (CDIP) Buoy 3601 measurements between 1994 and 2002 (Chapter 4). These provide the basis for combining individual hydrodynamic simulations into a comprehensive annual wave-current circulation climate for the study area.

CoastL grid development for north jetty

CoastL is a finite-difference nearshore circulation model. It is composed of two independent, dynamically coupled modules of combined wave refraction and diffraction and depth-averaged coastal flow. Each module is solved at every time step, based upon results of the other module from the previous time step. The wave model uses a wave-period averaged technique and can be applied over areas ranging from tens of meters to tens of kilometers. The CoastL model was developed under the assumption of a steady, monochromatic wave field with mild spatial variability. Random wave effects are represented in the CoastL model through the energy dissipation from wave breaking. Wave propagation characteristics within the surf zone, and all characteristics outside the surf zone, are still modeled as though the wave field was a regular wave field (i.e., a single direction, height, and frequency at each location in plan). The approach used for the simulation of this random wave breaking is based on the work of Battjes and Janssen (1978); which assumes that the wave height field is distributed according to a truncated Rayleigh probability distribution that is discontinuous at the breaking wave height. CoastL computes full wave-current interaction between internally or externally imposed flow fields. Depth-averaged flows are computed resulting from any combination of wave, wind, and tidal forcing.

The modeling for Grays Harbor was performed in two stages. A coarse 100-m computational grid was developed to transform waves from the Grays Harbor CDIP buoy located in deep water (Chapter 7) to shallow water to provide wave boundary conditions for a finer 20-m square inshore computational grid. The finer 20-m inshore grid was developed to simulate waves and currents near the north jetty. The configuration of the two grids is shown in Figure 8-1. The 100-m grid is aligned at an angle of 10.5 deg relative to True North, covers an area of 13 by 15 km, and contains 19,500 grid elements. The inshore grid is also aligned at 10.5 deg west, covers an area of 2 by 3 km, and contains 13,536 grid points. The bathymetry of the 100-m grid is shown in Figure 8-2.

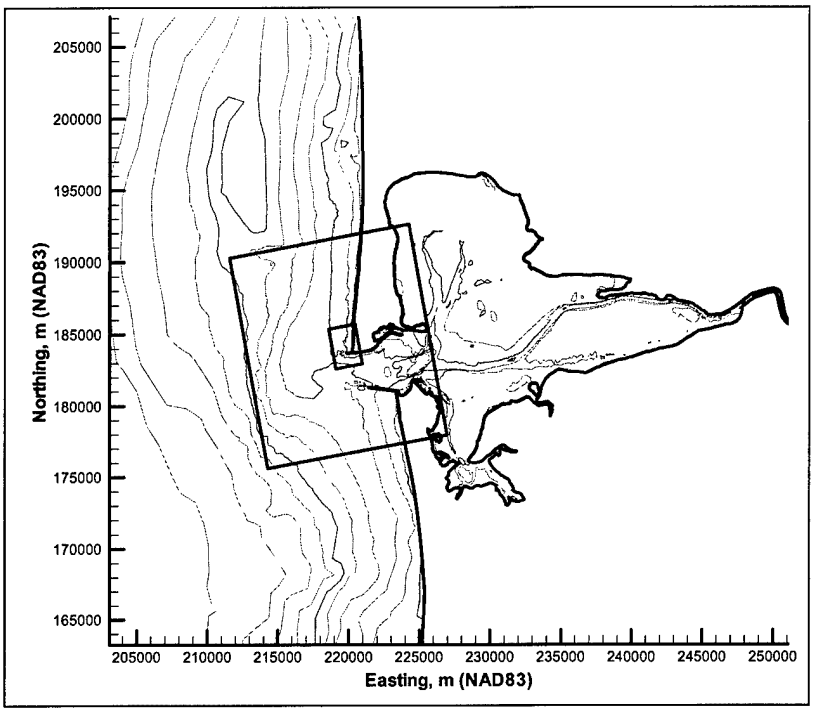

Figure 8-1. Location of offshore 100-m grid (outer blue box) and inshore 20-m grid (inner red box)

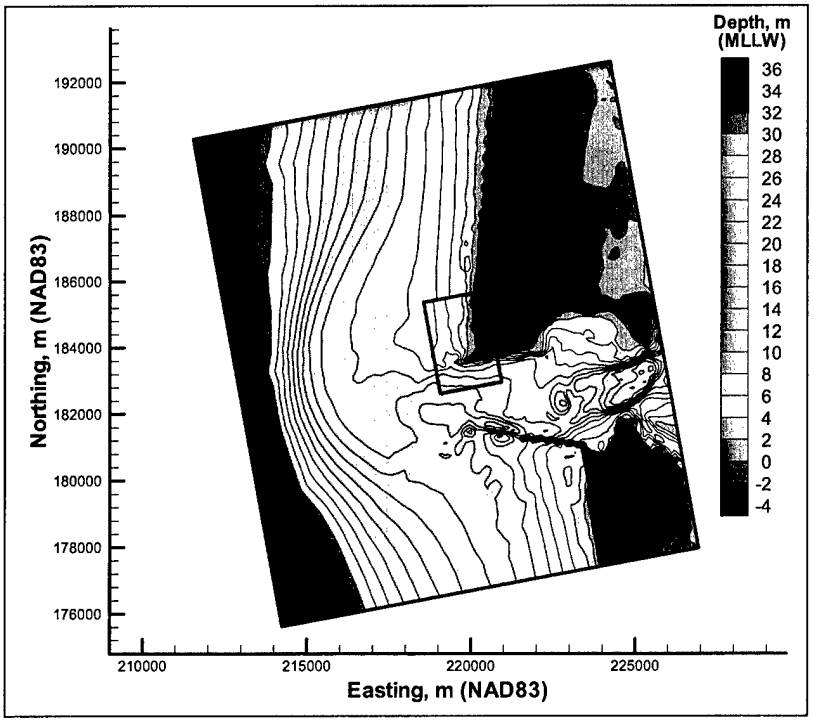

Figure 8-2. Bathymetry of offshore 100-m grid. Depths given to mean lower low water (mllw)

Offshore model

The depth-averaged currents at two stages of a spring tide cycle were extracted from a tide-only ADCIRC simulation to include the effect of the tidal currents on wave transformations and wave-induced currents. These were included in the CoastL simulations as steady-state current boundary conditions. At the offshore model, only the waves were computed. Wave-induced currents were not simulated owing to the coarse nature of the grid. Table 8-1 summarizes the combinations of water levels, background (tidal) currents, wave height, wave period, and direction used for the offshore simulations. In total, 144 combinations of tide, water level, wave height, period, and direction combinations were simulated on the offshore computational grid.

Incident waves were specified along the offshore boundary of the computational grid. Waves were allowed to radiate out the lateral (i.e., northern and southern) boundaries of the grid.

Table 8-1
Hydrodynamic Conditions for Offshore CoastL Model Simulations

Case	Water Level Above mllw (m)	Background Flow Field	Azimuth Wave Directions (deg)	Peak Wave Period (sec)	Significant Wave Height (m)
High water slack	3.0	None	210, 250, 280, 300	8, 13, 18	2, 5, 8
Low water slack	0.0	None	210, 250, 280, 300	8, 13, 18	2, 5, 8
Ebb	1.5	Ebb currents	210, 250, 280, 300	8, 13, 18	2, 5, 8
Flood	1.5	Flood currents	210, 250, 280, 300	8, 13, 18	2, 5, 8

An example of the computed wave height field for one case is presented in Figure 8-3, which shows the computed significant wave height for an incident wave from azimuth 280 deg, significant wave height H_s of 5.0 m, and peak spectral period T_p of 13.0 sec. This wave condition focuses wave energy at the north jetty.

Inshore model

The simulations with the offshore computational grid provided the boundary conditions for the fine-resolution simulations of circulation with the inshore computational grid. In the inshore model, the waves and currents were dynamically coupled (fully interactive at each time step), so that the waves could generate nearshore currents and these currents (interacting with tidal currents, if applicable) could contribute to the transformation of the waves.

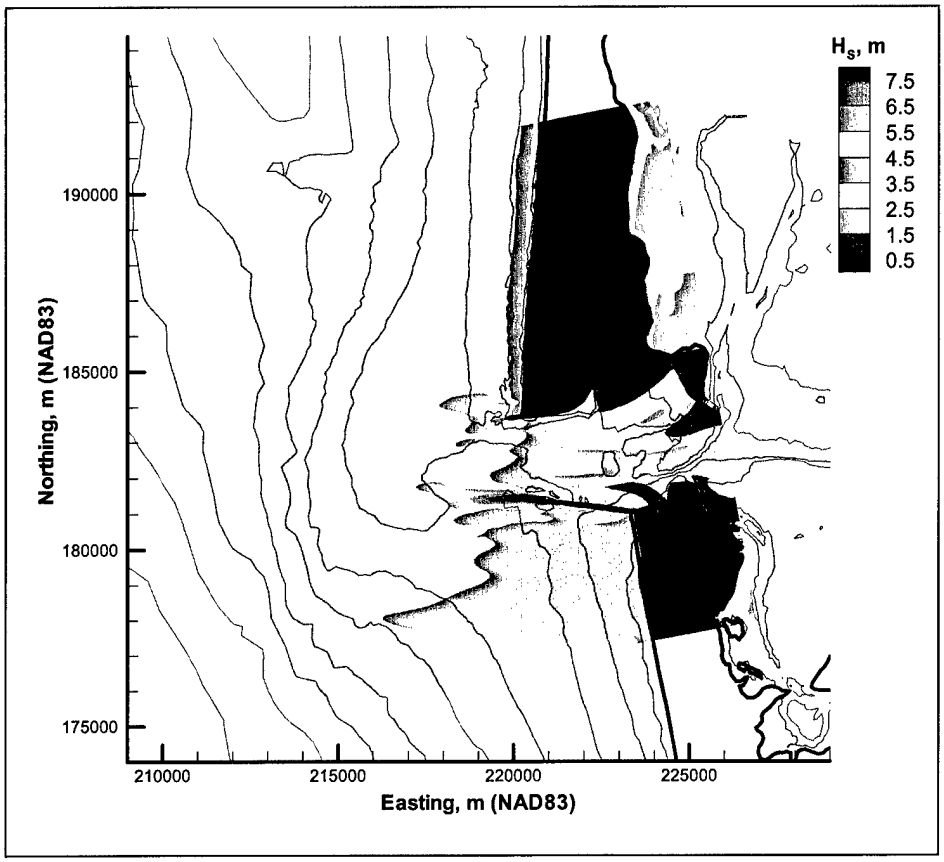

Figure 8-3. Computed significant wave height from 100-m offshore model for incident wave condition H_S = 5.0 m, T_p = 13.0 sec, and direction = 280 deg

Inshore simulations

Four sets of water depths were developed for simulations with the inshore computational grid domain for the years 1999, 2000, 2004, and 2029. It was assumed the bathymetry for the offshore grid did not vary. These water depths were created from several bathymetry surveys. The 1999 and 2001 bathymetry data were obtained from the U.S. Army Engineer District, Seattle annual survey, the Washington State Department of Ecology nearshore wave runner, and intertidal topography surveys (Ruggiero and Voigt 2000). The 2004 and 2029 depths were synthetically developed with the 1999-bathymetry data and the 2004 and 2029 shoreline positions derived from the GENESIS-T shoreline simulations described in Chapter 6. Separate 2004 and 2029 bathymetries were required for each alternative considered because each alternative resulted in a different shoreline position.

In total, 18 bathymetric configurations were developed (Table 8-2). The same combinations of water level, tidal currents, and wave parameters were simulated for each bathymetry. The wave climate consisted of four water levels representing the tidal range, four wave directions, two wave heights, and three wave periods resulting in a total of 96 combinations. The analysis of the offshore model results and some preliminary simulations with the nearshore grids

indicated that, because of the size of the domain, the simulations with H_s of 8 m were similar to those with H_s of 5 m. The H_s of 8 m was therefore omitted from the inshore analysis to reduce the number of simulations. Table 8-2 summarizes the configurations analyzed using the inshore CoastL model.

The 18 inshore grids are shown in Figures 8-4 through 8-21. Figures 8-4 through 8-9 show the 1999 bathymetry for existing condition and for Alt 2A, 2B, 3A, 3B, and 4. The bathymetry was not changed for these alternatives except for the adjustments necessary to position each structural alternative over the 1999 bathymetry.

Table 8-2
Bathymetric Configurations Studied with Inshore CoastL Model

Alternative	1999	2001	2004	2029
Existing condition	X			
Alt 1		X		
Alt 2A	X	X	X	X
Alt 2B	X		X	X
Alt 3A	X		X	X
Alt 3B	X		X	X
Alt 4	X		X	X
Total number of grids	6	2	5	5

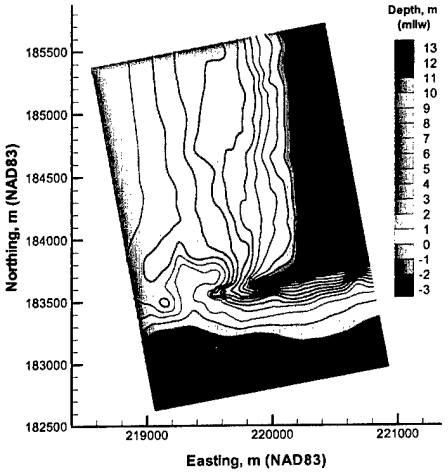

Figure 8-4. Existing condition 1999 bathymetry

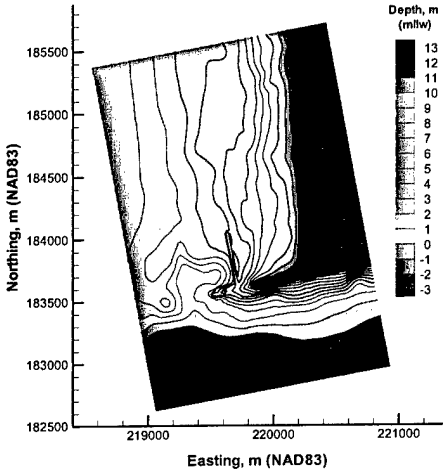

Figure 8-5. Alt 2A 1999 bathymetry

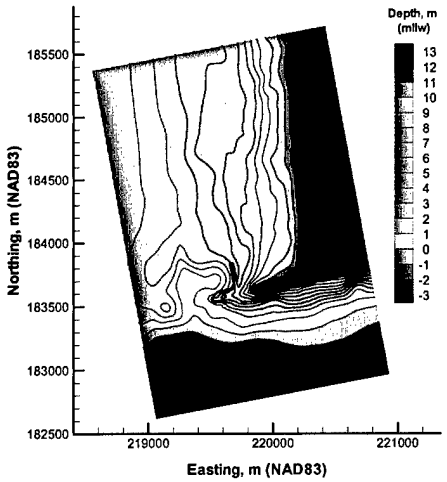

Figure 8-6. Alt 2B 1999 bathymetry

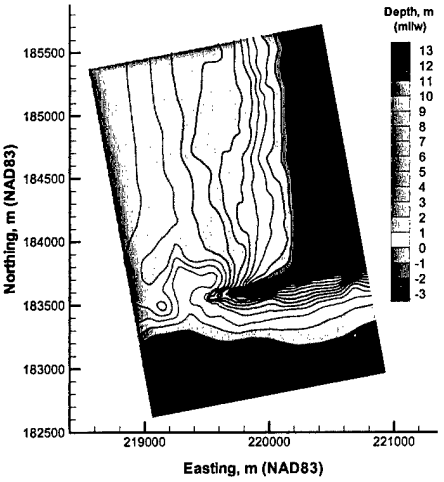

Figure 8-7. Alt 3A 1999 bathymetry

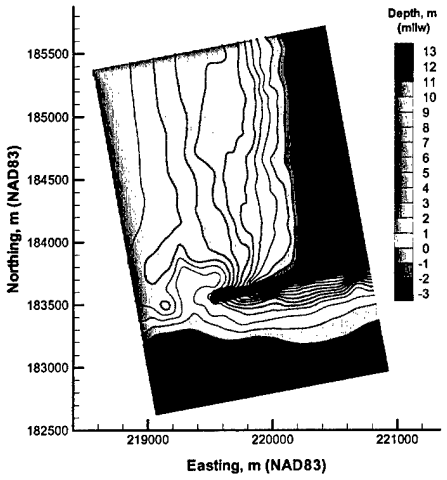

Figure 8-8. Alt 3B 1999 bathymetry

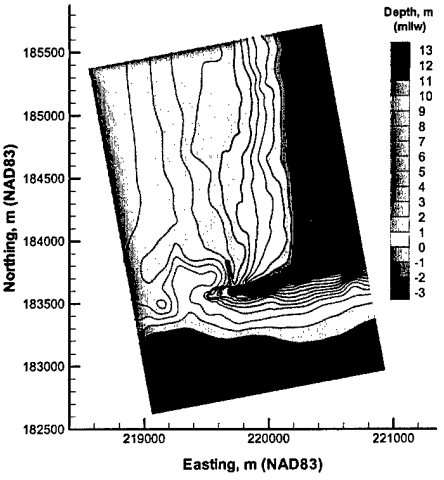

Figure 8-9. Alt 4 1999 bathymetry

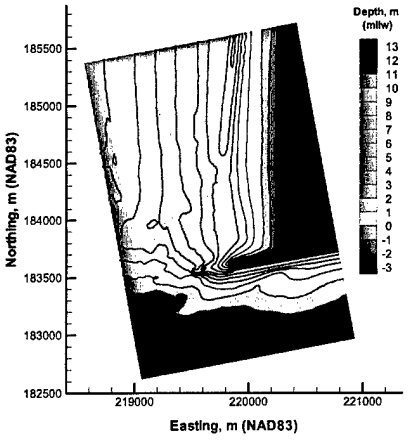

Figure 8-10. Alt 1 2001 bathymetry

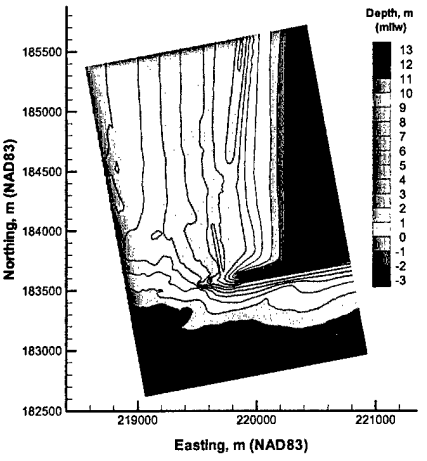

Figure 8-11. Alt 2A 2001 bathymetry

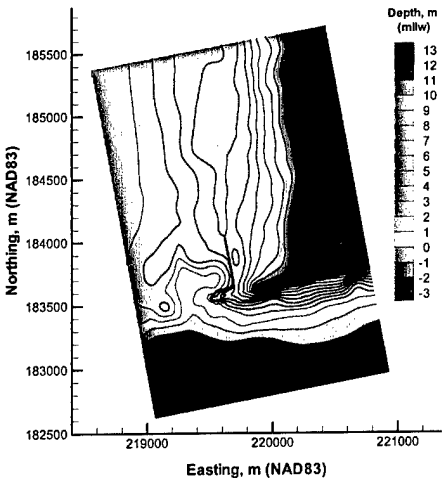

Figure 8-12. Alt 2A 2004 bathymetry

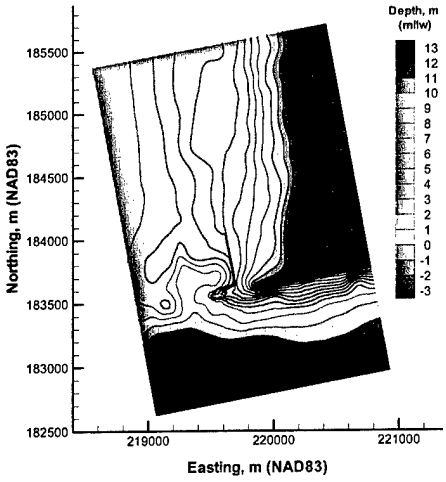

Figure 8-13. Alt 2A 2029 bathymetry

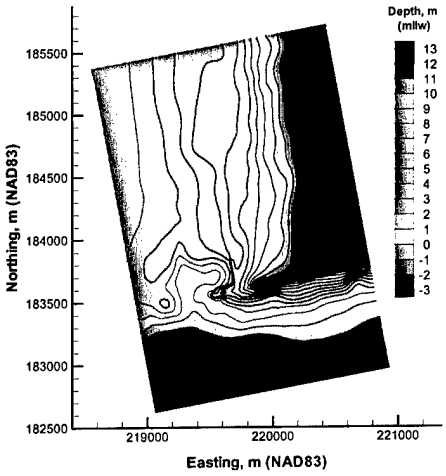

Figure 8-14. Alt 2B 2004 bathymetry

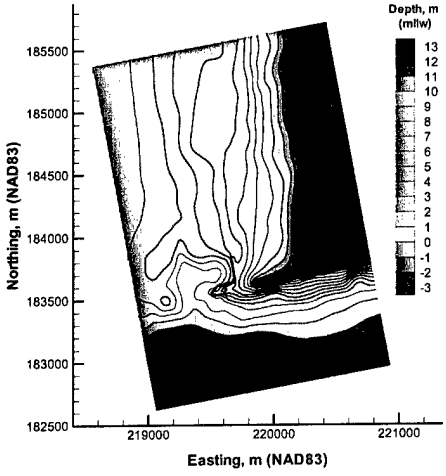

Figure 8-15. Alt 2B 2029 bathymetry

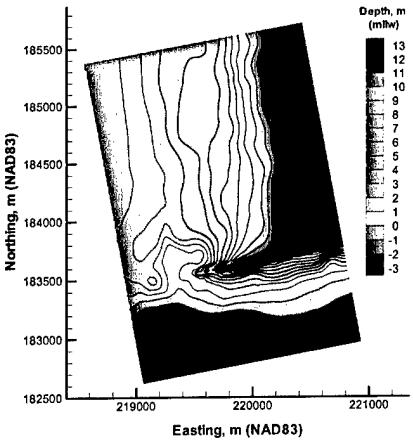

Figure 8-16. Alt 3A 2004 bathymetry

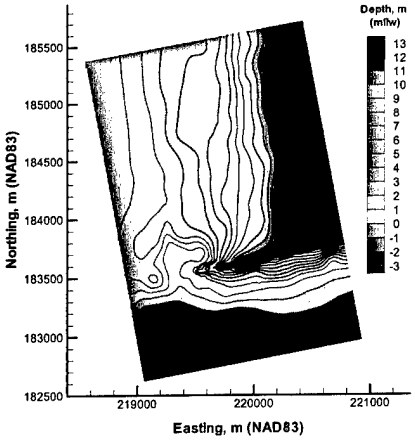

Figure 8-17. Alt 3A 2029 bathymetry

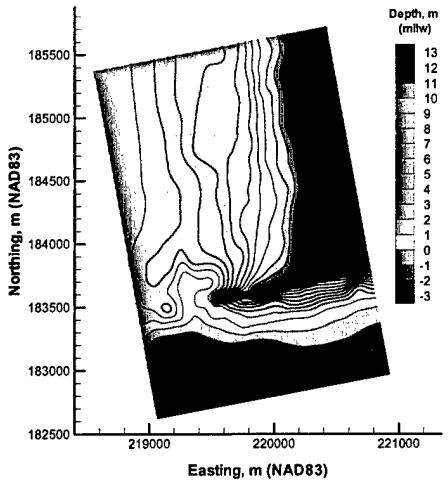

Figure 8-18. Alt 3B 2004 bathymetry

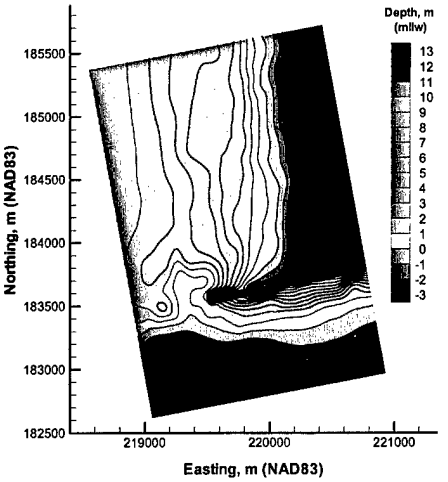

Figure 8-19. Alt 3B 2029 bathymetry

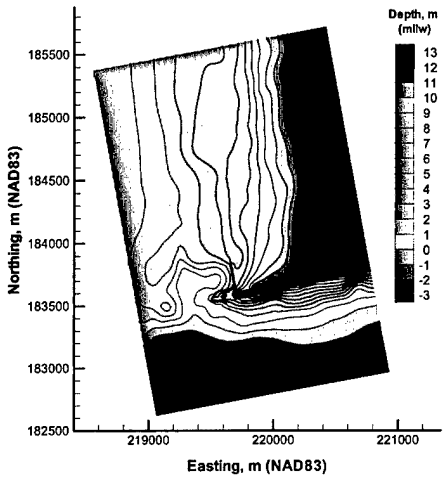

Figure 8-20. Alt 4 2004 bathymetry

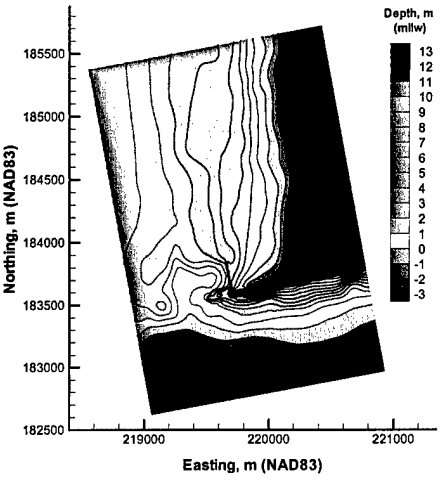

Figure 8-21. Alt 4 2029 bathymetry

Figures 8-10 and 8-11 show the 2001 bathymetry for Alts 1 and 2A. The main distinction between the 2001 bathymetry and the 1999 bathymetry is the absence of the scour trench on the northwest corner of the north jetty in the 2001 bathymetry. Maintaining the crest elevation of the spur alternatives at -10 ft mllw results in a much smaller structure (in terms of volume) in the 2001 bathymetry. As was the case for the 1999 bathymetry, Alt 2A (the long spur) was superimposed directly on the 2001 bathymetry.

Figures 8-12 through 8-21 show the synthetic 2004 and 2029 bathymetries associated with each of the alternatives (Alts 2A through 4). The shoreline configuration for each alternative was predicted by the GENESIS-T modeling described in Chapter 6. This information was used to adjust the 1999 bathymetry for each scheme by horizontally translating the beach profiles in the cross-shore direction for the predicted shoreline position change. A profile shifting

technique was developed that involved 17 separate steps of mapping, shifting, masking, and smoothing the bathymetry. The profile shift was applied between the mean water level and the -7 m mllw contour. Where shore profiles intersected the spur, no profile changes were made seaward of the spur.

Development of a representative annual climate

Evaluation of the overall changes to patterns of circulation and sediment transport potential induced by each alternative can be accomplished by consolidation of the simulation results in terms of the annual wave-current climate at the site. Assuming the combinations resulting from the four wave directions, three wave periods, and two wave heights are representative of the annual average wave climate, the joint annual frequency of occurrence of each combination was defined from the long-term buoy measurements (1994-2002).

The frequencies of occurrence were distributed evenly between the four tidal stages (high water slack, peak ebb flow, low water slack, and peak flood flow). This results in an annual expected frequency of occurrence of each of the hydrodynamic conditions (such that the sum of all frequencies is unity). An annual expected circulation climate can then be assembled as the sum of the velocity vectors for each combination of wave height, period, direction and tidal stage, with each hydrodynamic condition being multiplied by its frequency of occurrence. Table 8-3 shows the values used.

Simulation of nearshore currents at north jetty

The tidal currents on the upstream end of the domain were re-interpolated from tide-only ADCIRC simulations. Boundary conditions for currents varied along the boundaries because of setup and the wave-induced longshore current. Flows along most of the upstream boundary were constrained, whereas the free surface was not constrained. In areas where the ADCIRC and STWAVE simulations indicated strong wave-generated currents, the tidal boundary flow rate was not applied, and the wave-induced flows were allowed to control the boundary. The free surface was controlled along much of the downstream boundary. The determination of upstream or downstream was determined primarily from the direction of the longshore currents. This procedure will lead to some inaccuracies in the wave-generated currents in the direct vicinity of the boundaries. Because the model simulation periods were fairly short (1,000 sec), the boundary conditions are not expected to adversely alter results near the structural alternatives.

The water level, tidal current, wave height, period, and direction, and bathymetry combinations produce 96 simulations for each bathymetric configuration (Table 8-4) and 1,728 simulations with the inshore model (Table 8-5).

Table 8-3
Frequency of Occurrence of Selected Wave Conditions from CDIP Measurements (1994-2002)

Azimuth (deg)	T_p (sec)	H_s (m)	Frequency of Occurrence (percent)
210	8	2	4.481
210	8	5	1.205
210	13	2	2.322
210	13	5	0.523
210	18	2	0.342
210	18	5	0.109
250	8	2	10.011
250	8	5	2.482
250	13	2	3.664
250	13	5	0.829
250	18	2	0.487
250	18	5	0.126
280	8	2	29.445
280	8	5	3.565
280	13	2	14.271
280	13	5	1.843
280	18	2	2.464
280	18	5	0.301
300	8	2	14.555
300	8	5	0.062
300	13	2	6.048
300	13	5	0.031
300	18	2	0.833
300	18	5	0.003

Table 8-4
Hydrodynamic Conditions for Inshore CoastL Model Simulations

Case	Water Level Above Datum, m	Background Flow Field	Azimuth Wave Direction, deg	T_p, sec	H_s, m
High water slack	3.0	None	210, 250, 280, 300	8, 13, 18	2, 5
Low water slack	0.0	None	210, 250, 280, 300	8, 13, 18	2, 5
Ebb	1.5	Ebb currents	210, 250, 280, 300	8, 13, 18	2, 5
Flood	1.5	Flood currents	210, 250, 280, 300	8, 13, 18	2, 5

Table 8-5
Number of Simulations with Inshore CoastL Model

Structural Configuration	1999 Bathymetry	2001 Bathymetry	2004 Bathymetry	2029 Bathymetry
Existing condition	96			
Alt 1		96		
Alt 2A	96	96	96	96
Alt 2B	96		96	96
Alt 3A	96		96	96
Alt 3B	96		96	96
Alt 4	96		96	96
Total number of runs	576	192	480	480

Simulation of nearshore circulation – existing condition

Figures 8-22 and 8-23 show plan view maps of the nearshore circulation on the 1999 bathymetry for the existing condition with wave angles of 300 and 210 deg, respectively.

Waves from the northwest at high water slack (Figure 8-23) generate a longshore current directed to the south along the north beach. Wave refraction and set-up at the north jetty generate a shoreward current along the north side of the jetty and northward flow for several hundred meters to the north of the north jetty. The convergence of the longshore current with the refraction current creates a seaward-flowing rip current. The result is a counter clockwise gyre at the north jetty that resembles a topographically controlled rip circulation (e.g., Coutts-Smith and Short 2002) located 200 to 300 m north of the north jetty. A similar rip cell circulation is interpreted from the field measurements of nearshore currents presented in Chapter 4 that were acquired during periods of moderate incident wave energy (H_s between 2 and 4 m) and in the physical model. In particular, persistent northwesterly currents occurred at sta OS 2 a few hundred meters north of the jetty, while longshore currents varied from northerly to southerly at stations farther north (sta OS 3 and OS 4) in response to changing incident wave direction (Figure 8-4). Also, aerial photographs of the nearshore at the north jetty and three-dimensional (3-D) surface maps of nearshore topography consistently indicate the presence of an embayed shoreline under low to moderate incident wave energy. Shoreline embayments are often associated with rip cell circulation (Short 1985). The photograph shown in Figure 4-9, acquired during relatively low-energy summer waves, is a good example of the shoreline embayment and associated rip-cell features that occur to the north of the north jetty.

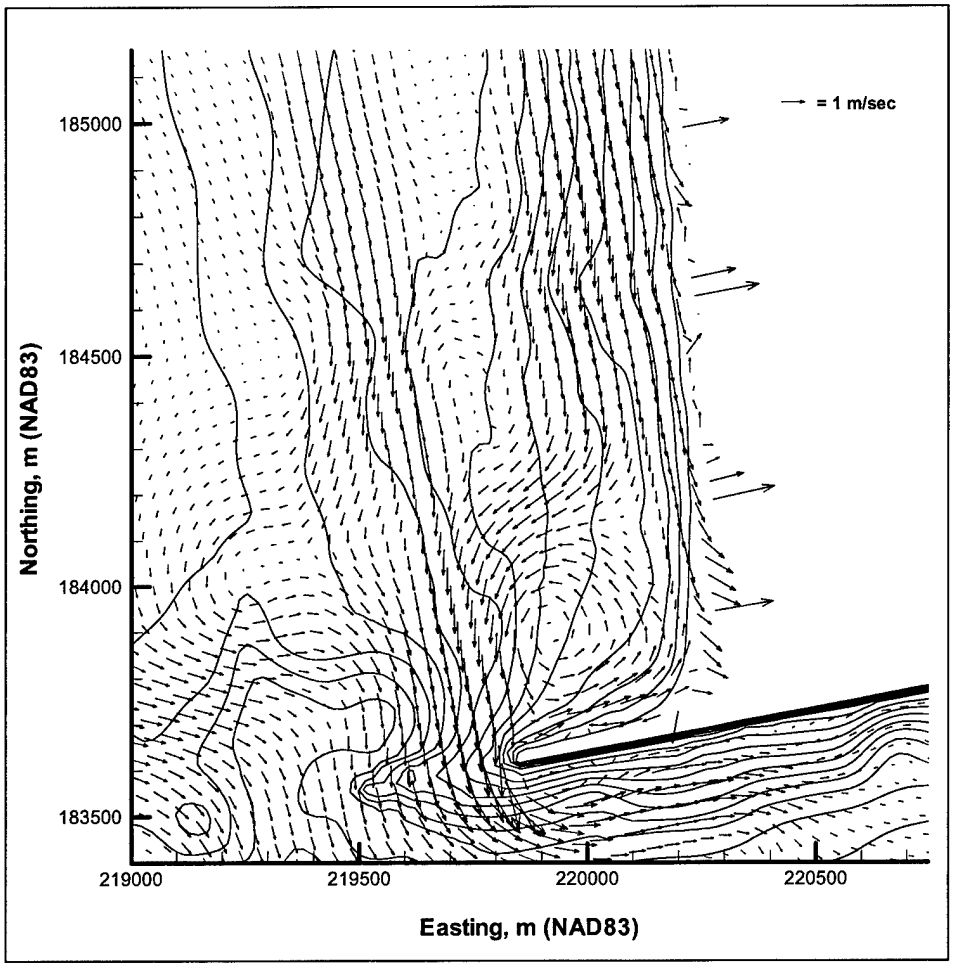

Figure 8-22. Wave-induced current pattern on 1999 bathymetry for offshore waves with direction of azimuth 300 deg, H_S of 5 m, and T_p of 13 sec at high water slack (every second vector shown in each orthogonal direction)

The 3-D physical model of the north beach at Grays Harbor (Chapter 5) produced a similar gyre for similar combinations of wave and tide forcing. The physical model tests indicate that this gyre is a controlling feature for flow patterns at the north jetty. These flows carry sediment offshore as well as to the south where it can enter the inlet.

CoastL predicts a similar gyre for many other combinations of tide, wave height, period, and direction. Waves from the southwest at high water slack (Figure 8-22) generate a counter-clockwise rotating gyre off the end of the north jetty. In this simulation, the longshore current does not develop fully for some distance to the north.

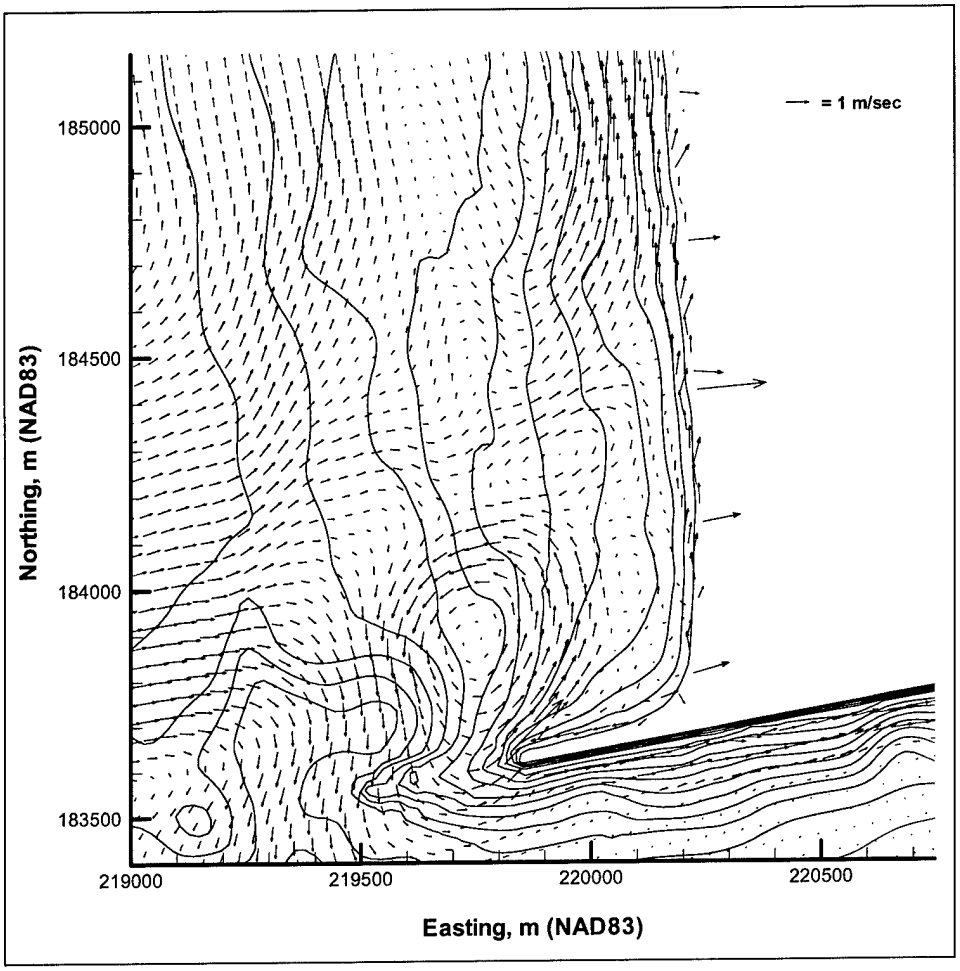

Figure 8-23. Wave-induced current pattern on 1999 bathymetry for offshore waves with direction of azimuth 210 deg, H_S of 5 m, and T_p of 13 sec at high water slack (every second vector shown in each orthogonal direction)

Figure 8-24 shows an example of a wave condition that does not produce a strong gyre system. This test at low water slack with offshore waves (direction of azimuth 280 deg, height H_S of 2 m, and period T_p of 18 sec) produces strong currents on the submerged part of the north jetty that drive a northward current along the north beach.

In general, simulations performed with the 2001 bathymetry produced a weaker gyre system than with the 1999 bathymetry (Figure 8-25). Although there is a slight difference in plan beach orientation between these two bathymetries, the largest difference is in profile. Cross-sections of the two bathymetries along a shore-normal transect located 135 m to the north of the north jetty are shown in Figure 8-26. The 2001 profile is more linear and is generally deeper towards the shore in the area where the gyre is produced in the 1999 simulations.

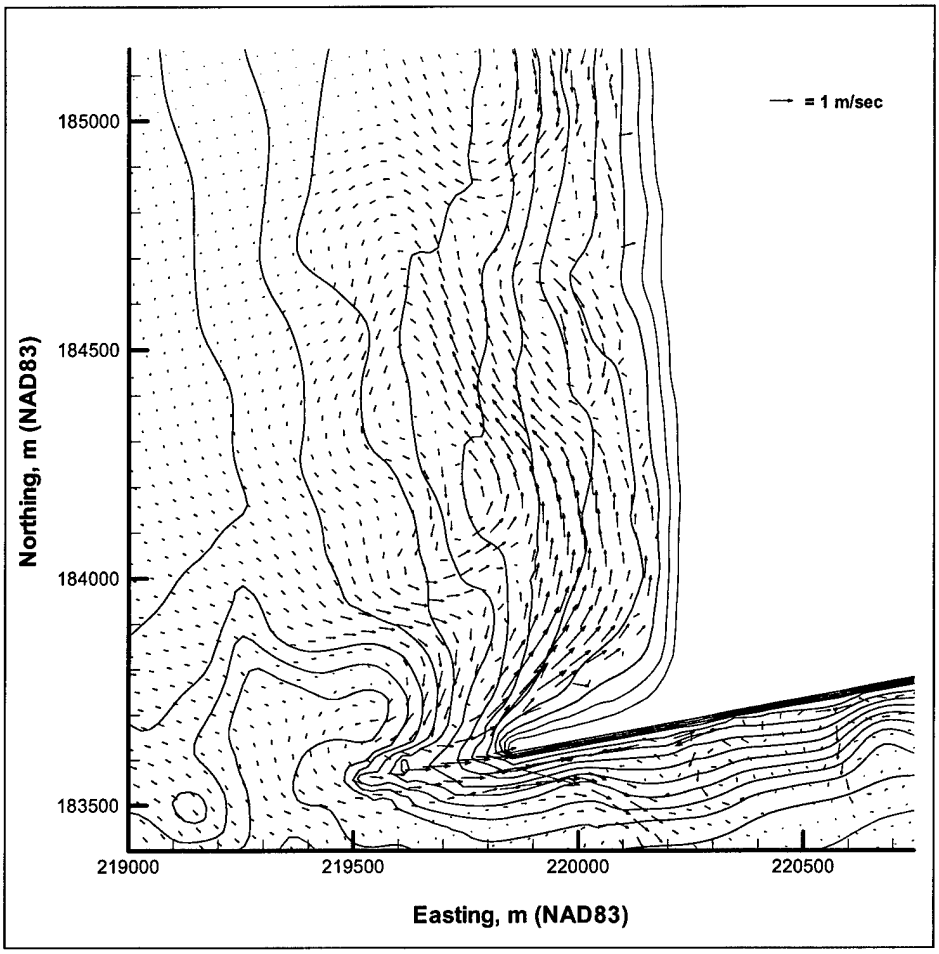

Figure 8-24. Wave-induced current pattern on 1999 bathymetry for offshore waves with direction of azimuth 280 deg, H_S of 2 m, and T_p of 18 sec at low water slack (every second vector shown in each orthogonal direction)

Comparisons of surveys from 1999, 2001, and 2002 show the nearshore exhibiting substantial changes in profile shape seasonally and annually. The CoastL results indicate sensitivity of the circulation patterns to variation in bathymetry. These observations and analysis provide an explanation for the differences in circulation patterns predicted by the ADCIRC model and the CoastL model for similar wave and tide combinations in the area near the north jetty. The grids for the depths in this area for the ADCIRC and CoastL models were developed independently, made use of different bathymetric data sets acquired in 1999, and involved different assumptions for interpolation of the finite element and finite difference grid elements. The resulting differences in the depth grids for the two models explains the somewhat differing circulation patterns predicted by the models and gives an indication of the variability in the hydrodynamic and sediment transport system.

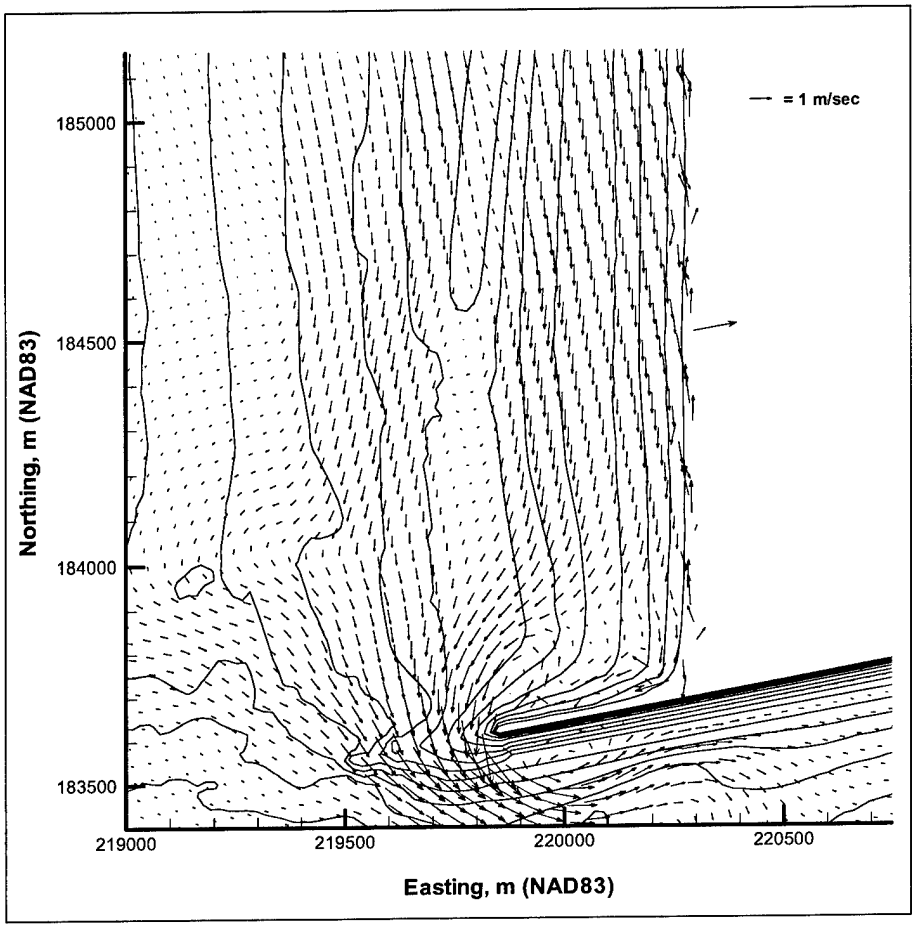

Figure 8-25. Wave-induced current pattern on 2001 bathymetry for offshore waves with direction of azimuth 300 deg, H_S of 5 m, and T_p of 13 sec at high water slack (every second vector shown in each orthogonal direction)

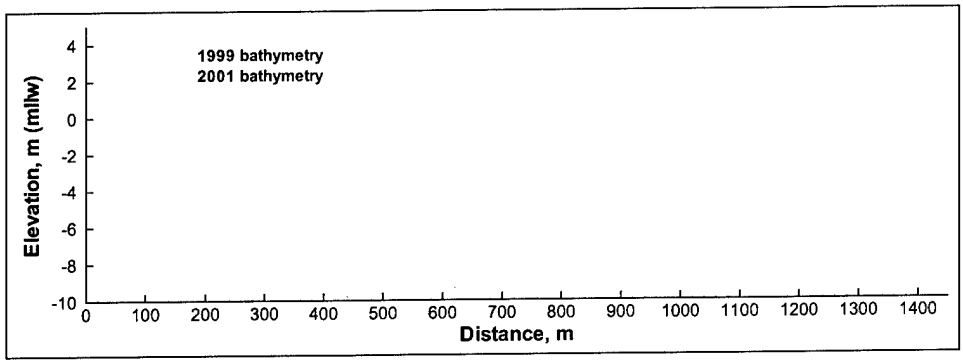

Figure 8-26. Shore-normal cross-sections from bathymetric grids taken 135 m north of north jetty. Distance is from edge of grid

Evaluation of alternatives

Numerical simulations of wave heights, wave and tide-induced currents, sediment transport potential and southward sediment bypassing rates were made to compare the existing condition and the five structural alternatives. Each of the alternatives was included in the numerical simulations, and the resulting currents, and sediment bypassing, were compared with the same respective parameters produced for existing condition.

Analyses have been performed for the 1999, 2001, 2004, and 2029 bathymetries. The discussion of results follows the analysis of existing condition (with the 1999 bathymetry) from hydrodynamics through to sediment transport and bypassing rates. The 2001, 2004, and 2029 bathymetries are then discussed in terms of their differences relative to 1999.

Submerged spur (Alts 2A and 2B)

The effectiveness of the spur at dissipating wave energy through breaking varies significantly with water depth because of the variation in relative submergence of the structure with changing water level (e.g., Chapter 6). Figures 8-27 through 8-30 show the spatial distribution of H_s predicted by CoastL for Alt 2A with waves of H_s = 5m, T_p = 13 sec, from azimuth 300 deg for ebb slack, flood slack, high water and low water, respectively. Three figures are shown in each plot: a plot of H_s for the existing condition, a plot of H_s for the alternative, and a plot of the difference between the two solutions of H_s.

Figure 8-27 shows a comparison of H_s for Alt 2A relative to existing condition (1999 bathymetry). The upper left and right plots show the spatial distribution of H_s for existing condition and Alt 2A, respectively. The lower plot shows the difference in H_s between the two cases. The difference is calculated as Alt 2A minus the existing condition, such that a positive change in H_s indicates larger wave heights higher in Alt 2A than for the existing condition. Figure 8-27 shows that, at low water, the spur produces a zone of reduced wave height shoreward of the structure.

Figure 8-28 compares wave heights for the ebb stage of tide, indicating a reduction in H_s shoreward of the spur. Wave height reductions also occur south of the jetty, most likely a result of wave-current interaction in this area. Figure 8-29 shows that similar patterns of wave height reduction occur shoreward of the spur on the flood as on the ebb. The wave-current induced changes in wave height south of the jetty are less with flood than with ebb. Figure 8-30 shows the distributions of both H_s and difference in H_s at high tide. The results show a reduction in H_s at the spur location and shoreward of the structure. The reduction is less at high tide than at lower water levels. This general pattern of reduced wave energy shoreward of the spur is consistent throughout all simulations. For the range of wave conditions and water levels examined, wave height reduction by the spur is typically 10 percent. The reduction in wave height increases with increasing offshore wave height and with increasing wave period. The affected area is typically located 100 to 200 m shoreward of the spur with the influence diminishing with distance shoreward.

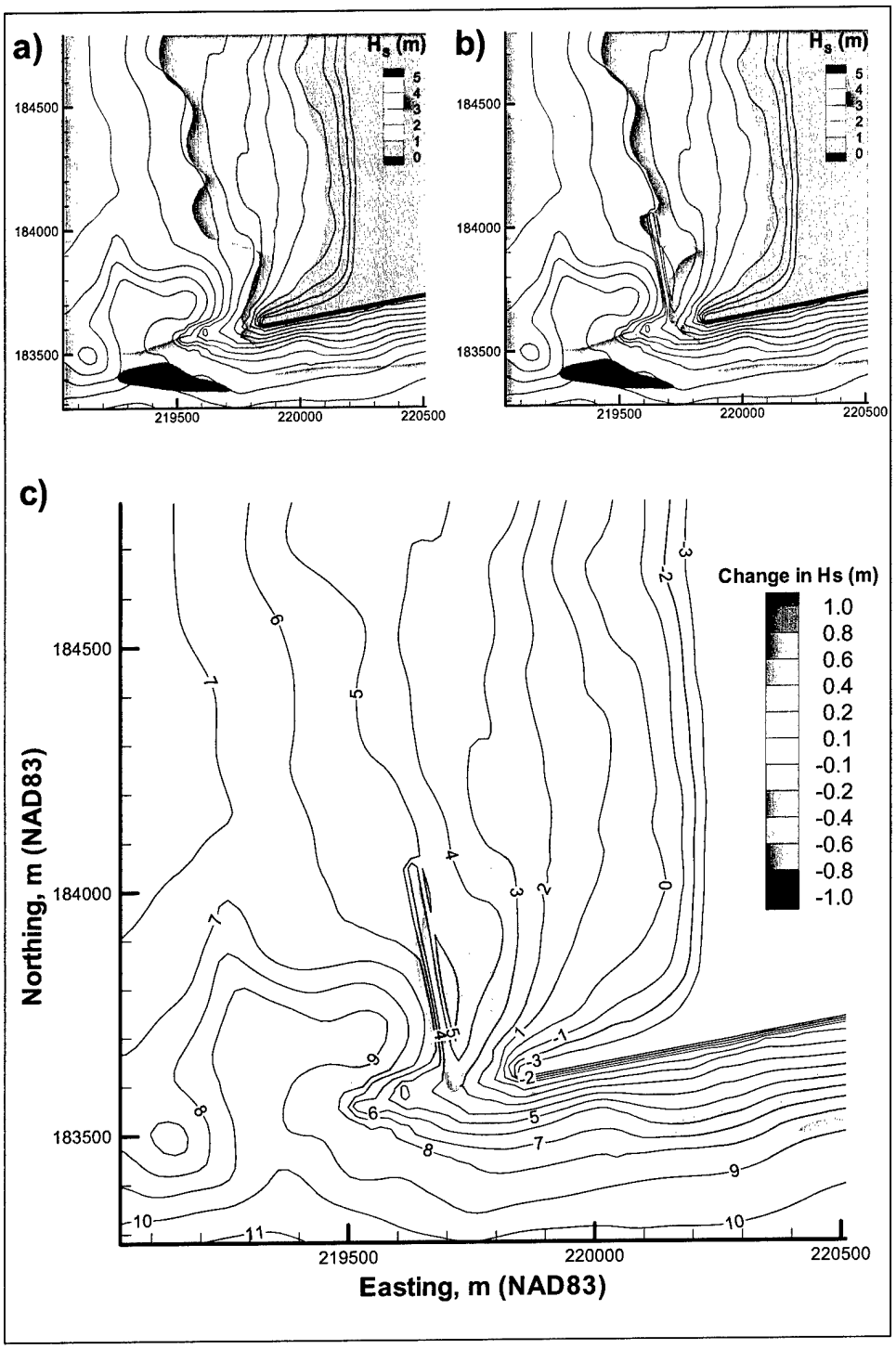

Figure 8-27. Results for waves of H_s = 5 m, T_p = 13 sec from azimuth 300 deg for low water slack: (a) H_s for existing condition, (b) H_s for Alt 2A, and (c) difference in H_s between Alt 2A and existing condition

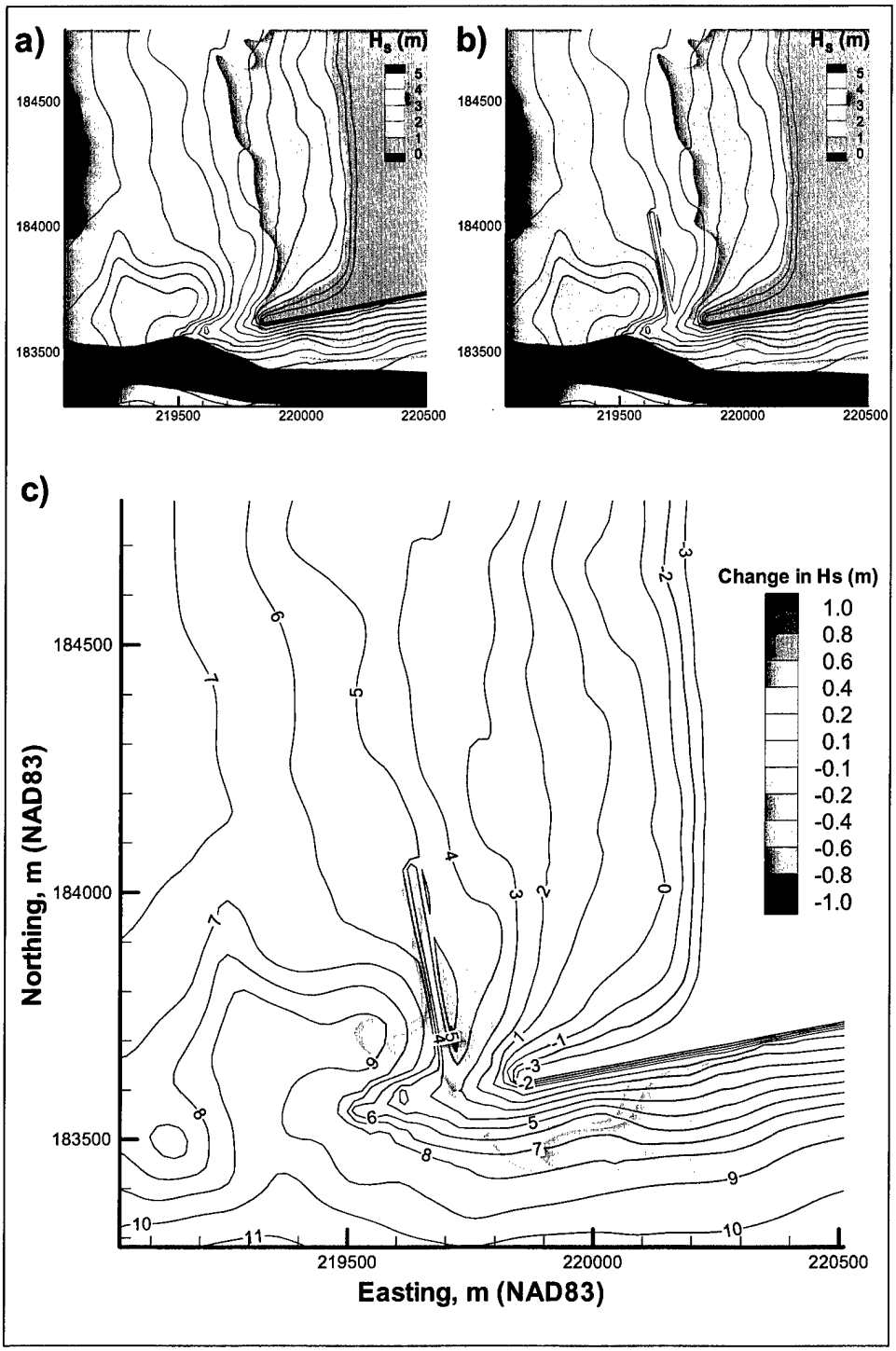

Figure 8-28. Results for waves of H_s = 5 m, T_p = 13 sec from azimuth 300 deg for peak ebb: (a) H_s for existing condition, (b) H_s for Alt 2A, and (c) difference in H_s between Alt 2A and existing condition

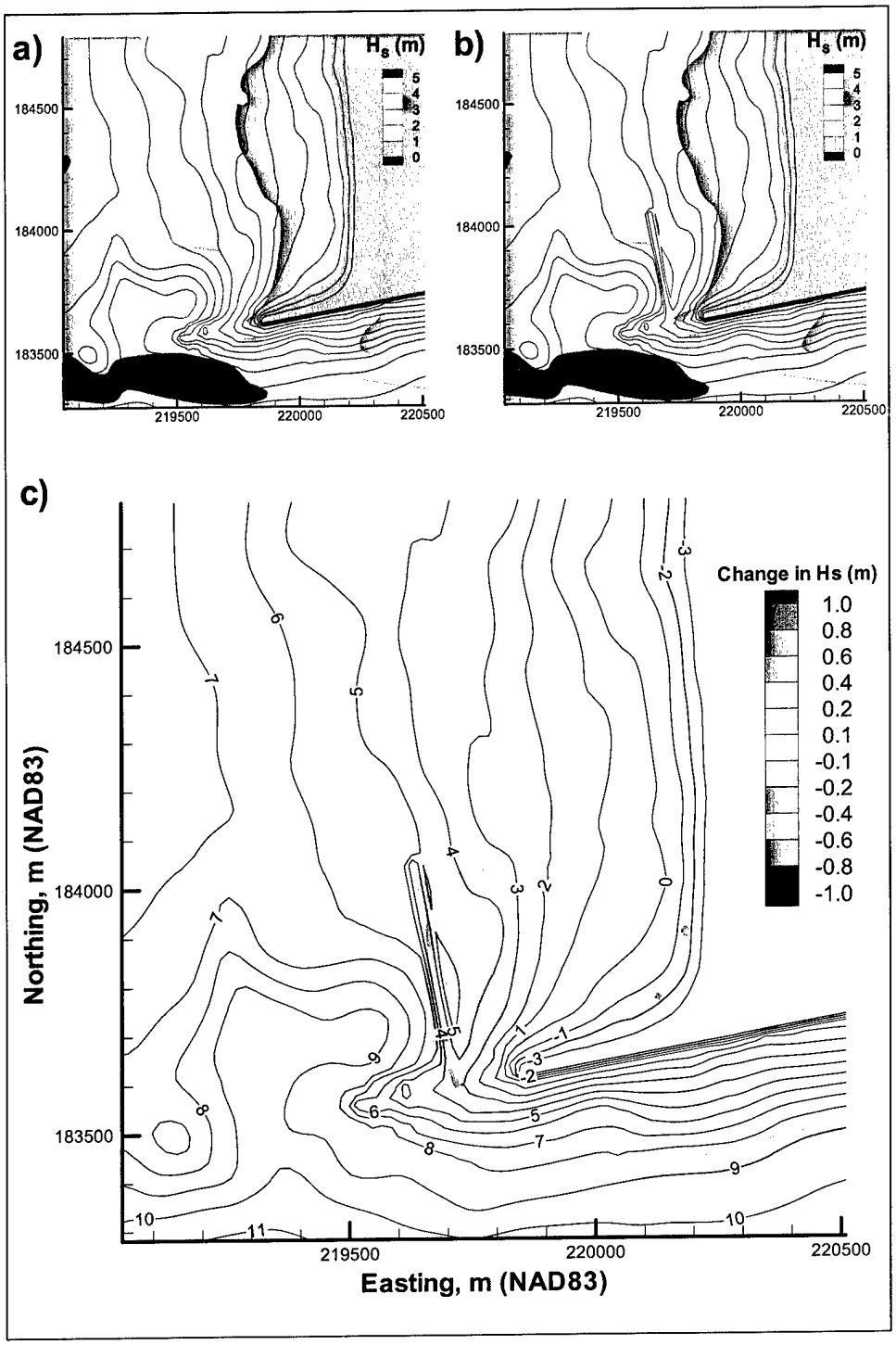

Figure 8-29. Results for waves of H_s = 5 m, T_p = 13 sec from azimuth 300 deg for peak flood: (a) H_s for existing condition, (b) H_s for Alt 2A, and (c) difference in H_s between Alt 2A and existing condition

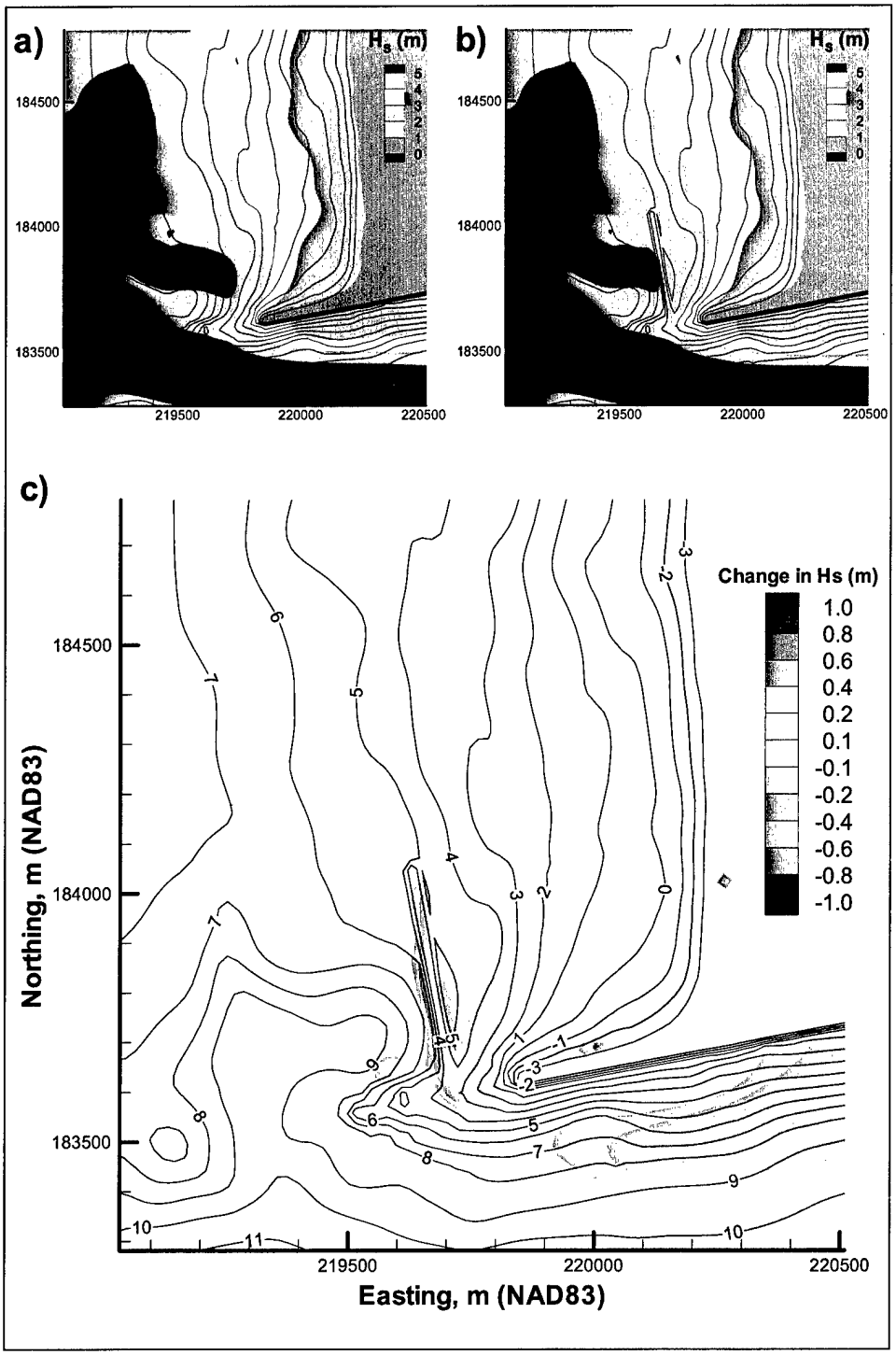

Figure 8-30. Results for waves of H_s = 5 m, T_p = 13 sec from azimuth 300 deg for high water slack: (a) H_s for existing condition, (b) H_s for Alt 2A, and (c) difference in H_s between Alt 2A and existing condition

The CoastL circulation patterns are analyzed with both vector field maps and contour maps. Representative examples are included here for the azimuth 300 deg, peak flood flow, H_s of 5 m, and T_p of 13 sec combination to illustrate the changes in circulation and wave conditions. This combination was chosen as being representative of waves from the northwest during a flood tide and is the condition that is most directly associated with sediments bypassing the north jetty to the south and entering the inlet.

Applying the existing 1999 bathymetry as a reference case, the simulations were analyzed for difference in the current field calculated as the magnitude of currents for Alt 2A minus the magnitude of currents for the existing condition. This calculation reveals the relative impact to nearshore circulation associated with each of the alternatives.

The change in current speed between Alt 2A flow and existing condition (1999 bathymetry) is presented in Figure 8-31. The current speed shoreward of the spur is reduced along almost the entire length of the spur. The bypassing current across the jetty tip and to the southeast is also reduced. Figure 8-32 shows the predicted circulation patterns. The counterclockwise gyre to the north of the north jetty is similar in size and shape with or without Alt 2A in place. Alternative 2A constrains the spatial extent of the gyre between the spur and the shore, shifts the rip current slightly southward and deflects the rip along the shoreward side of the spur. Velocity magnitudes shoreward of the spur are slightly reduced. At the tip of the jetty and to the south, currents are reduced slightly by Alt 2A relative to the existing condition.

Change in significant wave height from the existing condition to Alt 2A is shown in Figure 8-33. Wave height is reduced shoreward of the spur, most likely caused by wave breaking over the spur. Wave heights to the south of the jetty are increased or decreased, depending on location. This is likely caused by the change in circulation pattern to the south of the jetty, altering wave height through the wave-current interaction, giving a corresponding shift in the wave pattern.

Figure 8-34 compares Alt 2B (shorter spur) and the existing condition. The circulation patterns and the changes in circulation patterns are indistinguishable from those for Alt 2A. Comparing the velocity magnitudes, however, (Figure 8-35) it is evident that the reductions in velocity caused by Alt 2A are greater than the reductions caused by Alt 2B, even though the overall patterns are similar.

Current speeds predicted for Alts 2B and 2A are compared in Figure 8-36. The comparison shows that the only difference in current speed between Alts 2A and 2B is the spatial extent of the velocity reduction shoreward of the spur; the longer spur in Alt 2A causes a correspondingly larger zone of velocity reduction.

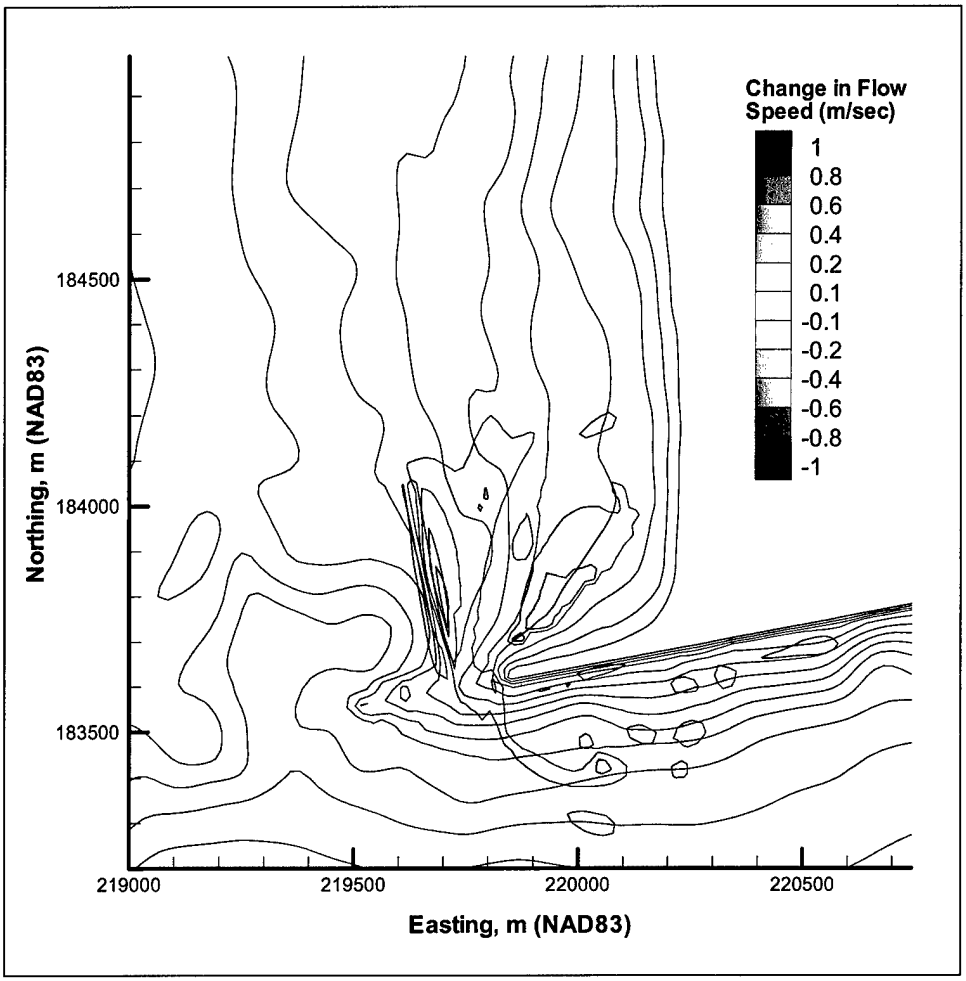

Figure 8-31. Change in current speed between Alt 2A and existing condition for H_s = 5 m, T_p = 13 sec, from azimuth 300 deg for peak flood

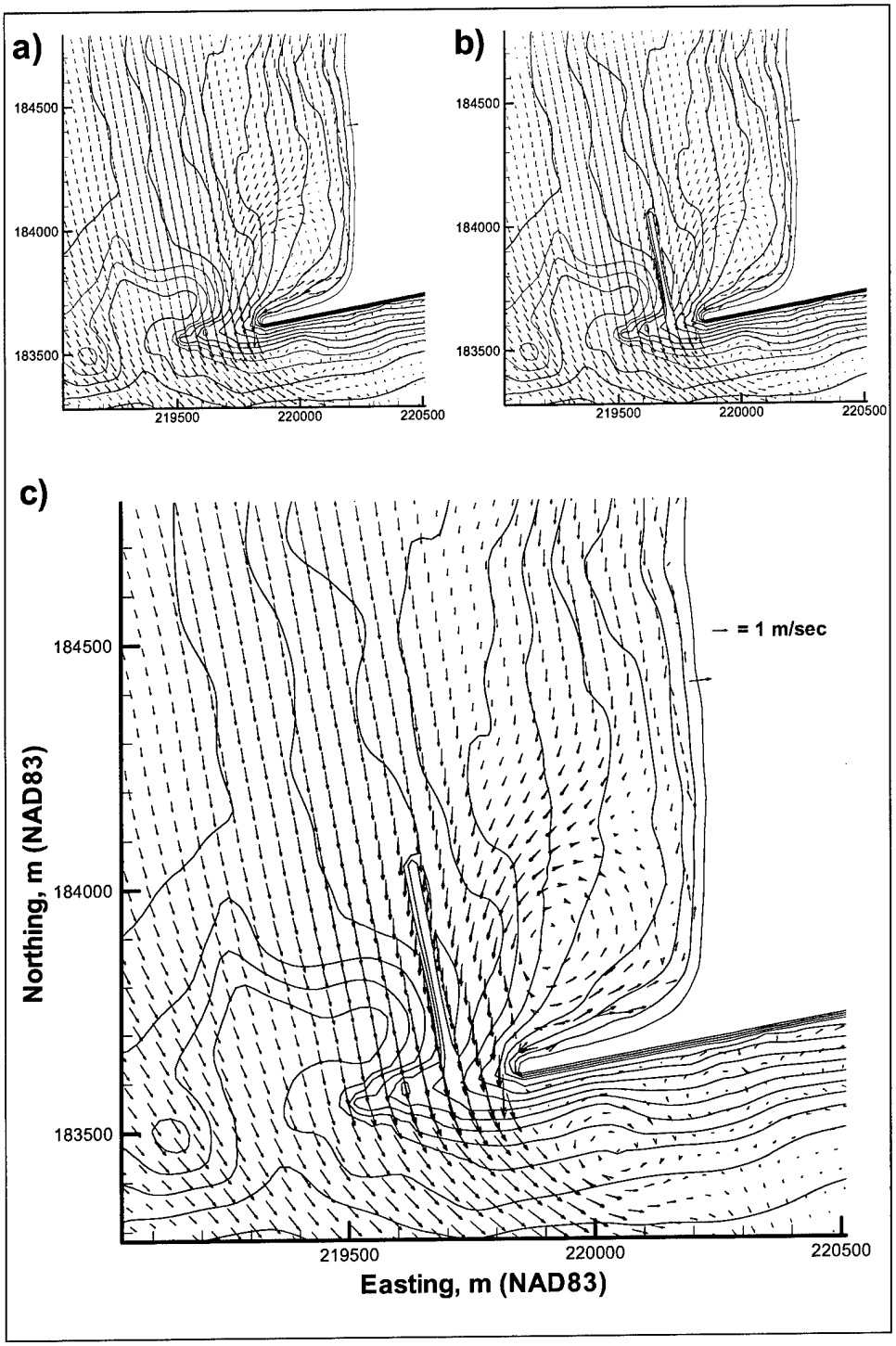

Figure 8-32. Current patterns for H_s = 5 m, T_p = 13 sec from azimuth 300 deg for peak flood: (a) existing condition, (b) Alt 2A, and (c) Alt 2A and existing condition

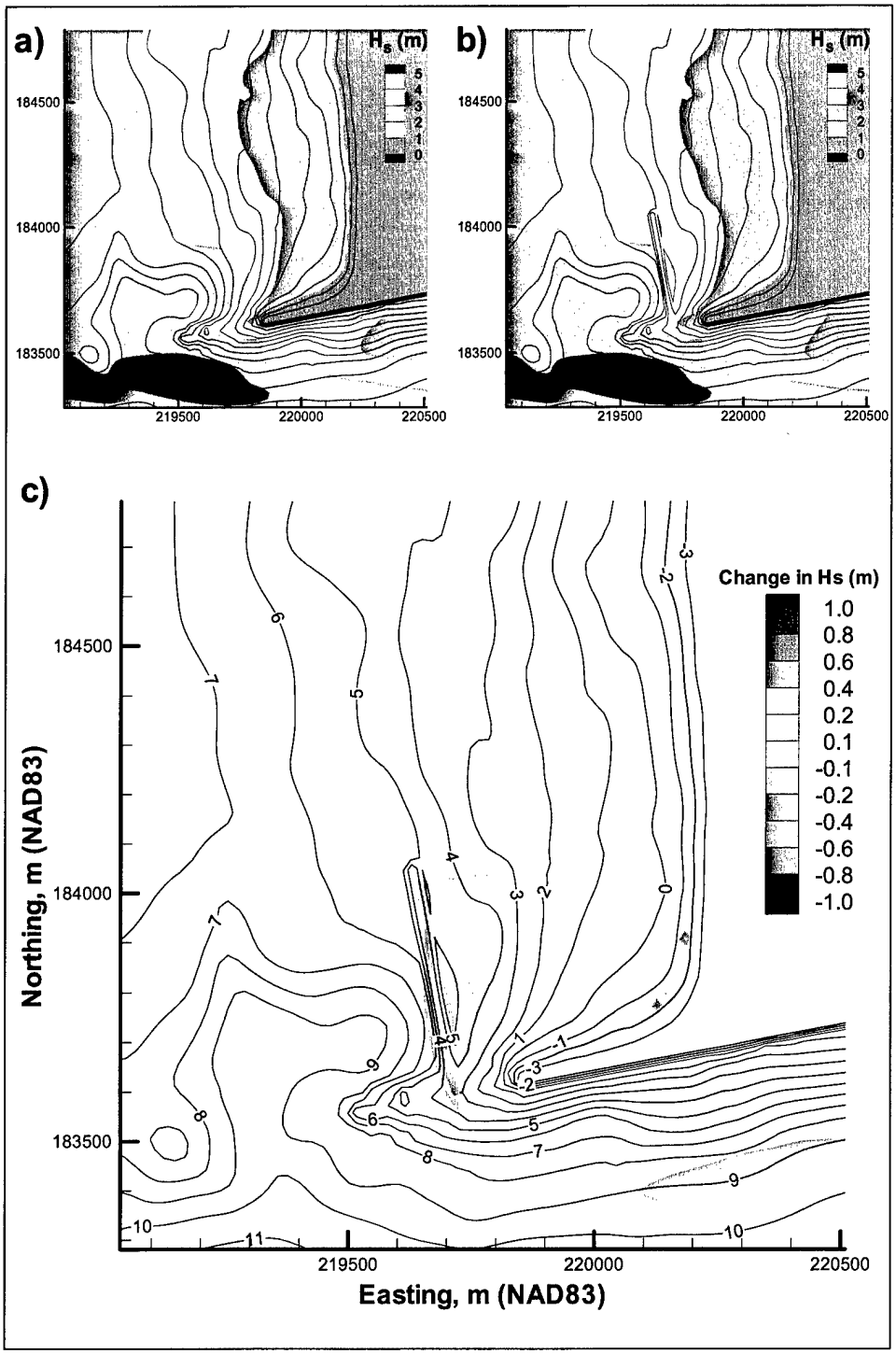

Figure 8-33. Results for waves of H_s = 5 m, T_p = 13 sec from azimuth 300 deg for peak flood: (a) H_s for existing condition, (b) H_s for Alt 2A, and (c) difference in H_s between Alt 2A and existing condition

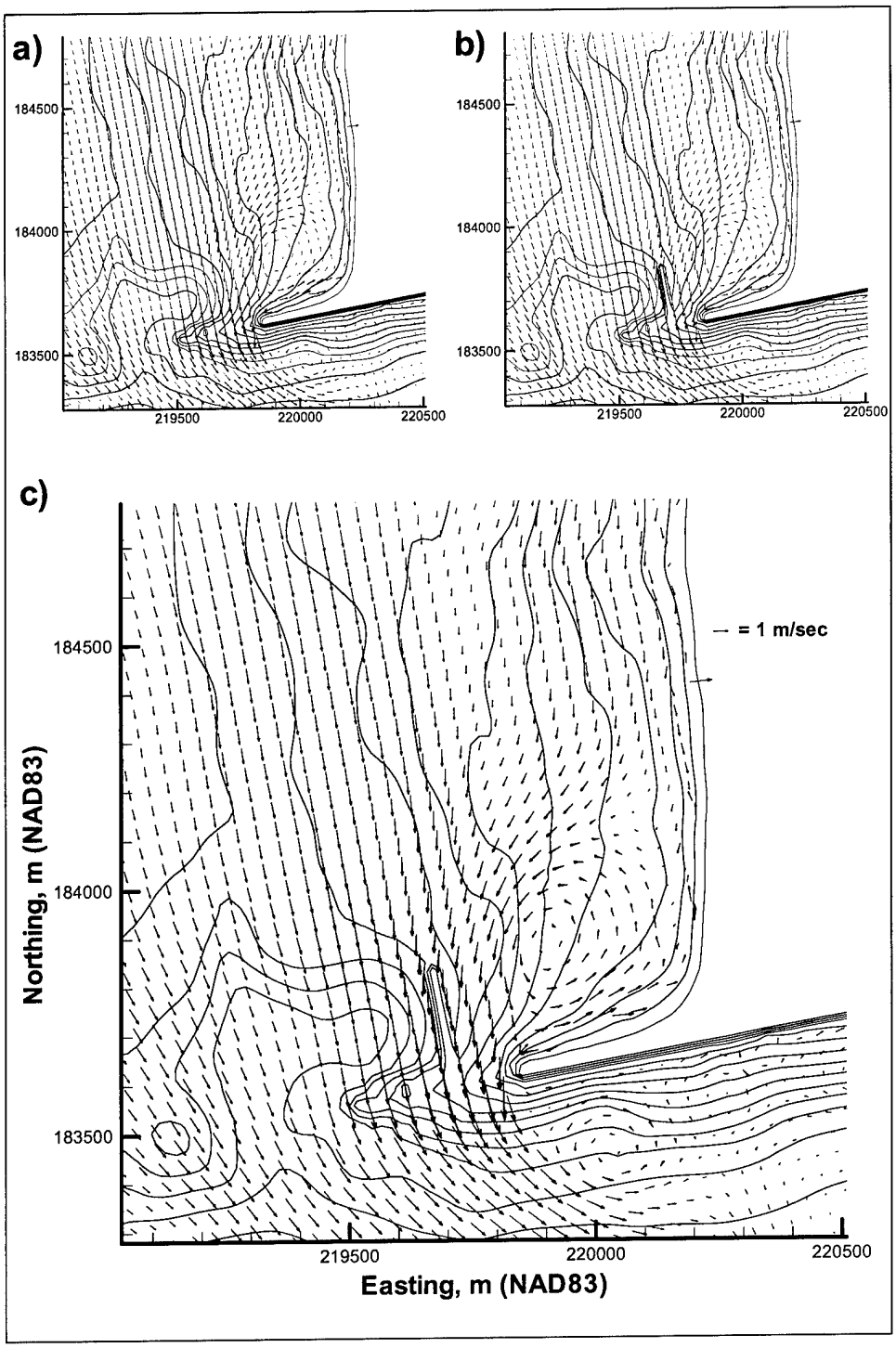

Figure 8-34. Current patterns for H_s = 5 m, T_p = 13 sec from azimuth 300 deg for peak flood: (a) existing condition, (b) Alt 2B, and (c) Alt 2B and existing condition

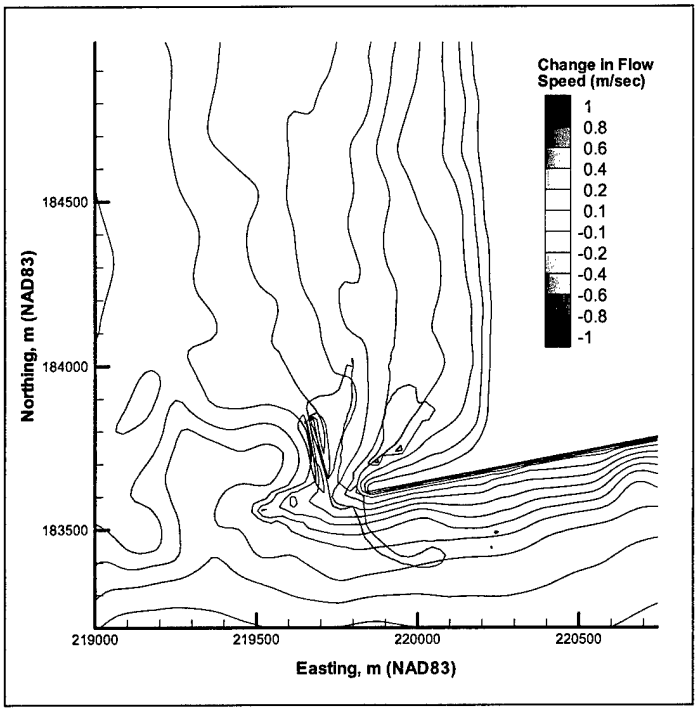

Figure 8-35. Change in current speed between Alt 2B and existing condition for H_s = 5 m, T_p = 13 sec from azimuth 300 deg for peak flood

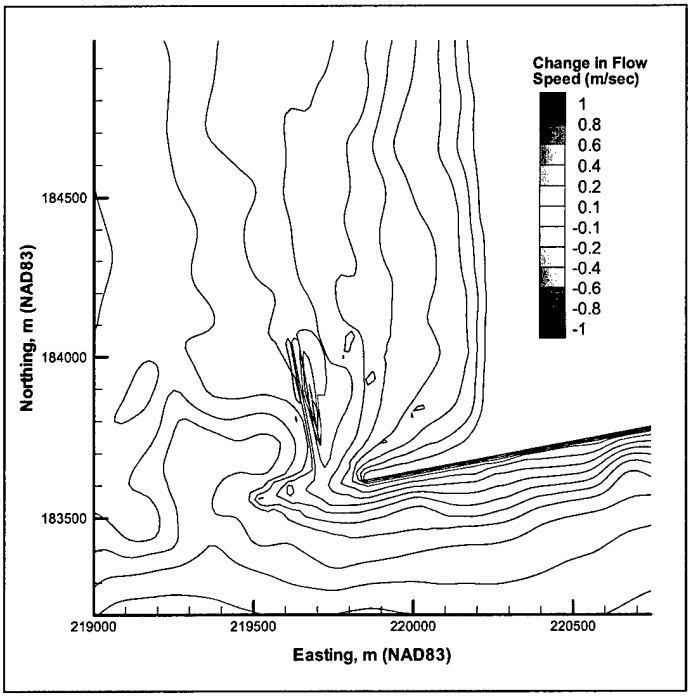

Figure 8-36. Change in current speed between Alt 2A and Alt 2B for H_s = 5 m, T_p = 13 sec from azimuth 300 deg for peak flood

Figure 8-37 shows the changes in H_s between the existing condition and Alt 2B. As was the case for Alt 2A, the main change is a reduction of about 10 percent in wave height shoreward of the spur. The shoreward extent of the wave height reduction is roughly the same as for Alt 2A, but the shore-parallel extent is reduced proportionately to the reduction in spur length.

Jetty rehabilitation (Alts 3A and 3B)

Figures 8-38 through 8-40 show results for the simulations with Alt 3A (partial jetty rehabilitation).

Alternative 3A significantly changes current speed and direction relative to the existing condition near the jetty (Figure 8-38). The bypassing current is shifted seaward to the new tip of the jetty; the current vectors near the tip are directed more toward the south than the southwest; and the current flows offshore (west-southwest) along the northern edge of the tip of the jetty, whereas under the existing condition, it flows south. In addition, the gyre to the north of the jetty shifts slightly to the north, and currents in the gyre are weaker. The rip current defined by the northern edge of the gyre also shifts slightly to the north relative to the existing condition.

The changes in the magnitude of the current for Alt 3A relative to the existing condition are shown in Figure 8-39. The changes in current speed near the tip of the jetty are mostly related to the westward translation of the bypassing current caused by extension of the jetty. Current speed in the area to the north of the jetty is slightly reduced. Current speed in the nearshore area adjacent to the jetty is increased. Some of these differences are caused by shifting of the current pattern (evidenced by current increases adjacent to current decreases).

The changes in wave height patterns associated with partial jetty rehabilitation are shown in Figure 8-40. Wave height to the north of the jetty is unchanged by the presence of the jetty rehabilitation. At the tip of the jetty, wave height increases to the northwest of the tip. This is likely caused by wave-current interaction. The changes in wave height to the south of the jetty are attributable to shifts in the bypassing current and associated changes in wave-current interactions.

The same pattern of increased current speeds further offshore and a south and westward shift of current directions near the tip of the jetty is seen for Alt 3B (Figure 8-41). For Alt 3B, the gyre location is the same as for Alt 3A, the reduction in current speed is more pronounced for Alt 3B, and the current at the north edge of the jetty is directed more toward offshore than for Alt 3A.

The changes in current speed caused by Alt 3B are shown in Figure 8-42. The current speed decreases to the north of the jetty (particularly offshore of the -5-m mllw contour). It increases in the nearshore corner north of the jetty, decreases to the south of the extended portion of the jetty, and greatly increases offshore and to the south of the tip of the jetty.

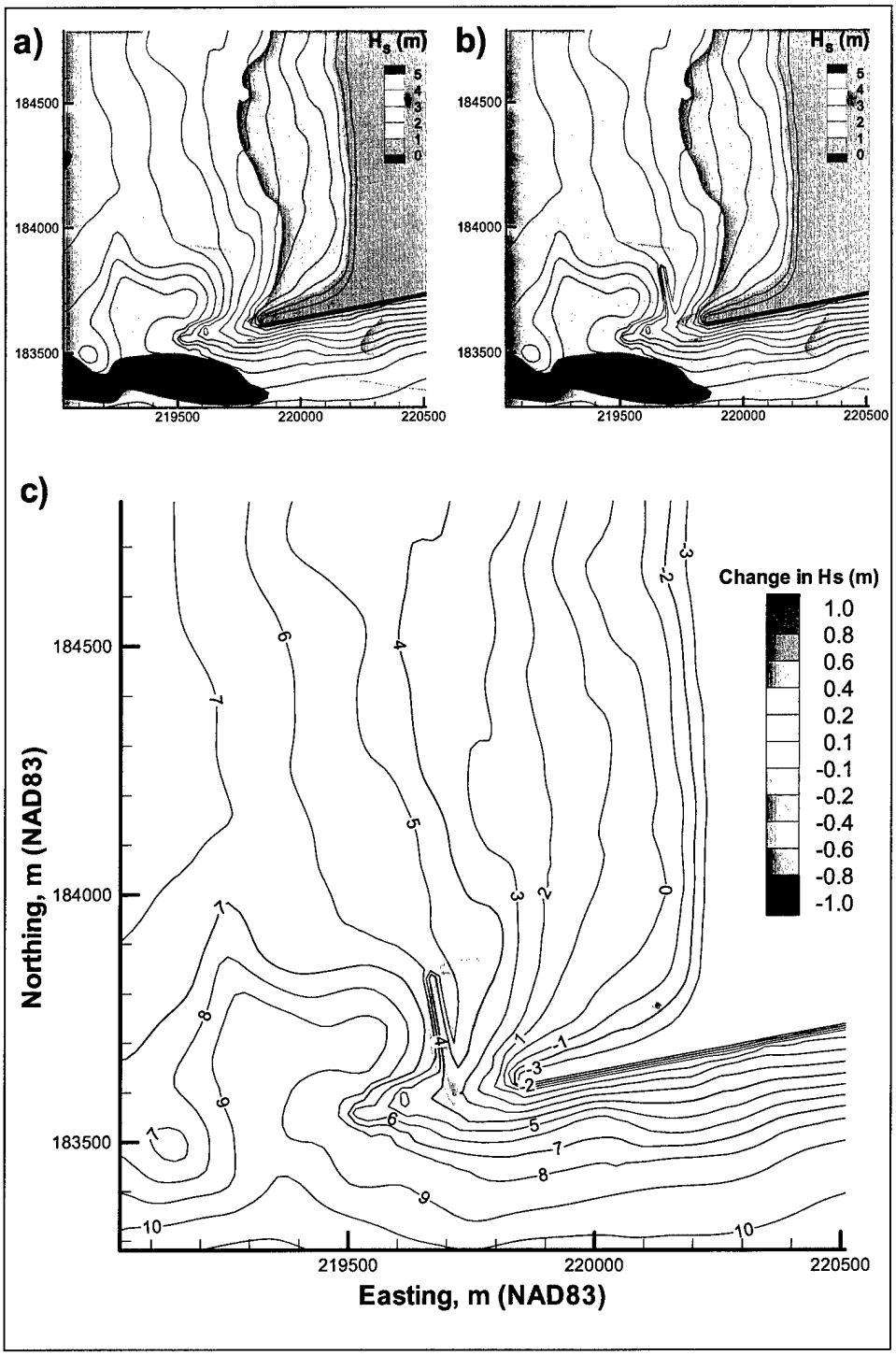

Figure 8-37. Results for waves of H_s = 5 m, T_p = 13 sec from azimuth 300 deg for peak flood: (a) H_s for existing condition, (b) H_s for Alt 2B, and (c) difference in H_s between Alt 2B and existing condition

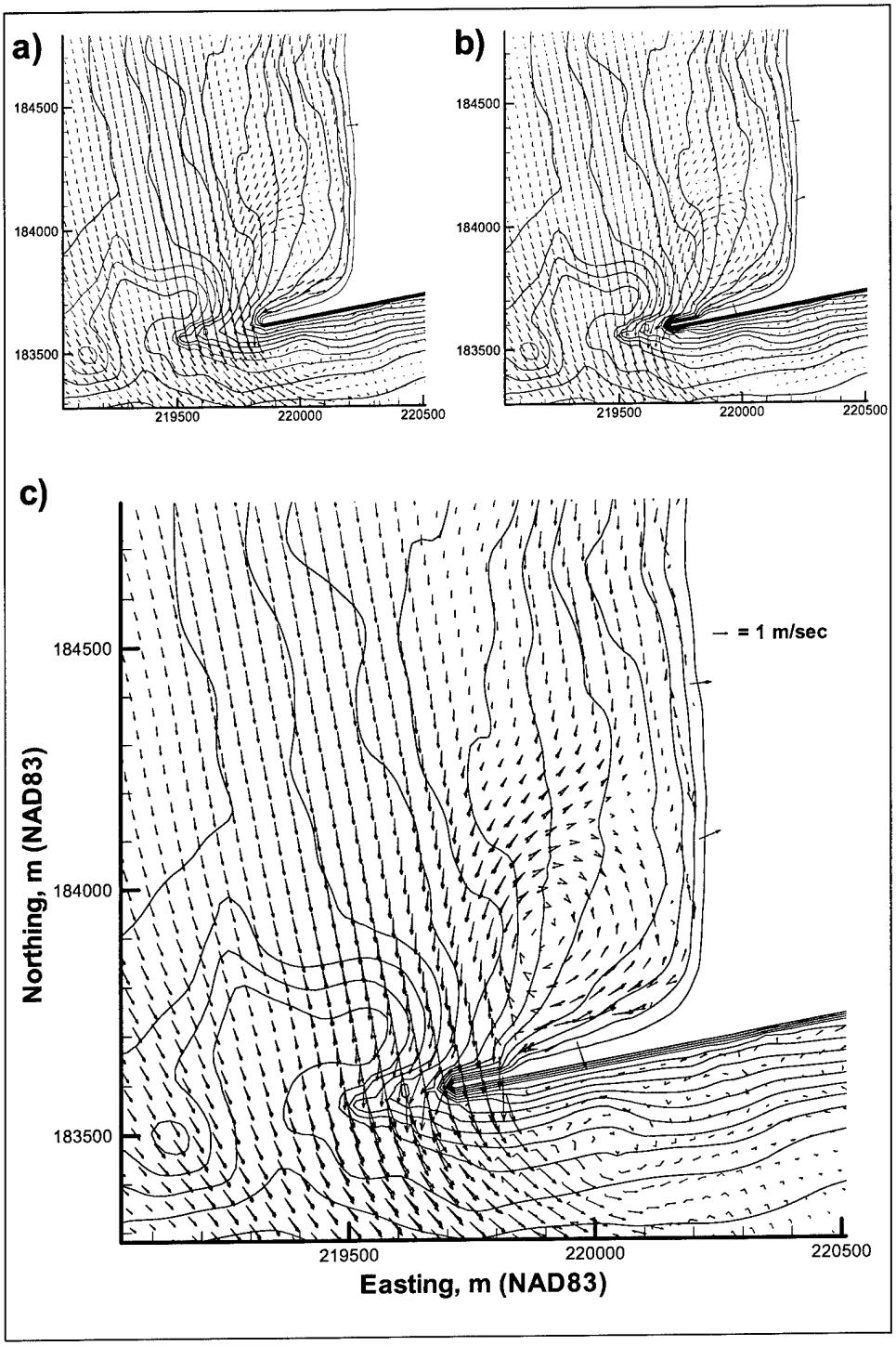

Figure 8-38. Current patterns for H_s = 5 m, T_p = 13 sec from azimuth 300 deg for peak flood: (a) existing condition, (b) Alt 3A, and (c) Alt 3A and existing condition

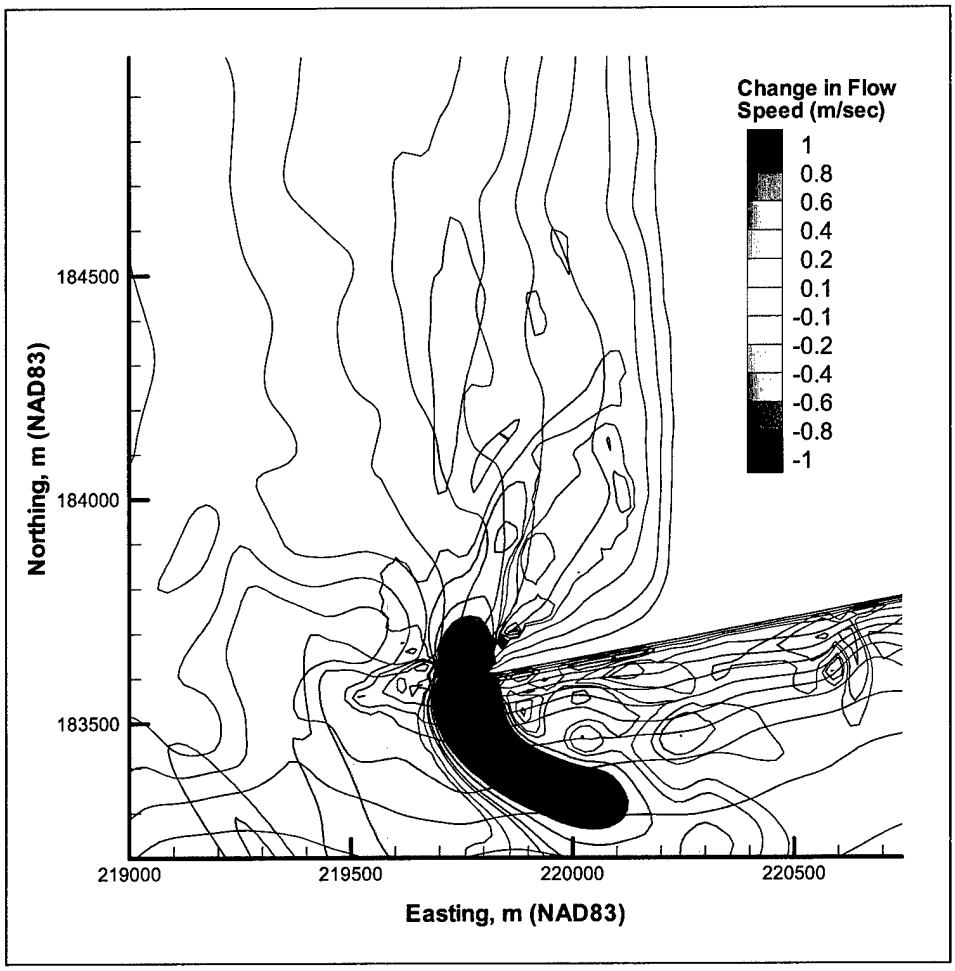

Figure 8-39. Change in current speed between Alt 3A and existing condition for H_s = 5 m, T_p = 13 sec from azimuth 300 deg for peak flood

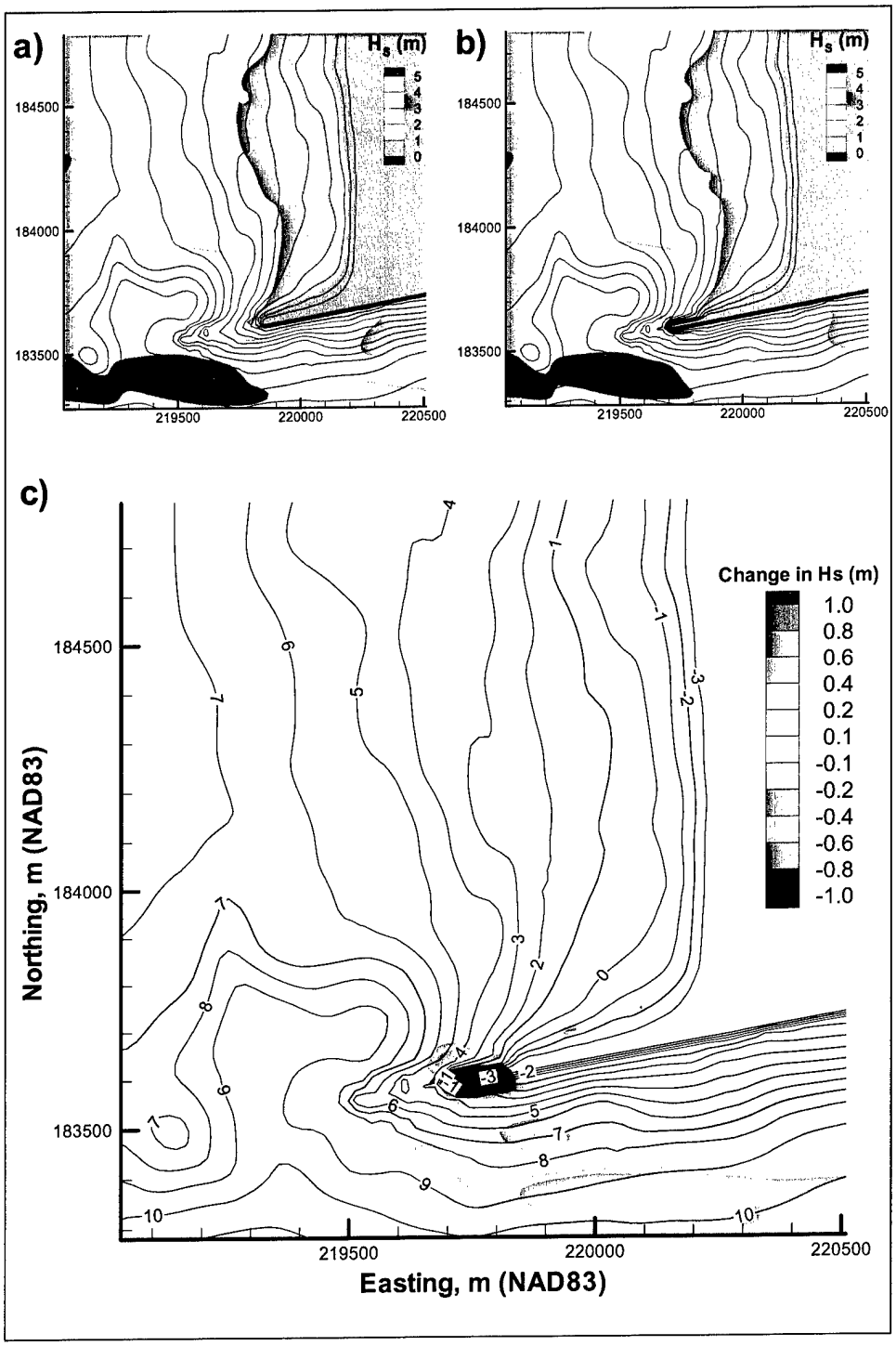

Figure 8-40. Results for waves of H_s = 5 m, T_p = 13 sec from azimuth 300 deg for peak flood: (a) H_s for existing condition, (b) H_s for Alt 3A, and (c) difference in H_s between Alt 3A and existing condition

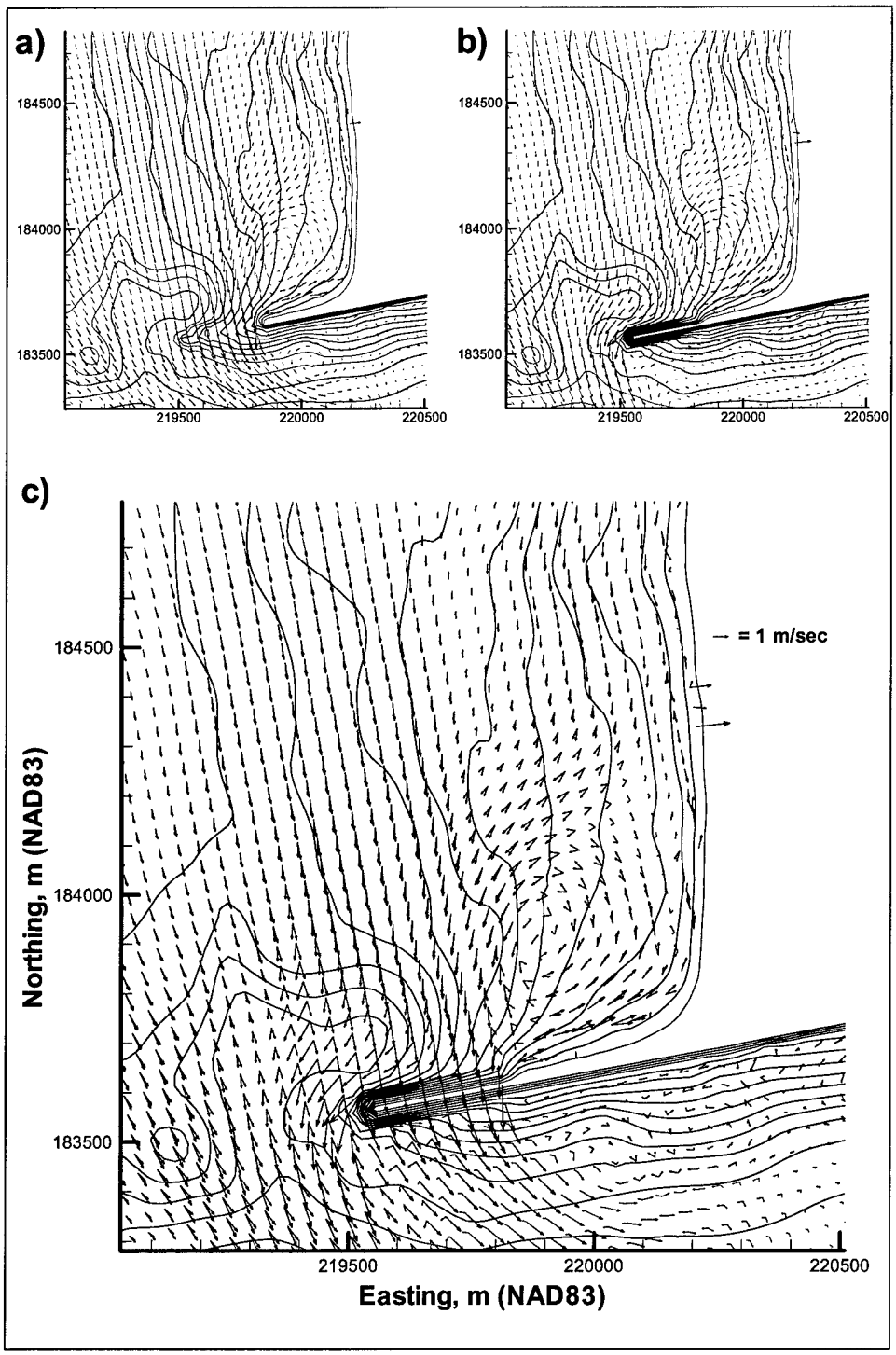

Figure 8-41. Current patterns for H_s = 5 m, T_p = 13 sec from azimuth 300 deg for peak flood: (a) existing condition, (b) Alt 3B, and (c) Alt 3B and existing condition

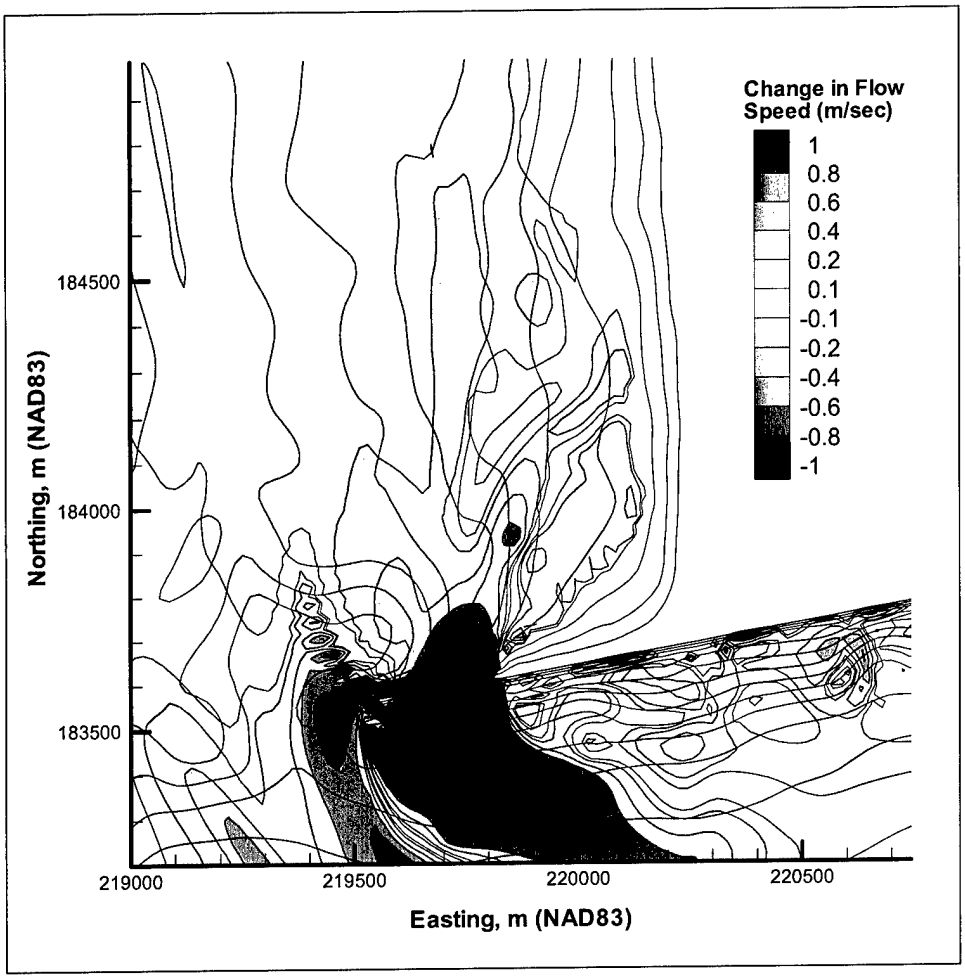

Figure 8-42. Change in current speed between Alt 3B and existing condition for H_s = 5 m, T_p = 13 sec from azimuth 300 deg for peak flood

Wave height changes associated with Alt 3B are shown in Figure 8-43. These patterns are similar to those observed for Alt 3A. There is no change in H_s for most of the area to the north of the jetty. The wave height H_s increases directly to the northwest of the jetty, and there is an eastward shifting of wave height pattern in the area south of the jetty.

Combination structure (Alt 4)

Alternative 4 is a combination of the short spur and the partial jetty rehabilitation. The changes in current patterns for Alt 4 tend to represent a combination of the changes attributable to both Alts 2B and 3A (Figure 8-44). The current speed is reduced in the area behind the spur, and the circulation patterns are shifted offshore by the jetty extension. The current along the north edge of the extended portion of the jetty flows more offshore, and the flow bypassing the jetty head is more southerly than with the existing condition.

Changes in current speed for Alt 4 are shown in Figure 8-45. As was the case for current vectors, the change in current speed shows the combined effects of Alts 2B and 3A; a reduction in current speed directly shoreward of the spur and a shift in current patterns near the tip of the jetty.

Changes in wave height caused by Alt 4 are shown in Figure 8-46. These changes include a reduction in wave height shoreward of the spur; a shift in wave height patterns at the tip and to the south of the jetty; and an increase in wave height at the northwest corner of the jetty tip.

Simulations with 2001 bathymetry

Simulations were performed for Alt 2A with the 2001 bathymetry to assess the sensitivity of the simulations to realistic variations in bathymetry. The change in current speed between Alt 2A and existing condition (2001 bathymetry) is minor (Figure 8-47). The current is reduced by 0.1 to 0.2 m/sec shoreward of the spur along almost the entire length of the spur. At the tip of the jetty, as well as to the south of the jetty, the current is reduced by 0.1 to 0.2 m/sec for Alt 2A relative to existing condition.

The predicted circulation patterns are shown in Figure 8-48. They differ from the patterns produced in the 1999 simulations in that the counter-clockwise gyre found in the 1999 bathymetry is absent in these simulations.

The changes in wave height caused by Alt 2A are shown in Figure 8-49. As with the 1999 condition, the most pronounced change is a 0.4 m reduction in H_s shoreward of the spur.

Simulations with 2004 and 2029 bathymetry

The range of hydrodynamic conditions (96 combinations of tide, wave direction, wave height, and wave period) was run on the predicted post-project 2004 and 2029 bathymetries. Figures 8-50 through 8-53 illustrate the influence of the predicted shoreline position and the predicted bathymetry response on circulation and bypassing currents.

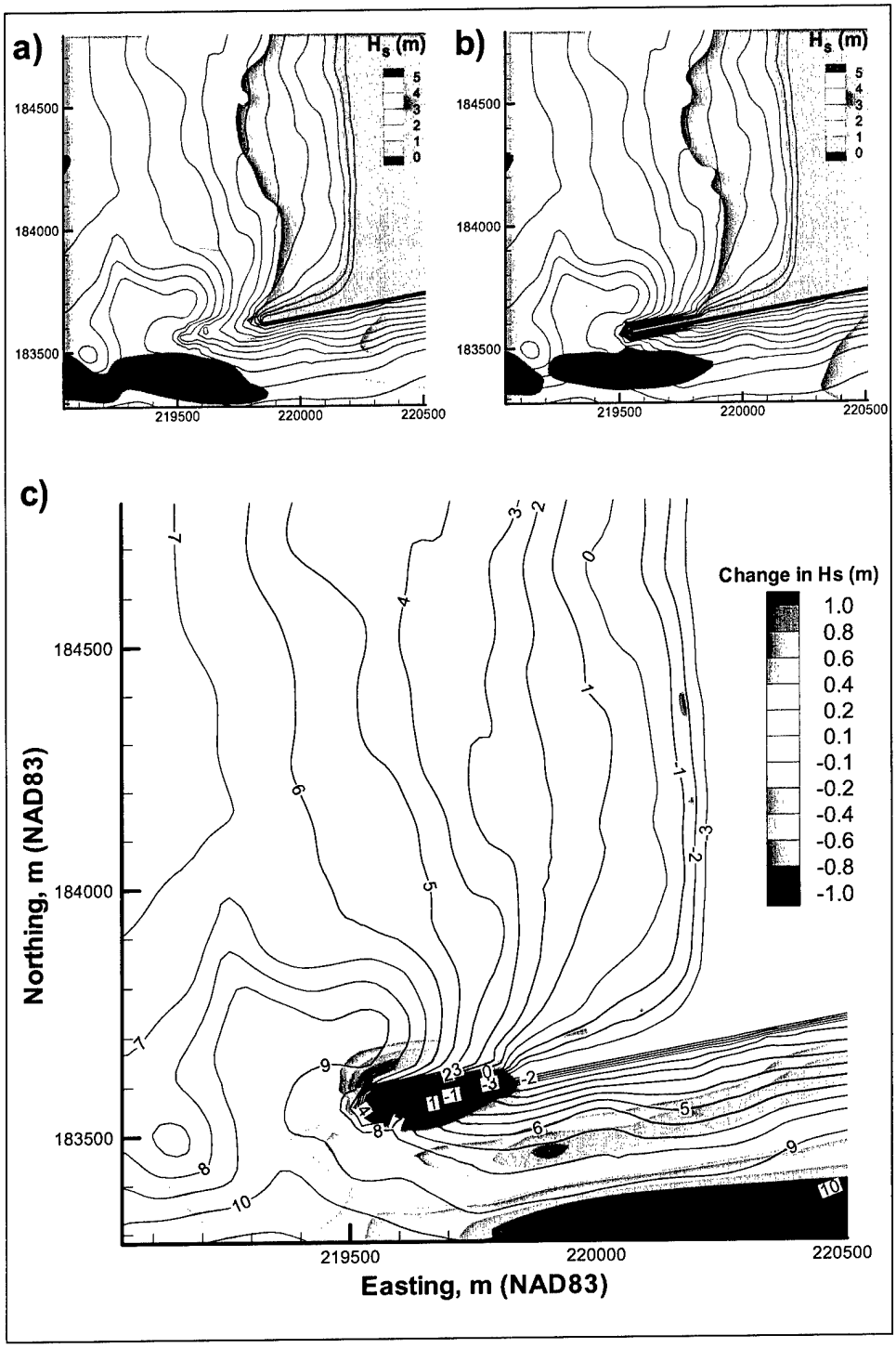

Figure 8-43. Results for waves of H_s = 5 m, T_p = 13 sec from azimuth 300 deg for peak flood: (a) H_s for existing condition, (b) H_s for Alt 3B, and (c) difference in H_s between Alt 3B and existing condition

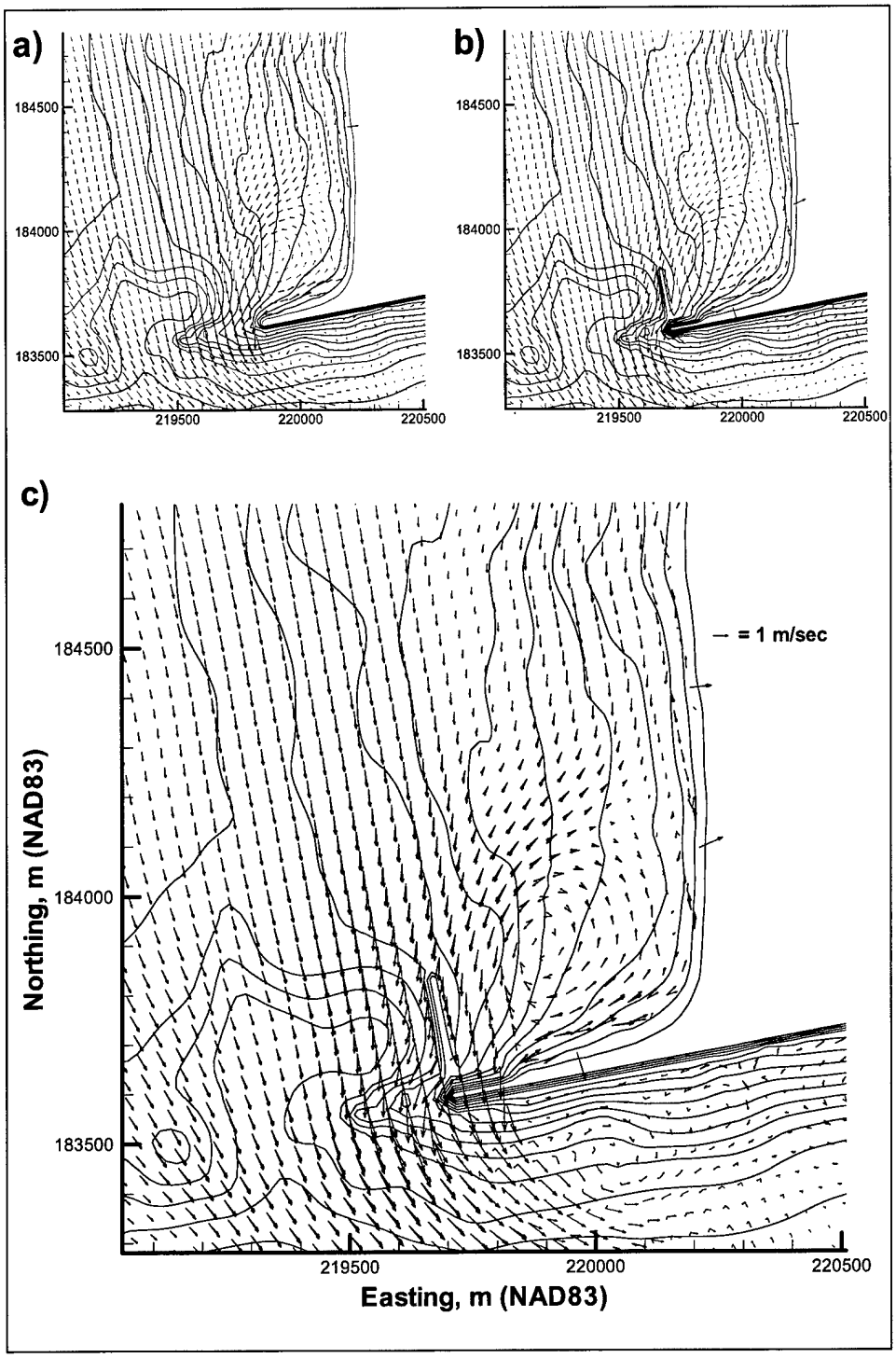

Figure 8-44. Current patterns for H_s = 5 m, T_p = 13 sec from azimuth 300 deg for peak flood: (a) existing condition, (b) Alt 4, and (c) Alt 4 and existing condition

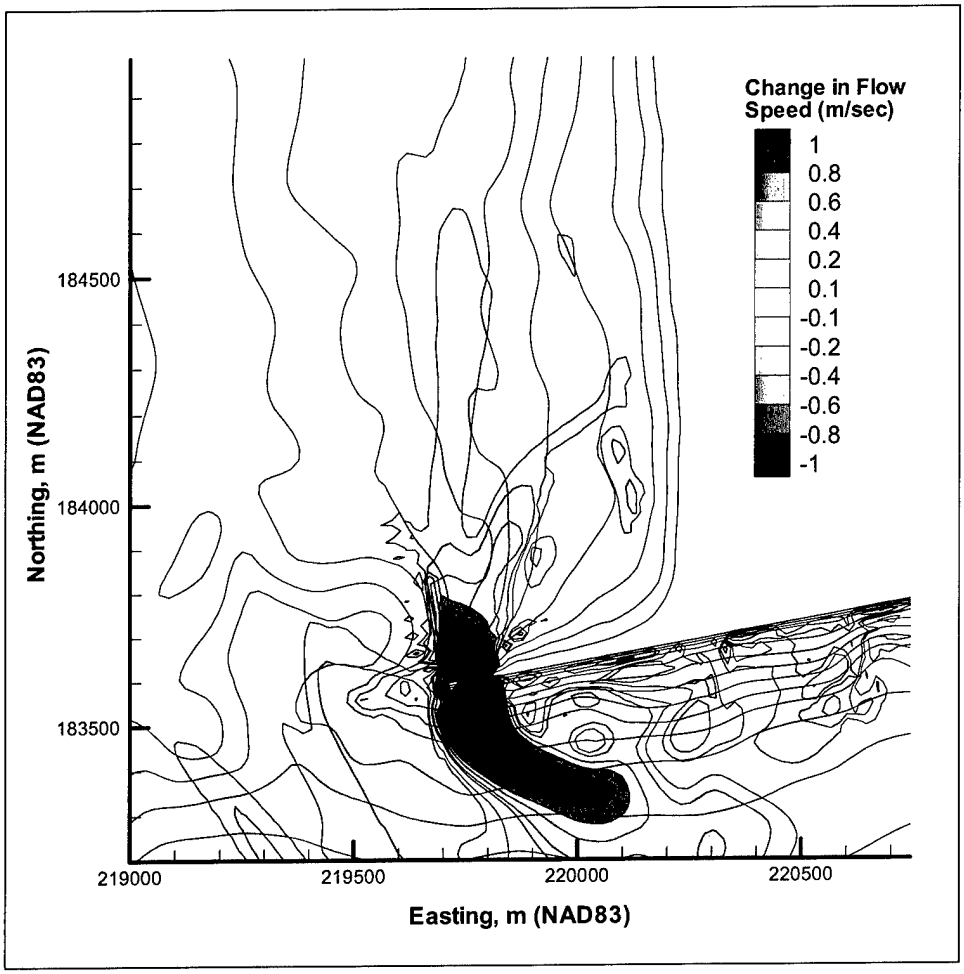

Figure 8-45. Change in current speed between Alt 4 and existing condition for H_s = 5 m, T_p = 13 sec from azimuth 300 deg for peak flood

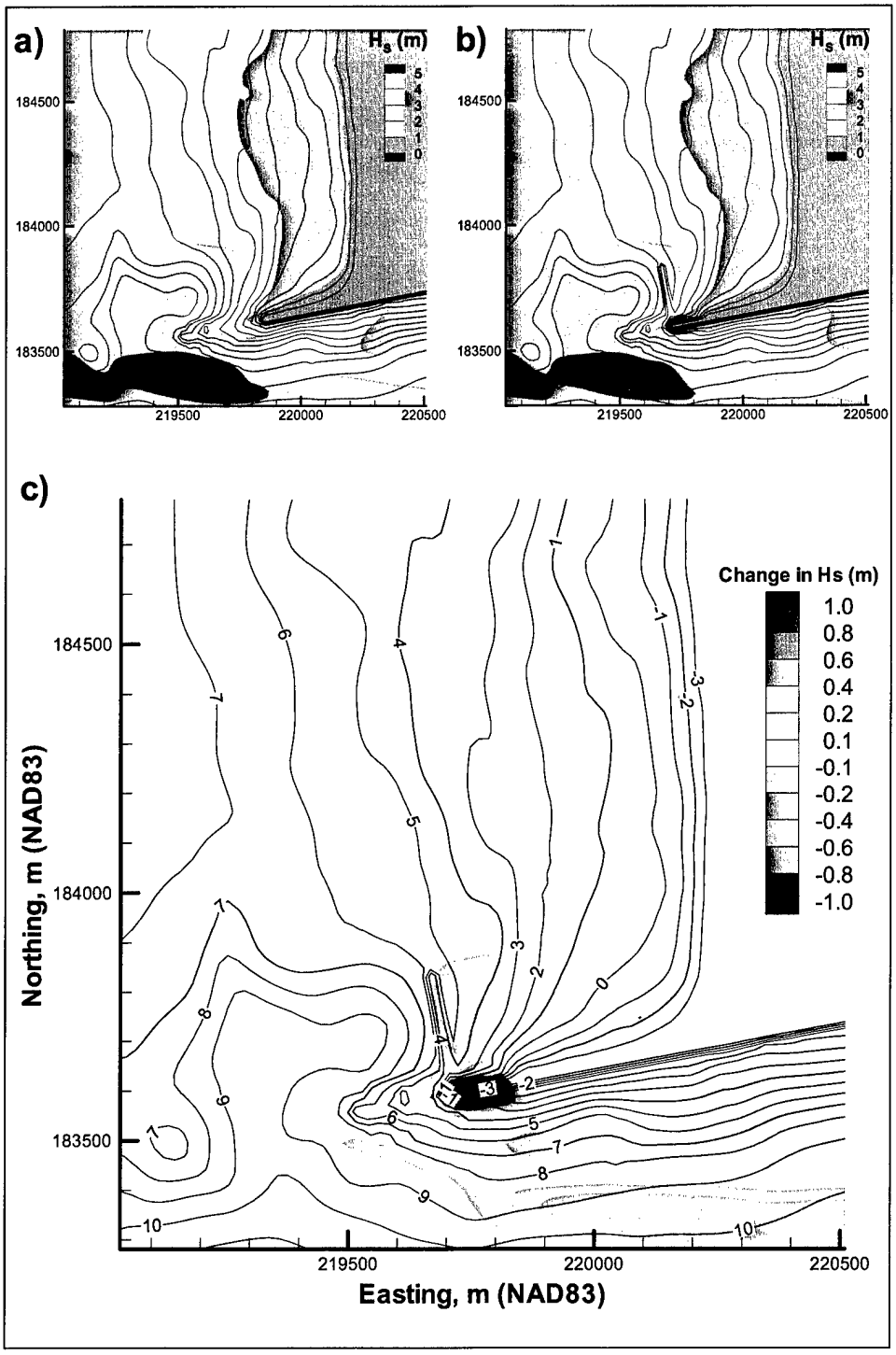

Figure 8-46. Results for waves of H_s = 5 m, T_p = 13 sec from azimuth 300 deg for peak flood: (a) H_s for existing condition, (b) H_s for Alt 4, and (c) difference in H_s between Alt 4 and existing condition

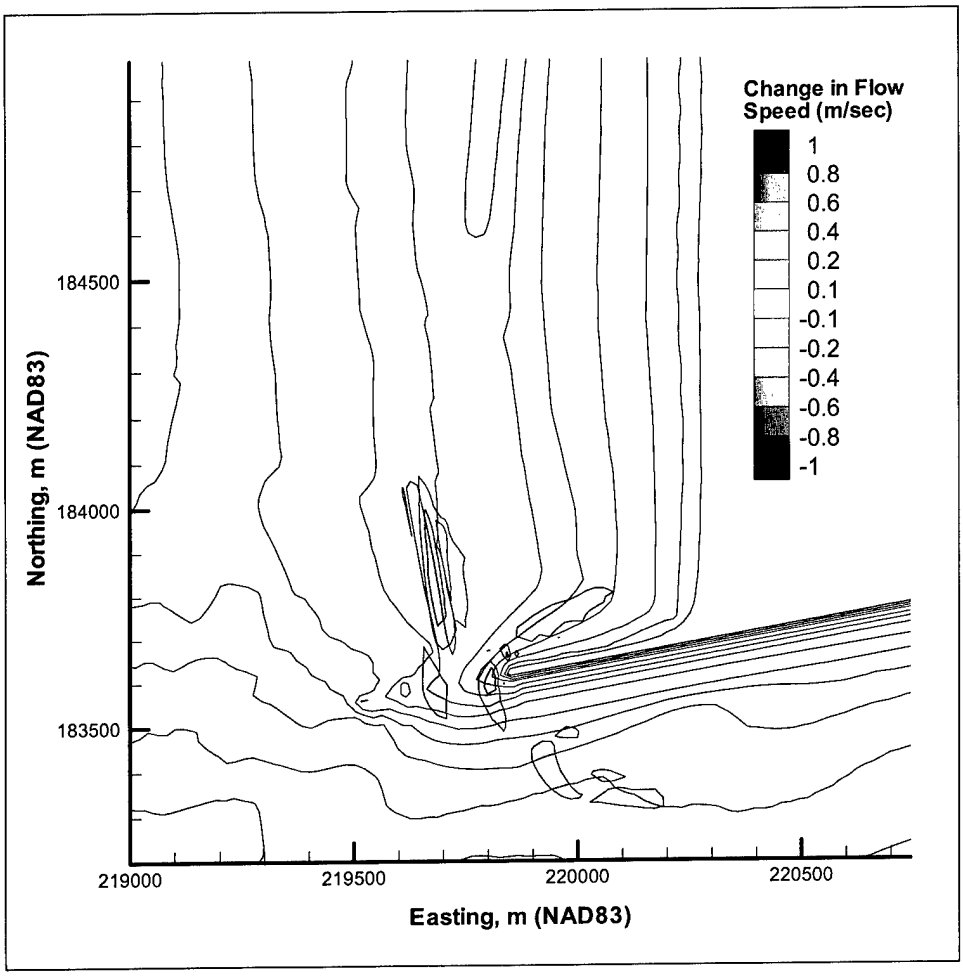

Figure 8-47. Change in current speed between Alt 4 and 2001 conditions for H_s = 5 m, T_p = 13 sec from azimuth 300 deg for peak flood

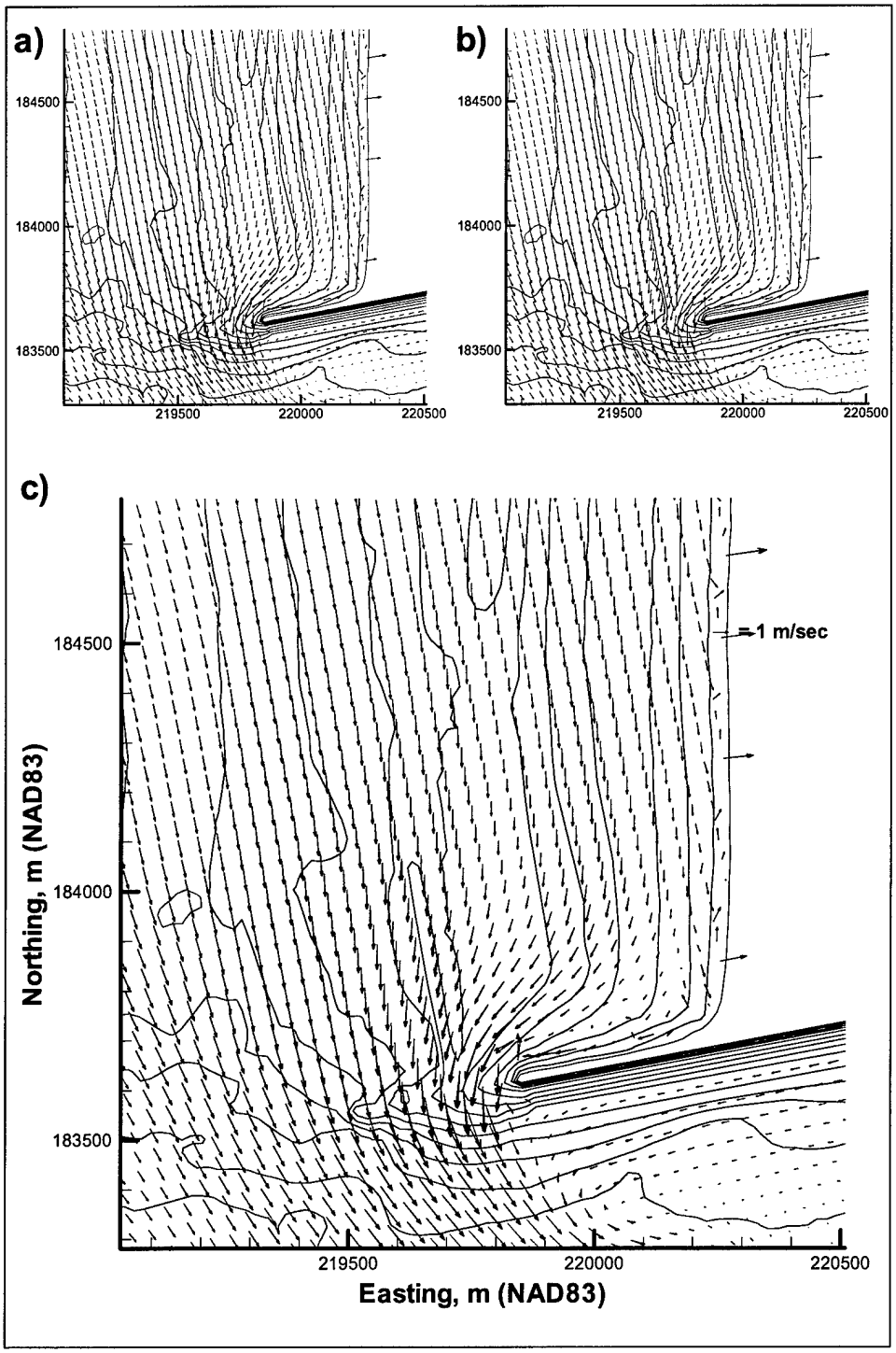

Figure 8-48. Current patterns for H_s = 5 m, T_p = 3 sec from azimuth 300 deg for peak flood: (a) 2001 conditions, (b) Alt 2A, and (c) Alt 2A and 2001 conditions

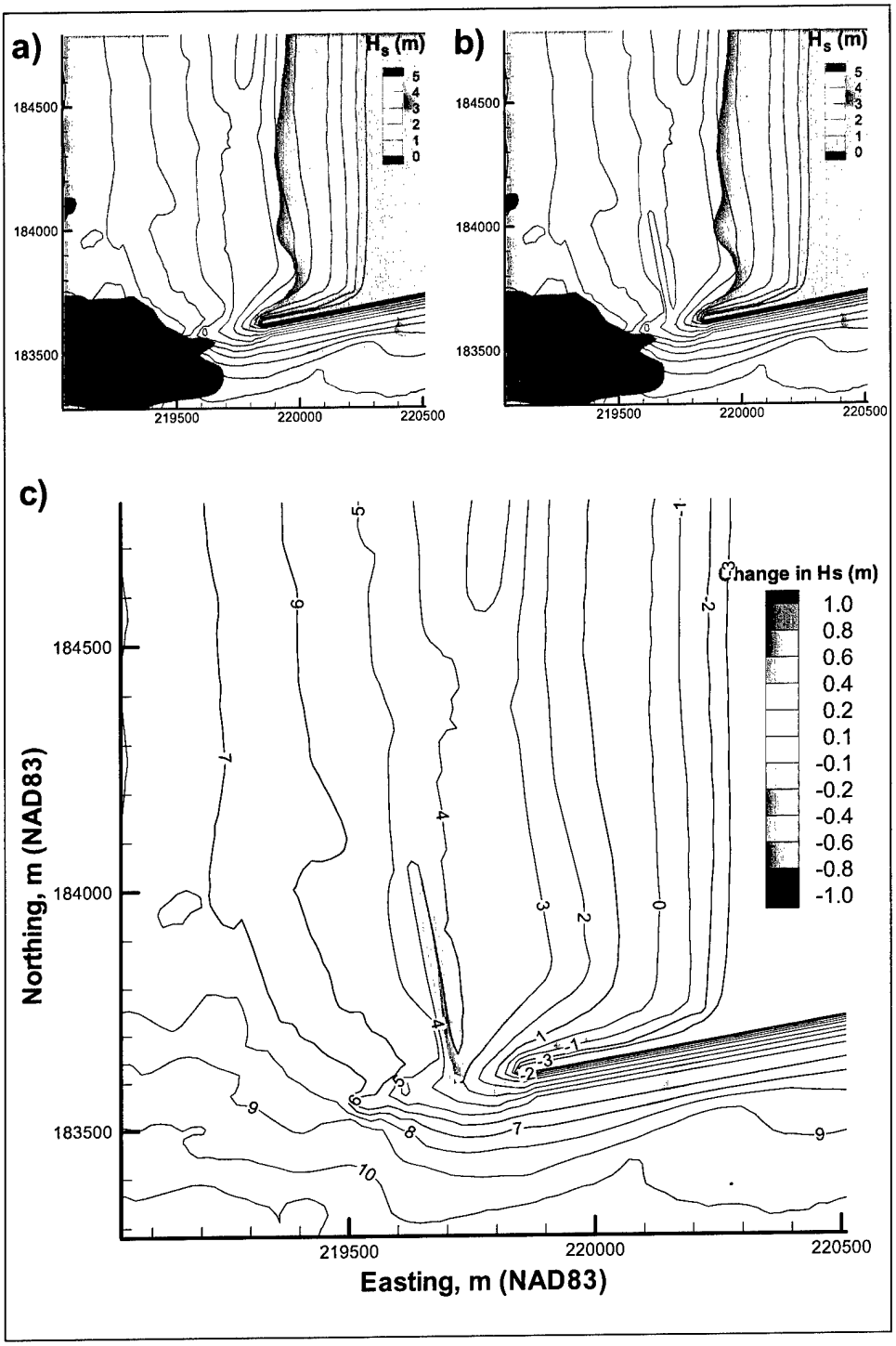

Figure 8-49. Results for waves of H_s = 5 m, T_p = 13 sec from azimuth 300 deg for peak flood: (a) H_s for 2001 conditions, (b) H_s for Alt 2A, and (c) difference in H_s between Alt 2A and 2001 conditions

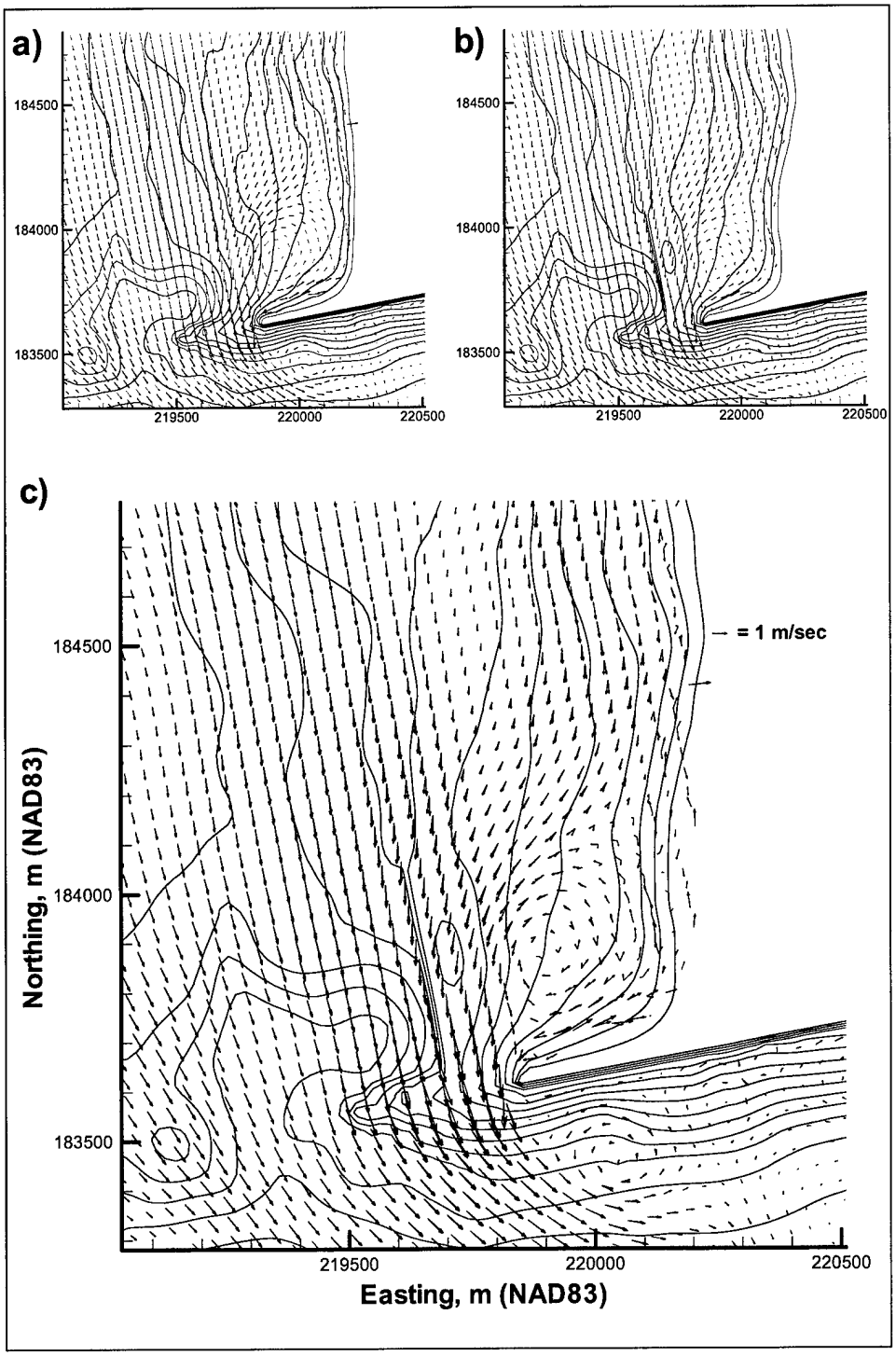

Figure 8-50. Current patterns for H_s = 5 m, T_p = 13 sec from azimuth 300 deg for peak flood: (a) 1999 existing condition, (b) 2004 with Alt 2A, and (c) both

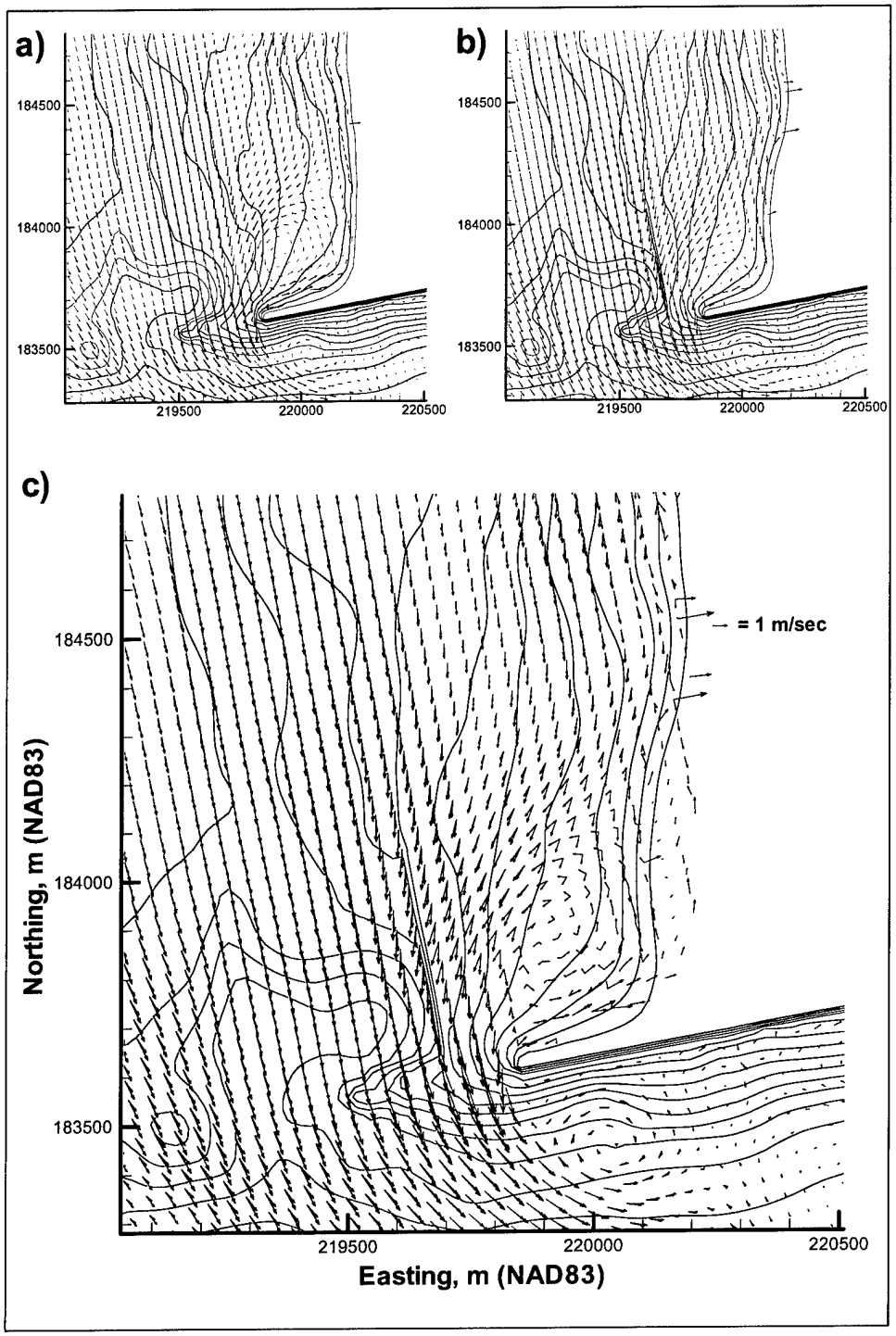

Figure 8-51. Current patterns for H_s = 5 m, T_p = 13 sec from azimuth 300 deg for peak flood: (a) 1999 existing condition, (b) 2029 with Alt 2A, and (c) both

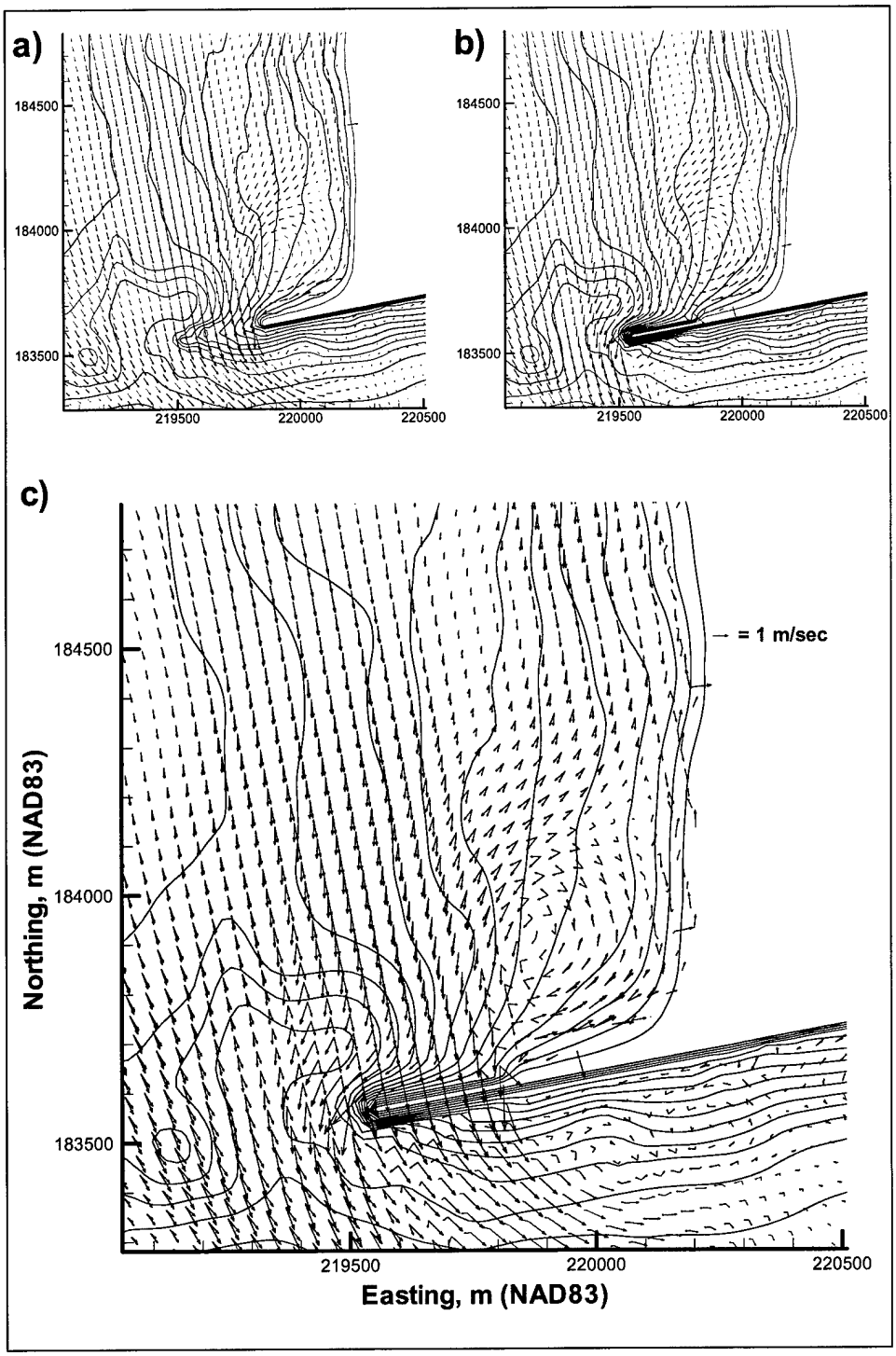

Figure 8-52. Current patterns for H_s = 5 m, T_p = 13 sec from azimuth 300 deg for peak flood: (a) 1999 existing condition, (b) 2004 with Alt 3B, and (c) both

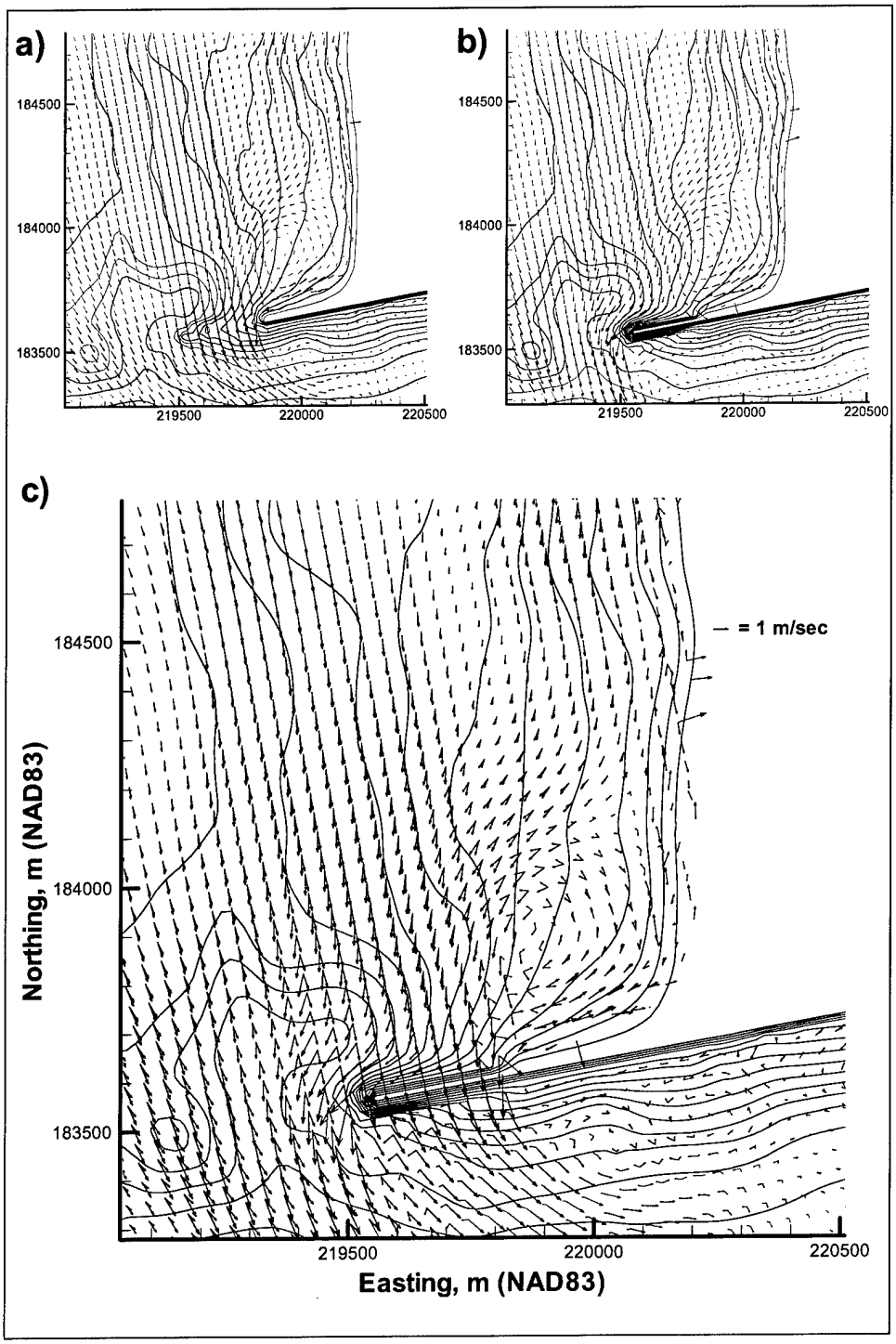

Figure 8-53. Current patterns for H_s = 5 m, T_p = 13 sec from azimuth 300 deg for peak flood: (a) 1999 existing condition, (b) 2029 with Alt 3B, and (c) both

Results of the modified bathymetries for Alt 2A are shown in Figures 8-50 and 8-51, comparing current vectors predicted for existing condition (1999 bathymetry) and the predicted bathymetries for Alt 2A immediately after 5 and 30 years (2004 and 2029 bathymetries, respectively). For the 2004 and 2029 bathymetries, the gyre adjacent to the north jetty becomes smaller, and its center shifts to the southeast, closer to the intersection point of the shore and the jetty.

Calculated modifications of the current for post-project bathymetries for Alt 3B are shown in Figures 8-51 and 8-52. Each compares current vectors predicted for the existing condition (1999 bathymetry) and the predicted bathymetries for Alt 3B after 5 and 30 years (2004 and 2029 bathymetries, respectively). For the 2004 and 2029 bathymetries, the gyre remains unchanged as the shoreline builds seaward.

In both cases, the calculated current patterns do not change significantly over time. The 2004 and 2029 bathymetries were constructed by translation of the 1999 profiles and so tend to preserve the circulation as calculated for the existing condition. The profiles offshore of the spur are identical in the three bathymetries. The reduced distance between the shoreline and the spur could be expected to increase the effectiveness of the spur in reducing flow intensities in its lee; however, it would seem that the overall shape of the shoreline and the orientation of the spur and jetty exert a larger control over circulation patterns than does the distance between the spur and the shoreline.

Annual change in bypassing flow

The results of the simulations can be assessed to determine the expected annual change in current speed by incorporating the frequency of occurrence of each event listed in Table 8-3. Because the results are being assessed to determine the impact of the alternatives on sediment bypassing into the inlet, the data set was reduced to include only those cases that contribute significantly to southward transport. Therefore, the results for waves from 210 and 250 deg were not included in this analysis.

The results for Alt 2A are shown in Figure 8-54, depicting the average current speed for waves from 280 and 300 deg: (a) the 1999 existing condition in the upper left-hand corner plot, (b) Alt 2A in the upper right-hand corner plot, and (c) the difference between the two configurations (Alt 2A minus existing condition) in the lower plot. There is a reduction in average current speed of between 8 to 12 percent over much of the area in the lee of the spur and a smaller area of increased current 4 to 12 percent on the seaward side. This reduction in average current speed is expected to lead to sediment deposition in the area behind the spur. As shown in Figure 8-54(a), the average current speed in this region is about 0.3 m/sec.

The changes in flow conditions were used to compute changes in the potential sediment transport rate. The potential sediment transport rate q_s is the rate predicted by van Rijn's (1993) equations under assumptions of steady-state equilibrium transport conditions. The actual transport rates at any point in the

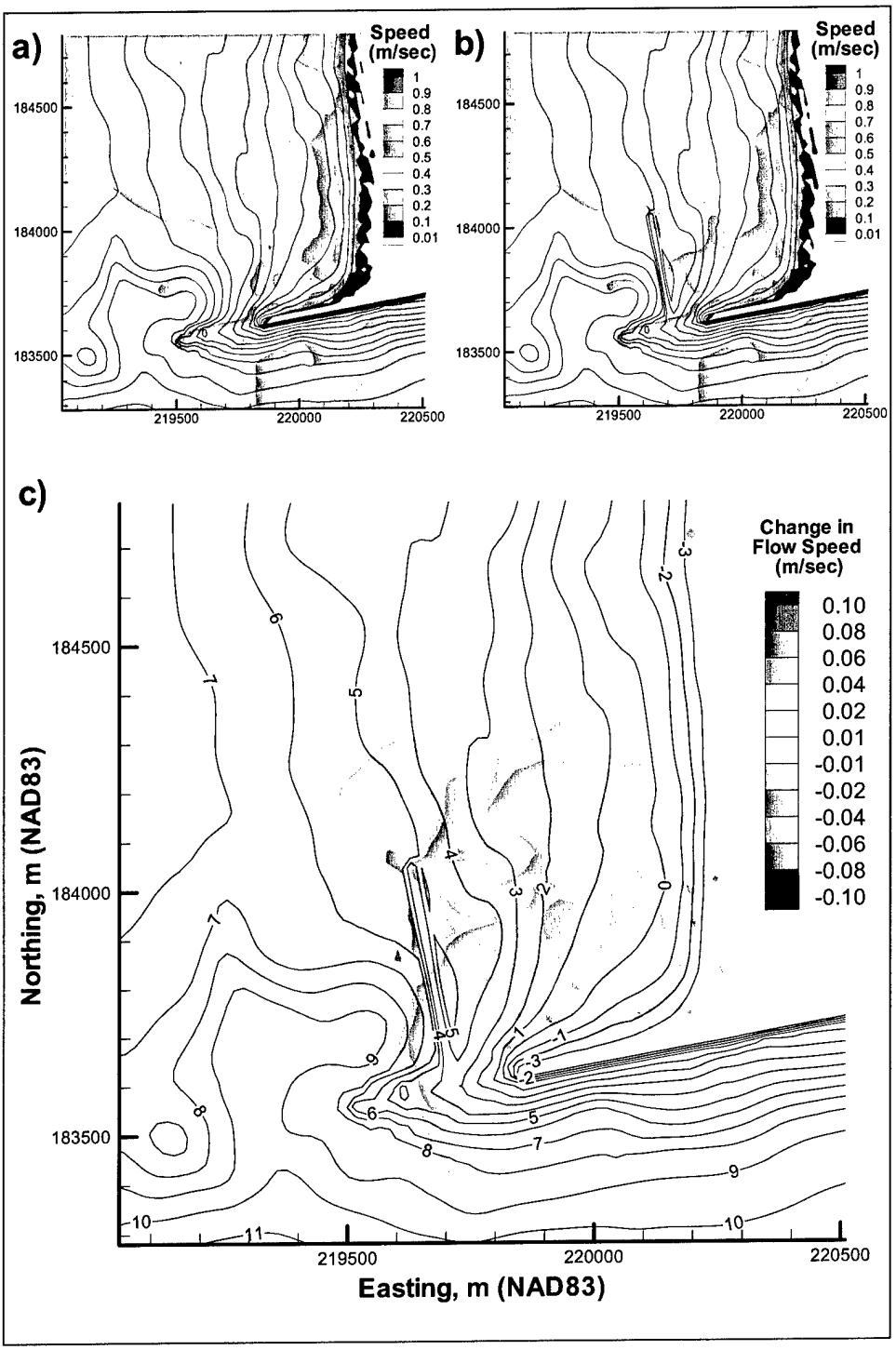

Figure 8-54. (a) Average current speed for 1999 existing condition, (b) Average current speed for 1999 with Alt 2A, and (c) difference in average current speed between Alt 2A and 1999 existing condition

domain are a function of the potential sediment transport rate and the flux of sediment being carried toward that point by the flow, by the rate at which sediment is entrained from the bed, and by the rate at which sediment settles onto the bed. A full sediment transport model is required to estimate these actual transport rates; however, such modeling was beyond the scope of the present study. Consequently, a simplified approach of calculating only the potential sediment transport rates was undertaken.

Figure 8-55 shows the average current speeds for Alt 2B. The pattern is similar to that of Alt 2A, but the differences occur in a smaller area consistent with the expected influence of the shorter spur.

Alternative 3A causes a large change in average current speed (Figure 8-56). The rehabilitation of the jetty increases current speed in the same area where the spur was seen to decrease current speed. These increases are between 1 and 8 percent. The extension of the jetty causes the southward bypassing current to shift offshore. This shift leads to a 16 to 20 percent reduction in annual average flow speed in the direct vicinity of the jetty extension, and a corresponding increase in flow speed further offshore. The flow depth is larger in this area, so this increase is only 4 to 8 percent. Because of an offshore shift in flow patterns, there is a general decrease in flow speed in the northern part of the model domain.

The pattern found for Alt 3A is repeated for Alt 3B (Figure 8-57) but with larger magnitude changes. The longer jetty rehabilitation increases average current speed by 8 to 20 percent in the same area where the spur was seen to decrease current speed. The extension of the jetty causes the southward bypassing current to shift offshore. This shift leads to a 16 to 20 percent reduction in annual average flow speed in the direct vicinity of the jetty extension, and a corresponding increase of 16 to 20 percent in flow speed further offshore. Because of an offshore shift in flow patterns, there is a general decrease in flow speed in the northern part of the model domain.

The result for the combination of a short spur and a short jetty rehabilitation (Alt 4) is shown in Figure 8-58. It is evident that the jetty rehabilitation dominates over the effect of the spur in causing overall changes in average speed. The patterns of change are similar to those for Alt 3B; however, the magnitude of the increase in average current speed for Alt 4 seems inconsistent with the results for Alts 2B and 3A.

Calculated currents for Alt 2A with the 2001 bathymetry are shown in Figure 8-59. The general pattern is similar to that for the 1999 bathymetry, although the magnitudes of the differences are smaller. The 1999 bathymetry showed reductions in flow speed landward of the spur of 8 to 12 percent, whereas the changes with the 2001 bathymetry are 4 to 10 percent.

Because of the large spatial shifts in flow patterns that occur with the predicted 2004 and 2029 bathymetries, the difference results are not readily analyzed. Therefore, this approach was not continued with results from the 2004 and 2029 bathymetry cases.

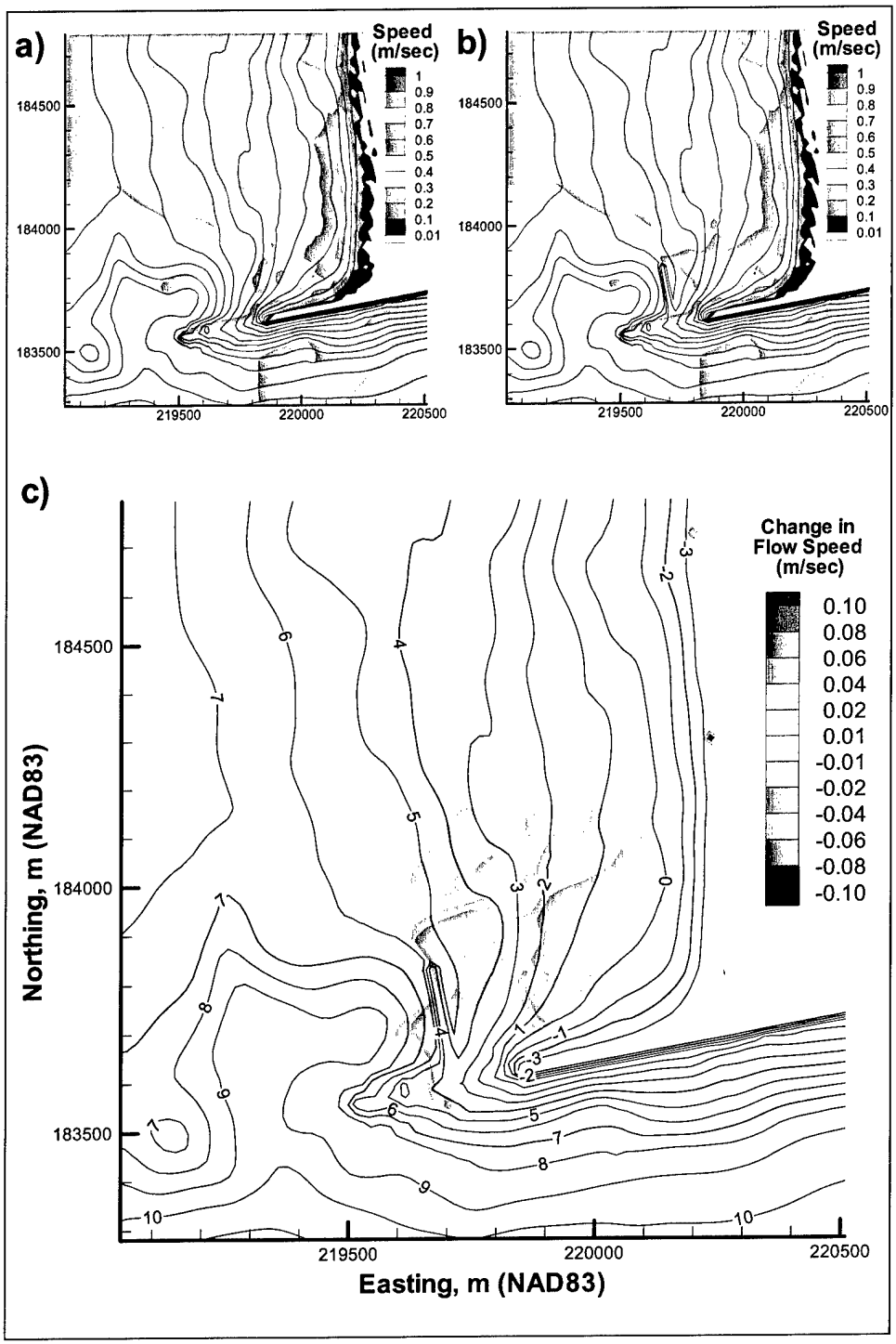

Figure 8-55. (a) Average current speed for 1999 existing condition, (b) average current speed for 1999 with Alt 2B, and (c) difference in average current speed between Alt 2B and 1999 existing condition

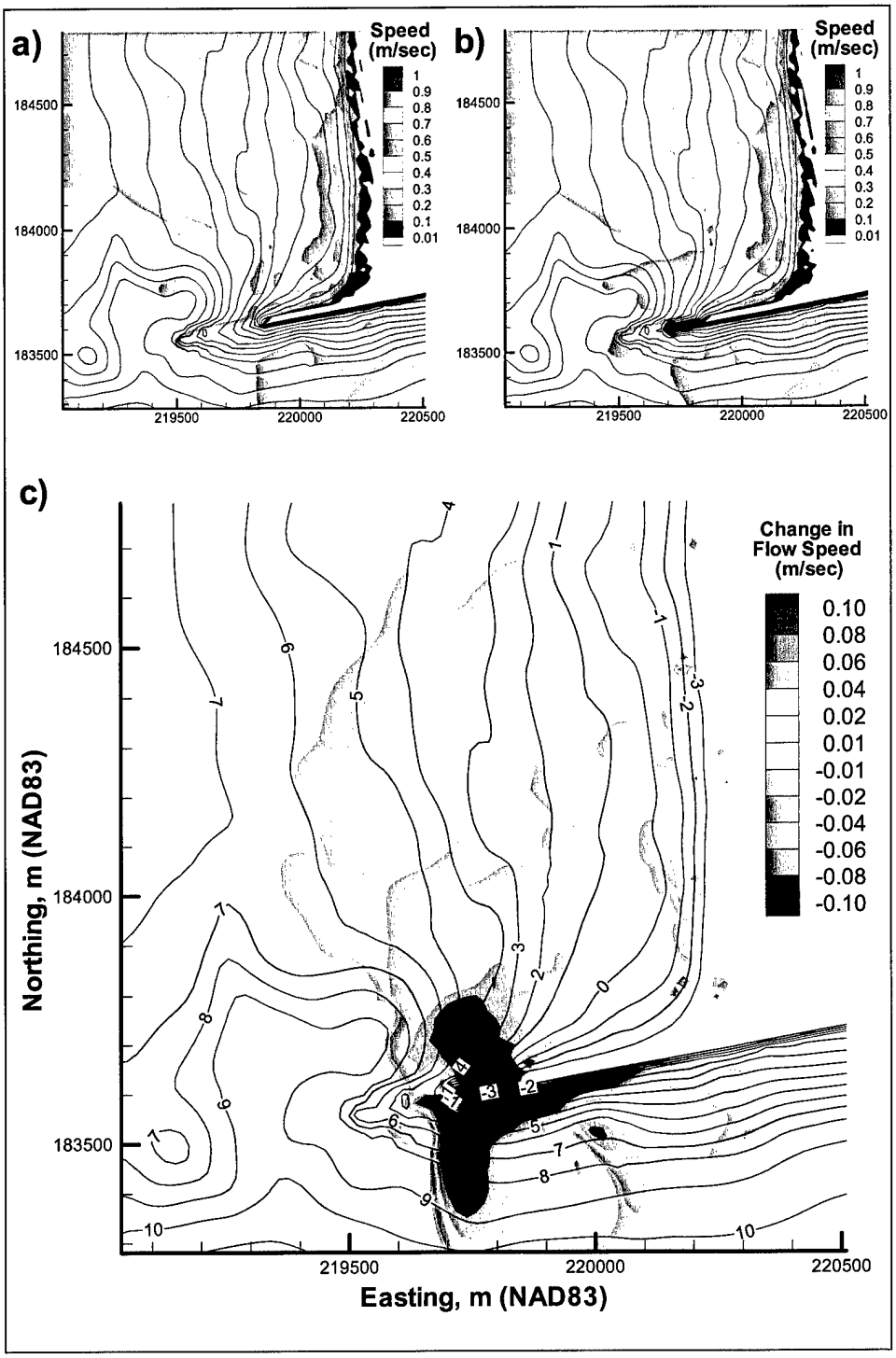

Figure 8-56. (a) Average current speed for 1999 existing condition, (b) average current speed for 1999 with Alt 3A, and (c) difference in average current speed between Alt 3A and 1999 existing condition

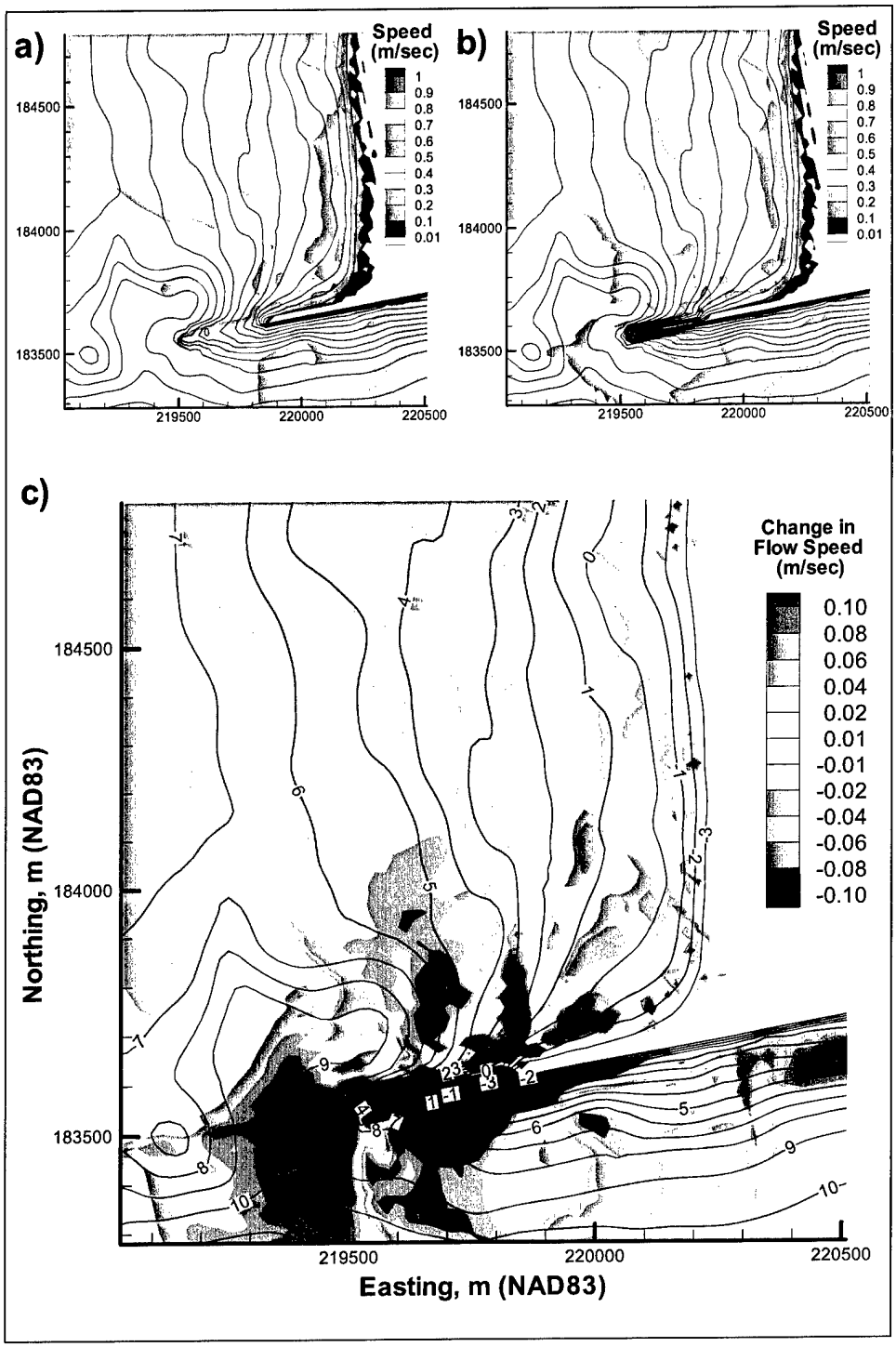

Figure 8-57. (a) Average current speed for 1999 existing condition, (b) average current speed for 1999 with Alt 3B, and (c) difference in average current speed between Alt 3B and 1999 existing condition

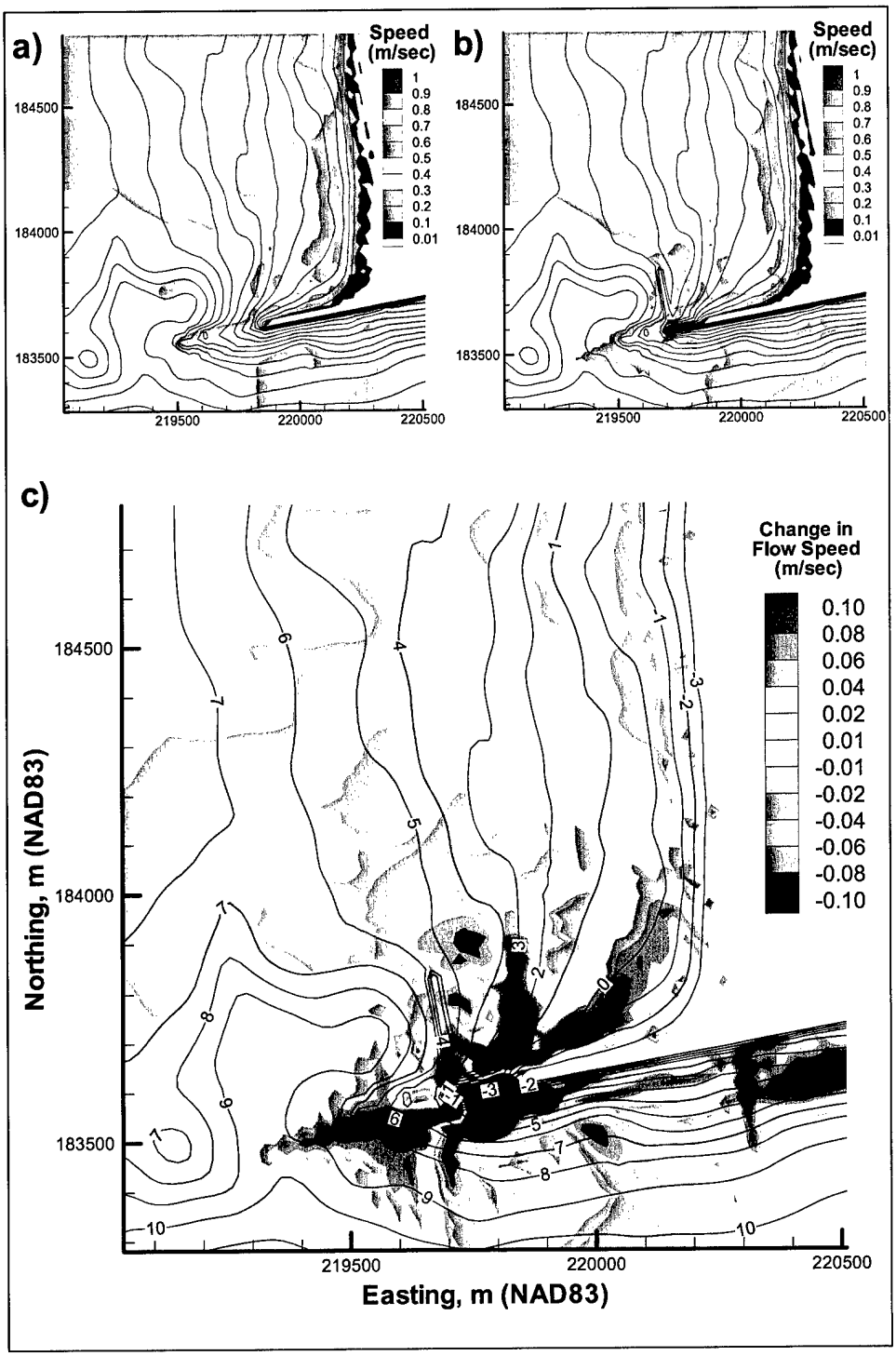

Figure 8-58. (a) Average current speed for 1999 existing conditions, (b) average current speed for 1999 with Alt 4, and (c) difference in average current speed between Alt 4 and 1999 existing condition

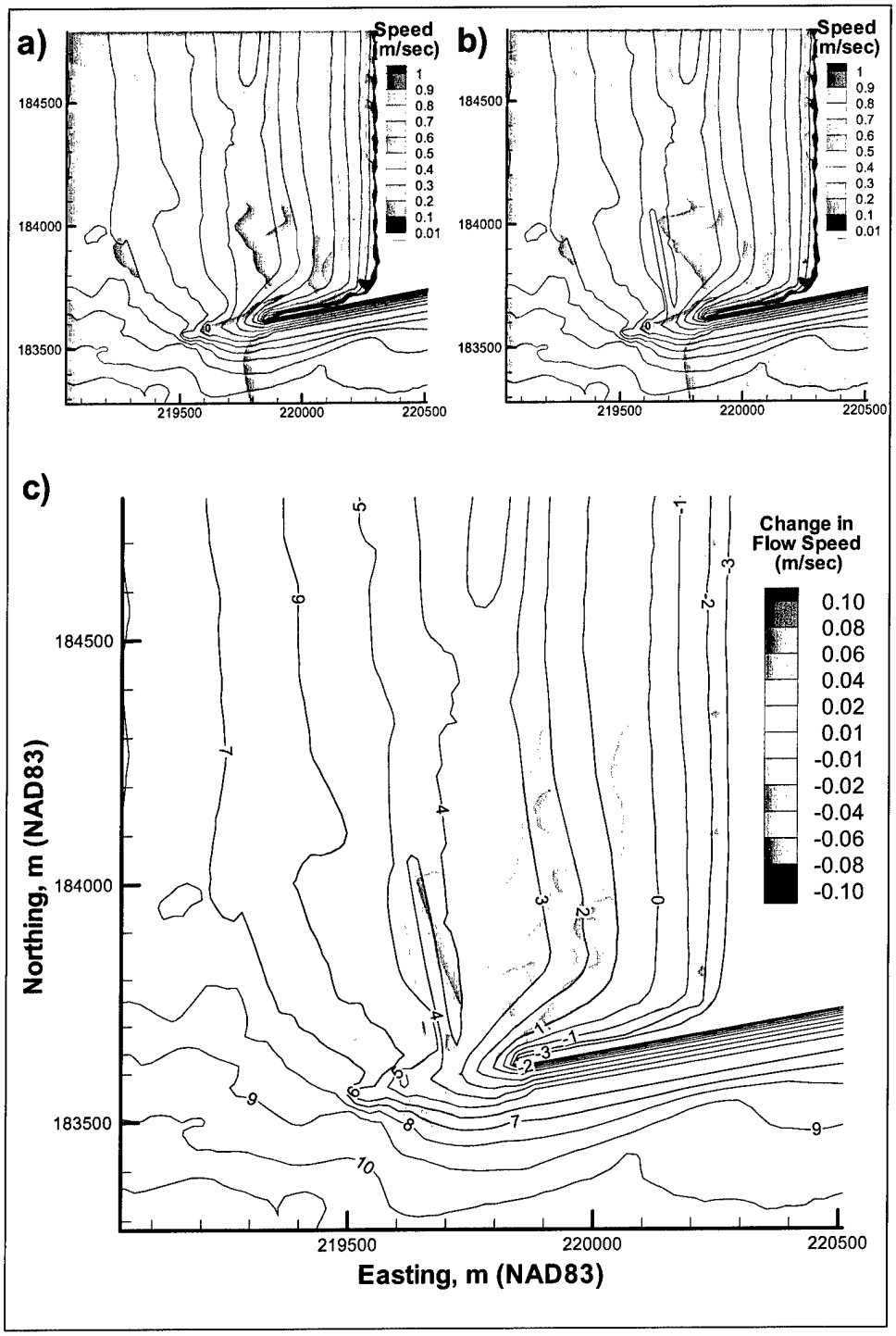

Figure 8-59. (a) Average current speed for 2001 existing condition, (b) average current speed for 2001 with Alt 2A, and (c) difference in average current speed between Alt 2A and 2001 existing condition

The results from the analysis for the 1999 and 2001 bathymetries indicates that construction of any of the alternatives under evaluation will decrease the average current speed near the north jetty, enhance the likelihood of sediment accretion in the area to the north of the north jetty, and consequently decrease sediment bypassing the north jetty into the inlet. It should be noted here that these calculations do not consider morphological feedback; in reality these flow patterns may change over time as the system adjusts to a new morphologic equilibrium.

Sediment transport potential

Sediment transport potential by waves and currents was computed by inputting the wave and current fields calculated by CoastL to the sediment transport algorithm by van Rijn (1993) as described in Appendix H. The sediment transport rate is the sum of both the suspended load and bed load components. This transport potential is the combined predicted sediment load caused by the action of both waves and currents. The direction of sediment transport was taken to be the same as the depth-averaged mean current. The formula is the same as discussed in Chapter 4 to evaluate sediment transport potential from the field measurements, adapted to provide estimates of the sediment transport potential at all nodes of the finite-difference grid. Potential sediment transport rates from a large number of combinations were reduced to an estimate of the annual bypassing sediment transport potential. No estimation of wave-driven mass transport was included in this analysis.

Methodology

The CoastL simulations provided finite-difference grids of water depth, wave height, wave direction, and depth-averaged currents (U and V). This information drove the sediment transport calculations. A median sediment grain size D_{50} of 0.2 mm and 35 percent size D_{35} of 0.16 mm were specified for the sediment transport simulations. These values are based on an analysis of grab samples and bottom sediment traps taken in the vicinity of the north jetty in May 2001. The resulting output is a grid of the potential sediment transport rate at each node (expressed as q_s-East and q_s-North). The units of sediment transport are kg/m/sec.

Evaluation of alternatives

Maps of transport potentials q_s for each alternative on the 1999 bathymetry are presented in comparison to existing condition in Figures 8-60 to 8-64. Here, a run with flood current with 5-m, 13-sec, 300-deg waves is shown as an example for southward bypassing. These plots illustrate the effects of changes in both wave height and current intensity for each alternative. In the following plots, the upper left and right contour maps show potential sediment transport rates for the 1999 existing condition and alternatives, respectively. The main lower plot shows a contour map of the difference in potential sediment transport rate created by

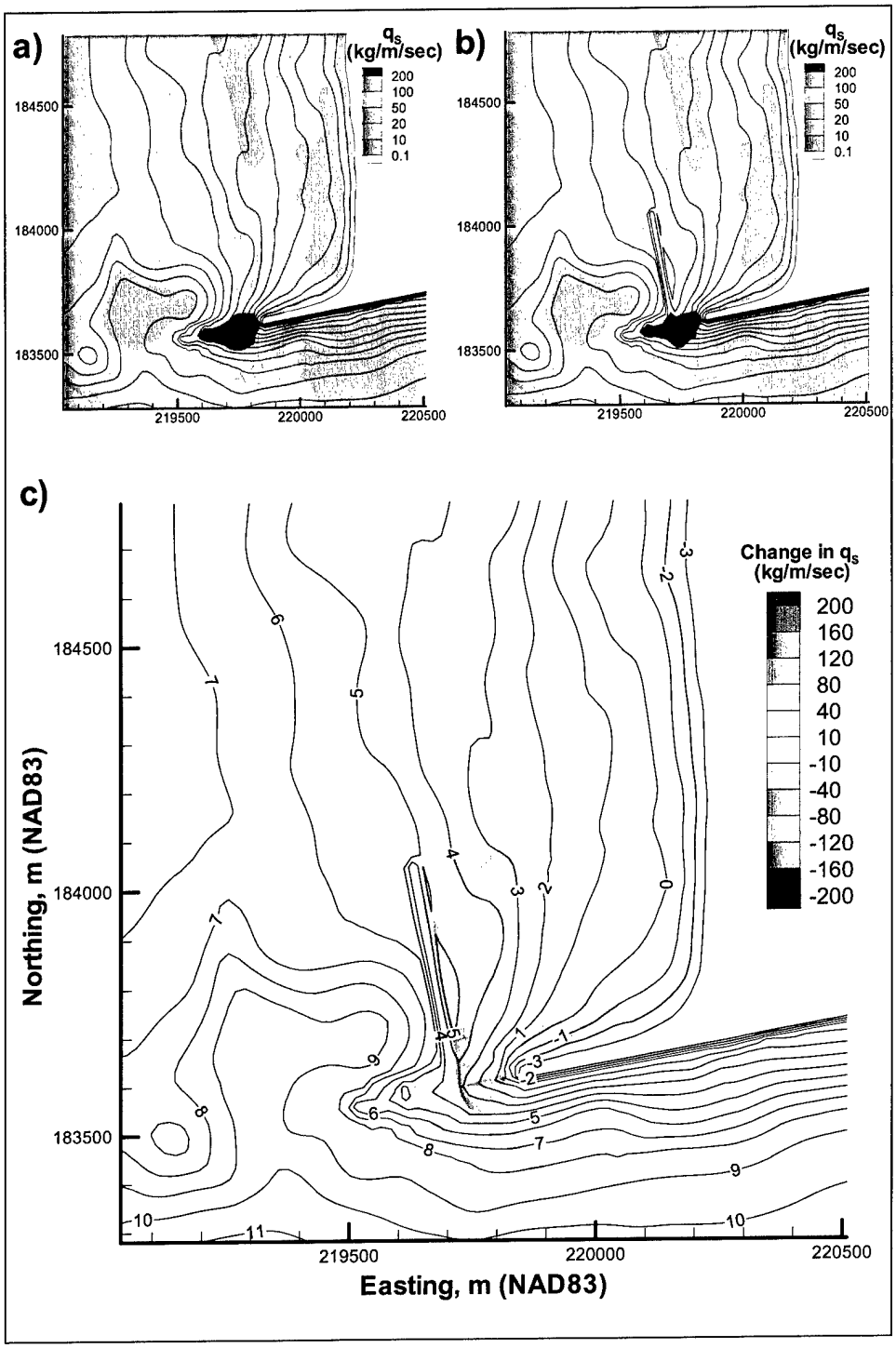

Figure 8-60. Transport potential results for waves of H_s = 5 m, T_p = 13 sec from azimuth 300 deg for peak flood: (a) q_s for 1999 existing condition, (b) q_s for Alt 2A, and (c) difference in q_s between Alt 2A and 1999 existing condition

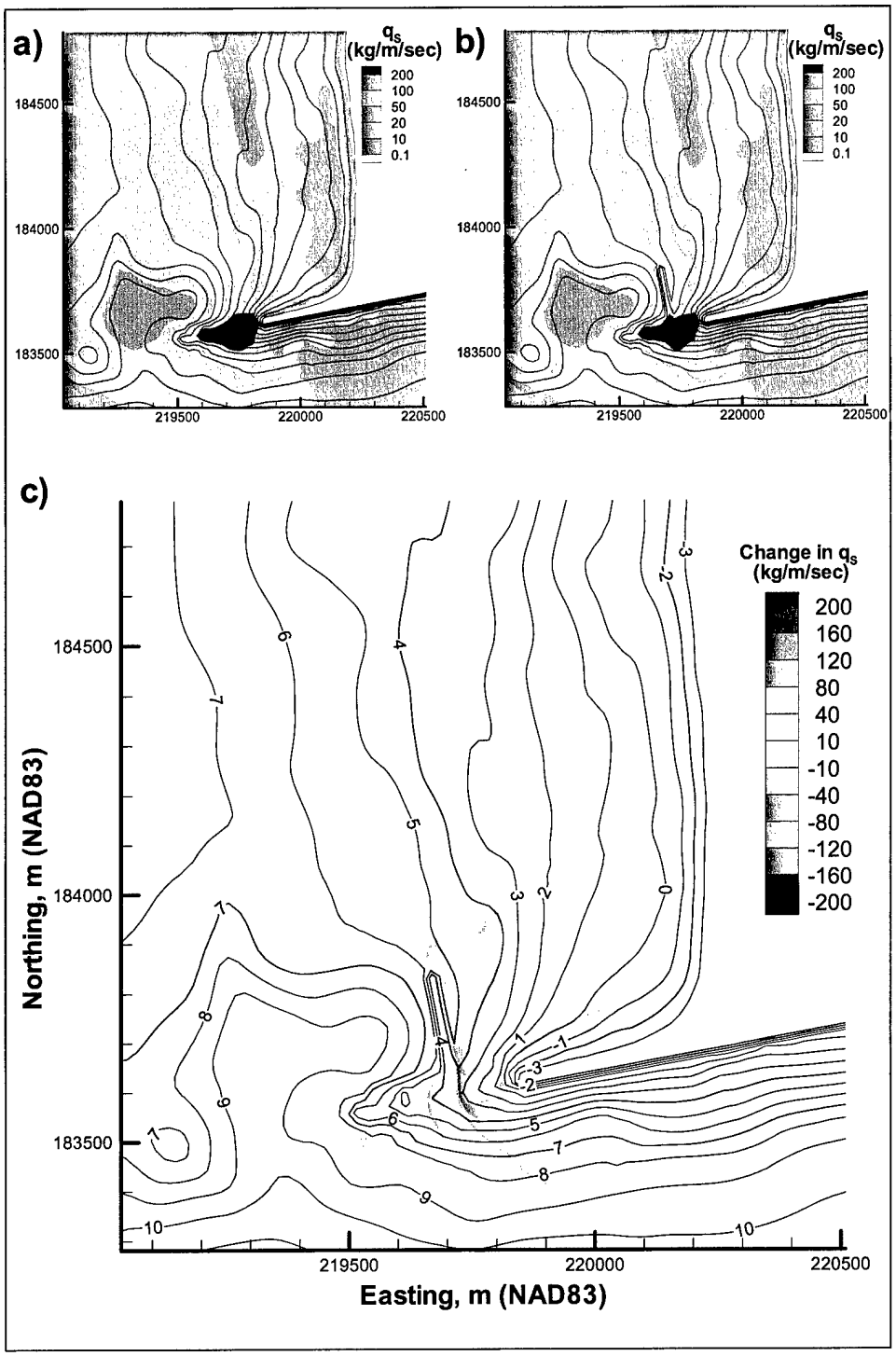

Figure 8-61. Transport potential results for waves of H_s = 5 m, T_p = 13 sec from azimuth 300 deg for peak flood: (a) q_s for 1999 existing condition, (b) q_s for Alt 2B, and (c) difference in q_s between Alt 2B and 1999 existing condition

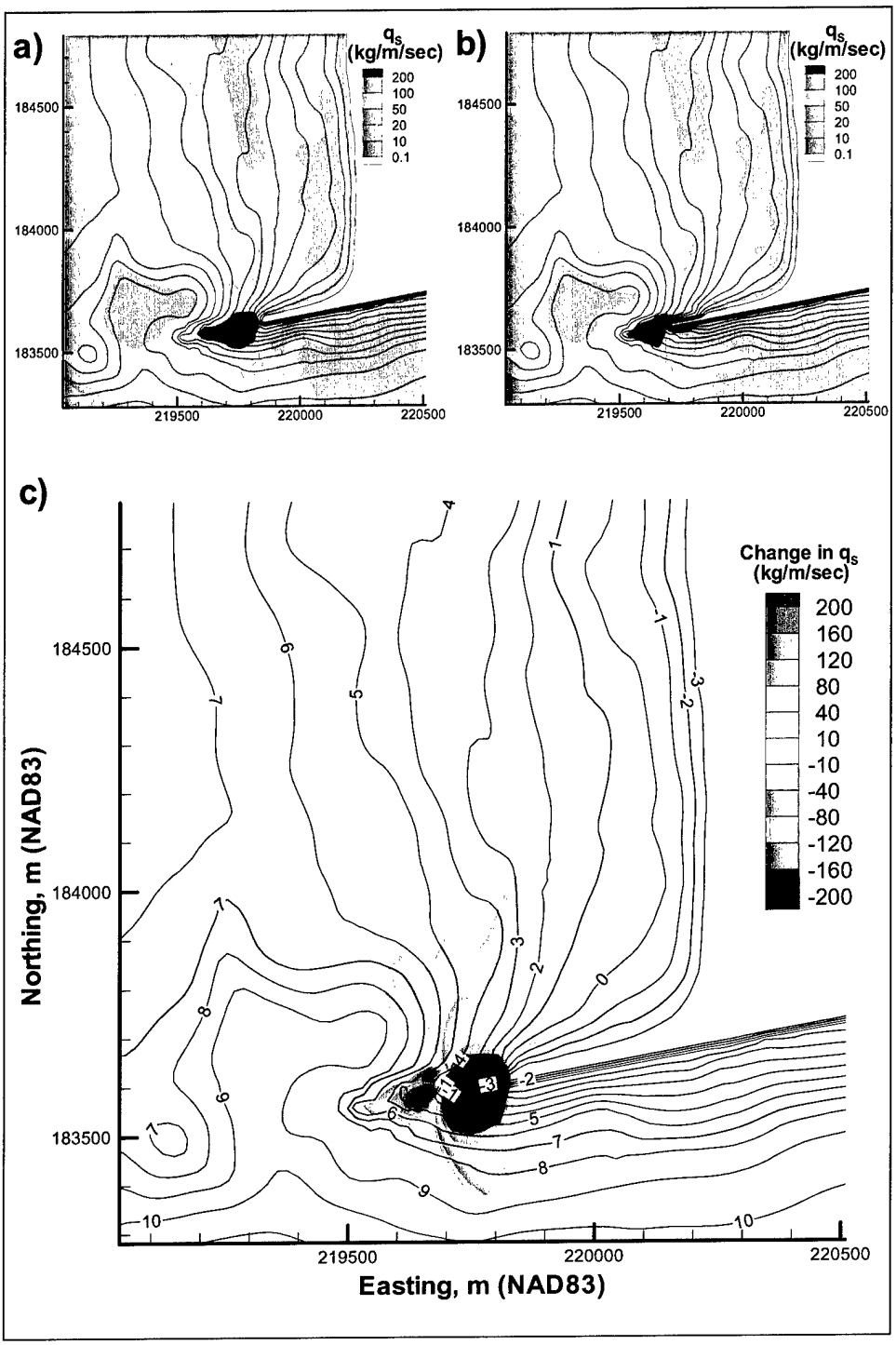

Figure 8-62. Transport potential results for waves of H_s = 5 m, T_p = 13 sec from azimuth 300 deg for peak flood: (a) q_s for 1999 existing conditions, (b) q_s for Alt 3A, and (c) difference in q_s between Alt 3A and 1999 existing condition

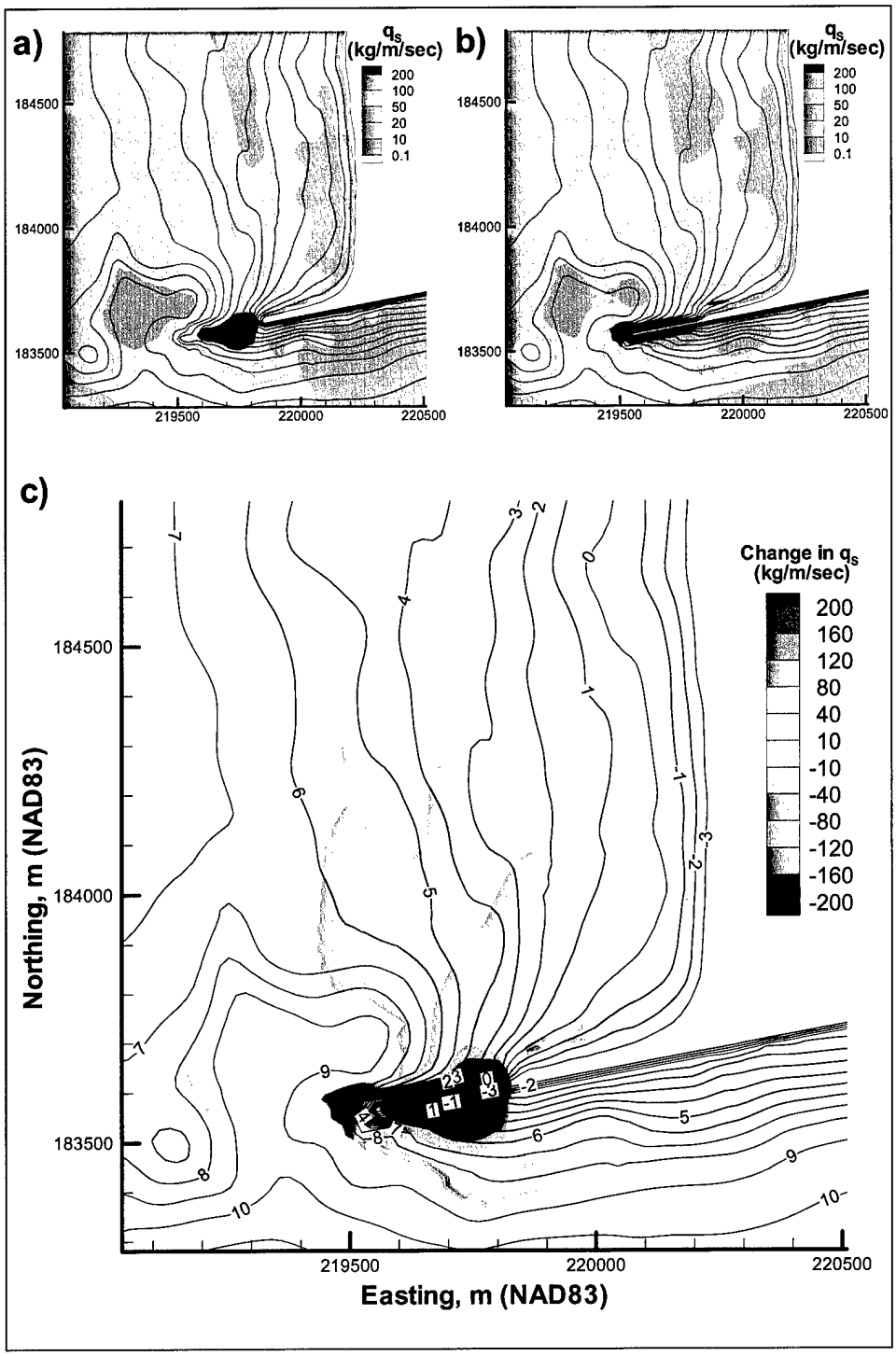

Figure 8-63. Transport potential results for waves of H_s = 5 m, T_p = 13 sec from azimuth 300 deg for peak flood: (a) q_s for 1999 existing condition, (b) q_s for Alt 3B, and (c) difference in q_s between Alt 3B and 1999 existing condition

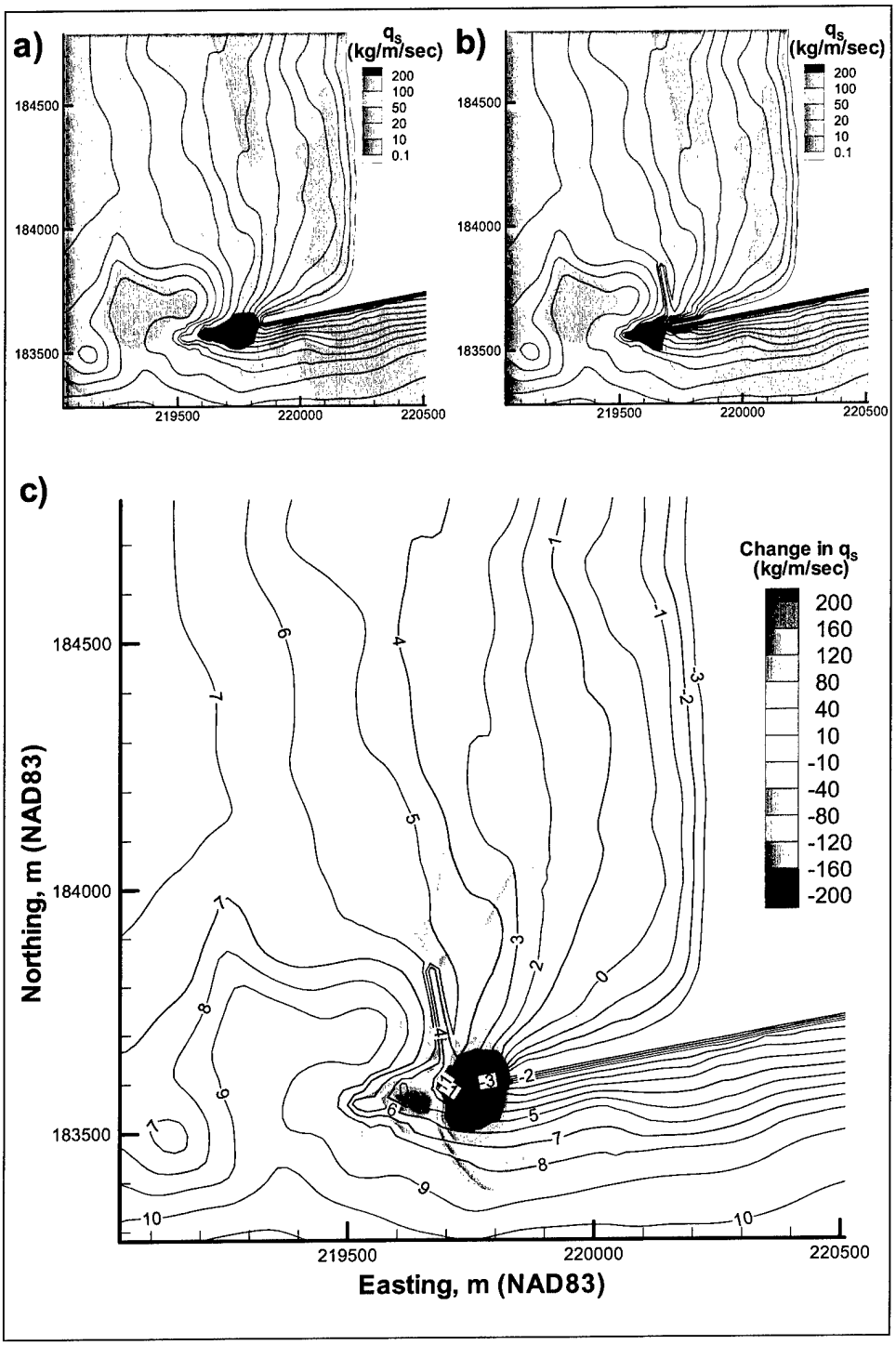

Figure 8-64. Transport potential results for waves of H_s = 5 m, T_p = 13 sec from azimuth 300 deg for peak flood: (a) q_s for 1999 existing condition, (b) q_s for Alt 4, and (c) difference in q_s between Alt 4 and 1999 existing condition

subtracting the potential transport rate for the existing condition from the rate for the alternative under consideration. Hence a positive value in this plot indicates an increase in potential sediment transport rate for the alternative under consideration.

Figure 8-60 shows the difference in q_s for Alt 2A. This plot shows a reduction in sediment transport shoreward of the spur and at the tip of the north jetty. The reduction in q_s at the tip of the jetty is offset somewhat by an increase in q_s to the south of the spur. Figure 8-61 shows the change in q_s for Alt 2B. This pattern is similar to that for Alt 2A with the extent of the reductions in q_s being roughly proportional to the reduced length of the spur.

Figures 8-62 through 8-64 show large differences in the transport rate q_s between the 1999 existing condition and the particular alternative. In most cases, however, this tends to be caused by the presence of the structural alternative (a straightforward result caused by the absence of transport where a structural alternative now exists, or a shift in the location of breaking at the end of a structure as a result of its lengthening). Figure 8-62 shows the change in q_s for Alt 3A. There is a shift in q_s seaward caused by the extension of the jetty (the reduction in q_s at the existing jetty tip is roughly offset by the increase in q_s at the new jetty tip). There is also a general reduction in q_s both to the north and south of the jetty. Figure 8-63 shows the changes in q_s for the longer jetty rehabilitation (Alt 3B). The general patterns are the same as those observed for Alt 3A. There is also an increase in q_s along the north face of the jetty and offshore of the jetty tip. Figure 8-64 shows the combined effects of the short spur and the short jetty rehabilitation (Alt 4). The seaward shift in q_s at the tip of the jetty is similar to that observed for Alt 3A. As was the case for the wave heights and currents, the changes in q_s for Alt 4 have the same characteristics as a superposition of the transport rates for Alts 2B and 3A.

Annual potential transport climate

Applying the estimated annual frequencies of occurrence of each of the hydrodynamic conditions, an annual potential sediment transport climate was computed for each alternative. Figures 8-65 through 8-69 show the potential sediment transport results for the various alternatives and the 1999 existing condition. The patterns of q_s (shown in the upper plots) are similar for all alternatives; sediment transport potential is greatest in the nearshore areas and around the north jetty, primarily caused by the local increase in velocity. In examining the difference plots (the lower plot in Figures 8-65 through 8-69), a distinction should be made between absolute changes (isolated areas of increase or decrease) and shifts (areas of paired increases and decrease, which suggest the translation of a phenomenon, such as around the north jetty in Figures 8-67 through 8-69).

The two spur alternatives (Figures 8-65 and 8-66) produce areas of decreased sediment transport potential in the lee of the spurs. Under the assumption that the 1999 existing condition bathymetry is in equilibrium, the existing rates of sediment supply to this area balance the sediment transported out of this area. The deficit in sediment transport potential caused by the presence of the spur

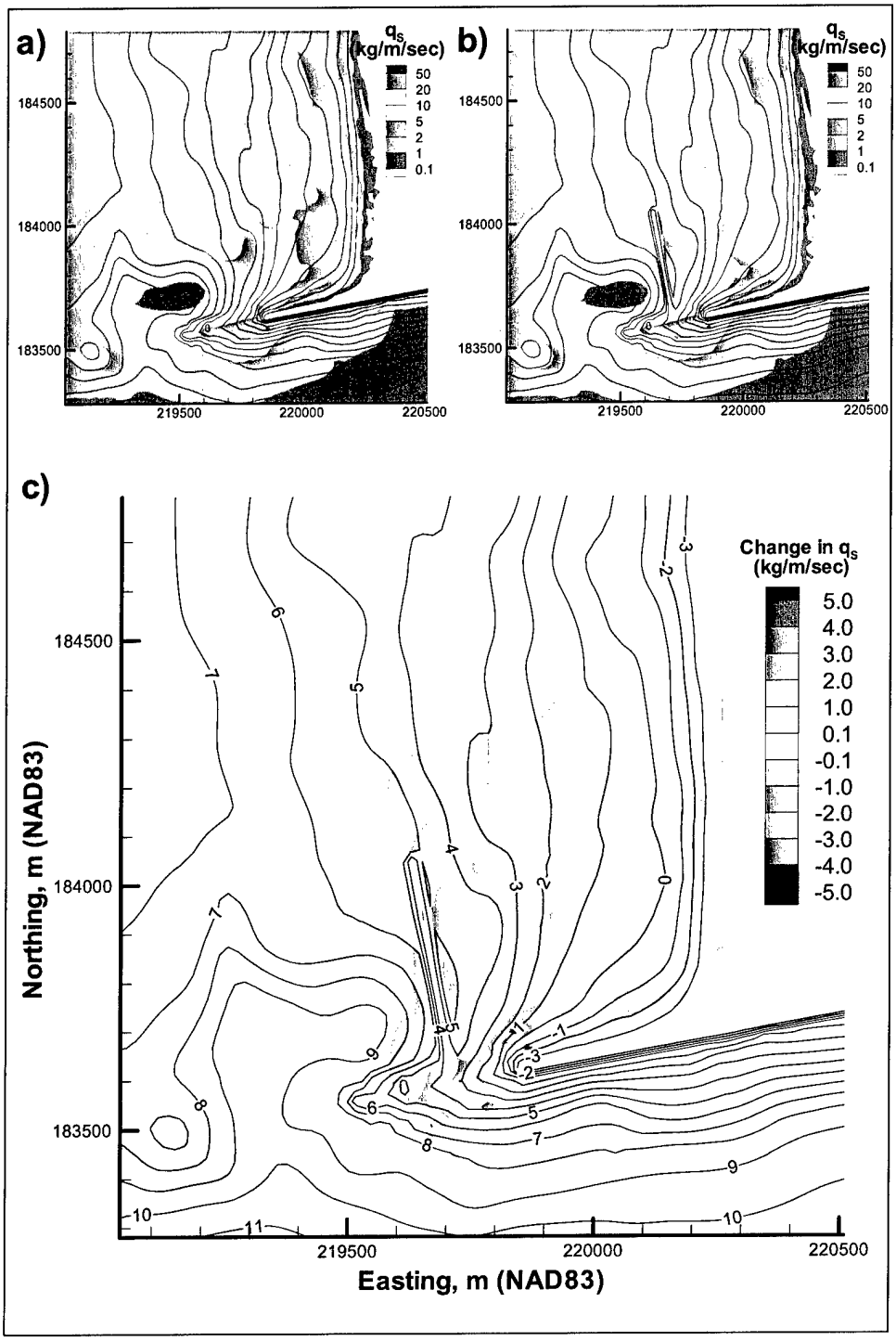

Figure 8-65. Expected annual change in q_s: (a) q_s for 1999 existing condition, (b) q_s for Alt 2A, and (c) difference in q_s between Alt 2A and 1999 existing condition

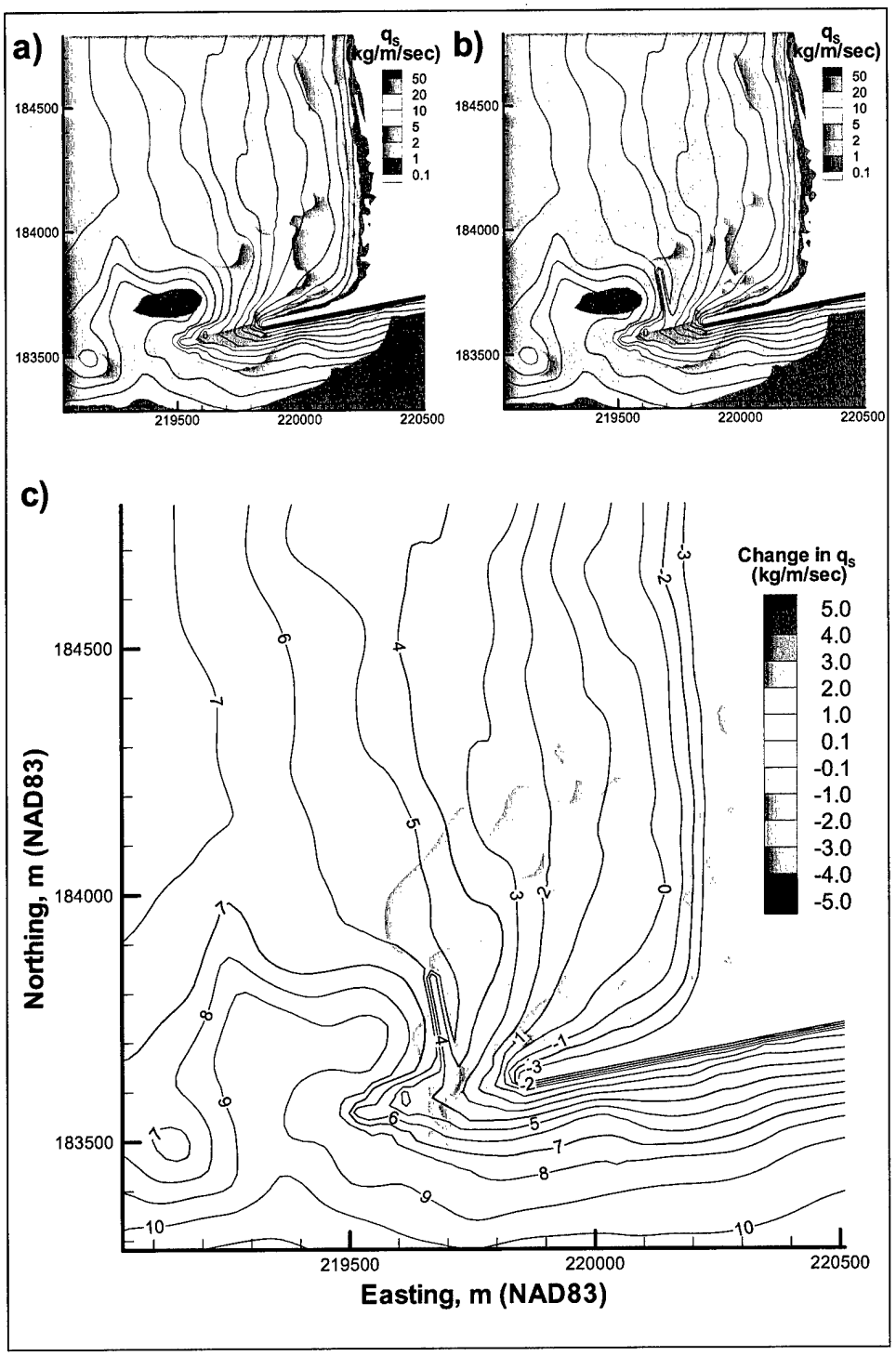

Figure 8-66. Expected annual change in q_s: (a) q_s for 1999 existing condition, (b) q_s for Alt 2B, and (c) difference in q_s between Alt 2B and 1999 existing condition

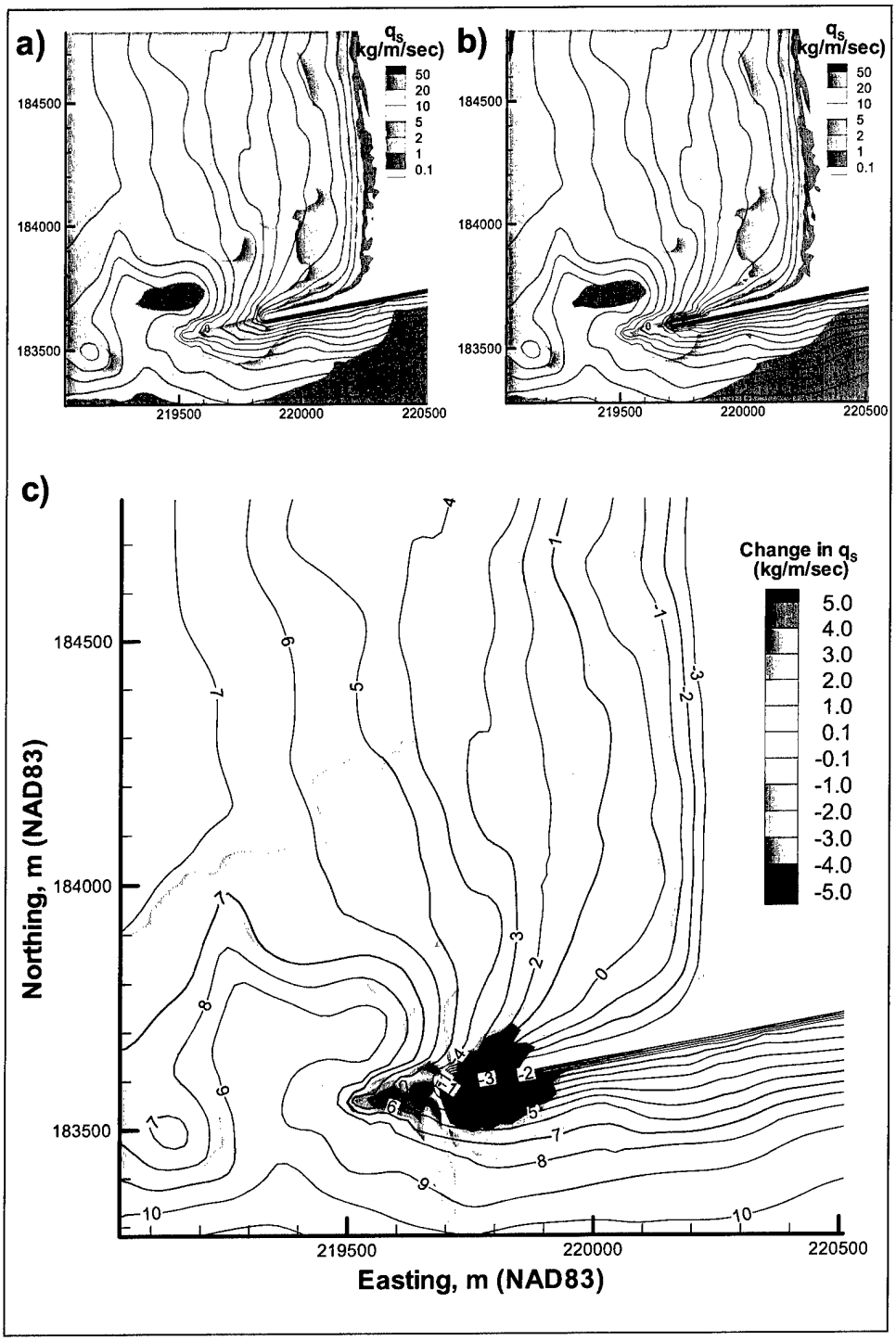

Figure 8-67. Expected annual change in q_s: (a) q_s for 1999 existing condition, (b) q_s for Alt 3A, and (c) difference in q_s between Alt 3A and 1999 existing condition

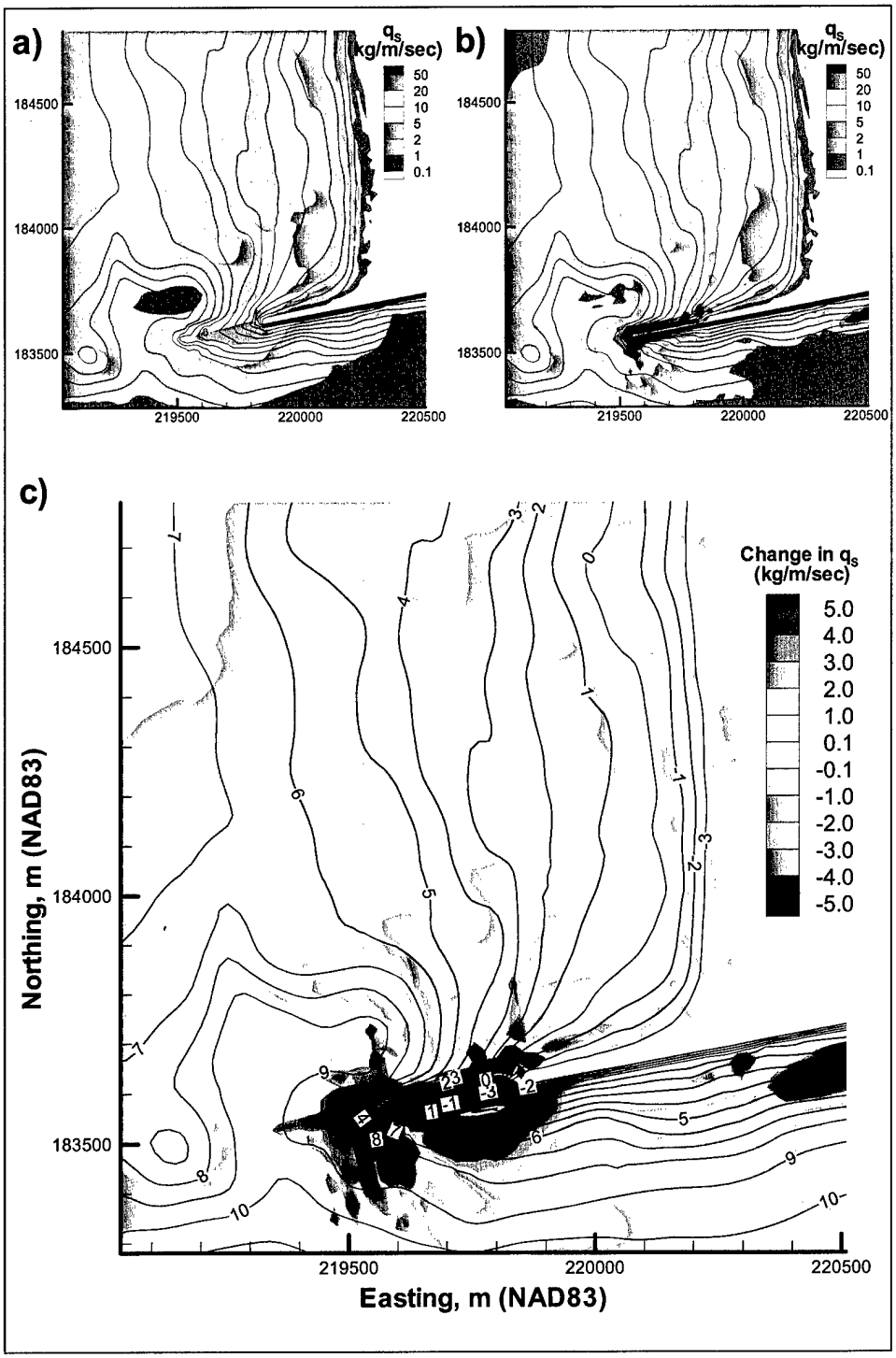

Figure 8-68. Expected annual change in q_s: (a) q_s for 1999 existing condition, (b) q_s for Alt 3B, and (c) difference in q_s between Alt 3B and 1999 existing condition

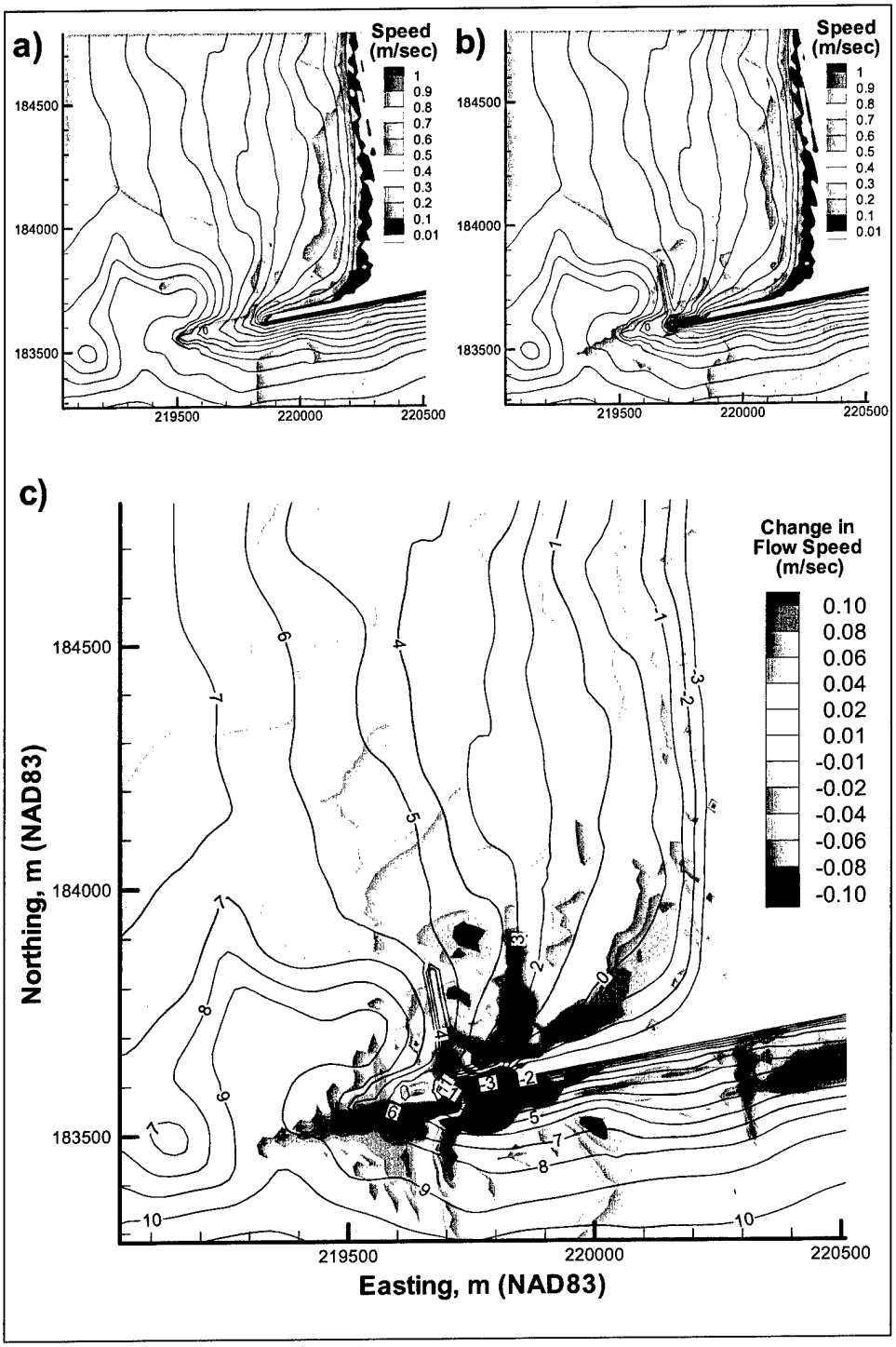

Figure 8-69. Expected annual change in q_s: (a) q_s for 1999 existing condition, (b) q_s for Alt 4, and (c) difference in q_s between Alt 4 and 1999 existing condition

suggests that there would be reduced sediment transport rates out of the area with the spur in place; with no change in the supply into the area, this deficit suggests that deposition of sediment may occur in this area. The three alternatives with jetty rehabilitation (Figures 8-67 through 8-69) have similar patterns; an increase of sediment transport potential towards the beach, accompanied by a decrease in sediment transport potential to the offshore. This pattern represents the general changes in current patterns near the structure.

The total annual change in the average annual transport rate q_s over the area to the north of the jetty is given in Table 8-6, expressed as a percentage of the 1999 existing rate. For these calculations, the average annual transport rate has been integrated over an area extending 1,400 m northward from the north jetty and 900 m offshore from the mean lower low water shoreline offshore. The calculations with the 1999 bathymetry indicate that all alternatives will lead to net deposition in this area. Alternative 3B shows the largest decrease in transport potential (4.8 percent). The long spur (Alt 2A) shows a 3.3 percent decrease in transport potential.

Table 8-6
Total Annual Change in Sediment Transport Potential to North of Jetty (Expressed as a Percentage of 1999 Existing Condition Value)

Alt 2A	-3.3
Alt 2B	-2.1
Alt 3A	-3.4
Alt 3B	-4.8
Alt 4	-1.8

In the evaluation of the alternatives with the 1999 bathymetry, only the hydrodynamics differ between the various alternatives and the existing condition. The tests with the 1999 bathymetry show results that are consistent with the expected behavior of these structural alternatives. In the tests with the 2004 and 2029 bathymetries, however, both the hydrodynamics and the bathymetry differ from the 1999 existing condition, negating the usefulness of the analysis.

The results of the analysis using the 2001 bathymetry for Alt 2A are shown in Figure 8-70. The total sediment transport potential was found to be 1.3 percent lower with Alt 2A than with the 2001 existing condition.

Lagrangian transport analysis

Analysis in the preceding section estimated changes in potential sediment transport rate associated with each alternative. In this section, a Lagrangian sediment modeling technique will be used to evaluate changes in the flux of southward bypassing of sediment at the north jetty. The methods used in the PSed model (Davies, Serrer, and Watson 2000) have been implemented as a custom,

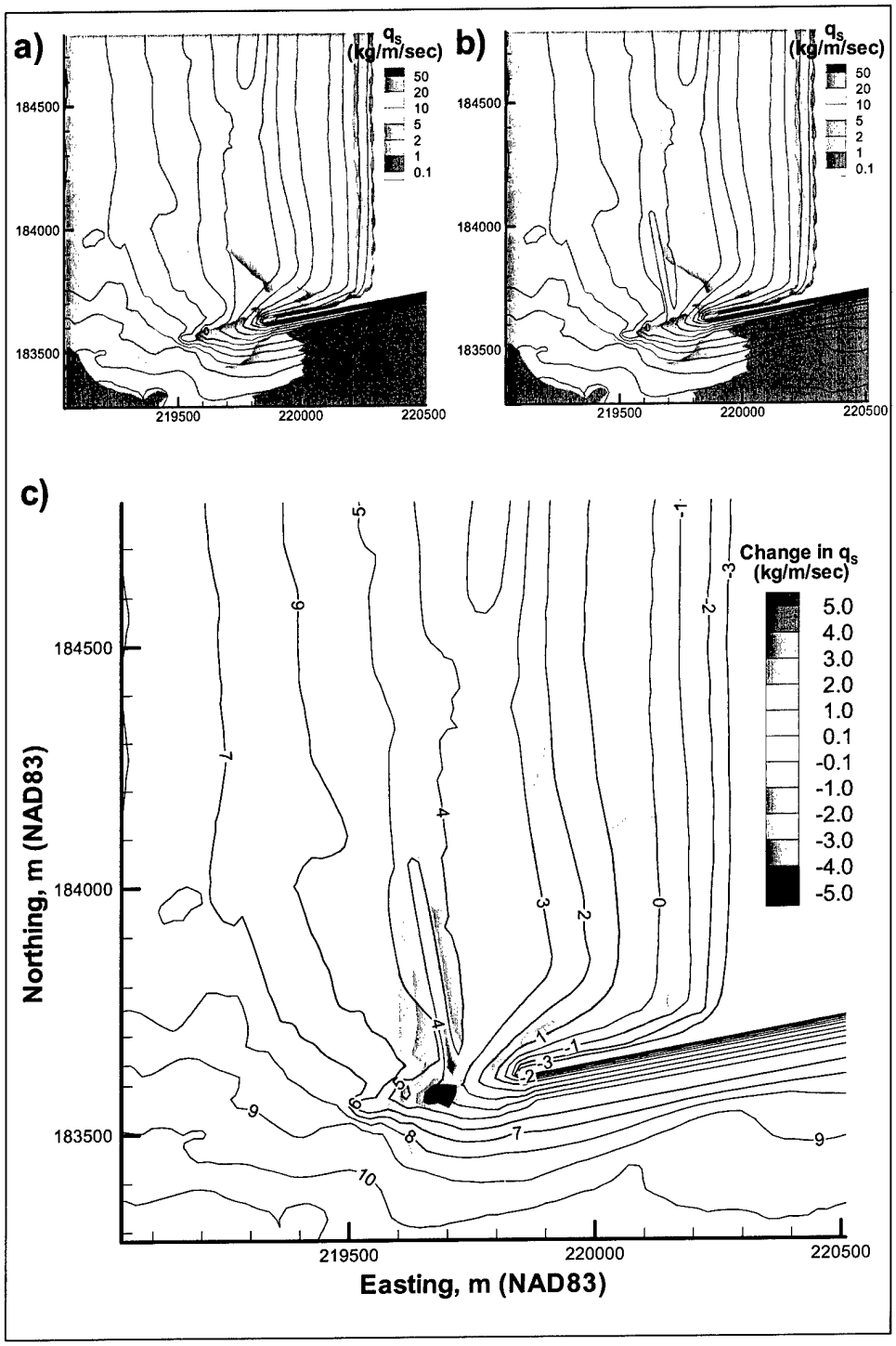

Figure 8-70. Expected annual change in q_s: (a) q_s for 2001 existing condition, (b) q_s for Alt 2A, and (c) difference in q_s between Alt 2A and 2001 existing condition

stand-alone finite-difference model structured to work with the van Rijn potential transport rate calculations and the CoastL hydrodynamics. This was necessary because the PSed model does not work with finite difference model data and does not have the capability to include waves as a forcing function. The van Rijn algorithm used to compute potential transport rates provided a convenient structure for the computation of combined wave-current-induced sediment transport, and the Lagrangian model was configured to work directly with the van Rijn formulation.

One approach considered for evaluation of bypassing rates was the comparison of the southward sediment transport potential along a line extending offshore from the tip of the north jetty. The sediment transport potential calculated at each grid node is an estimate of the equilibrium sediment transport rate at that location assuming an unlimited supply of sediment with the specified properties. The sediment transport rates predicted by this method are computed independently at each node as a function of local wave and current parameters. Therefore, the rates of southward bypassing computed along a line that extends seaward along the centerline of the north jetty are not significantly different for the various alternatives relative to the existing condition. Alternatives 2A and 2B, for example, cause only a minor direct change in wave height and current speed at the tip of the north jetty, and consequently, potential transport rates at that location are unchanged. A sediment transport model that represents the overall changes in wave intensity and circulation is required for an assessment of the bypassing.

This section describes sediment transport and bypassing based on the Lagrangian analysis. A grid of 120 source locations on the beach north of the north jetty was established for Lagrangian sediment transport modeling (Figure 8-71). Transport rates calculated with van Rijn's algorithm determined local sediment parcel release rates at each of these source locations. During the Lagrangian simulations, each source location released sediments continuously.

The advection rate for a sediment parcel is related to the potential transport rate at the location of the sediment parcel. A target advection rate is taken as the velocity of the flow at the elevation of the centroid of the total load sediment distribution. The centroid elevation is determined from integration of the vertically varying suspended sediment distribution and the bedload transport, which is assumed uniform over the saltation height. The local centroid height is the target elevation for a parcel and, as is explained below, parcels may not be at this height at all times.

Assuming a logarithmic velocity profile within the flow, a parcel is advected at the velocity associated with the computed parcel elevation. In a spatially varying flow field, the centroid height varies for a parcel from one time step to the next. If the parcel moves into an area of increased sediment mobility and it is below the local centroid height, the parcel will be advected upward at the fall velocity of the sediment. As a parcel moves into quiescent water, it settles toward the bed at the fall velocity. In this formulation, the movement of each parcel is independent of its neighbors; a more refined simulation would incorporate settling mechanisms once local concentrations exceed the potential transport rate and

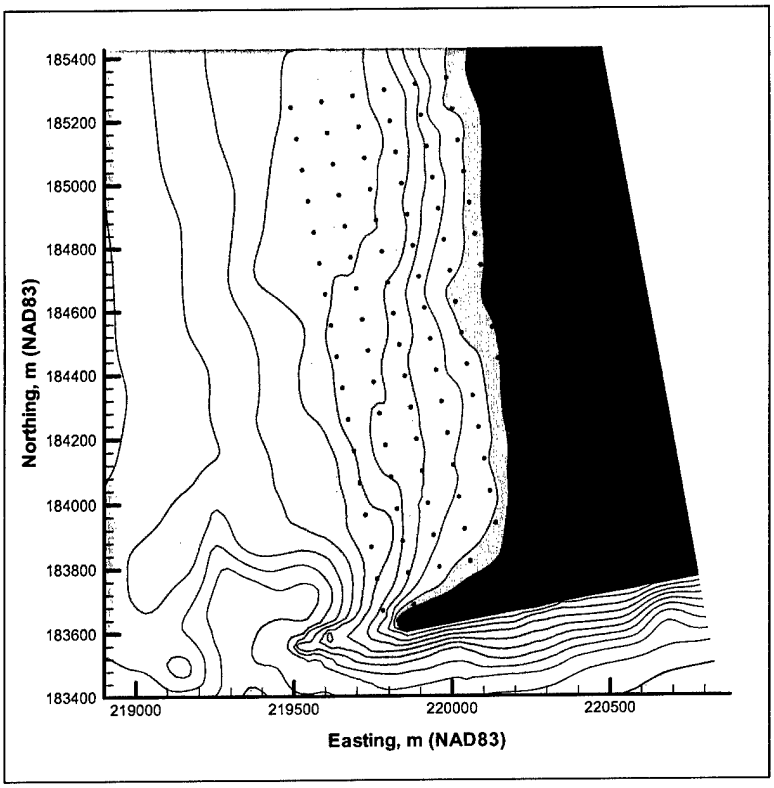

Figure 8-71. Sediment source locations for Lagrangian modeling

upward advection rates that scale to the turbulence intensity. However, this was beyond the scope of the present study. Consequently, sediment transport advection rates generally conform to the potential rates according to the van Rijn algorithm, and the overall transport patterns and bypassing rates represent a temporal and spatial integration of transport conditions along the north beach.

Figure 8-72 shows sediment pathways from a Lagrangian sediment transport simulation of the 1999 existing condition. A gyre and rip current are north of the jetty. The rip and longshore current combine to transport sediment southward past the tip of the jetty. Once past the jetty, the sediment path is directed toward the southeast. The long spur causes subtle changes to the sediment transport pathways (Figure 8-73); the gyre is slightly smaller and the flow of sediment is slightly closer to the tip of the jetty, possibly constrained by the presence of the spur. The gyre for Alt 2B (Figure 8-74) is slightly larger than for Alt 2A, and the bypassing flow of sediment extends the same distance seaward of the tip of the jetty, as it does under the existing condition. The patterns for the short jetty rehabilitation are generally similar to those of the existing condition (Figure 8-75) but shifted seaward commensurate with the extension of the jetty. The long jetty rehabilitation patterns (Figure 8-76) are similar to the existing condition but shifted further seaward. The sediment pathways for Alt 4 (Figure 8-77) are similar to a combination of the effects observed for the short spur and the short jetty rehabilitation.

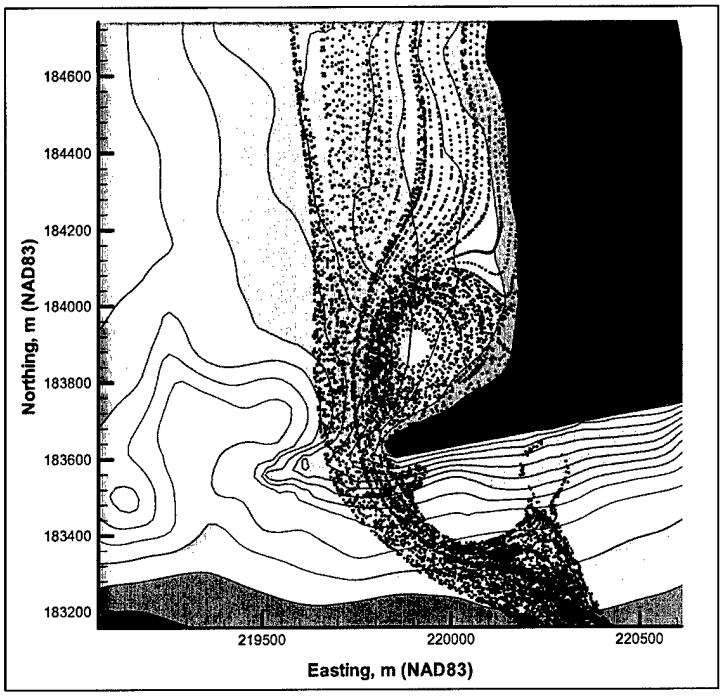

Figure 8-72. Lagrangian sediment parcel paths for H_s = 5 m, T_p = 13 sec from azimuth 300 deg for peak flood, existing condition, 1999 bathymetry

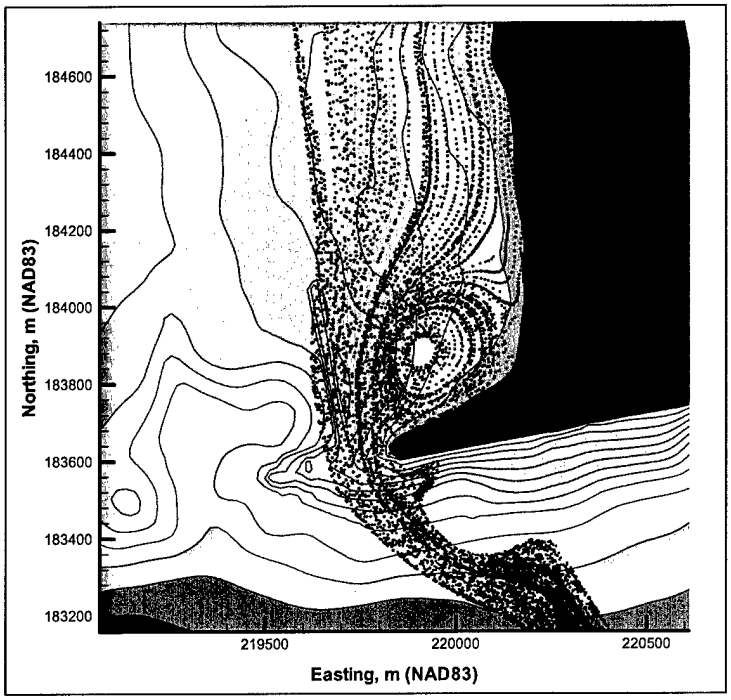

Figure 8-73. Lagrangian sediment parcel paths for H_s = 5 m, T_p = 13 sec from azimuth 300 deg for peak flood, Alt 2A, 1999 bathymetry

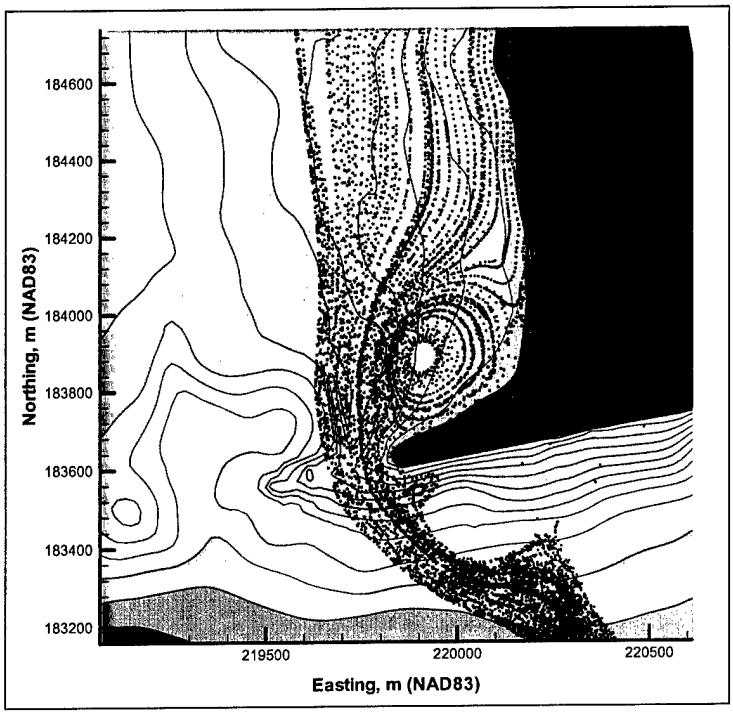

Figure 8-74. Lagrangian sediment parcel paths for H_s = 5 m, T_p = 13 sec from azimuth 300 deg for peak flood, Alt 2B, 1999 bathymetry

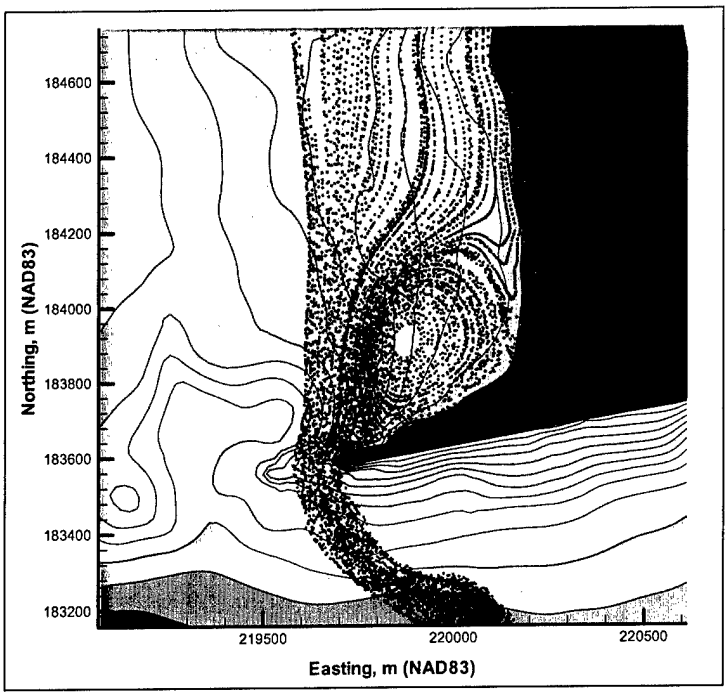

Figure 8-75. Lagrangian sediment parcel paths for H_s = 5 m, T_p = 13 sec from azimuth 300 deg for peak flood, Alt 3A, 1999 bathymetry

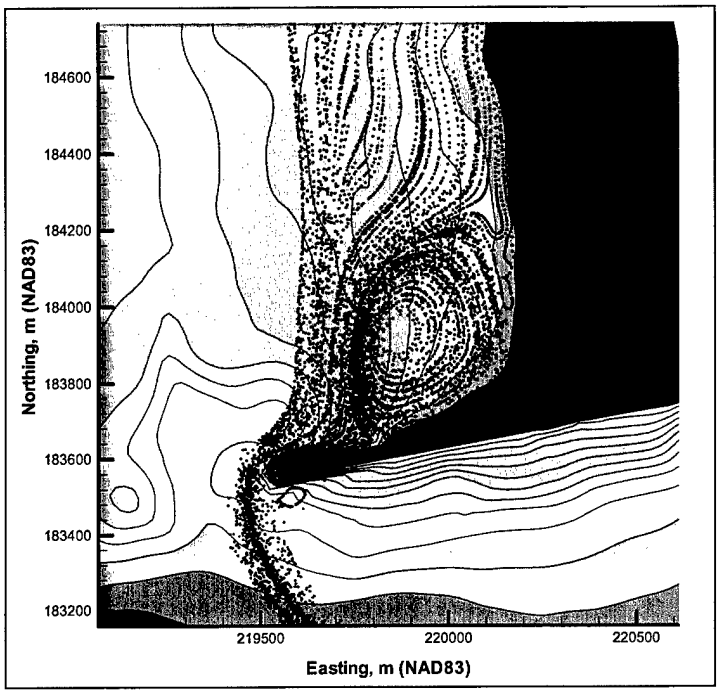

Figure 8-76. Lagrangian sediment parcel paths for H_s = 5 m, T_p = 13 sec from azimuth 300 deg for peak flood, Alt 3B, 1999 bathymetry

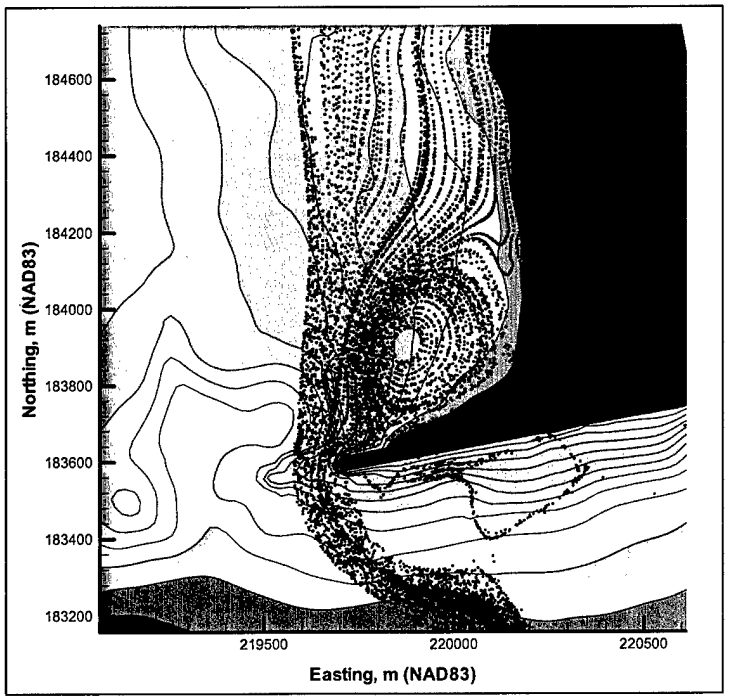

Figure 8-77. Lagrangian sediment parcels for H_s = 5 m, T_p = 13 sec from azimuth 300 deg for peak flood, Alt 4, 1999 bathymetry

Lagrangian bypassing rate analysis

During each Lagrangian sediment transport simulation, the number of sediment parcels moving to the south across a line through the major axis of the north jetty is recorded as the sediment-bypassing rate as though these parcels were being collected in a sediment trap. The following steps were taken to analyze southward bypassing of sediment:

a. During a simulation, the bypassing rate gradually increased with time and stabilized after about 5,000 to 10,000 sec. Figure 8-78 shows an example of the time-averaged (100-sec averaging period) bypassing rate. The bypassing rate for that hydrodynamic condition is taken to be the mean bypassing rate over a 5,000-sec interval during this stabilized portion.

b. The sediment bypassing rate for each hydrodynamic condition (tidal stage, wave height, period, and direction) is then weighted by the annual frequency of occurrence of that condition.

c. The bypassing rate is converted to a percentage deviation from the 1999 existing condition as the baseline.

d. The total annual average bypassing rate is computed as the sum of the weighted bypassing rates. This results in a single annual average bypassing rate for each alternative-bathymetry combination.

The results of this analysis are shown in tabular form for the 1999 bathymetry in terms of the change in the total annual bypassing rate for each hydrodynamic condition as well as an overall annual change. Table 8-7 lists the percentage change in predicted bypassing rates for waves from the west and north for the four tidal states relative to the existing condition.

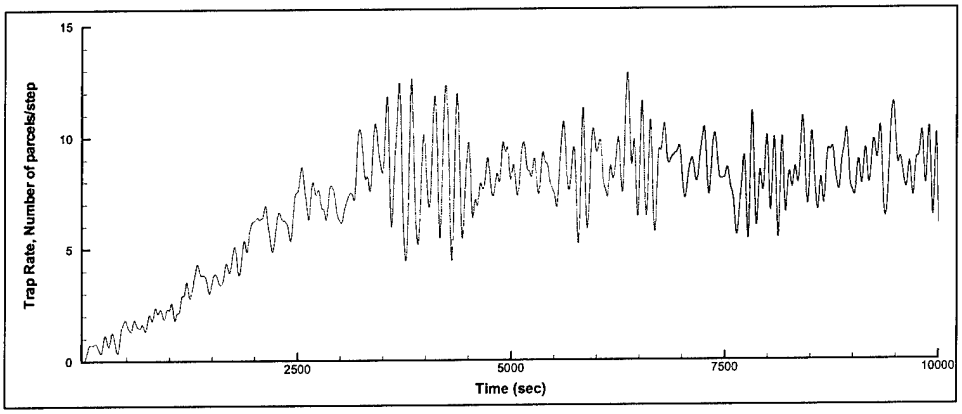

Figure 8-78. Example of time-averaged trap collection rate

Table 8-7
Change in Bypassing Rate (Percentage) for Southward Transport Conditions

Condition	Alternative				
	2A	2B	3A	3B	4
Low, 300-deg, 8-sec, 5-m	-11	-10	-15	-32	-21
Low, 300-deg, 8-sec, 2-m	-12	-2	22	-52	-25
Low, 300-deg, 18-sec, 5-m	-14	-10	-9	-25	-12
Low, 300-deg, 18-sec, 2-m	-16	-6	-2	-46	3
Low, 300-deg, 13-sec, 5-m	-10	-7	-15	-4	-12
Low, 300-deg, 13-sec, 2-m	-25	-8	-11	-74	14
Low, 280-deg, 8-sec, 5-m	-14	-4	-14	-14	-17
Low, 280-deg, 8-sec, 2-m	-58	-74	-12	-83	-100
Low, 280-deg, 18-sec, 5-m	-51	-41	13	62	-2
Low, 280-deg, 18-sec, 2-m	1700	200	2033	16833	22233
Low, 280-deg, 13-sec, 5-m	-24	-25	-13	-13	13
Low, 280-deg, 13-sec, 2-m	-1	124	213	-100	-79
High, 300-deg, 8-sec, 5-m	-8	-7	4	0	6
High, 300-deg, 8-sec, 2-m	-34	-9	-29	-100	-93
High, 300-deg, 18-sec, 5-m	-5	-4	-20	-26	-20
High, 300-deg, 18-sec, 2-m	-12	2	121	-35	19
High, 300-deg, 13-sec, 5-m	-7	-6	-12	-20	-16
High, 300-deg, 13-sec, 2-m	-17	26	90	-67	37
High, 280-deg, 8-sec, 5-m	-10	-7	4	-15	9
High, 280-deg, 8-sec, 2-m	-100	50	1600	-100	-100
High, 280-deg, 18-sec, 5-m	-20	-16	-83	-76	-86
High, 280-deg, 18-sec, 2-m	0	0	0	0	0
High, 280-deg, 13-sec, 5-m	-6	-1	-38	-58	-36
High, 280-deg, 13-sec, 2-m	39	-100	211	-100	225
Flood, 300-deg, 8-sec, 5-m	-6	-6	-15	-30	-13
Flood, 300-deg, 8-sec, 2-m	0	-1	-20	-33	-23
Flood, 300-deg, 18-sec, 5-m	-11	-6	-18	-35	-23
Flood, 300-deg, 18-sec, 2-m	-5	-6	-11	-38	-20
Flood, 300-deg, 13-sec, 5-m	-11	-8	-19	-28	-27
Flood, 300-deg, 13-sec, 2-m	0	0	-47	-36	-24
Flood, 280-deg, 8-sec, 5-m	-3	-3	-10	-29	-14
Flood, 280-deg, 8-sec, 2-m	-2	-4	-20	-40	-29
Flood, 280-deg, 18-sec, 5-m	-8	-10	-25	-64	-23
Flood, 280-deg, 18-sec, 2-m	-6	-1	-17	-52	-26
Flood, 280-deg, 13-sec, 5-m	-9	1	-5	-20	-4
Flood, 280-deg, 13-sec, 2-m	1	4	-20	-38	-13

(Continued)

Table 8-7 (Concluded)

Condition	Alternative				
	2A	2B	3A	3B	4
Ebb, 300-deg, 8-sec, 5-m	-14	-8	-22	-16	-39
Ebb, 300-deg, 8-sec, 2-m	-100	13	-100	-88	1313
Ebb, 300-deg, 18-sec, 5-m	-26	-12	-46	-62	-50
Ebb, 300-deg, 18-sec, 2-m	0	0	0	0	0
Ebb, 300-deg, 13-sec, 5-m	-17	-12	-25	-48	-40
Ebb, 300-deg, 13-sec, 2-m	0	0	0	0	0
Ebb, 280-deg, 8-sec, 5-m	2	-26	-100	-47	-100
Ebb, 280-deg, 8-sec, 2-m	0	0	0	0	0
Ebb, 280-deg, 18-sec, 5-m	-18	-26	-100	-100	-100
Ebb, 280-deg, 18-sec, 2-m	0	0	0	0	0
Ebb, 280-deg, 13-sec, 5-m	0	0	0	0	0
Ebb, 280-deg, 13-sec, 2-m	0	0	0	0	0

When expressed as percentage change in bypassing for a given hydrodynamic condition, this analysis does not take into account that certain conditions (e.g., flood tide with west-northwest waves) produce much more bypassing than others (e.g., ebb tide with west waves) and that, on an annual basis, some conditions have a higher frequency of occurrence than others. This is taken into account in Table 8-8, which summarizes by tidal state the percentage change in total bypassing on an annualized basis (the percentage change for each hydrodynamic condition has been multiplied here by its annual frequency of occurrence).

The results in Table 8-8 show that the alternatives can be ranked in order of their reduction of southward bypassing as: Alt 3B (largest reduction), Alts 4, 3A, 2A, and 2B (smallest reduction). Those alternatives that use a jetty rehabilitation component are most effective at reduction of sediment bypassing on flood tide. The two spur alternatives are most effective at reducing bypassing at low water, because of the inverse relationship between spur effectiveness and depth of water over the spur (i.e., freeboard).

Table 8-8
Change in Bypassing Expressed as Percentage of Total Bypassing, 1999 Bathymetry

Tidal State	Alternative				
	2A	2B	3A	3B	4
Low	-2.9	-1.3	0.4	-6.6	-1.6
High	-1.1	-0.5	0.0	-3.7	-0.7
Ebb	-0.1	-0.1	-0.3	-0.1	0.7
Flood	-1.5	-0.6	-15.4	-27.6	-14.9
Total	-5.5	-2.4	-15.3	-38.1	-16.5

The same procedure was conducted with the 2001 bathymetry, but only Alt 2A was studied (Table 8-9). Bypassing decreases for all conditions. Again, the largest reduction is in the low water slack case. For the 2001 bathymetry, the decreases in bypassing are larger than those for the corresponding 1999 bathymetry but, because the flood results make up a smaller percentage of the total bypassing in the 2001 results, the total reduction in bypassing is the same as for the 1999 results.

Table 8-9
Change in Bypassing Expressed as Percentage of Total Bypassing, 2001 Bathymetry

Tidal Stage	Alt 2A
Low	-15.7
High	-4.4
Ebb	-6.9
Flood	-3.7
Total	-5.5

Post-project bathymetry

Tables 8-10 and 8-11 show the results of similar analysis conducted for the 2004 and 2029 bathymetry surveys, respectively. The analysis shows a large amount of variability, as was seen in the integrated annual potential calculations. Alternative 3B shows a large and consistent decrease in transport. Results for the other alternatives vary considerably. The interpretation is that the synthetically prograded bathymetry results in an increase in the bypassing rate for each alternative. Alternative 3B is the only alternative that does not cause a net increase in bypassing relative to the existing condition. A significant factor here may be that these post-project bathymetries are not morphologically coupled to the CoastL hydrodynamic simulations.

Table 8-10
Change in Bypassing Expressed as Percentage of Total Bypassing, 2004 Bathymetry

	Alternative				
Tidal Stage	2A	2B	3A	3B	4
Low	-3.4	0.1	6.6	-6.5	-0.7
High	-1.9	-1.8	8.8	3.5	7.1
Ebb	0.3	0.0	-0.3	-0.3	-0.3
Flood	-2.5	-0.2	30.6	-28.3	1.0
Total	-7.5	-1.8	45.7	-31.6	7.1

Table 8-11
Change in Bypassing Expressed as Percentage of Total Bypassing, 2029 Bathymetry

Tidal State	Alternative				
	2A	2B	3A	3B	4
Low	1.7	5.3	8.8	-4.7	0.0
High	-0.2	17.0	15.3	-0.9	12.4
Ebb	0.8	0.1	-0.3	-0.3	-0.3
Flood	53.7	97.6	49.6	-26.5	43.6
Total	55.9	119.9	73.4	-32.4	55.7

Review of assumptions

The following list summarizes some of the uncertainties in, and limitations of, the analysis presented in this section:

a. The calculation domain was necessarily limited to enable representation of many hydrodynamic conditions for four bathymetries and the alternatives, focusing on the gyre at the north jetty and the fate of sediment near it. There are some situations, particularly at peak ebb and flood tide, for which the boundaries of the model may influence the sediment transport predictions. An attempt was made to minimize this contamination by careful application of the boundary conditions.

b. The Lagrangian simulation incorporates a restricted set of arbitrarily placed sediment sources in the nearshore. It is not known to what extent the solution is sensitive to this selection of sources. They have been chosen to be representative sediment source sites along the beach north of the jetty.

c. The hydrodynamic simulations were snapshots of steady-state peak wave and tide combinations. The sediment transport simulations incorporate these snapshot hydrodynamics to drive the Lagrangian sediment transport model until equilibrium of the bypassing rate occurs. Actual sediment transport under a continuously varying tidal regime may differ.

d. Waves smaller than H_s = 1 m have not been included in this analysis (except that the energy at the beach caused by 1 m waves was included in the estimated duration of H_s = 2 m waves). Waves of H_s = 1 m and smaller may be most significantly influenced by the presence of the jetty. Therefore, the effectiveness of the jetty rehabilitation alternatives may be underestimated.

e. Some aspects of on- and offshore sediment transport have not been represented. Onshore sediment transport is likely to be more prevalent during low-energy waves and, therefore, promote lower bypassing rates in low-energy conditions. Conversely, offshore transport associated with undertow is likely to be more significant during high-energy waves, leading to increased bypassing.

f. The sediment transport rate calculations are vertically integrated. In some situations, waves will induce bedload transport to the north whereas waves and currents will induce suspended load transport to the south. Conditions may exist where the depth-averaged approach has net offshore movement.

The analysis has been restricted to a large, but nevertheless limited number of wave parameter combinations to include a wide range of structural alternatives and bathymetries.

Summary

Modeling of waves, circulation, and potential sediment transport near the north jetty and along the southern portion of the north beach was interpreted through calculation of the following quantities:

a. Changes in wave height.

b. Changes in mean current direction and speed.

c. Average annual change in current speed.

d. Change in potential sediment transport rate (both event-by-event and on an average annualized basis).

e. Changes in Lagrangian sediment pathways and resulting estimates in changes to bypassing conditions.

On the basis of this analysis, the following conclusions can be drawn:

a. The two spur options, Alts 2A and 2B, produced decreases in estimated bypassing of 3.3 and 2.1 percent, respectively, as calculated by the potential sediment transport rate analysis and 5.5 and 2.4 percent, respectively, by the Lagrangian sediment transport rate analysis. The jetty extension alternatives, Alts 3A, 3B, and 4, produced decreases in bypassing of 3.4, 4.8, and 1.8 percent, respectively, as calculated by the potential sediment transport rate analysis, and 15.3, 38.1, and 16.5 percent, respectively, by the Lagrangian sediment transport rate analysis.

b. The presence of the spur (Alts 2A, 2B) will reduce wave heights (which will reduce sediment entrainment) and will reduce currents (which will reduce sediment advection) in the area between the spur and the shore, leading to reduced sediment transport in that area and reduced sediment bypassing.

c. The long spur (Alt 2A) is more effective than the short spur (Alt 2B) at reducing sediment bypassing.

d. The long jetty rehabilitation (Alt 3B) provides the largest reduction in southward-bypassing rate.

e. The patterns of velocity change caused by the short jetty rehabilitation (Alt 3A) are similar to those for the long jetty rehabilitation, but the changes are smaller in magnitude.

f. The effectiveness of the various structural alternatives in reducing sediment bypassing at the north jetty can be ranked, in order of most to least effective, as: Alts 3B, 3A, 2A, and 2B.

g. The performance of the combined short spur-partial rehabilitation (Alt 4) was found to be similar to that of Alt 3A.

h. The beneficial effects of the spur are most pronounced for the 1999 bathymetry. The same general patterns of current and wave height reduction are predicted for the 2001 bathymetry, but the magnitudes of the changes are smaller because the 2001 bathymetry results in the spur occupying a smaller portion of the water column.

References

Battjes, J. A., and Janssen, J. P. F. M. (1978). "Energy loss and set-up due to breaking of random waves," *Proceedings 16th Coastal Engineering Conference,* American Society of Civil Engineers (ASCE), 569-587.

Coutts-Smith, A. J., and Short, A. D. (2002) "Topographically controlled rips (mega-rips): An embayment scale process," Abstracts of the *28th International Conference on Coastal Engineering*, ASCE, paper no. 41.

Davies, M. H., Serrer, M., and Watson, D. A. W. (2000). "PSed 2000 – A Lagrangian sediment transport model," Preliminary Technical Report HYD-TR-051, Canadian Hydraulics Centre, National Research Council, Canada, 41 pp.

MacDonald, N. J. (1998). "Numerical modelling of non-linear wave-induced nearshore circulation," Ph.D diss., Department of Civil Engineering, University of Liverpool, United Kingdom, 566 pp.

Ruggiero, P., and Voigt, B. (2000). "Beach monitoring in the Columbia River Littoral Cell, 1997-2000," Publication Number 00-06-26, Washington State Department of Ecology, July 2000.

Short, A. D. (1985). "Rip current type, spacing and persistence, Narabeen Beach, Australia," *Marine Geology* 65, 47-71.

Van Rijn, L. C. (1993). *Principles of sediment transport in rivers, estuaries and coastal seas*. Aqua Publishers, Amsterdam, Netherlands.

9 Synthesis of Study Results and Conclusions[1]

The goal of this study was to identify and evaluate feasible methods for reducing annual maintenance dredging in the outer Federal navigation channel at Grays Harbor, WA, by modification of the north jetty. This chapter summarizes key findings and conclusions of the study as documented in Chapters 1-8 of this report and associated technical appendices in an accompanying volume. The study was an interdisciplinary effort involving field measurements; analysis of shoreline position, bathymetry, morphology, and engineering activities in the area; numerical modeling of waves, currents, sediment transport, and shoreline evolution; and physical modeling of the waves and currents, including use of sediment tracers.

Approximately 1.1 million cu yd of sediment is dredged annually from the outer channel of Grays Harbor. Most dredging in the outer harbor occurs at South and Crossover Reaches of the navigation channel located in the eastern end of the outer harbor, followed in volume of dredging at the Entrance Reach, Point Chehalis Reach, and Bar Channel. Table 1-1 in Chapter 1 summarizes the alternatives that were evaluated for reducing sediment bypassing around the north jetty. Two rubble mound submerged spurs were studied as a longer design, Alt 2A, and a shorter design, Alt 2B. Alternatives 3A and 3B denote, respectively, partial (shorter) and full (longer) rehabilitation of the north jetty, and Alt 4 is a combination of Alts 2B and 3A (shorter spur and shorter jetty rehabilitation).

Findings of This Study

This study provided new information, predictive capabilities, and insights into the sediment transport and morphological processes at Grays Harbor. The scale and complexity of these processes necessitated that the evaluation of structural alternatives at the north jetty be examined within a system-wide context. The system-wide evaluation encompassed the regional sediment budget, morphology change, and changes in water and sediment circulation patterns.

---

[1] Written by Nicholas C. Kraus, U.S. Army Engineer Research and Development Center, Coastal and Hydraulics Laboratory, Vicksburg, MS, and Hiram T. Arden, U.S. Army Engineer District, Seattle, WA.

Key processes

Key processes identified from the field measurements and physical and numerical modelings are:

a. Field measurements indicate clear seasonal patterns in coastal flow and sediment transport at the entrance to Grays Harbor. These patterns and trends are well replicated by the ADCIRC-STWAVE circulation numerical model. The major features of the seasonal flow and transport are:

(1) Winter storms and southwest waves promote northward and offshore transport of sediment along the Washington coast. Measurements on the ebb shoal indicate net northward transport of approximately 30,000 cu yd/year per 500 m width of seabed between the 10- and 20-m depths.

(2) At the entrance to Grays Harbor, storm-driven northward currents are diverted seaward by ebb shoal morphology, the south jetty, and ebb-dominated tidal currents on the ebb shoal. In 10- to 20-m water depth, near-bottom currents flow to the northwest with speed reaching 0.8 m/sec during storms. The strong north-directed current indicates that northerly moving sediment bypasses the inlet entrance, but may contribute to sedimentation of the bar channel.

(3) In the summer, waves from the northwest and swell waves promote southward and onshore transport of sediment on the Washington Coast.

b. Sediment bypassing the north jetty and entering Grays Harbor is in part controlled by the presence of a persistent large rip current located just north of the jetty. The rip current transports sediment to the outer surf zone where an accelerating southward-directed wave- and tide-induced current carries sediment into the inlet. Field measurements, numerical simulations with CoastL, and the physical model confirm this circulation pattern at the north jetty. Field measurements and numerical simulations with the CoastL and ADCIRC-STWAVE models confirm southward sediment transport at the north jetty into the inlet. Sediment flux estimates for material passing the seaward tip of the north jetty as derived from field measurements are consistent with the estimate of 400,000 cu yd/year derived from the morphological change analysis.

c. The tidal and wave-induced circulation along the south side of the north jetty is flood dominated. Residual sediment transport in this area is directed eastward into Grays Harbor. Most of this sediment is deposited along Damon Point. The deposited sediment preserves the integrity of the spit and extends it. Sediment stripped from the southeastward extension of Damon Point by North Bay ebb currents contributes to shoaling in the navigation channel.

d. The ADCIRC-STWAVE simulations indicate that the ebb current in the inlet achieves a maximum near the tip of Damon Point. This finding is confirmed by field measurements. Ebb currents run south from Damon Point toward the south jetty where they are redirected seaward. PSED numerical simulations and field observations indicate that these strong

currents carry sediment toward the navigation channel and to other parts of the estuary. The ebb current also returns a portion of the sediment to the ebb shoal outside the inlet.

Evaluation of alternatives

Sediment-control alternatives were evaluated relative to the existing condition (Alt 1) by means of physical and numerical modeling. Key findings of the various modeling activities are summarized in Table 9-1 in terms of performance criteria or their physical processes surrogates.

a. All of the alternatives reduce the wave height in the nearshore and the current speed in the area between the spur and the shore. These reductions would lead to reduced sediment transport and sediment bypassing in this area, and increase the volume of sand on the north beach.

b. CoastL sediment transport modeling indicates that the effectiveness of the various structural alternatives in reducing sediment bypassing at the north jetty can be ranked in order of most to least effective as: Alts 3B, 3A, 2A, and 2B.

c. GENESIS-T modeling indicates that longshore transport accounts for approximately 10 to 15 percent of the sediment that bypasses the north jetty, with the remainder of the bypassed material being associated with the rip current located near the jetty. All of the structural alternatives reduce longshore transport bypassing relative to the existing condition. The spur alternatives (Alts 2A and 2B) reduce this bypassing by 33 percent, Alt 3A by 17 percent, Alt 3B by 30 percent, and Alt 4 by 50 percent.

d. The GENESIS-T model indicates that the pattern of shoreline response is similar for all five structural alternatives, whereas the magnitude of the responses differs. Each alternative promotes beach accretion adjacent to the jetty relative to Alt 1 (existing conditions). The larger structures (Alts 2A and 3B) and the combination structure (Alt 4) create the greatest change, with maximum advance in shoreline position relative to Alt 1 of approximately 250 ft. The smaller structures (Alts 2B and 3A) also produce shoreline advance relative to Alt 1 with a maximum advance of approximately 150 ft. Relative shoreline advance is greatest at the jetty and tapers off within 0.5 miles to the north.

e. Morphological analysis indicates that approximately 40 percent of the sediment reaching the north beach is transported south around the north jetty and into the entrance. Assuming that an equivalent portion (40 percent) of the additional volume of sediment impounded by each alternative relative to Alt 1 as predicted by the GENESIS-T model is prevented from bypassing the north jetty to the south, the alternatives would be expected to reduce southward bypassing into the inlet by 16,000 to 80,000 cu yd/year (Table 9-1). The larger structures (Alts 2A and 3B) and combination structure (Alt 4) produce a greater reduction in bypassing than the smaller structures (Alts 2B and 3A).

f. The findings indicate that a relatively large portion of the sediment bypassing the north jetty is deposited at Damon Point. A relatively small portion bypasses Damon Point and is transported to the navigation channel. Information is not available to determine the absolute quantity of sediment bypassing Damon Point.

Conclusions

Study findings concerning the response of major morphological elements of the inlet system (ebb shoal, inlet throat/entrance, inlet shoals), dredging, and navigation channel infill patterns over time since jetty construction are as follows:

a. Changes in morphologic patterns indicate that the regional net longshore sediment transport is directed to the north at Grays Harbor, although there is a local reversal of longshore transport north of the entrance. These trends are consistent prior to and after jetty construction. A local reversal of transport on the updrift side of an inlet is typical for inlets and entrances with ebb-tidal shoals.

b. Bathymetry and shoreline position analysis indicates that major changes in the inlet throat, ebb shoal region, and nearshore regions followed jetty construction. The entrance area deepened rapidly after jetty construction and immediately after rehabilitation in the 1940s. The outer portion of Grays Harbor became a net exporter of marine sediment. A strong ebb current, the presence of which can be seen in figures contained in Appendix E, transports sediment from the harbor to far offshore. As a result, the ebb shoal translated seaward to depths greater than 50 ft. The outer edge of the modern ebb shoal is located in 90-100 ft of water.

c. The large seaward advance and growth in volume of the beach adjacent to the north jetty that occurred after jetty construction is a result of onshore movement or collapse of the northern portion of the originally broad ebb shoal and southward longshore transport within about 3,000 ft of the south end of north beach. The amount of material supplied from the relic shoal to the beach is decreasing with time.

d. Approximately 40 percent of sediment reaching the north beach (adjacent to the north jetty) from offshore is transported south, around the jetty, and into the entrance area. Flood currents and wave-induced currents transport this bypassed sediment toward Damon Point, where most of it is deposited in a large subaqueous spit to the south and west of the tip of the spit.

e. Channel shoaling and dredging requirements decreased significantly after the entrance deepening associated with jetty construction and rehabilitation in the 1940s.

f. Realignment of the navigation channel from Sand Island Reach to South Reach in the mid-1970s also caused a local reduction in dredging requirements. Overall reduction in dredging following the 1975 rehabilitation of the north jetty is unclear, owing to the realignment of reaches.

g. During the last decade, the average annual volume of sand dredged from the lower navigation channel (Bar Channel, Entrance Reach, Point Chehalis Reach, South Reach, and Crossover Reach) has been 1,106,000 cu yd/year, assuming that only 50 percent of the dredged material from Crossover Reach is marine sand.

Discussion

The scale of change in southward-directed bypassing of sediment expected to occur after construction of any of the evaluated alternatives is small compared to the scale of transport at the Grays Harbor entrance from sources originating outside the entrance or by being reworked and redistributed within the entrance. Modification of the north jetty is one of relatively few options for controlling sedimentation in the outer navigation channel; others include channel realignment and modifications to the south jetty.

Table 9-1
Predicted Changes in Key Performance Criteria Relative to Existing Conditions

Performance Criteria	Model	Spur Alternatives		Jetty Rehabilitation Alternatives		Combination
		2A	2B	3A	3B	4
Reduce southward bypassing flux at the north jetty	CoastL	Yes	Yes	Yes	Yes	Yes
	GENESIS-T	Yes	Yes	Yes	Yes	Yes
	Volume reduction, 1,000 cu yd per year	36-80	24-56	16-28	28-60	28-68
Reduce wave height in the nearshore	Physical Model	Yes	Yes	Yes	Yes	
	ADCIRC-STWAVE	Yes	Yes	Yes	Yes	Yes
	CoastL	Yes	Yes	Yes (for SW waves)	Yes (for SW waves)	Yes
Reduce currents nearshore	Physical Model	Yes	No	No	Yes	
	ADCIRC-STWAVE	No	No	Yes (shifted seaward)	Yes (shifted seaward)	Yes
	CoastL	Yes	Yes	Yes (shifted seaward)	Yes (shifted seaward)	Yes
Reduce currents at jetty tip (percent reduction)	Physical-Model	Yes	No	No	Yes	
	ADCIRC-STWAVE	Yes (14)	Yes (12)	Yes (33)	Yes (17)	Yes (33)
Increase beach volume up to 0.5 mile from jetty (1,000 cu yd accreted over 5 years)	GENESIS-T	Yes (450-1,000)	Yes (300-700)	Yes (200-350)	Yes (350-370)	Yes (350-380)

Notes:
Yes - indicates performance criteria supported.
No - indicates performance criteria not supported.

REPORT DOCUMENTATION PAGE

Form Approved
OMB No. 0704-0188

Public reporting burden for this collection of information is estimated to average 1 hour per response, including the time for reviewing instructions, searching existing data sources, gathering and maintaining the data needed, and completing and reviewing this collection of information. Send comments regarding this burden estimate or any other aspect of this collection of information, including suggestions for reducing this burden to Department of Defense, Washington Headquarters Services, Directorate for Information Operations and Reports (0704-0188), 1215 Jefferson Davis Highway, Suite 1204, Arlington, VA 22202-4302. Respondents should be aware that notwithstanding any other provision of law, no person shall be subject to any penalty for failing to comply with a collection of information if it does not display a currently valid OMB control number. **PLEASE DO NOT RETURN YOUR FORM TO THE ABOVE ADDRESS.**

1. REPORT DATE *(DD-MM-YYYY)*	2. REPORT TYPE	3. DATES COVERED *(From - To)*
September 2003	Final report	

4. TITLE AND SUBTITLE

North Jetty Performance and Entrance Navigation Channel Maintenance, Grays Harbor, Washington; Volume I: Main Text

5a. CONTRACT NUMBER

5b. GRANT NUMBER

5c. PROGRAM ELEMENT NUMBER

6. AUTHOR(S)

Nicholas C. Kraus and Hiram T. Arden, editors
With contributions by Hiram T. Arden, Jessica L. Baker, Mark R. Byrnes, Mary A. Cialone, Julie A. Cohen, Michael H. Davies, David Hericks, Nicholas c. Kraus, Neil J. McDonald, Philip D. Osborne, Ty V. Wamsley, Donald L. Ward

5d. PROJECT NUMBER

5e. TASK NUMBER

5f. WORK UNIT NUMBER

7. PERFORMING ORGANIZATION NAME(S) AND ADDRESS(ES)

U.S. Army Engineer Research and Development Center
Coastal and Hydraulics Laboratory
3909 Halls Ferry Road
Vicksburg, MS 39180-6199

8. PERFORMING ORGANIZATION REPORT NUMBER

ERDC/CHL TR-03-12

9. SPONSORING / MONITORING AGENCY NAME(S) AND ADDRESS(ES)

U.S. Army Engineer District, Seattle
P.O. Box 3755, Seattle, WA 98124-3755

10. SPONSOR/MONITOR'S ACRONYM(S)

11. SPONSOR/MONITOR'S REPORT NUMBER(S)

12. DISTRIBUTION / AVAILABILITY STATEMENT

Approved for public release; distribution is unlimited.

13. SUPPLEMENTARY NOTES

14. ABSTRACT

This report documents a study performed for the U.S. Army Engineer District, Seattle to identify and evaluate feasible methods for reducing annual maintenance dredging in the outer Federal navigation channel at Grays Harbor, WA, by modification of the north jetty. Main interest was in potential reduction of southward sand bypassing the north jetty and preservation of the jetty should the neighboring beach erode. Considerable information and predictive capability were generated concerning the behavior of the Federal navigation channel and adjacent coastal and inlet shorelines. The study was conducted as a coordinated multi-disciplinary approach involving field measurement, physical modeling of the hydrodynamics and potential sediment pathways, geomorphic analysis and sediment budget formulation, and numerical modeling of waves, circulation and sediment transport, including modeling of shoreline change and bypassing.

Numerous alternatives were considered and subjected to a screening process to identify feasible engineering and physically constructible alternatives within broad criteria. Six alternatives passed the screening and were evaluated. The alternatives concerned an innovative submerged spur that would be placed parallel to the shoreline along the north jetty, partial and full rehabilitation of the north jetty, and a combination of these alternatives with structures of different lengths.

(Continued)

15. SUBJECT TERMS

See reverse.

16. SECURITY CLASSIFICATION OF:			17. LIMITATION OF ABSTRACT	18. NUMBER OF PAGES	19a. NAME OF RESPONSIBLE PERSON
a. REPORT	b. ABSTRACT	c. THIS PAGE			19b. TELEPHONE NUMBER *(include area code)*
UNCLASSIFIED	UNCLASSIFIED	UNCLASSIFIED		492	

14. ABSTRACT (continued)

The sediment-control alternatives were evaluated relative to the existing condition. The study revealed many wide-area processes controlling sedimentation in and around Grays Harbor. The scale of change in southward-directed bypassing of sediment expected to occur after construction of any of the evaluated alternatives was found to be small compared to the scale of transport at the Grays Harbor entrance from sources originating outside the entrance or by being reworked and redistributed within the entrance. Modification of the north jetty is one of relatively few options for controlling sedimentation in the outer navigation channel; others include channel realignment and modifications to the south jetty.

15. SUBJECT TERMS

Dredging
Channel maintenance
Field measurement
Grays Harbor, Washington
Jetty
Navigation channel
Numerical modeling
Physical modeling
Rip current
Sand bypassing
Sediment budget
Sediment transport